

NASA CR-159749
R79AEG395



National Aeronautics and
Space Administration

CORE NOISE INVESTIGATION OF THE CF6-50 TURBOFAN ENGINE

FINAL REPORT

by

V.L. DOYLE
AND
M.T. MOORE

GENERAL ELECTRIC COMPANY
AIRCRAFT ENGINE GROUP
CINCINNATI, OHIO 45215

January 1980

Prepared For

National Aeronautics and Space Administration

(NASA-CR-159749) CORE NOISE INVESTIGATION
OF THE CF6-50 TURBOFAN ENGINE Final Report
(General Electric Co.) 520 p HC A22/MP A01

CSCI 21F

N80-16062

Unclass
46988

63/07

CONTRACT NAS3-21260

NASA-Lewis Research Center

FOREWORD

This report, prepared by the Advanced Engineering and Technical Programs Department, Aircraft Engine Group, General Electric Company, Evendale, Ohio, was sponsored by the National Aeronautics and Space Administration, Lewis Research Center, 21000 Brookpark Road, Cleveland, Ohio, under Contract NAS3-21260. Mr. R.G. Huff was the NASA Project Manager and Mr. M.T. Moore was the Program Technical Manager for the General Electric Company. The authors express their gratitude to Mr. L.E. Langenbrunner and Mrs. J.A. Gilbert for their assistance in the preparation of the report information.

PRECEDING PAGE BLANK NOT FILLED

PRECEDING PAGE BLANK NOT FILLED

TABLE OF CONTENTS

<u>Section</u>	<u>Page</u>
1.0 SUMMARY	1
2.0 INTRODUCTION	2
3.0 TEST DESCRIPTION	3
3.1 CF6-50 Engine Test Vehicle	3
3.2 CF6-50 Standard Production Combustor	3
3.3 Test Objectives	7
3.4 Test Setup	7
3.4.1 Engine Installation	9
3.4.2 Acoustic Arena	9
3.4.3 Data Acquisition System	9
3.5 Test Matrix	9
3.6 Instrumentation	13
3.6.1 Internal Sensors	13
3.6.2 Far-Field Microphones	13
3.7 Data Reduction and Processing	18
3.7.1 Data Analysis Methods	18
3.7.2 Time Series Analysis Parameter Optimization	21
3.7.2.1 Time Series Parameter Study	21
3.7.2.2 Use of Digital Processing Techniques	31
3.7.2.3 Error Evaluation of Time Series Estimates	37
3.7.3 Signal Polarity Identification	41
3.7.4 Data Processing	52
3.7.4.1 Frequency Response Corrections	52
3.7.4.2 Power Level Calculation	52
3.7.4.3 Engine Measurements Verification	55
4.0 ANALYSIS AND DISCUSSION OF RESULTS	58
4.1 Direct Analysis of Engine Acoustic Measurements	58
4.1.1 Internal and Far-Field Spectra Comparison	58
4.1.1.1 Internal Measurements	58
4.1.1.2 Far-Field Measurements	75
4.1.2 Internal Spectra Comparison from Engine Out- door Stand and Test Cell	86
4.1.3 Comparison of Engine Test to Duct-Rig Results with Standard Combustor	90
4.1.4 Aerodynamic Parameters	95

TABLE OF CONTENTS (Concluded)

<u>Section</u>	<u>Page</u>
4.2 Source Location from Internal Measurements	95
4.2.1 Identification of Source Location from Vectoring of Cross-Correlation Time Delays	98
4.2.2 Source Content Evaluation from Cross- Spectra Phase	98
4.2.3 Summary of Source Location Investigation	110
4.3 Coherence and Transfer Function Analysis	110
4.3.1 Internal Coherence and Transfer Function Results	110
4.3.2 Coherence and Transfer Function Results to the Far Field	121
4.3.3 Turbine Transfer Function Comparison with Previous Test Results and Present Theory	130
4.3.4 Summary of Coherence and Transfer Function Results	132
4.4 Output Power	134
4.4.1 Duct Power Level Comparison with Predictions	134
4.4.2 Far-Field Coherent Output Power	136
4.4.3 Coherent Output Power Summary	145
5.0 CONCLUSIONS	150
5.1 Observations on the Acquisition and Processing of Measurements	150
5.2 Core Noise Spectra Comparisons with ECCP Phases II and III Results	150
5.3 Apparent Primary Core Noise Source Location	151
5.4 Turbine Transmission Loss	151
5.5 Coherence and Transfer Function to Far Field	152
5.6 Core Nozzle and Combustor PWL's	152
5.7 Coherent Output Power Observations	152
APPENDIX A - Coherence Functions and Transfer Functions for Internal and Far-Field Sensors	153
B - Turbine Transfer Function Results	406
C - Coherent Output Spectra Results	411
D - Nomenclature	486
REFERENCES	490

LIST OF ILLUSTRATIONS

<u>Figure</u>		<u>Page</u>
3.1-1.	CF6-50 Engine and Nacelle.	4
3.2-1.	CF6-50 Combustor Design Features.	6
3.4-1.	CF6-50 Engine Installation at Peebles, Site 4D Thrust Stand.	10
3.4-2.	Far-Field Microphone Array for CF6-50 Core Noise Measurements.	11
3.4-3.	Acoustic Data Acquisition System.	12
3.6-1.	Internal Sensor Locations for Engine Combustor Noise Measurements.	15
3.6-2.	Typical Kulite Waveguide Sensor Installations for CF6-50 Core Noise Acoustic Test (7708283).	16 ---
3.6-3.	Sound Separation Probe Location on CF6-50 Engine.	17
3.7-1.	Effect of Data Bandwidth on Cross-Correlation.	24
3.7-2.	Effect of Sampling Rate on Cross-Correlation.	26
3.7-3.	Effect of Sampling Rate on Coherence.	27
3.7-4.	Effect of Sampling Rate on Phase Angles.	28
3.7-5.	Effect of Averages on Coherence.	29
3.7-6.	Effect of Averages on Phase Angles.	30
3.7-7.	Effect of Not Removing Time Delay from Phase.	34
3.7-8.	Effect of Removing Two Different Time Delays on Cross-Spectrum Phase.	35
3.7-9.	Coherent Spectra Error Estimates.	38
3.7-10.	Coherence Function Error Estimates.	39
3.7-11.	Transfer Function Gain and Phase Error Estimates.	40

LIST OF ILLUSTRATIONS (Continued)

<u>Figure</u>		<u>Page</u>
3.7-12.	Polarity Check of Far-Field Microphones Using Shotgun Blast.	42
3.7-13.	Polarity Check of Core Probe Kulites Using Shotgun Blast.	43
3.7-14.	Gross-Correlation Between Core Probe and 90° Far-Field Microphone.	44
3.7-15.	Cross-Correlation Between Core Probe and 100° Far-Field Microphone.	44
3.7-16.	Far-Field Microphone Polarity Verification from Core Probe Cross-Correlations.	46
3.7-17.	Polarity Check of Internal Sensors Using Shotgun Blast.	47
3.7-18.	ECCP Phase III Cross-Correlation Results from Internal Combustor Sensors.	48
3.7-19.	Cross-Correlations from Internal Combustor Sensors Used on CF6-50 Core Noise Program.	49
3.7-20.	Cross-Correlations Between Fuel Nozzle Sensors and Associated Waveguide Sensors.	50
3.7-21.	Ambient Frequency Response Results from Combustor Waveguide Sensors.	53
3.7-22.	Comparison of Core Probe Power Levels with Far-Field Measured Power Levels.	57
4.1-1.	Plane 3.0 (16°) Internal Spectra Variation with Engine Core Speed.	61
4.1-2.	Variation of Plane 3.0 One-Third-Octave-Band Spectra with Percent Net Thrust.	62
4.1-3.	Plane 3.5 (282°) Internal Spectra Variation with Engine Core Speed.	63
4.1-4.	Variation of Plane 3.5 One-Third-Octave-Band Spectra with Percent Net Thrust.	64
4.1-5.	CF6-50 Fuel System Schematic.	65

LIST OF ILLUSTRATIONS (Continued)

<u>Figure</u>		<u>Page</u>
4.1-6.	CF6 Fuel Nozzles.	67
4.1-7.	Primary-Secondary Fuel Nozzle (102°) Spectra Variation with Engine Core Speed.	68
4.1-8.	Secondary-Only Fuel Nozzle (42°) Spectra Variation with Engine Core Speed.	69
4.1-9.	Plane 3.5 (42°) Internal Spectra Variation with Engine Core Speed.	71
4.1-10.	Plane 3.5 (102°) Internal Spectra Variation with Engine Core Speed.	72
4.1-11.	Comparison of Primary-Secondary Fuel Nozzle Spectra with Plane 3.5 Sensor (102°).	73
4.1-12.	Comparison of Secondary-Only Fuel Nozzle Spectra with Plane 3.5 Sensor (42°).	74
4.1-13.	Plane 4.0 (92°) Internal Spectra Variation with Engine Core Speed.	76
4.1-14.	Variation of Plane 4.0 One-Third-Octave-Band Spectra with Percent Net Thrust.	77
4.1-15.	Plane 8.0A (270°) Internal Spectra Variation with Engine Core Speed.	78
4.1-16.	Variation of Plane 8.0A One-Third-Octave-Band Spectra with Percent Net Thrust.	79
4.1-17.	Internal Pressure Spectra Variation with Engine Speed.	80
4.1-18.	Far-Field Spectra Variation at 30° Acoustic Angle.	81
4.1-19.	Far-Field Spectra Variation at 60° Acoustic Angle.	82
4.1-20.	Far-Field Spectra Variation at 90° Acoustic Angle.	83
4.1-21.	Far-Field Spectra Variation at 120° Acoustic Angle.	84
4.1-22.	Far-Field Spectra Variation at 150° Acoustic Angle.	85

LIST OF ILLUSTRATIONS (Continued)

<u>Figure</u>		<u>Page</u>
4.1-23.	Variation of Far-Field Spectra with Engine Power Setting.	87
4.1-24.	CF6-50 Internal Power Spectra Comparison at Idle.	88
4.1-25.	CF6-50 Internal Power Spectra Comparison at Approach.	89
4.1-26.	CF6-50 Internal Power Spectra Comparison at Takeoff.	91
4.1-27.	Acoustic Probe Locations for Duct-Rig Test.	92
4.1-28.	Comparison of Engine and Duct-Rig Power Spectra for Standard Combustor at Approach.	93
4.1-29.	Comparison of Engine and Duct-Rig Power Spectra for Standard Combustor.	94
4.2-1.	Cross-Correlation Results Between Combustor Sensors at Plane 3.0 and 3.5.	100
4.2-2.	Cross-Correlation Results Between Combustor Sensors at Plane 3.5 and 4.0.	101
4.2-3.	Cross-Correlation Results Between Combustor Sensors at Plane 3.5.	102
4.2-4.	Time Delay Vectoring for Combustor Source Location Identification.	103
4.2-5.	Correlated Frequency Regions Between Combustor Sensors from Plane 3.0 (16°) to 3.5 (42°) for Approach.	105
4.2-6.	Correlated Frequency Region Between Combustor Sensors from Plane 3.5 (102°) to 4.0 (92°) for Approach.	106
4.2-7.	Correlated Frequency Region Between Combustor Sensors from Plane 3.5 (42°) to 3.5 (102°) for Approach.	107
4.2-8.	Correlated Frequency Regions Between Combustor Sensors from Plane 3.0 (16°) to 3.5 (42°) for Takeoff.	108
4.2-9.	Correlated Frequency Region Between Combustor Sensors from Plane 3.5 (102°) to 4.0 (92°) for Takeoff.	109

LIST OF ILLUSTRATIONS (Continued)

<u>Figure</u>		<u>Page</u>
4.2-10.	Correlated Frequency Region Between Combustor Sensors from Plane 3.5 (42°) to 3.5 (102°) for Takeoff.	111
4.3-1.	Coherence Function for Plane 3.0 (16°) to 3.5 (42°).	114
4.3-2.	Coherence Function for Plane 3.5 (102°) to 4.0 (92°).	116
4.3-3.	Coherence Function for Plane 3.5 (282°) to 8.0A (270°).	117
4.3-4.	Coherence Function for Plane 8.0A to 8.0B (270°).	118
4.3-5.	Transfer Function (Gain and Phase) for Plane 3.5 (102°) to 4.0 (92°).	119
4.3-6.	Transfer Function (Gain and Phase) for Plane 3.5 (282°) to 8.0A (270°).	120
4.3-7.	Transfer Function (Gain and Phase) for Plane 8.0A to 8.0B (270°).	122
4.3-8.	Far-Field Coherence Level Comparison Between Planes 3.5 (102°) and 8.0A for 50 Hz.	123
4.3-9.	Far-Field Coherence Level Comparison Between Planes 3.5 (102°) and 8.0A for 100 Hz.	124
4.3-10.	Far-Field Coherence Level Comparison Between Planes 3.5 (102°) and 8.0A for 400 Hz.	125
4.3-11.	Coherence Function Far-Field Spectral Distribution Relative to Plane 8.0A.	127
4.3-12.	Transfer Function Gain Relative to Plane 8.0A for 120° Far-Field Angle.	128
4.3-13.	Transfer Function Phase Relating to Plane 8.0A for 120° Far-Field Angle.	129
4.3-14.	Comparison of Measured Turbine Attenuation from Coherent Spectra at Approach.	131
4.3-15.	Comparison of Measured Turbine Attenuation from Coherent Spectra at 45.5% Thrust.	133

LIST OF ILLUSTRATIONS (Continued)

<u>Figure</u>		<u>Page</u>
4.4-1.	Comparison of Internal Sensor FPWL _{meas} to PWL _{GE} .	135
4.4-2.	Comparison of Core Probe Coherent PWL _{meas} to PWL _{GEFAA} .	137
4.4-3.	Comparison of Far-Field Raw and Coherent SPL Spectra at Peak Angle.	138
4.4-4.	Coherent Power Level Spectra Comparison.	140
4.4-5.	Directivity Comparison of Coherent Far-Field OASPL Relative to Plane 8.0.	141
4.4-6.	Directivity Comparison of Coherent Far-Field PWL Relative to Plane 8.0.	142
4.4-7.	Directivity Comparison of Coherent Far-Field OASPL Relative to Plane 3.5.	143
4.4-8.	Directivity Comparison of Coherent Far-Field PWL Relative to Plane 3.5.	144
4.4-9.	Directivity Index Comparison from Far-Field Coherent Measurements Relative to Plane 8.0.	147
4.4-10.	Directivity Index Comparison from Far-Field Coherent Measurements Relative to Plane 3.5.	148
4.4-11.	Directivity Index Comparison Between Coherent Measurements and Predicted Results.	149
A-1.	Coherence and Transfer Functions for Plane 3.0 (16°) to Plane 3.5 (42°) at 3.8% Thrust.	154
A-2.	Coherence and Transfer Functions for Plane 3.5 (102°) to Plane 4.0 (92°) at 3.8% Thrust.	155
A-3.	Coherence and Transfer Functions for Plane 3.5 (282°) to Plane 8.0A (270°) at 3.8% Thrust.	156
A-4.	Coherence and Transfer Functions for Plane 8.0A to Plane 8.0B (270°) at 3.8% Thrust.	157
A-5.	Coherence and Transfer Functions for Fuel Nozzle (42°) to Plane 3.5 (42°) at 3.8% Thrust.	158

LIST OF ILLUSTRATIONS (Continued)

<u>Figure</u>		<u>Page</u>
A-6.	Coherence and Transfer Functions for Fuel Nozzle (102°) to Plane 3.5 (102°) at 3.8% Thrust.	159
A-7.	Coherence and Transfer Functions for Plane 3.0 (16°) to Plane 3.5 (42°) at 15.0% Thrust.	160
A-8.	Coherence and Transfer Functions for Plane 3.5 (102°) to Plane 4.0 (92°) at 15.0% Thrust.	161
A-9.	Coherence and Transfer Functions for Plane 3.5 (282°) to Plane 8.0A (270°) at 15.0% Thrust.	162
A-10.	Coherence and Transfer Functions for Plane 8.0A to Plane 8.0B (270°) at 15.0% Thrust.	163
A-11.	Coherence and Transfer Functions for Fuel Nozzle (42°) to Plane 3.5 (42°) at 15.0% Thrust.	164
A-12.	Coherence and Transfer Functions for Fuel Nozzle (102°) to Plane 3.5 (102°) at 15.0% Thrust.	165
A-13.	Coherence and Transfer Functions for Plane 3.0 (16°) to Plane 3.5 (42°) at 22.8% Thrust.	166
A-14.	Coherence and Transfer Functions for Plane 3.5 (102°) to Plane 4.0 (92°) at 22.8% Thrust.	167
A-15.	Coherence and Transfer Functions for Plane 3.5 (102°) to Plane 8.0A (270°) at 22.8% Thrust.	168
A-16.	Coherence and Transfer Functions for Plane 8.0A to Plane 8.0B (270°) at 22.8% Thrust.	169
A-17.	Coherence and Transfer Functions for Fuel Nozzle (42°) to Plane 3.5 (42°) at 22.8% Thrust. —	170
A-18.	Coherence and Transfer Functions for Fuel Nozzle (102°) to Plane 3.5 (102°) at 22.8% Thrust.	171
A-19.	Coherence and Transfer Functions for Plane 3.0 (16°) to Plane 3.5 (42°) at 26.7% Thrust.	172
A-20.	Coherence and Transfer Functions for Plane 3.5 (102°) to Plane 4.0 (92°) at 26.7% Thrust.	173

LIST OF ILLUSTRATIONS (Continued)

<u>Figure</u>		<u>Page</u>
A-21.	Coherence and Transfer Functions for Plane 3.5 (282°) to Plane 8.0B (270°) at 26.7% Thrust.	174
A-22.	Coherence and Transfer Functions for Plane 8.0A to Plane 8.0B (270°) at 26.7% Thrust.	175
A-23.	Coherence and Transfer Functions for Fuel Nozzle (42°) to Plane 3.5 (42°) at 26.7% Thrust.	176
A-24.	Coherence and Transfer Functions for Fuel Nozzle (102°) to Plane 3.5 (102°) at 26.7% Thrust.	177
A-25.	Coherence and Transfer Functions for Plane 3.0 (16°) to Plane 3.5 (42°) at 30.8% Thrust.	178
A-26.	Coherence and Transfer Functions for Plane 3.5 (102°) to Plane 4.0 (92°) at 30.8% Thrust.	179
A-27.	Coherence and Transfer Functions for Plane 3.5 (282°) to Plane 8.0A (270°) at 30.8% Thrust.	180
A-28.	Coherence and Transfer Functions for Plane 8.0A to Plane 8.0B (270°) at 30.8% Thrust.	181
A-29.	Coherence and Transfer Functions for Fuel Nozzle (42°) to Plane 3.5 (42°) at 30.8% Thrust.	182
A-30.	Coherence and Transfer Functions for Fuel Nozzle (102°) to Plane 3.5 (102°) at 30.8% Thrust.	183
A-31.	Coherence and Transfer Functions for Plane 3.0 (16°) to Plane 3.5 (42°) at 36.5% Thrust.	184
A-32.	Coherence and Transfer Functions for Plane 3.5 (102°) to Plane 4.0 (92°) at 36.5% Thrust.	185
A-33.	Coherence and Transfer Functions for Plane 3.5 (282°) to Plane 8.0A (270°) at 36.5% Thrust.	186
A-34.	Coherence and Transfer Functions for Plane 8.0A to Plane 8.0B (270°) at 36.5% Thrust.	187
A-35.	Coherence and Transfer Functions for Fuel Nozzle (42°) to Plane 3.5 (42°) at 36.5% Thrust.	188

LIST OF ILLUSTRATIONS (Continued)

<u>Figure</u>		<u>Page</u>
A-36.	Coherence and Transfer Functions for Fuel Nozzle (102°) to Plane 3.5 (102°) at 36.5% Thrust.	189
A-37.	Coherence and Transfer Functions for Plane 3.0 (16°) to Plane 3.5 (42°) at 45.5% Thrust.	190
A-38.	Coherence and Transfer Functions for Plane 3.5 (102°) to Plane 4.0 (92°) at 45.5% Thrust.	191
A-39.	Coherence and Transfer Functions for Plane 3.5 (282°) to Plane 8.0A (270°) at 45.5% Thrust.	192
A-40.	Coherence and Transfer Functions for Plane 8.0A to Plane 8.0B (270°) at 45.5% Thrust.	193
A-41.	Coherence and Transfer Functions for Fuel Nozzle (42°) to Plane 3.5 (42°) at 45.5% Thrust.	194
A-42.	Coherence and Transfer Functions for Fuel Nozzle (102°) to Plane 3.5 (102°) at 45.5% Thrust.	195
A-43.	Coherence and Transfer Functions for Plane 3.5 (102°) to 10° Far-Field Microphone at 3.8% Thrust.	196
A-44.	Coherence and Transfer Functions for Plane 3.5 (102°) to 30° Far-Field Microphone at 3.8% Thrust.	197
A-45.	Coherence and Transfer Functions for Plane 3.5 (102°) to 40° Far-Field Microphone at 3.8% Thrust.	198
A-46.	Coherence and Transfer Functions for Plane 3.5 (102°) to 50° Far-Field Microphone at 3.8% Thrust.	199
A-47.	Coherence and Transfer Functions for Plane 3.5 (102°) to 60° Far-Field Microphone at 3.8% Thrust.	200
A-48.	Coherence and Transfer Functions for Plane 3.5 (102°) to 70° Far-Field Microphone at 3.8% Thrust.	201
A-49.	Coherence and Transfer Functions for Plane 3.5 (102°) to 80° Far-Field Microphone at 3.8% Thrust.	202

LIST OF ILLUSTRATIONS (Continued)

<u>Figure</u>		<u>Page</u>
A-50.	Coherence and Transfer Functions for Plane 3.5 (102°) to 90° Far-Field Microphone at 3.8% Thrust.	203
A-51.	Coherence and Transfer Functions for Plane 3.5 (102°) to 100° Far-Field Microphone at 3.8% Thrust.	204
A-52.	Coherence and Transfer Functions for Plane 3.5 (102°) to 110° Far-Field Microphone at 3.8% Thrust.	205
A-53.	Coherence and Transfer Functions for Plane 3.5 (102°) to 120° Far-Field Microphone at 3.8% Thrust.	206
A-54.	Coherence and Transfer Functions for Plane 3.5 (102°) to 130° Far-Field Microphone at 3.8% Thrust.	207
A-55.	Coherence and Transfer Functions for Plane 3.5 (102°) to 140° Far-Field Microphone at 3.8% Thrust.	208
A-56.	Coherence and Transfer Functions for Plane 3.5 (102°) to 150° Far-Field Microphone at 3.8% Thrust.	209
A-57.	Coherence and Transfer Functions for Plane 3.5 (102°) to 160° Far-Field Microphone at 3.8% Thrust.	210
A-58.	Coherence and Transfer Functions for Plane 8.0A (270°) to 10° Far-Field Microphone at 3.8% Thrust.	211
A-59.	Coherence and Transfer Functions for Plane 8.0A (270°) to 30° Far-Field Microphone at 3.8% Thrust.	212
A-60.	Coherence and Transfer Functions for Plane 8.0A (270°) to 40° Far-Field Microphone at 3.8% Thrust.	213
A-61.	Coherence and Transfer Functions for Plane 8.0A (270°) to 50° Far-Field Microphone at 3.8% Thrust.	214
A-62.	Coherence and Transfer Functions for Plane 8.0A (270°) to 60° Far-Field Microphone at 3.8% Thrust.	215
A-63.	Coherence and Transfer Functions for Plane 8.0A (270°) to 70° Far-Field Microphone at 3.8% Thrust.	216
A-64.	Coherence and Transfer Functions for Plane 8.0A (270°) to 80° Far-Field Microphone at 3.8% Thrust.	217

LIST OF ILLUSTRATIONS (Continued)

<u>Figure</u>		<u>Page</u>
A-65.	Coherence and Transfer Functions for Plane 8.0A (270°) to 90° Far-Field Microphone at 3.8% Thrust.	218
A-66.	Coherence and Transfer Functions for Plane 8.0A (270°) to 100° Far-Field Microphone at 3.8% Thrust.	219
A-67.	Coherence and Transfer Functions for Plane 8.0A (270°) to 110° Far-Field Microphone at 3.8% Thrust.	220
A-68.	Coherence and Transfer Functions for Plane 8.0A (270°) to 120° Far-Field Microphone at 3.8% Thrust.	221
A-69.	Coherence and Transfer Functions for Plane 8.0A (270°) to 130° Far-Field Microphone at 3.8% Thrust.	222
A-70.	Coherence and Transfer Functions for Plane 8.0A (270°) to 140° Far-Field Microphone at 3.8% Thrust.	223
A-71.	Coherence and Transfer Functions for Plane 8.0A (270°) to 150° Far-Field Microphone at 3.8% Thrust.	224
A-72.	Coherence and Transfer Functions for Plane 8.0A (270°) to 160° Far-Field Microphone at 3.8% Thrust.	225
A-73.	Coherence and Transfer Functions for Plane 3.5 (102°) to 10° Far-Field Microphone at 15% Thrust.	226
A-74.	Coherence and Transfer Functions for Plane 3.5 (102°) to 30° Far-Field Microphone at 15% Thrust.	227
A-75.	Coherence and Transfer Functions for Plane 3.5 (102°) to 40° Far-Field Microphone at 15% Thrust.	228
A-76.	Coherence and Transfer Functions for Plane 3.5 (102°) to 50° Far-Field Microphone at 15% Thrust.	229
A-77.	Coherence and Transfer Functions for Plane 3.5 (102°) to 60° Far-Field Microphone at 15% Thrust.	230
A-78.	Coherence and Transfer Functions for Plane 3.5 (102°) to 70° Far-Field Microphone at 15% Thrust.	231
A-79.	Coherence and Transfer Functions for Plane 3.5 (102°) to 80° Far-Field Microphone at 15% Thrust.	232

LIST OF ILLUSTRATIONS (Continued)

<u>Figure</u>		<u>Page</u>
A-80.	Coherence and Transfer Functions for Plane 3.5 (102°) to 90° Far-Field Microphone at 15% Thrust.	233
A-81.	Coherence and Transfer Functions for Plane 3.5 (102°) to 100° Far-Field Microphone at 15% Thrust.	234
A-82.	Coherence and Transfer Functions for Plane 3.5 (102°) to 110° Far-Field Microphone at 15% Thrust.	235
A-83.	Coherence and Transfer Functions for Plane 3.5 (102°) to 120° Far-Field Microphone at 15% Thrust.	236
A-84.	Coherence and Transfer Functions for Plane 3.5 (102°) to 130° Far-Field Microphone at 15% Thrust.	237
A-85.	Coherence and Transfer Functions for Plane 3.5 (102°) to 140° Far-Field Microphone at 15% Thrust.	238
A-86.	Coherence and Transfer Functions for Plane 3.5 (102°) to 150° Far-Field Microphone at 15% Thrust.	239
A-87.	Coherence and Transfer Functions for Plane 3.5 (102°) to 160° Far-Field Microphone at 15% Thrust.	240
A-88.	Coherence and Transfer Functions for Plane 8.0A (270°) to 10° Far-Field Microphone at 15% Thrust.	241
A-89.	Coherence and Transfer Functions for Plane 8.0A (270°) to 30° Far-Field Microphone at 15% Thrust.	242
A-90.	Coherence and Transfer Functions for Plane 8.0A (270°) to 40° Far-Field Microphone at 15% Thrust.	243
A-91.	Coherence and Transfer Functions for Plane 8.0A (270°) to 50° Far-Field Microphone at 15% Thrust.	244
A-92.	Coherence and Transfer Functions for Plane 8.0A (270°) to 60° Far-Field Microphone at 15% Thrust.	245
A-93.	Coherence and Transfer Functions for Plane 8.0A (270°) to 70° Far-Field Microphone at 15% Thrust.	246
A-94.	Coherence and Transfer Functions for Plane 8.0A (270°) to 80° Far-Field Microphone at 15% Thrust.	247

LIST OF ILLUSTRATIONS (Continued)

<u>Figure</u>		<u>Page</u>
A-95.	Coherence and Transfer Functions for Plane 8.0A (270°) to 90° Far-Field Microphone at 15% Thrust.	248
A-96.	Coherence and Transfer Functions for Plane 8.0A (270°) to 100° Far-Field Microphone at 15% Thrust.	249
A-97.	Coherence and Transfer Functions for Plane 8.0A (270°) to 110° Far-Field Microphone at 15% Thrust.	250
A-98.	Coherence and Transfer Functions for Plane 8.0A (270°) to 120° Far-Field Microphone at 15% Thrust.	251
A-99.	Coherence and Transfer Functions for Plane 8.0A (270°) to 130° Far-Field Microphone at 15% Thrust.	252
A-100.	Coherence and Transfer Functions for Plane 8.0A (270°) to 140° Far-Field Microphone at 15% Thrust.	253
A-101.	Coherence and Transfer Functions for Plane 8.0A (270°) to 150° Far-Field Microphone at 15% Thrust.	254
A-102.	Coherence and Transfer Functions for Plane 8.0A (270°) to 160° Far-Field Microphone at 15% Thrust.	255
A-103.	Coherence and Transfer Functions for Plane 3.5 (102°) to 10° Far-Field Microphone at 22.8% Thrust.	256
A-104.	Coherence and Transfer Functions for Plane 3.5 (102°) to 30° Far-Field Microphone at 22.8% Thrust.	257
A-105.	Coherence and Transfer Functions for Plane 3.5 (102°) to 40° Far-Field Microphone at 22.8% Thrust.	258
A-106.	Coherence and Transfer Functions for Plane 3.5 (102°) to 50° Far-Field Microphone at 22.8% Thrust.	259
A-107.	Coherence and Transfer Functions for Plane 3.5 (102°) to 60° Far-Field Microphone at 22.8% Thrust.	260
A-108.	Coherence and Transfer Functions for Plane 3.5 (102°) to 70° Far-Field Microphone at 22.8% Thrust.	261
A-109.	Coherence and Transfer Functions for Plane 3.5 (102°) to 80° Far-Field Microphone at 22.8% Thrust.	262

LIST OF ILLUSTRATIONS (Continued)

<u>Figure</u>		<u>Page</u>
A-110.	Coherence and Transfer Functions for Plane 3.5 (102°) to 90° Far-Field Microphone at 22.8% Thrust.	263
A-111.	Coherence and Transfer Functions for Plane 3.5 (102°) to 100° Far-Field Microphone at 22.8% Thrust.	264
A-112.	Coherence and Transfer Functions for Plane 3.5 (102°) to 110° Far-Field Microphone at 22.8% Thrust.	265
A-113.	Coherence and Transfer Functions for Plane 3.5 (102°) to 120° Far-Field Microphone at 22.8% Thrust.	266
A-114.	Coherence and Transfer Functions for Plane 3.5 (102°) to 130° Far-Field Microphone at 22.8% Thrust.	267
A-115.	Coherence and Transfer Functions for Plane 3.5 (102°) to 140° Far-Field Microphone at 22.8% Thrust.	268
A-116.	Coherence and Transfer Functions for Plane 3.5 (102°) to 150° Far-Field Microphone at 22.8% Thrust.	269
A-117.	Coherence and Transfer Functions for Plane 3.5 (102°) to 160° Far-Field Microphone at 22.8% Thrust.	270
A-118.	Coherence and Transfer Functions for Plane 8.0A (270°) to 10° Far-Field Microphone at 22.8% Thrust. ---	271
A-119.	Coherence and Transfer Functions for Plane 8.0A (270°) to 30° Far-Field Microphone at 22.8% Thrust. — —	272
A-120.	Coherence and Transfer Functions for Plane 8.0A (270°) to 40° Far-Field Microphone at 22.8% Thrust.	273
A-121.	Coherence and Transfer Functions for Plane 8.0A (270°) to 50° Far-Field Microphone at 22.8% Thrust.	274
A-122.	Coherence and Transfer Functions for Plane 8.0A (270°) to 60° Far-Field Microphone at 22.8% Thrust.	275
A-123.	Coherence and Transfer Functions for Plane 8.0A (270°) to 70° Far-Field Microphone at 22.8% Thrust.	276
A-124.	Coherence and Transfer Functions for Plane 8.0A (270°) to 80° Far-Field Microphone at 22.8% Thrust.	277

LIST OF ILLUSTRATIONS (Continued)

<u>Figure</u>		<u>Page</u>
A-125.	Coherence and Transfer Functions for Plane 8.0A (270°) to 90° Far-Field Microphone at 22.8% Thrust.	278
A-126.	Coherence and Transfer Functions for Plane 8.0A (270°) to 100° Far-Field Microphone at 22.8% Thrust.	279
A-127.	Coherence and Transfer Functions for Plane 8.0A (270°) to 110° Far-Field Microphone at 22.8% Thrust.	280
A-128.	Coherence and Transfer Functions for Plane 8.0A (270°) to 120° Far-Field Microphone at 22.8% Thrust.	281
A-129.	Coherence and Transfer Functions for Plane 8.0A (270°) to 130° Far-Field Microphone at 22.8% Thrust.	282
A-130.	Coherence and Transfer Functions for Plane 8.0A (270°) to 140° Far-Field Microphone at 22.8% Thrust.	283
A-131.	Coherence and Transfer Functions for Plane 8.0A (270°) to 150° Far-Field Microphone at 22.8% Thrust.	284
A-132.	Coherence and Transfer Functions for Plane 8.0A (270°) to 160° Far-Field Microphone at 22.8% Thrust.	285
A-133.	Coherence and Transfer Functions for Plane 3.5 (102°) to 10° Far-Field Microphone at 26.7% Thrust.	286
A-134.	Coherence and Transfer Functions for Plane 3.5 (102°) to 30° Far-Field Microphone at 26.7% Thrust.	287
A-135.	Coherence and Transfer Functions for Plane 3.5 (102°) to 40° Far-Field Microphone at 26.7% Thrust.	288
A-136.	Coherence and Transfer Functions for Plane 3.5 (102°) to 50° Far-Field Microphone at 26.7% Thrust.	289
A-137.	Coherence and Transfer Functions for Plane 3.5 (102°) to 60° Far-Field Microphone at 26.7% Thrust.	290
A-138.	Coherence and Transfer Functions for Plane 3.5 (102°) to 70° Far-Field Microphone at 26.7% Thrust.	291
A-139.	Coherence and Transfer Functions for Plane 3.5 (102°) to 80° Far-Field Microphone at 26.7% Thrust.	292

LIST OF ILLUSTRATIONS (Continued)

<u>Figure</u>		<u>Page</u> _____
A-140.	Coherence and Transfer Functions for Plane 3.5 (102°) to 90° Far-Field Microphone at 26.7% Thrust.	293
A-141.	Coherence and Transfer Functions for Plane 3.5 (102°) to 100° Far-Field Microphone at 26.7% Thrust.	294
A-142.	Coherence and Transfer Functions for Plane 3.5 (102°) to 110° Far-Field Microphone at 25.7% Thrust.	295
A-143.	Coherence and Transfer Functions for Plane 3.5 (102°) to 120° Far-Field Microphone at 26.7% Thrust.	296
A-144.	Coherence and Transfer Functions for Plane 3.5 (102°) to 130° Far-Field Microphone at 26.7% Thrust.	297 —
A-145.	Coherence and Transfer Functions for Plane 3.5 (102°) to 140° Far-Field Microphone at 26.7% Thrust.	298
A-146.	Coherence and Transfer Functions for Plane 3.5 (102°) to 150° Far-Field Microphone at 26.7% Thrust.	299
A-147.	Coherence and Transfer Functions for Plane 3.5 (102°) to 160° Far-Field Microphone at 26.7% Thrust.	300
A-148.	Coherence and Transfer Functions for Plane 8.0A (270°) to 10° Far-Field Microphone at 26.7% Thrust.	301
A-149.	Coherence and Transfer Functions for Plane 8.0A (270°) to 30° Far-Field Microphone at 26.7% Thrust.	302
A-150.	Coherence and Transfer Functions for Plane 8.0A (270°) to 40° Far-Field Microphone at 26.7% Thrust.	303
A-151.	Coherence and Transfer Functions for Plane 8.0A (270°) to 50° Far-Field Microphone at 26.7% Thrust.	304
A-152.	Coherence and Transfer Functions for Plane 8.0A (270°) to 60° Far-Field Microphone at 26.7% Thrust.	305
A-153.	Coherence and Transfer Functions for Plane 8.0A (270°) to 70° Far-Field Microphone at 26.7% Thrust.	306
A-154.	Coherence and Transfer Functions for Plane 8.0A (270°) to 80° Far-Field Microphone at 26.7% Thrust.	307

LIST OF ILLUSTRATIONS (Continued)

<u>Figure</u>		<u>Page</u>
A-155.	Coherence and Transfer Functions for Plane 8.0A (270°) to 90° Far-Field Microphone at 26.7% Thrust.	308
A-156.	Coherence and Transfer Functions for Plane 8.0A (270°) to 100° Far-Field Microphone at 26.7% Thrust.	309
A-157.	Coherence and Transfer Functions for Plane 8.0A (270°) to 110° Far-Field Microphone at 26.7% Thrust.	310
A-158.	Coherence and Transfer Functions for Plane 8.0A (270°) to 120° Far-Field Microphone at 26.7% Thrust.	311
A-159.	Coherence and Transfer Functions for Plane 8.0A (270°) to 130° Far-Field Microphone at 26.7% Thrust.	312
A-160.	Coherence and Transfer Functions for Plane 8.0A (270°) to 140° Far-Field Microphone at 26.7% Thrust. —	313
A-161.	Coherence and Transfer Functions for Plane 8.0A (270°) to 150° Far-Field Microphone at 26.7% Thrust.	314
A-162.	Coherence and Transfer Functions for Plane 8.0A (270°) to 160° Far-Field Microphone at 26.7% Thrust.	315
A-163.	Coherence and Transfer Functions for Plane 3.5 (102°) to 10° Far-Field Microphone at 30.8% Thrust.	316
A-164.	Coherence and Transfer Functions for Plane 3.5 (102°) to 30° Far-Field Microphone at 30.8% Thrust.	317
A-165.	Coherence and Transfer Functions for Plane 3.5 (102°) to 40° Far-Field Microphone at 30.8% Thrust.	318
A-166.	Coherence and Transfer Functions for Plane 3.5 (102°) to 50° Far-Field Microphone at 30.8% Thrust.	319
A-167.	Coherence and Transfer Functions for Plane 3.5 (102°) to 60° Far-Field Microphone at 30.8% Thrust.	320
A-168.	Coherence and Transfer Functions for Plane 3.5 (102°) to 70° Far-Field Microphone at 30.8% Thrust.	321
A-169.	Coherence and Transfer Functions for Plane 3.5 (102°) to 80° Far-Field Microphone at 30.8% Thrust.	322

LIST OF ILLUSTRATIONS (Continued)

<u>Figure</u>		<u>Page</u>
A-170.	Coherence and Transfer Functions for Plane 3.5 (102°) to 90° Far-Field Microphone at 30.8% Thrust.	323
A-171.	Coherence and Transfer Functions for Plane 3.5 (102°) to 100° Far-Field Microphone at 30.8% Thrust.	324
A-172.	Coherence and Transfer Functions for Plane 3.5 (102°) to 110° Far-Field Microphone at 30.8% Thrust.	325
A-173.	Coherence and Transfer Functions for Plane 3.5 (102°) to 120° Far-Field Microphone at 30.8% Thrust.	326
A-174.	Coherence and Transfer Functions for Plane 3.5 (102°) to 130° Far-Field Microphone at 30.8% Thrust.	327
A-175.	Coherence and Transfer Functions for Plane 3.5 (102°) to 140° Far-Field Microphone at 30.8% Thrust.	328
A-176.	Coherence and Transfer Functions for Plane 3.5 (102°) to 150° Far-Field Microphone at 30.8% Thrust.	329
A-177.	Coherence and Transfer Functions for Plane 3.5 (102°) to 160° Far-Field Microphone at 30.8% Thrust.	330
A-178.	Coherence and Transfer Functions for Plane 8.0A (270°) to 10° Far-Field Microphone at 30.8% Thrust.	331
A-179.	Coherence and Transfer Functions for Plane 8.0A (270°) to 30° Far-Field Microphone at 30.8% Thrust.	332
A-180.	Coherence and Transfer Functions for Plane 8.0A (270°) to 40° Far-Field Microphone at 30.8% Thrust.	333
A-181.	Coherence and Transfer Functions for Plane 8.0A (270°) to 50° Far-Field Microphone at 30.8% Thrust.	334
A-182.	Coherence and Transfer Functions for Plane 8.0A (270°) to 60° Far-Field Microphone at 30.8% Thrust.	335
A-183.	Coherence and Transfer Functions for Plane 8.0A (270°) to 70° Far-Field Microphone at 30.8% Thrust.	336
A-184.	Coherence and Transfer Functions for Plane 8.0A (270°) to 80° Far-Field Microphone at 30.8% Thrust.	337

LIST OF ILLUSTRATIONS (Continued)

<u>Figure</u>		<u>Page</u>
A-185.	Coherence and Transfer Functions for Plane 8.0A (270°) to 90° Far-Field Microphone at 30.8% Thrust.	338
A-186.	Coherence and Transfer Functions for Plane 8.0A (270°) to 100° Far-Field Microphone at 30.8% Thrust.	339
A-187.	Coherence and Transfer Functions for Plane 8.0A (270°) to 110° Far-Field Microphone at 30.8% Thrust.	340
A-188.	Coherence and Transfer Functions for Plane 8.0A (270°) to 120° Far-Field Microphone at 30.8% Thrust.	341
A-189.	Coherence and Transfer Functions for Plane 8.0A (270°) to 130° Far-Field Microphone at 30.8% Thrust.	342
A-190.	Coherence and Transfer Functions for Plane 8.0A (270°) to 140° Far-Field Microphone at 30.8% Thrust.	343
A-191.	Coherence and Transfer Functions for Plane 8.0A (270°) to 150° Far-Field Microphone at 30.8% Thrust.	344
A-192.	Coherence and Transfer Functions for Plane 8.0A (270°) to 160° Far-Field Microphone at 30.8% Thrust. —	345
A-193.	Coherence and Transfer Functions for Plane 3.5 (102°) to 10° Far-Field Microphone at 36.5% Thrust.	346
A-194.	Coherence and Transfer Functions for Plane 3.5 (102°) to 30° Far-Field Microphone at 36.5% Thrust.	347
A-195.	Coherence and Transfer Functions for Plane 3.5 (102°) to 40° Far-Field Microphone at 36.5% Thrust.	348
A-196.	Coherence and Transfer Functions for Plane 3.5 (102°) to 50° Far-Field Microphone at 36.5% Thrust.	349
A-197.	Coherence and Transfer Functions for Plane 3.5 (102°) to 60° Far-Field Microphone at 36.5% Thrust.	350
A-198.	Coherence and Transfer Functions for Plane 3.5 (102°) to 70° Far-Field Microphone at 36.5% Thrust.	351
A-199.	Coherence and Transfer Functions for Plane 3.5 (102°) to 80° Far-Field Microphone at 36.5% Thrust.	352

LIST OF ILLUSTRATIONS (Continued)

<u>Figure</u>		<u>Page</u>
A-200.	Coherence and Transfer Functions for Plane 3.5 (102°) to 90° Far-Field Microphone at 36.5% Thrust.	353
A-201.	Coherence and Transfer Functions for Plane 3.5 (102°) to 100° Far-Field Microphone at 36.5% Thrust.	354
A-202.	Coherence and Transfer Functions for Plane 3.5 (102°) to 110° Far-Field Microphone at 36.5% Thrust.	355
A-203.	Coherence and Transfer Functions for Plane 3.5 (102°) to 120° Far-Field Microphone at 36.5% Thrust.	356
A-204.	Coherence and Transfer Functions for Plane 3.5 (102°) to 130° Far-Field Microphone at 36.5% Thrust.	357
A-205.	Coherence and Transfer Functions for Plane 3.5 (102°) to 140° Far-Field Microphone at 36.5% Thrust.	358
A-206.	Coherence and Transfer Functions for Plane 3.5 (102°) to 150° Far-Field Microphone at 36.5% Thrust.	359
A-207.	Coherence and Transfer Functions for Plane 3.5 (102°) to 160° Far-Field Microphone at 36.5% Thrust.	360
A-208.	Coherence and Transfer Functions for Plane 8.0A (270°) to 10° Far-Field Microphone at 36.5% Thrust.	361
A-209.	Coherence and Transfer Functions for Plane 8.0A (270°) to 30° Far-Field Microphone at 36.5% Thrust.	362
A-210.	Coherence and Transfer Functions for Plane 8.0A (270°) to 40° Far-Field Microphone at 36.5% Thrust.	363
A-211.	Coherence and Transfer Functions for Plane 8.0A (270°) to 50° Far-Field Microphone at 36.5% Thrust.	364
A-212.	Coherence and Transfer Functions for Plane 8.0A (270°) to 60° Far-Field Microphone at 36.5% Thrust.	365
A-213.	Coherence and Transfer Functions for Plane 8.0A (270°) to 70° Far-Field Microphone at 36.5% Thrust.	366
A-214.	Coherence and Transfer Functions for Plane 8.0A (270°) to 80° Far-Field Microphone at 36.5% Thrust.	367

LIST OF ILLUSTRATIONS (Continued)

<u>Figure</u>		<u>Page</u>
A-215.	Coherence and Transfer Functions for Plane 8.0A (270°) to 90° Far-Field Microphone at 36.5% Thrust.	368
A-216.	Coherence and Transfer Functions for Plane 8.0A (270°) to 100° Far-Field Microphone at 36.5% Thrust.	369
A-217.	Coherence and Transfer Functions for Plane 8.0A (270°) to 110° Far-Field Microphone at 36.5% Thrust.	370
A-218.	Coherence and Transfer Functions for Plane 8.0A (270°) to 120° Far-Field Microphone at 36.5% Thrust.	371
A-219.	Coherence and Transfer Functions for Plane 8.0A (270°) to 130° Far-Field Microphone at 36.5% Thrust.	372
A-220.	Coherence and Transfer Functions for Plane 8.0A (270°) to 140° Far-Field Microphone at 36.5% Thrust.	373
A-221.	Coherence and Transfer Functions for Plane 8.0A (270°) to 150° Far-Field Microphone at 36.5% Thrust.	374
A-222.	Coherence and Transfer Functions for Plane 8.0A (270°) to 160° Far-Field Microphone at 36.5% Thrust.	375
A-223.	Coherence and Transfer Functions for Plane 3.5 (102°) to 10° Far-Field Microphone at 45.5% Thrust.	376
A-224.	Coherence and Transfer Functions for Plane 3.5 (102°) to 30° Far-Field Microphone at 45.5% Thrust.	377
A-225.	Coherence and Transfer Functions for Plane 3.5 (102°) to 40° Far-Field Microphone at 45.5% Thrust.	378
A-226.	Coherence and Transfer Functions for Plane 3.5 (102°) to 50° Far-Field Microphone at 45.5% Thrust. — — —	379
A-227.	Coherence and Transfer Functions for Plane 3.5 (102°) to 60° Far-Field Microphone at 45.5% Thrust.	380
A-228.	Coherence and Transfer Functions for Plane 3.5 (102°) to 70° Far-Field Microphone at 45.5% Thrust.	381
A-229.	Coherence and Transfer Functions for Plane 3.5 (102°) to 80° Far-Field Microphone at 45.5% Thrust. —	382

LIST OF ILLUSTRATIONS (Continued)

<u>Figure</u>		<u>Page</u>
A-230.	Coherence and Transfer Functions for Plane 3.5 (102°) to 90° Far-Field Microphone at 45.5% Thrust.	383
A-231.	Coherence and Transfer Functions for Plane 3.5 (102°) to 100° Far-Field Microphone at 45.5% Thrust.	384
A-232.	Coherence and Transfer Functions for Plane 3.5 (102°) to 110° Far-Field Microphone at 45.5% Thrust.	385
A-233.	Coherence and Transfer Functions for Plane 3.5 (102°) to 120° Far-Field Microphone at 45.5% Thrust.	386
A-234.	Coherence and Transfer Functions for Plane 3.5 (102°) to 130° Far-Field Microphone at 45.5% Thrust.	387
A-235.	Coherence and Transfer Functions for Plane 3.5 (102°) to 140° Far-Field Microphone at 45.5% Thrust.	388
A-236.	Coherence and Transfer Functions for Plane 3.5 (102°) to 150° Far-Field Microphone at 45.5% Thrust.	389
A-237.	Coherence and Transfer Functions for Plane 3.5 (102°) to 160° Far-Field Microphone at 45.5% Thrust.	390
A-238.	Coherence and Transfer Functions for Plane 8.0A (270°) to 10° Far-Field Microphone at 45.5% Thrust.	391
A-239.	Coherence and Transfer Functions for Plane 8.0A (270°) to 30° Far-Field Microphone at 45.5% Thrust.	392
A-240.	Coherence and Transfer Functions for Plane 8.0A (270°) to 40° Far-Field Microphone at 45.5% Thrust.	393
A-241.	Coherence and Transfer Functions for Plane 8.0A (270°) to 50° Far-Field Microphone at 45.5% Thrust.	394
A-242.	Coherence and Transfer Functions for Plane 8.0A (270°) to 60° Far-Field Microphone at 45.5% Thrust.	395
A-243.	Coherence and Transfer Functions for Plane 8.0A (270°) to 70° Far-Field Microphone at 45.5% Thrust.	396
A-244.	Coherence and Transfer Functions for Plane 8.0A (270°) to 80° Far-Field Microphone at 45.5% Thrust.	397

LIST OF ILLUSTRATIONS (Continued)

<u>Figure</u>		<u>Page</u>
A-245.	Coherence and Transfer Functions for Plane 8.0A (270°) to 90° Far-Field Microphone at 45.5% Thrust.	398
A-246.	Coherence and Transfer Functions for Plane 8.0A (270°) to 100° Far-Field Microphone at 45.5% Thrust.	399
A-247.	Coherence and Transfer Functions for Plane 8.0A (270°) to 110° Far-Field Microphone at 45.5% Thrust.	400
A-248.	Coherence and Transfer Functions for Plane 8.0A (270°) to 120° Far-Field Microphone at 45.5% Thrust.	401
A-249.	Coherence and Transfer Functions for Plane 8.0A (270°) to 130° Far-Field Microphone at 45.5% Thrust.	402
A-250.	Coherence and Transfer Functions for Plane 8.0A (270°) to 140° Far-Field Microphone at 45.5% Thrust.	403
A-251.	Coherence and Transfer Functions for Plane 8.0A (270°) to 150° Far-Field Microphone at 45.5% Thrust.	404
A-252.	Coherence and Transfer Functions for Plane 8.0A (270°) to 160° Far-Field Microphone at 45.5% Thrust.	405
B-1.	Turbine Attenuation Comparisons from Coherent Spectra on the CF6-50 Engine.	407
C-1.	Coherent Output SPL Spectra from Plane 3.5 (102°) to Far-Field Microphones at 3.8% Thrust.	412
C-2.	Coherent Output SPL Spectra from Plane 3.5 (102°) to Far-Field Microphones at 15.0% Thrust.	417
C-3.	Coherent Output SPL Spectra from Plane 3.5 (102°) to Far-Field Microphones at 22.8% Thrust.	422
C-4.	Coherent Output SPL Spectra from Plane 3.5 (102°) to Far-Field Microphones at 26.7% Thrust.	427
C-5.	Coherent Output SPL Spectra from Plane 3.5 (102°) to Far-Field Microphones at 30.8% Thrust.	432
C-6.	Coherent Output SPL Spectra from Plane 3.5 (102°) to Far-Field Microphones at 36.5% Thrust.	437

LIST OF ILLUSTRATIONS (Concluded)

<u>Figure</u>		<u>Page</u>
C-7.	Coherent Output SPL Spectra from Plane 3.5 (102°) to Far-Field Microphones at 45.6% Thrust.	442
C-8.	Coherent Output SPL Spectra from Plane 8.0A (270°) to Far-Field Microphones at 3.8% Thrust.	447
C-9.	Coherent Output SPL Spectra from Plane 8.0A (270°) to Far-Field Microphones at 15.0% Thrust.	452
C-10.	Coherent Output SPL Spectra from Plane 8.0A (270°) to Far-Field Microphones at 22.8% Thrust.	457
C-11.	Coherent Output SPL Spectra from Plane 8.0A (270°) to Far-Field Microphones at 26.7% Thrust.	462
C-12.	Coherent Output SPL Spectra from Plane 8.0A (270°) to Far-Field Microphones at 30.8% Thrust.	467
C-13.	Coherent Output SPL Spectra from Plane 8.0A (270°) to Far-Field Microphones at 36.5% Thrust.	472
C-14.	Coherent Output SPL Spectra from Plane 8.0A (270°) to Far-Field Microphones at 45.5% Thrust.	477

LIST OF TABLES

<u>Table</u>		<u>Page</u>
3.1-1.	CF6-50C Engine Specifications.	5
3.2-1.	CF6-50 Combustor Design Parameters.	8
3.5-1.	Summary of CF6-50 Core Noise Acoustic Test Conditions.	14
3.7-1.	Time Series Analysis Formulas Using Discrete Finite Fourier Transform (DFT).	23
3.7-2.	Time Series Computation Procedures for Cross-Correlation Using Time/Data Analyzer with PDP 11/35.	32
3.7-3.	Time Series Computation Procedures for Cross-Spectra, Coherence, Coherent Spectra, and Transfer Function Using Time/Data Analyzer with PDP 11/35.	33
3.7-4.	Summary of Microphone and Kulite Signal Polarities for Core Noise Measurements.	51
3.7-5.	Ambient Frequency Response Corrections for CF6-50 Core Noise Waveguide Sensors.	54
4.1-1.	Test Conditions for Comparison of CF6-50 Core Noise Results with ECCP Phases II and III.	59
4.1-2.	Engine Aerodynamic Performance Summary for CF6-50 Core Noise Program.	96
4.1-3.	CF6-50 Core Noise Aerodynamic Parameters.	97
4.2-1.	Time Delay Vectoring Source Location Summary.	99
4.2-2.	Summary of Source Location Parameters for CF6-50 Combustor.	112
4.4-1.	Summary of Far-Field Directivity Indices from Coherent Measurements.	146
C-1.	Overall Pressure Level from CF6-50 Measurements Referenced to Plane 3.5.	482
C-2.	Overall Power Level from CF6-50 Measurements Referenced to Plane 3.5.	483
C-3.	Overall Pressure Level from CF6-50 Measurements Referenced to Plane 8.0.	484
C-4.	Overall Power Level from CF6-50 Measurements Referenced to Plane 8.0.	485

1.0 SUMMARY

The Core Noise Investigation of the CF6-50 Turbofan Engine, sponsored by the NASA-Lewis Research Center under Contract NAS3-21260, was an experimental research program that provided for the acquisition of simultaneously recorded internal and far-field fluctuating pressure measurements. Those measurements were used to determine the contribution of the combustor to the far-field noise signature of the CF6-50 high-bypass turbofan engine. The program objectives were to (1) investigate the internal source locations in the combustor region; (2) determine coherence functions and transfer functions (magnitude and phase), with time delay removed, for pairs of internal sensors and from internal to far field; and (3) to determine the coherent output power in the far-field measurements.

Engine internal narrowband spectra showed peak frequencies to occur between 315 to 630 Hz, typical of core noise spectra. Engine power level spectra comparisons from fluctuating pressure measurements were made between previous engine results and full-scale combustor component duct rig results. The apparent primary source location within the combustor was investigated using the vectoring of time delays from cross-correlations between pairs of fluctuating pressure signals. Groups of frequencies corresponding to the time delays were identified from cross-spectrum phase results. Ordinary coherence functions determined in the far field relative to internal measurements gave generally low coherence levels (0.1 to 0.4) over a limited frequency range (50 to 100 Hz). Transfer function (gain and phase) plots were obtained for a range of engine conditions from idle to 45.5% net thrust (including approach power). Turbine transfer functions, determined from the coherent portion of the fluctuating pressure measurements at combustor discharge and core nozzle discharge relative to the combustor inlet spectra, were compared to previous engine results and present theory. The coherent output power, determined from the ordinary coherence analysis of the far-field measurements relative to the internal measurements on the CF6-50 engine, gave low values. The above results were obtained at several points covering the operating range of the CF6-50 engine and concentrated around the approach power region. The program provided an opportunity to acquire a unique set of data on the CF6-50 engine that will add to the engine data bank for noise investigation.

2.0 INTRODUCTION

The Core Noise Investigation of the CF6-50 turbofan engine was an experimental research program sponsored by the National Aeronautics and Space Administration's Lewis Research Center of Cleveland, Ohio, that examined combustor internally generated noise and its influence on noise measurements in the far field. This program was built on earlier work conducted under the Experimental Clean Combustor Program, Phase III (NAS3-19736) on a CF6-50 engine in a test cell.

The primary objective of the Core Noise Investigation program was to obtain simultaneous internal and far-field dynamic pressure measurements on a CF6-50 high-bypass turbofan engine in order to determine the acoustic contribution of the combustor to the far-field noise signature of the engine.

A standard production-type annular combustor used for the engine test provided comparative data with full-scale component results of a similar combustor tested under the Experimental Clean Combustor Program, Phase II (NAS3-18551).

The secondary objectives of this program, to be determined or evaluated from the measurements, included the following:

- The turbine acoustic transfer and coherence function from the present engine test and comparison with existing data and theory
- The location of the apparent primary noise source in the core engine
- The acoustic power level in the combustor and in the core nozzle exhaust duct, comparing these results with the General Electric core noise predictions

The data acquired under this program will form a unique set of measurements on the CF6-50 engine which expands the data base for core noise investigation.

3.0 TEST DESCRIPTION

3.1 CF6-50 ENGINE TEST VEHICLE

The vehicle used in the acoustic test for the Core Noise Investigation program was the CF6-50 engine (Serial Number 455-768) with a standard production-type annular combustor.

The CF6-50 engine is a dual rotor, axial flow turbofan powerplant having a high-bypass ratio. It is comprised of a 14-stage high-pressure compressor driven by a 2-stage high-pressure turbine, and has an integrated front fan and low pressure compressor, driven by a 4-stage low-pressure turbine. The annular combustor converts fuel and compressor discharge air into energy to drive the turbines. The accessory drive system extracts energy from the high-pressure, high-speed rotor to drive the engine accessories and the engine-mounted aircraft accessories.

The core exhaust on this test vehicle was fitted with a long, fixed (non-reversing) annular plug nozzle. A bellmouth lip was mounted to the engine inlet. Figure 3.1-1 is an illustration of a typical CF6-50 engine and nacelle without a bellmouth inlet. Some key specifications of the CF6-50C engine are listed in Table 3.1-1.

3.2 CF6-50 STANDARD PRODUCTION COMBUSTOR

The CF6-50 standard production combustor is a high-performance annular combustor incorporating a low-pressure-loss step diffuser, carbureting swirl-cup-dome design and a short burning length. The step diffuser has a pressure loss of about 1% of the total pressure and does not vary significantly over the engine cycle. The design of the step diffuser provides a uniform, steady airflow distribution into the combustor. Thirty vortex-inducing, axial swirl cups with venturi tubes are used (one for each of its corresponding fuel nozzles) to provide flame stabilization and mixing of the fuel-air mixture. The combustion liner skirts are composed of a series of circumferentially stacked rings which are continuously film-cooled to protect the skirts from the high convective and radiant heat. Primary combustion zone cooling air entry is provided by closely spaced dilution holes in each ring. These holes augment the recirculation for flame stabilization and admit the balance of the primary combustion air. Figure 3.2-1(a) illustrates the mechanical design features of the combustor system in the CF6-50 engine.

The combustor airflow distribution is illustrated in Figure 3.2-1(b). Compressor discharge air (W_3) enters the prediffuser passage and is split into three streams: outer, center, and inner at diffuser discharge. The combustion airflow enters the combustion zone through either swirl cups, dilution holes, or film cooling slots. The air used in the combustion process,

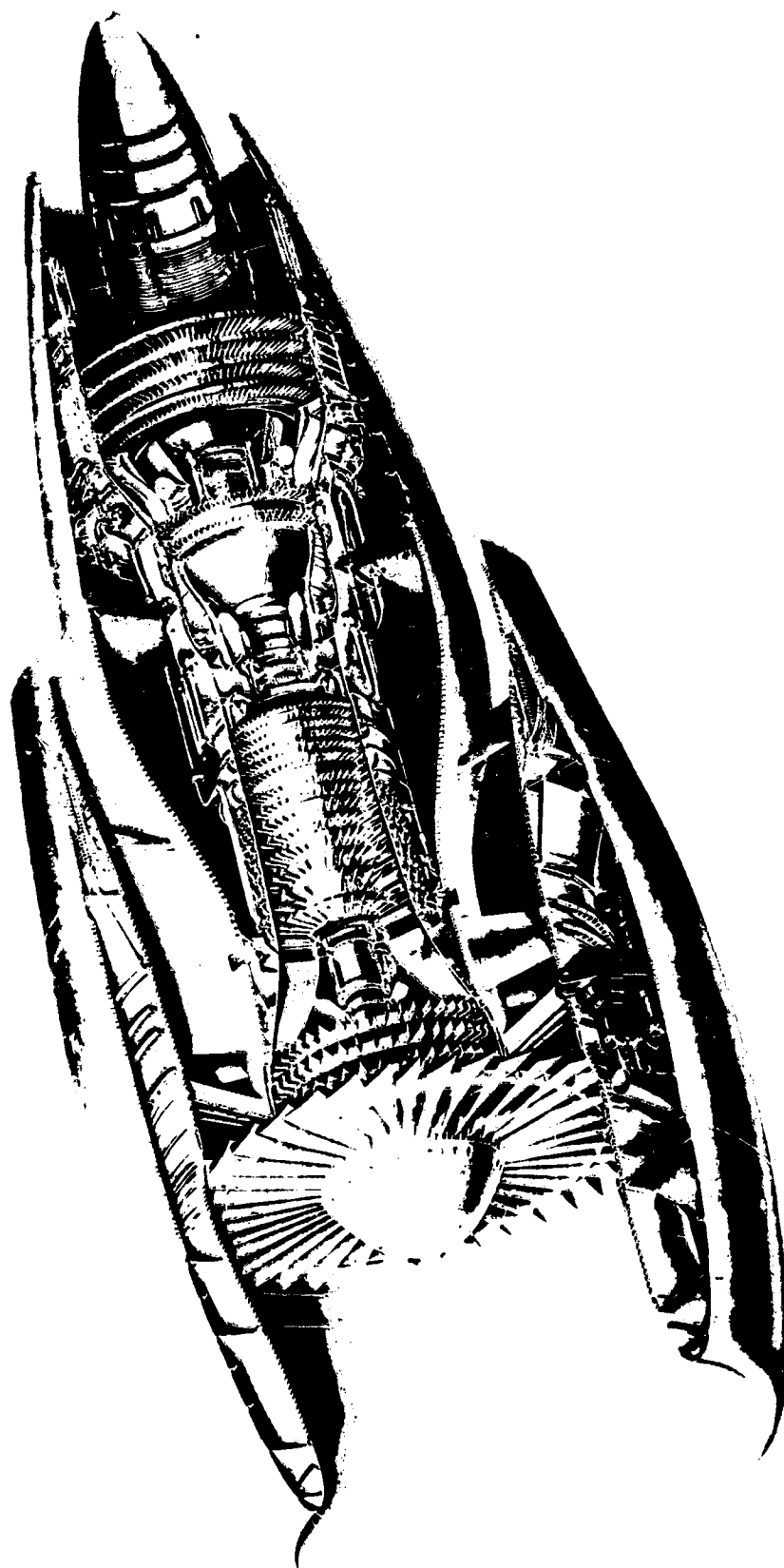
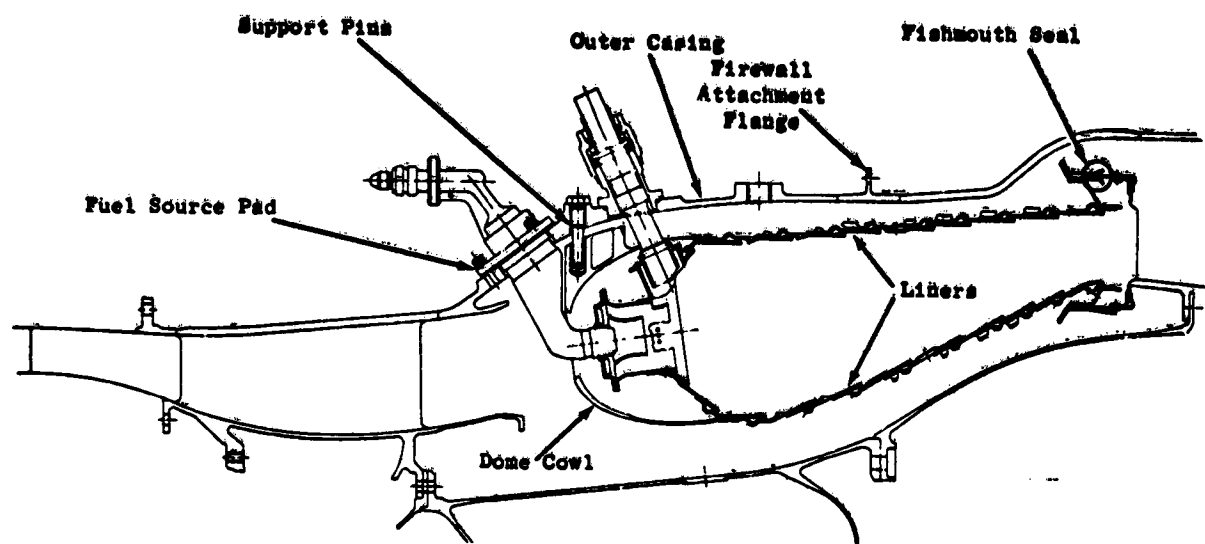


Figure 3.1-1. CF6-50 Engine and Nacelle.

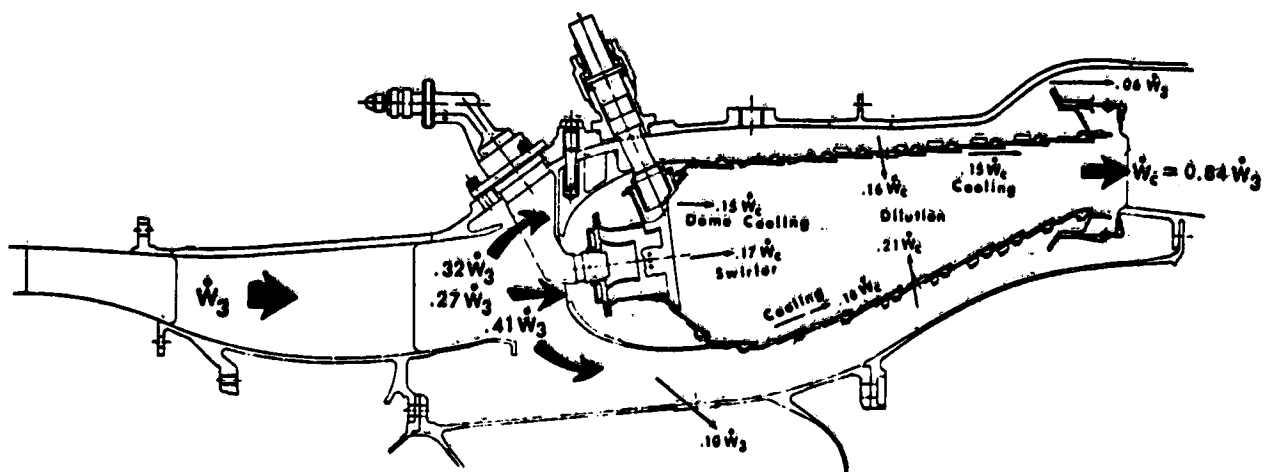
ORIGINAL PAGE IS
OF POOR QUALITY

Table 3.1-1. CF6-50C Engine Specifications.

• Takeoff Rating (SLS)	
Thrust	224.2 kN (50,400 lbf)
Specific Fuel Consumption	10.7 mg/Ns (0.377 lbm/lbf-hr)
• Maximum Cruise (Mach 0.85/10.7 km)	
Thrust	48 kN (10,800 lbf)
Specific Fuel Consumption	18.6 mg/Ns (0.656 lbm/lbf-hr)
• Weight	3780 kg (8330 lb)
• Length	482 cm (190 in.)
• Maximum Diameter	272 cm (107 in.)
• Pressure Ratio	
Takeoff	29.4
Maximum Cruise	31.4
• Bypass Ratio (Takeoff)	4.4
• Total Airflow (Takeoff)	659 kg/s (1452 lbm/s)



(a) CF6-50 Combustor Mechanical Design Features



(b) CF6-50 Combustor Air Flow Paths

Figure 3.2-1. CF6-50 Combustor Design Features.

either directly or indirectly, is only that air (W_c) that exits the combustor. The outer and inner flow streams are smoothly accelerated around the combustor cowl and enter the combustion zone through the outer and inner passages which consist of holes and slots. Thirty percent of W_c is liner cooling flow which enters the combustion reaction zone through film cooling slots. The center stream flows into the combustor primary zone through the dome cowl to the swirl cups. The cowl opening is sized to provide free-stream diffusion of the dome flow. This results in higher pressure recovery in the center stream. The higher pressure recovery generates higher pressure drops across the dome and therefore higher velocities through the swirl cups and other dome flow openings.

The combustion process of chemically reacting a liquid fuel with air, for heat release, is nonhomogeneous by nature. The local fuel-air ratio is a function of the location in the combustor. When fuel enters the primary zone close to the swirl cups, the fuel-air ratio is close to stoichiometric and decreases from that value as the fuel-air mixture travels axially down the combustor. The dilution holes and film cooling slots dilute the primary zone mixture and, to an extent, react with it. Typically, the fuel-air ratio determined from the airflow that exits the combustor is used in analysis.

Relevant design parameters for the CF6-50 combustor are shown in Table 3.2-1.

3.3 TEST OBJECTIVES

The primary objective of the acoustic test on the CF6-50 engine was to obtain simultaneous internal and far-field fluctuating pressure measurements for the purpose of determining the influence of the internally generated combustor noise on the far-field signature of the engine. Comparisons of the internal measurements from this engine test with a standard production combustor were to be made with previous full-scale component test results on a similar type of combustor.

Other objectives to be determined or evaluated from the engine measurements included the turbine acoustic-transfer function (magnitude and phase) and coherence function from the present test, the location of the apparent primary noise source in the core engine, the coherent output power in the far field, and the acoustic power level in the combustor and in the core nozzle exhaust duct, comparing these results with the General Electric Core Noise Predictions.

3.4 TEST SETUP

The setup for the test of the CF6-50 engine was done at the outdoor acoustic test Site 4D, located at the General Electric's Proving Ground Facility 144.81-km (90-mi) east of Cincinnati in Peebles, Ohio.

Table 3.2-1. CF6-50 Combustor Design Parameters.

Combustor Airflow (W_c)	103.42 kg/s (228.0 lb/sec)
Compressor Exit Mach Number	0.27
Overall System Length	75.95 cm (29.90 in.)
Burning Length (L_B)	34.8 cm (13.70 in.)
Dome Height (H_D)	11.43 cm (4.50 in.)
L_B/H_D	3.0
Reference Velocity	25.9 m/s (85 ft/sec)
Reference Area	3729 cm ² (578 in. ²)
Space Rate	$602.91 \frac{\text{watt}}{\text{m}^3\text{-Pa}} \left(5.905 \times 10^6 \frac{\text{Btu}}{\text{hr-ft}^3\text{-atm}} \right)$
$\Delta P_T/P_{T_3}$	4.3% (Total)
Number of Fuel Nozzles	30
Fuel Nozzle Spacing (B)	6.91 cm (2.72 in.)
L_B/B	5.0
B/H_D	0.60

3.4.1 Engine Installation

The engine was installed on the open trussed cantilever support stand at Site 4D with a long boattail fairing. The engine was horizontally suspended from the thrust stand at an engine centerline height of 3.96 m (13 ft) above the concrete surface of the sound-field arena. Figure 3.4-1 is a photograph of the engine installed on the test stand. All performance rakes were removed from the fan inlet, fan exhaust, and core exhaust ducts for the acoustic test.

Internal dynamic pressure sensors were installed in available access ports on the engine in the region of the combustor and in the core exhaust nozzle.

3.4.2 Acoustic Arena

The acoustic arena was set up within the level, flat, semicircular area with a concrete surface of up to 152.4-m (500-ft) diameter which was located on the open cantilever side of the engine stand. The far-field microphone array of 16 ground-mounted microphones was placed on the concrete area of Site 4D, equally spaced around a 45.7-m (150-ft) arc encompassing angles from 10° to 160° relative to the engine inlet axis as illustrated in Figure 3.4-2. The microphone arc was centered at the fan nozzle exit. The microphones were positioned at a height of 1.27 m (0.5 in.) above the ground plane and oriented vertically with the microphone head pointed at the concrete.

3.4.3 Data Acquisition System

The data acquisition system setup included all the necessary equipment to obtain analog magnetic tape recordings of all fluctuating pressure signals (internal and far field) along with the digital, steady-state aerodynamic signals of the engine parameters. Online data analysis capability of the internal sensors was provided with a real-time narrow-band spectrum analyzer connected to the tape recorder with single-channel output displayed on an X-Y recorder through means of a selector switch. This information provided a check of the internal measurements and an indication of sensor signal validity. Signal monitoring equipment was used to visually check each far field and internal sensor during the run. The acoustic data acquisition system for Kulite and microphone measurements is shown schematically in Figure 3.4-3.

The signals from the individual systems (Kulites and microphones) were recorded on a Sangamo Sabre IV, 28-channel, FM magnetic tape recorder set for operation in wide-band Group I with a center frequency of 108 kHz and run at a tape speed of 76.2 cm/sec (30 ips).

3.5 TEST MATRIX

The test points for the core noise investigation covered the sea level static operating line of the CP6-50 engine. Data were obtained at a total of 14 steady-state conditions which encompassed all required points including idle, approach, and takeoff conditions plus 4 repeat points and 2 intermediate

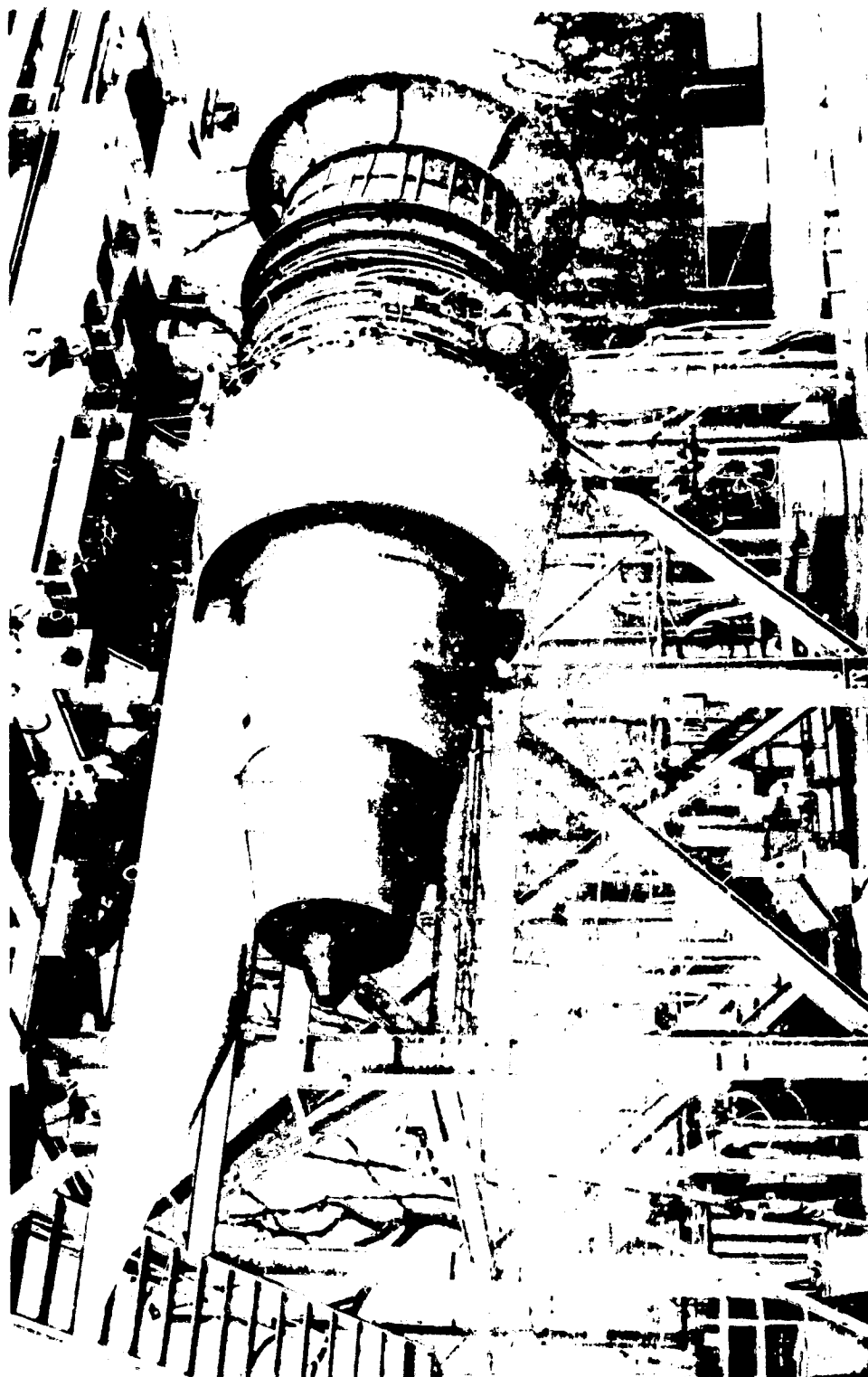


Figure 3.4-1. CF6-50 Engine Installation on Peebles Site 4D Thrust Stand.

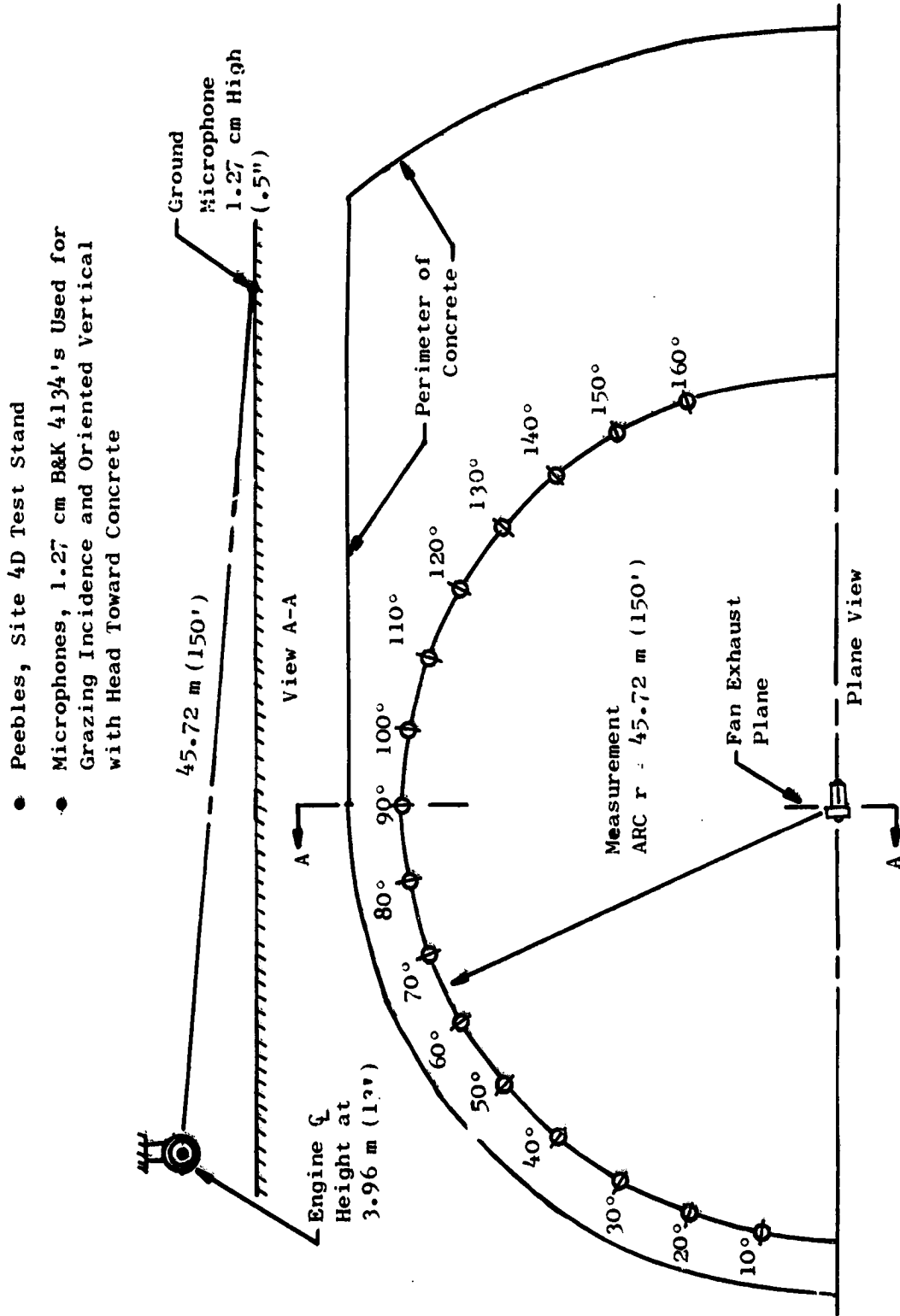


Figure 3.4-2. Far-Field Microphone Array for CF6-50 Core Noise Measurements.

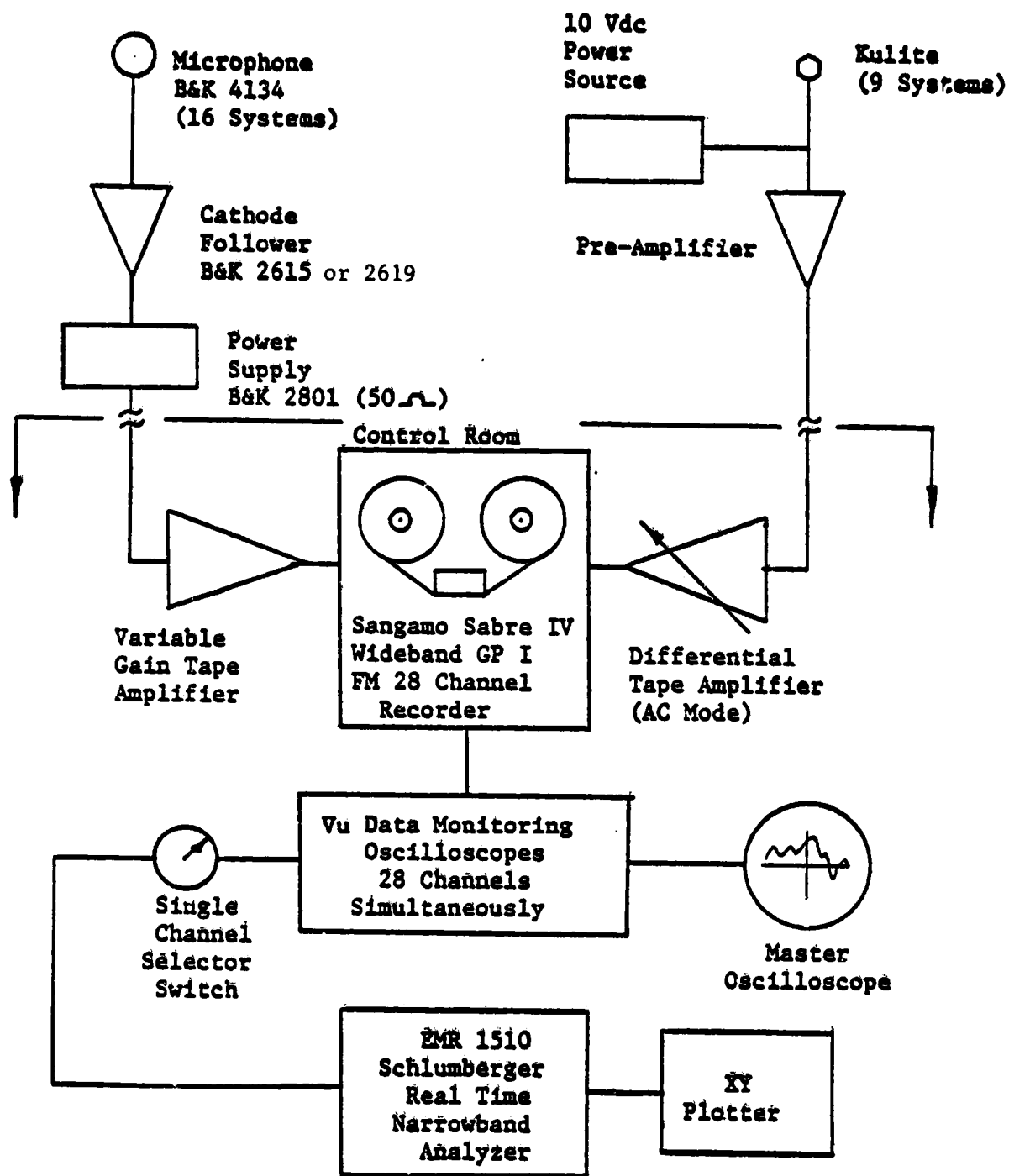


Figure 3.4-3. Acoustic Data Acquisition System.

power settings at the low end of the operating range. Table 3.5-1 lists the test conditions.

The aerodynamic performance data for each test condition were provided by the two online DMS (Data Management System) readings at the beginning and end of each steady-state condition. The data were supplemented by cross plots from the sea level static cycle for this engine to complete the performance information.

3.6 INSTRUMENTATION

The instrumentation used on this test included internal and far-field acoustic sensors as well as standard engine performance monitor instrumentation for tracking engine operation during the test run, and safety monitor instrumentation which ensured safe operation and control during the test run. Dynamic pressure measurements were taken simultaneously on the internal pressure transducers and on the far-field microphones at all test points.

3.6.1 Internal Sensors

The dynamic pressure instrumentation was installed in available access ports at the three axial planes in the combustor region and at the core nozzle exit. Dynamic pressures in the main fuel supply were obtained from redundant Kulite sensors located in the fuel nozzle region.

The internal sensors consisted of five Kulite pressure transducers (XGE-15-375-200D) installed in the air-cooled tee-block mountings of waveguide systems having capped semi-infinite coils and relatively short [approximately 20.32 cm (8 in.) to 33.02 cm (13 in.) long] standoff tubes. The location of these sensors was in the region of the combustor as illustrated in Figure 3.6-1. A photograph of the waveguide sensors installed on the engine is shown in Figure 3.6-2.

Measurements of internal fluctuating pressures were obtained from Kulite transducers flush mounted in the wall of two fuel nozzles upstream of the nozzle flow divider valve. One nozzle was a secondary-only type located at 42° and the other, a primary-secondary type at the 102° circumferential positions (clockwise from top, aft looking forward).

A dual-element, water-cooled sound separation probe with 12.7-cm (5.0-in.) spacing between Kulites was positioned at the core nozzle discharge plane as shown in Figure 3.6-3. The probe was set at an area-weighted central immersion of the core nozzle annulus and supported external to the engine.

3.6.2 Far-field Microphones

The microphones used for this test were Bruel and Kjaer (B&K) Type 4134, 1.27-cm (0.5-in.) diameter condenser microphones oriented vertically with the

Table 3.5-1. Summary of CF6-50 Core Noise Acoustic Test Conditions.

<u>Nominal % F_n</u>	<u>Core Speed $N_2/\sqrt{\theta_2}$</u>	<u>Fuel- Air Ratio, f/a</u>	<u>Condition</u>	<u>Remarks</u>
3.8	6,564	0.0101	Idle	Repeat Point
15.0	8,034	0.0109		Intermediate Point
22.8	8,452	0.0120		
26.7	8,660	0.0120		Intermediate Point
30.8	8,686	0.0131	Approach	Repeat Point
36.5	8,882	0.0139		
45.6	9,106	0.0154		Repeat Point
67.8	9,668	0.0182		
85.5	9,964	0.0201		Repeat Point
99.8	10,281	0.0230	Takeoff	

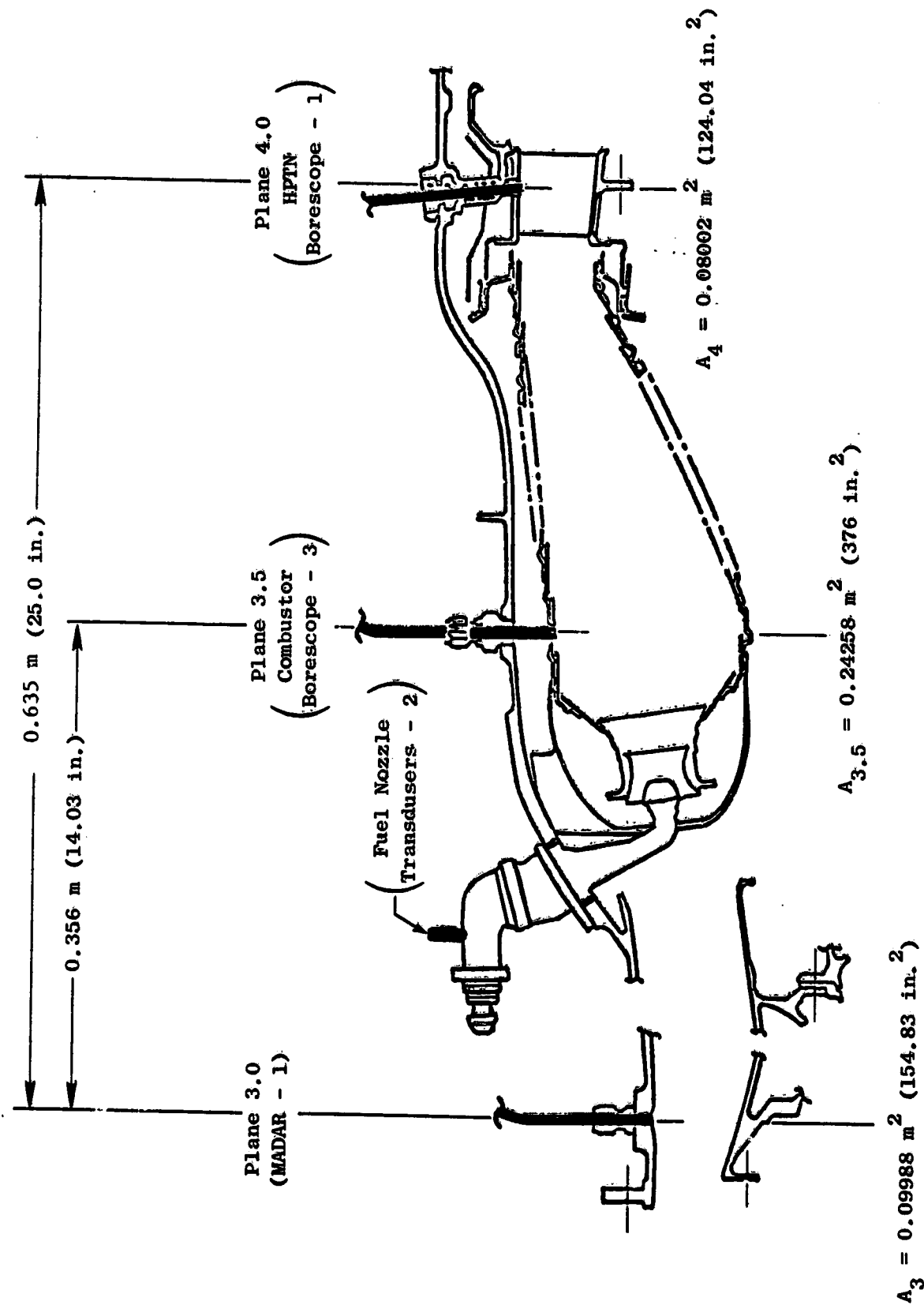


Figure 3.6-1. Internal Sensor Locations for Engine Combustor Nozzle Measurements.

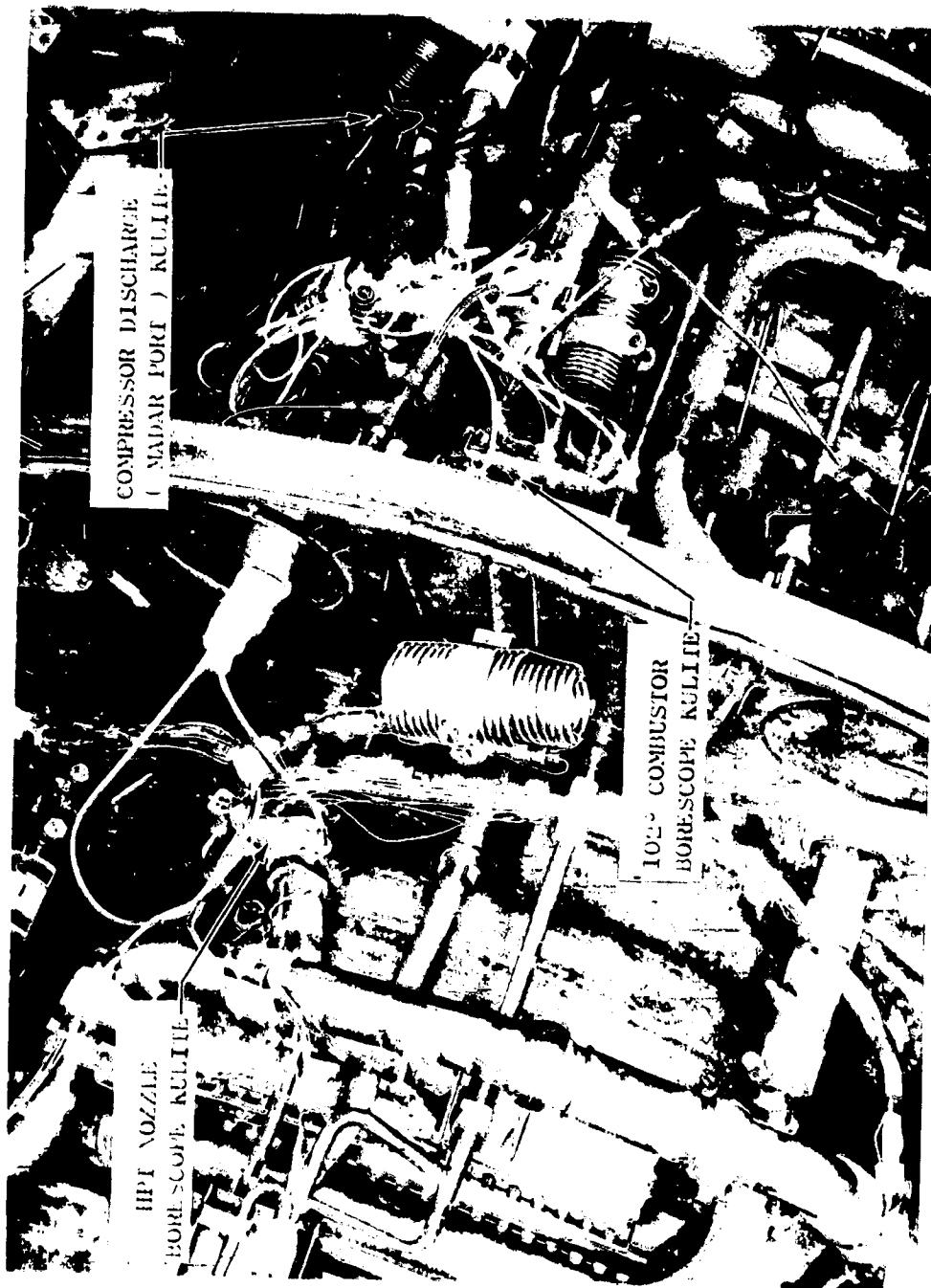


Figure 3.6-2. Typical Kulite Waveguide Sensor Installations for CF6-50 Core Noise Acoustic Test (7708283).

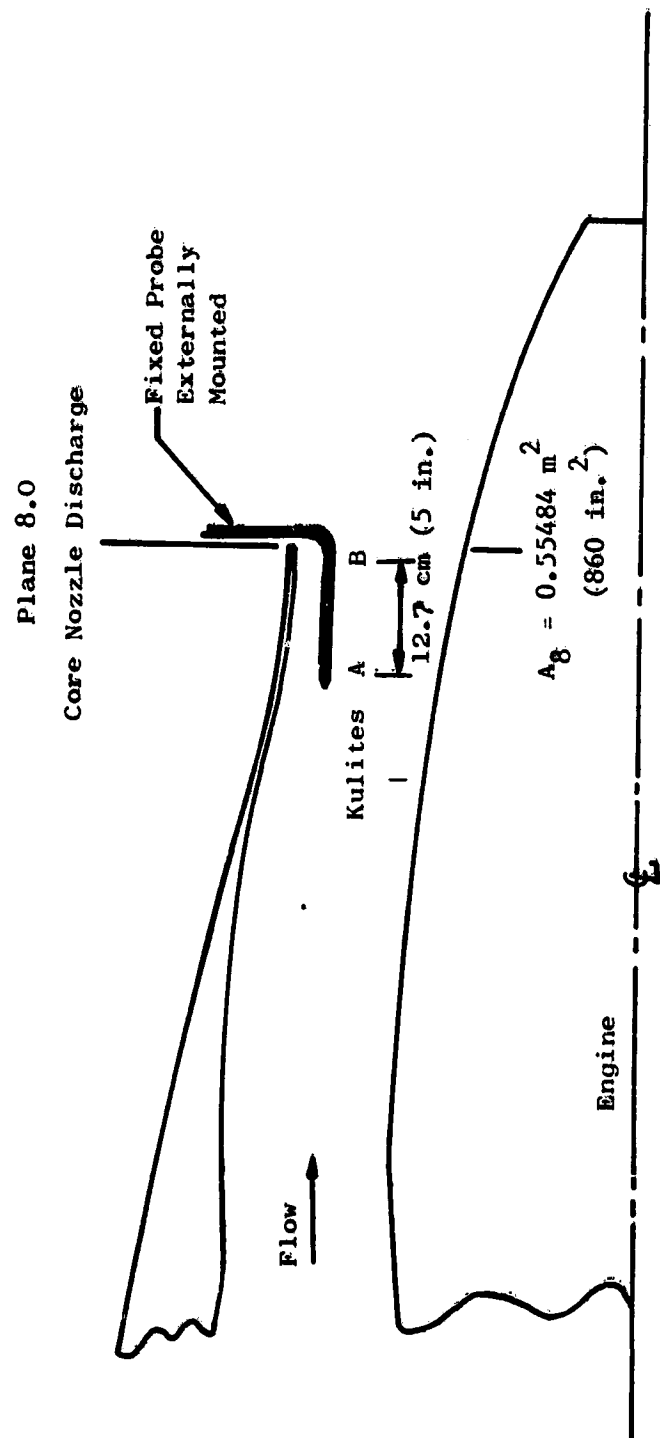


Figure 3.6-3. Sound-Separation Probe Location on CF6-50 Engine.

microphone head pointed toward the ground. The microphones were positioned 1.27 cm (0.5 in.) above the ground plane to ensure that the ground nulls were sufficiently above the frequencies of interest for this test (calculated frequency of the first null is 77.5 kHz).

All microphone systems utilized either the B&K 2615 or B&K 2619 cathode follower and B&K 2801 power supply with the 50 Ω output option to provide a flat response through the 10 kHz region of interest.

3.7 DATA REDUCTION AND PROCESSING

3.7.1 Data Analysis Methods

The methods used in analysis of the data from the core noise engine test included 1/3-octave-band and narrowband spectral analysis and digital fast Fourier transform (DFT) techniques of cross-correlation, coherence, and transfer function (amplitude and phase) analysis.

One-Third-Octave-Band Spectral Analysis

The 1/3-octave-band spectra were processed from the recorded data by standard techniques and by DFT procedures. Those processed by standard techniques included the internal data processed over a range of 1/3-octave bands from 50 to 5,000 Hz while the far-field data were processed from 50 to 10,000 Hz. Internal spectra were obtained from measured data which were corrected for probe ambient frequency response. The far-field data were corrected to Standard Day, 288.1 K (59° F) 70% R.H., and free-field conditions.

The 1/3-octave-band spectra determined for all test conditions were used for evaluating the combustor internal measurement trends and for comparisons with the component combustor data in ECCP Phase II (Reference 1) and the engine data from ECCP Phase III (Reference 2). The overall fluctuating pressure level (OAFPL) obtained from the 1/3-OBFPL spectra were used to determine the measured power level (PWL_{meas}) assuming the total pressure signal was acoustic. The far-field arc 1/3-octave-band spectra were used to evaluate raw signal content. The overall levels were used to obtain directivity and sound power levels with engine tones removed. Coherent 1/3-octave-band spectra were obtained between selected pairs of sensors using time-series analyses and DFT procedures.

Digital Fast Fourier Transform Techniques

The digital fast Fourier transform techniques used for the data analysis included both frequency and time-domain techniques. Detailed explanations of these various methods, briefly described below, are found in Reference 3. The

techniques in the frequency domain include auto spectrum, cross spectrum, coherence function, coherent output spectrum, and transfer function gain and phase.

Time-series analysis views continuous data records in finite increments or samples. The samples acquired at sequential times over the record length are stored in blocks for subsequent conversion by finite Fourier transform from the time domain to the frequency domain. The data stored in these blocks are truncated segments of the continuous data record. The spectral bandwidth, B_s , is defined as the ratio of the sampling rate (SR) to the transform block size (N). The signal waveforms are expressed as functions of time with $x(t)$ as the input signal and $y(t)$ as the output signal. For these signals the auto spectra are defined by

$$\text{Input: } G_{xx}(f) = F_x(t) \cdot F_x^*(t) \quad (1)$$

$$\text{Output: } G_{yy}(f) = F_y(t) \cdot F_y^*(t) \quad (2)$$

where F is the Fourier transform operation, and F^* is the complex conjugate of the Fourier transform.

The narrowband analysis of the engine data was processed through a digital Fourier transform analyzer using a block size of 4096 and a sampling rate of 8192 samples/sec to obtain 2-Hz bandwidth spectra over a range of frequencies from 0 to 2000 Hz. The number of block averages employed was 20 which results in a total sample record length of 10 seconds being used in the analysis of the data. The narrowband spectra obtained through this analysis were computed for 9 internal sensors and 15 far-field microphones for 8 conditions over the operating range. The results from this analysis are presented in Reference 4. The internal spectra were used to assist in evaluating trends from the internal Kulite measurements. Fluctuating pressure level (FPL) was used instead of sound pressure level (SPL) for these sensors since the pressure signal contains turbulence in addition to sound. The far-field data used sound pressure level (SPL) since the signals that reach the microphone locations in the far field are principally acoustic.

The cross spectrum, $G_{xy}(f)$, is obtained from the product of the Fourier transform of the input signal record $F_x(t)$, times the complex conjugate of the Fourier transform of the output signal, $F_y^*(t)$, and is expressed as

$$G_{xy}(f) = F_x(t) F_y^*(t) \quad (3)$$

The square of the magnitude of this cross spectrum divided by the auto spectra of the input and output signals defines the ordinary coherence function which is expressed as

$$\gamma^2 = \frac{|G_{xy}|^2}{G_{xx} \cdot G_{yy}} \quad (4)$$

The coherence function expresses the degree of similarity between the input and output signals in the frequency domain.

The coherent output spectrum is a means of expressing the amount of the output signal that is coming from the input signal. It is defined as the auto spectrum of the output signal multiplied by the coherence function and is expressed as

$$(CO)G_{yy} = \gamma^2 G_{yy} \quad (5)$$

Another term used in the analysis of the data is the transfer function, normally defined as the ratio of the output-to-input autospectra. However, since the far-field signals contain many source contributions, the most effective way to determine the transfer function from internal to far field was to use the cross spectrum in place of the output autospectrum.

$$H^2 = \frac{G_{xy}}{G_{xx}} \quad (6)$$

This yields a complex quantity which can be used to determine the gain and phase between the output and input as a function of frequency.

The time delays between two signals separated by a large distance (i.e., internal to far field) and by smaller internal separations must be removed from the data to properly align the data records in order to minimize bias errors in the results. The technique used to identify these time delays was cross-correlation analysis. Cross-correlation analysis is a measure of the propagation-time-delay characteristics of signal transmission in the time domain. In cross-correlation, the input signal is compared with the time-delayed output signal to determine the amount of similarity between the two signals. The cross-correlation function is expressed as

$$R_{xy}(\tau) = \lim_{T \rightarrow \infty} \frac{1}{T} \int_0^T x(t)y(t+\tau)dt \quad (7)$$

The normalized correlation coefficient is expressed as

$$\rho_{xy}(\tau) = \frac{R_{xy}(\tau)}{R_{xx}(0) R_{yy}(0)} \quad (8)$$

where $R_{xx}(0)$ and $R_{yy}(0)$ are the zero-time-delay values of the autocorrelation of the input and output signal, respectively.

With large spacings between sensors (distances much greater than the quarter wavelengths of the frequencies of interest), only the acoustic signal is well correlated and peaks will occur in the cross-correlogram at values of time delay that correspond to the distance between the sensors divided by the local speed of sound. This is typical of cross-correlations between the internal sensors and the far-field microphones.

The identification of source locations can be determined through the vectoring of time delays obtained from cross-correlation analysis. The direction of the propagating signal can be related to the sign (\pm) of the time delay. Comparing time delays between several pairs of sensors identifies regions where the time delay goes through zero, which can be related to the apparent location of the sources.

The location of the source can be pinpointed as occurring in regions where the time delay goes through zero (changes sign) or is near zero. For instance, if the acoustic signal originates halfway between an upstream and downstream sensor the delay time will be zero (for a no flow condition) since the signal travel times to each sensor are identical. If the source is located less than, or more than, halfway between sensors, the time delay from upstream to downstream will be near zero but will change sign depending on the conditions.

3.7.2 Time Series Analysis Parameter Optimization

The analysis of the data by digital time series techniques required the optimization of several parameters in order to construct a procedure that yielded the desired results. The approach condition at 30.8% F_n was selected as the focal point of the study since it appeared to give a reasonable degree of signal correlation with the majority of the sensors and also was representative of a condition influenced by core noise.

Variations of the time series parameters were conducted to determine their influence on the analysis results.

3.7.2.1 Time Series Parameter Study

The parameters investigated for the study included the following:

1. Sample Rate, SR (samples/sec)
2. Transform Block Size, N (samples)
3. Sample Averages, M
4. Sample Interval, Δt (sec/sample)
where $\Delta t = 1/SR$ (9)
5. Sample Length, t (sec)
where $t = N\Delta t = N/SR$ (10)
6. Record Length, T (sec)
where $T = Mt$ (11)
7. Resolution Bandwidth, B_e (Hz)
where $B_e = 1/t = SR/N$ (12), (13)

$$\begin{aligned} 8. \quad & \text{Resolution Frequency, } f \text{ (Hz)} \\ & \text{where } f = SR/2 \text{ (Nyquist or Folding Frequency)} \end{aligned} \quad (14)$$

$$\begin{aligned} 9. \quad & \text{Random Error, } \epsilon \text{ for autospectra} \\ & \text{where } \epsilon = 1/\sqrt{B_e T} \end{aligned} \quad (15)$$

or substituting equations (9) through (14) into (15) yields

$$\epsilon = 1/\sqrt{M} \quad (16)$$

which says that the amount of random error in a spectral calculation varies inversely with the square root of the number of sample averages.

These parameters represent the control available to the operator when performing time-series analysis on the digital fast Fourier transform analyzer.

The time series parameters were used to establish operating regions for employing the time series analysis formulas noted in Table 3.7-1.

The parametric study evaluated several effects on the analysis result. Among these were:

1. The effect of data bandwidth on cross-correlation (keeping sampling rate and block size constant but varying the analysis window).
2. The effect of sampling rate on cross-correlation coherence, and transfer function phase angle for internal sensors and internal to far-field pairs.
3. The effect of averaging on cross-correlation, coherence, and transfer function phase angle for internal sensors and internal to far-field pairs.

The effect of varying the frequency bands of the data to be analyzed was found to be significant for internal/external results. Some typical examples of this effect are shown in figure 3.7-1. Data bandwidths of 0-1000, 100-1000, and 500-1000 Hz were used in cross-correlations of an internal pair of sensors and the core probe to a far-field microphone. Too broad a range of frequencies results in broad time-delay peaks that obscure the real peaks in internal/external data. Narrowing the window by cutting off the low frequency below 100 Hz while maintaining an upper limit of 1000 Hz enhances the time-delay peaks in both sets of data. Further reduction of the low-frequency end below 500 Hz minimizes one of the peaks in the internal correlations and washes out the resolution in the far-field data, indicating removal of the correlated signal. The best overall cross-correlation results were obtained with a window of 100 to 1000 Hz for both internal pairs of internal to external sensors.

Table 3.7-1 Time-Series Analysis Formulas Using Discrete Finite Fourier Transform (DFT).

Autospectrum	$G_{xx}(f) = \text{DFT } x(t) \cdot \text{DFT}^* x(t); G_{yy}(f) = \text{DFT } y(t) \cdot \text{DFT}^* y(t)$
Autocorrelation	$R_{xx}(\tau) = \text{DFT}^{-1} G_{xx}(f); R_{yy}(\tau) = \text{DFT}^{-1} G_{yy}(f)$
Cross-Spectrum	$G_{xy}(f) = \text{DFT } x(t) \cdot \text{DFT}^* y(t)$
Cross-Correlation	$R_{xy}(\tau) = \text{DFT}^{-1} G_{xy}(f)$
Normalized Cross-Cor	$\rho_{xy}(\tau) = R_{xy}(\tau)/R_{xx}(0)/R_{yy}(0)$
Coherence Function	$\gamma^2(f) = G_{xy}(f) \cdot 2/G_{xx}(f)/G_{yy}(f)$
Coherent Spectrum	$\gamma^2 G_{yy}(f) = G_{xy}(f) \cdot 2/G_{xx}(f)$
Transfer Spectrum	$H(f) = G_{xy}(f)/G_{xx}(f)$

- Time Series Parameter Effects
- 30.8% F_n

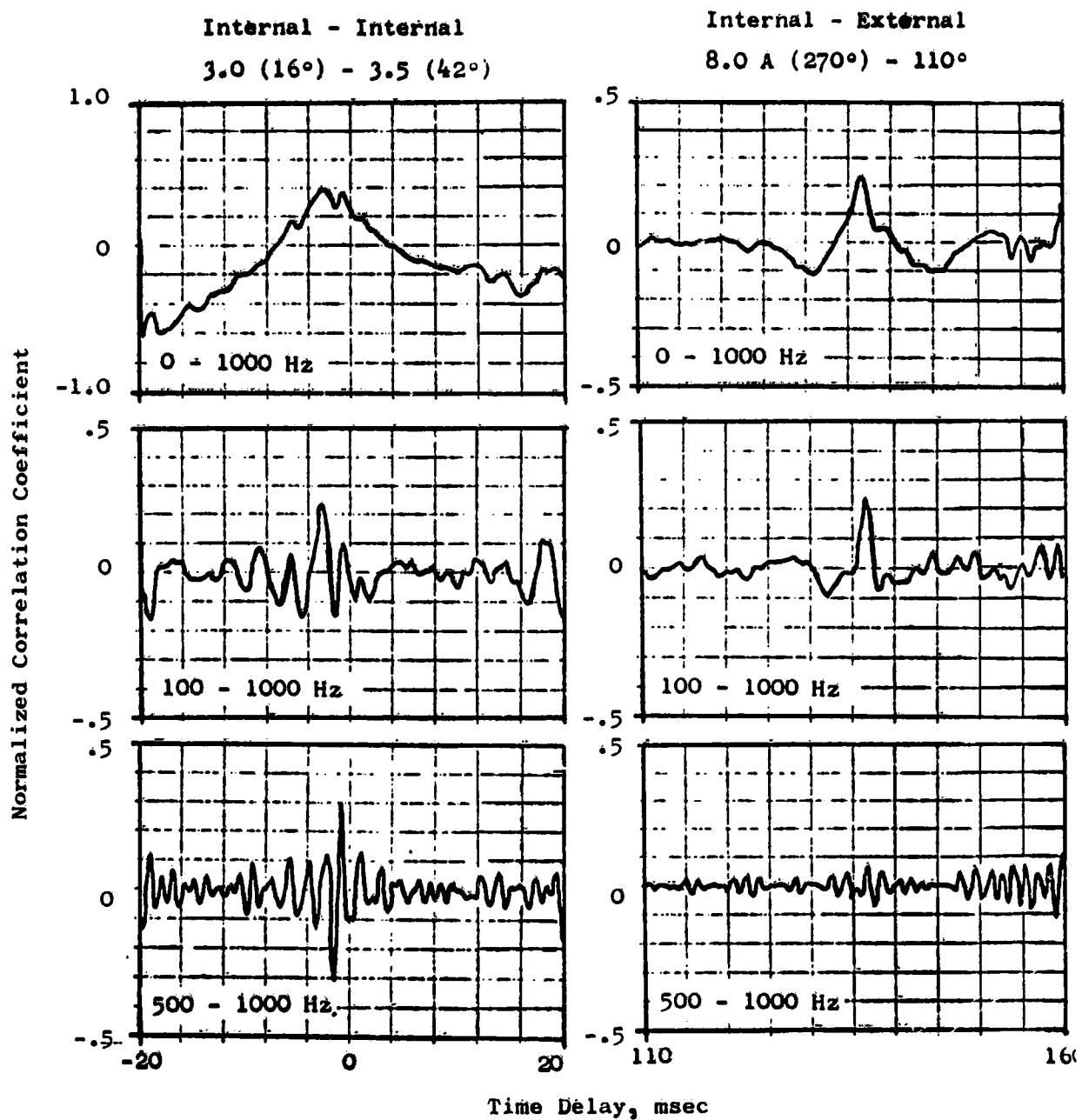


Figure 3.7-1. Effect of Data Bandwidth on Cross-Correlation.

The sampling rate effect on cross-correlations in this study was determined at a data bandwidth of 100-500 Hz. Cross-correlations from internal sensor pairs were checked at 51,200, 25,600, and 12,800 sps, while the external data were checked at 6,400, 3,200 and 1,600 sps. Figure 3.7-2 shows the results. The higher the sampling rate the greater the number of peaks appear in the data, often resulting in spurious peaks that do not clarify the true peaks. The midrange sample rates of 25,600/32,000 sps for the internal/external results proved to be best for the analysis.

A similar study with the coherence function in Figure 3.7-3 shows the effect of increasing the sampling rate to increase the resolution of the signal and eliminate much of the "hash" on the spectrum.

The results with sampling rate on transfer function phase in Figure 3.7-4 are in agreement with these observations.

The effect of increasing the number of averages on coherence is shown in Figure 3.7-5. The number of averages was increased from 50 to 100, and then to 200. Doubling the number of averages reduces the random background noise by 3 dB. The internal sensors at a sample rate of 2560 sps show a small difference in level going from 50 to 100 averages, but no change for increasing the number of averages to 200. This indicates the coherence function is achieved with the 100 averages.

The internal to far-field comparison shows successive level reductions with increasing number of averages at a sample rate of 5120 sps. This indicates that the internal to far-field results would benefit from increased averaging.

The results of the transfer phase angle study with number of averages indicates similar effects as shown in Figure 3.7-6.

● Observations on Parametric Study Results

Several noteworthy observations about the data from the CF6-50 measurements from this time series parameter evaluation were made. They include the following:

1. Cross-correlations between poorly correlated signals are very sensitive to computation parameters.
2. Distinguishable cross-correlation peaks are required to precisely determine time delays.
3. Phase angle plots indicate different propagation time delays for different frequency bands.
4. Internal-to-internal cross-correlations are best when frequency bands are restricted to 100-1000 Hz.

• Time Series Parameter Effects

• Data Bandwidth = 100 - 500 Hz

• 30.8% F_n

Internal - Internal
3.0 (16°) - 3.5 (42°)

Internal - External
8.0A (270°) - 110°

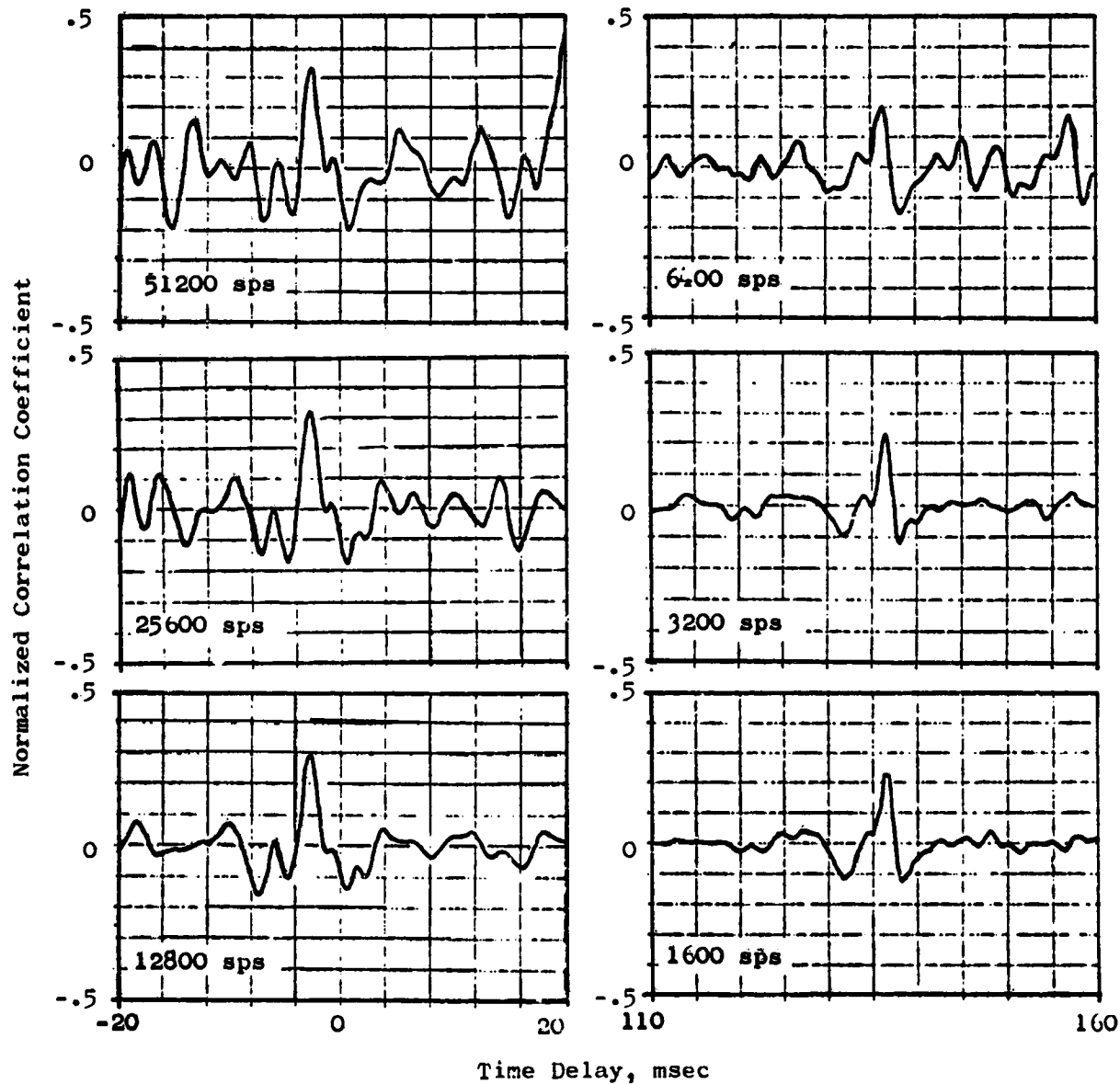


Figure 3.7-2. Effect of Sampling Rate on Cross-Correlation.

- Time Series Parameter Effects
- 100 Averages

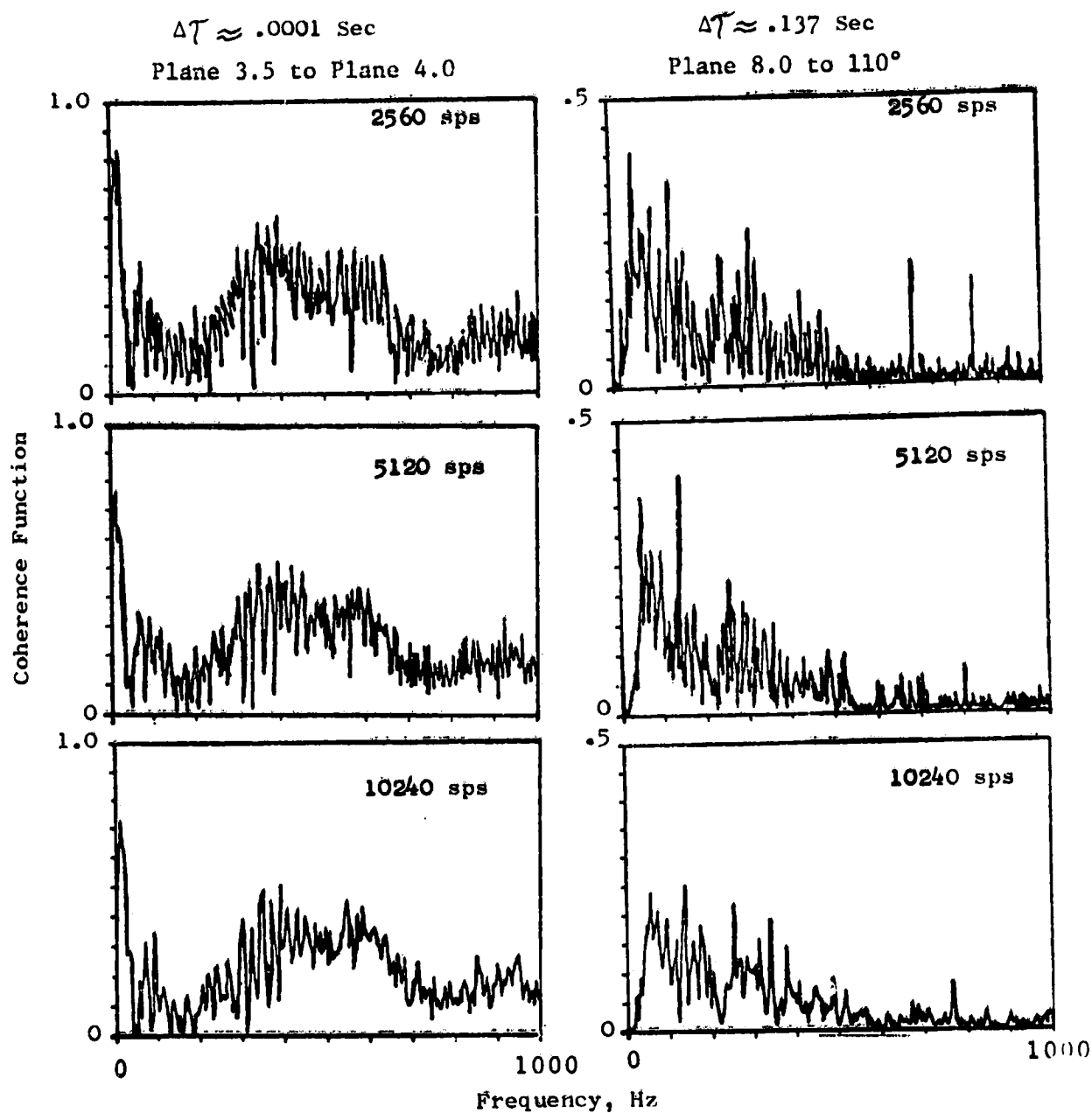


Figure 3.7-3. Effect of Sampling Rate on Coherence.

- Time Series Parameter Effects
- 100 Averages

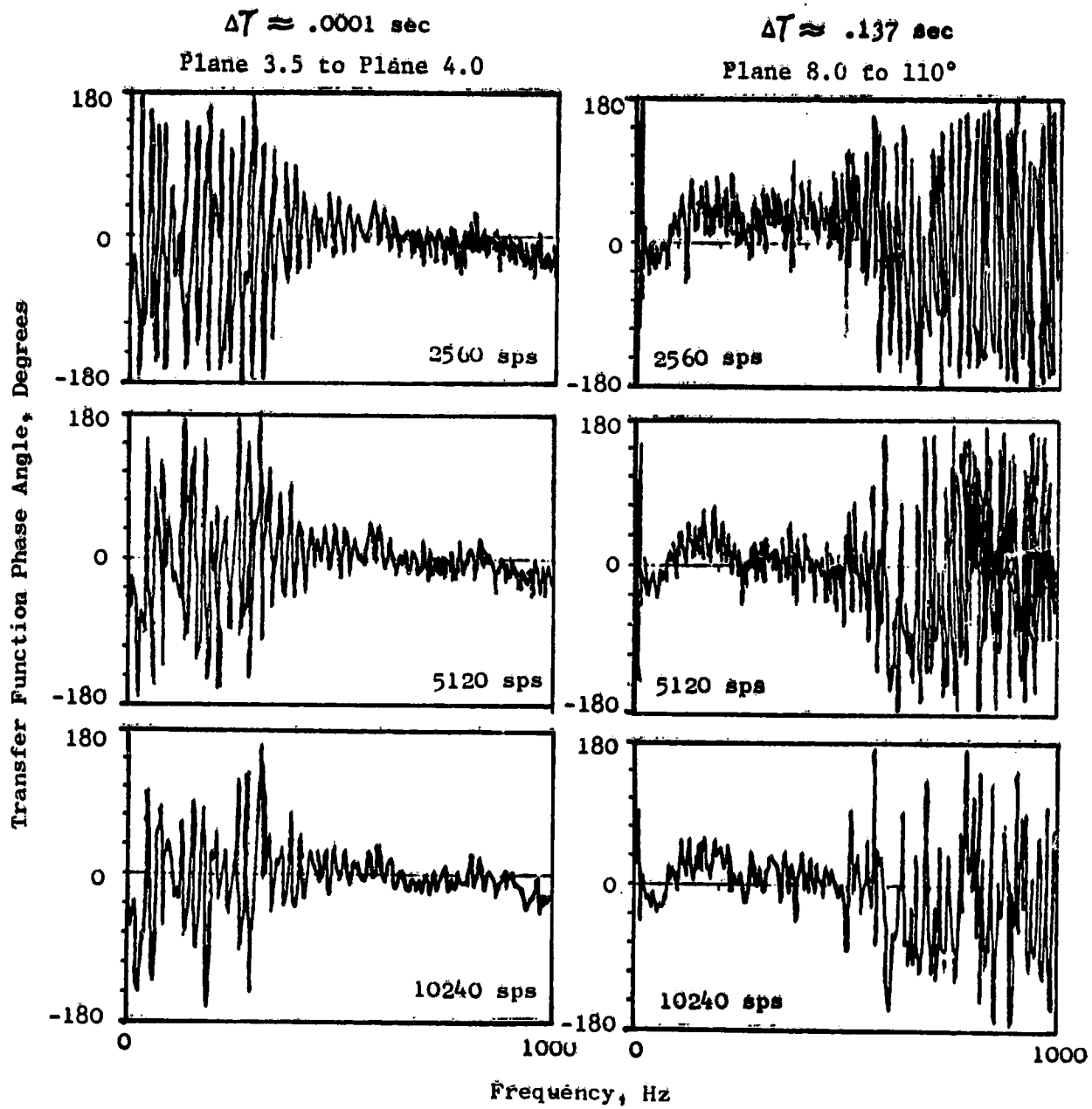


Figure 3.7-4. Effect of Sampling Rate on Phase Angles.

- Time Series Parameter Effects
- 2560 sps/5120 sps

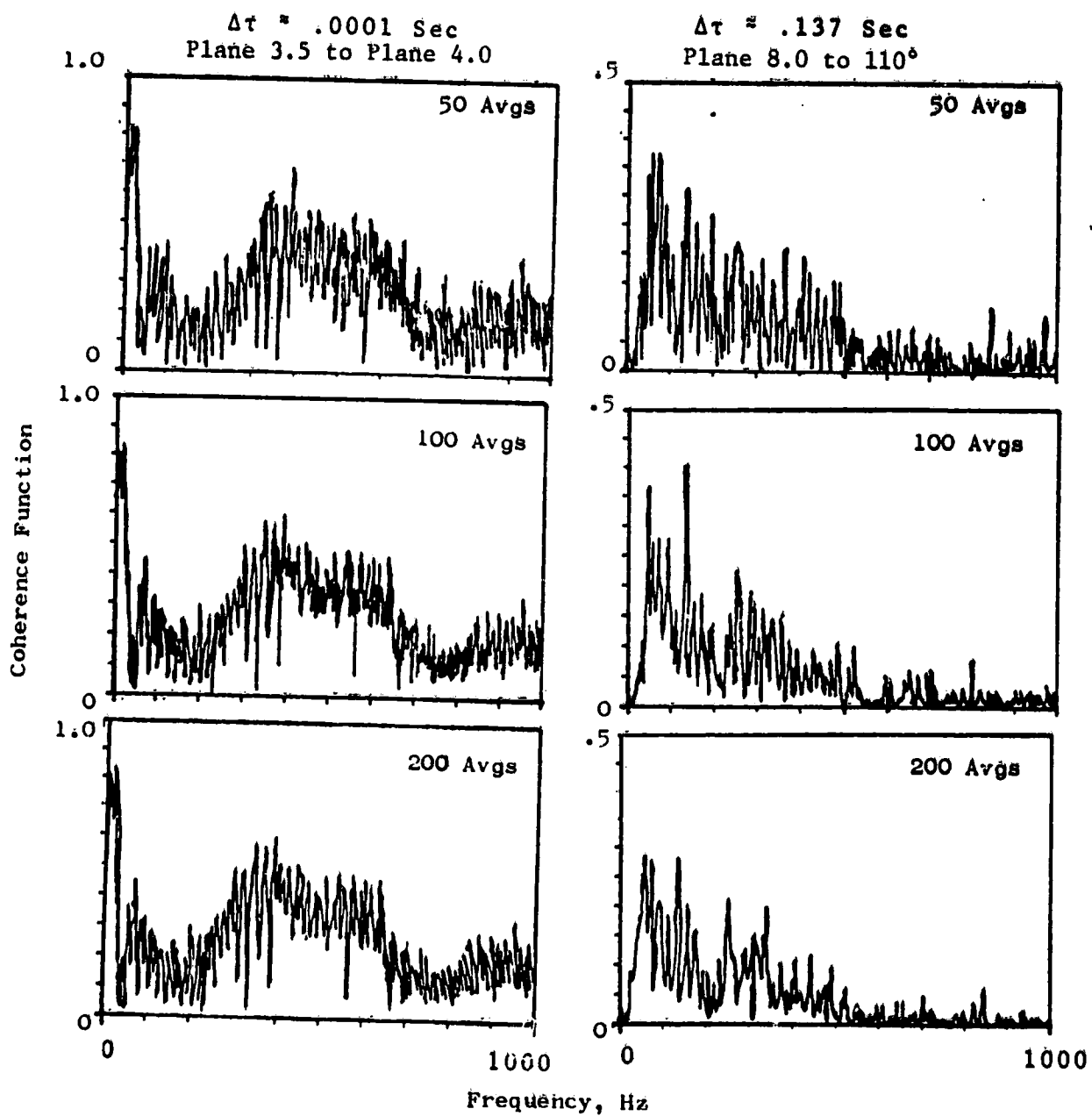


Figure 3.7-5. Effect of Averages on Coherence.

- Time Series Parameter Effects
- 2560 sps / 5120 sps

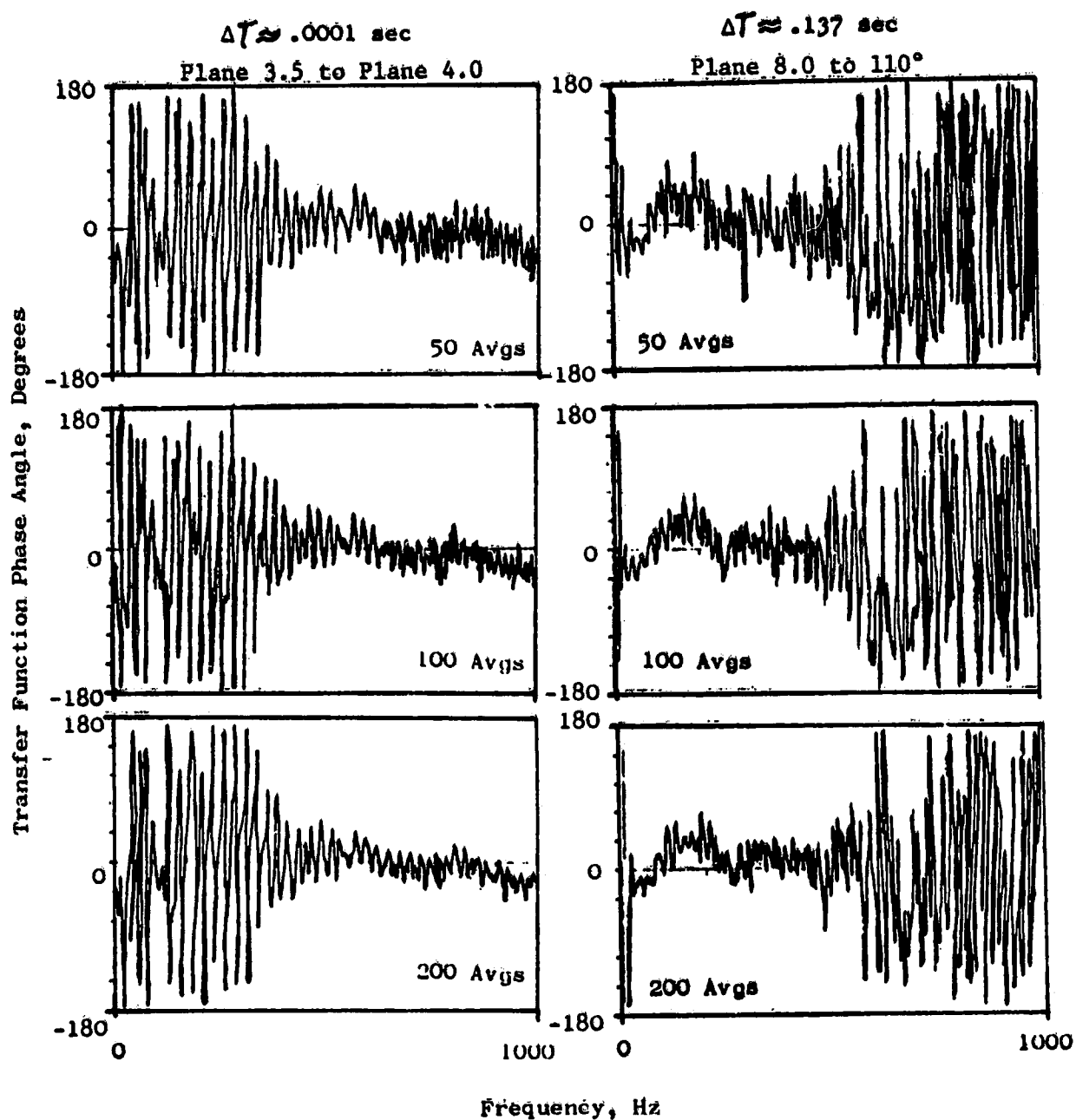


Figure 3.7-6. Effect of Averages on Phase Angles.

5. Internal-to-external cross-correlations are best when frequency bands are restricted to 100-500 Hz.
6. High correlation occurs between tailpipe to far-field and combustor-to-combustor.
7. Coherence results indicate 0-1000-Hz energy in the combustor but only 50-500 Hz propagates to the far field.

These observations were used in the selection of parameter combinations which appeared to optimize the results of the study. A summary of these parameters for the cross-correlation analysis was found in Table 3.7-2. Two sets of parameters are listed, one for internal sensor pairs and another for internal to far-field sensor combinations. This is to be expected due to the relative magnitudes of the time delays involved. A similar set of optimized parameters for the coherence, coherent spectra, and transfer function analysis is listed in Table 3.7-3. These optimized time-series analysis parameters were used in the analysis of the core noise data.

3.7.2 2 Use of Digital Processing Techniques

The digital FFT processing techniques used in the analysis of the internal and far-field data obtained in the core noise investigation program included those in the time domain (i.e., cross-correlation) as well as the frequency domain (i.e., cross-spectrum phase).

Time delays associated with acoustic wave propagation speeds were removed from the internal and far-field data. The removal of the time delay between the signal pairs was necessary to account for the requirements of the digital analysis. The effects of time delay removal on the analysis results vary depending on the type of analysis used and the magnitude of the time delay. For example, the idealized phase plot in Figure 3.7-7 shows the effect of not removing a positive time delay in the analysis to result in a sawtoothed curve starting at zero with a positive slope to 180° , then shifting to -180° and continuing with the same positive slope to $+180^\circ$ over the rest of the frequency range. The frequency at which the 180° phase shift occurs can be related to this time delay by

$$f_{180^\circ} = \frac{1}{2\tau}, \text{ where } \tau \text{ is the time delay} \quad (17)$$

Several time-delay peaks are also possible. Some of these may be in the negative direction as illustrated in Figure 3.7-8(a). Removal of each time delay from the cross-spectrum phase results in certain groups of frequencies being in phase as indicated by the horizontal portion of the spectrum in Figure 3.7-8(b). The negative-sloped region of the spectrum in the lower frequencies indicates that this region is out of phase for the time delay τ_1 , and that still a greater negative delay time is required to bring this region into phase. Removal of this second time-delay peak, τ_2 , in Figure 3.7-8(c), places the

Table 3.7-2. Time Series Computation Procedures for Cross-Correlation
Using Time/Data Analyzer with PDP 11/35.

Normalized Cross-Correlation

Internal-Internal

Block Size = 512 + 512 Zeros

Sample Rate = 25,600 sps

Sample Interval = 39 μ sec

Maximum Delay = \pm 0.01 sec

Internal-External

Block Size = 512 + 512 Zeros

Sample Rate = 3,200 sps

Sample Interval = 313 μ sec

Maximum Delay = 0.16 sec

Table 3.7-3. Time Series Computation Procedures for Coherence, Coherent Spectra, and Transfer Function Using Time/Data Analyzer with PDP 11/35.

Internal-Internal

Block Size	2,048 Samples
Sample Rate	12,800 s/sec
Resolution	6.25 Hz
Maximum Data	1,000 Hz
Record Length	8.0 sec

Internal-External

Block Size	2,048 Samples
Sample Rate	5,120 s/sec
Resolution	2.5 Hz
Maximum Data	2,000 Hz
Record Length	0.40 sec

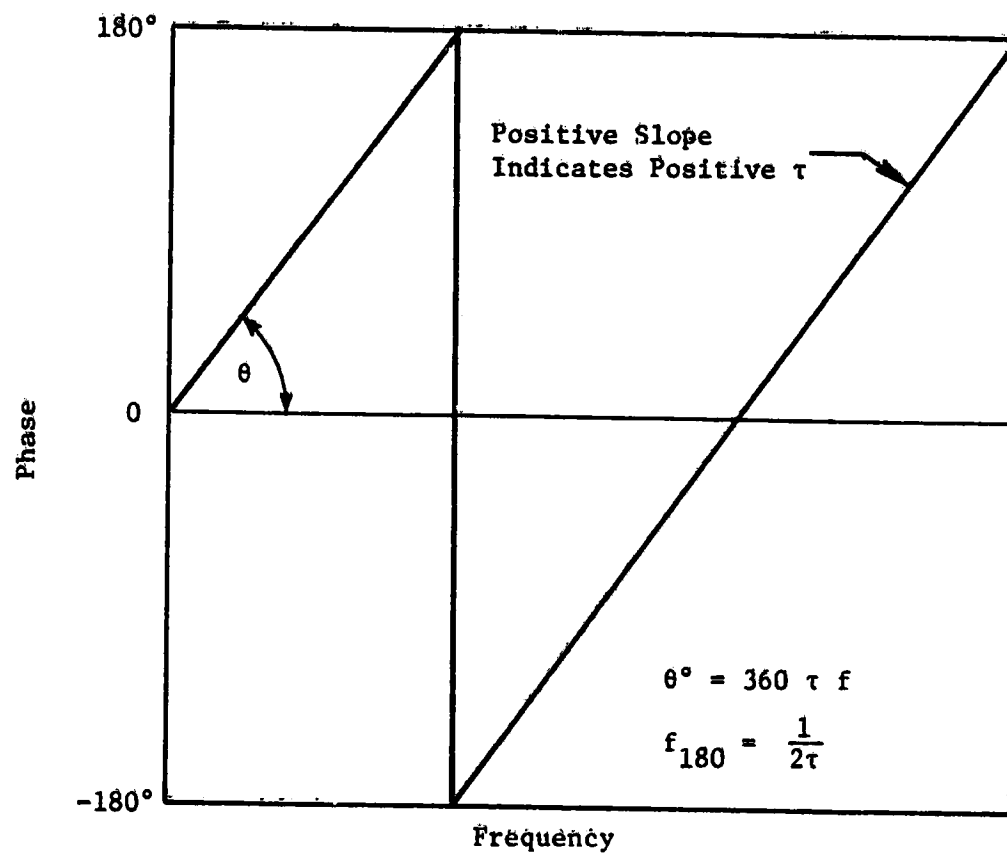


Figure 3.7-7. Effect of Not Removing Time Delay from Phase.

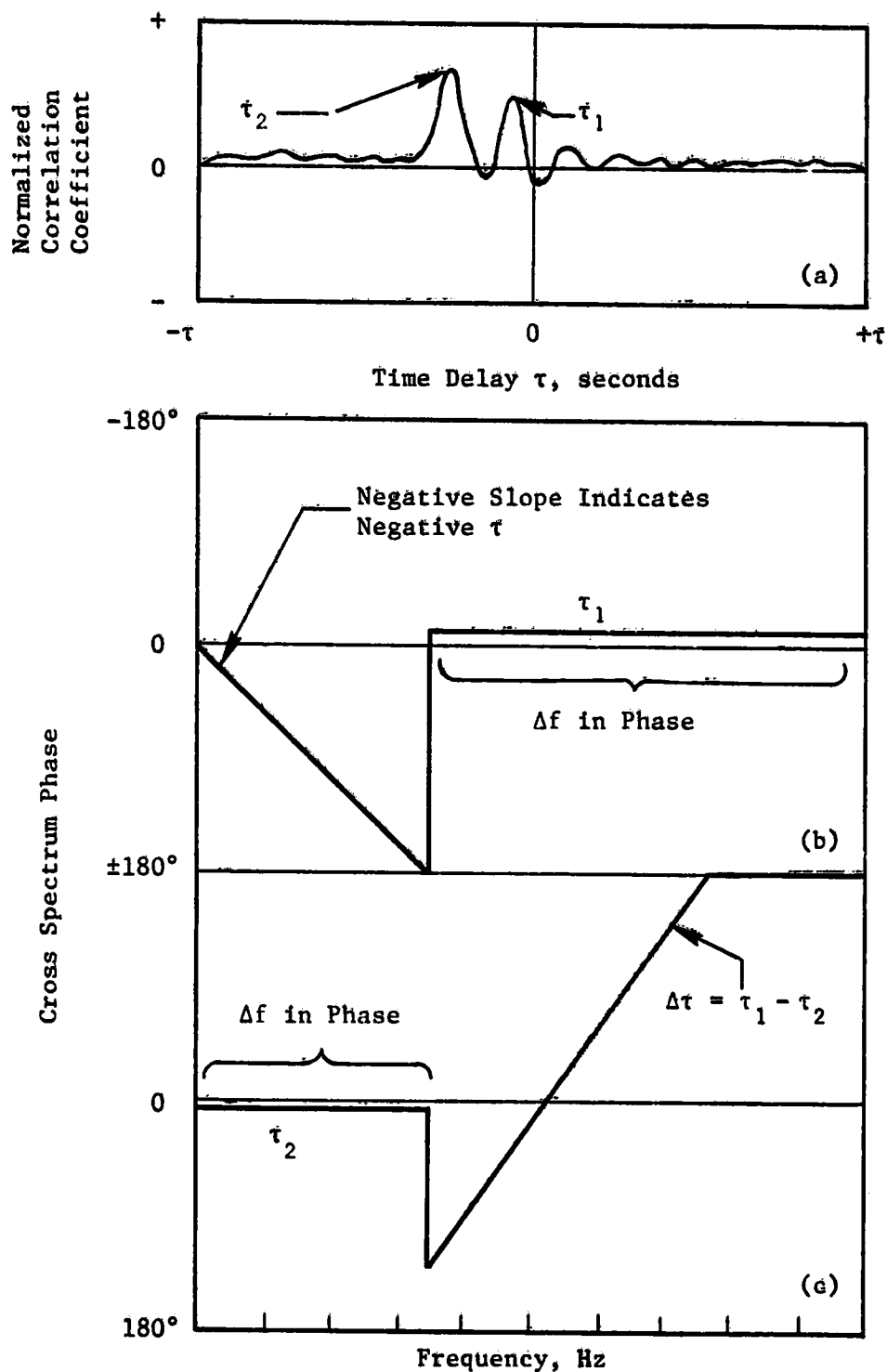


Figure 3.7-8. Effect of Removing Two Different Time Delays on Cross-Spectrum Phase.

lower frequency region in phase but not the higher frequencies. This region is now positively sloped, indicating a positive change in time delay is required for this region (less negative τ). These results indicate that different groups of frequencies are travelling at different time delays.

The effect on the coherence function determined with only one time delay removed is that they are not appreciably in error since the amount of the time delay difference is quite small, and the error associated with this difference is also small. Reference 5 gives a relationship for determining the effect of bias errors on coherence due to time delays as

$$\hat{\gamma}^2 = \gamma^2 \left(1 - \frac{\tau}{t}\right)^2 \quad (18)$$

where $\hat{\gamma}^2$ = Estimated (measured) value of the coherence function between two sensors

γ^2 = True value of the coherence function

τ = Time delay between two signals

t = Sample length (Equation 10)

The error estimate is

$$\frac{\hat{\gamma}^2}{\gamma^2} = \left(1 - \frac{|\tau|}{t}\right)^2 \approx 1 \quad \text{where } t = .16 \text{ sec}$$

Then, for some typical values of time delays as found in Figure 3.7-8 of $\tau_1 = -0.000625$ sec and $\tau_2 = -0.00250$ sec, the respective estimates on coherence are 0.99220 and 0.96899 of the actual value. Using only the primary time delay, and neglecting the multiple time delays in the coherence function, does not seriously influence the quality of the result. This is also true for the transfer function amplitude (gain).

The coherence function γ^2 , transfer function amplitude, expressed as gain, $|H|^2$ and transfer function phase angle ϕ in degrees were computed with a block size of 2048, in a sample bandwidth of 2.5 Hz over a record time of 40 seconds with 100 averages. The data are presented on a log frequency scale at frequencies from 50 to 1600 Hz. The high-frequency cutoff is at 2000 Hz. The log scale highlights the frequency regions of interest in each spectrum.

In order to minimize the large amount of error associated with the very low coherence levels with the number of averages set at 100 (which was the amount established as the optimum number of averages based on a trade between computational time and signal resolution), the data below coherence function values of less than 0.1 were ignored.

The transfer functions for the internal to far-field sensors were determined with the loss due to spherical divergence removed which allows for a clearer definition of any additional losses. The far-field transfer functions (amplitude) are denoted $|H^*|^2$, as opposed to the internal transfer functions $|H|^2$ which include all losses. The magnitude of the transfer function to the far-field is obtained from:

$$|H^*|^2 = |H|^2 - \frac{r^2}{R^2} \quad (19)$$

where r is the distance to the far-field microphone and R is the reference distance.

3.7.2.3 Error Evaluation of Time Series Estimates

The analysis methods used on the data have an inherent amount of error associated with each estimated value. The random error calculations used in this report are based on results formulated in Reference 6 dealing with single input/output problems. These error formulas are based primarily on the number of averages and on the magnitude of the parameter in question, and they are rederived versions of the formulas found in Reference 3.

- Coherent output spectrum estimates

$$\epsilon[\hat{S}] \approx [2 - \gamma^2]^{1/2} / |\gamma| \sqrt{M}$$

- Coherence function estimates

$$\epsilon(\hat{\gamma}^2) \approx \sqrt{2} (1 - \gamma^2) / |\gamma| \sqrt{M}$$

- Transfer gain factor estimates

$$\epsilon[|\hat{H}|^2] \approx 2(1 - \gamma^2)^{1/2} / |\gamma| \sqrt{2M}$$

- Transfer phase factor estimates

$$\Delta\hat{\phi} \approx \epsilon[|\hat{H}|]$$

In each case, the normalized random error formula is a function of the actual coherence function γ^2 , and the number of averages (M). The estimated value of γ^2 is used in place of γ^2 along with the number of averages to find the random error for each estimate.

These confidence-limit relationships are found in graphical form for 100 averages in Figures 3.7-9 through 3.7-11. Typical values of the coherence function estimates for the data ran from 0.8 to 0.1 which convert to maximum and minimum confidence limits on these graphs.

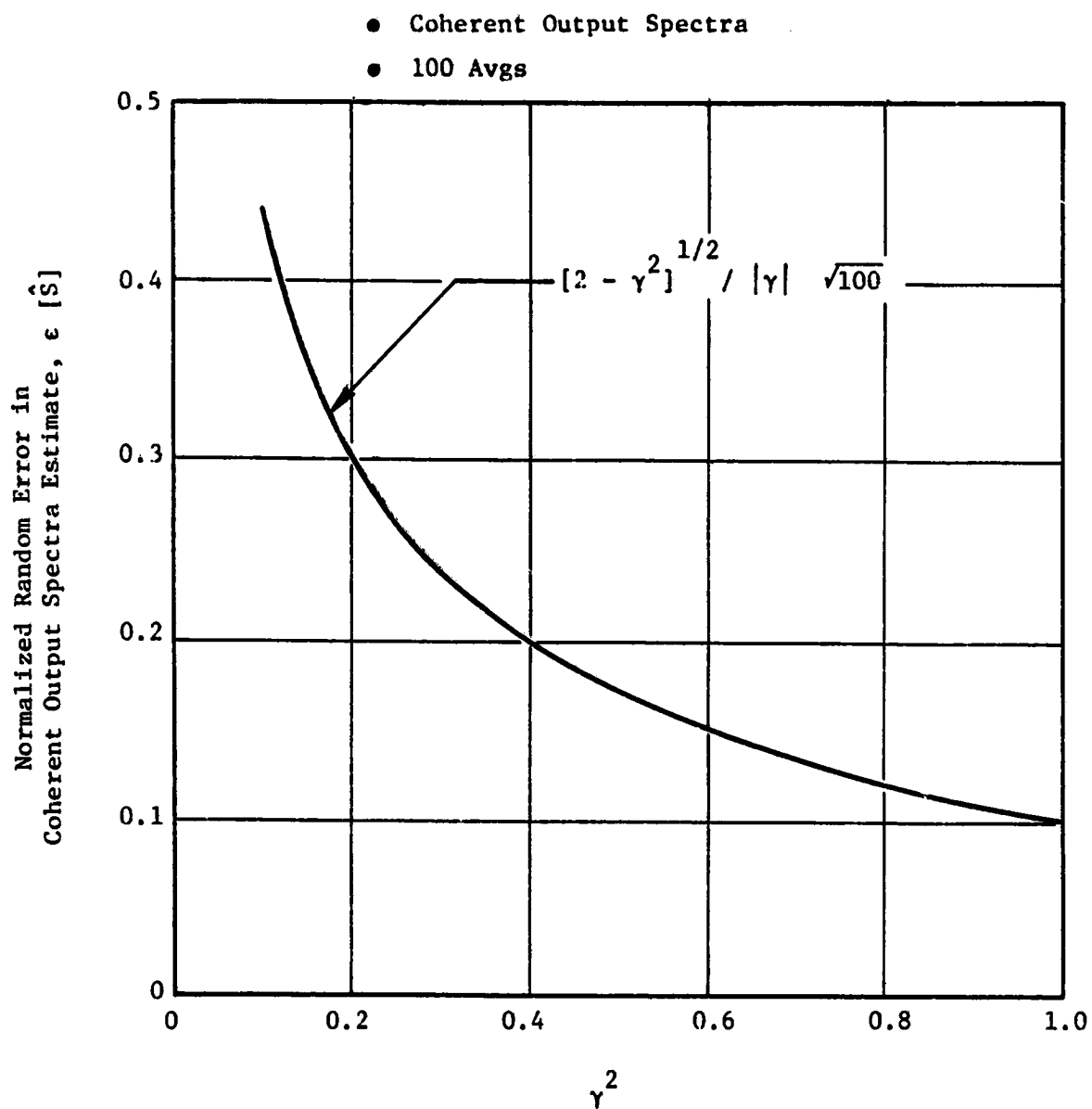


Figure 3.7-9. Coherent Spectra Error Estimates.

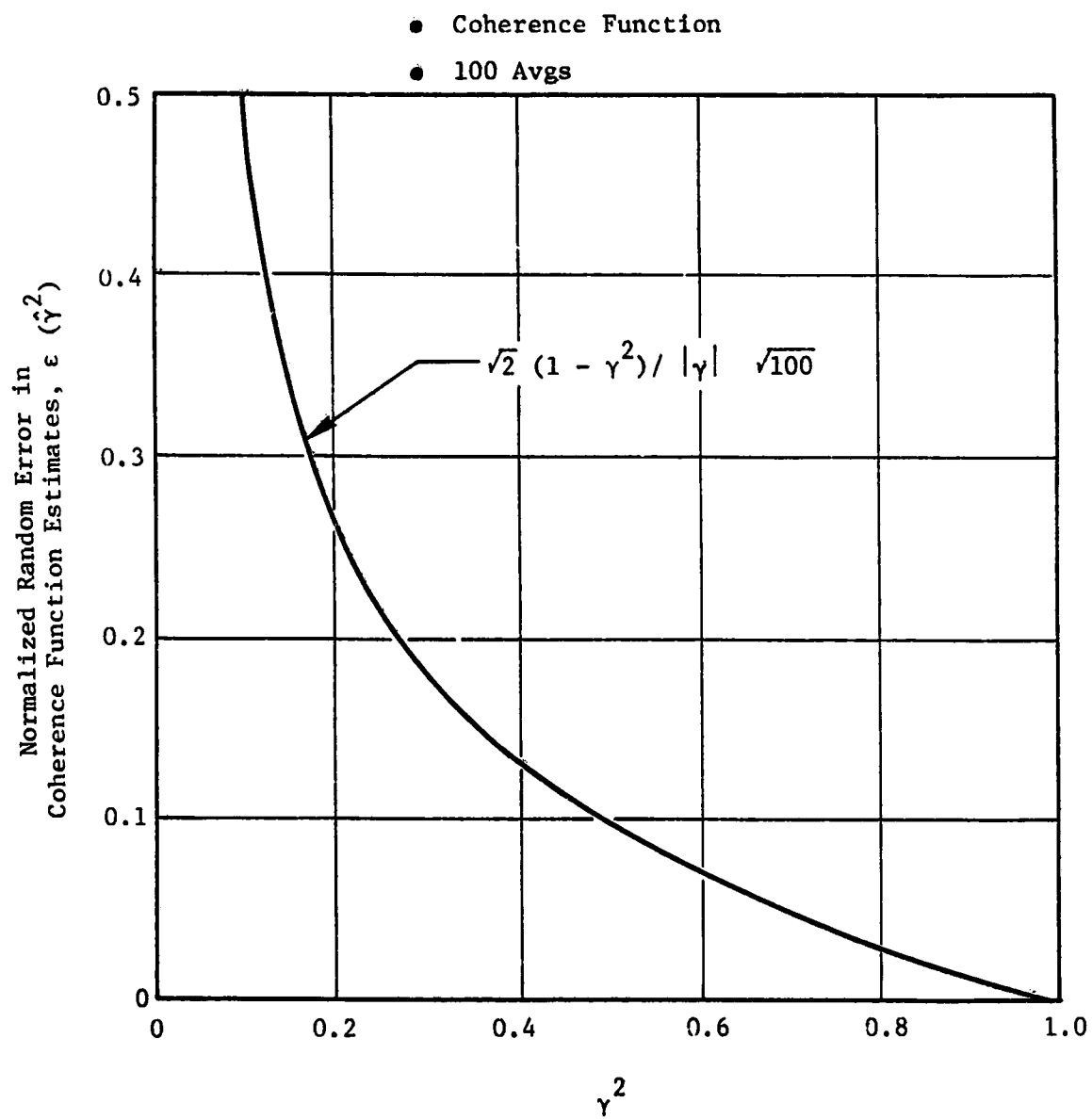


Figure 3.7-10. Coherence Function Error Estimates.

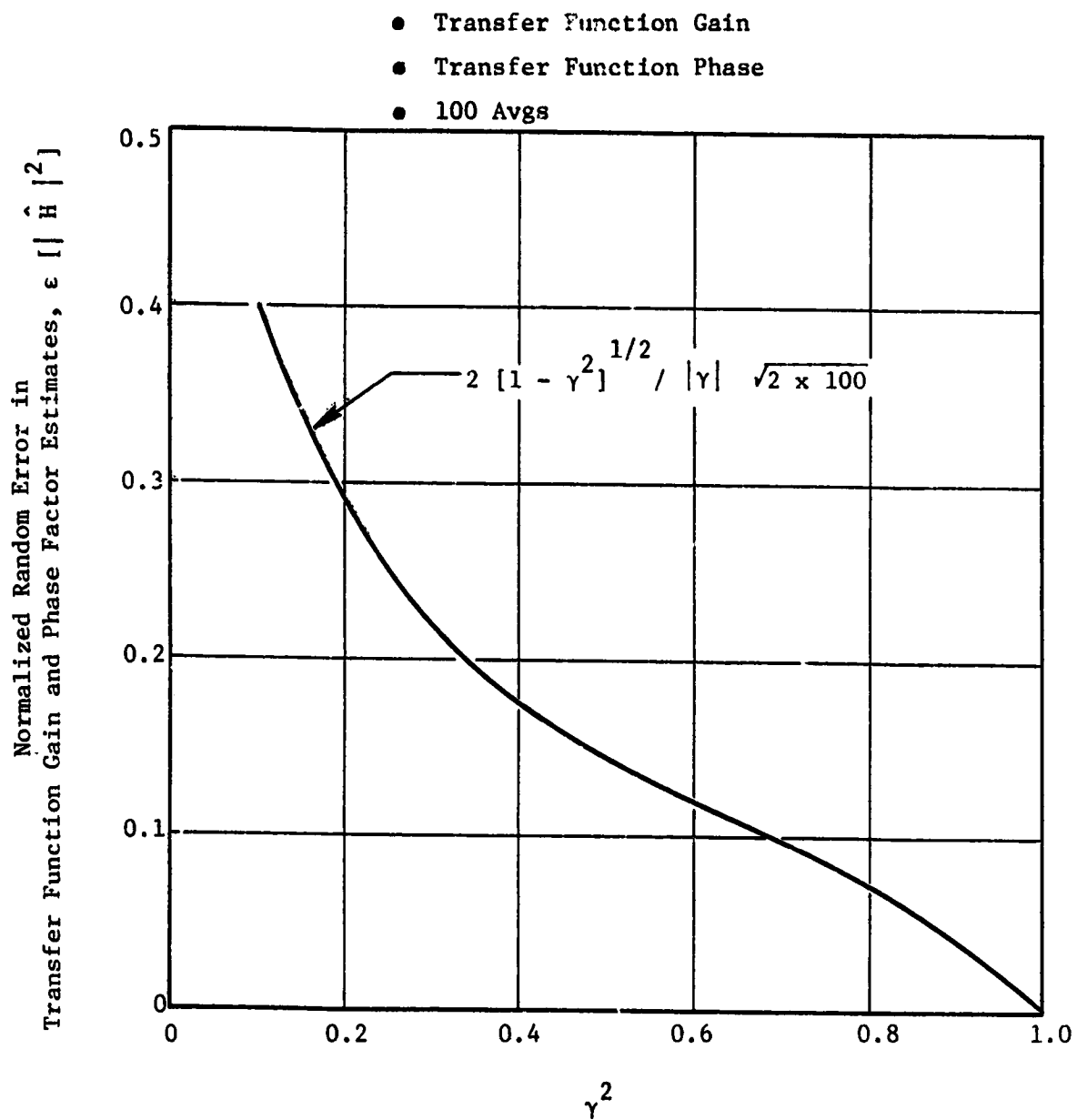


Figure 3.7-11. Transfer Function Gain and Phase Error Estimates.

3.7.3 Signal Polarity Identification

A requirement of this program was to provide a verification of signal polarity to each of the internal Kulites and far-field microphones simultaneously, in order to perform the phase analysis between internal to far-field sensors as detailed by the contract. This polarity verification was provided by a combination of an impulse signal input to all sensors simultaneously and through cross-correlations between sensors of known-to-unknown signal polarities.

Prior to actual engine running, a check of the microphone and Kulite signal polarities was made simultaneously on all sensors after all instrumentation had been set up. The acoustic instrumentation included 9 internal Kulites and 16 far-field microphones. A blast from a 12-gauge shotgun fired in the region of the core exhaust toward the center of the microphone array provided an impulse signal which was recorded on all tape recorder channels. The direction of the pressure pulse on the signal waveform was to indicate the polarity of each system.

A review of the impulse signal waveforms during data reduction showed varying degrees of clarity on the far-field microphone array. Clear pulses were evident on the 90° and 100° microphones which were of opposite sign as shown in Figure 3.7-12. The amplitudes of the impulse on the other microphones were less prominent, but also indicated polarity differences. The impulse signals on the internal Kulites were only discernible on the Plane 4.0 sensor and on the sound-separation probe in the core exhaust (Plane 8.0). Conclusive evidence of an impulse on the other internal sensors in the combustor and in the fuel nozzles was insufficient, primarily due to the sensor locations inside the engine and to the low sensitivities of the high-pressure Kulite systems (even with the amplifiers set at high gain).

The shotgun blast established the polarity of the 90° microphone to be negative (-) and that of the 100° microphone to be positive (+) as shown in Figure 3.7-12. The polarities of the Kulites in the core probe are similarly indicated from the shotgun blast to be of opposite sign as indicated in Figure 3.7-13. Probe element A displays a positive (+) pulse while probe element B suggests a negative (-) pulse.

Verification of the probe signal polarities was accomplished using cross-correlation analysis between each of the probe Kulites with the 90° and 100° microphones. Since cross-correlations between signals of the same polarity (either positive or negative) will give a positive amplitude to the correlation coefficient, R_{xy} , signals with opposite polarities processed through the cross-correlation procedure will yield a negative correlation coefficient. Therefore, a negative R_{xy} amplitude should occur for the cross-correlation between core probe A (+) to the 90° microphone (-), while the cross-correlation between core probe B (-) and the 90° microphone should be positive. Figure 3.7-14 shows test results at the 22.8% thrust power setting and verifies the anticipated cross-correlation results of the 90° microphone with the core

• Angle re to Fan Exit

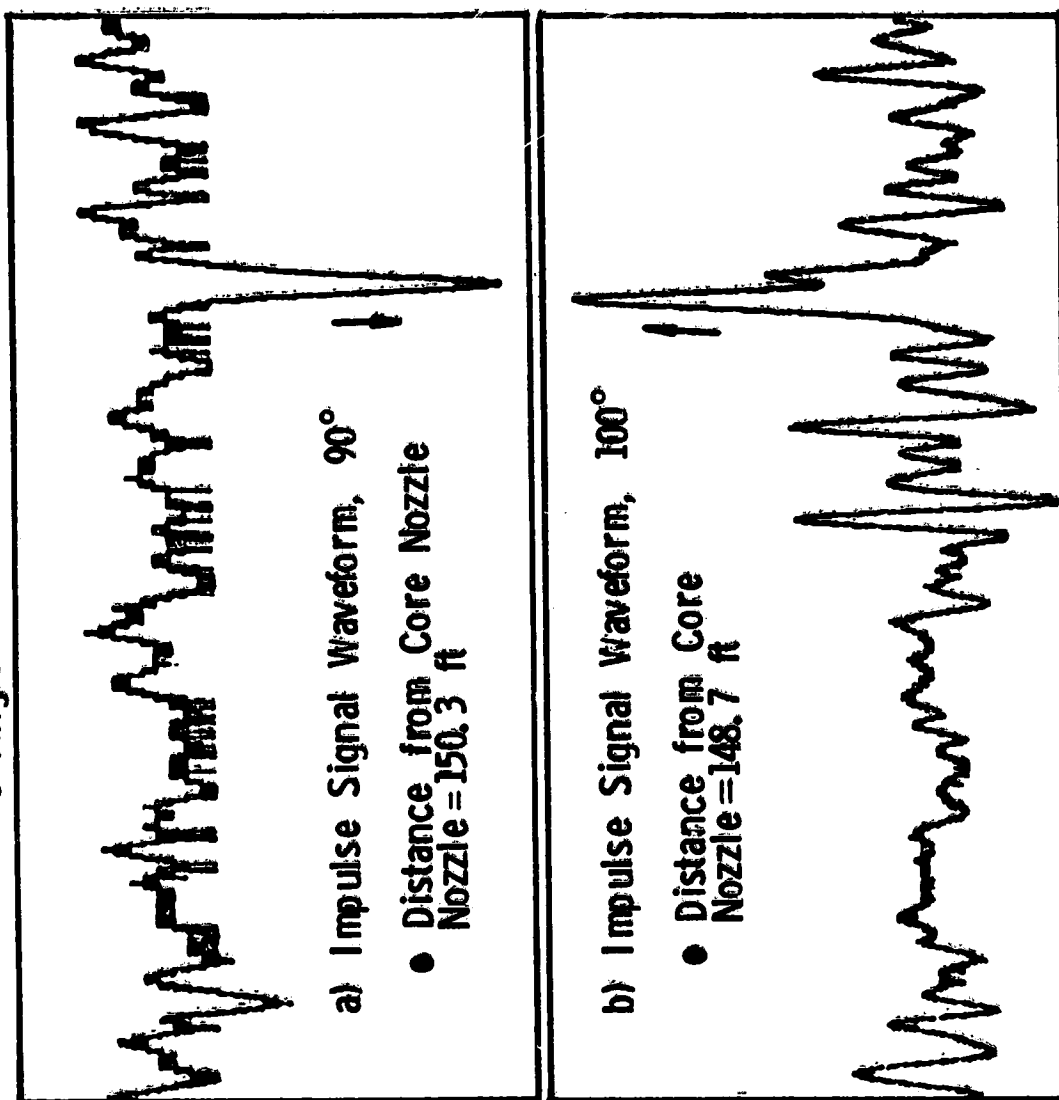


Figure 3.7-12. Polarity Check of Far-Field Microphones Using Shotgun Blast.

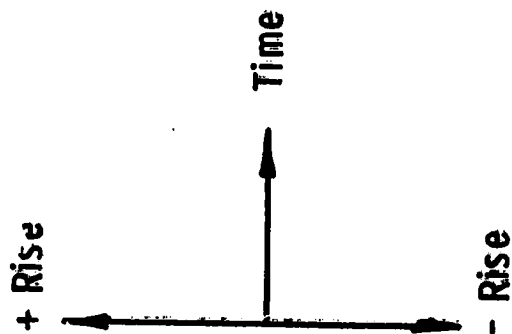
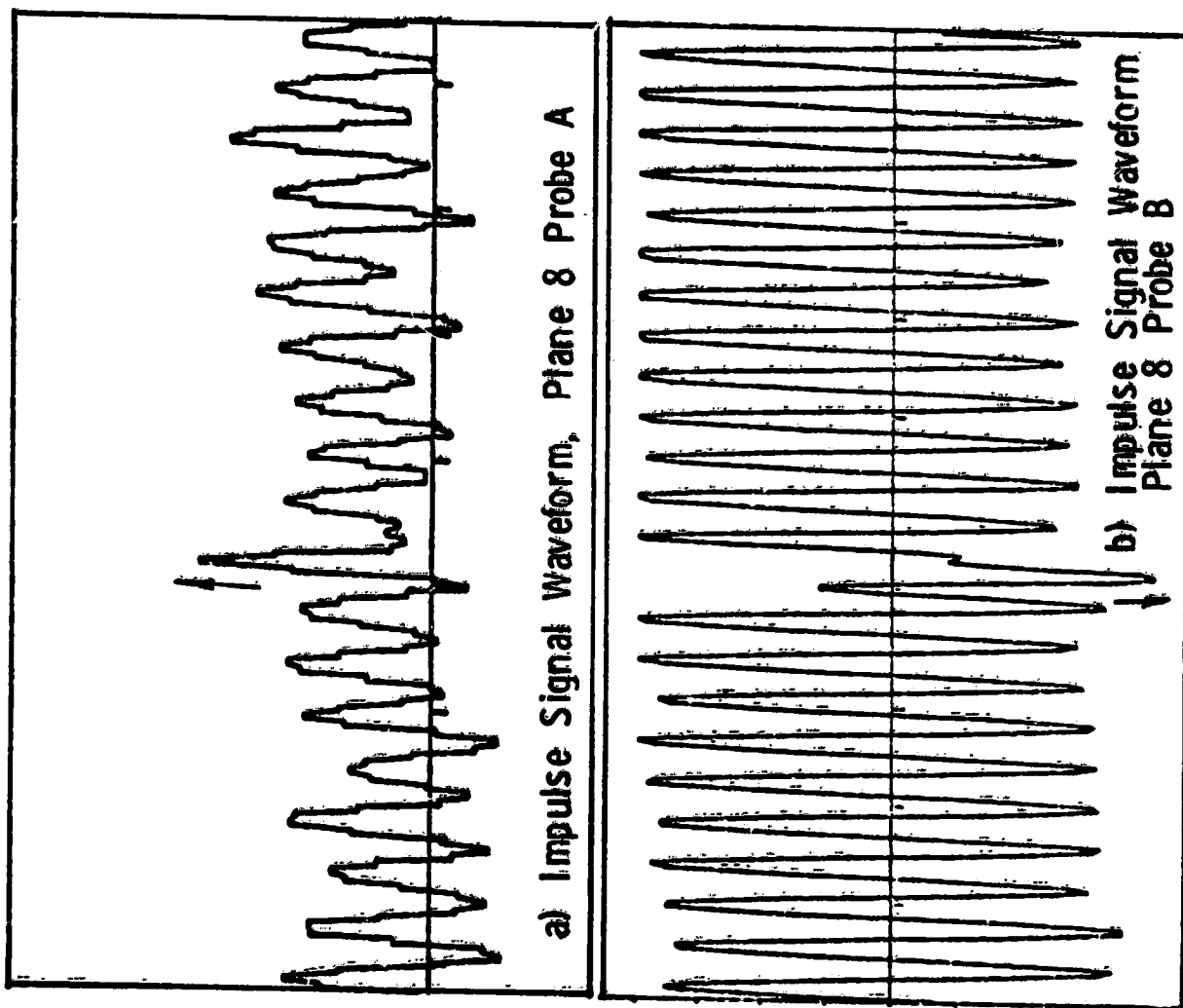


Figure 3.7-13. Polarity Check of Core Probe Kulites Using Shotgun Blast.

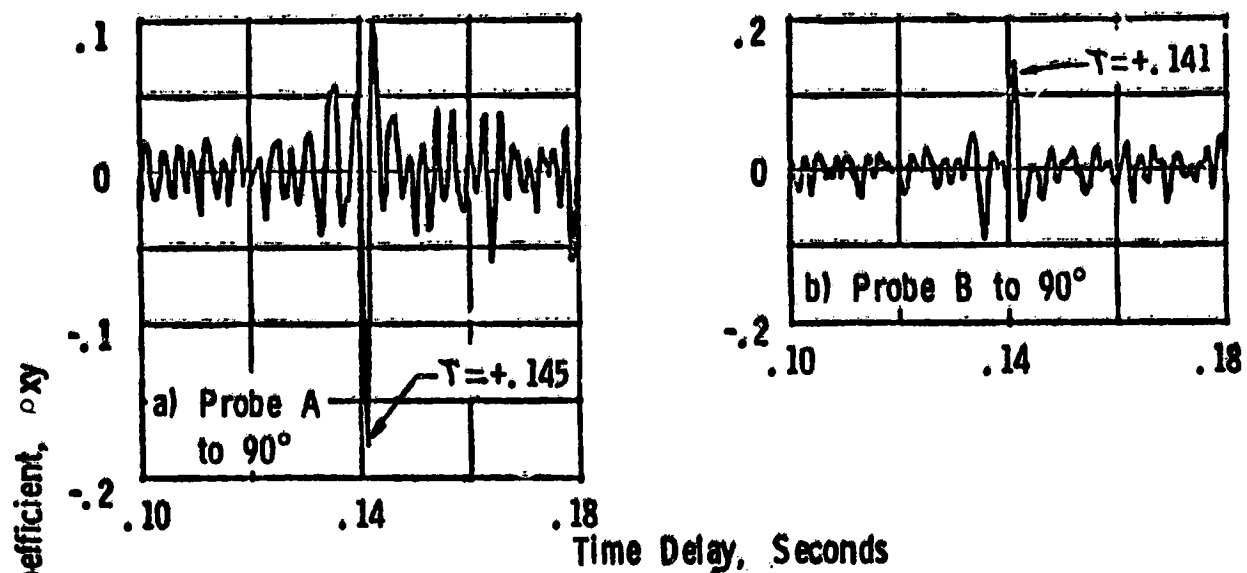


Figure 3.7-14. Cross-Correlation Between Core Probe and 90° Far-Field Microphone.

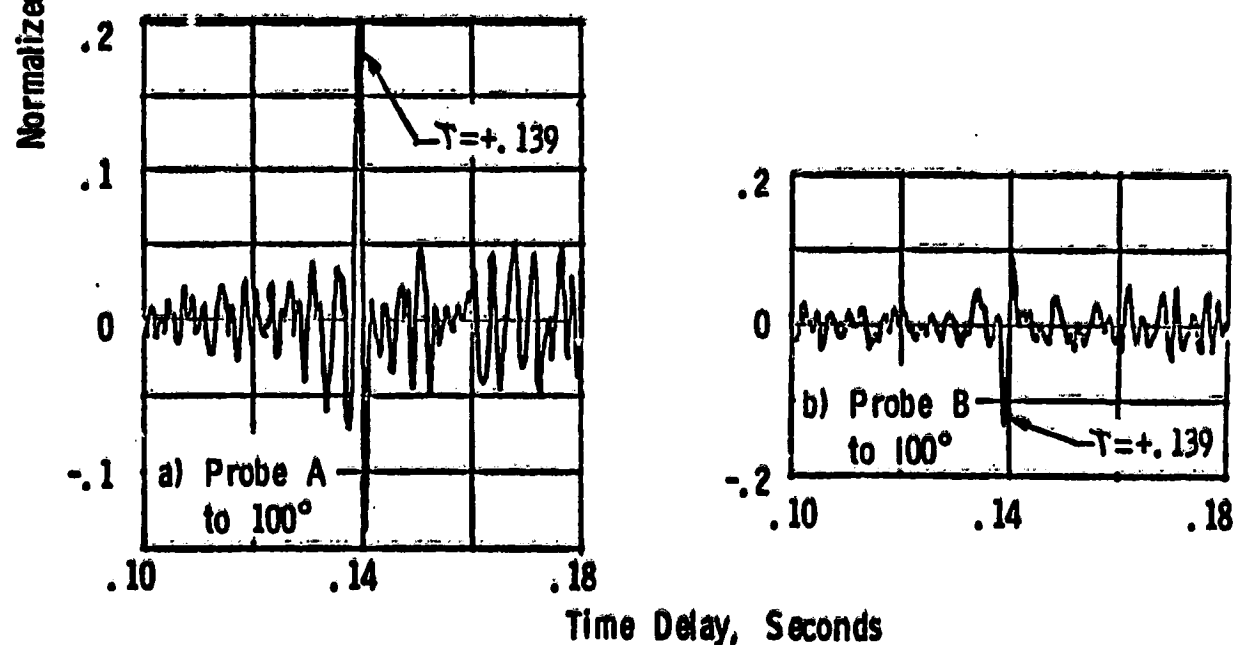


Figure 3.7-15. Cross-Correlation Between Core Probe and 100° Far-Field Microphone.

probe Kulites. Similar verification is apparent in Figure 3.7-15 from the results obtained at this condition with the 100° microphone (+) and the core probe Kulites. These results confirm the polarities of the core probe A as positive (+) and the probe B as negative (-). The polarities of the remaining far-field microphones were established using the cross-correlation results of core probe A with each microphone, as illustrated in Figure 3.7-16.

Six out of 15 microphones had negative (-) polarity. The setup of the B&K microphone systems included the 1.27 cm (0.5 in.) microphone head (Type 4134), cathode follower (Type 2615 or 2619) and power supply (Type 2801) set for 50Ω output impedance. Each system was single-end connected to the tape recorder amplifiers. A check of the individual 90° and 100° microphone systems as they were used in the field was made in the laboratory with the same results. This suggests that differences in the wiring and/or electronics resulted in reversed polarities with these systems, and that they must be checked prior to each setup.

The only clear impulse signal obtained from the shotgun blast with the internal sensors was at the Plane 4.0 sensor (92° from top, clockwise aft looking forward). Figure 3.7-17 illustrates the signal waveform for this sensor and indicates a positive pulse. Previous cross-correlation results between internal sensors from the Experimental Clean Combustor Program (ECCP), Phase III, at 30% thrust all gave positive correlation coefficients as indicated in Figure 3.7-18. The Kulites for the ECCP test were checked for polarity prior to the run by applying a known pressure to the reference side of each Kulite individually and observing the signal displacements to ensure that all had the same polarity (a positive pressure on the Kulite reference side gives a negative displacement if the sensor polarity is positive).

Cross-correlations between each of the internal waveguide sensors and the Plane 4.0 (92°) sensor of known positive (+) polarity for the 22.8% thrust condition for this program yielded results as shown in Figure 3.7-19. These results were in complete agreement with the ECCP Phase III results of Figure 3.7-18. The time delays associated with the average speed of sound between internal measurement locations were used to identify the correlation peaks which turned out to be of positive amplitude in each case and confirmed the positive polarity of the waveguide sensors.

The polarity of the fuel nozzle sensors was determined from cross-correlations between the individual fuel nozzles and their associated waveguide sensors at 42° and 102°. Results from this procedure indicated a positive polarity for both fuel nozzle sensors as shown in Figure 3.7-20. The polarity summary for the complete array of sensors used for the CF6-50 core noise measurements is listed in Table 3.7-4.

• Significance of Findings

1. If phase analysis is to be performed, the determination of signal polarity is critical. An impulse signal such as a blast from a shotgun, or horn, etc., recorded simultaneously on all channels

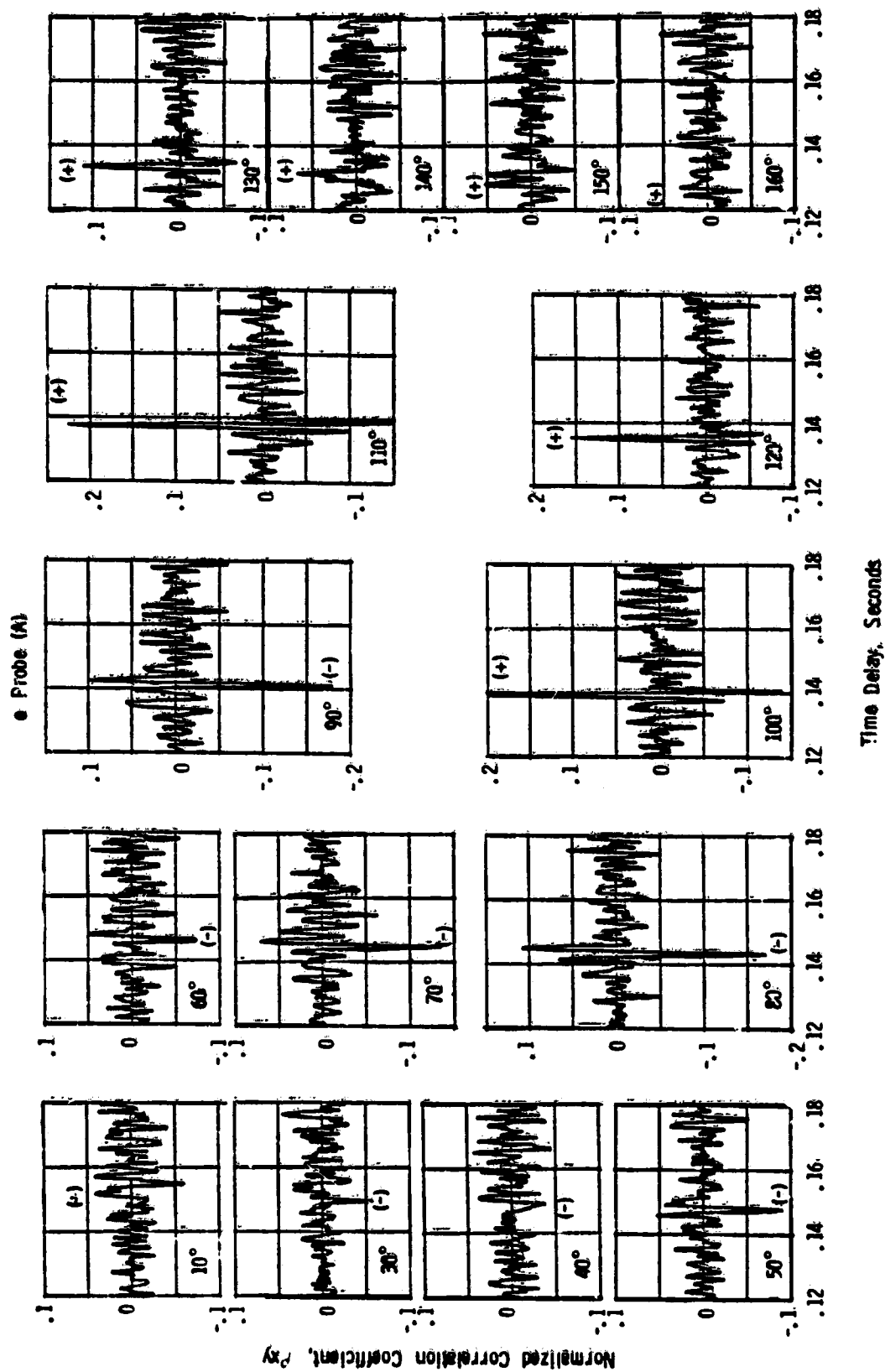


Figure 3.7-16. Far-Field Microphone Polarity Verification from Core Probe Cross-Correlations.

- CF6 - 50 Core Noise Program
- Impulse Signal Waveform, Plane 4.0, (92°)

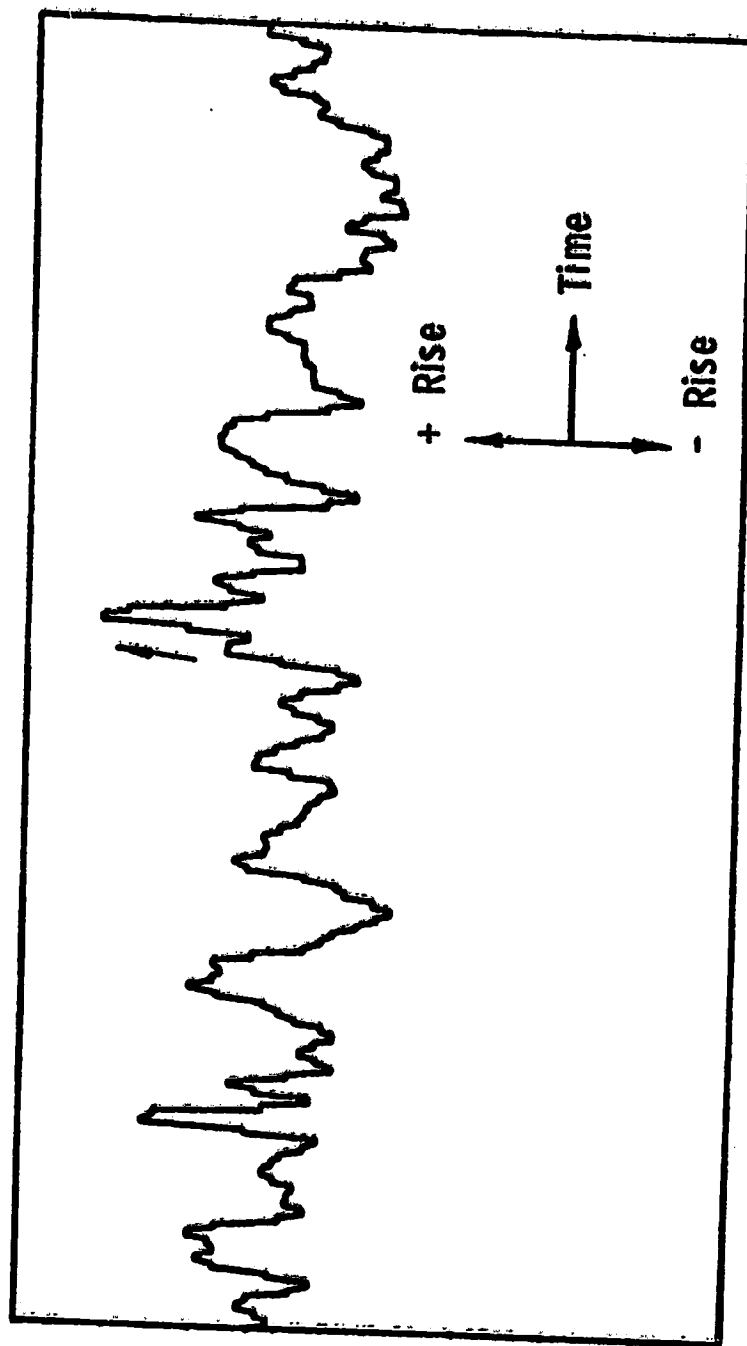
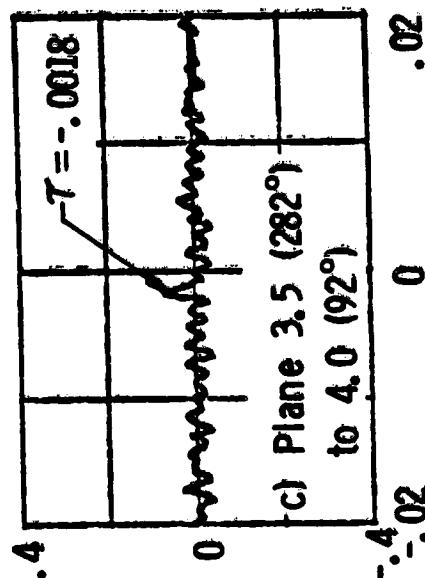
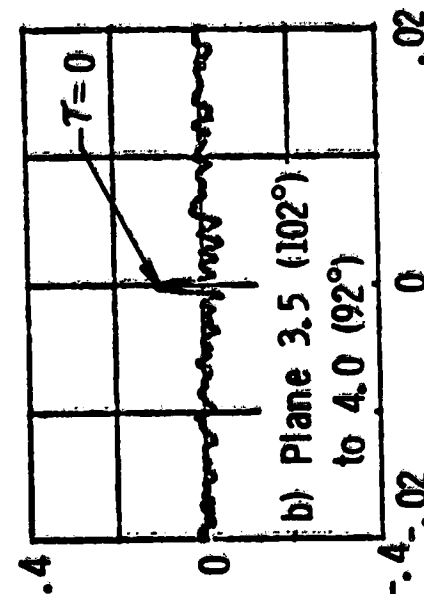
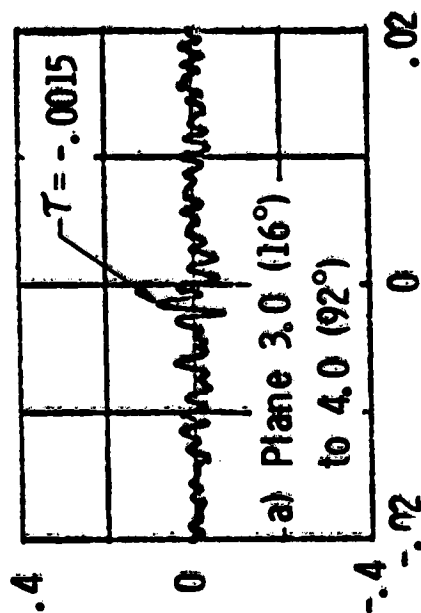


Figure 3.7-17. Polarity Check of Internal Sensors Using Shotgun Blast.

● NAS3 - 19736

● 30% Fm



Time Delay, Seconds

Figure 3.7-18. ECCP Phase III Cross-Correlation Results from Internal Combustor Sensors.

Normalized Correlation Coefficient, ρ_{xy}

● NAS3 - 21260

● 22.5% Fr

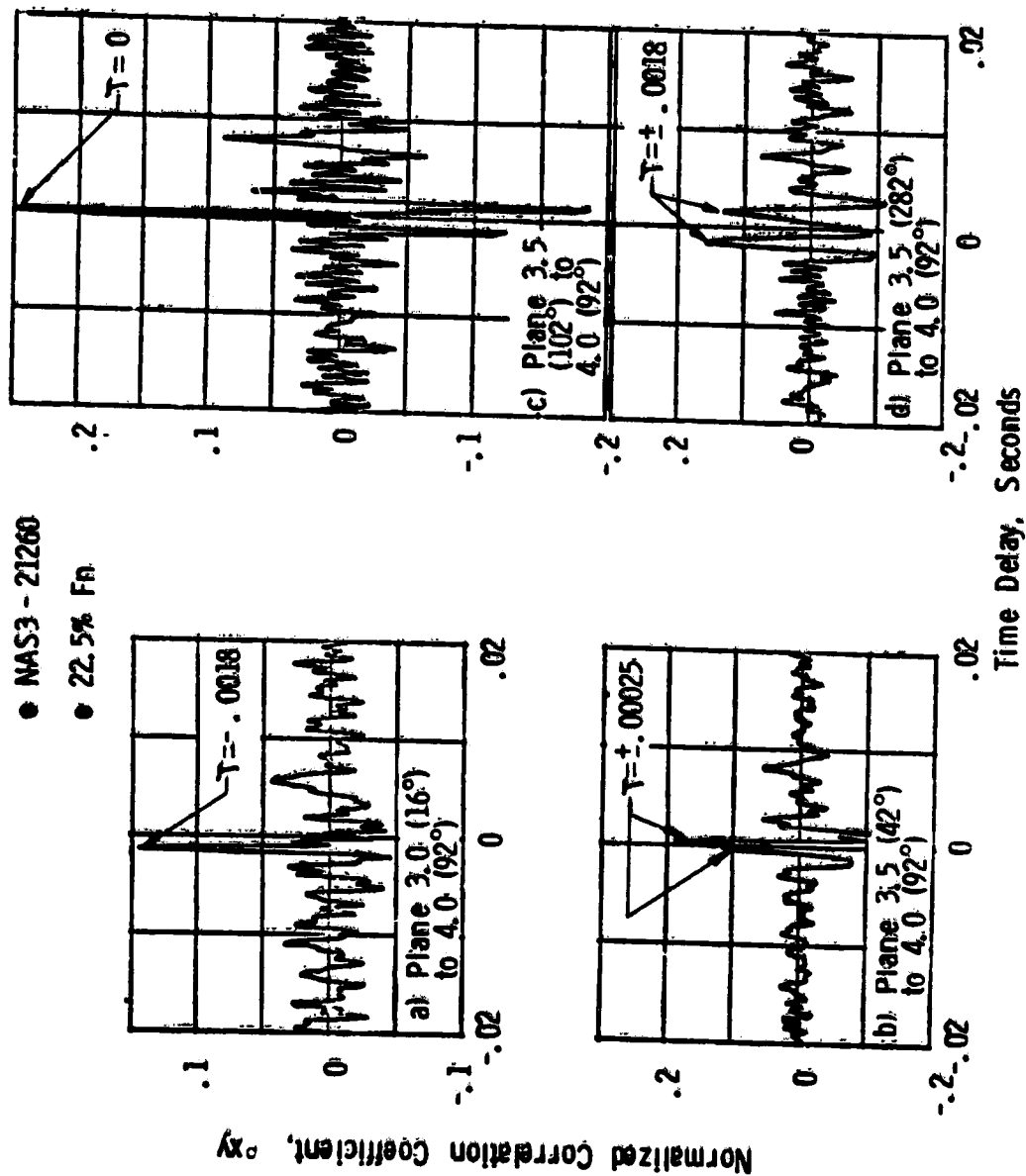


Figure 3.7-19. Cross-Correlation Between Upstream Combustor Sensors with Plane 4.0.

● NAS3 - 21260

● 22.5% Fn

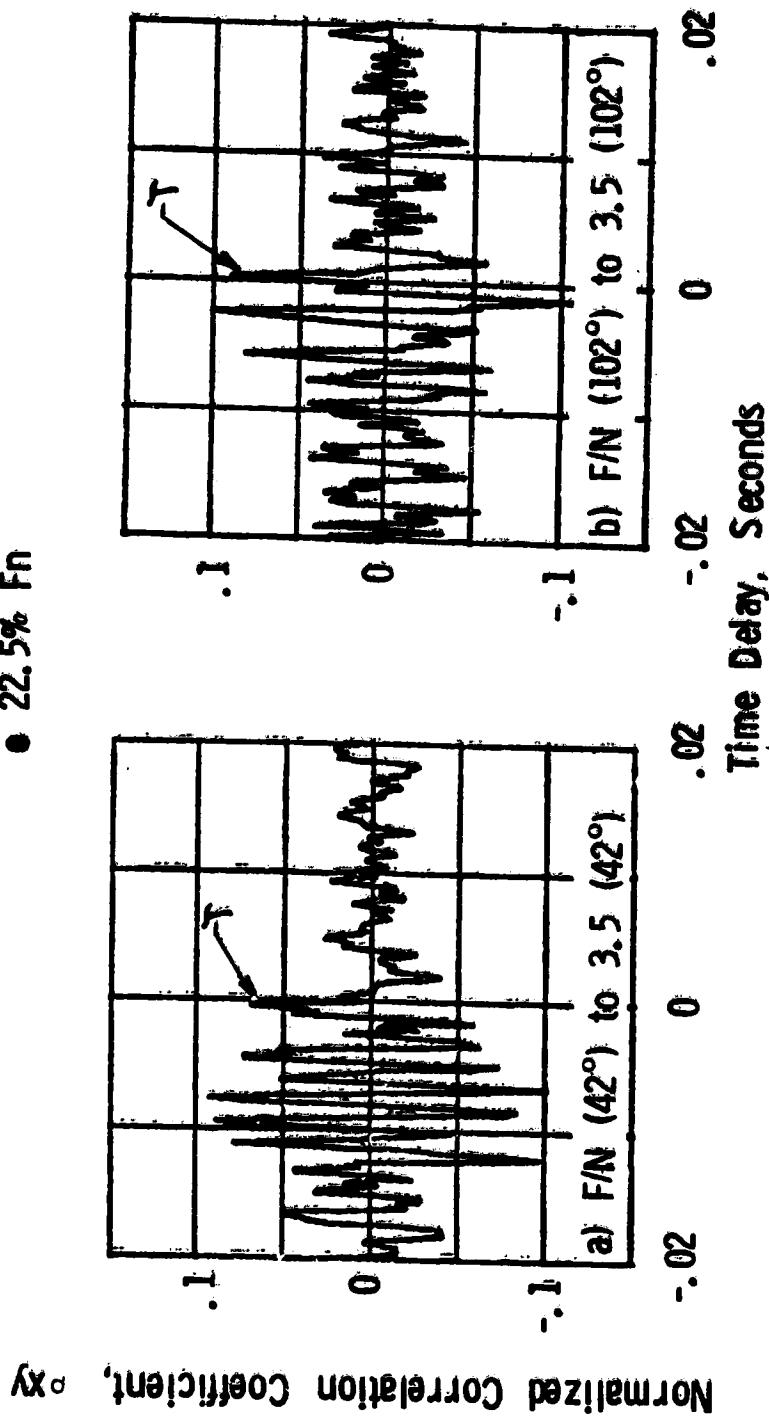


Figure 3.7-20. Cross-Correlations Between Fuel Nozzle Sensors and Associated Waveguide Sensors.

Table 3.7-4. Summary of Microphone and Kulite Signal Polarities for Core Noise Measurements.

<u>Sensor</u>		<u>Verified Signal Polarity</u>
<u>Microphone</u>	10°	+
	30°	-
	40°	-
	50°	-
	60°	-
	70°	-
	80°	-
	90°	-
	100°	+
	110°	+
	120°	+
	130°	+
	140°	+
	150°	+
	160°	+
<u>Kulite Plane</u>	3.0 (16°)	+
	Plane 3.5 (42°)	+
	3.5 (102°)	+
	3.5 (282°)	+
	Plane 4.0 (92°)	+
	Plane 8.0A. (270°)	+
	8.0B. (270°)	-
	Fuel Nozzle (42°)	+
	Fuel Nozzle (102°)	+

provides a quick setup and time-saving effort during a test run (as opposed to individual pressure checks to both Kulite and microphone systems).

2. Kulites should be pressure-checked for signal polarity during hookup by applying a positive pressure to the reference side of the transducer (gives negative displacement if polarity is positive).
3. Microphone systems are not always of the same polarity and must be checked.

3.7.4 Data Processing

3.7.4.1 Frequency Response Corrections

The internal and far field measurements obtained during the test run were corrected for frequency response, where applicable, as part of the data reduction procedure. The acoustic waveguide systems in the combustor region underwent ambient frequency response calibration using the plane-wave tube apparatus and procedure as described in Reference 2. The frequency response calibrations were required for these systems to account for probe losses resulting from the length of the standoff tube on each sensor. Typical frequency response calibration results are shown in Figure 3.7-21 for the waveguide sensors. Tabulation of the corrections for each 1/3-octave-band frequency is found in Table 3.7-5.

The flush-mounted Kulites located in the core exhaust probe and fuel nozzles did not require calibration since previous calibration for the acoustic probe showed a flat frequency response of up to 10 kHz over the range of interest. The fuel nozzle Kulite system frequency response for liquid measurement is typically flat up to 1000 Hz.

The far-field microphone systems were corrected for pink-noise frequency response which was recorded as part of the far-field system setup prior to test. These corrections were applied to the measured data during data reduction.

3.7.4.2 Power Level Calculation

The measured power level, $\bar{P}PWL_{meas}$, was calculated at each measurement plane assuming the entire fluctuating pressure measurement was acoustic signal propagating as a plane wave axially through the engine. The power level was calculated using Blokhintsev's results (as noted in Reference 7), for the acoustic intensity flux vector which can be written:

$$\vec{I} = \frac{p^2}{\rho c^3} (\vec{c} + \vec{V} \hat{e}_p) (\vec{c} \hat{e}_p + \vec{V}) \quad (20)$$

P , ρ , and c are used in the conventional sense, where \vec{V} is the absolute flow velocity and \hat{e}_p the unit vector normal to the acoustic wave front.

• Plane Wave Tube Calibration, Flush Mounted Reference Kulites

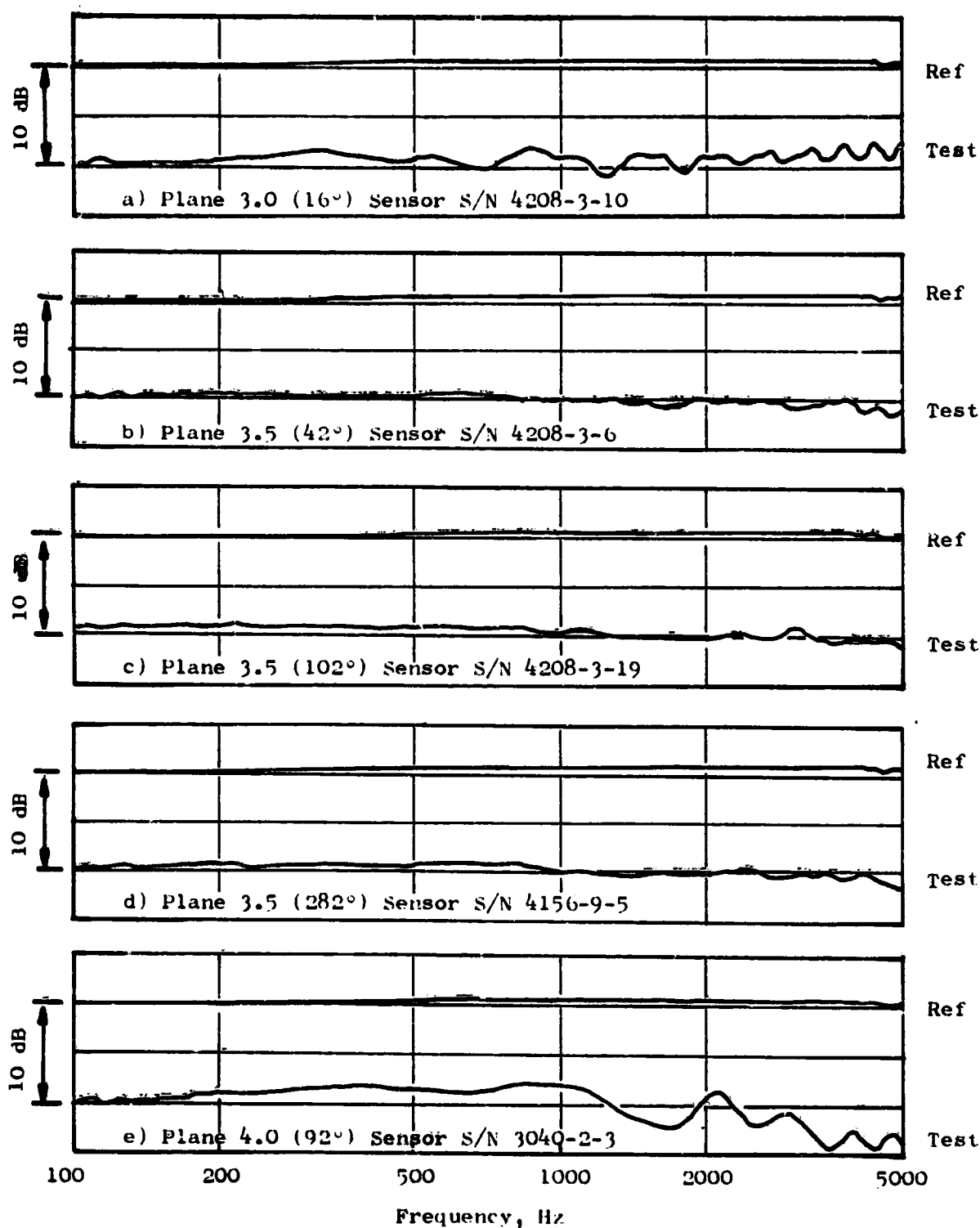


Figure 3.7-21. Ambient Frequency Response Results from Combustor Waveguide Sensors.

Table 3.7-5. Ambient Frequency Response Corrections for CF6-50 Core Noise Waveguide Sensors.

Frequency, Hz	Plane 3.0 16°	Plane 3.5			Plane 4.0 92°
		42°	102°	282°	
50	0	0	0	0	0
63	0	0	0	0	0
80	0	0	0	0	0
100	0	-0.1	-0.8	-0.3	0
125	-0.2	-0.5	-1.0	-0.2	-0.3
160	-0.3	-0.4	-1.0	-0.5	-0.5
200	-0.6	-0.5	-1.0	-0.6	-0.9
250	-1.0	-0.4	-1.0	-0.5	-1.3
315	-1.5	-0.1	-1.0	-0.6	-1.5
400	-0.8	0	-0.9	-0.3	-1.7
500	-0.5	-0.1	-0.8	-0.2	-1.2
630	0.3	0	-0.6	-0.2	-0.8
800	-0.9	0.4	-0.6	-0.2	-1.4
1000	-0.4	0.7	0.1	-0.6	-1.3
1250	1.6	0.8	0.4	1.1	0.4
1600	-0.3	1.1	0.5	0.8	2.7
200	-0.3	0.8	0.5	0.8	-0.3
2500	-2.5	0.8	0.5	0.8	2.7
3150	-0.5	1.4	0	0.9	2.7
4000	-0.3	1.0	0.7	1.0	3.1
5000	-1.7	2.1	1.2	2.1	4.3

• Applied to Measured 1/3-Octave-Band Values

We are interested primarily in the axial component, hence

$$\begin{aligned}
 I_x &= \vec{I} \cdot \hat{e}_x \\
 &= \frac{p^2}{\rho c} (c + \vec{V} \cdot \hat{e}_p) (c \hat{e}_p + \vec{V}) \cdot \hat{e}_x \\
 &= \frac{p^2}{\rho c} (1 + M \cos \theta) (\cos \theta + M \cos \phi)
 \end{aligned} \tag{21}$$

where θ and ϕ are the angles made by the acoustic wave front and the flow with the axial direction. M is the flow Mach number. The flow at the measuring planes is near axial and if a plane wave assumption is used here,

$$I_x = \frac{p^2}{\rho c} (1 + M)^2 \tag{22}$$

The plane-wave assumption also permits the acoustic power to be computed from a measurement at any point of the cross section. Using a consistent set of reference pressure (P_0) and specific impedance ($\rho_0 c_0$), the acoustic power level (PWL referenced to 10^{-13} watts) is given by:

$$PWL = SPL + 20 \log (1 + M) + 10 \log \left(\frac{\rho_0 c_0}{\rho c} \right) + 10 \log A + 9.9 \tag{23}$$

or

$$PWL = SPL + 20 \log (1 + M) + 10 \log \left(\frac{P_0}{P_S} \sqrt{\frac{T_S}{T_0}} \right) + 10 \log A + 9.9 \tag{24}$$

where SPL = sound pressure level re 2×10^{-5} N/m²

P_S, T_S = static pressure and temperature at the measuring station

P_0, T_0 = ambient (standard day) pressure and temperature

A = cross-sectional area in m²

3.7.4.3 Engine Measurements Verification

The data acquired during the core noise measurements on the CF6-50 engine were checked to ensure the validity of the measurements. The far-field data from the low microphones were compared to previous test results obtained from a similar test setup and found in shape and level to agree within ± 2 dB. On-line 10-Hz narrowband spectra from the internal measurements on the CF6-50 engine with the standard combustor were compared to similar spectra obtained for the same sensor locations on a previous test with a double annular combustor. The levels were of the same order of magnitude for both tests.

The core probe overall FPWL (re 10^{-13} watts) was compared to the far-field power levels to evaluate the region of potential core noise dominance over the engine operating line. The far-field results are from standard day and free-field corrected data obtained from measurements around a 45.72 m (150 ft) arc. Both sets of data are for the low-frequency region between 50 to 2000 Hz. Figure 3.7-22 illustrates the results of the core probe FPWL plotted against core velocity and the far-field PWL plotted against the effective jet velocity (V_e) brought about by the merging of the fan and core streams. This velocity V_e was determined from the fan bypass ratio (BPR) and jet velocities of the fan (V_{18}) and core (V_8) streams using:

$$V_e = \frac{(BPR) V_{18} + V_8}{BPR + 1} \quad (25)$$

The figure shows that the core-generated power dominates the lower velocities below approximately 230 m/sec (755 ft/sec). This corresponds to conditions below 45% F_n . The engine generated power level at velocities above 230 m/sec (755 ft/sec) is primarily controlled by jet noise. These results suggest that the most promising conditions for core noise investigation are at the power settings of approach and below. Above approach, the other engine noise sources overtake the core noise. This observation parallels those for a similar comparison reported in Reference 8.

• CF6-50 Engine Test

• $\Delta f = 50 - 2000 \text{ Hz}$

○ Core Probe (A) FPWL

□ Far-Field PWL at $V_e = \frac{(BPR) V_{18} + V_8}{BPR + 1}$
(Tone Corrected)
(feet/second)

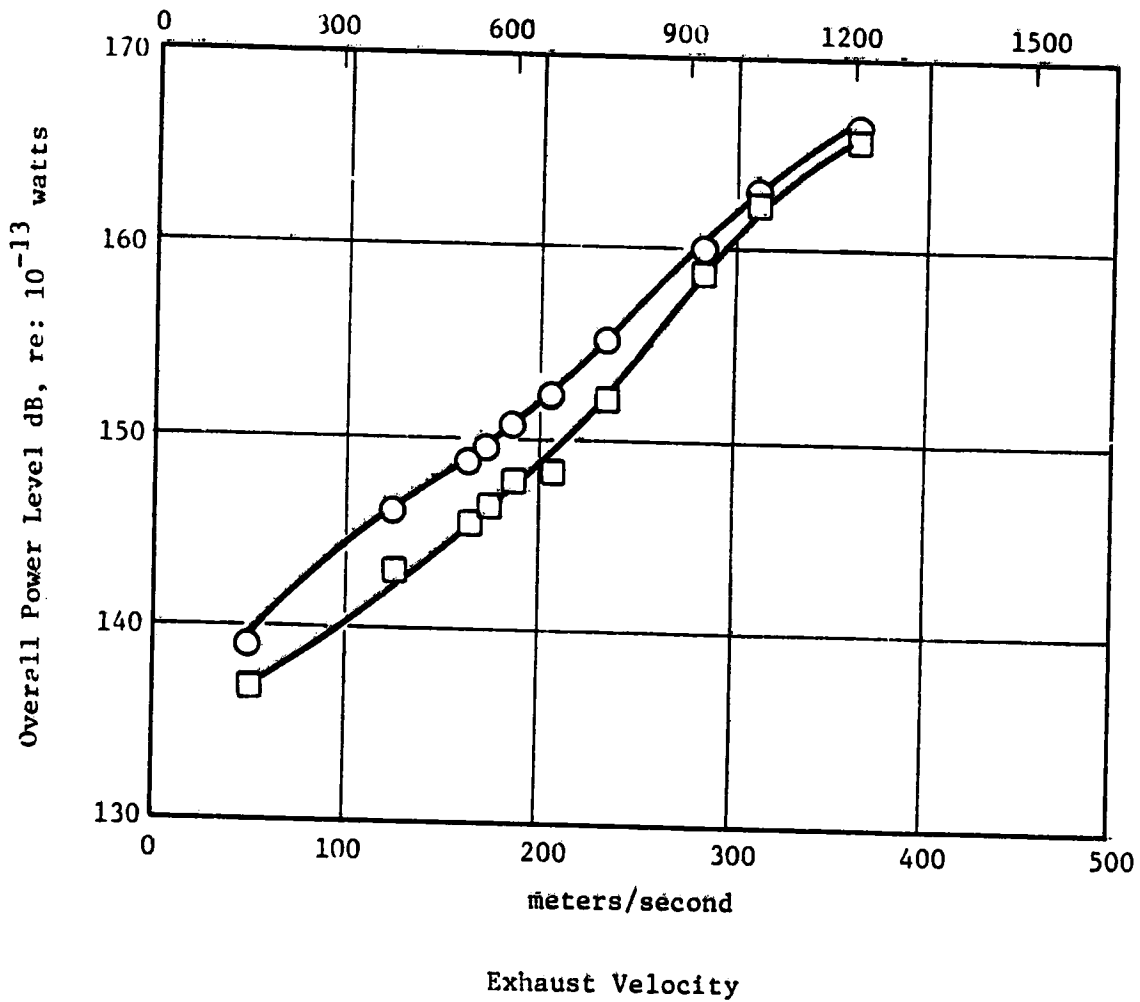


Figure 3.7-22. Comparison of Core Probe Power Levels with Far-Field Measured Power Levels.

4.0 ANALYSIS AND DISCUSSION OF RESULTS

4.1 DIRECT ANALYSIS OF ENGINE ACOUSTIC MEASUREMENTS

The engine acoustic measurements obtained from the core noise test of the CF6-50 were processed through 2-Hz narrowband and 1/3-octave-band analysis procedures to display pressure spectra from each sensor at all test conditions. A direct analysis of these spectra was performed to (1) identify characteristics common to internal and far-field measurements, (2) compare internal spectra with similar engine measurements previously acquired in a test cell (ECCP Phase III, Reference 2), and (3) compare engine to full-scale annular combustor rig results with a standard production-type combustor (ECCP Phase II, Reference 1). Table 4.1-1 summarizes the ECCP Phases II and III test points for comparison with the core noise program test data. Tabulations of required aerodynamic performance parameters are included in this subsection.

4.1.1 Internal and Far-field Spectra Comparison

The internal and far-field measurements processed as 2-Hz narrowband spectra were obtained directly from the measured data. The 1/3-octave-band spectra from the internal sensors are corrected for ambient frequency response only, while the far-field measurements are corrected to 288.3 K (59° F), 70% R.H. standard day and free-field conditions.

The internal spectral comparisons were made over five representative test conditions covering the complete engine sea level static operating range and included 3.8% (idle), 22.8, 30.8% (approach), 67.8 and 99.8% (takeoff) net thrust settings (% F_n). Comparisons of the fuel nozzle spectra with the associated spectra from the waveguide probes included an additional low power point at 15% F_n . Similar comparisons with the far-field spectra included all of the above six power settings. The narrowband and 1/3-octave-band spectra for all sensors at each of the original eight data points in the test matrix are found in Reference 4.

The internal measurements consist of fluctuating pressures and include both turbulence and sound (FPL spectra). The far-field measurements are considered to represent the engine acoustic signature which is comprised of many sources (i.e., fan, combustor, turbine and jet, etc.). The turbulent contribution, however, is not present due to the distant location of the microphones in the far field. The far-field spectra, therefore, are sound pressure level (SPL) spectra.

4.1.1.1 Internal Measurements

The purpose of the internal spectra comparison was to identify characteristic trends in the fluctuating pressure level spectra that might be observed in the far field.

Table 4.1-1. Test Conditions for Comparison of CF6-50 Core Noise Results with ECCP Phases II and III.

Condition	Program Identification	Rdg No.	f/a	Metric Units					
				PT3 atm	TT3 K	W3 kg/sec	PT4 atm	TT4 K	(W/TT ³ /PT ³) (Kg √K/sec-atm)
Idle	Core Noise ECCP Ph III	544	0.0101	3.14	419.4	12.5	3.02	826.7	81.5
		6	0.0156	2.95	442.8	12.5	2.85	1042.8	89.2
Approach	Core Noise ECCP Ph III ECCP Ph II	551	0.0131	11.65	602.2	49.9	11.12	1097.2	105.1
		39	0.0166	11.48	642.8	45.0	10.98	1256.7	99.4
		317	0.0141	6.87	661	29.9	6.45	1174	111.9
Takeoff	Core Noise ECCP Ph III ECCP Ph II	567	0.0230	28.31	772.2	95.3	27.08	1516.1	93.5
		33	0.0275	26.95	830.6	88.9	25.76	1733.3	95.1
		321	0.0229	9.59	811.0	33.1	9.16	1583	98.3

Condition	Program Identification	Rdg No.	f/a	English Units					
				PT3 psia	TT3 ° R	W3 lb/sec	PT4 psia	TT4 ° R	(W/TT ³ /PT ³) (ft ² /° R/sec)
Idle	Core Noise ECCP Ph III	544	0.0101	46.16	755	27.6	44.39	1488	0.1141
		6	0.0156	43.36	797	27.6	41.90	1877	0.1248
Approach	Core Noise ECCP Ph III ECCP Ph II	551	0.0131	171.26	1084	110.0	163.46	1975	0.1468
		39	0.0166	168.76	1157	99.2	161.41	2262	0.1388
		317	0.0141	100.99	1190	65.9	94.82	2113	0.1563
Takeoff	Core Noise ECCP Ph III ECCP Ph II	567	0.0230	416.16	1390	210.1	398.08	2729	0.1307
		33	0.0275	396.16	1495	196.0	378.67	3120	0.1328
		321	0.0229	140.97	1460	73.0	134.65	2849	0.1374

Plane 3.0, Compressor Discharge

The Plane 3.0 sensor, located in the Madar port between the diffuser struts (16° clockwise from top, aft looking forward), measures fluctuating pressures from the compressor and combustor regions. Figure 4.1-1 shows the 2-Hz narrowband FPL spectra to 2000 Hz for the Plane 3.0 waveguide probe and illustrates the spectra variation with engine core speed. Predominant frequency regions appear between 200 to 400 Hz and 700 to 1300 Hz. The 1/3-octave band spectra shown in Figure 4.1-2 for the compressor discharge plane reflect the high-energy, dual-frequency regions at higher power settings.

Plane 3.5, Combustor Inlet

The three waveguide-type sensors, located at the combustor inlet plane in the 42°, 102°, and 282° borescope inspection ports, all displayed similar spectral shapes and FPL's indicating circumferential uniformity of the fluctuating pressures in this region, which is just aft of the fuel nozzles and ignitors. Typical 2-Hz narrowband results from the sensor at the 282° position are shown in Figure 4.1-3 for five representative conditions including idle (3.8% F_n), approach (30.8% F_n), and takeoff (99.8% F_n) power. A general increase in FPL is apparent with increasing speed. A bilobed characteristic is evident above idle setting in the frequency regions between 200-500 and 900-1300 Hz. A similar observation is noted from the 1/3-octave-band results in Figure 4.1-4.

Fuel Nozzle Sensors

Two fuel nozzles located at the 42° and 102° positions were instrumented with Kulite transducers. Measurements of liquid (fuel) pressure pulsations were made along with the fluctuating pressure measurements acquired with the waveguide sensors in the gaseous media. Comparisons were made of the spectra from the fuel nozzles and associated waveguide sensors in the same vicinity, using a common fluctuating pressure level (FPL) reference pressure of 2×10^{-5} N/m², ignoring the impedance difference between the liquid and gas. As such, the fuel nozzle spectra were used to compare signal content and shape rather than absolute magnitude.

Fuel System Operation

The CF6-50 fuel system, as related to the combustor noise measurements, consists of the main fuel pump, main engine control, fuel manifold, and fuel nozzles.

The main fuel pump is the prime mover of fuel to the fuel nozzles and contains rotating parts that transmit signals to the liquid fuel. A schematic of the CF6-50 fuel system and main fuel pump showing the path of combustor fuel flow is illustrated in Figure 4.1-5. Fuel enters the pump from the fuel supply. The fuel for combustion is directed into a centrifugal boost impeller which discharges the fuel through a debris screen and into a high-pressure

- CF6-50 Core Noise Program
- As Measured Data

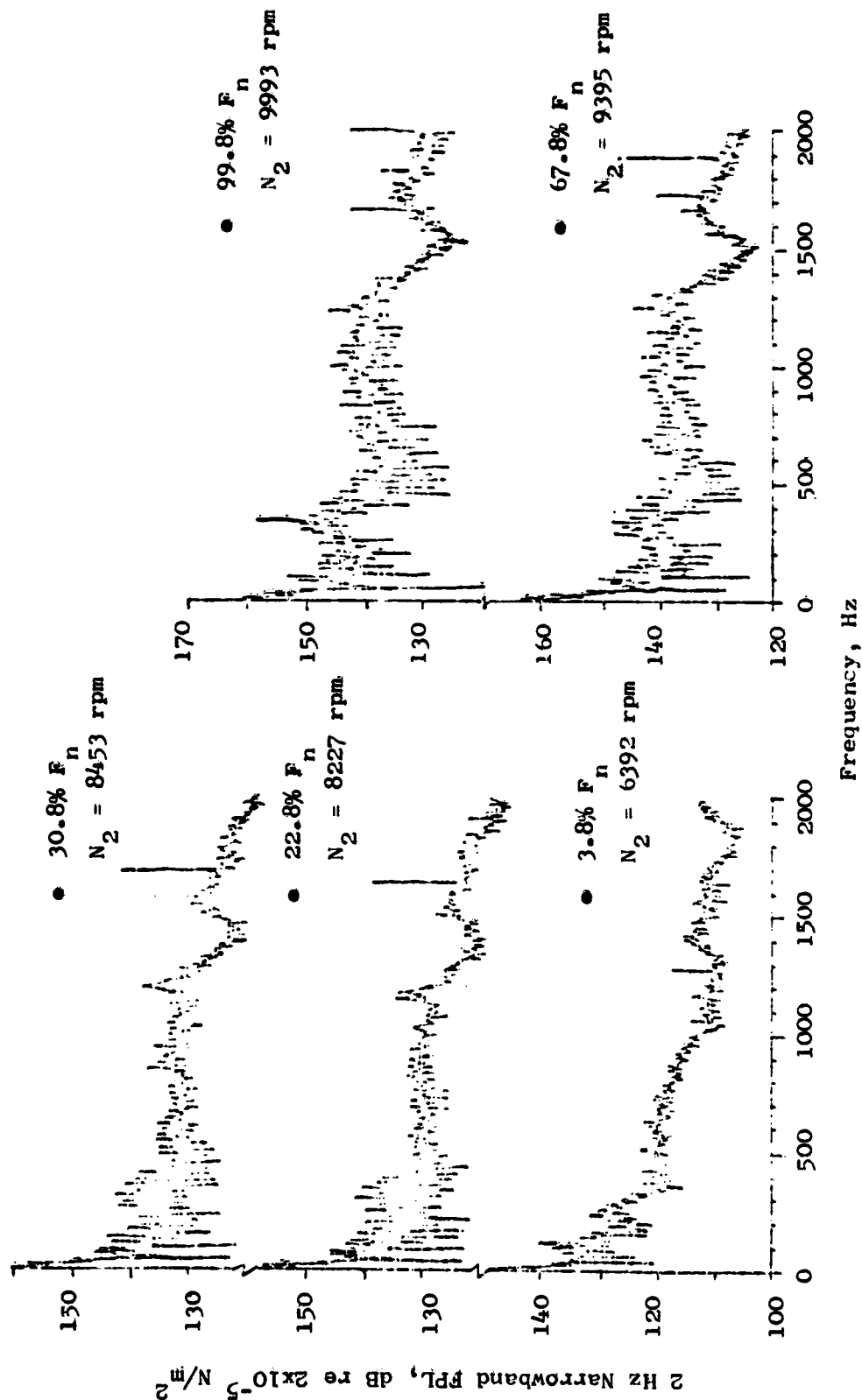


Figure 4.1-1. Plane 3.0 (16°) Internal Spectra Variation with Engine Core Speed.

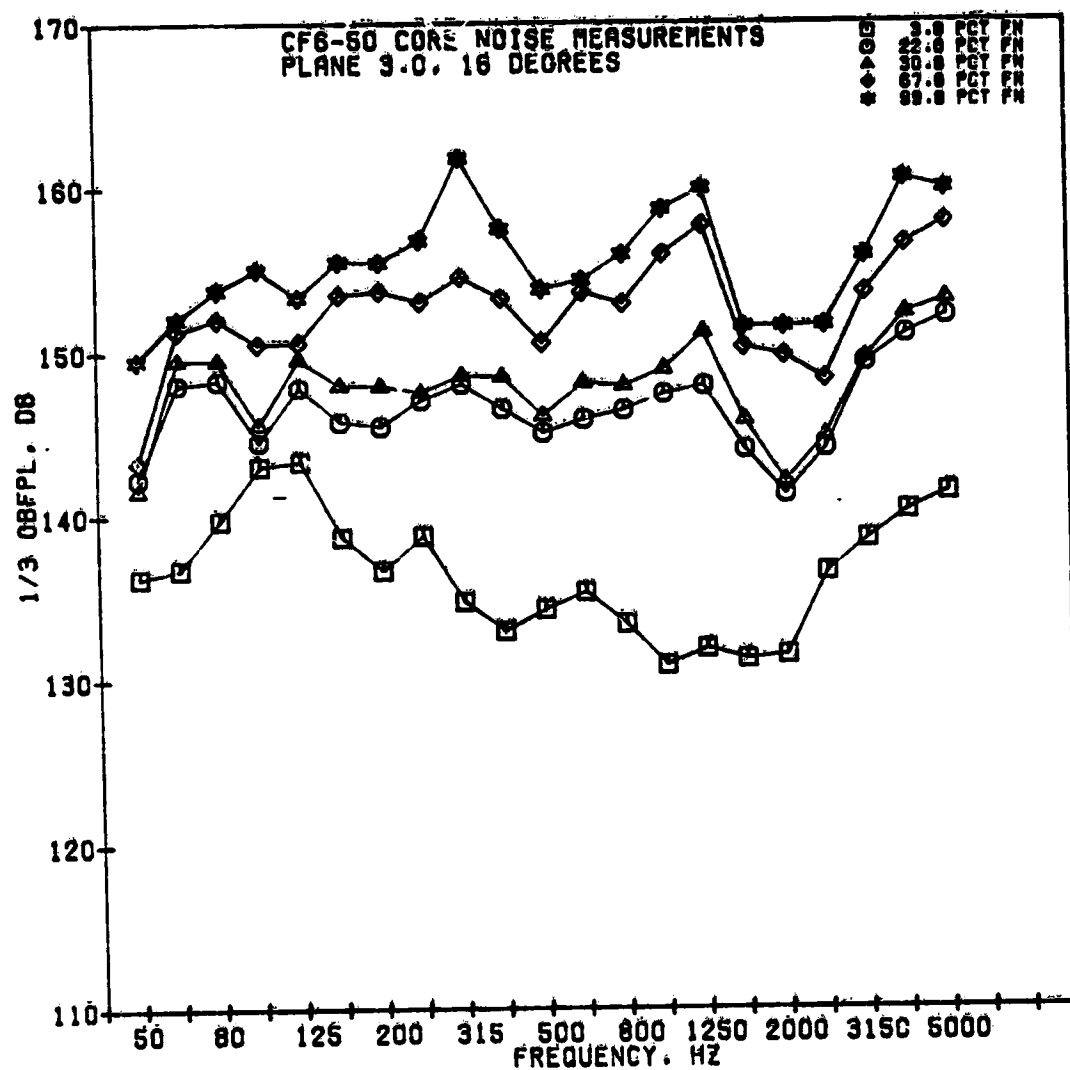


Figure 4.1-2. Variation of Plane 3.0 One-Third-Octave-Band Spectra with Percent Net Thrust.

• CF6-50 Core Noise Program

• As Measured Data

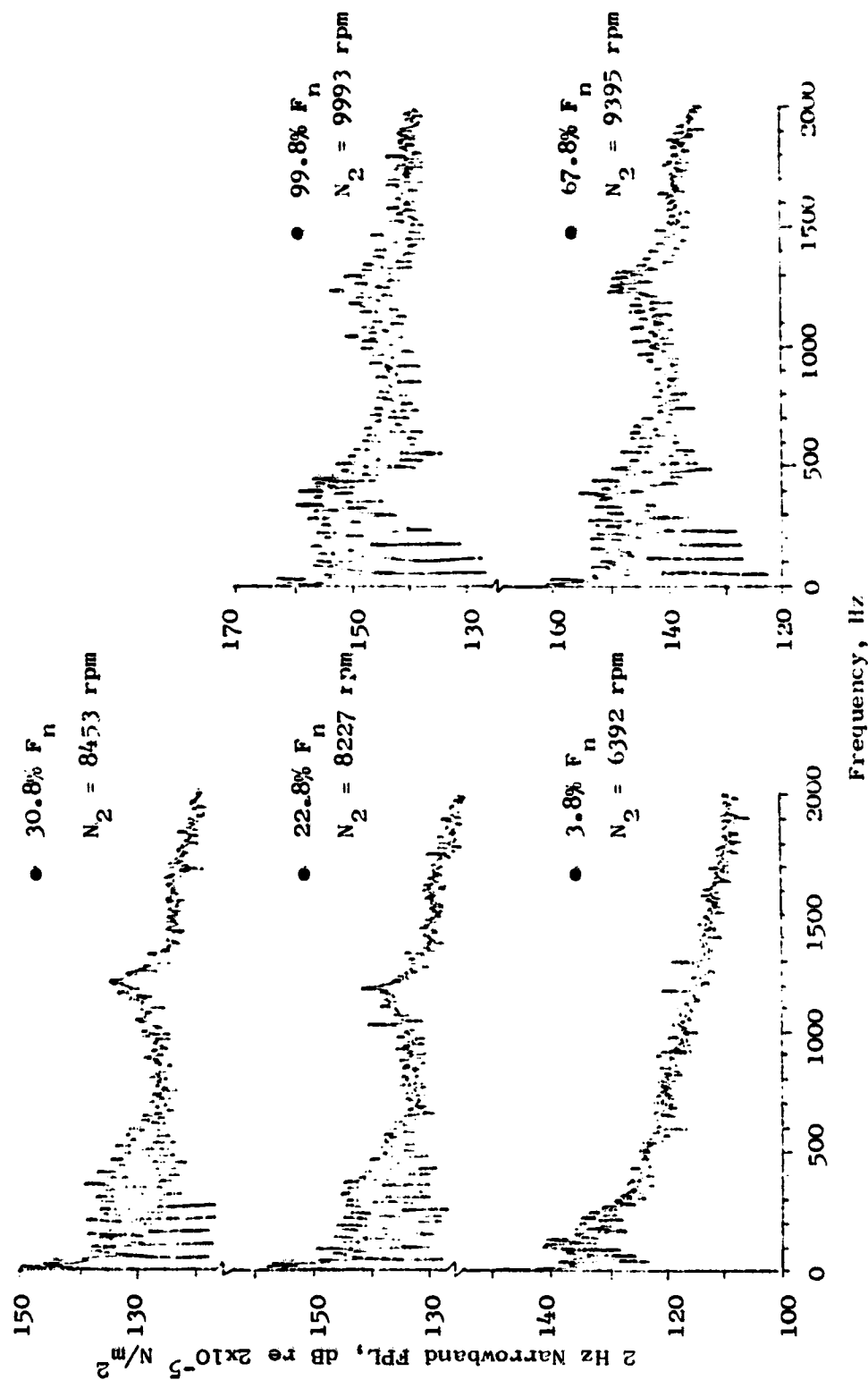


Figure 4.1-3. Plane 3.5 (282°) Internal Spectra Variation with Engine Core Speed.

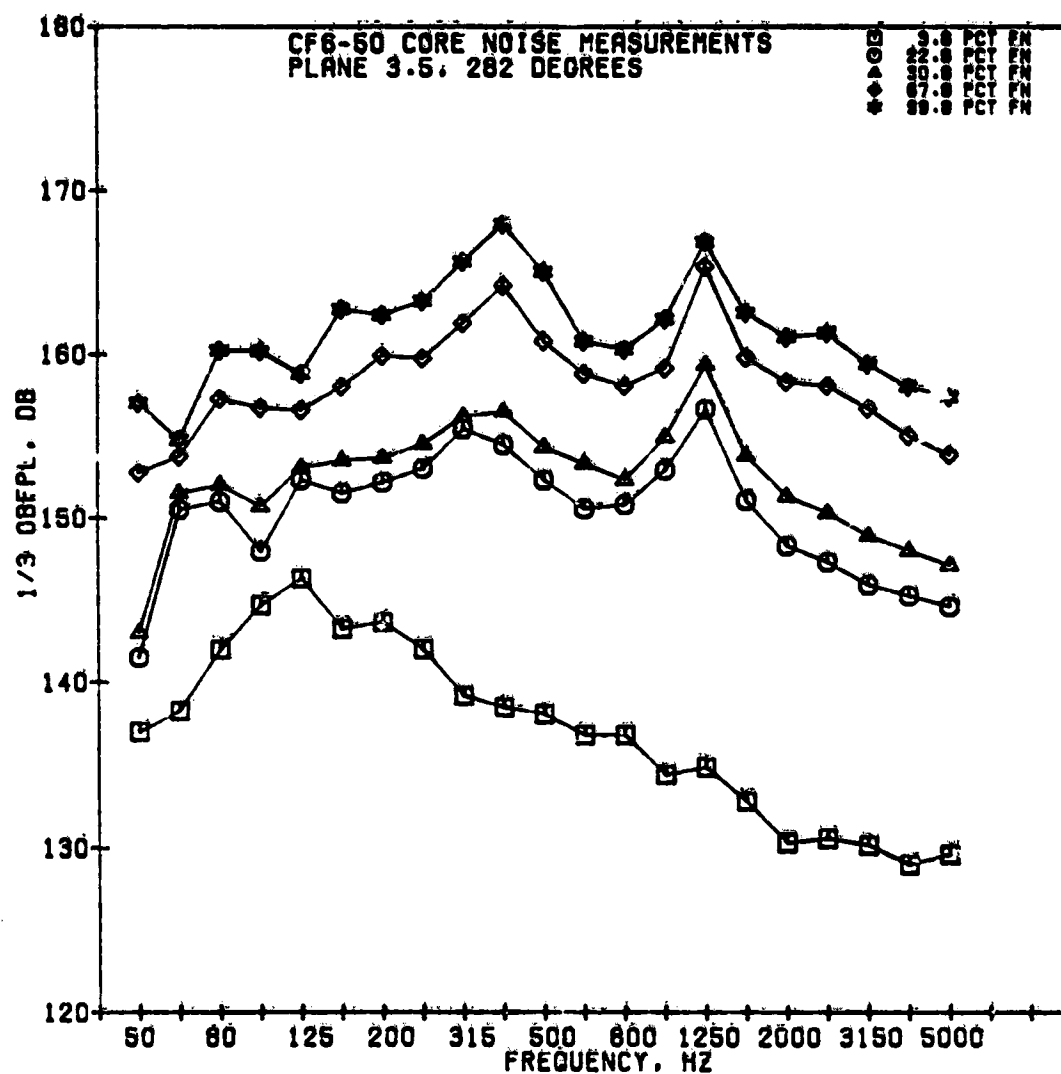


Figure 4.1-4. Variation of Plane 3.5 One-Third-Octave-Band Spectra with Percent Net Thrust.

● COMBUSTOR FUEL FLOW PATH

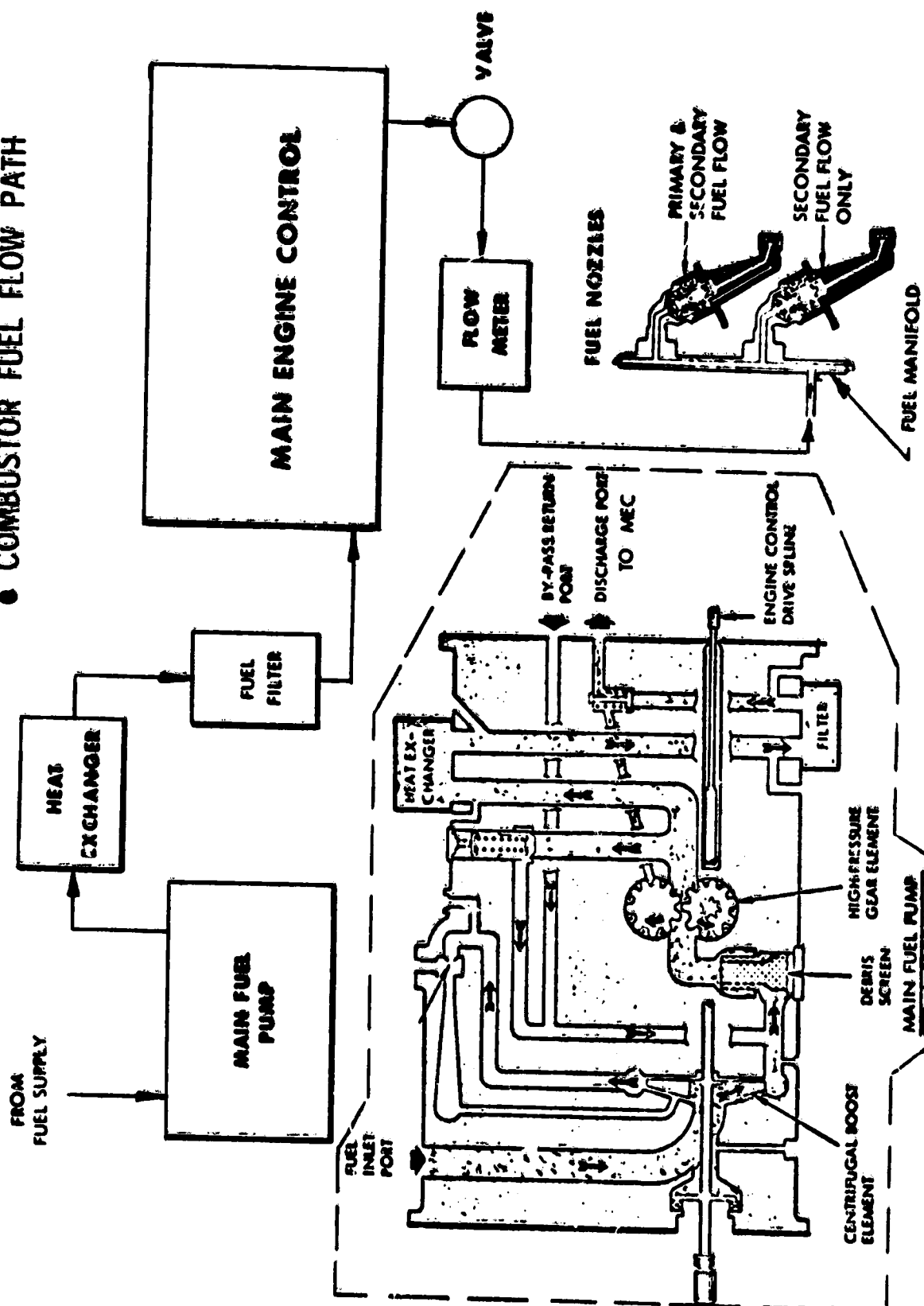


Figure 4.1-5. CF6-50 Fuel System Schematic.

ORIGINAL PAGE IS
OF POOR QUALITY

gear element, increasing the pressure of the fuel delivered to the main engine control and eventually to the fuel manifold and fuel nozzles.

The high-pressure gear element contains two positive displacement, counter rotating, 12-tooth gears. Fuel flows around the gears, and the gear teeth push the fuel through the passages. This action is similar to an air chopper siren device (previously used for acoustic tests) which allows air to pass through a rotating disc containing numerous uniform slots and then discharging the air through a single orifice to generate multiple tones.

The combustion fuel delivered to the fuel manifold is of high pressure (>69.03 atm, 1015 psig). The fuel manifold supplies fuel to the 30 fuel nozzles which consist of 3 different types. A fuel nozzle schematic is shown in Figure 4.1-6. One-half of the fuel nozzles are the dual flow primary-secondary type. The primary passage is always open and fuel flows through it anytime it is present in the nozzle (at all conditions). Fuel flows through the secondary passages only when the pressure differential across the fuel divider valve is sufficient to open the valve (about 14.28 atm, 210 psi).

There are 14 secondary-only type fuel nozzles. Fuel flows through these nozzles when the flow divider valve ΔP reaches approximately 16.33-17.0 atm (240-250 psi). These nozzles cut on at higher power settings than the primary-secondary nozzles. A special dual-flow nozzle is used between the igniter plugs to provide a primary flow for better flame cross propagation at light off.

Comparison of Fuel Nozzle and Plane 3.5 Spectra

The narrowband FPL spectra from the fuel nozzle sensors are displayed in Figures 4.1-7 and -8 for six speeds covering the CF6-50 operating line. Several distinct tones are noted throughout the frequency range. A few of these tones have been identified as being directly related to the fuel system. A predominate tone around 200 Hz is thought to be associated with the fuel nozzle flow divider valve spring critical frequency which was determined from vibration tests to occur at approximately 200 Hz. The first harmonic of this tone is apparent in the 400-Hz region of both nozzles at each speed. The two 12-tooth drive gears which pressurize the fuel in the main fuel pump were identified as the source of two more prominent tones. They are related to the gear tooth passing frequencies, occurring as a 12/rev and 24/rev of the fuel pump speed which forms a 0.584 ratio with the engine core speed.

The broadband of the primary-secondary nozzle spectra in Figure 4.1-7 suggests a bilobed spectral characteristic. The first notable region occurs between 250 and 500 Hz, while the second occurs between 1200 and 1600 Hz. A more dramatic display of the broadband characteristic is found in the secondary-only fuel nozzle spectra in Figure 4.1-8. The most predominant broadband lobe occurs at the higher frequencies between 1200 to 1600 Hz, while another lobe is found in the region between 400 to 700 Hz, but is not as well defined.

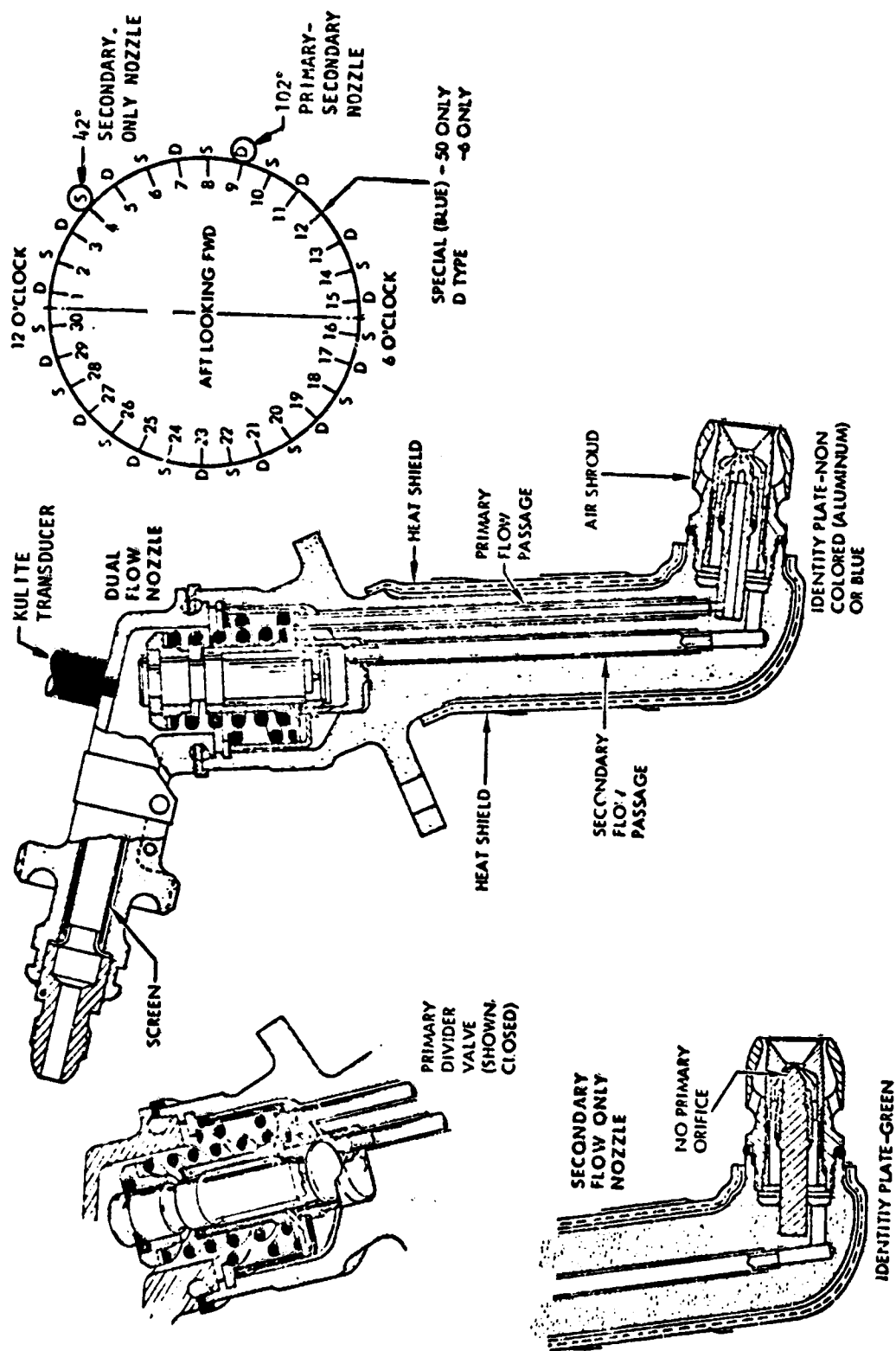


Figure 4.1-6. CF6 Fuel Nozzles.

- CF6-50 Core Noise Program
- As Measured Data
- Physical Speed

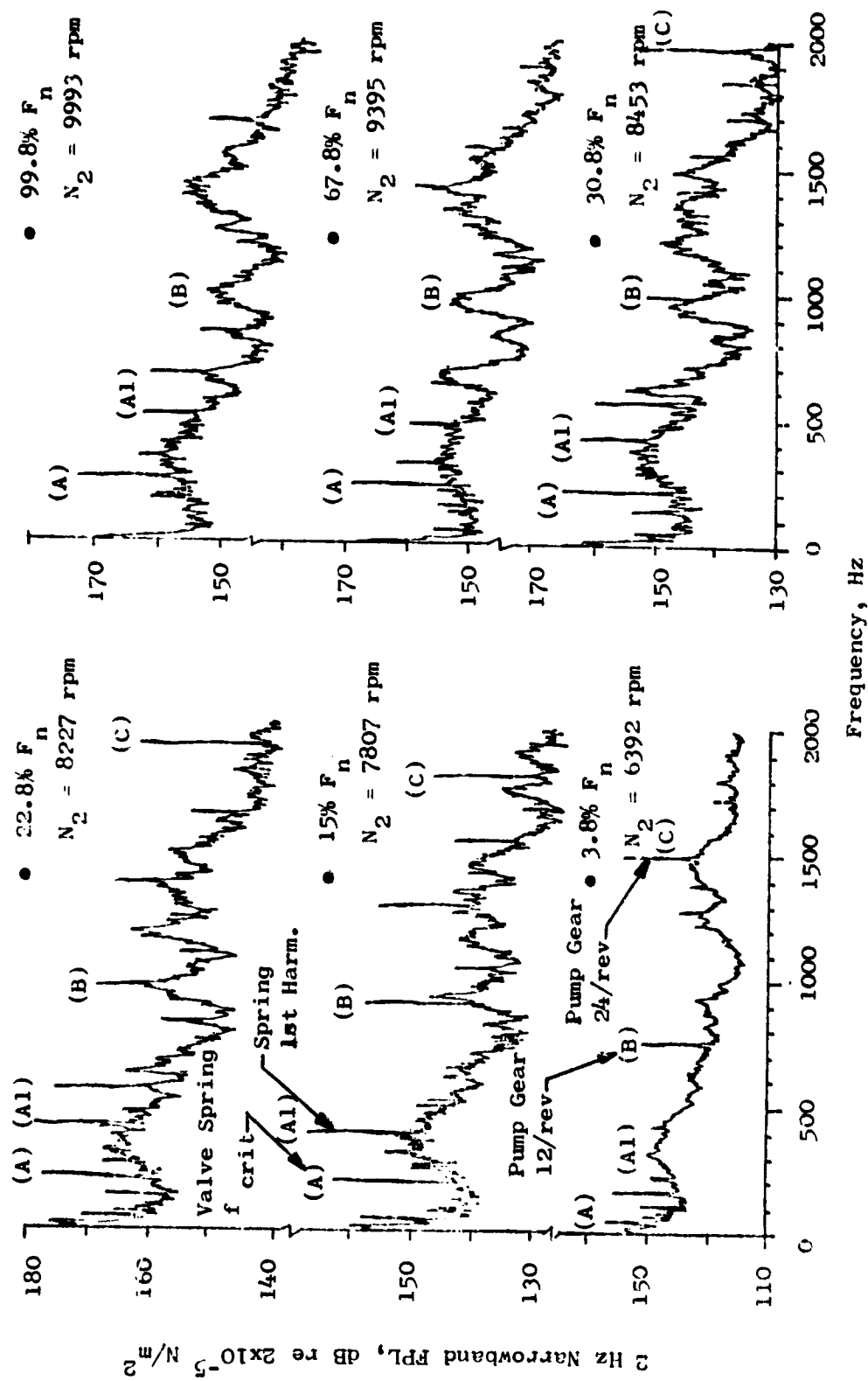


Figure 4.1-7. Primary-Secondary Fuel Nozzle (102°) Spectra Variation with Engine Core Speed.

• CF6-50 Core Noise Program

• As Measured Data

• Physical Speed

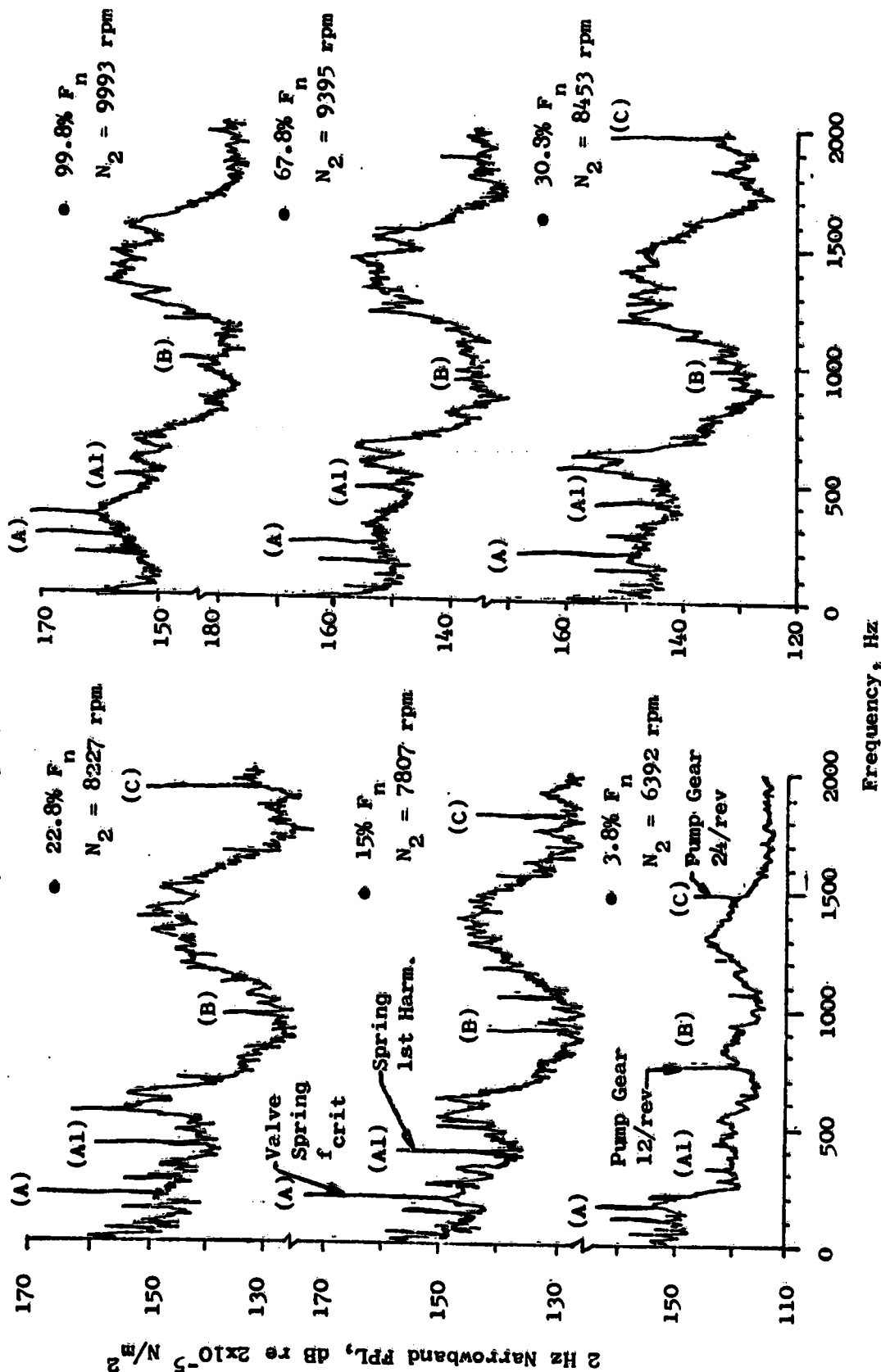


Figure 4.1-8. Secondary-Only Fuel Nozzle (42°) Spectra Variation with Engine Core Speed.

The narrowband spectra from the waveguide sensors located at 42° and 102° in the combustor inlet, Plane 3.5, and at the same circumferential positions as the instrumented fuel nozzles, are shown in Figures 4.1-9 and 4.1-10, respectively. The spectral variation with engine core speed of the 42° waveguide sensor in Figure 4.1-9 shows that the spectra develops a bilobed shape that is constant with increasing speed. Peak regions occur between 300 to 400 Hz and 1200 to 1300 Hz. They correspond to similar regions noted for the associated secondary-only fuel nozzle spectra. The waveguide spectra at 102° (Figure 4.1-10) indicates a similar bilobed characteristic with peaks occurring in the same frequency regions as indicated for the primary-secondary fuel nozzle spectra in Figure 4.1-7.

A comparison of the fuel nozzle 1/3-OBFPL spectra to the spectra of the corresponding waveguide sensor at the same circumferential position indicates the regions of spectral shape similarity on a 1/3-octave basis over the range of operating conditions as illustrated in Figures 4.1-11 and -12. The plots in Figure 4.1-11 show that the primary-secondary nozzle exhibits peaks between the 250- to 500-Hz 1/3-octave bands and between the 1000- and 2000-Hz bands which tend to match similar regions in the waveguide sensor at 102° for conditions above idle.

The secondary-only nozzle spectra forms three prominent peaks after the valve cuts on and reaches full operation at conditions above idle as shown in Figure 4.1-12. A low-frequency peak occurs in the 200-Hz band and is apparent in both nozzles at all speeds. This is a tone-dominated region as seen from the narrowbands of Figures 4.1-7 and -8. The tone is attributed to the fuel nozzle valve spring critical frequency which occurs at about 200 Hz.

The midfrequency peak in Figure 4.1-12 overlaps with the 250-500 Hz region in the primary-secondary nozzle in Figure 4.1-11. It extends from approximately 400 to 630 Hz. But at takeoff, it matches the primary-secondary region. This region has been typically denoted as the region where the peak in the core noise spectra occurs.

A third peak is apparent in the region between the 1000- to 2000-Hz bands in both fuel nozzles and waveguide sensors. This is most probably the result of the large broadband lobe and not the tones identified in this region from the narrowband spectra.

Observations from Fuel Nozzle Comparisons

1. The spectral shapes of the fuel nozzle and combustor waveguide sensor measurements are similar. The degree of similarity increases with increased speed. However, the peak regions do not vary with speed but remain in fixed frequency bands.
2. The internal spectra exhibit a bilobed shape with peaks occurring between 300 to 600 Hz and 1200 to 1600 Hz. The low frequency peak corresponds to the typical frequency range associated with combustor noise.

- CF6-50 Core Noise Program
- As Measured Data
- Physical Speed

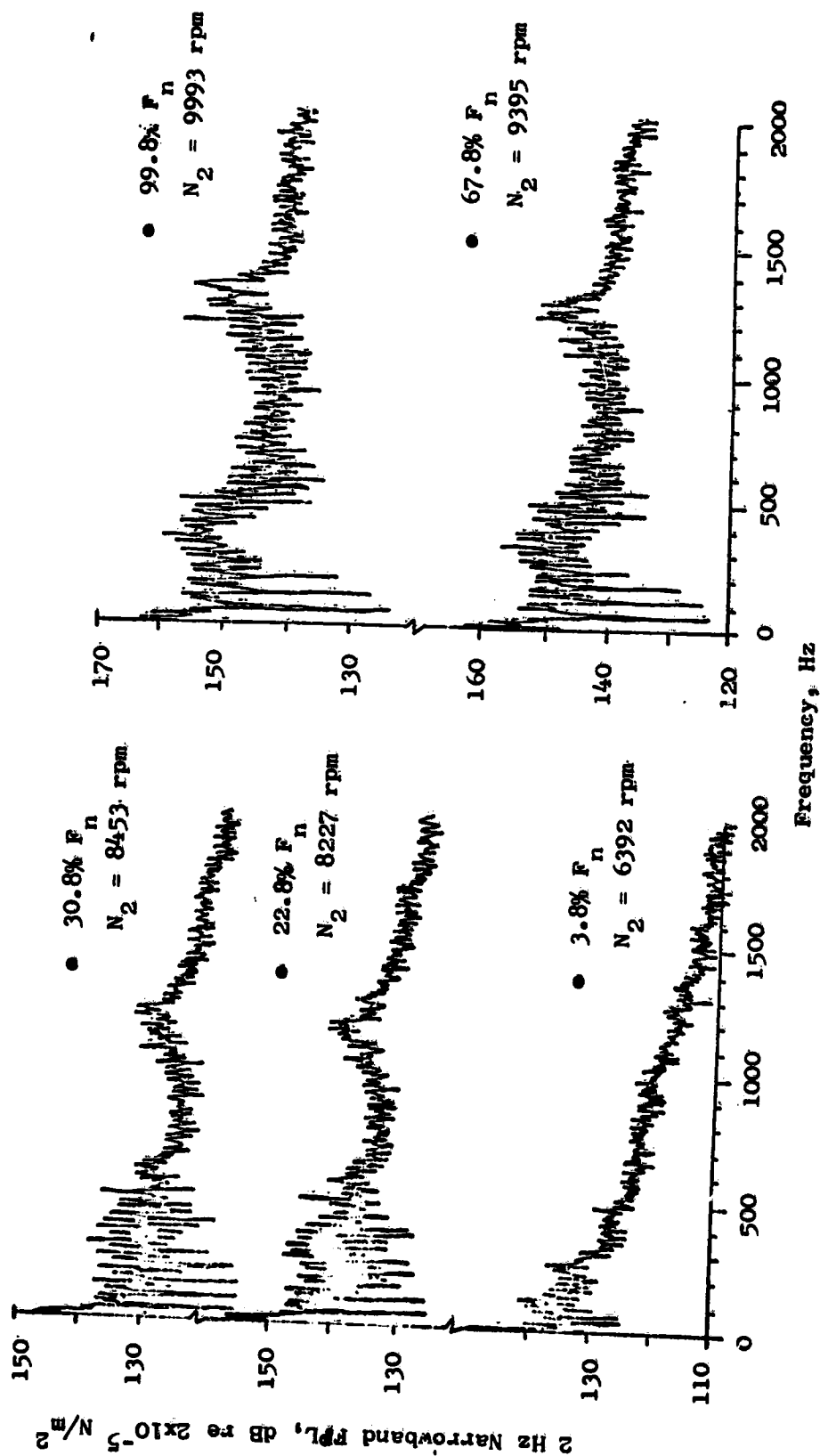


Figure 4.1-9. Plane 3.5 (42°) Internal Spectra Variation with Engine Core Speed.

- CF6-50 Core Noise Program

- As Measured Data

- Physical Speed

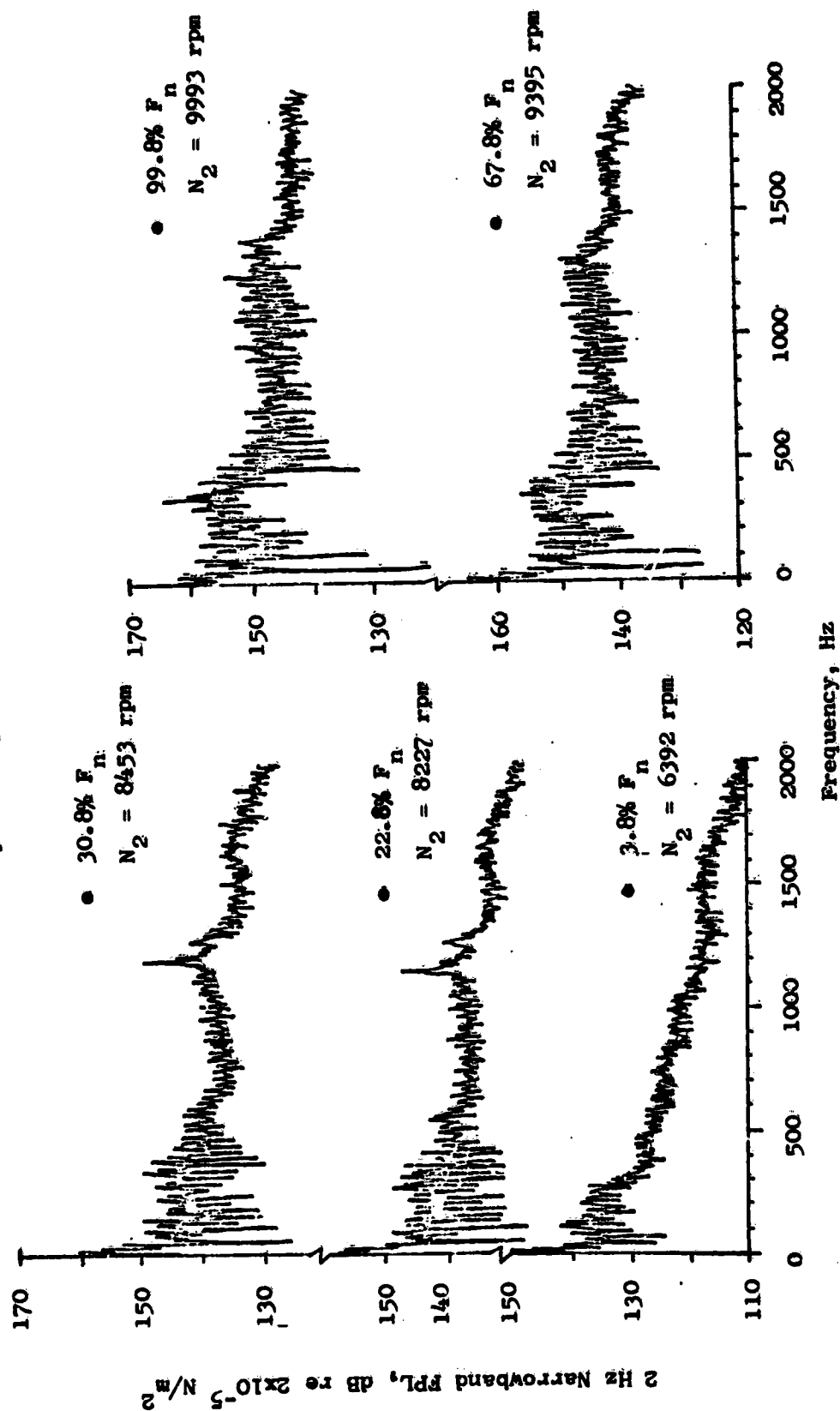


Figure 4.1-10. Plane 3.5 (102°) Internal Spectra Variation with Engine Core Speed.

- CF6-50 Core Noise Program
- 1/3 Octave Band Internal Spectra

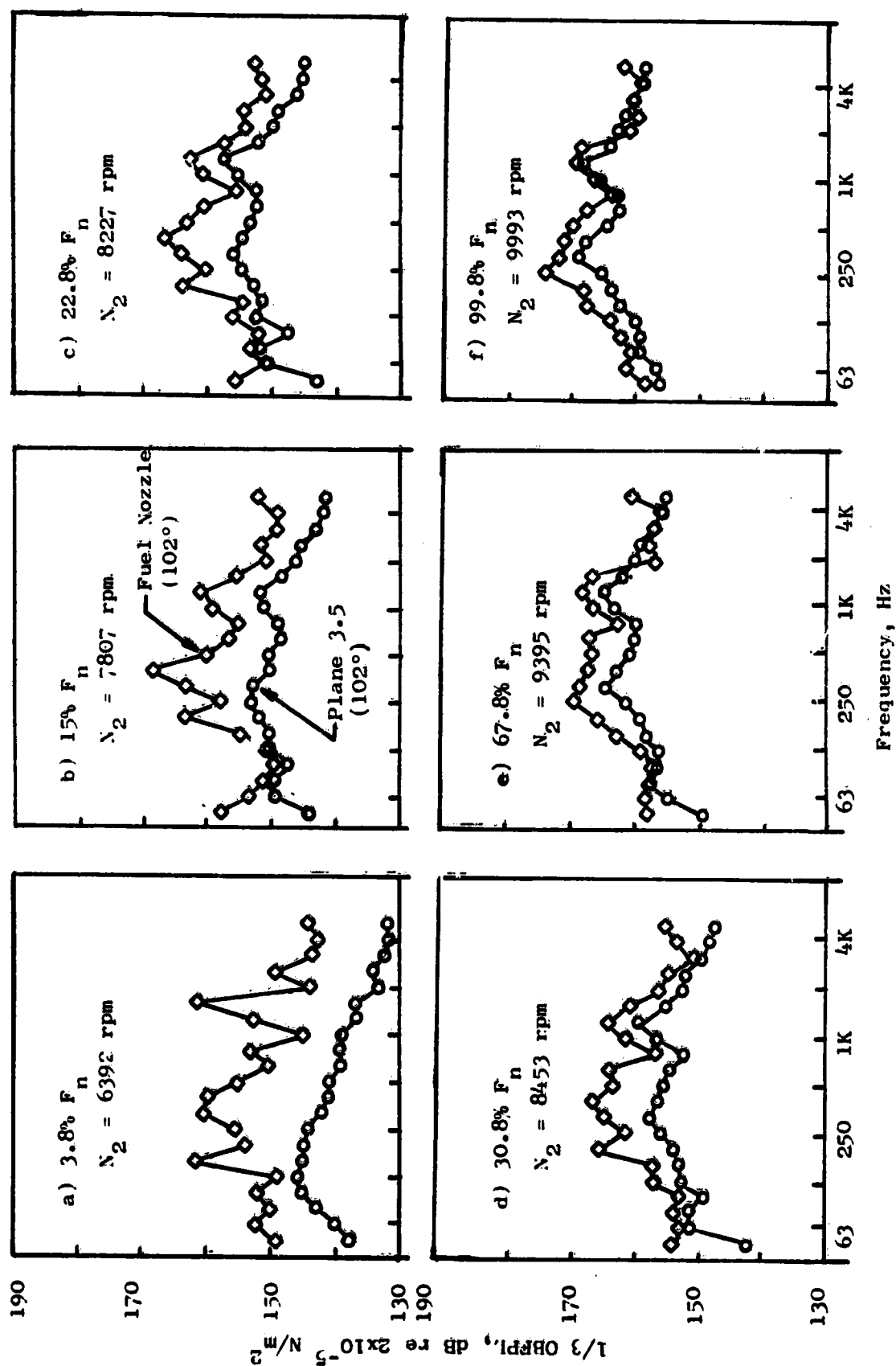


Figure 4.1-11. Comparison of Primary-Secondary Fuel Nozzle Spectra with Plane 3.5 Sensor (102°).

- CF6-50 Core Noise Program
- 1/3 Octave Band Internal Spectra

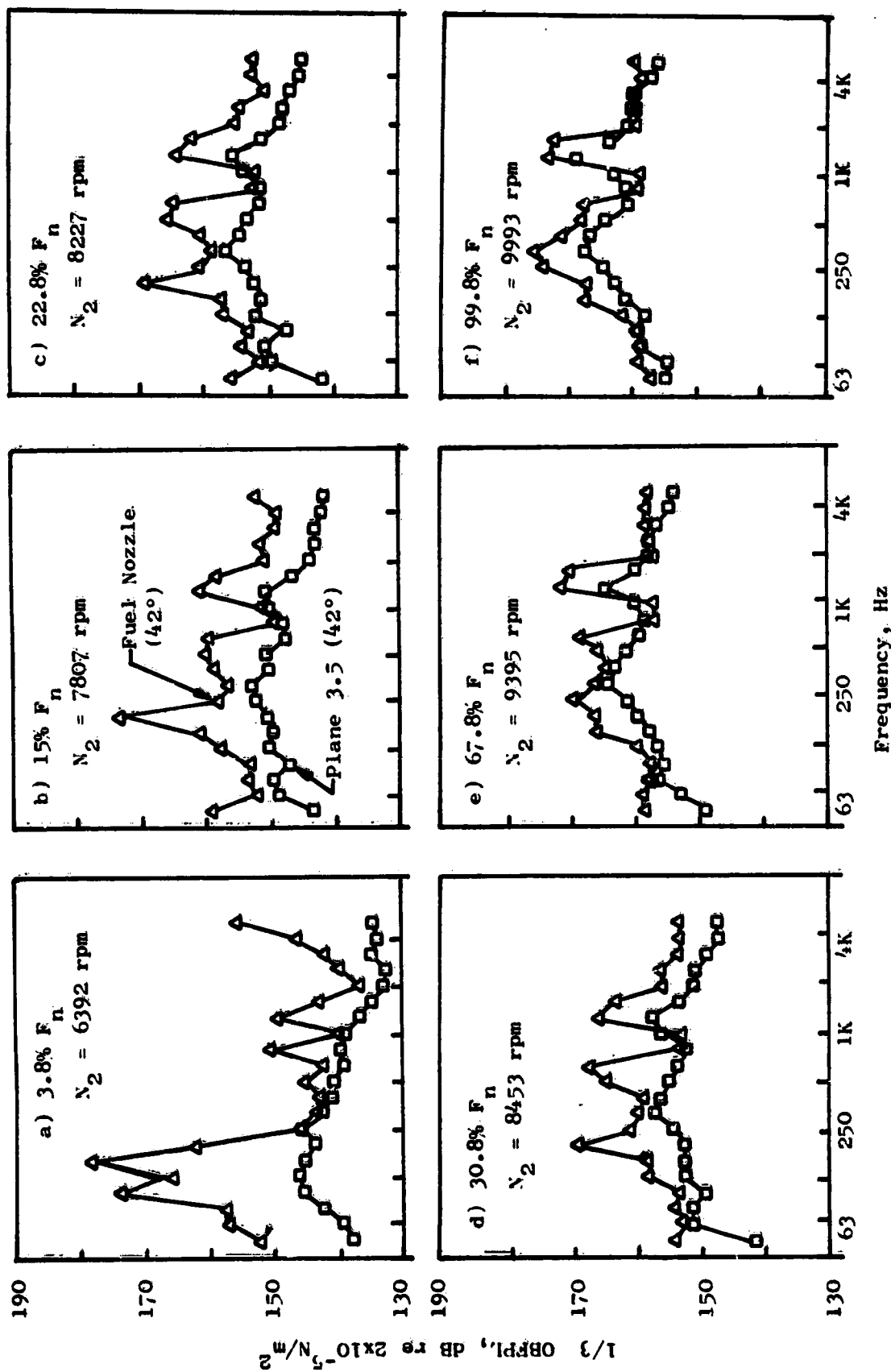


Figure 4.1-12. Comparison of Secondary-Only Fuel Nozzle Spectra with Plane 3.5 Sensor (42°).

3. The fuel system components are the source of several of the tones apparent in the narrowband spectra of the fuel nozzle measurements. Some of these tones have been identified in the far-field measurements at idle condition (see Reference 4).

Plane 4.0 Combustor Discharge

The measurements at the combustor discharge plane, 4.0, were made within the high-pressure-turbine nozzle diaphragm. The flow through the nozzle diaphragm is choked at the exit (throat) over most of the operating conditions above idle. The Mach number at the sensor location is a relatively constant 0.55. Figure 4.1-13 illustrates the narrowband spectra variation with core speed. A similarity between spectra shape at this plane with the combustor inlet is apparent from a comparison with Figure 4.1-3. The 1/3-octave-band spectra (Figure 4.1-14) shows a lobe in the 250- to 800-Hz frequency region. The higher frequencies (>800 Hz) show a general increase in FPL at all core speeds.

Plane 8.0, Core Nozzle Discharge

The sound-separation probe used at the exit of the core exhaust nozzle was positioned at a central immersion in the exhaust annulus. Figure 4.1-15 illustrates the variation with engine core speed of the narrowband spectra from the forward (A) Kulite on the probe. The low pressure turbine BPF's of the first, second, and third stages are noted at the idle power setting of $3.8\% F_n$. These tones disappear from the spectra range at higher speed points. The shape of the spectra remain about the same throughout the engine operating range. The 1/3-octave-band spectra displayed in Figure 4.1-16 show similar trends. The lower power settings ($<30.8\% F_n$) indicate a peaked frequency region around 200 to 630 Hz which spans the typical combustor noise region.

A summary of the internal pressure spectra (FPL) variation with engine speed is presented in Figure 4.1-17 for the six conditions covering the operating range. This figure illustrates the trends from each of the internal sensors in relation to each other.

4.1.1.2 Far-field Measurements

The far-field measurements taken in conjunction with the internal measurements at each test condition were processed in 2-Hz narrowband and 1/3-octave-band spectra. An indication of the variation of narrowband spectra content with engine core speed is illustrated in Figures 4.1-18 through 4.1-22 for acoustic far-field angles of 30° , 60° , 90° , 110° , 120° , and 150° , respectively.

The narrowband spectra at idle show several tones at various angles around the arc, some of which occur at higher frequencies as a function of core speed. The most predominant tone in the far field at all speeds is the fan blade passing frequency (BPF) (A). Other tones at idle power, in addition

- CF6-50 Core Noise Program
- As Measured Data

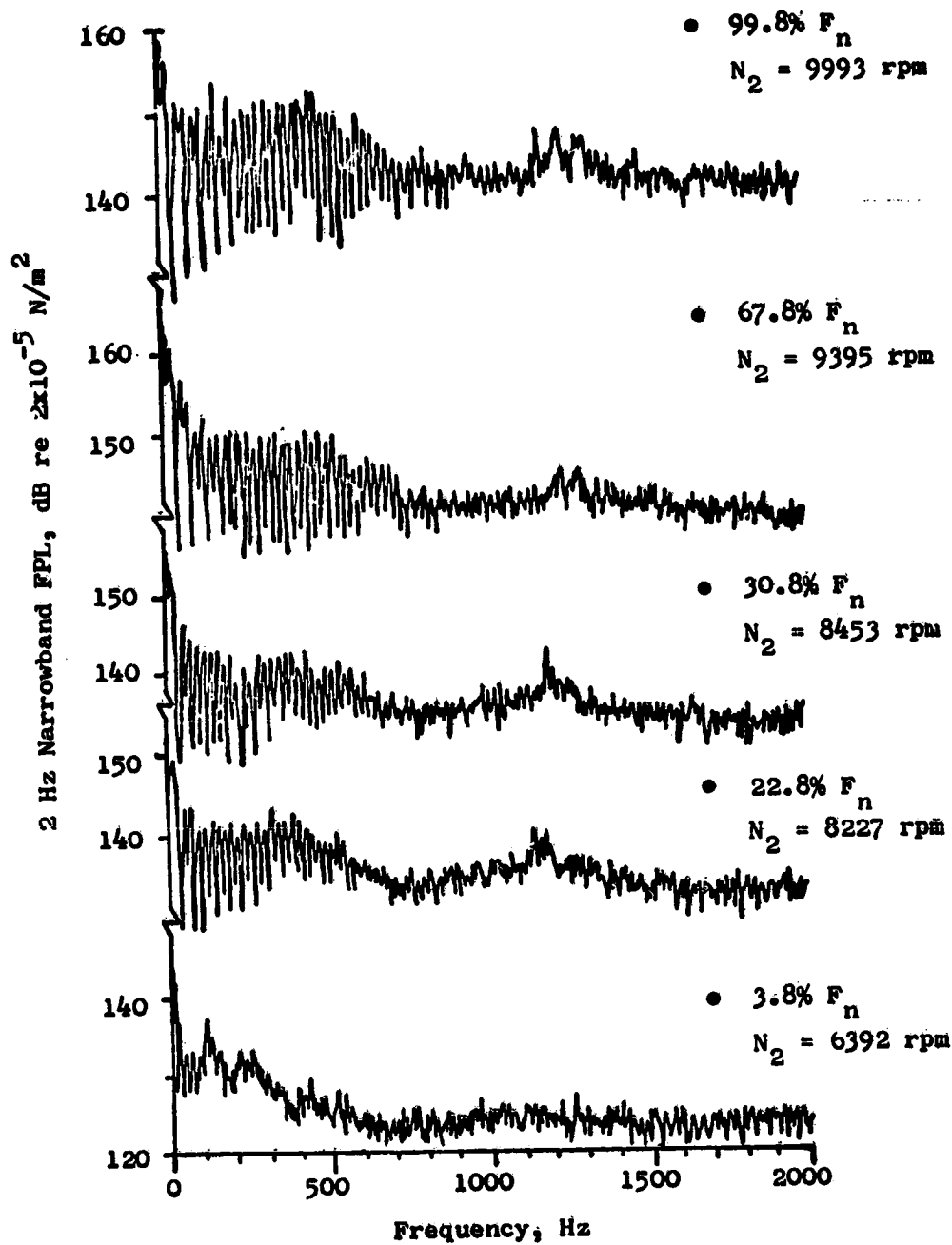


Figure 4.1-13. Plane 4.0 (92°) Internal Spectra Variation with Engine Core Speed.

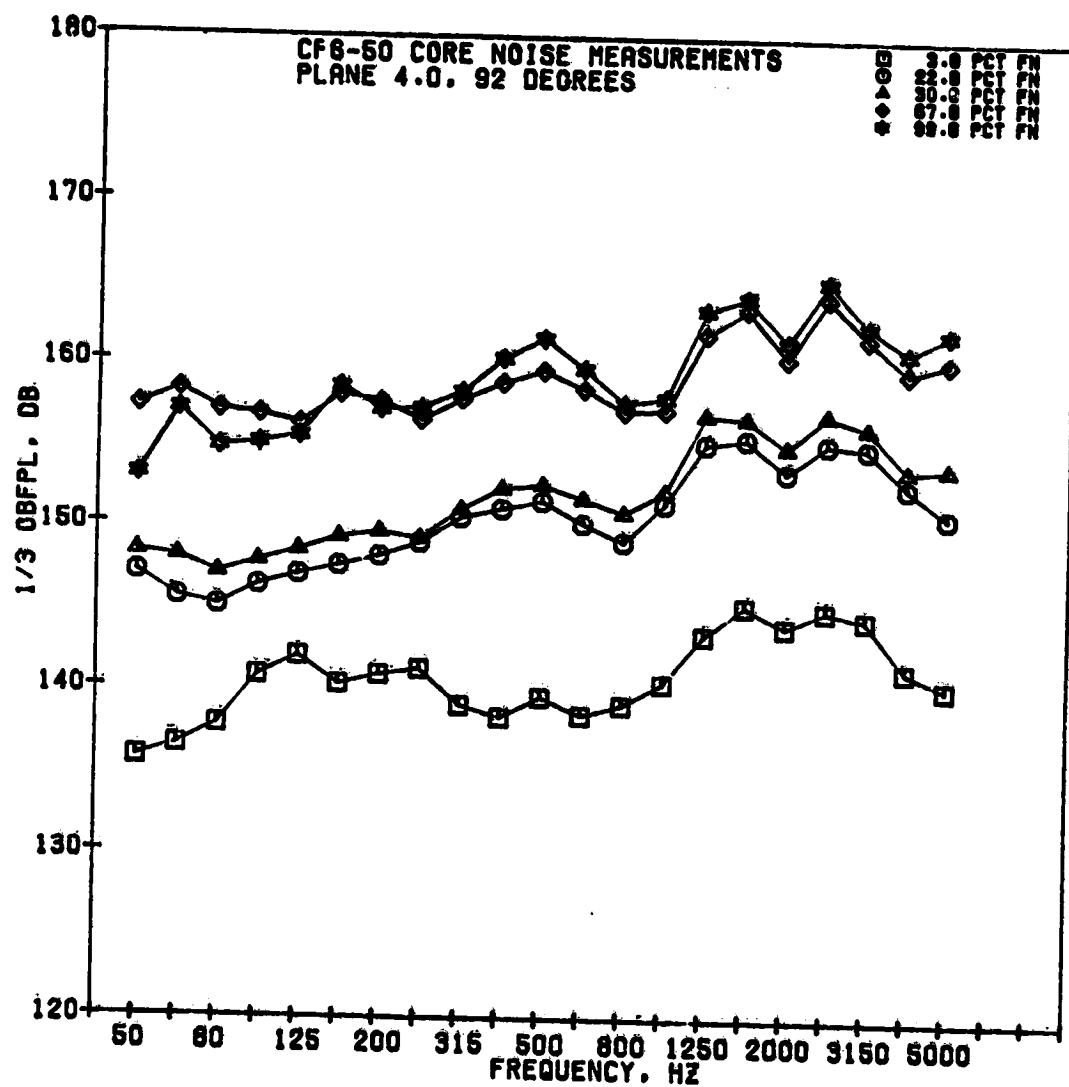


Figure 4.1-14. Variation of Plane 4.0 One-Third-Octave-Band Spectra with Percent Net Thrust.

● CF6-50 Core Noise Program

● As Measured Data

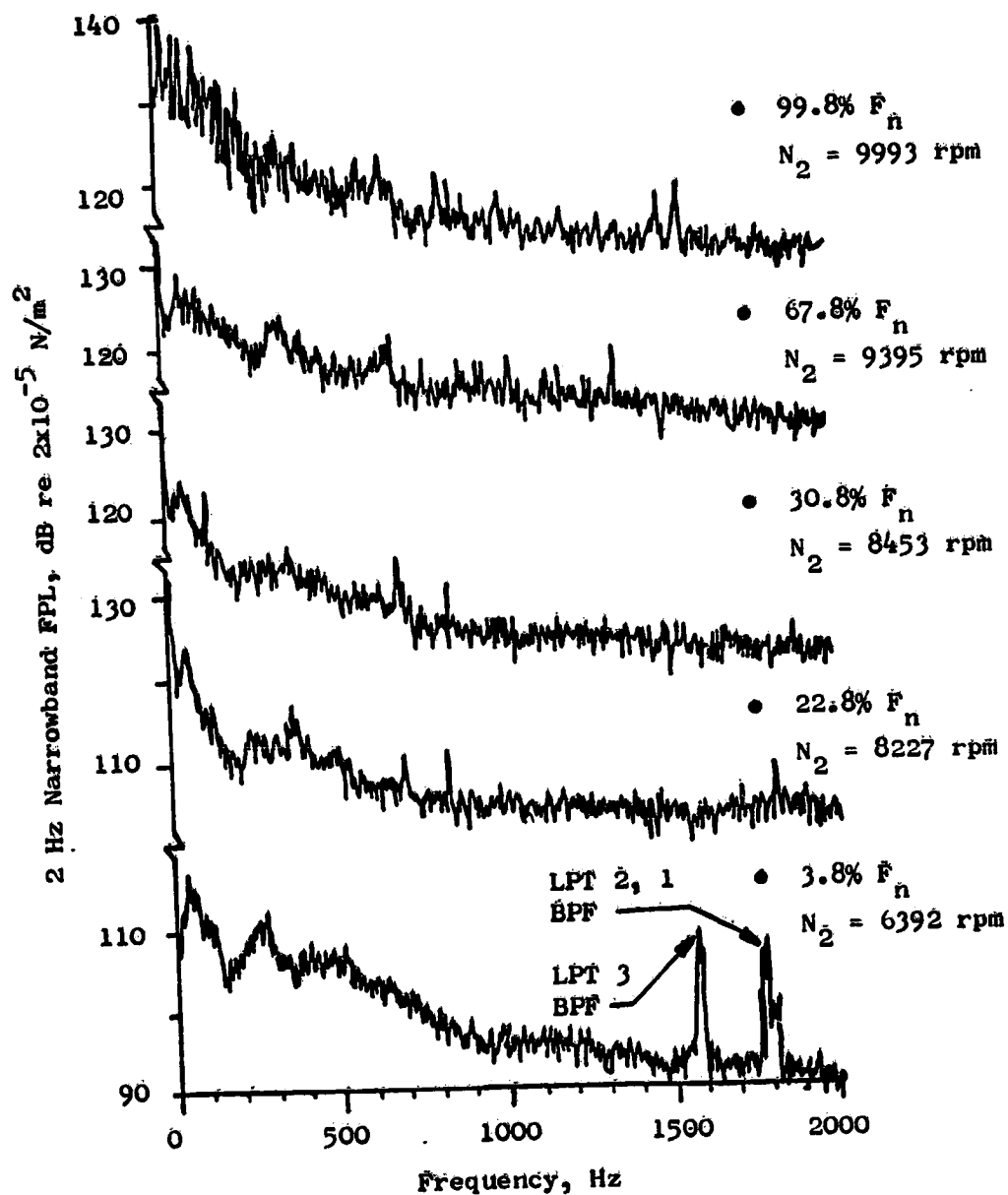


Figure 4.1-15. Plane 8.0A (270°) Internal Spectra Variation with Engine Core Speed.

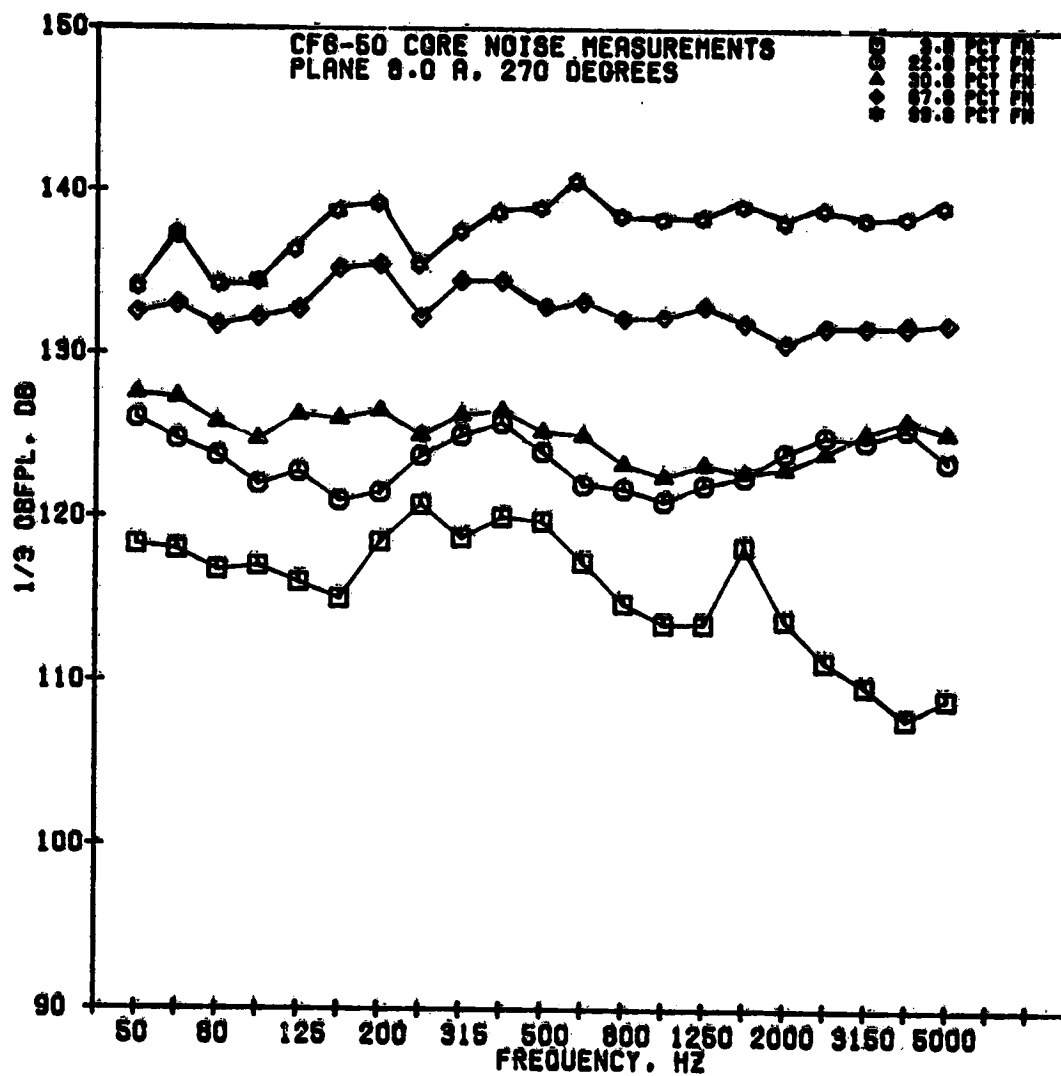


Figure 4.1-16. Variation of Plane 8.0A One-Third-Octave-Band Spectra with Percent Net Thrust.

- CF6-50 Core Noise Program
- 1/3 Octave Band Internal Spectra
- Corrected For Frequency Response

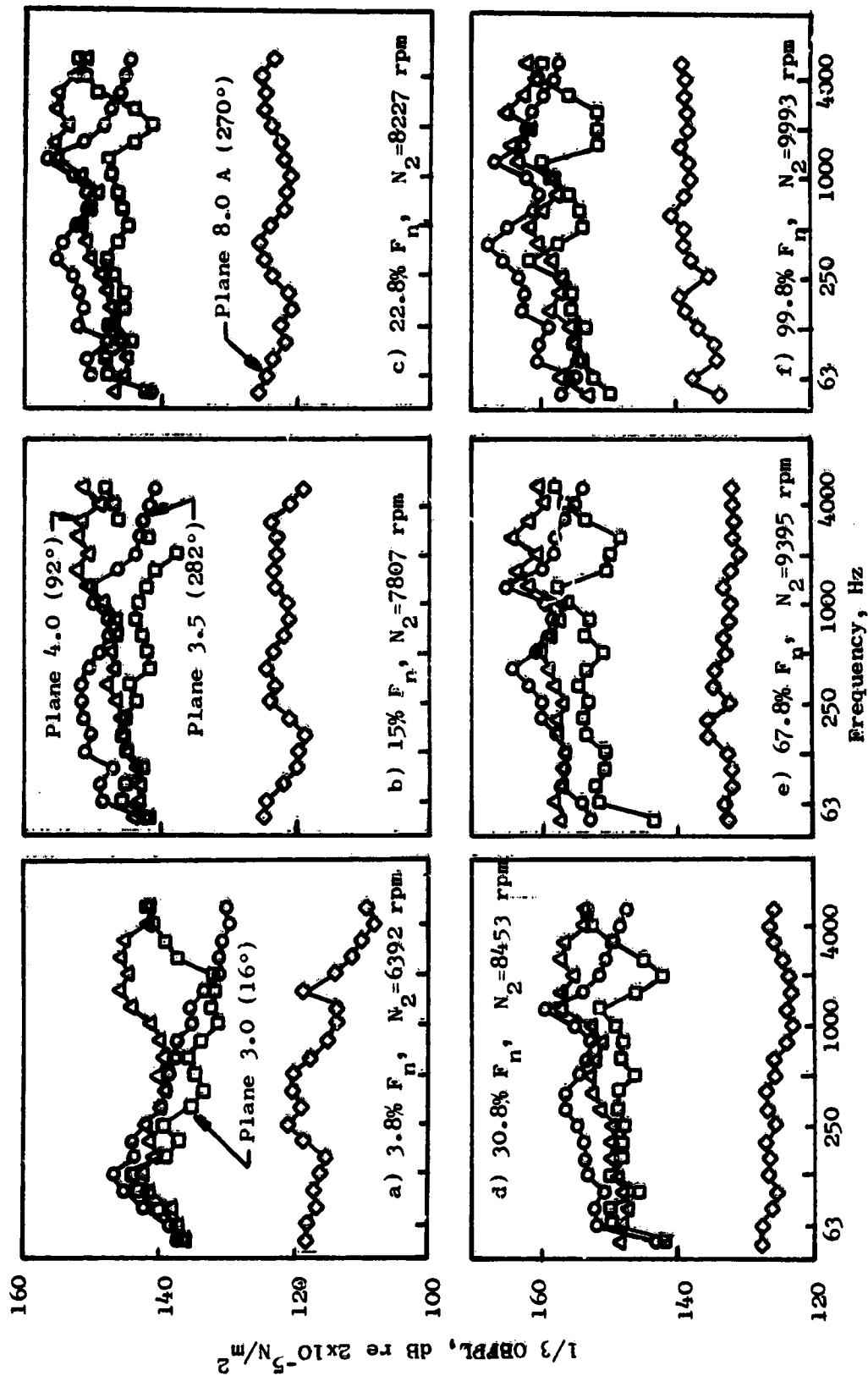


Figure 4.1-17. Internal Pressure Spectra Variation with Engine Speed.

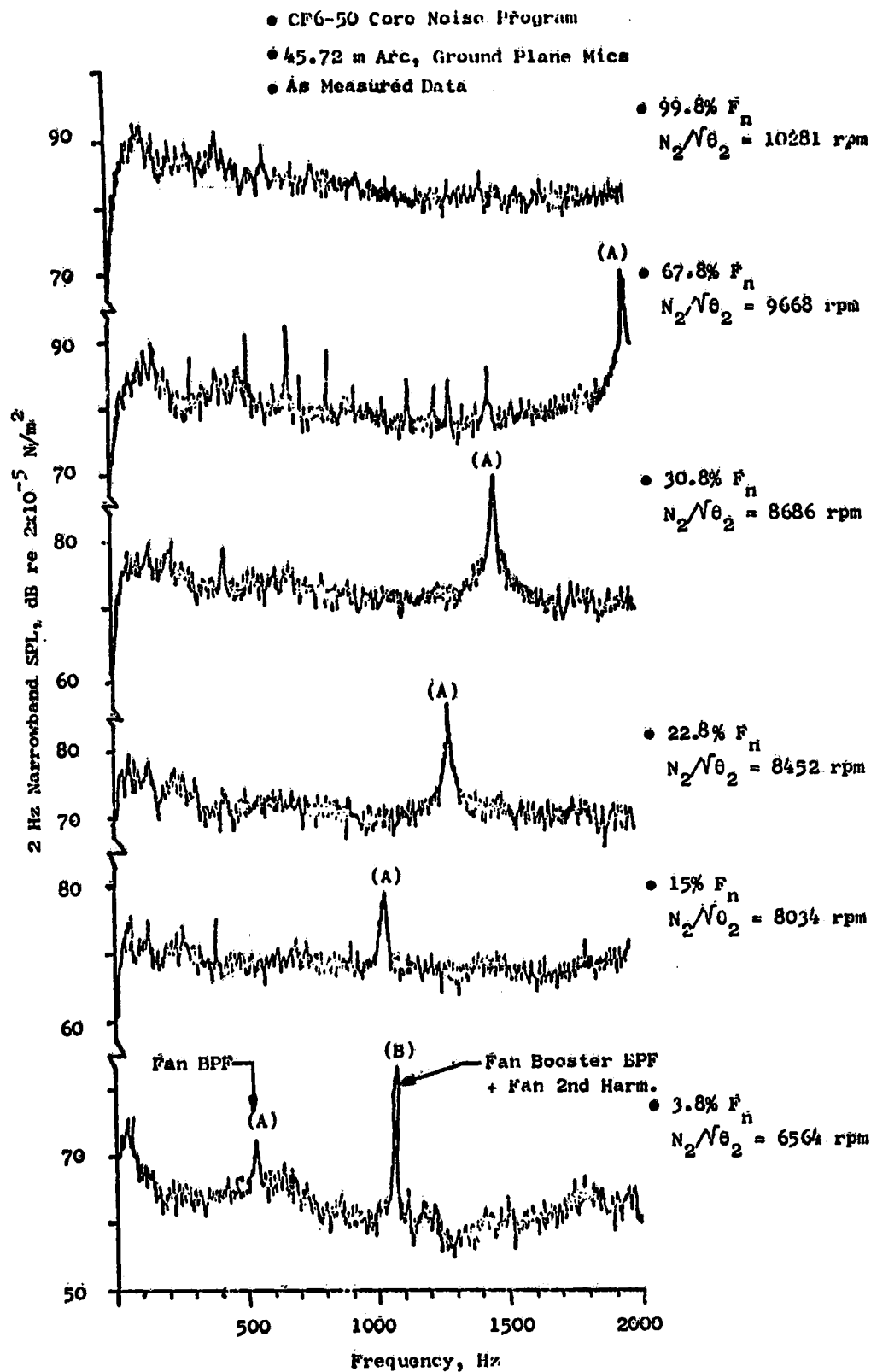


Figure 4.1-18. Far-Field Spectra Variation at 30° Acoustic Angle.

- CF6-50 Core Noise Program
- 45.72 m Arc, Ground Plane Mics
- As Measured Data

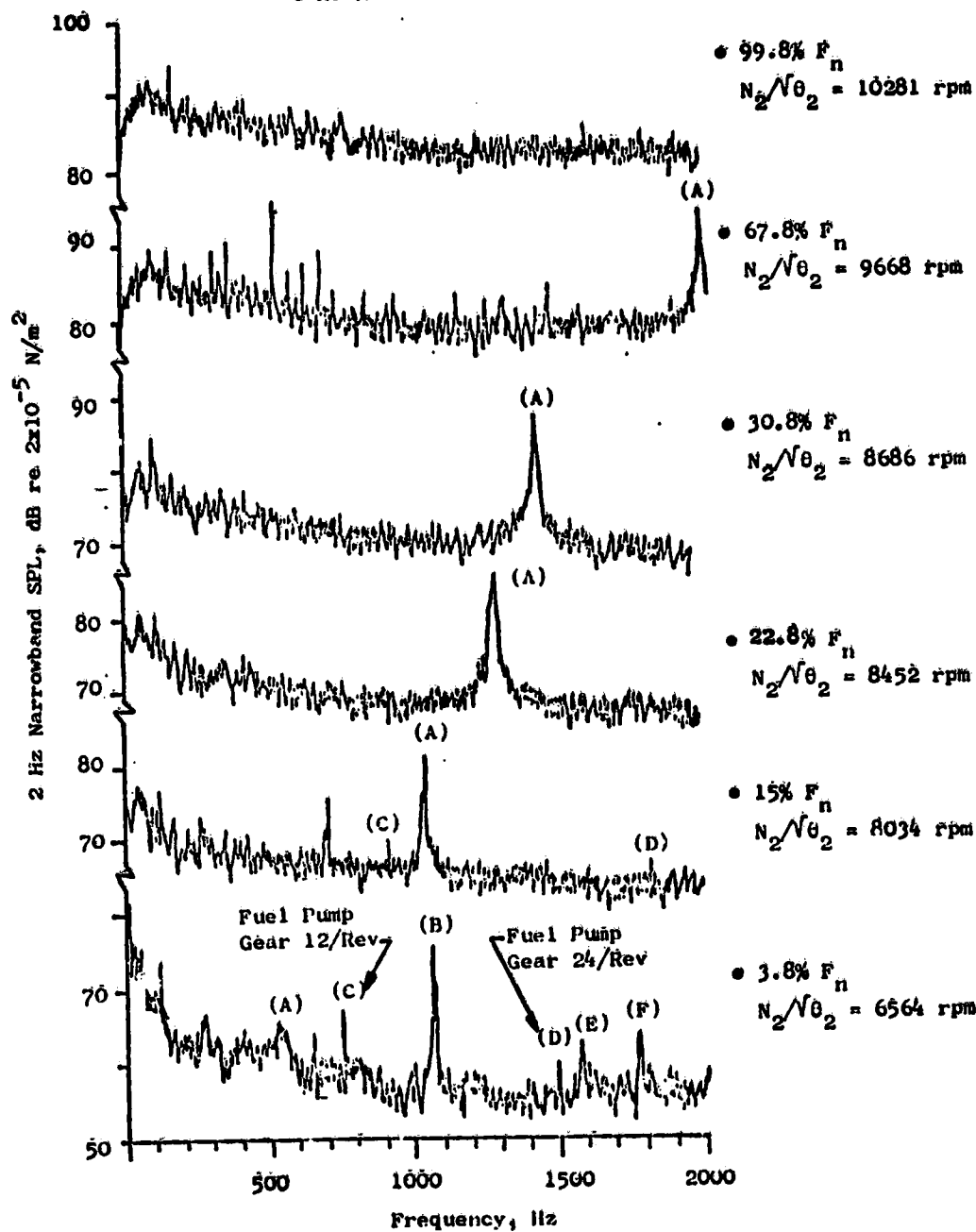


Figure 4.1-19. Far-Field Spectra Variation at 60° Acoustic Angle.

- CF6-50 Core Noise Program
- 45.72 m Arc, Ground Plane Mics
- An Measured Data

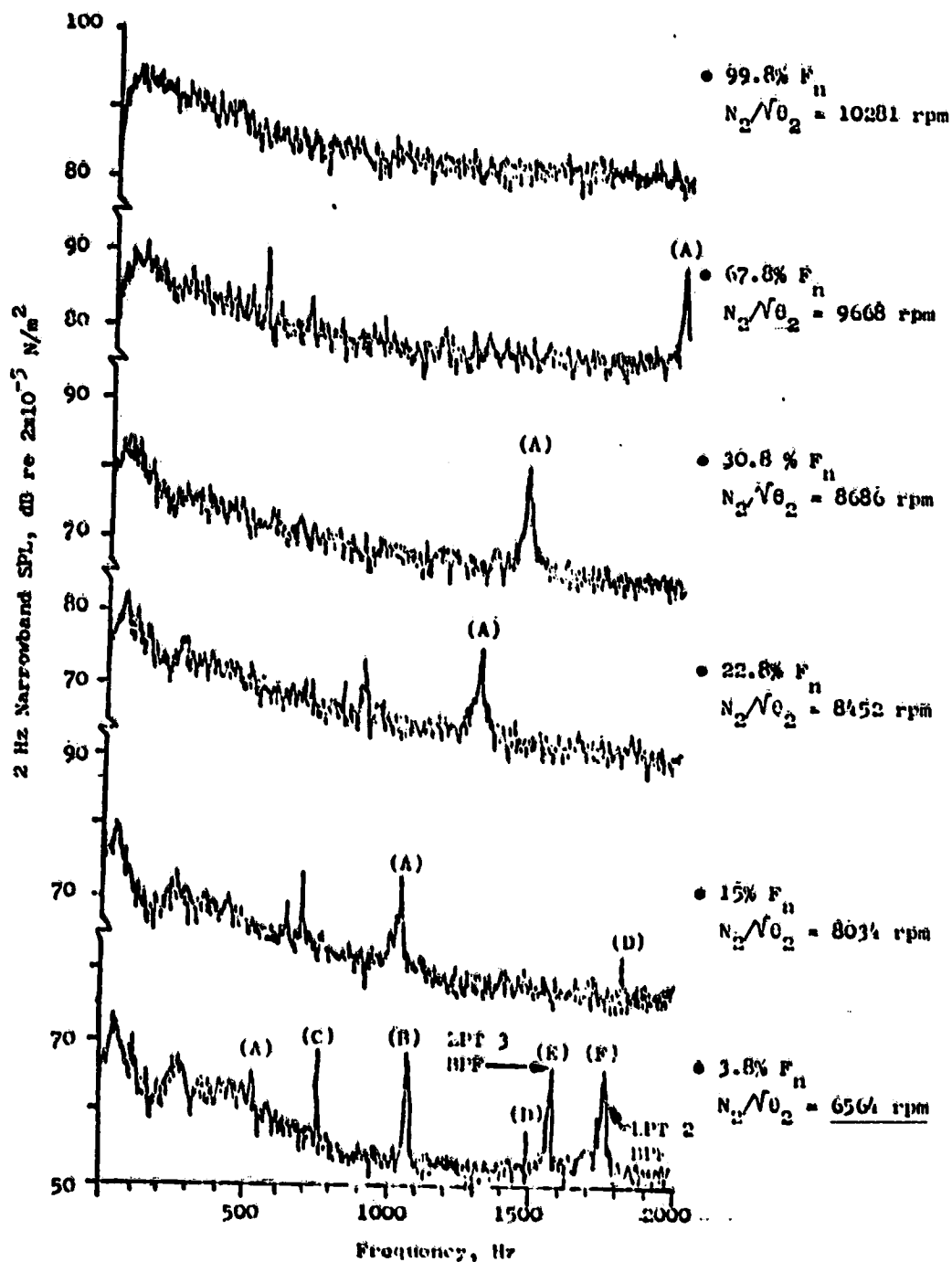


Figure 4.1-20. Far-Field Spectra Variation at 90° Acoustic Angle.

- CF6-50 Core-Noise Program
- 45.72 m Arc, Ground Plane Micro
- As Measured Data

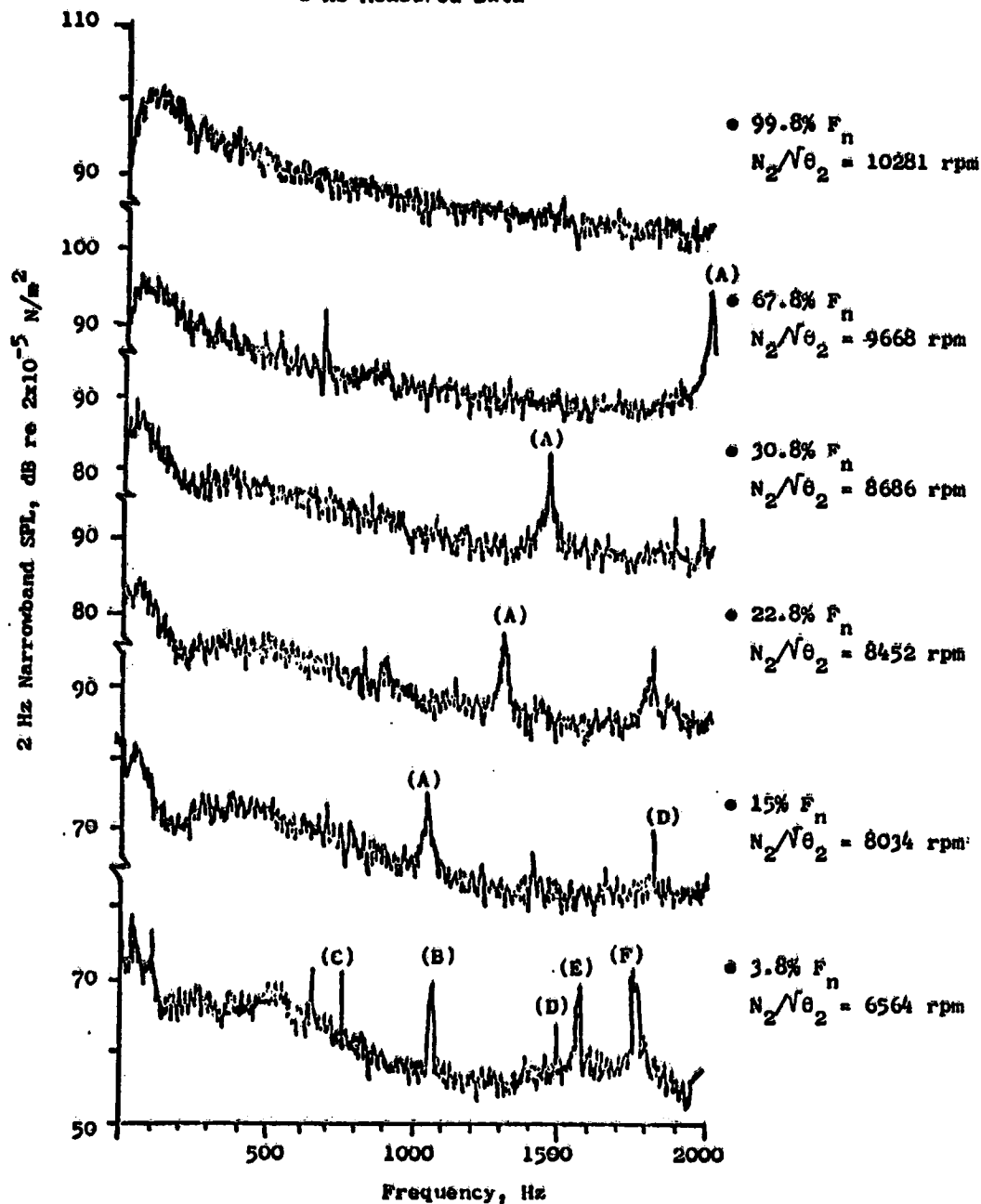


Figure 4.1-21. Far-Field Spectra Variation at 120° Acoustic Angle.

ORIGINAL PAGE IS
OF POOR QUALITY

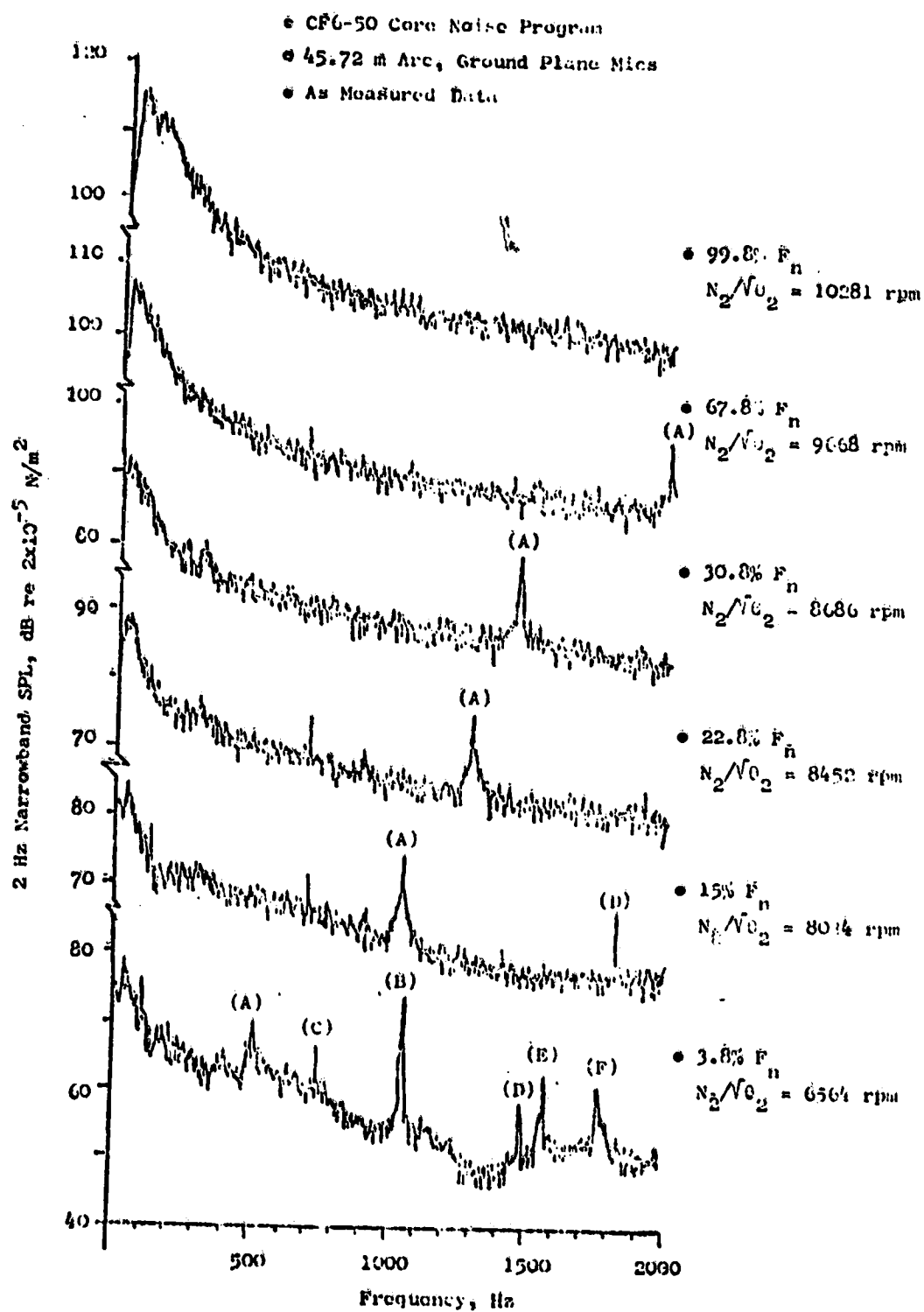


Figure 4.1-22. Far-Field Spectra Variation at 150° Acoustic Angle.

to the fan BPF, include the fan booster BPF and fan second harmonic (B), those from the fuel pump gear (C and D), and low-pressure turbine third and second stage BPF's (E and F).

The fuel pump gear tones (C and D) were identified in the internal FPL spectra from the fuel nozzle sensors. These results show that the fuel system components are the sources of several tones apparent in the far-field data at low power settings near idle.

The 1/3-octave-band far-field spectra presented in Figure 4.1-23 illustrate the spectra variation at selected angles versus core speed. They support the narrowband results previously discussed. The spectra at the typical peak core noise angle of 120° shows the SPL to peak around 400-500 Hz for conditions below $30.8\% F_n$. Similar peaked regions are noted at 110° and 90° .

4.1.2 Internal Spectra Comparison from Engine Outdoor Stand and Test Cell

The CF6-50 engine internal measurements acquired during the core noise investigation with the standard production annular combustor were compared with similar measurements obtained on a CF6-50 engine with a double annular combustor run in a test cell (Reference 2). The purpose of the comparison was to check the general spectra levels within each combustor and note differences. The idle, approach, and takeoff power settings were selected for comparison. Engine results were compared on a 1/3-octave-band FPWL spectra basis to account for differences in state properties and combustor areas.

Figure 4.1-24 shows the CF6-50 internal power spectra comparison at idle for Planes 3.0, 3.5, 4.0, and 8.0. The open symbols represent the standard annular combustor results obtained in the core noise program, while the solid symbols represent the results obtained in ECCP Phase III on the double annular combustor.

The power spectra at Planes 3.0, 3.5, and 8.0 agree within 5 to 8 dB above 250 Hz (except for the 400-Hz tone in the ECCP Phase III data). The spectra shapes are also similar. A large difference is noted at Plane 4.0 with the standard combustor data falling 10 to 15 dB below the double annular results. One possible explanation of the differences observed between the two combustors could be the pilot-fuel-only operation of the double annular combustor at idle as opposed to the alternate fuel nozzle operation for the standard combustor. The pilot-fuel-only operation at those low power settings generally produced higher FPWL's as noted in Reference 2.

The approach-power comparison illustrated in Figure 4.1-25 shows a much closer agreement of both spectral shape and level. This condition has all fuel nozzles operating for both the standard and double annular combustors. The difference of about 10 dB at the low frequencies (<250 Hz) in the core exhaust (Plane 8.0) may be the result of higher turbulence experienced on the core probe with the factory plug nozzle installed for the test cell run (ECCP Phase III). A long fixed nozzle was used on the core exhaust for the outdoor test of the engine. It offered a smoother, more gradual expansion path to the exhaust flow through nozzle.

● CF6-50 Core Noise Ground Plane Microphone Data

● Standard Day, Freefield Corrected on 45.72 m Arc

□ 3.8% F_n ▽ 15.0% F_n

○ 22.8% F_n △ 30.8% F_n

◇ 67.8% F_n ● 99.8% F_n

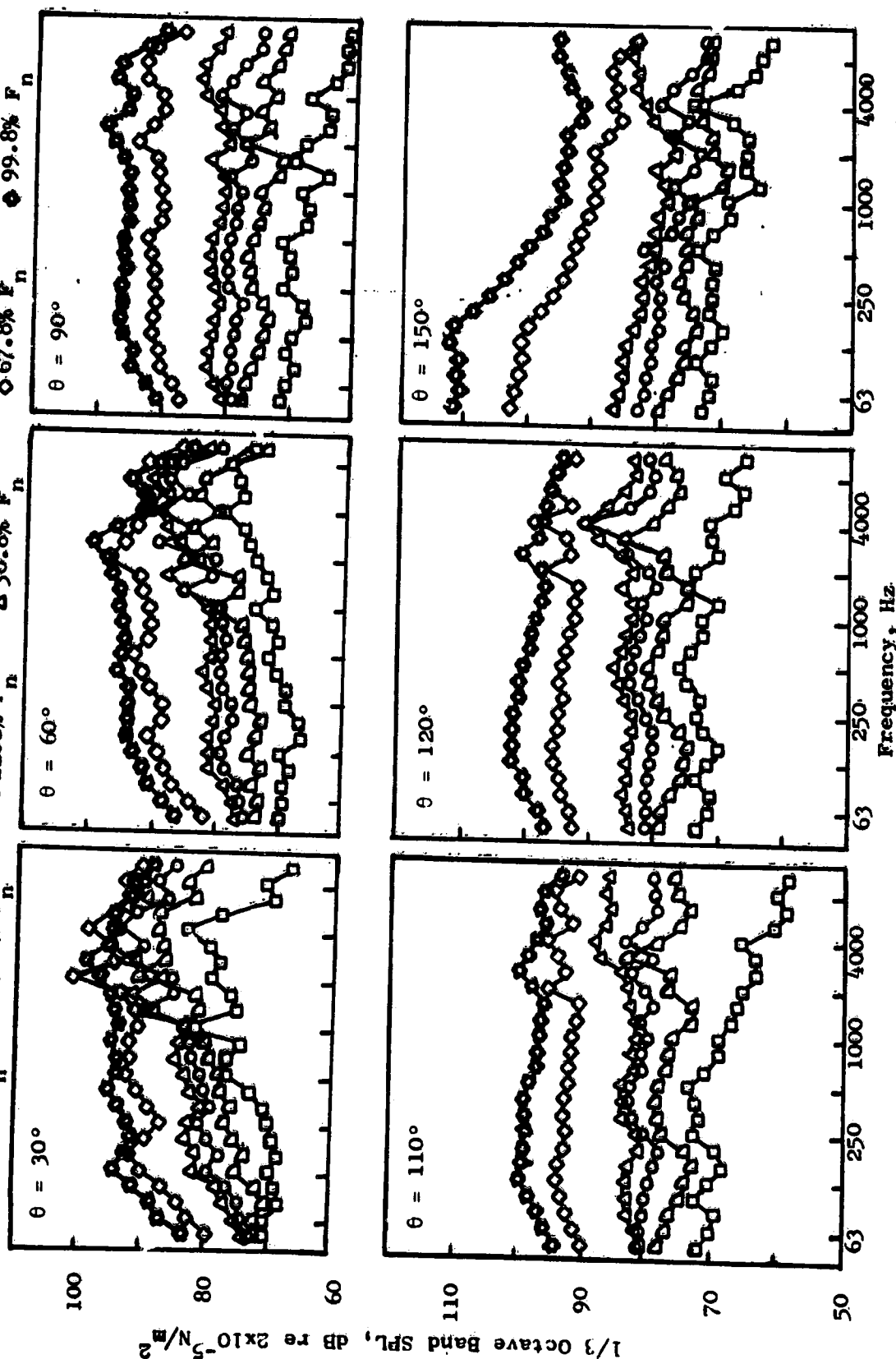


Figure 4.1-23. Variation of Far-Field Spectra with Engine Power Setting.

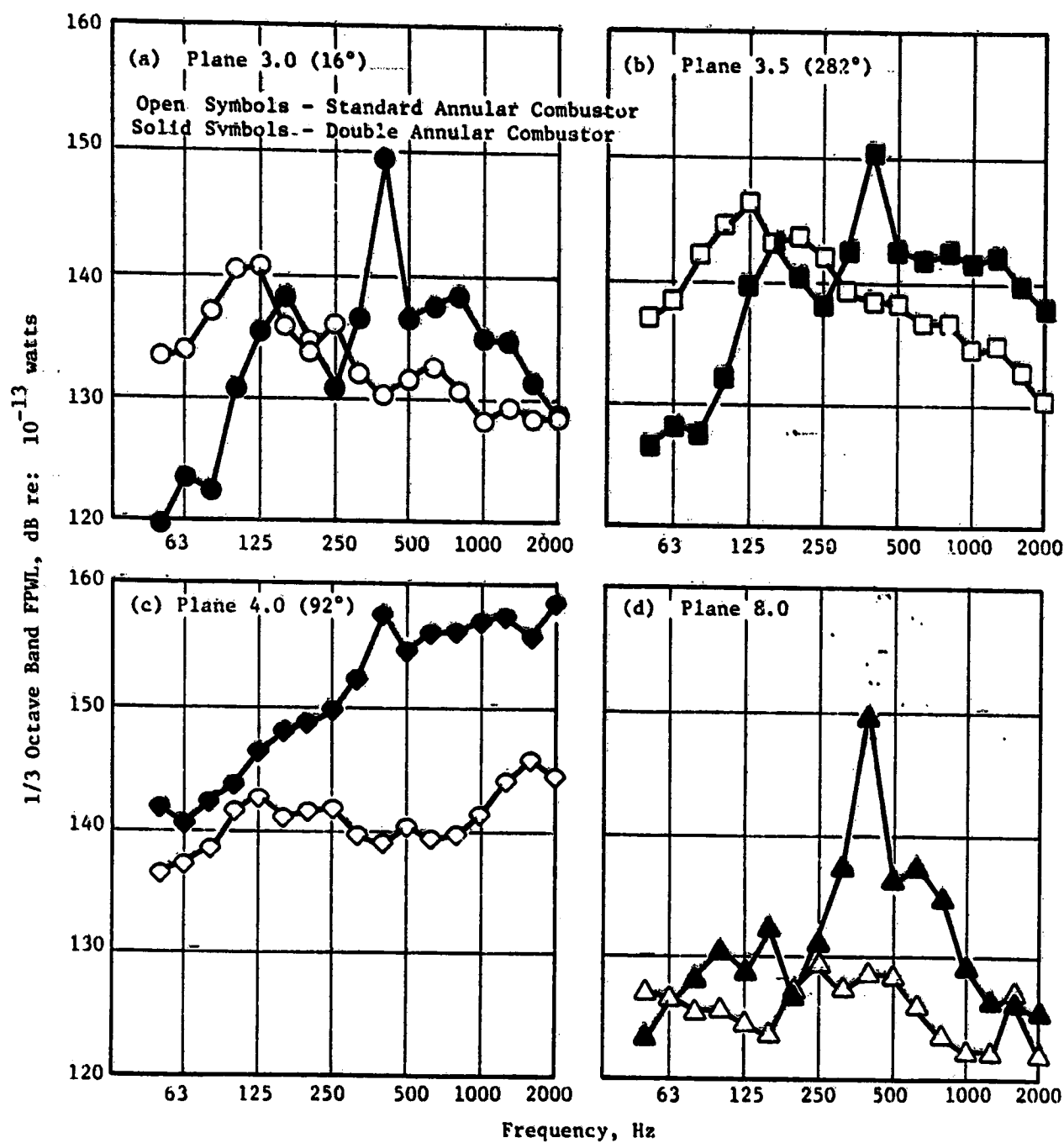


Figure 4.1-24. GF6-50 Internal Power Spectra Comparison at Idle.

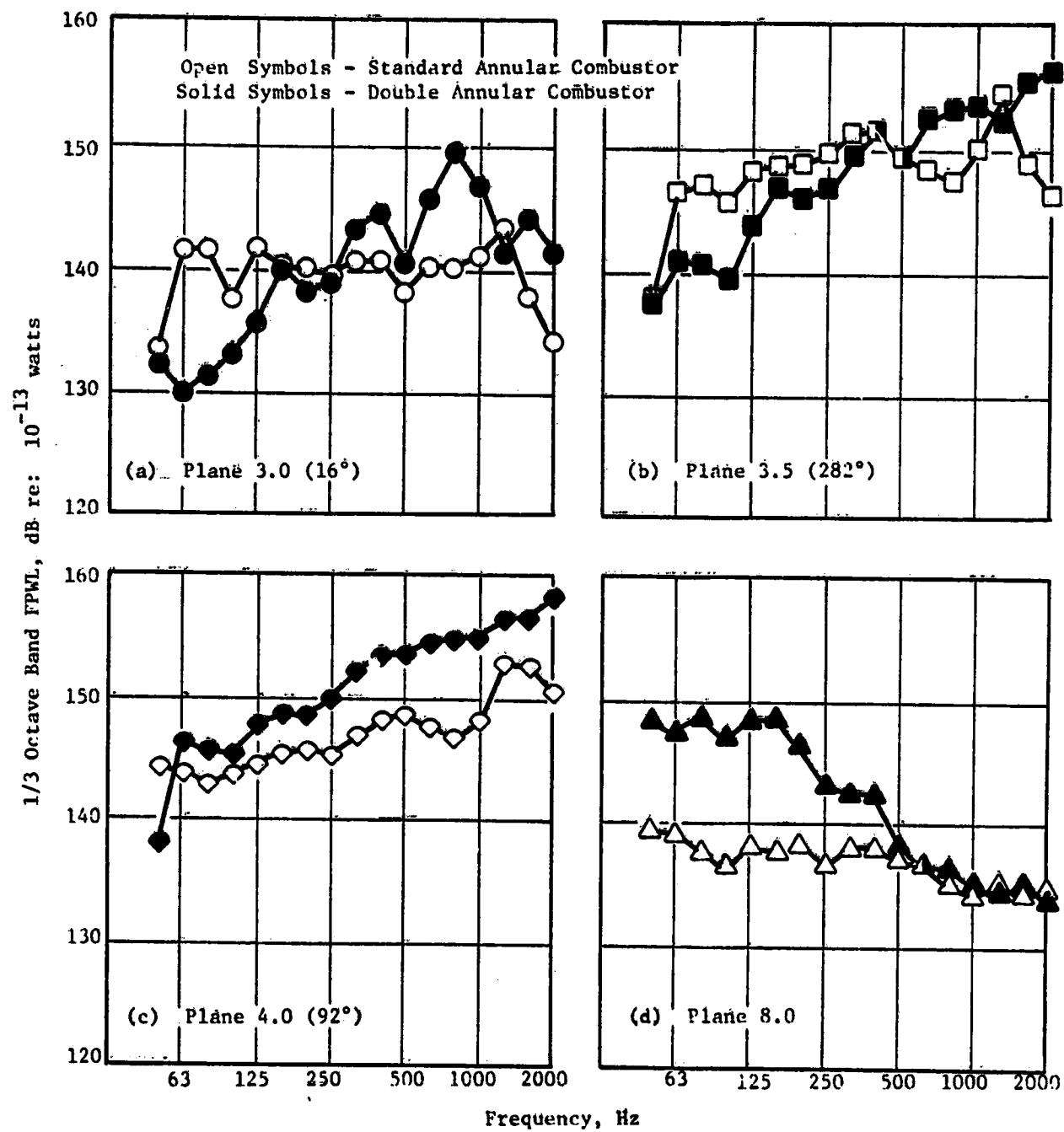


Figure 4.1-25. CF6-50 Internal Power Spectra Comparison at Approach.

The comparison at takeoff power in Figure 4.1-26 shows agreement in spectra shape at Planes 3.0, 4.0, and 8.0. The Plane 3.5 spectra for the standard combustor are more peaked in the 315-500 Hz region than the generally flat rising shape of the double annular spectrum. Differences of 5 to 8 dB lower FPWL are noted at Plane 4.0 with the standard combustor.

These comparisons indicate general agreement of spectra levels for both tests of the CF6-50 engine. Differences in spectral shape are expected since the combustors are not the same.

4.1.3 Comparison of Engine Test to Duct-Rig Results with Standard Combustor

The internal measurements obtained on the CF6-50 engine with the standard production annular combustor were compared with measurements previously obtained on a similar type combustor during full-scale annular combustor rig tests (Reference 1) for the Experimental Clean Combustor Program. Two points were selected for comparison based on similarity of fuel-air ratios and inlet flow functions ($Wc/\sqrt{T_{T3}/P_{T3}}$). The selected conditions are shown in Table 4.1-1 and include the approach and takeoff power settings. They are Readings 317 and 321 from ECCP Phase II and Readings 551 and 567 from the current program.

The setup for the duct-rig test is detailed in the ECCP Phase II final report (Reference 1). The acoustic probe locations for these tests were as illustrated in Figure 4.1-27. The engine and duct-rig acoustic measurement plane locations were not identical, as noted in reviewing the engine plane locations in Figure 3.6-1.

The data for comparison included the inlet and discharge measurements from the component test and Planes 3.0, 3.5, and 4.0 from the CF6-50 engine test. The differences associated with the state properties, measurement plane area, and flow Mach numbers were accounted for by using the measured 1/3-octave-band power level spectra which were based on fluctuating pressure measurements at each plane. An assumption was made that the noise generated in the combustor propagated in the plane-wave mode past each sensor.

The approach power setting comparison in Figure 4.1-28 indicates agreement of engine and duct-rig data in the low frequencies (<250 Hz) at both inlet and discharge stations. The duct-rig results above 315 Hz show differences of 10 to 15 dB above the engine data.

The engine power spectra at Plane 4.0 from this program agree well in shape and level with the component data in the discharge for the low frequencies. The Plane 3.5 sensor in the borescope port is about 3 dB higher than the duct-rig data over the same frequency range.

The engine-to-duct-rig spectra comparison for the takeoff condition in Figure 4.1-29 shows a much wider separation between the data sets over the frequency range for both inlet and discharge. In general, the shapes of the power spectra from the engine and duct-rig are similar, especially in the discharge region.

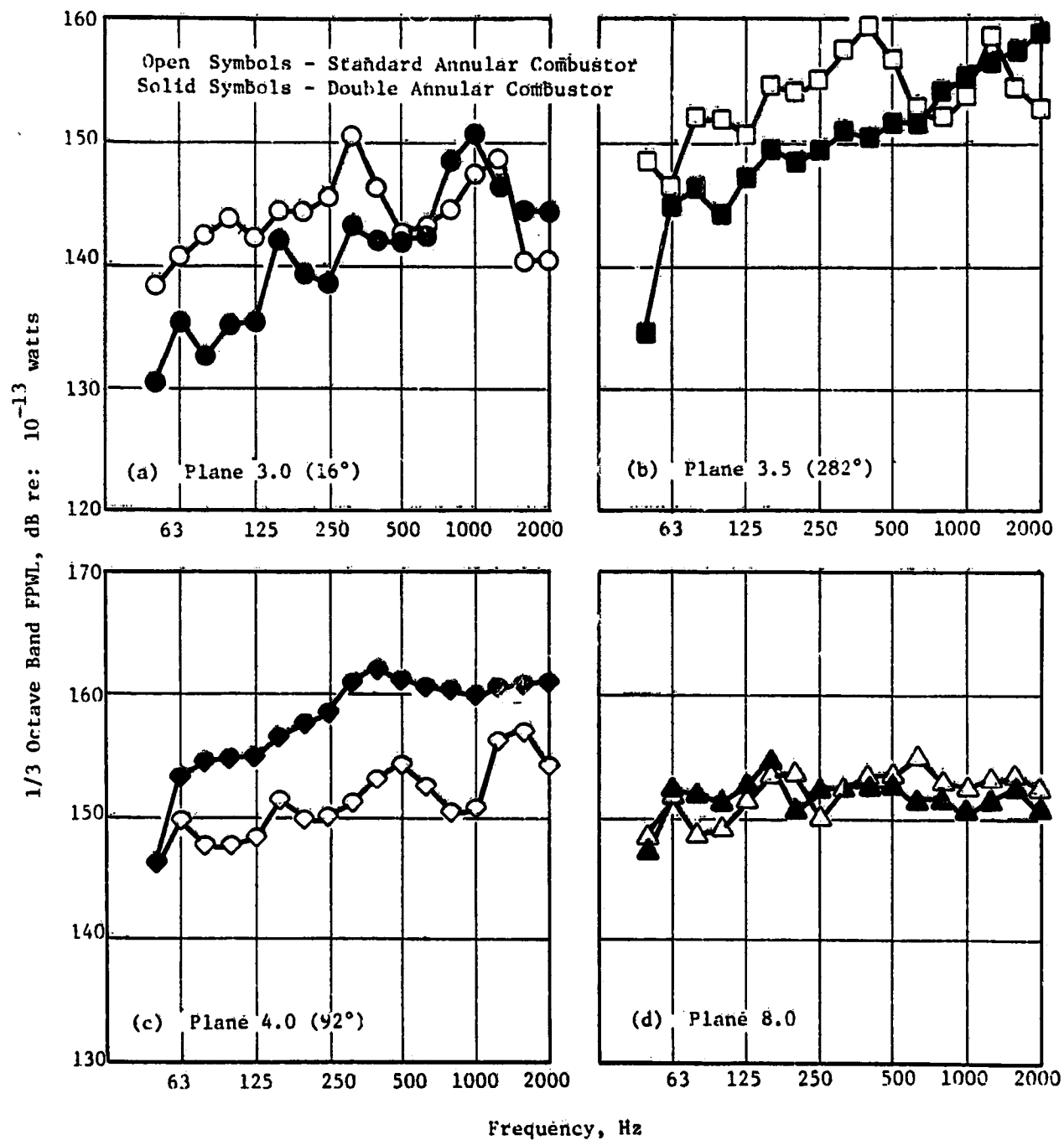
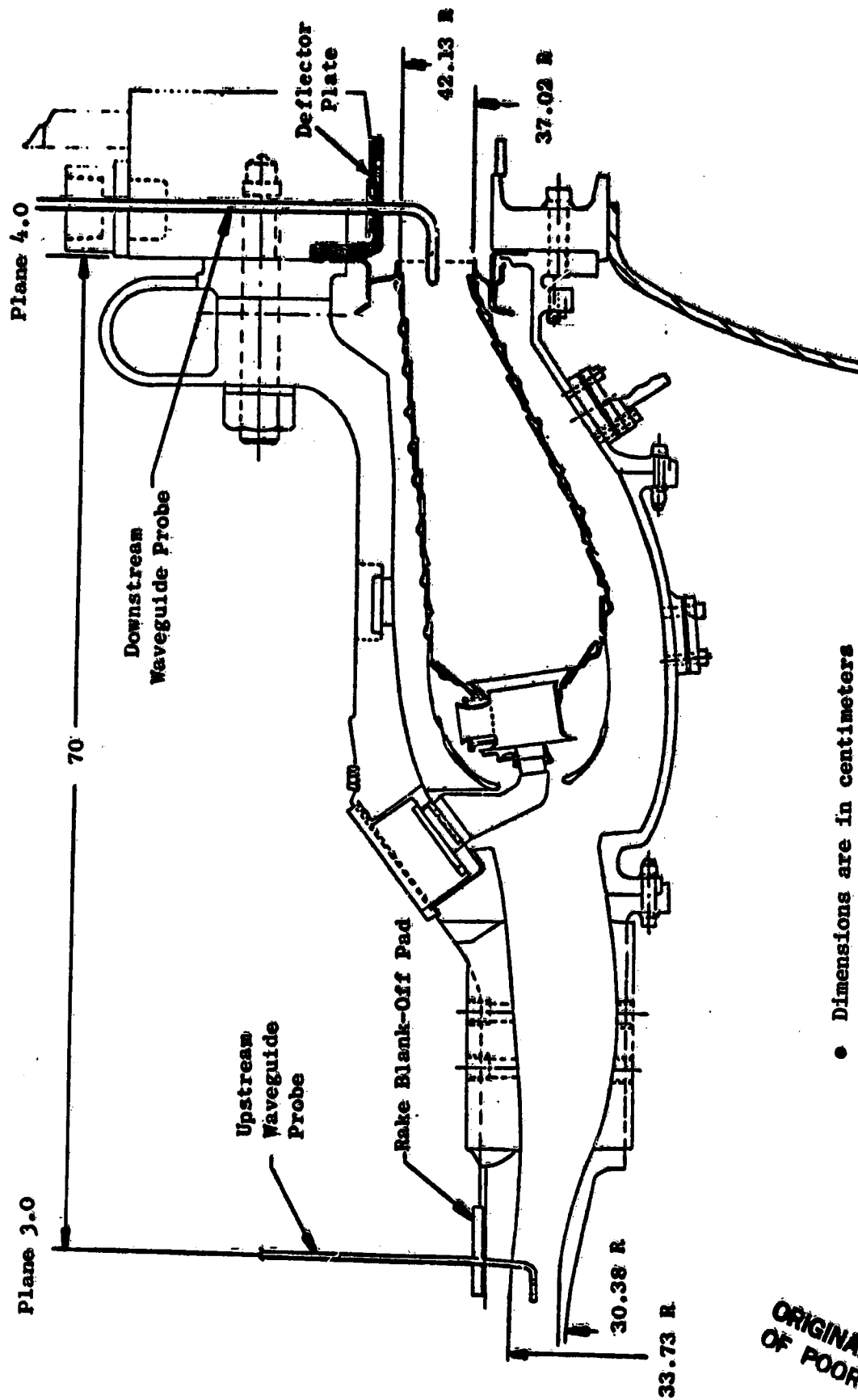


Figure 4.1-26. CF6-50 Internal Power Spectra Comparison at Takeoff.



• Dimensions are in centimeters

Figure 4.1-27. Acoustic Probe Locations for Duct-Rig Test.

ORIGINAL PAGE IS
OF POOR QUALITY

NOTE: The filled symbols represent duct rig test data.

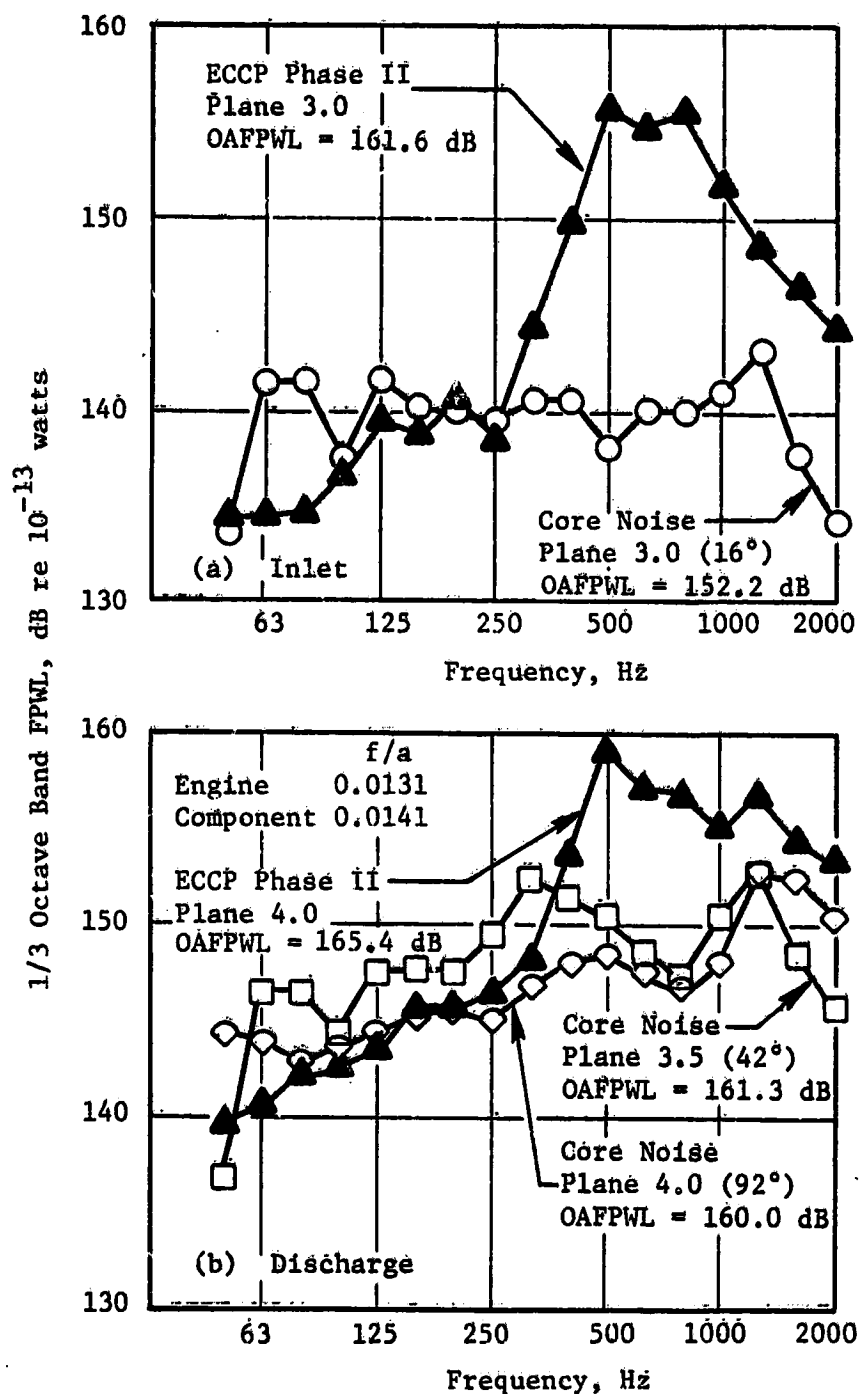


Figure 4.1-28. Comparison of Engine and Duct-Rig Power Spectra for Standard Combustor at Approach.

NOTE: The filled symbols represent duct rig test data.

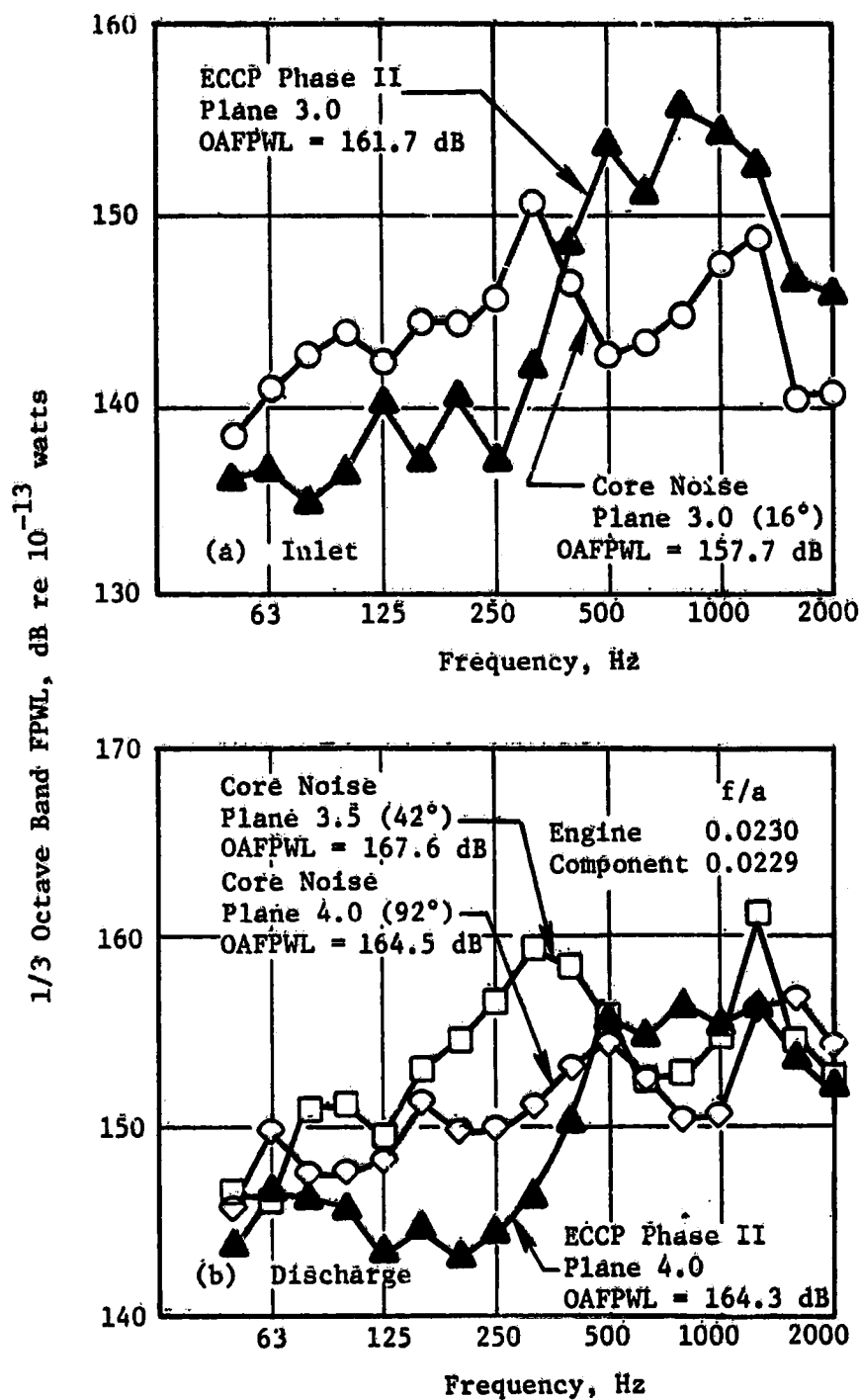


Figure 4.1-29. Comparison of Engine and Duct-Rig Power Spectra for Standard Combustor at Takeoff.

A number of differences exist between the engine and duct-rig combustor configuration as noted in Reference 2. They include differences in measurement plane location, instrumentation, the presence of a choked turbine nozzle diaphragm in the engine, and the variations in test conditions which all contribute to the differences in levels apparent between engine and duct rig. However, the overall engine-to-duct-rig comparisons with the standard combustor show good results.

4.1.4 Aerodynamic Parameters

A summary of the engine aerodynamic performance information for the CF6-50 core noise program is found in Table 4.1-2. The performance data were obtained from an average of two DMS (Data Management System) readings taken online at the beginning and end of each steady-state condition. The data were supplemented by data from the engine-run logs and cross plots from the sea level static cycle for this engine to complete the performance information. Static pressures and temperatures determined from isentropic relationships are included in the table along with an estimate of the local Mach number at each measurement plane. A total of 14 points is listed in the table which include repeat readings at 3.8% F_n (idle), 30.8% F_n (approach), 45.6% F_n , and 85.5% F_n (climbout) which were taken to check data repeatability over the operating line.

The CF6-50 core noise aerodynamic parameters computed from the engine performance information are listed in Table 4.1-3 for each test condition.

4.2 SOURCE LOCATION FROM INTERNAL MEASUREMENTS

The identification of the primary noise source location within the CF6-50 combustor was accomplished through the vectoring of the time delays from cross-correlations between pairs of internal sensors. The sensor pairs consisted of a forward sensor which provided the input signal and an aft sensor for the output signal. A review of the signal resolution with various combinations of internal sensors, including the downstream sensors in the core exhaust nozzle probe, showed the best combination of sensor pairs for this analysis to be between Plane 3.0 to Plane 3.5, Plane 3.5 to Plane 4.0, and the sensors between Plane 3.5 (42°) to 3.5 (102°) and Plane 3.5 (102°) to 3.5 (282°). Cross-correlations between any of the combustor sensors and the downstream probe in the core exhaust gave poor resolution ($\rho_{xy} < 0.1$) and, consequently, were not used in the source location investigation. A quantitative evaluation of the frequency bands associated with the time delays from the cross-correlations was determined through the use of the cross-spectrum phase for each sensor pair.

The conditions investigated included five low-power settings from idle to approach and three higher power points above approach to the takeoff condition. Restricting the majority of the source location investigation to the low power settings gave better resolution to the cross-correlations between sensors.

Table 4.1-2. Engine Aerodynamic Performance Summary for CF6-50 Core Noise Program.

Metric Units

Point No.	WPS Bldgs (Average)	WPS (km)	N_1/ϕ_2 rpm	N_2/ϕ_2 rpm	902	P_{T3} atm	P_{S3} atm	T_{S3} K	S_3	$P_{T3.5}$ atm	$P_{S3.5}$ atm	$T_{S3.5}$ K	$S_{3.5}$	W_{36} kg/sec	$W_{36.5}$ kg/sec	$W_{36.5}$ lb/hr	P_{T4} atm	P_{S4} atm	T_{4} K	N_4	P_{T4} atm	P_{S4} atm	T_{4} K	N_4
1	544-545	3.8	867	6564	9753	3.16	3.03	419.4	417.2	3.16	3.03	419.4	417.2	12.5	453.6	453.6	3.02	2.53	826.7	791.1	1.01	0.90	825.0	622.9
2	546-547	3.8	862	6464	9753	3.16	3.03	419.4	417.2	3.16	3.03	419.4	417.2	11.8	451.3	451.3	3.02	2.53	822.8	787.8	1.01	0.90	822.8	622.9
3	548-549	3.8	852	6364	9753	3.16	3.03	419.4	417.2	3.16	3.03	419.4	417.2	36.0	1905.0	1905.0	3.02	2.53	822.8	787.8	1.01	0.90	822.8	622.9
4	550-551	3.8	842	6264	9753	3.16	3.03	419.4	417.2	3.16	3.03	419.4	417.2	46.7	2023.0	2023.0	3.02	2.53	822.8	787.8	1.01	0.90	822.8	622.9
5	552-553	3.8	832	6164	9753	3.16	3.03	419.4	417.2	3.16	3.03	419.4	417.2	49.9	2350.7	2350.7	3.02	2.53	822.8	787.8	1.01	0.90	822.8	622.9
6	554-555	3.8	822	6064	9753	3.16	3.03	419.4	417.2	3.16	3.03	419.4	417.2	55.6	2709.5	2709.5	3.02	2.53	822.8	787.8	1.01	0.90	822.8	622.9
7	556-557	3.8	812	5964	9753	3.16	3.03	419.4	417.2	3.16	3.03	419.4	417.2	62.1	3470.9	3470.9	3.02	2.53	822.8	787.8	1.01	0.90	822.8	622.9
8	558-559	3.8	802	5864	9753	3.16	3.03	419.4	417.2	3.16	3.03	419.4	417.2	80.8	5204.4	5204.4	3.02	2.53	822.8	787.8	1.01	0.90	822.8	622.9
9	560-561	3.8	792	5764	9753	3.16	3.03	419.4	417.2	3.16	3.03	419.4	417.2	89.6	6404.4	6404.4	3.02	2.53	822.8	787.8	1.01	0.90	822.8	622.9
10	562-563	3.8	782	5664	9753	3.16	3.03	419.4	417.2	3.16	3.03	419.4	417.2	95.3	7892.5	7892.5	3.02	2.53	822.8	787.8	1.01	0.90	822.8	622.9

 $A_{3.5} = 0.24258 \text{ m}^2$ $A_3 = 0.09988 \text{ m}^2$

Compressor Cross-Sectional Areas at Measurement Planes

 $A_0 = 0.55484 \text{ m}^2$

English Units

Point No.	WPS Bldgs (Average)	WPS (km)	N_1/ϕ_2 rpm	N_2/ϕ_2 rpm	902	P_{T3} psia	P_{S3} psia	T_{S3} R	S_3	$P_{T3.5}$ psia	$P_{S3.5}$ psia	$T_{S3.5}$ R	$S_{3.5}$	W_{36} lb/sec	$W_{36.5}$ lb/sec	$W_{36.5}$ lb/hr	P_{T4} psia	P_{S4} psia	T_{4} R	N_4	P_{T4} psia	P_{S4} psia	T_{4} R	N_4
1	544-545	3.8	867	6564	9753	46.2	44.5	755	751	46.2	44.5	755	751	27.5	1000	1000	44.4	37.2	1488	1424	14.8	13.4	1424	1121
2	546-547	3.8	862	6464	9753	46.2	44.5	755	751	46.2	44.5	755	751	26.0	995	995	44.4	37.2	1488	1424	14.8	13.4	1424	1121
3	548-549	3.8	852	6364	9753	46.2	44.5	755	751	46.2	44.5	755	751	75.0	2950	2950	44.4	37.2	1488	1424	14.8	13.4	1424	1121
4	550-551	3.8	842	6264	9753	46.2	44.5	755	751	46.2	44.5	755	751	103.0	4460	4460	44.4	37.2	1488	1424	14.8	13.4	1424	1121
5	552-553	3.8	832	6164	9753	46.2	44.5	755	751	46.2	44.5	755	751	110.0	5215	5215	44.4	37.2	1488	1424	14.8	13.4	1424	1121
6	554-555	3.8	822	6064	9753	46.2	44.5	755	751	46.2	44.5	755	751	122.5	6150	6150	44.4	37.2	1488	1424	14.8	13.4	1424	1121
7	556-557	3.8	812	5964	9753	46.2	44.5	755	751	46.2	44.5	755	751	137.0	7600	7600	44.4	37.2	1488	1424	14.8	13.4	1424	1121
8	558-559	3.8	802	5864	9753	46.2	44.5	755	751	46.2	44.5	755	751	178.2	11650	11650	44.4	37.2	1488	1424	14.8	13.4	1424	1121
9	560-561	3.8	792	5764	9753	46.2	44.5	755	751	46.2	44.5	755	751	197.5	14300	14300	44.4	37.2	1488	1424	14.8	13.4	1424	1121
10	562-563	3.8	782	5664	9753	46.2	44.5	755	751	46.2	44.5	755	751	210.0	17400	17400	44.4	37.2	1488	1424	14.8	13.4	1424	1121

Compressor Cross-Sectional Areas at Measurement Planes

 $A_{3.5} = 0.376 \text{ in}^2$ $A_3 = 0.154 \text{ in}^2$ $A_0 = 880 \text{ in}^2$

Table 4.1-3. CF6-50 Core Noise Aerodynamic Parameters.

• Metric Units

Point No.	DMS Rngs (Average)	% F ₀ (Nom)	N ₂ /√θ ₂ rpm	W ₂₅ kg/sec	W ₃ kg/sec	$\frac{W_{36}/T_{T3}}{P_{T3} A_3}$ kg./K sec-atm-m ²	f/a kgf/Kga	ΔP ₄₃ atm	ΔP ₄₃ /P _{T3} %	ΔT ₃₄ K	V _R m/sec	HRR kw	S _c watt/m ² -Pa
1	544-545	3.8	6564	15.8	14.9	816.2	.0101	.12	3.82	407.3	12.6	5439.0	295.9
1R	569-570	3.8	6444	14.9	14.0	793.7	.0106	.01	0.30	408.4	12.1	5411.8	305.1
2	571-572	15.0	8034	42.8	40.5	1072.7	.0109	.36	4.92	388.3	18.7	16045.0	374.9
3	547-548	22.8	8452	55.4	52.4	1024.4	.0120	.47	4.76	450.6	19.5	22843.8	394.9
4	549-550	26.7	8660	58.8	55.6	1081.7	.0120	.42	4.01	468.3	19.7	24257.9	395.7
5	551-552	30.8	8686	62.9	59.4	1052.4	.0131	.53	4.55	495.0	19.5	28282.8	414.7
5R	573-574	30.8	8697	62.9	59.4	1049.7	.0132	.57	4.88	493.4	19.5	28364.4	414.4
6	557-558	36.5	8882	70.1	66.2	1045.1	.0139	.61	4.58	529.5	19.8	33449.8	432.3
7	561-562	45.6	9106	78.2	73.9	1027.9	.0154	.67	4.33	571.1	19.9	41336.4	456.7
7R	575	45.6	9106	78.4	74.0	1027.8	.0155	.69	4.46	571.7	19.8	41608.4	459.1
8	563-564	67.8	9668	101.8	96.2	1025.2	.0182	.91	4.33	658.3	20.6	63364.4	515.1
9	565-566	85.5	9964	112.6	106.4	991.0	.0201	1.11	4.52	703.4	20.4	77777.7	540.9
9R	578	85.5	9964	112.9	106.6	992.9	.0204	1.06	4.30	711.1	20.5	78756.7	545.7
10	567-568	99.8	10281	120.1	113.4	936.6	.0230	1.23	4.34	743.9	19.7	94638.6	571.0

• English Units

Point No.	DMS Rngs (Average)	% F ₀ (Nom)	N ₂ /√θ ₂ rpm	W ₂₅ lb/sec	W ₃ lb/sec	$\frac{W_{36}/T_{T3}}{P_{T3} A_3}$ lb √°/R sec-lb	f/a lbf/lba	ΔP ₄₃ psi	ΔP ₄₃ /P _{T3} %	ΔT ₃₄ °R	V _R ft/sec	HRR kw	S _c × 10 ⁶ Btu H _T -ft ² -atm
1	544-545	3.8	6564	34.8	32.8	0.1100	.0101	1.76	3.82	733.1	41.4	5439.0	2.898
1R	569-570	3.8	6444	32.8	30.9	0.1028	.0106	0.15	0.30	735.1	39.8	5411.8	2.988
2	571-572	15.0	8034	94.4	89.3	0.1394	.0109	5.29	4.92	699.0	61.3	16045.0	3.672
3	547-548	22.8	8452	122.1	115.5	0.1391	.0120	6.91	4.76	811.0	63.9	22843.8	3.868
4	549-550	26.7	8660	129.6	122.6	0.1405	.0120	6.17	4.01	843.0	64.8	24257.9	3.876
5	551-552	30.8	8686	138.7	131.0	0.1366	.0131	7.79	4.55	891.0	64.1	28282.8	4.062
5R	573-574	30.8	8697	138.7	131.0	0.1362	.0132	8.38	4.88	888.0	63.9	28364.4	4.059
6	557-558	36.5	8882	154.5	145.9	0.1356	.0139	8.97	4.58	953.0	64.8	33449.8	4.205
7	561-562	45.6	9106	172.4	162.9	0.1336	.0154	9.85	4.33	1028.0	65.2	41336.4	4.473
7R	575	45.6	9106	172.8	163.1	0.1336	.0155	10.14	4.46	1029.0	65.1	41608.4	4.503
8	563-564	67.8	9668	224.4	212.1	0.1331	.0182	13.38	4.33	1185.0	67.7	63364.4	5.046
9	565-566	85.5	9964	248.2	234.6	0.1287	.0201	16.32	4.52	1266.0	66.9	77777.7	5.298
9R	578	85.5	9964	248.9	235.0	0.1289	.0204	15.58	4.30	1280.0	67.2	78756.7	5.345
10	567-568	99.8	10281	264.8	250.0	0.1215	.0230	18.08	4.34	1339.0	64.5	94638.6	5.593

4.2.1 Identification of Source Location from Vectoring of Cross-Correlation Time Delays

A low power setting of 15% F_n was used to illustrate the cross-correlation results from the eight conditions investigated. The results presented for this condition are, in general, typical of all of the other power settings. A summary tabulation of the time delays from sensor pairs at all test points is presented in Table 4.2-1.

The internal sensor pairs from Plane 3.0 (16°) to 3.5 (42°) indicate a negative time delay (-0.85 msec), as seen in Figure 4.2-1, for the predominant peak which corresponds to a velocity of 485 m/s (1591 ft/sec) when using a linear distance between the sensors of 0.4125 m (1.353 ft). This velocity is close to the acoustic velocity of 460.2 m/s (1510 ft/sec) computed for this condition at this location. The negative time delay indicates that a wave moving at acoustic propagation speed is traveling in an upstream direction from Plane 3.5 to 3.0. Similar results are determined from negative time delays obtained between the Plane 3.0 sensor with Plane 3.5 (102°) and 3.5 (282°) sensors.

The Plane 3.5 sensors paired with the Plane 4.0 sensor in the HPT nozzle diaphragm at the combustor discharge showed primarily positive or very near zero time delays. Figure 4.2-2 illustrates the slightly positive time delay (0.04 msec) for the Plane 3.5 (42°) to 4.0 (92°) sensor pair, while Figure 4.2-2(b) indicates a slightly negative time delay (-0.03 msec) for the Plane 3.5 (102°) to 4.0 (92°) sensor combination. This very small (\pm) time delay suggests the acoustic signals in this vicinity are reaching both the Plane 3.5 (42°), 3.5 (102°), and 4.0 (92°) sensors almost simultaneously. The wave directions are suggested to be generally normal to the linear distances between sensors at each plane and propagating in an aft direction. The double-peaked time delay resulting from the cross-correlation between Plane 3.5 (272°) to Plane 4.0 (42°) in Figure 4.2-2(c) illustrates the forward and aft movement of acoustic waves between these sensors.

A look at the time delays associated with the Plane 3.5 sensors at different circumferential locations indicate a positive delay time of 0.2 msec between Plane 3.5 (42°) to 3.5 (102°) in Figure 4.2-3. The Plane 3.5 (102°) to 3.5 (282°) cross-correlation shows a double peak with positive and negative time delays in Figure 4.2-3(b) which is similar to the results between Plane 4.0 (92°) to Plane 3.5 (282°) (see Figure 4.2-2). This suggests that the two or more sets of waves are moving circumferentially around the combustor in this region. Figure 4.2-4 summarizes the results of this comparison and illustrates the time-delay vectoring at 15% F_n , which is typical of other conditions.

4.2.2 Source Content Evaluation from Cross-Spectra Phase

The cross-spectra phase associated with each cross-correlation between interval sensor pairs was determined to quantitatively identify the frequency regions associated with each time delay peak, since there was often more than

Table 4.2-1. Time Delay Vectoring Source Location Summary.

• Direction of Time Delays from Cross-Correlations
Between Combustor Sensor Pairs

Input/ Output	3.0 (16°) 3.5 (42°)	3.0 (16°) 3.5 (102°)	3.0 (16°) 3.5 (282°)	3.5 (42°) 4.0 (92°)	3.5 (102°) 4.0 (92°)	3.5 (282°) 4.0 (92°)	3.5 (42°) 3.5 (102°)	3.5 (102°) 3.5 (282°)
Z F _n								
3.8	-	-	-	0	-	±	+	±
15.0	-	-	-	+	-	±	±	±
22.8	-	-	-	+	0	+	±	±
26.7	-	-	-	+		±	±	±
30.8	-	-	-	+	-	±	+	±
36.5	-	-	-	+	0	±	±	
45.5	-	-	-	+	-	±	+	
99.8	-	-	-	+	-	+	+	

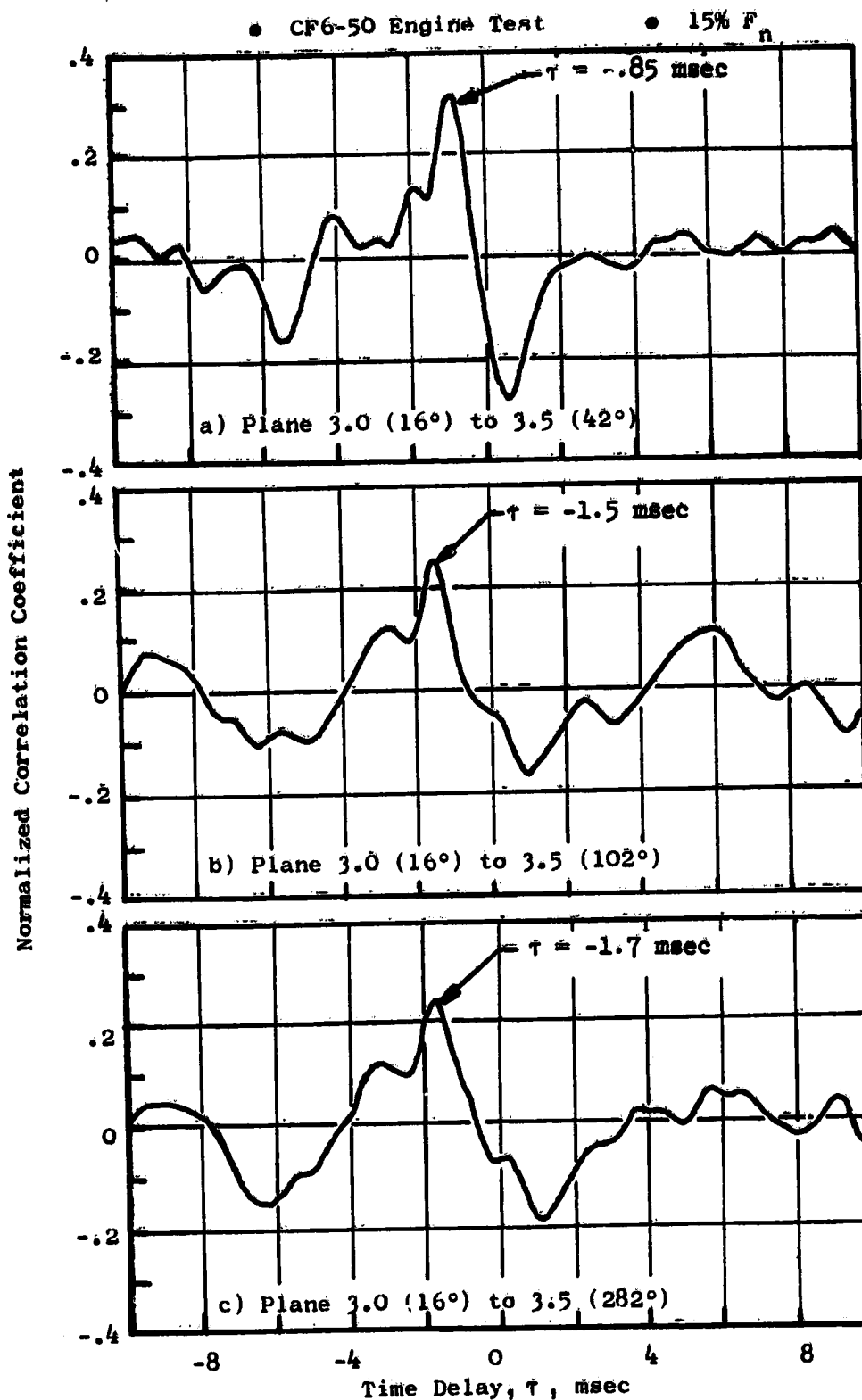


Figure 4.2-1. Cross-Correlation Results Between Combustor Sensors at Plane 3.0 and 3.5.

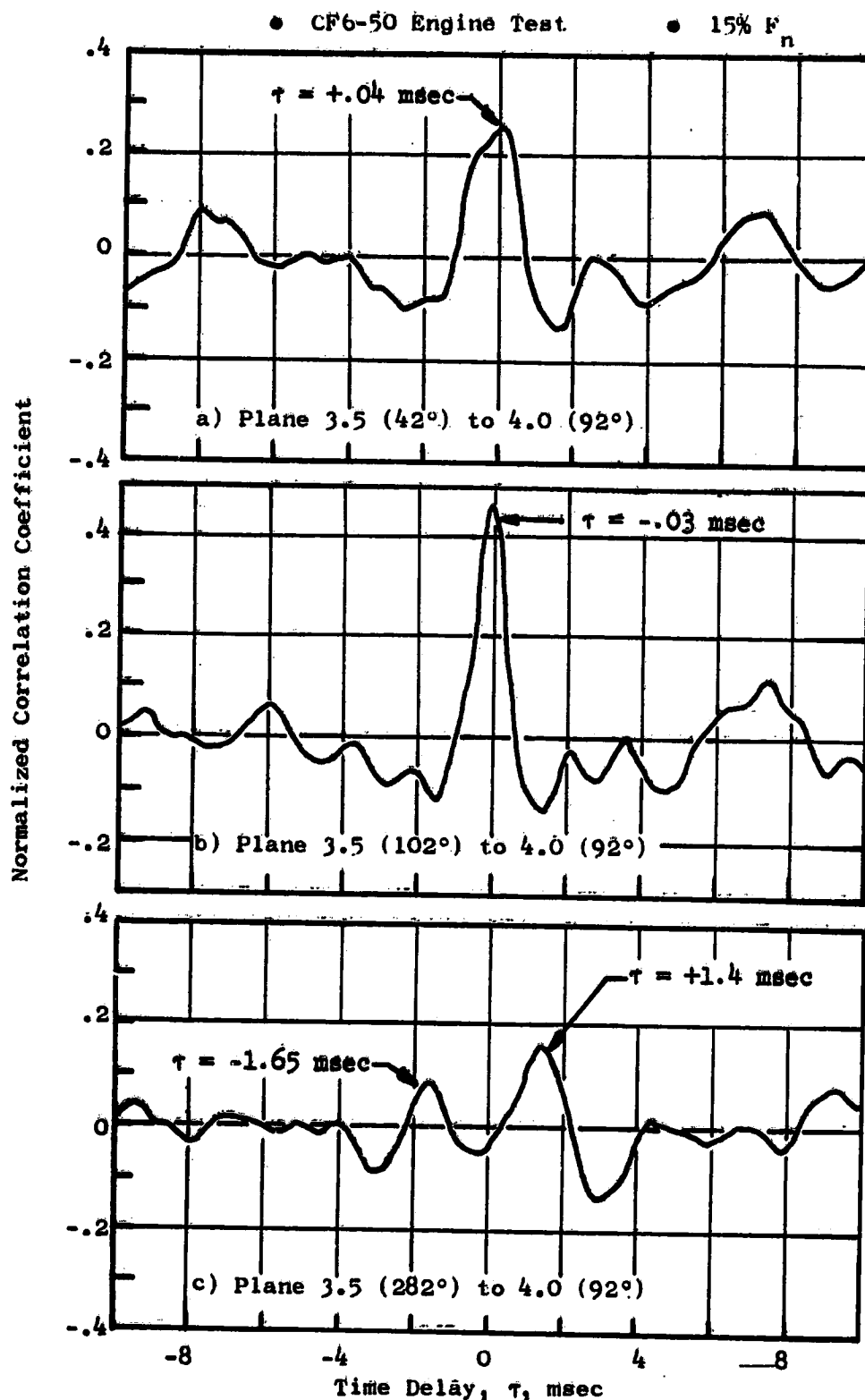


Figure 4.2-2. Cross-Correlation Results Between Combustor Sensors at Plane 3.5 and 4.0.

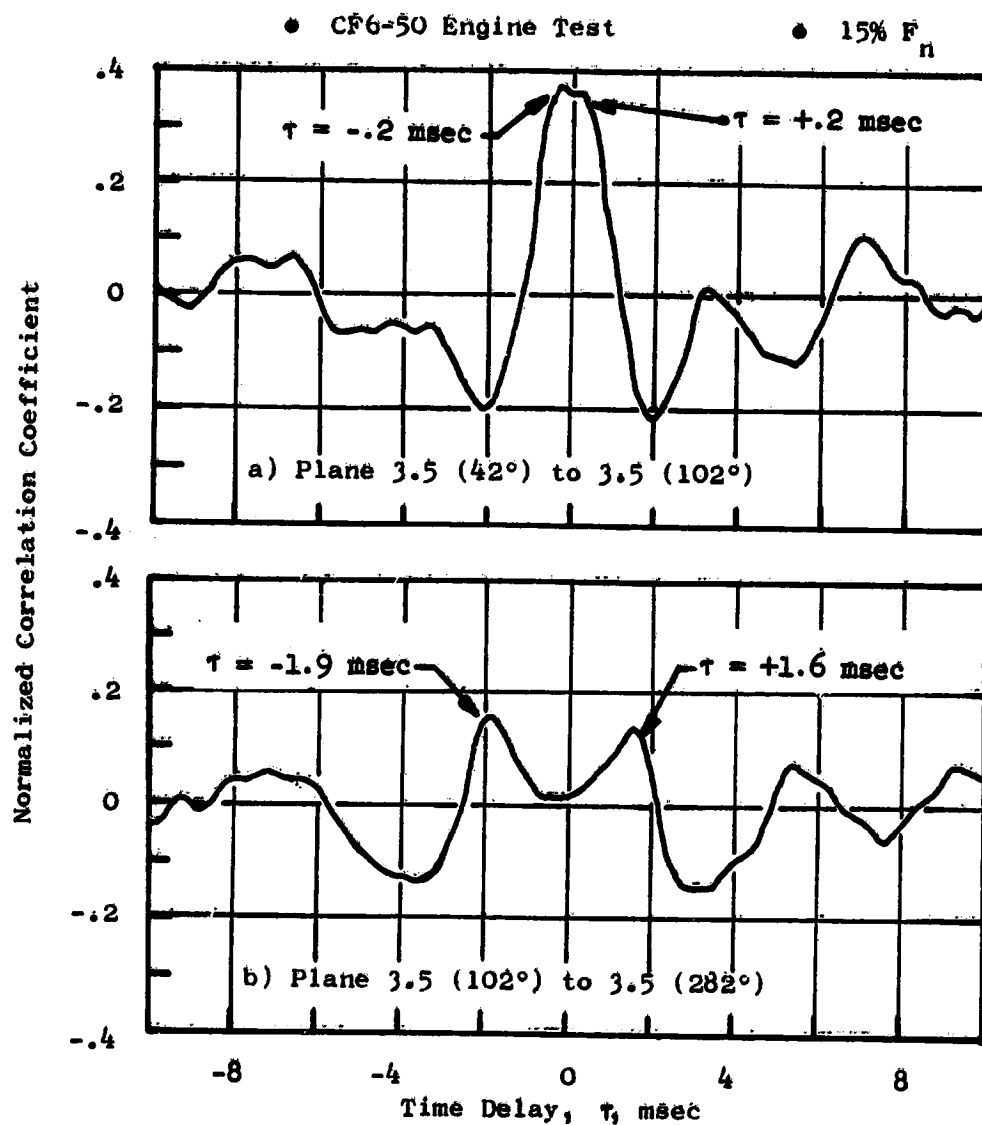


Figure 4.2-3. Cross-Correlation Results Between Combustor Sensors at Plane 3.5.

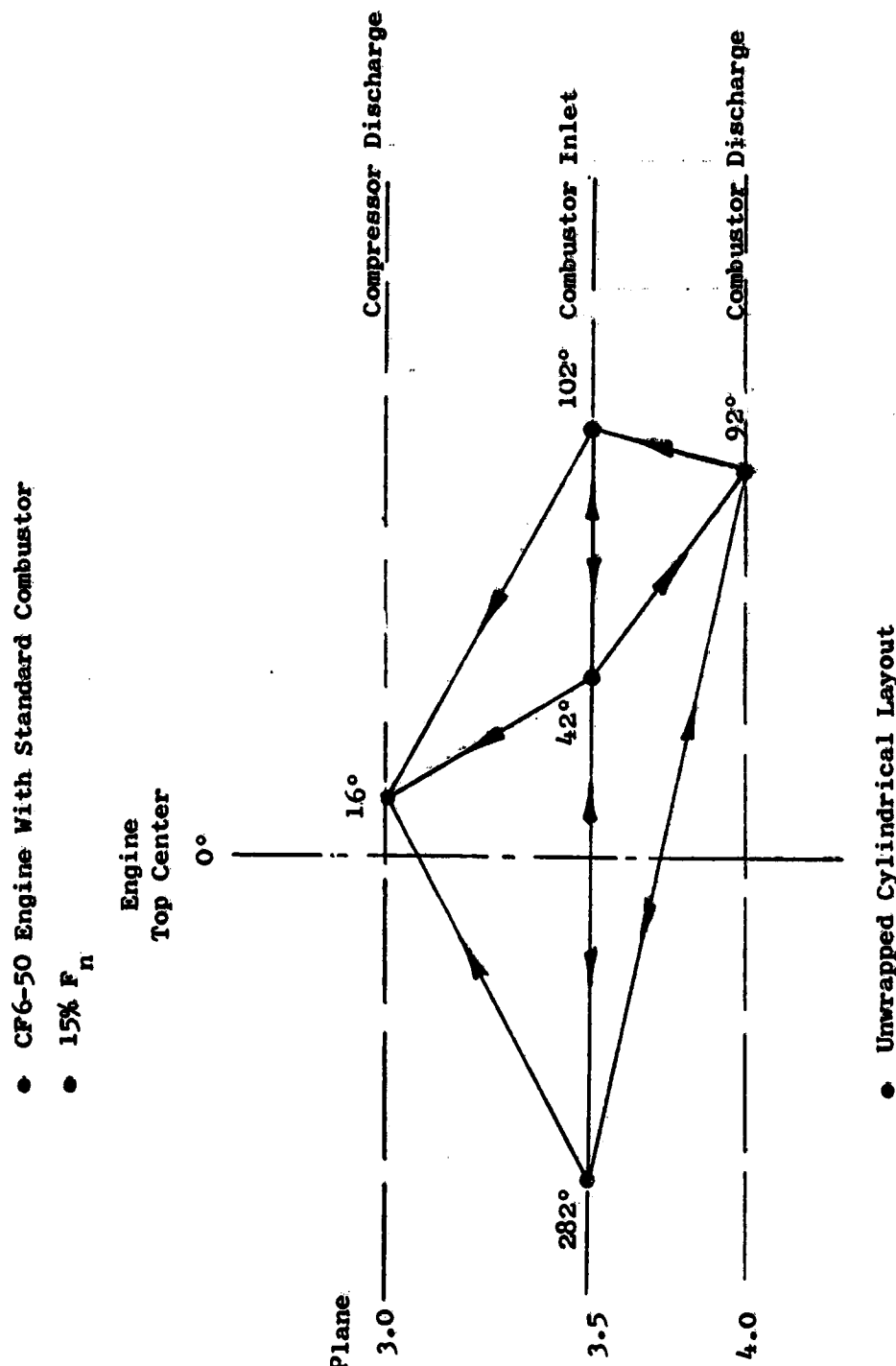


Figure 4.2-4. Time Delay Vectoring for Combustor Source Location Identification.

one peak. The time delay of the cross-correlation was removed from the cross-spectrum phase (within the limits of computational practicality) to give a near zero phase shift to selected frequency regions. Identification of correlated frequency regions associated with the predominant time delays from the cross-correlations between combustor sensor pairs was accomplished through the use of the cross-spectrum phase at the output signal. The cross-spectrum phase plots indicate the frequency regions that have near zero phase shift. These zero phase frequency regions are the frequencies that move at the wave propagation speeds defined by the time delay peaks.

Figure 4.2-5 illustrates the zero phase frequency regions in the cross-spectrum phase plot that correspond to the time delay peaks in the cross-correlogram of a pair of sensors from 3.0 to 3.5 (42°) for the 30.8% F_n (approach) condition. The first correlation peak in Figure 4.2-5(a) is at a negative time delay of -0.625 msec and is associated with a region of frequencies between 500 to 850 Hz, illustrated by the near zero phase region of the cross-spectrum in Figure 4.2-5(b). The second correlation peak at -2.50 msec in Figure 4.2-5(a) is associated with a lower frequency region between 100 and 350 Hz as seen in Figure 4.2-5(c). Both of these bands of frequencies are traveling upstream but at different times which may suggest different propagation paths in the same general direction.

Figure 4.2-6 illustrates that the frequency band associated with the time delay peak between the Plane 3.5 sensor and the one at Plane 4.0 (92°) for the 30.8% F_n condition is concentrated at frequencies from 500 to 1000 Hz. The slightly negative time delay suggests that this zero phase shift band of frequencies reaches both sensors almost simultaneously, but that the signals have a generally forward direction of propagation at this location.

The results from the circumferentially displaced sensors at Plane 3.5 show in Figure 4.2-7 that the signal is traveling from the sensor at 42° to the one at 102° and is comprised of the lower frequencies between 100 to 400 Hz which generally are attributed to combustion noise... The higher frequencies are associated with the small peak at zero time delay. The phase angle is increasing at a very slow rate above 500 Hz due to the small time delay associated with these frequencies.

A similar comparison conducted at the takeoff condition (99.8% F_n) shows that correlated frequency regions between 600 to 1000 Hz and 200 to 400 Hz occur (Figure 4.2-8) for the Plane 3.0 to 3.5 (42°) sensors which correspond to the time delays of -0.8 and -1.9 msec noted in the cross-correlogram. The low (negative) amplitude of the -0.8 msec peak is the result of the 100- to 1000-Hz frequency band influence on the high frequencies above 600 Hz. Since both of the time delays are negative, the waves are moving forward and contain acoustic energy regions comprised of the frequencies identified above.

Figure 4.2-9 shows the frequencies above 500 Hz to be at zero phase with a time delay of -0.078 msec for the Plane 3.5 (102°) to 4.0 (92°) sensors at the takeoff condition. These frequencies dominate the region between the sensors and appear to move in a forward direction.

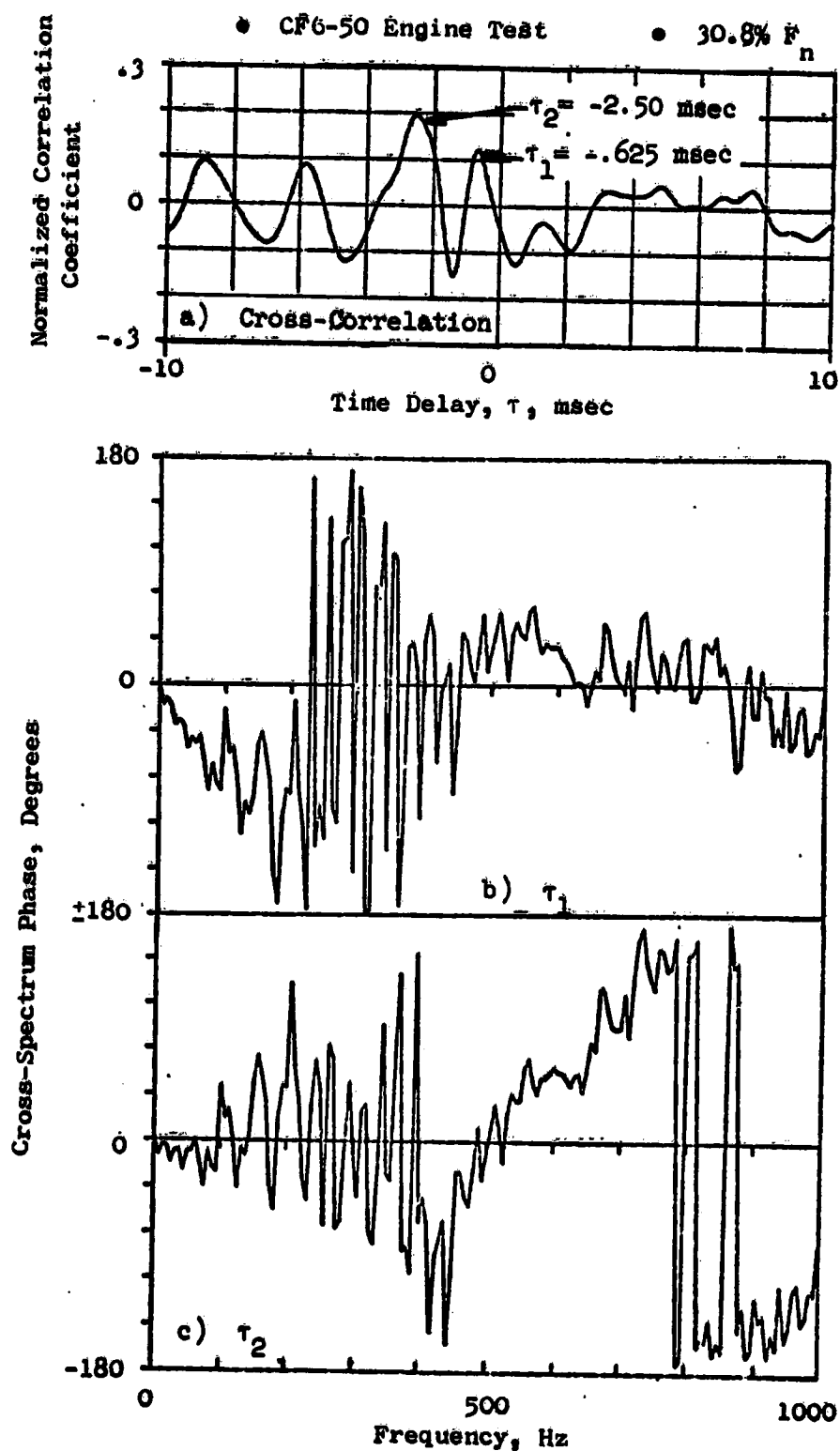


Figure 4.2-5. Correlated Frequency Regions Between Combustor Sensors from Plane 3.0 (16°) to 3.5 (42°) for Approach.

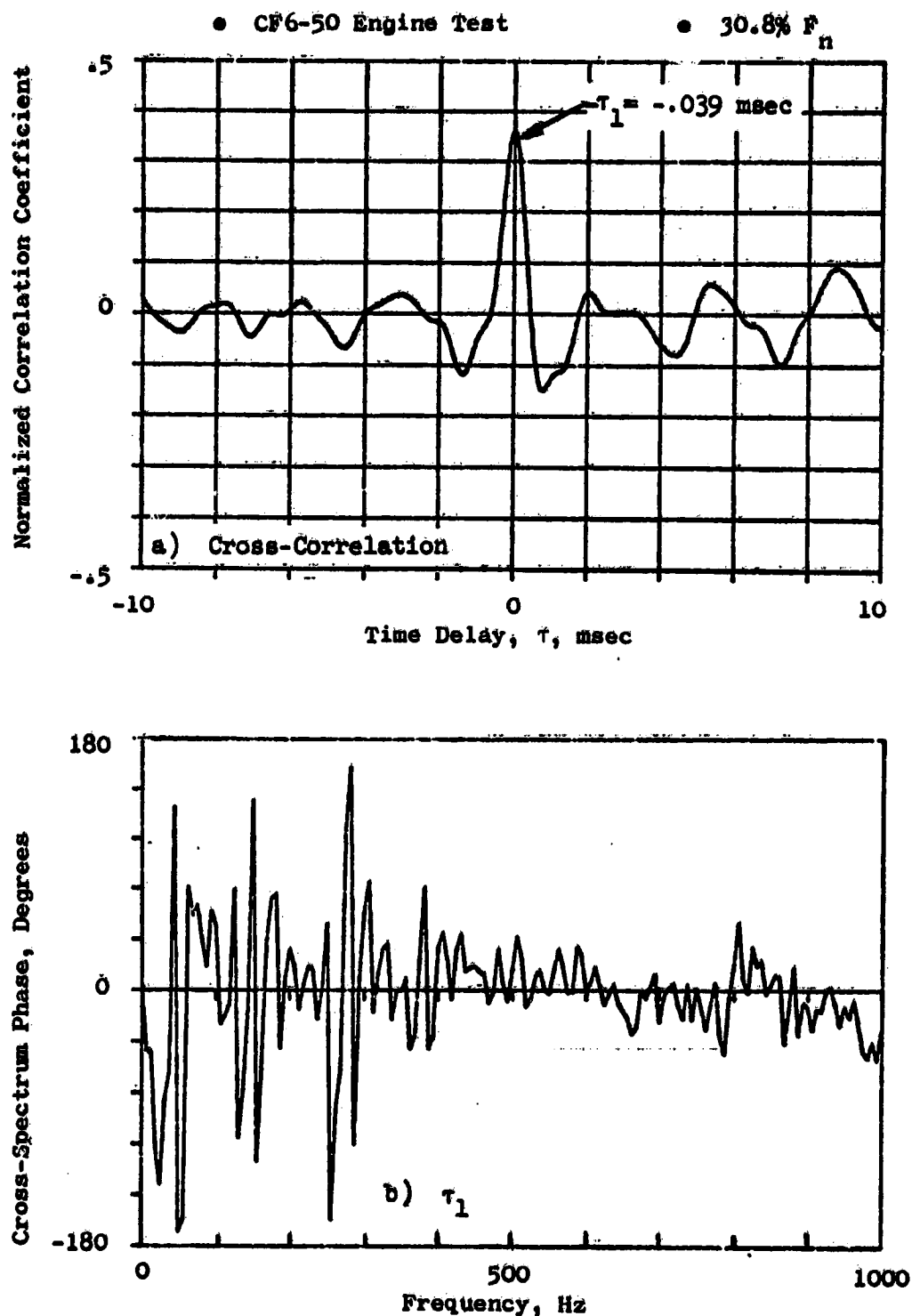


Figure 4.2-6. Correlated Frequency Region Between Combustor Sensors from Plane 3.5 (102°) to 4.0 (92°) for Approach.

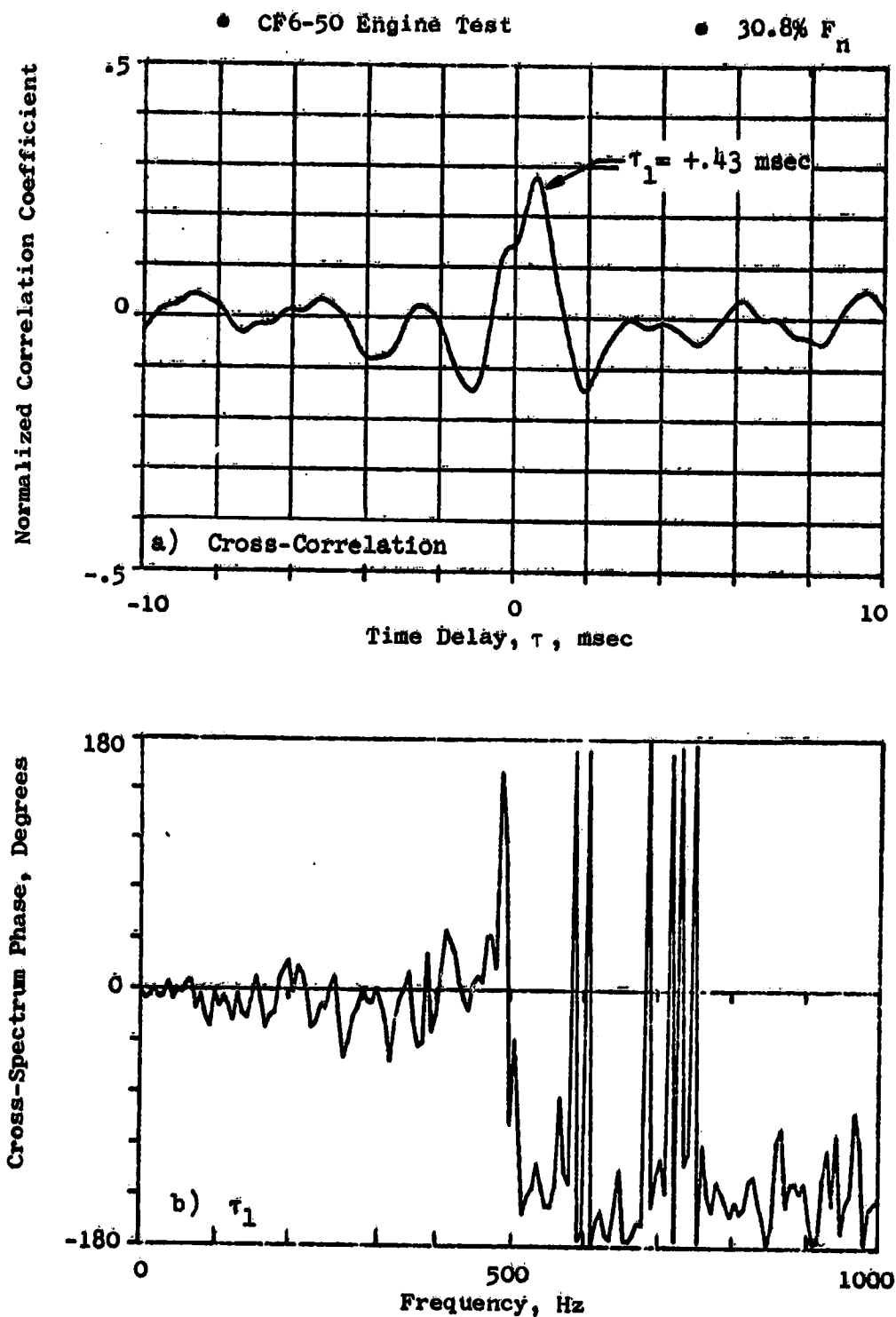


Figure 4.2-7. Correlated Frequency Region Between Combustor Sensors from Plane 3.5 (42°) to 3.5 (102°) for Approach.

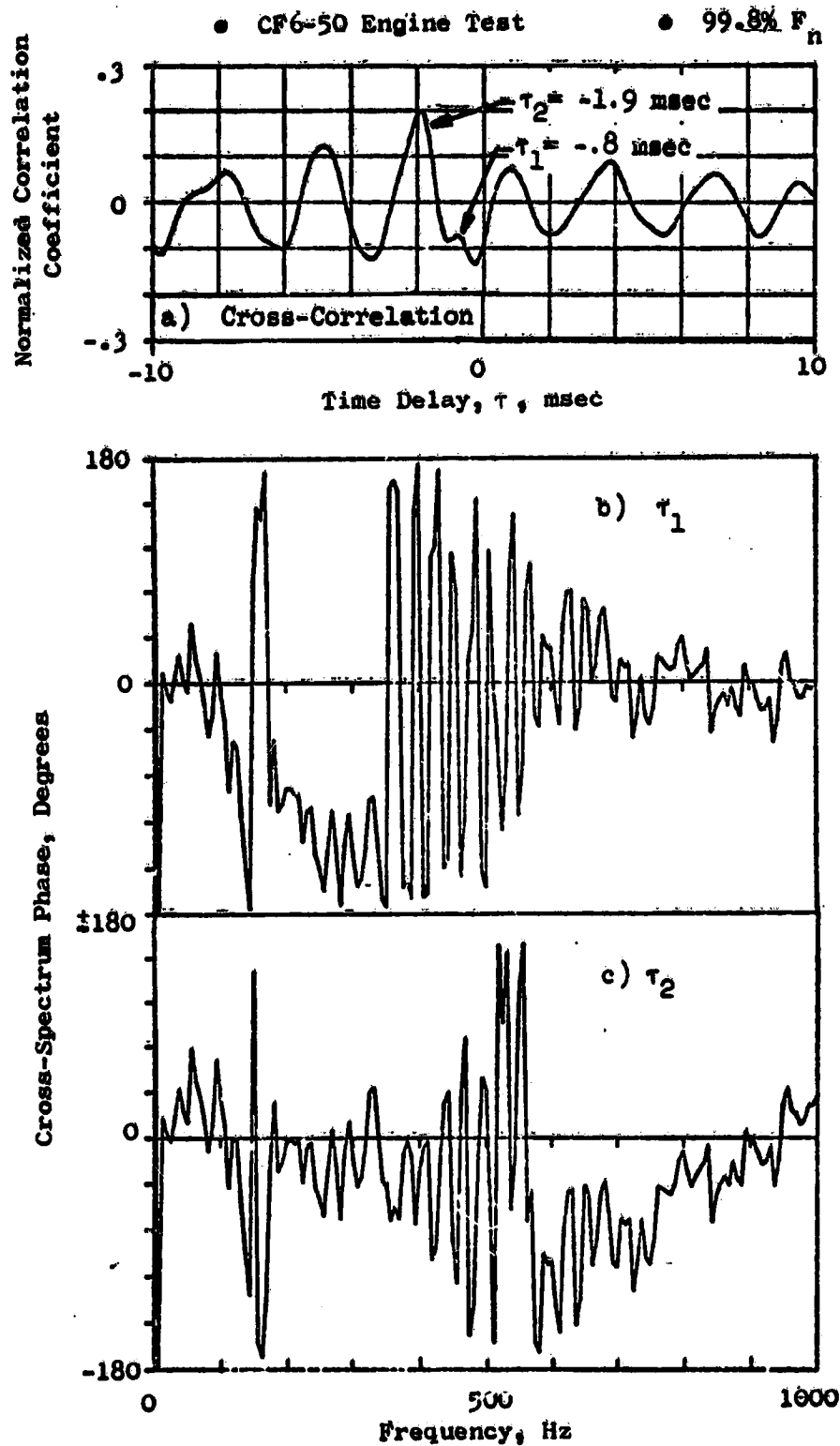


Figure 4.2-8. Correlated Frequency Regions Between Combustor Sensors from Plane 3.0 (16°) to 3.5 (42°) for Takeoff.

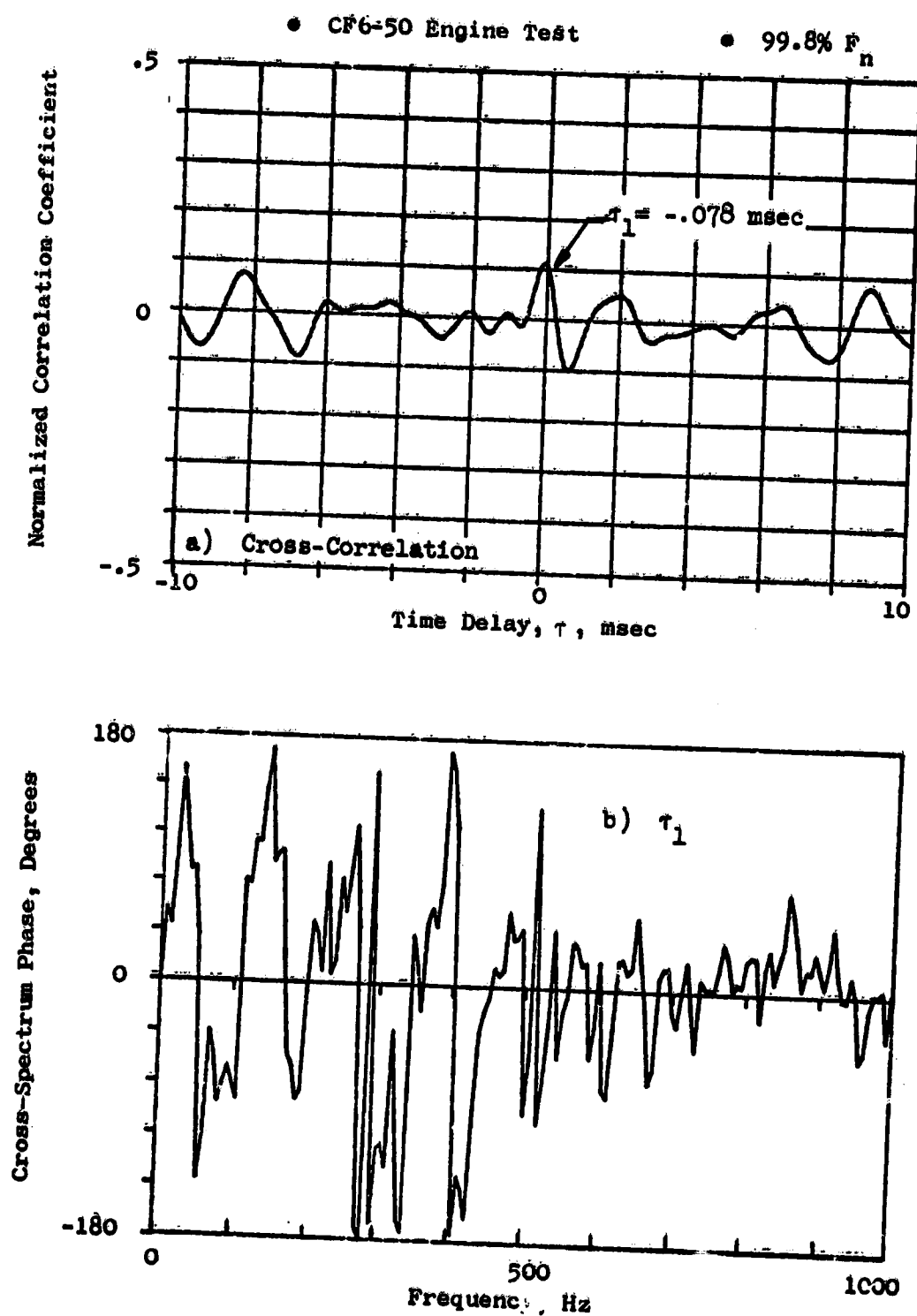


Figure 4.2-9. Correlated Frequency Region Between Combustor Sensors from Plane 3.5 (102°) to 4.0 (92°) for Takeoff.

The correlated frequency region in Figure 4.2-10 between the combustor sensors from Plane 3.5 (42°) to 3.5 (102°) is primarily comprised of low frequencies (100-500 Hz) which travel with a positive time delay (+0.703 msec), apparently in a circumferential path around the combustor.

4.2.3 Summary of Source Location Investigation

The predominate time delays and correlated frequency regions for all test conditions used in this analysis were determined and are found in Table 4.2-2. The amplitude of the normalized correlation coefficient at each of the time delay peaks is also listed in the table along with an estimate of the acoustic velocity obtained from the usual sonic velocity equation and approximate magnitude of the time delay (not direction), based on the linear distance between sensor pairs.

A review of this table indicates that the estimated time delays between Plane 3.0 to 3.5 agree well with the test results, except for the direction. The results between Plane 3.5 to 4.0 are not as clear since it has been previously shown that acoustic waves are traveling all over this region and not necessarily in the aft direction.

The vectoring of the time delays from the cross-correlations indicates that the location of the primary noise source within the standard production combustor is between Plane 3.5 and 4.0 as defined by the presence of near zero time delays. It is also apparent that more than one group of frequencies contributes to the sources within the combustor, and that these groups of frequencies travel different paths and, sometimes, in different directions.

4.3 COHERENCE AND TRANSFER FUNCTION ANALYSIS

4.3.1 Internal Coherence and Transfer Function Results

Comparisons of coherence function results at each measurement plane were reviewed along with selected results from the transfer analysis. Appendix A presents the coherence and transfer function results for seven power settings (3.8, 15, 22.8, 26.7, 30.8, 36.5, and 45.5% F_n). Positive time delays determined from cross-correlations between pairs of sensors were incorporated into the data to account for phase differences between sensors. Where negative time delays were observed (which indicated that the signals were traveling opposite to the assumed direction), a zero time delay was input. The error introduced by this procedure was estimated by the method outlined in Section 3.7. It results in an error of approximately 0.004% of the true coherence value, which is negligible.

Coherence function comparisons are shown in Figure 4.3-1 for the compressor discharge to combustor inlet Planes 3.0 (16°) and Plane 3.5 (42°) at conditions of 15, 30.8, and 45.5% F_n . The coherence levels range from 0.2 to 0.5, or more, over the engine power settings investigated; the spectral shapes are similar.

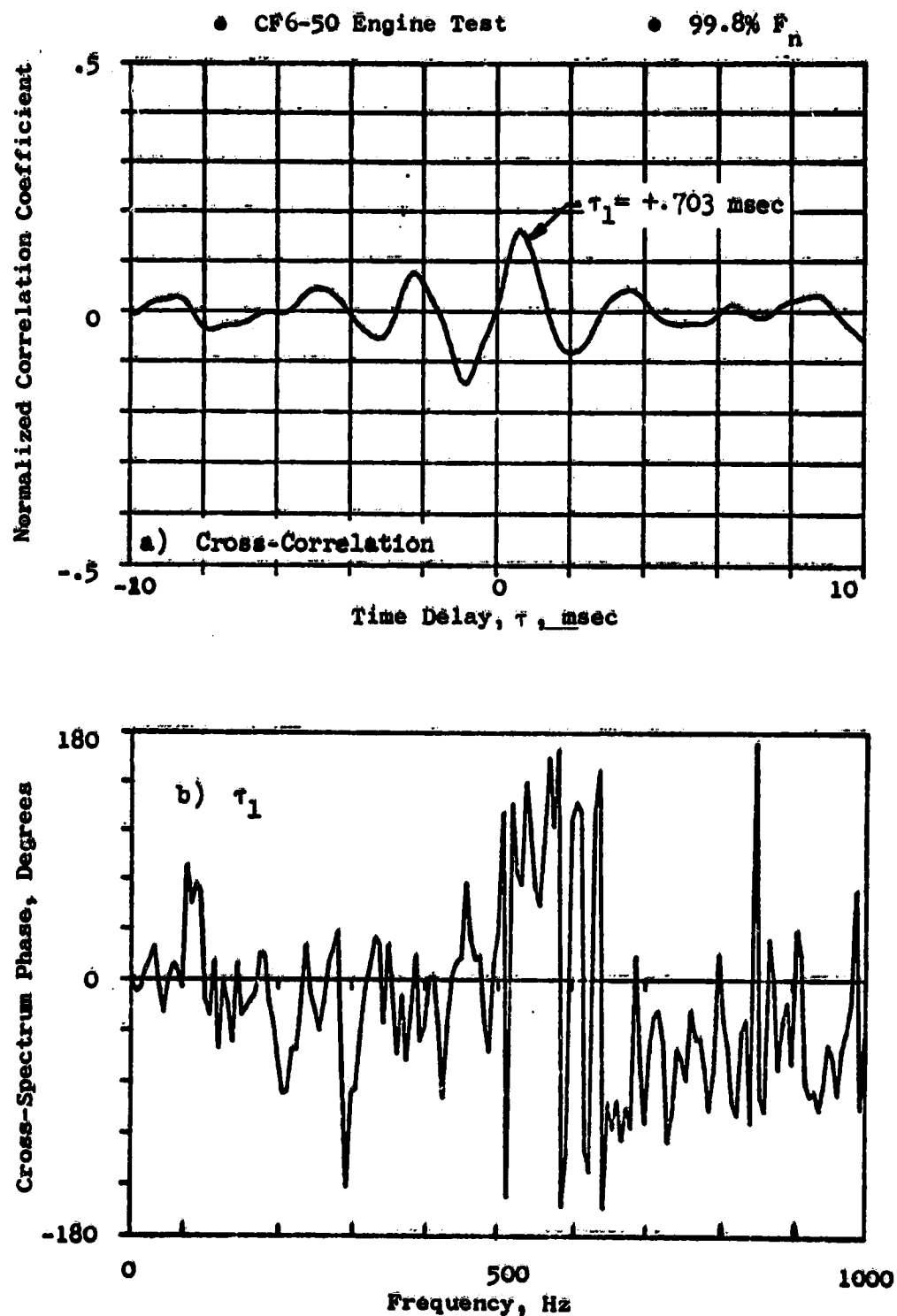


Figure 4.2-10. Correlated Frequency Region Between Combustor Sensors from Plane 3.5 (42°) to 3.5 (102°) for Takeoff.

Table 4.2-2. Summary of Source Location Parameters for CF6-50 Combustor.

Percent Net Thrust, % Fn Corrected Core Speed, rpm Cross-Correlation Pair	3.8 6582	15.0 8034	22.8 8452	26.7 8660	30.8 8688	36.5 8881	45.5 9106	99.6 10281
• Plane 3.0 (16°) to 3.5 (42°)								
	Linear Distance d = 0.4125 m (1.353 ft)							
(msec) τ 1	-1.0	-0.85	-0.9	-0.8	-0.625	-0.664	-0.781	-0.8
2					-2.50	-2.578	-1.953	-1.9
ρ_{xy} 1	0.54	0.32	0.21	0.17	0.124	0.097	0.150	-
2					0.198	0.253	0.243	0.2
(KHz) Δf 1	0.2-0.8	0.45-0.8	0.5-0.7	0.5-0.8	0.5-1.0	0.5-0.8	0.6-0.9	0.6-1.0
2					0.1-0.4	0.1-0.4	0.1-0.3	0.1-0.4
(m/s) \bar{C}	409.3	460.2	480.4	484.0	490.4	499.3	510.8	555.3
(msec) $ \tau_{est} $	1.007	0.896	0.858	0.852	0.841	0.826	0.807	0.742
• Plane 3.0 (16°) to 3.5 (102°)								
	Linear Distance d = 0.7404 m (2.429 ft)							
(msec) τ 1	-1.7	-1.5	-1.5	-1.5	-1.406	-1.367	-1.328	-
2					-2.734	-2.656	-2.617	-
ρ_{xy} 1	0.44	0.25	0.18	0.19	0.179	0.134	0.175	-
2					0.127	0.150	0.109	-
(KHz) Δf 1	0.45-0.8	0.4-0.8	0.5-0.8	0.5-0.8	0.5-0.9	0.5-0.9	0.5-0.9	-
2					0.1-0.3	0.1-0.3	0.1-0.2	-
(m/s) \bar{C}	409.3	460.2	480.4	484.0	490.4	499.3	510.8	555.3
(msec) $ \tau_{est} $	1.809	1.609	1.541	1.529	1.510	1.483	1.449	1.333
• Plane 3.0 (16°) to 3.5 (282°)								
	Linear Distance d = 0.7622 m (2.50 ft)							
(msec) τ 1	-1.8	-1.7	-1.6	-1.6	-1.406	-1.65	-1.445	-1.10
2								
ρ_{xy} 1	0.44	0.24	0.15	0.15	0.131	0.115	0.109	0.08
2								
(KHz) Δf 1	0.4-0.7	0.4-0.7	0.5-0.7	0.5-0.7	0.5-0.8	0.4-0.8	0.5-0.8	-
2								
(m/s) \bar{C}	409.3	460.2	480.4	484.0	490.4	499.3	510.8	555.3
(msec) $ \tau_{est} $	1.862	1.656	1.586	1.574	1.554	1.526	1.492	1.372
• Plane 3.5 (42°) to 4.0 (92°)								
	Linear Distance d = 0.4679 m (1.535 ft)							
(msec) τ 1	0	0.04	0.1	0.1	0.195	-0.117	0.117	0.156
2								
ρ_{xy} 1	0.25	0.26	0.23	0.2	0.21	0.182	0.1499	0.08
2								
(KHz) Δf 1	0.1-0.4	0.3-0.5	0.4-0.5		0.4-0.6	0.4-0.6	0.4-0.6	0.5-0.8
2								
(m/s) \bar{C}	486.5	527.3	554.1	559.9	569.4	581.6	597.4	658.4
(msec) $ \tau_{est} $	0.962	0.887	0.844	0.836	0.822	0.804	0.783	0.711

Table 4.2-2. Summary of Source Location Parameters for CF6-50 Combustor (Concluded).

Percent Net Thrust, % Fn Corrected Core Speed, rpm Cross-Correlation Pair	3.8 6582	15.0 8034	22.8 8452	26.7 8660	30.8 8688	36.5 8881	45.5 9106	99.8 10281
• Plane 3.5 (102°) to 4.0 (92°)	Linear Distance d = 0.2860 m (0.938 ft)							
(msec) τ 1	-0.10	-0.03	0	-	-0.039	0	-0.039	-0.078
2								
ρ_{xy} 1	0.62	0.46	0.38	0.08	0.362	0.343	0.288	0.13
2								
(KHz) Δf 1	0.1-0.7	0.4-0.6	0.4-0.7	-	0.3-1.0	0.4-0.9	0.4-0.9	0.5-1.0
2								
(m/s) \bar{C}	486.5	527.3	554.1	559.9	569.4	581.6	597.4	658.4
(msec) $ \tau_{est} $	0.588	0.542	0.516	0.511	0.502	0.492	0.478	0.434
• Plane 3.5 (282°) to 4.0 (92°)	Linear Distance d = 1.2883 m (4.227 ft)							
(msec) τ 1	1.2	1.4	-	1.45	1.523	1.35	1.4	1.1
2	-1.9	-1.65	-	-1.52	-1.602	-1.60	-1.7	-1.3
ρ_{xy} 1	0.05	0.16	0.09	0.08	0.137	0.07	0.08	0.05
2	0.26	0.085	-	0.08	0.105	0.07	0.095	0.05
(KHz) Δf 1	-	-	-	-	-	-	-	-
2	-	-	-	-	-	-	-	-
(m/s) \bar{C}	486.5	527.3	554.1	559.9	569.4	581.6	597.4	658.4
(msec) $ \tau_{est} $	2.648	2.443	2.325	2.301	2.263	2.215	2.157	1.957
• Plane 3.5 (42°) to 3.5 (102°)	Linear Distance d = 0.4409 m (1.446 ft)							
(msec) τ 1	0.3	0.2	0.3	0.35	0.43	0.469	0.430	0.703
2	-	-0.2	-0.5	-0.5	-	-0.352	-	-
ρ_{xy} 1	0.48	0.36	0.27	0.26	0.3185	0.262	0.27	0.16
2	-	0.36	0.27	0.23	-	0.136	-	-
(KHz) Δf 1	0.1-0.4	0.1-0.3	0.1-0.4	0.1-0.5	0.1-0.5	0.1-0.5	0.1-0.5	0.1-0.5
2	-	-	-	-	-	-	-	-
(m/s) \bar{C}	409.3	460.2	480.4	484.0	490.4	499.3	510.8	555.3
(msec) $ \tau_{est} $	1.077	0.958	0.918	0.911	0.879	0.883	0.863	0.794
• Plane 3.5 (102°) to 3.5 (282°)	Linear Distance d = 1.3230 m (4.340 ft)							
(msec) τ 1	1.7	1.6	1.5	1.6	1.7	-	-	-
2	-1.7	-1.9	-1.7	-1.9	-1.9	-	-	-
ρ_{xy} 1	0.27	0.14	0.125	0.06	0.07	0.09	0.085	0.06
2	0.07	0.15	0.16	0.08	0.09	-	-	-
(KHz) Δf 1	0.3-0.4	-	0.3-0.5	-	-	-	-	-
2	-	-	-	-	-	-	-	-
(m/s) \bar{C}	409.3	460.2	480.4	484.0	490.4	499.3	510.8	555.3
(msec) $ \tau_{est} $	3.232	2.875	2.754	2.734	2.698	2.650	2.590	2.382

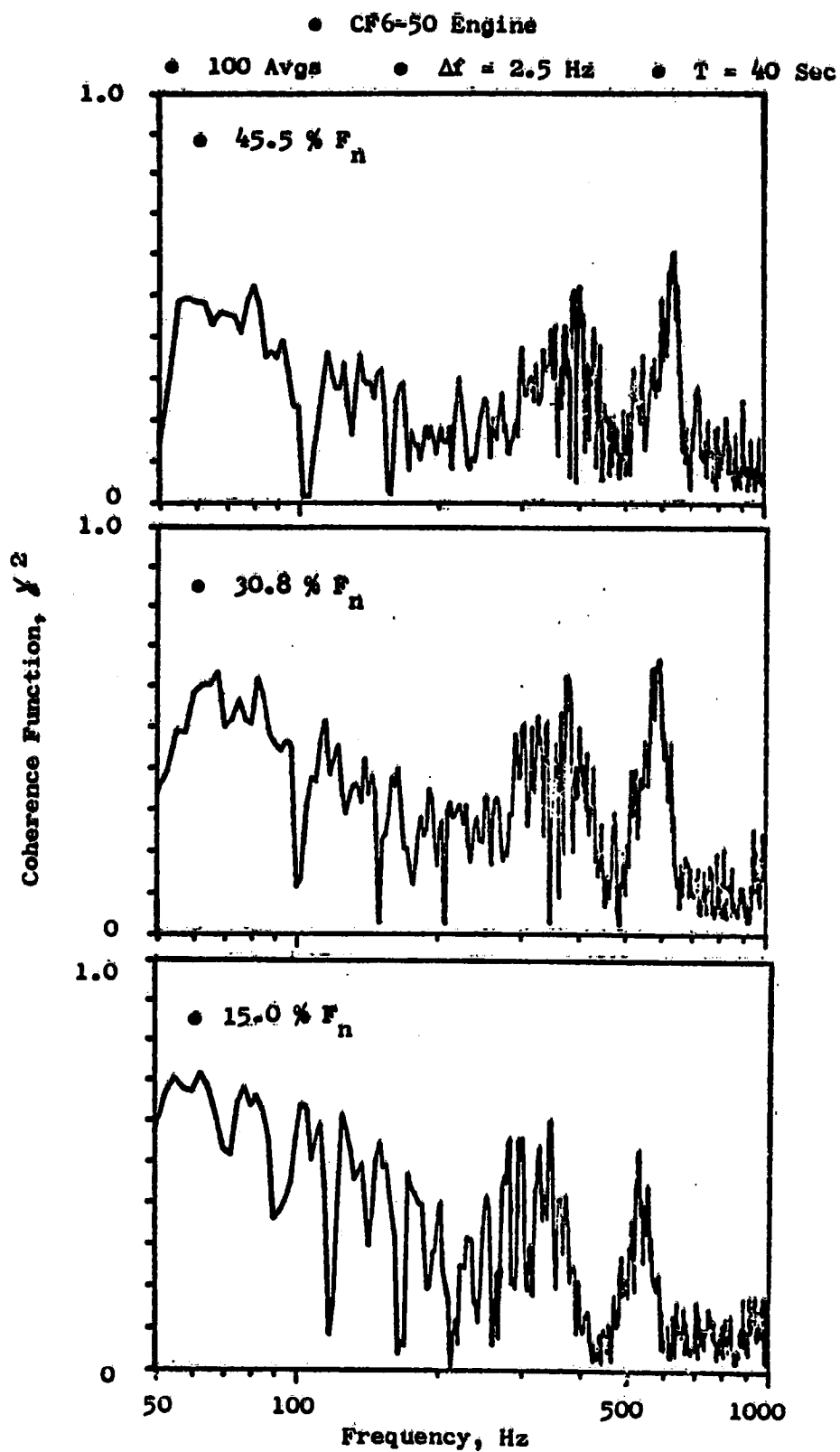


Figure 4.3-1. Coherence Function for Plane 3.5 (16°) to 4.0 (42°).

Figure 4.3-2 compares the coherence function for Plane 3.5 (102°) to Plane 4.0 (92°) at the same power settings. At the lower power setting of $15\% F_n$, the coherence levels remain at 0.4 to 0.5 over the low-frequency region up to 500 Hz. With increasing thrust (speed), the coherence level in the low-frequency region (<300 Hz) is reduced, while the levels at the higher frequencies between 400 and 600 Hz remain essentially the same. The relatively high coherence levels between the Plane 3.5 to 4.0 sensors suggests that a large amount of acoustic energy is present in this region. This observation is supported by the results of the source location survey (Section 4.2).

Between the combustor and the core nozzle, only a small group of frequencies below 100 Hz shows any significant level of coherence (0.3 to 0.4) at the $15\% F_n$ point. Figure 4.3-3 shows the comparison for Plane 3.5 (282°) to Plane 8.0A (270°). The higher power settings show coherence levels around 0.1 and below, indicating little or no similarity between the signals at the combustor inlet plane and the core nozzle.

Figure 4.3-4 shows the coherence function in the core nozzle (Planes 8.0A to 8.0B) to possess high levels (>0.5) up to 500 Hz at all test conditions compared. At the $15\% F_n$ point, the spectral distribution of the coherence function peaks in a region between 250 to 600 Hz, which includes the frequencies associated with core noise. With increasing thrust, the coherence levels in the low frequencies between 100-200 Hz increase from 0.3 to 0.7, indicating an increase in signal similarity on both probe elements which may be attributed to increased turbulence over the probe.

Typical examples of the resulting transfer functions (gain and phase) between sensors at Planes 3.5 (102°) and 4.0 (92°) are illustrated in Figure 4.3-5 for the low power setting of $15\% F_n$. A zero time delay was used in this region because of the small (± 0.4 ms) delay times determined from cross-correlation analysis indicating the close proximity of the source between these planes. The transfer function calculations were accomplished with 100 averages of the 2.5-Hz bandwidth data having a total record length of 40 seconds. The relatively high level of coherence (Figure 4.3-2) for these sensors at this condition is reflected in the average transfer function magnitude (gain) of approximately 0.1 over the low frequency range from 50 to 500 Hz. The phase angle plot, Figure 4.3-5(b), is basically horizontal over the same frequency range, indicating these frequencies are in phase.

In contrast, Figure 4.3-6 illustrates the transfer function results for the same condition between the combustor sensor at Plane 3.5 (282°) to the core nozzle Plane 8.0A (270°). Recalling that the coherence levels for this pair of sensors were quite low (Figure 4.3-3) for this condition above 100 Hz, the transfer function gain in Figure 4.3-6(a) shows levels of about 0.001 in this region. The frequencies above 100 Hz show even lower transfer function magnitudes.

The phase plot for these sensors is erratic and does not show any apparent frequency regions in phase with the delay time computed from cross-correlation analysis. These results are directly related to the low coherence levels obtained for this pair of sensors at all conditions.

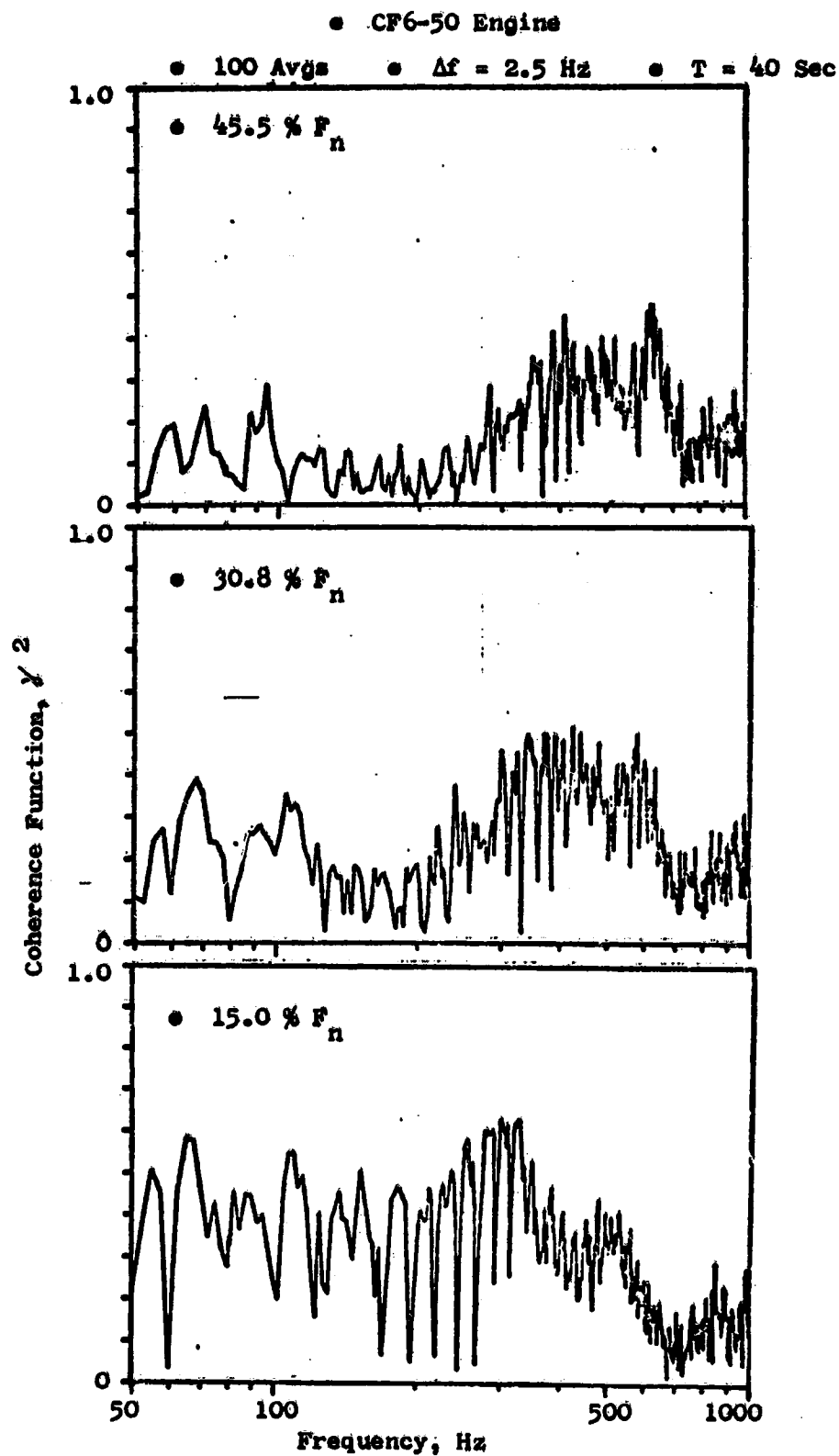


Figure 4.3-2. Coherence Function for Plane 3.5 (102°) to 4.0 (92°).

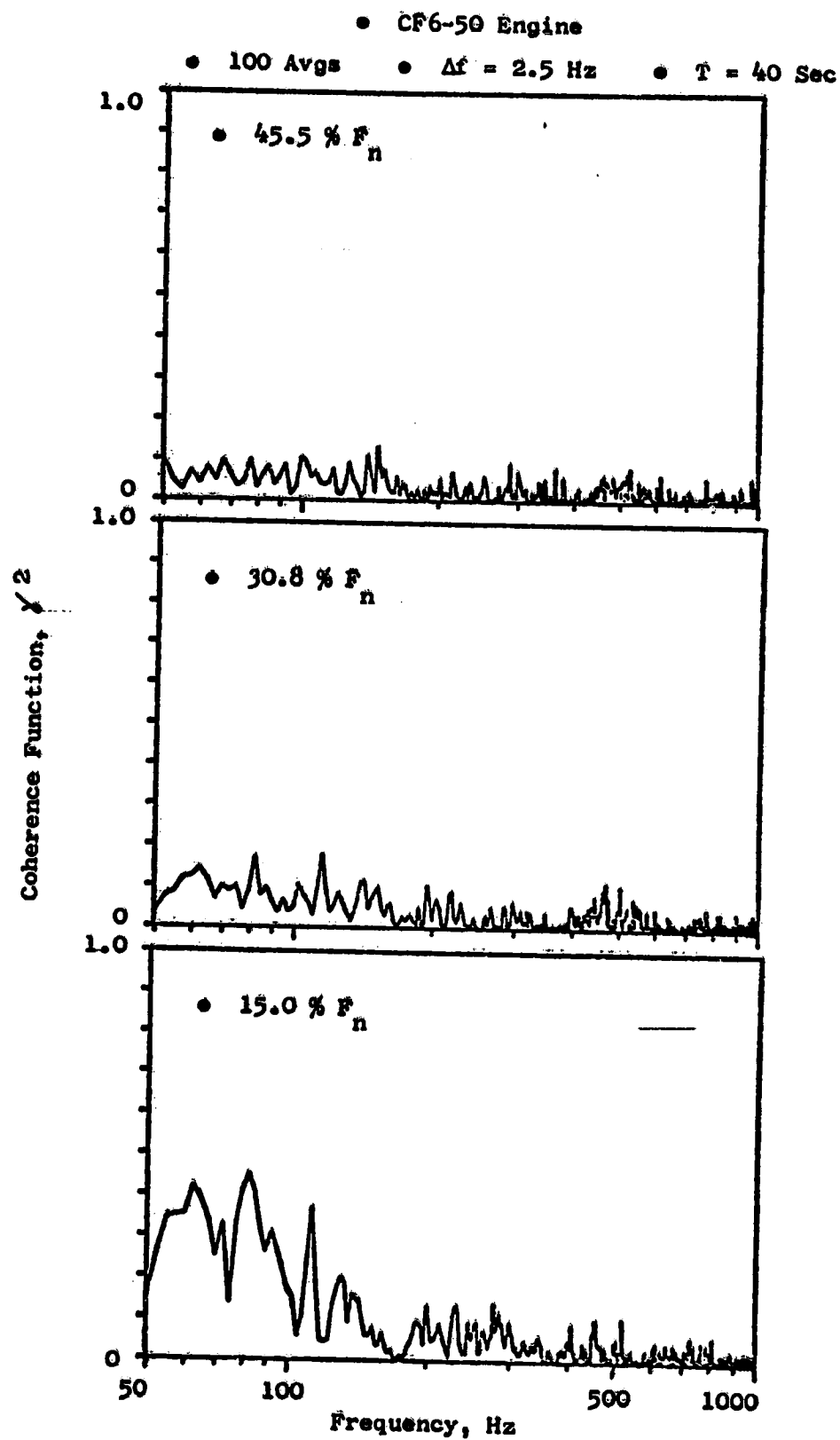


Figure 4.3-3. Coherence Function for Plane 3.5 (282°) to 8.0A (270°).

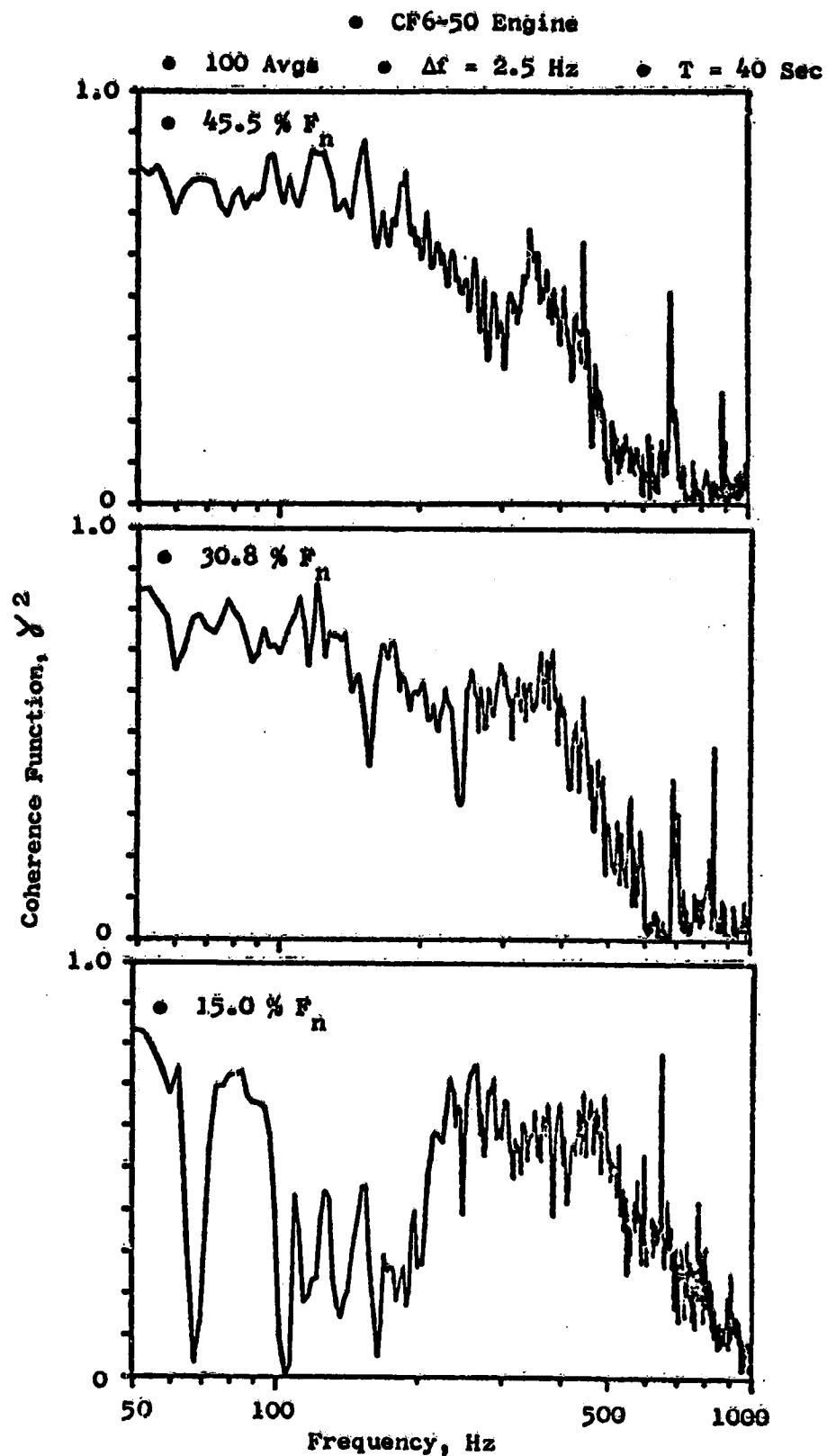


Figure 4.3-4. Coherence Function for Plane 8.0A to 8.0B (270°).

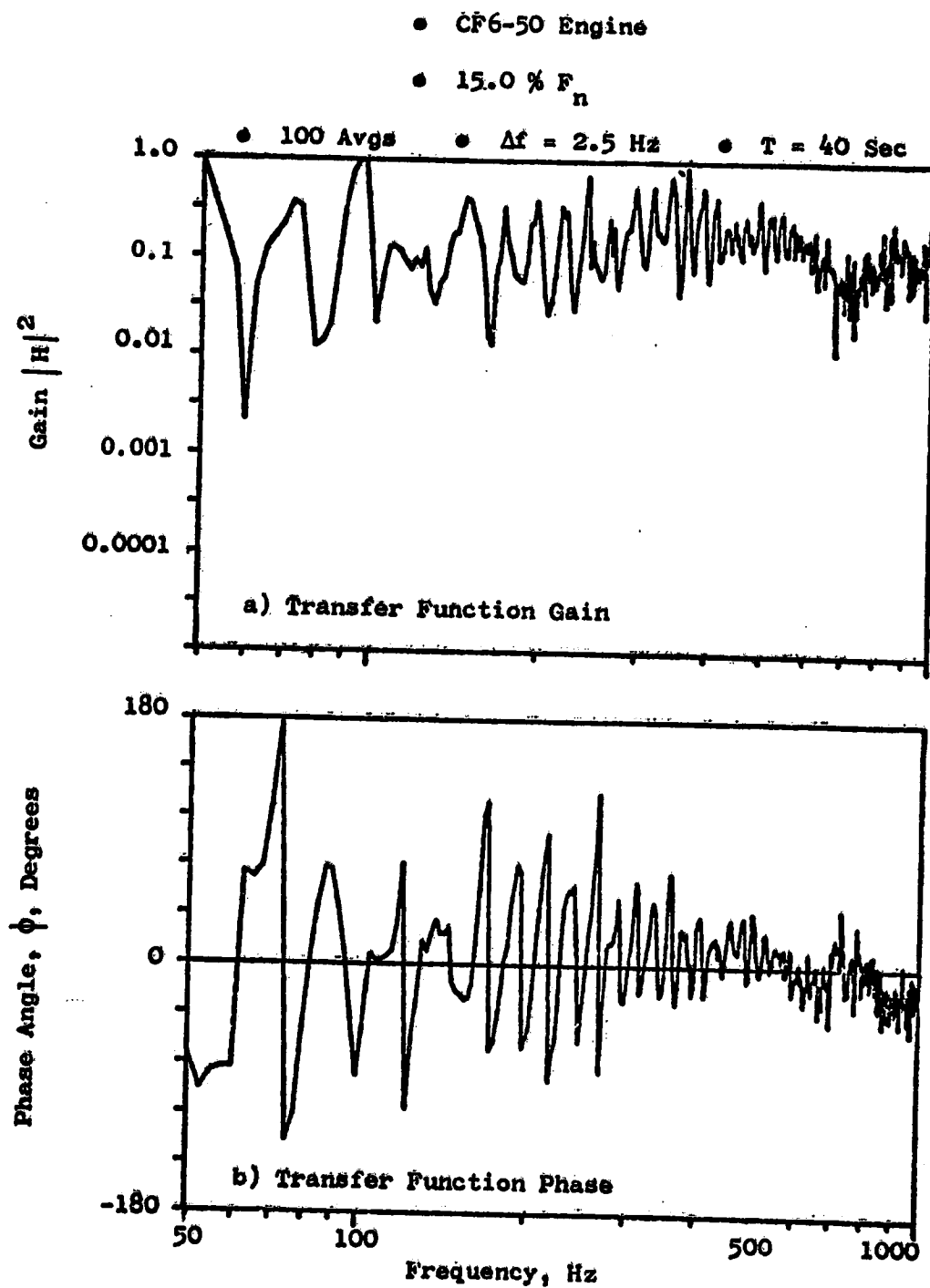


Figure 4.3-5. Transfer Function (Gain and Phase) for Plane 3.5 (102°) to 4.0 (92°).

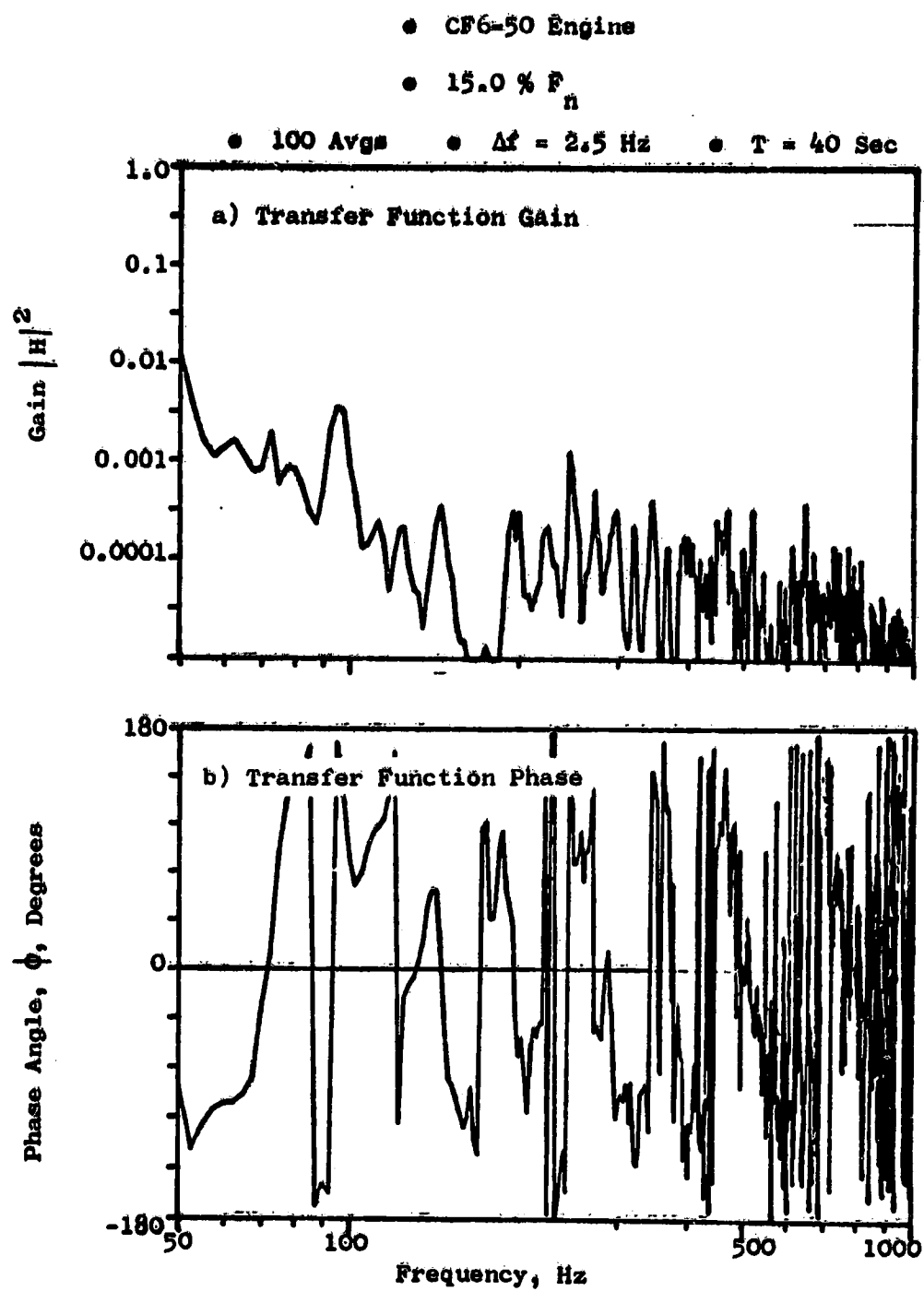


Figure 4.3-6. Transfer Function (Gain and Phase) for Plane 3.5 (282°) to 8.0A (270°).

The transfer function results within the core nozzle between the Plane 8.0 probe Kulites A to B are shown in Figure 4.3-7 for the high power setting at 45.5% F_n . A high level of transfer function magnitude ($0.1 < |H|^2 < 1.0$) is apparent from 50 to 400 Hz. This range of frequencies is also in phase, as seen from the horizontal line in Figure 4.3-7(b) for this region. The high level of coherence in Figure 4.3-4 for this condition is the basis for these transfer results.

4.3.2 Coherence and Transfer Function Results to the Far Field

Coherence and transfer functions (gain and phase), with time delay removed, were computed between the CP6-50 engine and each far-field microphone for the seven test conditions evaluated. Two different internal sensors were used as reference signal inputs. They included the Plane 3.5 (102°) sensor in the combustor and the core probe sensor at Plane 8.0A (270°). The complete coherence and transfer analysis results to the far field are found in Appendix A. Selected examples from the analysis are presented in the discussion which covers the conditions tested.

The coherence levels achieved with the two sets of engine to far-field measurements are graphically summarized for the 15% F_n and 45.5% F_n settings at three selected frequencies (50, 100, and 400 Hz). The frequency selections were based on the observations that the higher coherence values were generally found between 50 and 100 Hz, while the peak core noise frequency is typically identified with 400 Hz. A similar coherent low-frequency region peaking around 120 Hz was observed by the investigators of Reference 9.

Figure 4.3-8 shows the 50-Hz comparison of the far-field coherence levels relative to Planes 3.5 (102°) and 8.0A (270°) for the 15 and 45.5% points, respectively. The figure shows the high degree of coherence relative to Plane 8.0A for this frequency at low power setting over the Plane 3.5 (102°) reference. The coherence levels referenced to Plane 3.5 concentrate around 0.1 at 15% F_n , while at the higher power setting (45.5% F_n) the levels are below the 0.1 coherence value established as a minimum level for analysis purposes.

Similar comparisons of the Plane 3.5 and Plane 8.0 coherence results with the far field are illustrated in Figure 4.3-9 for 100 Hz and Figure 4.3-10 for 400 Hz, the typical core noise peak frequency. The 100-Hz comparison shows coherence levels of 0.1 to 0.25 in the aft quadrant angles for the low-power point. At the higher speed, however, coherence levels of 0.1 and below are apparent for both reference plane sensors.

Figure 4.3-10 shows the 400-Hz coherence level for both planes to fall essentially at or below the 0.1 coherence value at all angles for the conditions shown. This is typical for the coherence values of the higher frequencies at all conditions.

From Reference 3, for the ideal case of a constant parameter linear system with a single clearly defined input and output, the coherence function will be unity. If the input and output signals are totally unrelated, the coherence will be zero. If the coherence function is greater than zero but less than unity, one or more of three possible situations exists.

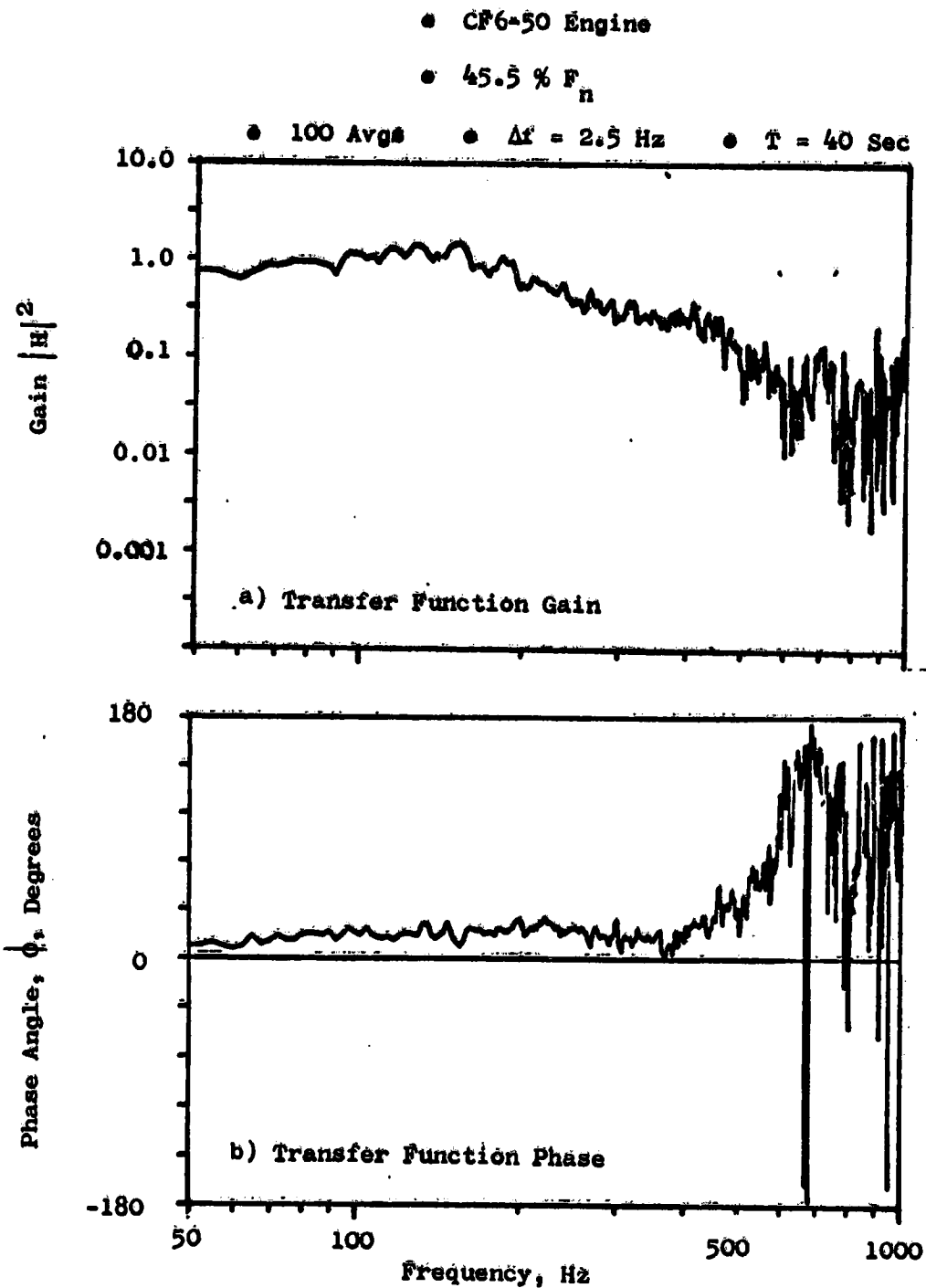


Figure 4.3-7. Transfer Function (Gain and Phase) for Plane 8.0A to 8.0B (270°).

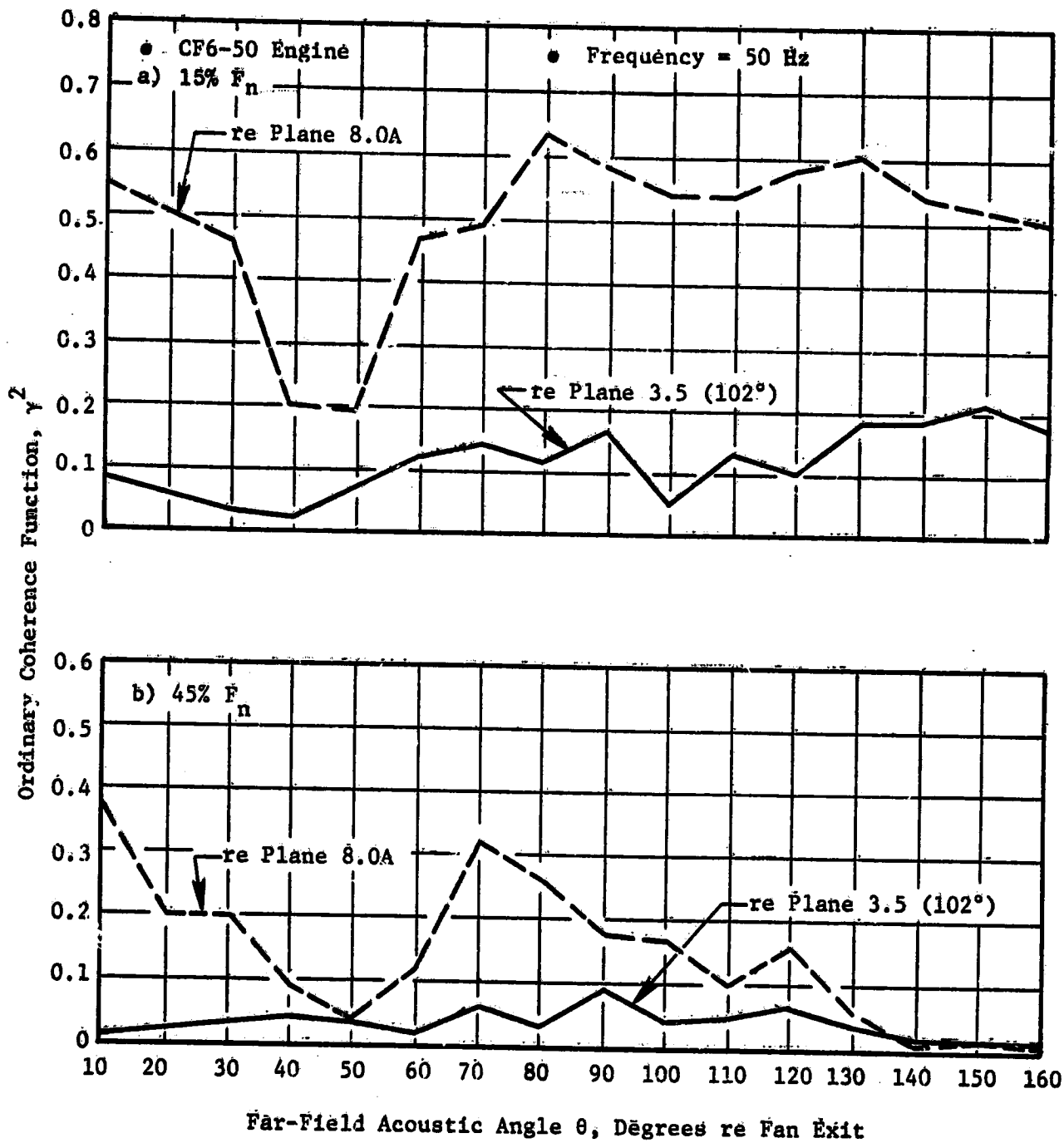


Figure 4.3-8. Far-Field Coherence Level Comparison Between Planes 3.5 (102°) and 8.0A for 50 Hz.

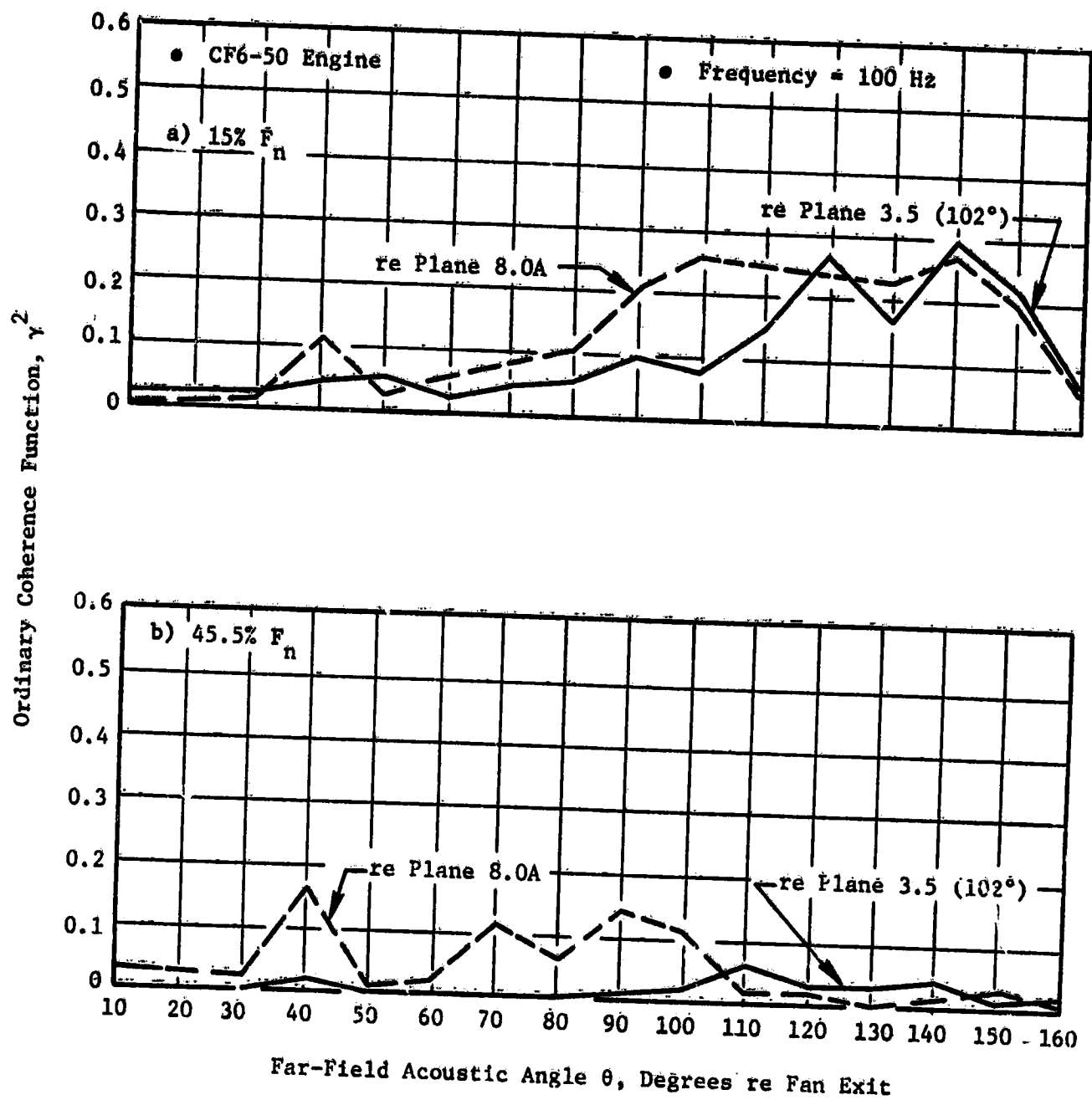


Figure 4.3-9. Far-Field Coherence Level Comparison Between Planes 3.5 (102°) and 8.0A for 100 Hz.

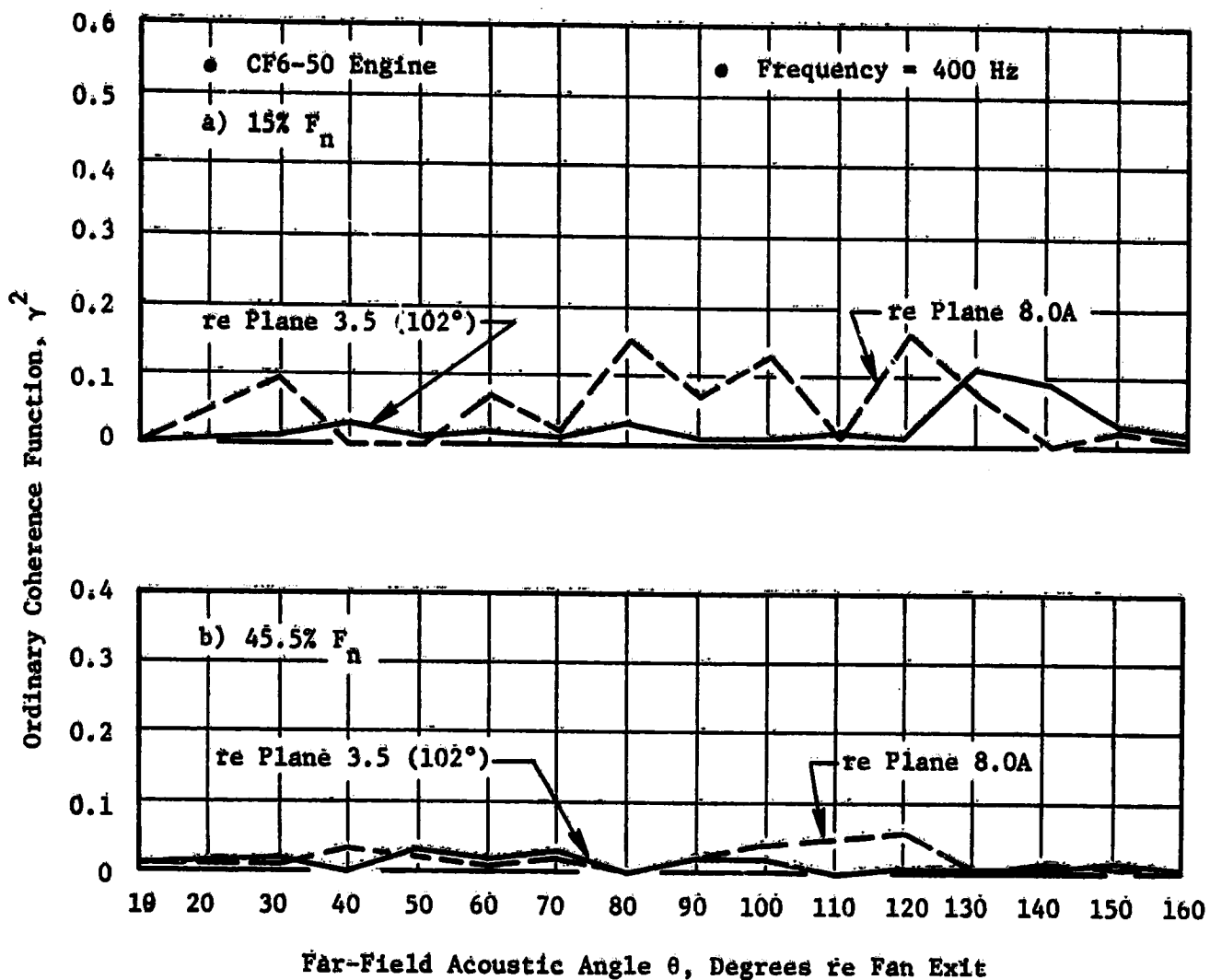


Figure 4.3-10. Far-Field Coherence Level Comparison Between Planes 3.5 (102°) and 8.0A for 400 Hz.

1. The measurements are influenced by extraneous noise - both internal and external measurements are above the noise floor; therefore, this can be eliminated.
2. The system relating the input and output signal is not linear - several noise paths are possible which are not linear.
3. The output signal is a function of more than one input - at higher power settings this is true since jet noise dominates the engine noise. The lower power settings are more likely to be controlled by core noise.

A review of the far-field results from the Plane 3.5 and Plane 8.0A references with the above situations was performed in an attempt to identify a reason for the low coherence which appeared to be associated more with the Plane 3.5 reference than Plane 8.0. Without an extensive survey, which is beyond the scope of this contract, the most probable reason appears to be the nonlinear paths the noise takes from the combustor to the far field (e.g., casing radiated noise).

The spectral distribution of the coherence function at selected far-field angles relative to the core nozzle Plane 8.0A sensor is compared in Figure 4.3-11. Angles of 60°, 90°, 120°, and 150° on the 45.72-m (150-ft) measurement arc for the approach power setting (30.8% F_n) were used in the comparison. The time delays due to acoustic propagation to each microphone location were removed. The values of the coherence function ranged between 0.15 to 0.35 at 60°, 90°, and 120°. At 150° the coherence levels are less than 0.1 over the frequency range from 50 to 1000 Hz. The regions of frequencies with coherence level greater than 0.1 are concentrated with the low frequencies (400 Hz) with the most prominent regions between 50 to 150 Hz.

The transfer function results (gain and phase) with the far field relative to the Plane 8.0A sensor were compared at the peak core noise angle in the far field (120°). Figure 4.3-12 illustrates the transfer function gain for the 120° microphone at 15, 30.8, and 45.5% F_n . The gain ($|H^*|^2$) in the far field has the transmission loss due to spherical divergence removed in order to depict the actual loss of coherent signal due to influences other than proximity to the source. The transfer function values are about 0.1 between 50 and 300 Hz for all power settings. The loss is greater at the higher frequencies where the coherence is less than 0.1.

Figure 4.3-13 shows the transfer function phase results for the 120° at the same conditions. The nearly horizontal region of the plot in the low frequencies below 200 Hz, indicates that about the proper amount of delay time was removed. Above 200 Hz the coherence levels are less than 0.1, except for a small band of frequencies around 300 Hz (Figure 4.3-11). Therefore, the phase information at the higher frequencies is meaningless due to the large amount of error associated with using low coherence values (~0.1) as described in Section 3.7.

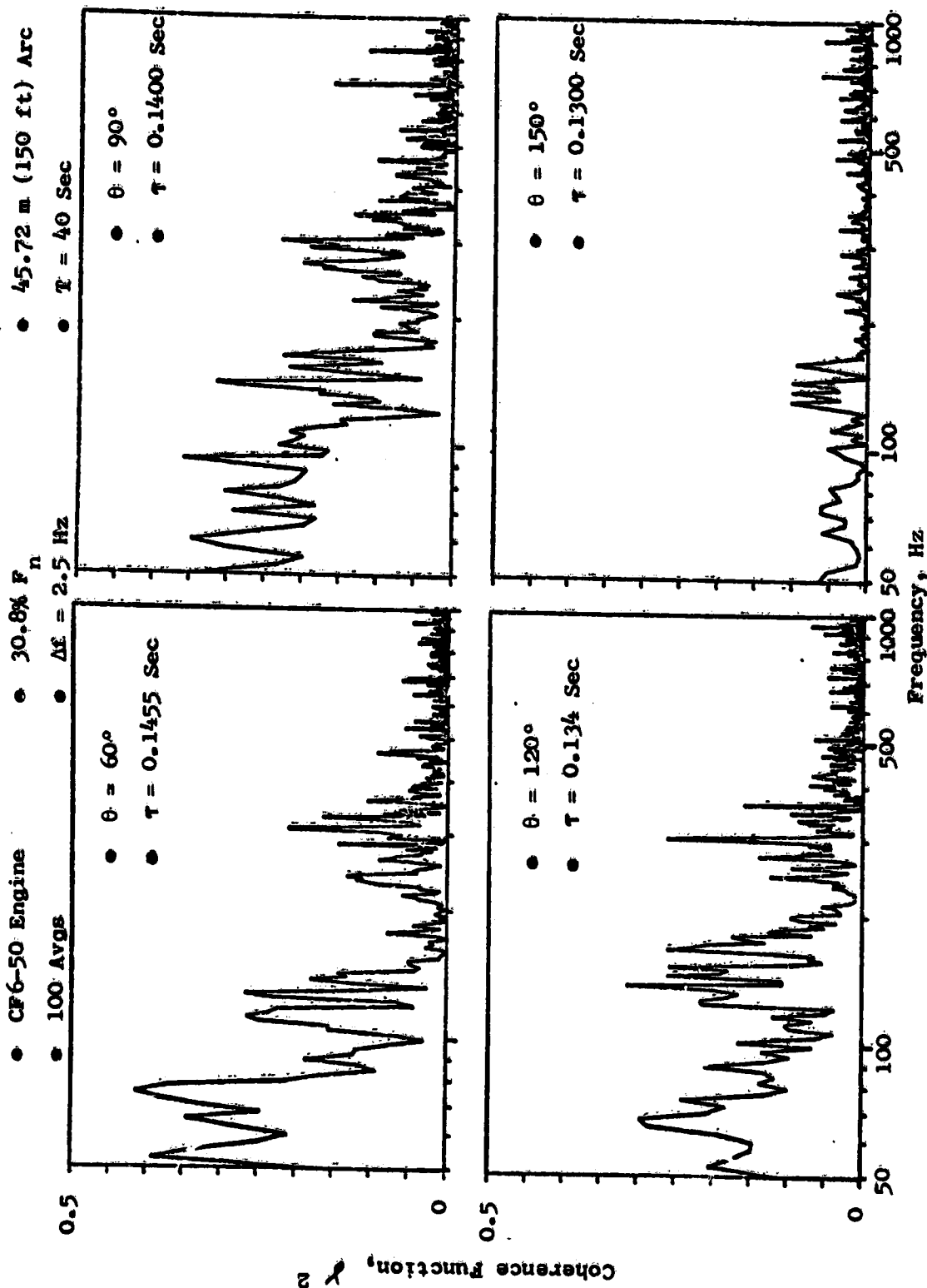


Figure 4.3-11. Coherence Function Far-Field Spectral Distribution Relative to Plane 8.0A.

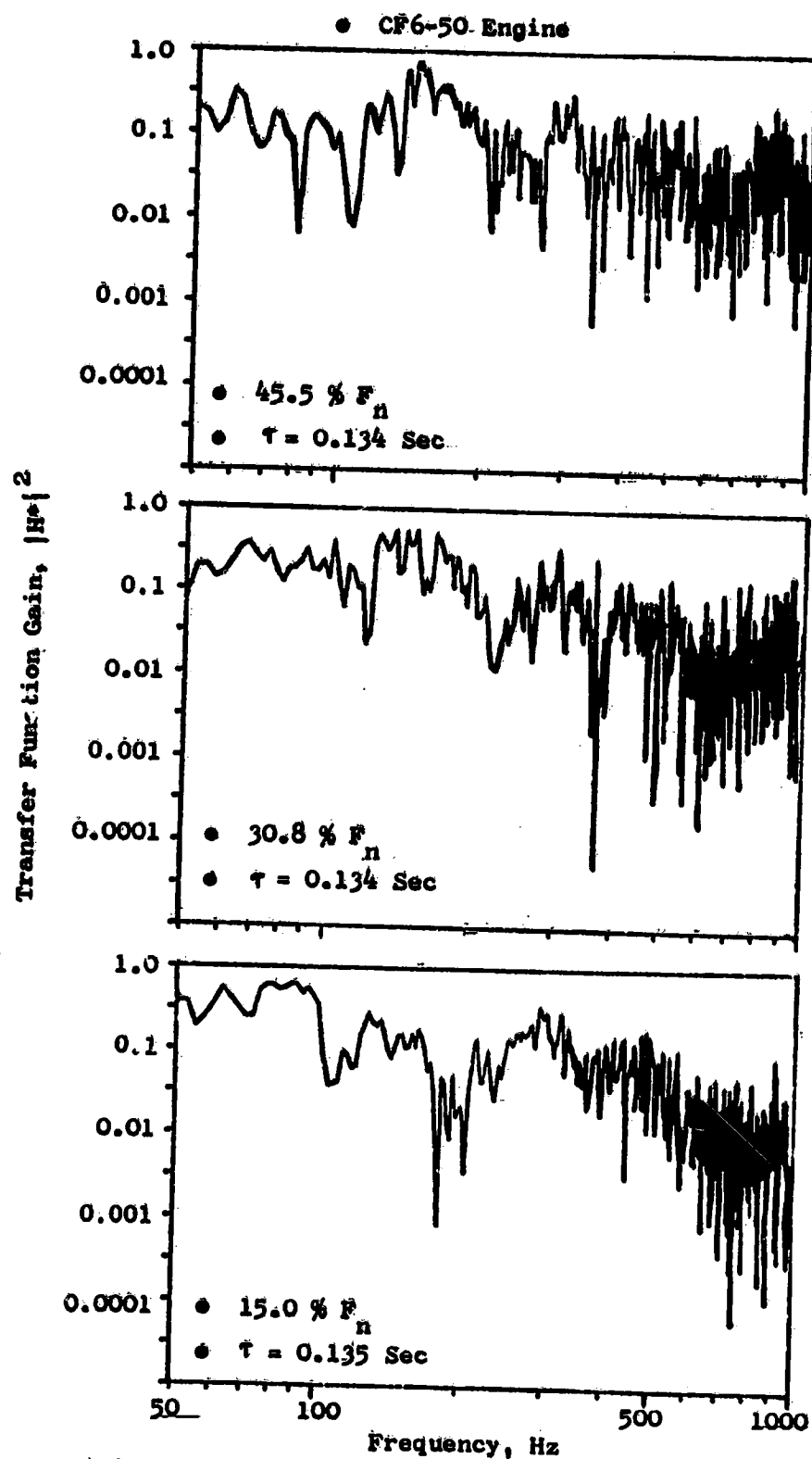


Figure 4.3-12. Transfer Function Gain Relative to Plane 8.0A for 120° Far-Field Angle.

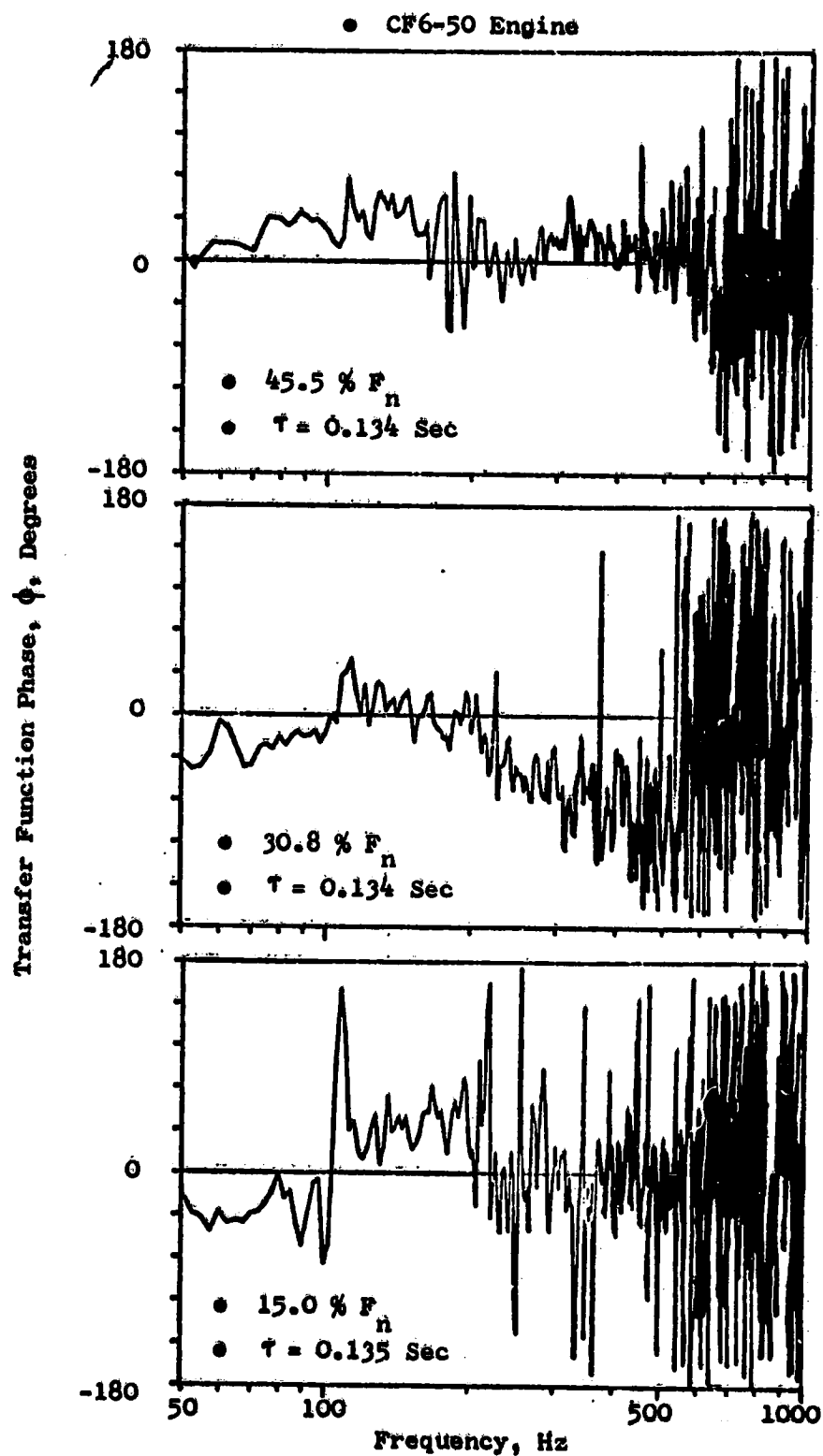


Figure 4.3-13. Transfer Function Phase Relative to Plane 8.0A for 120° Far-Field Angle.

4.3.3 Turbine Transfer Function Comparison with Previous Test Results and Present Theory

The transmission loss of acoustic signals across the turbine of the CF6-50 turbofan engine was determined as an attenuation, or loss of coherent signal level from the combustor discharge Plane 4.0 to the core nozzle exit, Plane 8.0. The coherent levels at each of these planes were obtained relative to an upstream input signal level at the combustor inlet, Plane 3.5. The procedure used here is similar to that described in Reference 2. The coherent SPL spectra at Planes 4.0 and 8.0 were compared at each of the seven low-power settings. The difference between the spectra represents the amount of energy transferred in SPL across the turbine. The results of these comparisons at each test condition are found in Appendix B.

• Comparison with Previous Test Results

Comparisons of the turbine attenuation results on a PWL basis were made with similar results obtained during the running of the ECCP Phase III test with a double annular combustor on the same type of engine (see Reference 2). Conditions at approach power ($\sim 30\% F_n$) and about $45\% F_n$ were selected for the comparison. The attenuations determined in the form of ΔSPL 's at each 1/3-octave-band frequency from 50 to 1600 Hz between the coherent spectra plots at Planes 4.0 and 8.0 relative to the upstream combustor signal at Plane 3.5 were converted to PWL attenuations to account for impedance changes, Mach number effects, and area differences at the measurement planes.

Figure 4.3-14 illustrates the PWL attenuation comparison at approach for the $30.8\% F_n$ point on the core noise test and the $29.7\% F_n$ point on the ECCP Phase III test. (The $29.7\% F_n$ condition was selected for comparison since both sets of pilot and main burners of the double annular combustor were operational.) The attenuations for the core noise test range from ΔdB_{PWL} of about 10 to 25 dB, while the ECCP results show about 6- to 18.5-dB attenuation over the frequency range. The core noise attenuation increases rapidly between 160 to 400 Hz. A similar rate of increase is apparent for the ECCP results between 315 to 500 Hz.

A higher power setting comparison of turbine attenuations is presented in Figure 4.3-15 for the conditions around $45\% F_n$. The core noise attenuations range from about 8 to 25 dB over the frequency range, remaining constant in the low frequencies below 160 Hz and increasing from there to about 1250 Hz. The ECCP results behave similarly, but at levels that are below the core noise attenuations by 3 to 6 dB in the low frequencies (<160 Hz) and 10 to 15 dB in the higher frequencies.

• Comparison with Present Theory

The theoretical turbine transmission loss (attenuation), as predicted for supersonic blade rows by the procedure in Reference 10, was determined for the six-stage turbine on the CF6-50 engine. The takeoff condition was selected for the analysis comparison due to cycle condition availability. This condition is considered to be representative of the other operating conditions

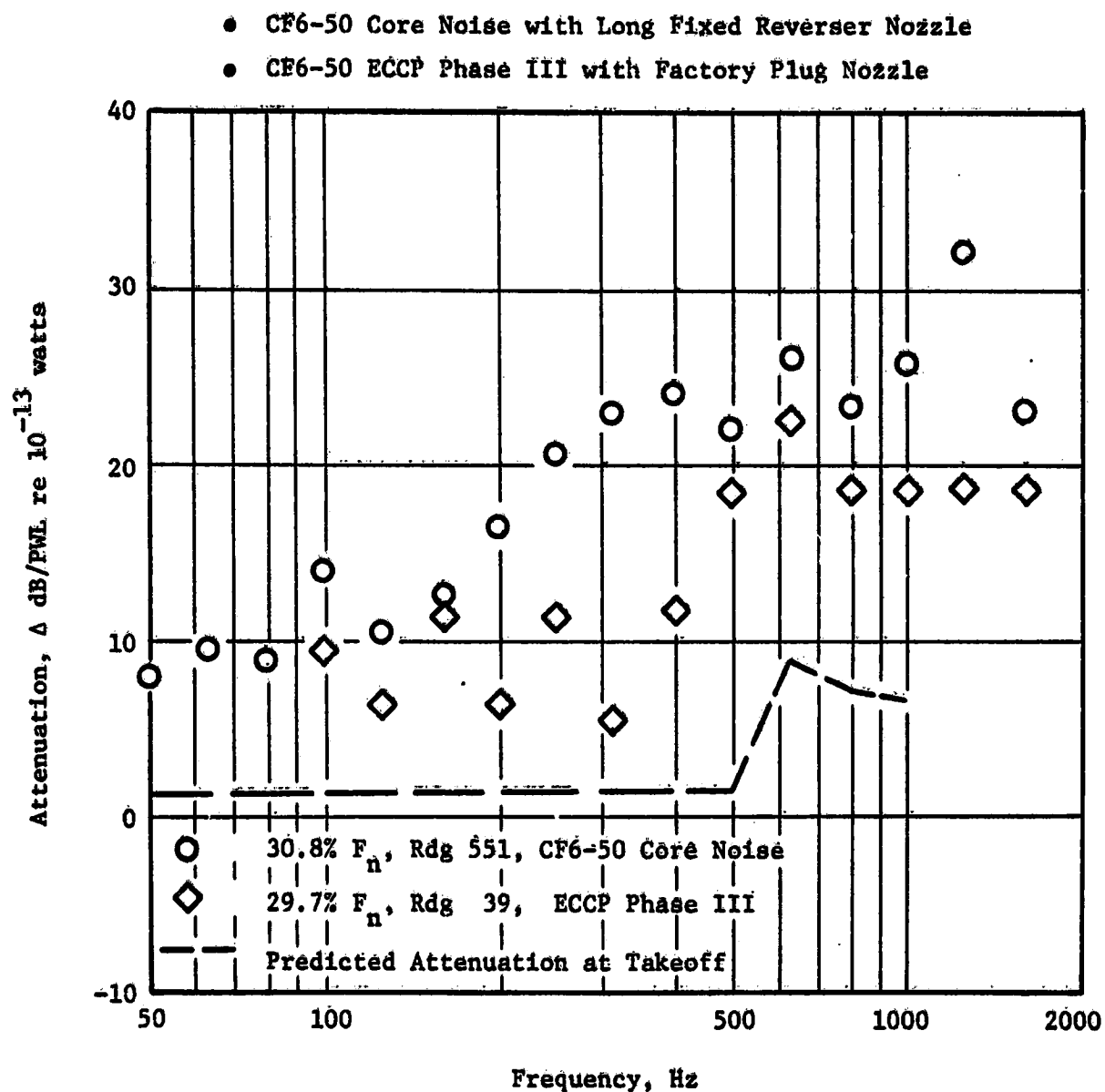


Figure 4.3-14. Comparison of Measured Turbine Attenuation from Coherent Spectra at Approach.

since, above idle, the turbine nozzle (Plane 4.0) operates near choked conditions. The prediction program was set up following the recommendations noted in Reference 10 for the CF6-50 turbine. The attenuation results of the theoretical predictions are shown in comparison with the engine results in Figures 4.3-14 and -15. A maximum attenuation of 8.54 dB is obtained at 630 Hz after reaching the first cut-on frequency of 570 Hz. Prior to cut-on, less than 1.5-dB attenuation is computed. The attenuation drops off from the maximum to 7.12 and 6.72 dB at 800 and 1000 Hz, respectively.

The shape of the theoretically predicted attenuation curve is similar to the data trends observed for the 30.8 and 45.5% F_n conditions in Figures 4.3-14 and -15, respectively. The attenuation levels for the theoretical prediction are lower than the core noise test results by as much as 20 dB, primarily in the frequencies above 125-160 Hz. This amount of difference may be due to the limited coherent signal content at the higher frequencies at both Planes 4.0 and 8.0 relative to the input signal Plane 3.5.

4.3.4 Summary of Coherence and Transfer Function Results

The coherence levels within the CF6-50 engine combustor were of sufficient magnitude to achieve reasonable transfer function gain and phase information. Between the combustor and the core nozzle, the coherence levels were quite low (~ 0.1) which resulted in a minimum amount of transfer function information.

The far-field results showed that only a small amount of correlated signal reached the far field and was coherent in a small band of low frequencies (< 200 Hz). Nonlinear effects, due to the various paths the internally generated signal takes before reaching the far field, were reasoned to be a possible cause for the low coherence levels observed with this engine.

The method of analysis (ordinary coherence) may also have an influence on the strength of the coherent signal in the far-field. Other noise sources, even at low power settings, may have contributed to the low coherence levels achieved. There is a possibility that the use of multiple coherence with the three Plane 3.5 sensors or the two Plane 8.0 sensors as input may improve the results of the coherence and transfer function analyses.

The turbine transfer functions determined for the CF6-50 with the standard production combustor, in the form of ΔdB_{PWL} attenuation, were compared with the ECCP Phase III results (Reference 2) and present theory (Reference 10). The results of the comparison showed the CF6-50 core noise attenuation to be generally higher than the ECCP data, especially at the frequencies above 160 Hz. The theoretical prediction is lower than both sets of data but the spectral shape is similar.

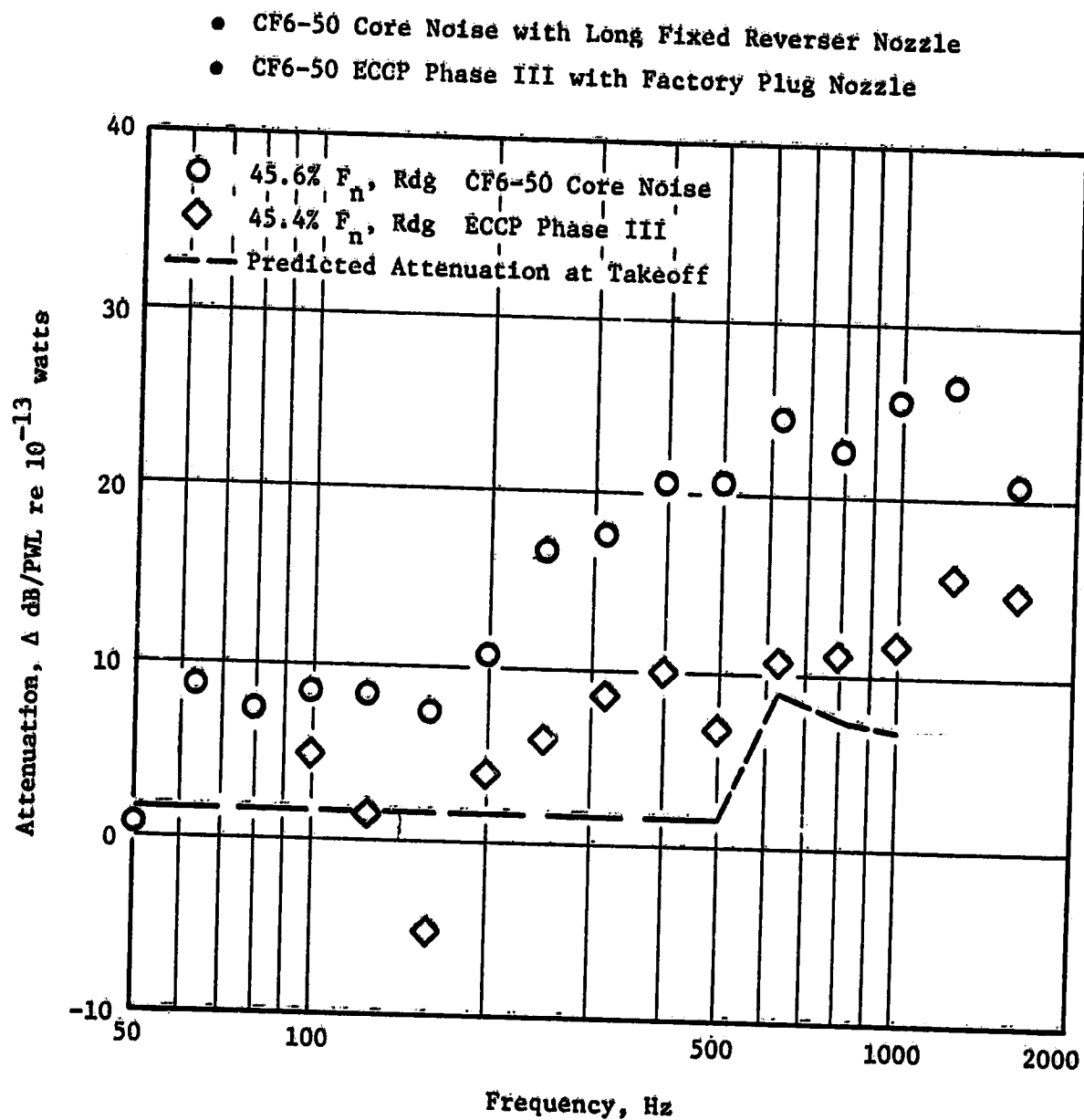


Figure 4.3-15. Comparison of Measured Turbine Attenuation from Coherent Spectra at 45.5 Percent Thrust.

4.4 OUTPUT POWER

4.4.1 Duct Power Level Comparison with Predictions

Comparisons were made with predicted values of measured and coherent duct PWL's computed inside the CF6-50 engine combustor and core nozzle, respectively.

Internal Combustor FPWL Versus Component Prediction

A comparison of the combustor sensor measured power level was made with a simplified component prediction derived for the ECCP of Phase II component test data (Reference 1). The overall power level PWL_{GE} is calculated from:

$$PWL_{GE} = 100.2 + 10 \log [W_{36}(T_4 - T_3) \sqrt{T_3}]$$

re 10^{-13} watts

where P_{T3} = Combustor inlet total pressure, KN/m²
 T_{T3} = Combustor inlet total temperature, K
 T_{T4} = Combustor exit total temperature, K
 W_{36} = Total combustor airflow, kg/sec

The aero parameters used in calculating the PWL_{GE} values are found in Table 4.1-2.

The measured results were based on an overall power level determined from the internal fluctuating pressure measurements reduced to 1/3-octave-band spectra and corrected for frequency response loss. The overall levels determined from these pressure measurements (considered to be acoustic plane wave signals) were converted to power level accounting for impedance changes due to differences in test conditions, Mach number effects, and area differences at each measurement plane as described in Section 3.7. The resulting power level was designated $FPWL_{meas}$ with units in dB re 10^{-13} watts. The parameters used in the conversion to $FPWL_{meas}$ are found in Table 4.1-2.

The comparison of $FPWL_{meas}$ to PWL_{GE} for the combustor internal sensors at Planes 3.0, 3.5, and 4.0 are shown in Figure 4.4-1. Good agreement is apparent in the slope of the data at all planes. The measured levels at Plane 3.0 are 2 to 4 dB lower than the equal power level line, which may be due to the transmission loss through the combustor liner, while at Planes 3.5 and 4.0, the levels are about 4 dB higher than the line. These results indicate that the internal power levels are predicted quite accurately with the PWL_{GE} simplified correlation over the entire operating range of the engine.

Coherent PWL in Core Exhaust Compared to Engine Prediction

The PWL_{GEFAA} engine prediction is based on a correlation derived from engine far-field data and core probe results obtained during tests conducted

- CF6-50 Standard Combustor
- Engine Test Results
- 1/3-Octave-Band Results $\Delta f = 50 \sim 5000 \text{ Hz}$

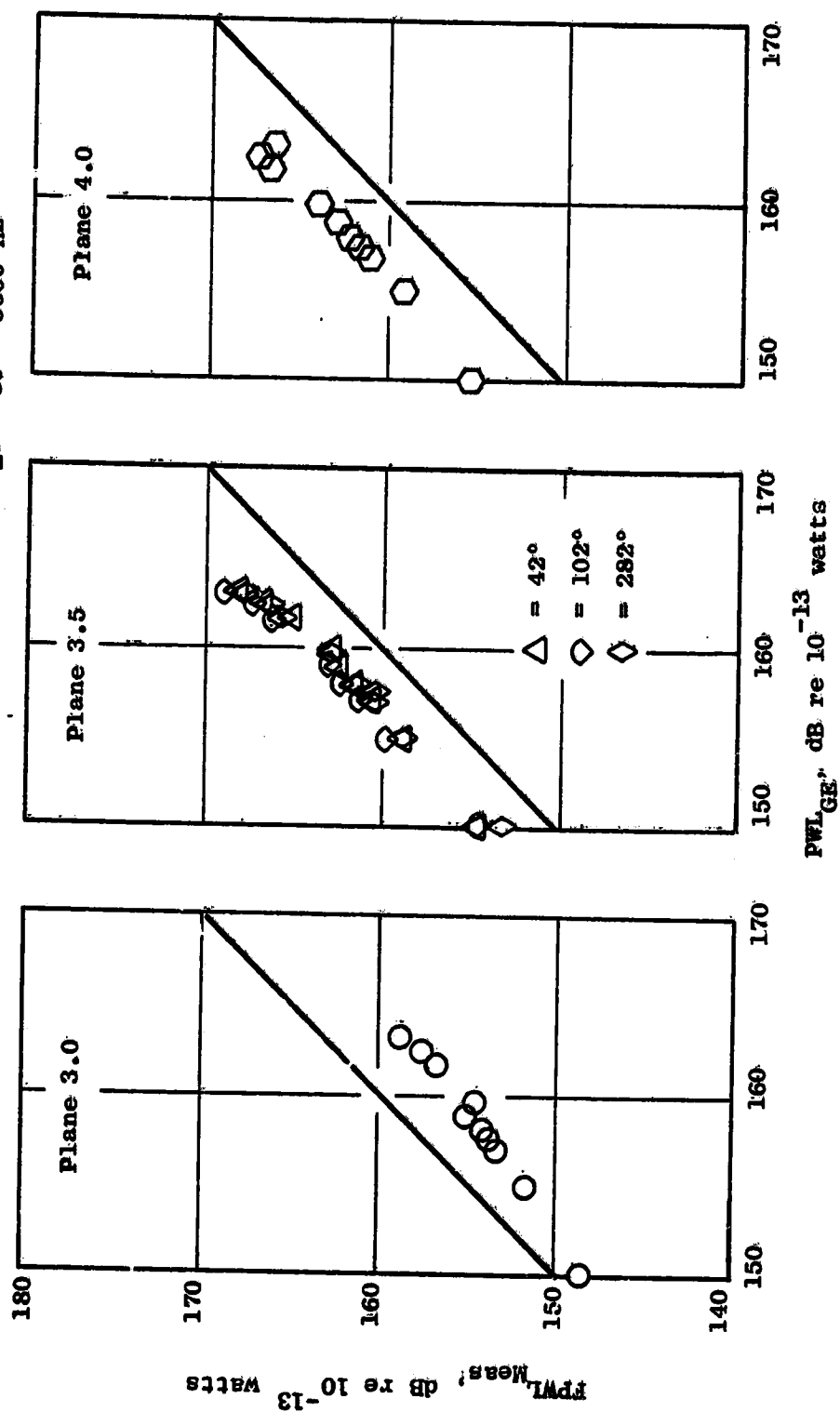


Figure 4.4-1. Comparison of Internal Sensor $FPWL_{Meas}$ to PWL_{GE} .

under the Core Engine Program, Reference 11. The overall power level from the engine correlation is calculated from

$$PWL_{GEFFA} = 169.3 + 10 \log W_{36}(T_{T4} - T_{T3})^2 (\rho_3 / \rho_0)^2 - 40 \log (T_{T4} - T_{T3})_{\text{Design}}$$

re 10⁻¹³ watts

where the nomenclature is described above and $(T_{T4} - T_{T3})_{\text{Design}}$ is the total temperature drop across the high and low pressure turbines at the cycle design point.

The comparison with the measured power level is based on the pressure measurements taken with the sound-separation probe in the core nozzle. The power level determined from the as-measured fluctuating pressure measurements in the core exhaust was higher than the predicted power level from the engine correlation. To more accurately compare the ECCP Phase III data with the engine correlating parameter, the coherent part of the probe Kulite A spectra with the Kulite B signal was used to compute the PWL_{meas} .

Figure 4.4-2 illustrates the comparison of the coherent PWL_{meas} with PWL_{GEFFA} . The results show reasonable agreement in level and good agreement in data slope of the measurement (coherent) results with the ECCP Phase III results (Reference 2) and predicted levels. These results support the credibility of the engine correlation procedure. It also shows the potential for acquiring core noise data from internal probe measurements at a single central immersion.

4.4.2 Far-field Coherent Output Power

Coherent Output Spectra Comparison from Plane 3.5 and Plane 8.0

The coherent output spectra were determined between the internal sensors at Plane 3.5 (102°) and each far-field microphone. A similar set of spectra was determined between the Plane 8.0A core probe Kulite and the far-field microphones. The complete set of far-field coherent output SPL spectra (corrected to free field) for the seven lowest power settings is found in Appendix C along with tabulations of raw and coherent OASPL and OAPWL.

A typical comparison between the raw (measured) spectra on the 45.72 m (150 ft) arc corrected to free field and the coherent spectra at peak angle is presented in Figure 4.4-3. Figure 4.4-3(a) shows the coherent spectrum at 45.5% F_n to fall about 10 to 20 dB below the raw spectrum and indicates very little of the typical core noise dominated shape. In contrast, Figure 4.4-3(b) shows the coherent spectrum at 15% F_n to exhibit a peaked region between 200 to 630 Hz level in this region. The low frequencies (<100 Hz) of the coherent spectrum, which is only 6 to 10 dB below the spectrum, are 2.5 dB below the raw level. This condition is representative of one that contains a large amount of core generated noise. The result from the spectra comparison in Figure 4.4-3 enhances the results presented in Figure 3.7-22 showing the regions of core noise influence on the far-field measurements to fall below 45.5% F_n (230 m/s core velocity).

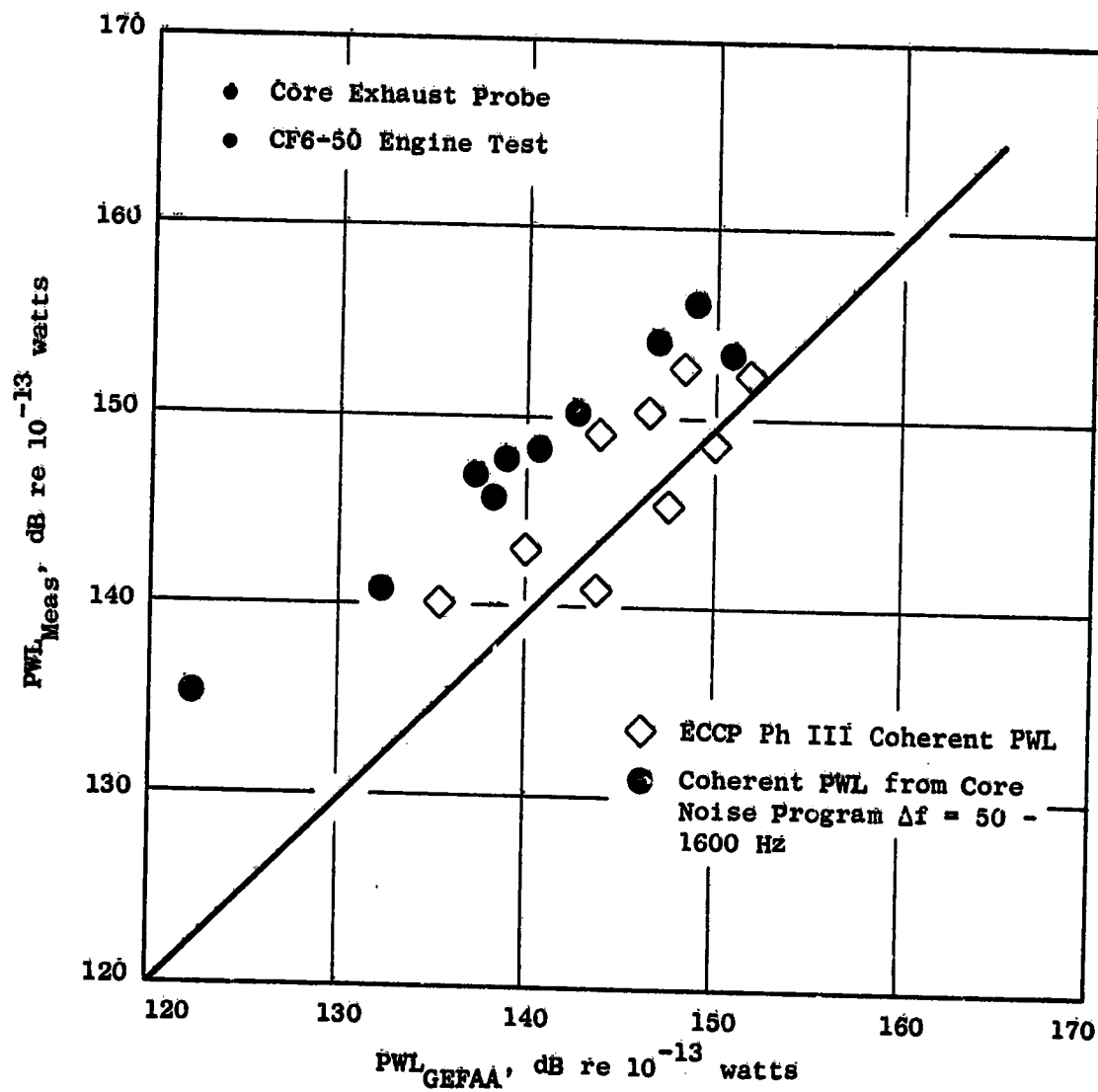


Figure 4.4-2. Comparison of Core Probe Coherent PWL_{Meas} to PWL_{GEFAA}.

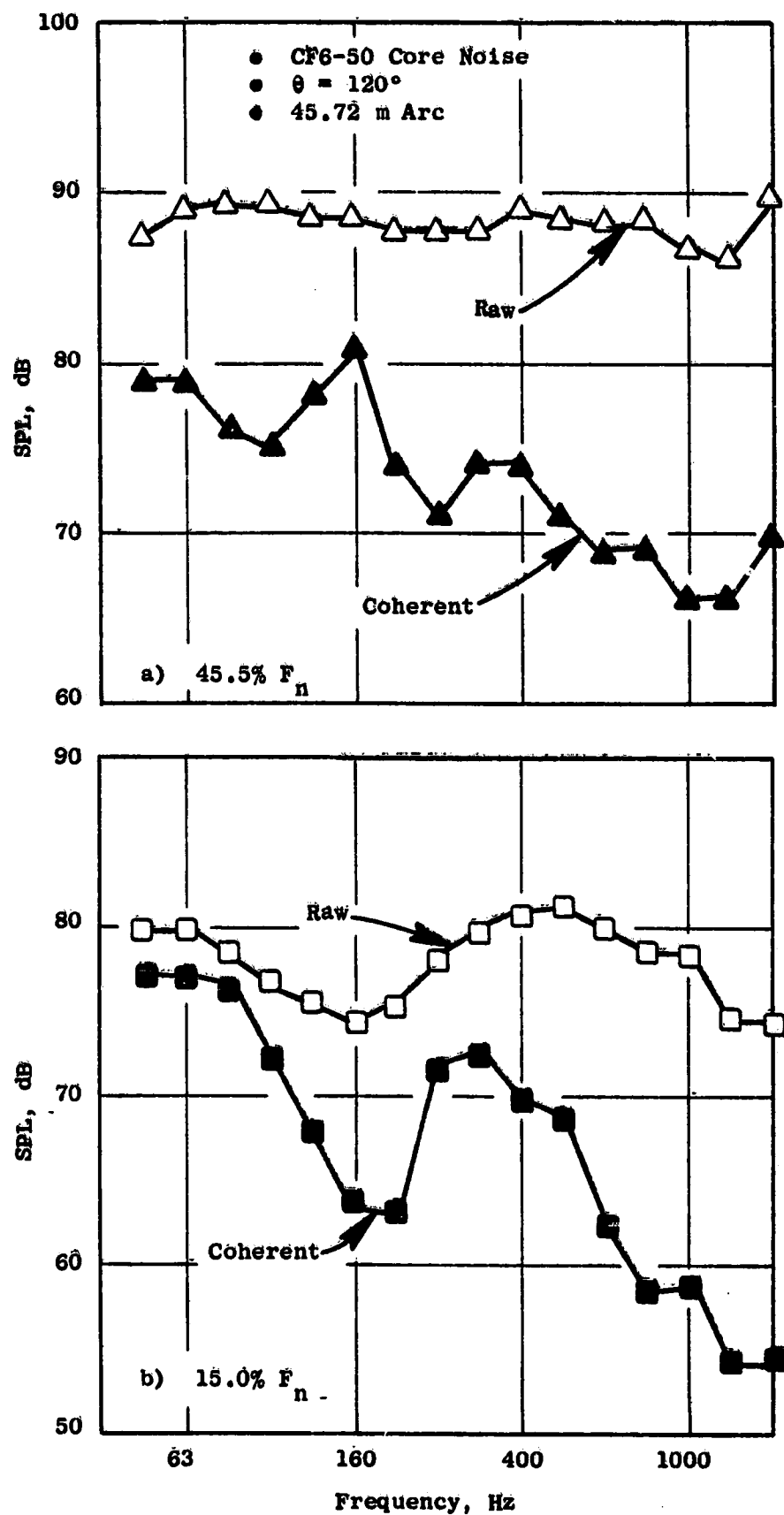


Figure 4.4-3. Comparison of Far-Field Raw and Coherent SPL Spectra at Peak Angle.

The overall coherent power level spectra determined in the far field relative to the internal sensors at Planes 3.5 and 8.0 were compared at three representative power settings covering the engine operating range for this analysis. The PWL was calculated by applying a spherical surface area segment to the intensities determined at each angle. Figures 4.4-4(a) and 4.4-4(b) illustrate the overall coherent power spectra variation at 15, 30.8, and 45.5% F_n relative to Plane 3.5 [Figure 4.4-4(a)] and Plane 8.0 [Figure 4.4-4(b)]. Both figures indicate peaked spectra at 15% F_n in the region between 250 to 630 Hz which is typically associated with core noise. This peaked shape disappears at the higher power settings, more so in Figure 4.4-4(a) (Plane 3.5) due to the smaller amount of coherent signal over the frequency range in the far field.

Coherent OASPL and PWL Directivity Comparisons

The OASPL from the coherent output spectra were determined at each angle for seven test conditions. Figure 4.4-5 shows the comparison of the Plane 8.0A probe to the far field for 15, 30.8, and 45.5% F_n . The peak angle shifts from 130° at the low power setting (15% F_n) to 120° above approach (30.8% F_n). The dark symbols on the figure illustrate the OASPL from the raw signal at 30.8% F_n which is 10 to 17 dB above the coherent OASPL.

The coherent PWL was determined from the acoustic intensity at each angle and the area segment associated with a spherical surface with radius equal to the measurement arc radius (45.72 m, 150 ft) and origin at fan exit center. A PWL directivity comparison of Plane 8.0A results is shown in Figure 4.4-6 for the above three power settings in the survey. The peak of the PWL directivity is at 120° at 15% F_n and moves between 110° and 120° at the higher speeds. The raw PWL (solid symbols) for the 30.8% F_n point shows a 4dB spread between the coherent levels as illustrated in Figure 4.4-5.

A similar comparison is shown in Figures 4.4-7 and 4.4-8 for the coherent output spectra from Plane 3.5 (102°) to the far-field angles. Since this set of data contained some very low coherence values (<0.1) over much of the frequency range of interest in the forward angles, it is not surprising to see a general flattening of the directivity in the forward angles at the three representative conditions of 15, 30.8, and 45.5% F_n . The aft angles exhibit a peaking of the OASPL (Figure 4.4-7) and PWL (Figure 4.4-8) at all thrust settings in the 130° region. This is because of the increased coherence (>0.1) at some of the lower frequencies (see Section 4.3.2). The raw levels of OASPL and PWL (solid symbols) show even larger differences than with the Plane 8.0A results. These results suggest a peak core noise far-field angle region between 110° and 130° which is consistent with past results.

Directivity Index Comparisons

The Directivity Indices (DI) of the far-field coherent output spectra relative to Plane 3.5 and Plane 8.0 were determined for all seven lower speed points using the ratio of the acoustic intensities at each angle, calculated from the coherent SPL spectra, and the average intensity computed

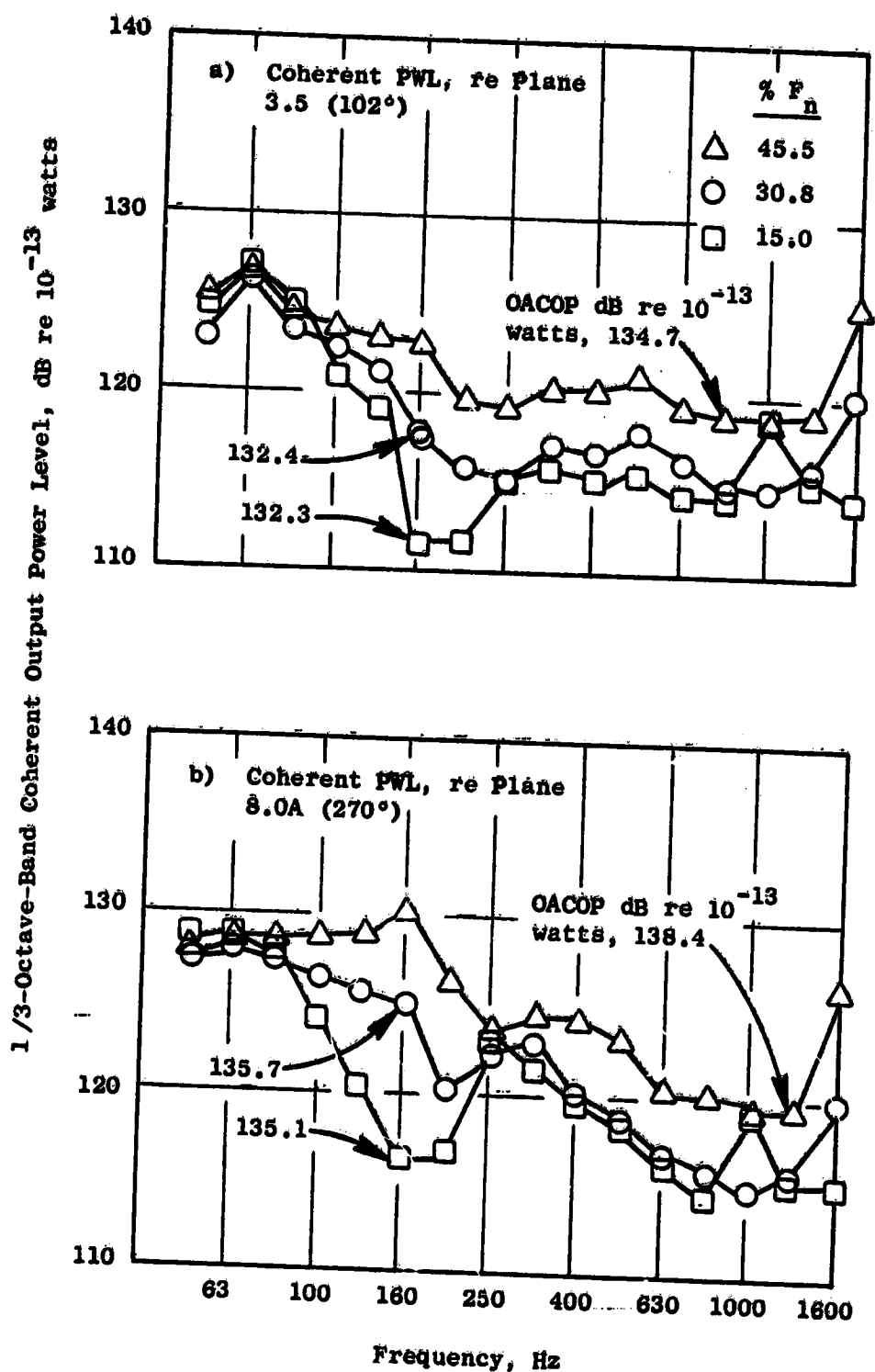


Figure 4.4-4. Coherent Power Level Spectra Comparison for the CF6-50 Engine.

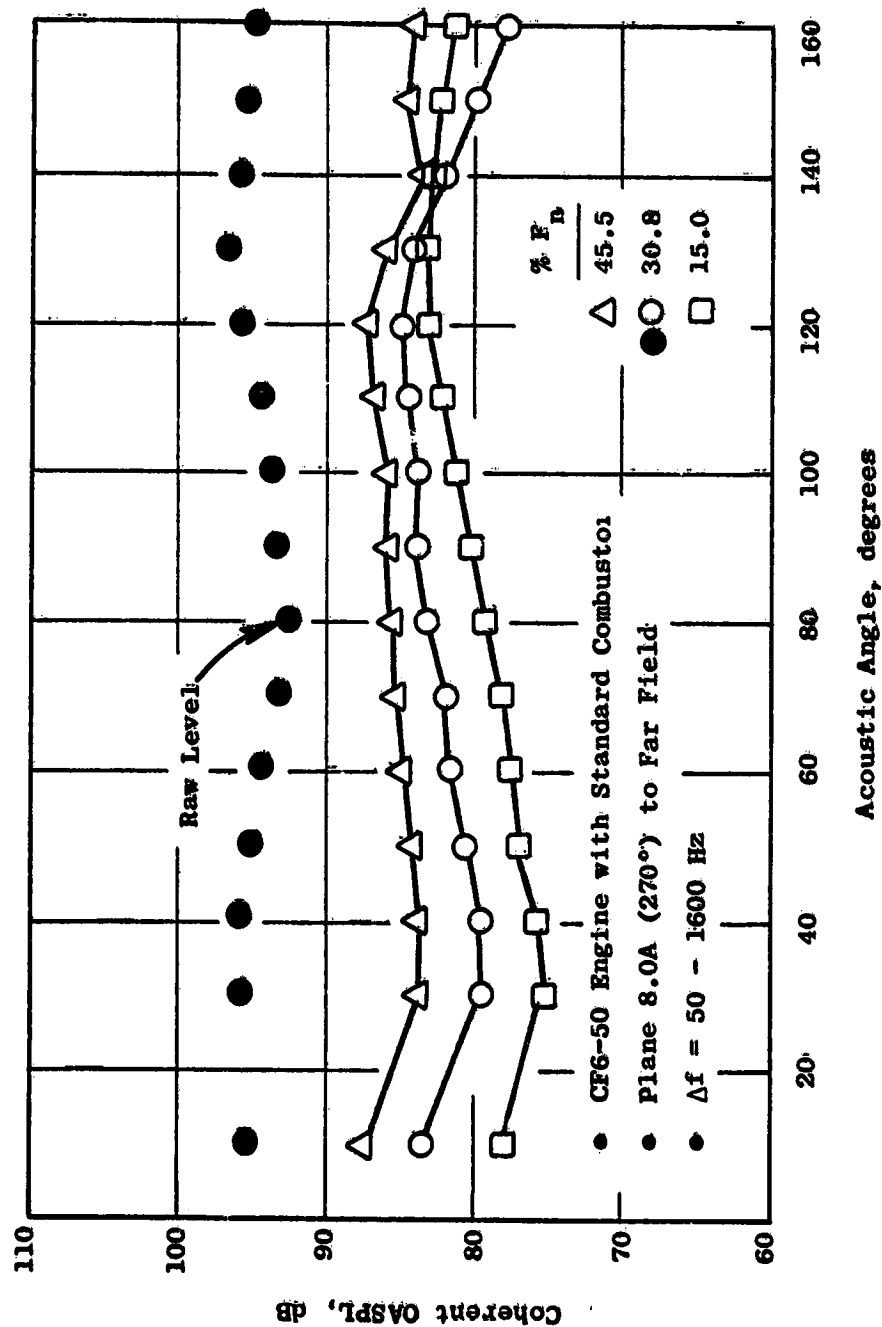


Figure 4.4-5. Directivity Comparison of Coherent Far-Field OASPL Relative to Plane 8.0.

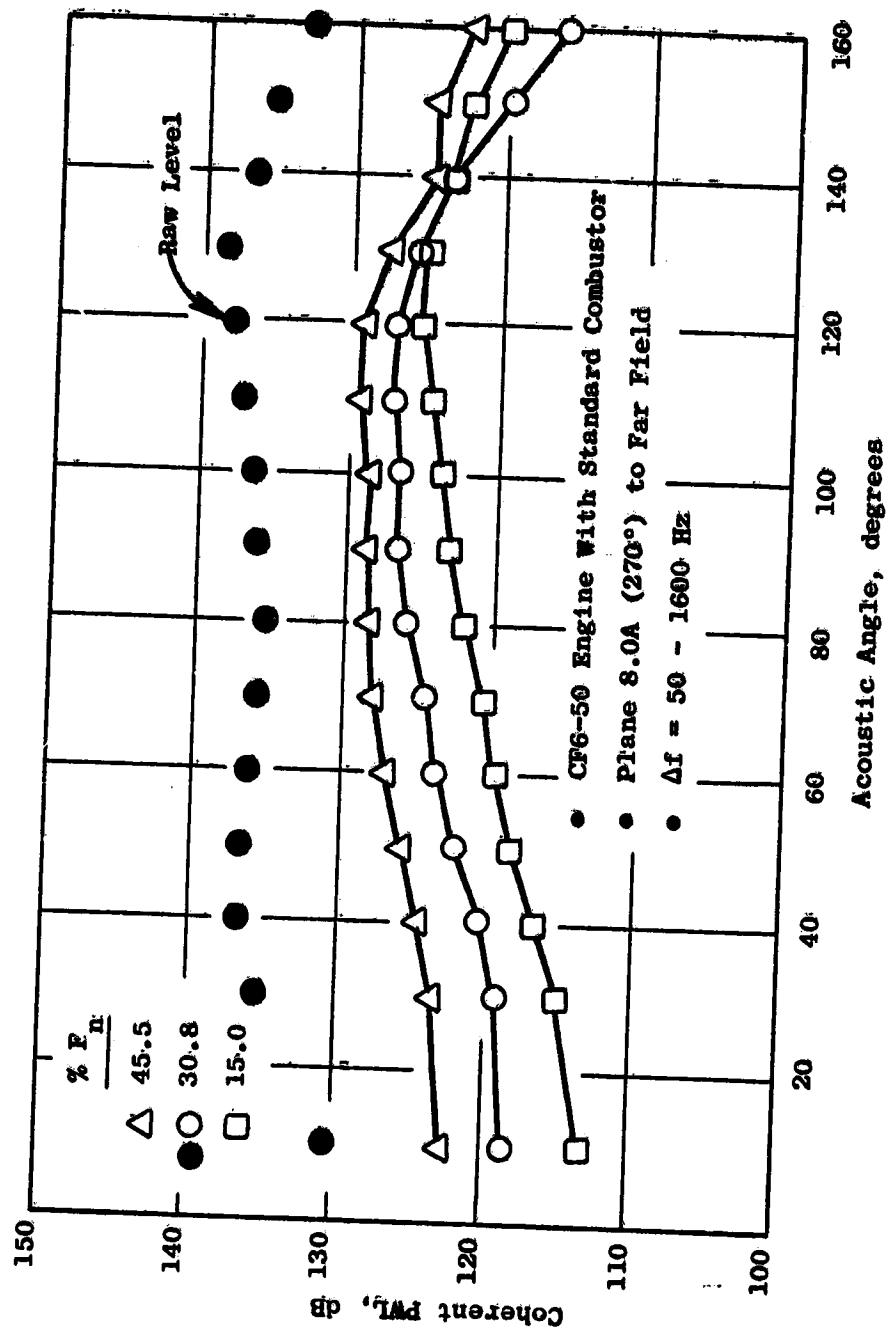


Figure 4.4-6. Directivity Comparison of Coherent Far-Field PWL Relative to Plane 8.0.

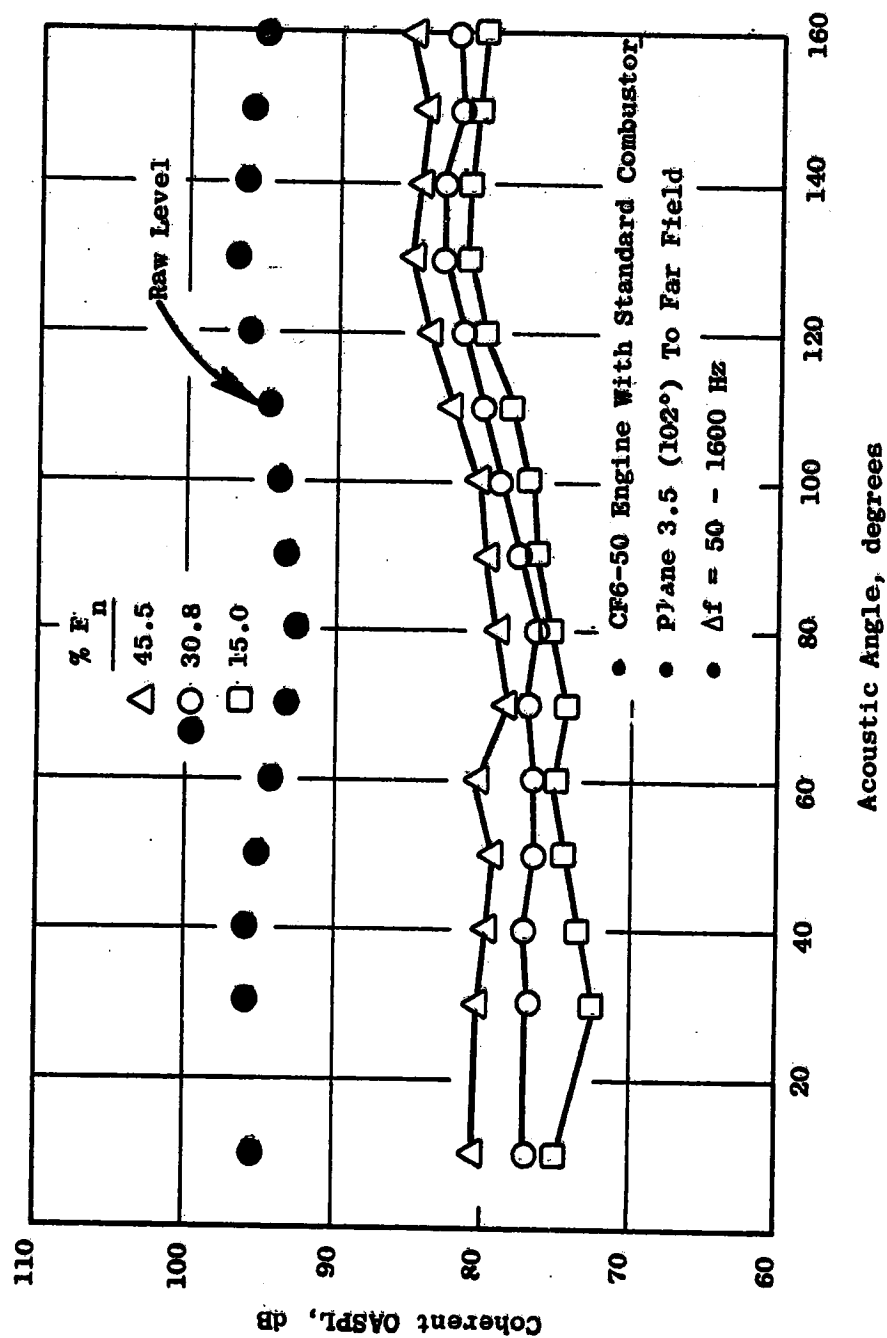


Figure 4.4-7. Directivity Comparison of Coherent Far-Field OASPL Relative to Plane 3.5.

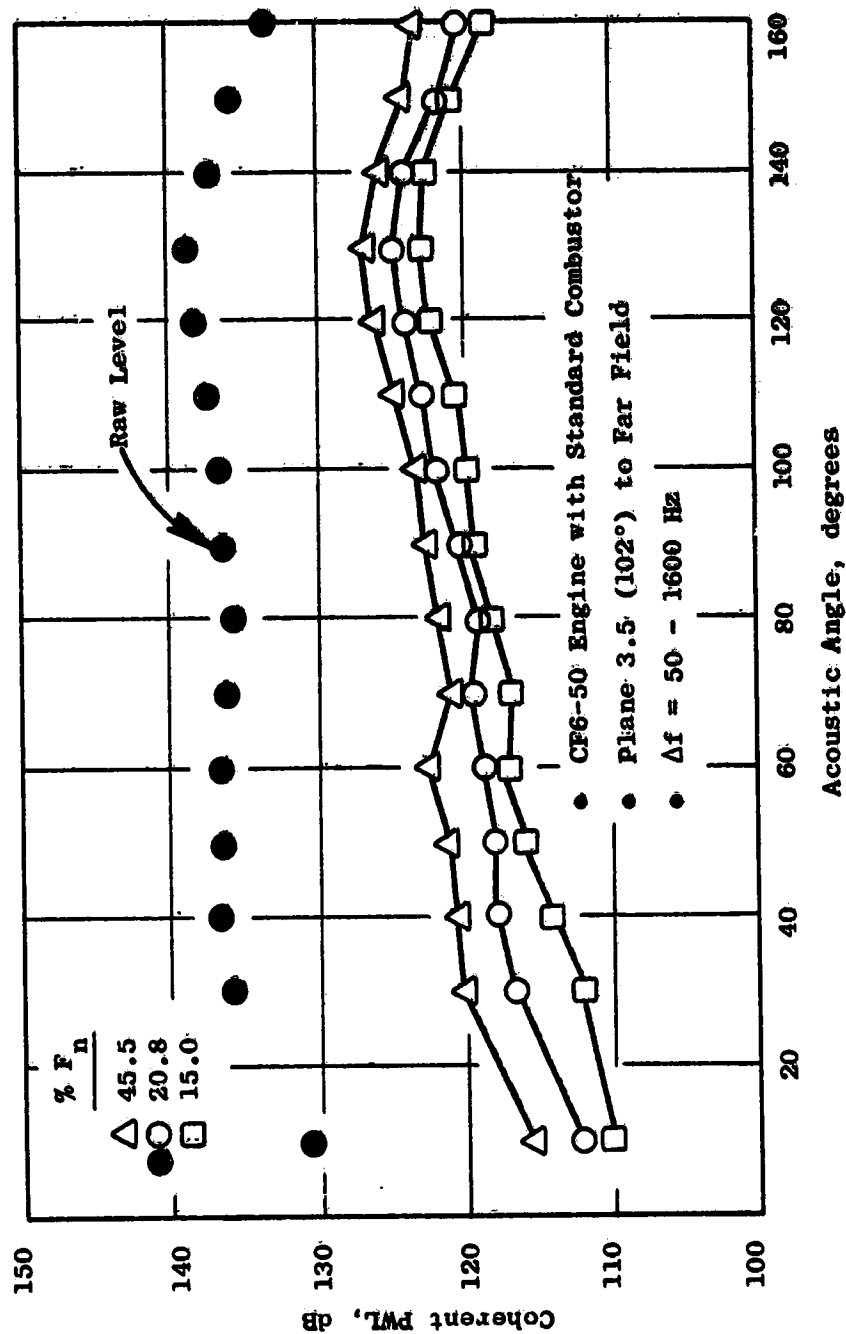


Figure 4.4-8. Directivity Comparison of Coherent Far-Field PWL Relative to plane 3.5.

from the mean square average sound pressure. Table 4.4-1 lists these Directivity Indices for all test conditions. Figure 4.4-9 shows the DI distribution referenced to the Plane 8.0 internal sensor for the three power settings of 15, 30.8, and 45.5% F_n . The figure indicates a peak directivity index at 130° for the low-power point with a shift to 120° at the higher power settings. The shapes of the DI distributions are similar but are not identical.

In contrast, the DI distribution referenced to Plane 3.5 in Figure 4.4-10, shows close agreement in both shape and level for angles above 60°. The peak values occur at 140° for 15% F_n and 130° for the higher thrust conditions.

Figure 4.4-11 shows the comparison of the directivity index determined from the measured data at 30.8% F_n (referenced to Plane 8.0) and the predicted DI from the GE core noise prediction (Reference 11). The comparison shows the prediction to underpredict (-4 dB) the forward angles (<100°) and over predict (+3 dB) in the peak angle region of 110° to 130°.

4.4.3 Coherent Output Power Summary

The results from the internally generated power levels determined from the measured pressures in the standard combustor of the CF6-50 engine match the simplified component prediction defined in Reference 1. The coherent power level computed from the CF6-50 core exhaust duct measurements obtained with the sound separation probe agrees with the GE core noise prediction described in Reference 11 and with similar PWL's calculated for past tests (Reference 2). This result indicates that valid core noise data can be obtained with duct probe measurements at a single immersion.

The core noise contribution to the overall engine noise can be seen from the coherent power calculated from the far-field measurements. The coherent power in the far-field appears to be better defined by the set of far-field coherent spectra determined relative to the core nozzle discharge Plane 8.0 rather than Plane 3.5 in the combustor. The coherent OASPL and PWL directivities peaked between 110° and 130°, which is in the region of peak core noise directivity (~120°).

The directivity index determined from the acoustic intensities was compared with the prediction (Reference 11). Results of the comparison showed the engine data to be greater than the prediction (by 3 dB) in the peak angle region (110°-140°) and less than the prediction (by 4 dB) in the forward angles (<100°).

Table 4.4-1. Summary of Far-Field Directivity Indices from Coherent Measurements.

• Directivity Index, dB

θ (deg)	3.8 Plane		15.0 Plane		22.8 Plane		26.7 Plane		30.8 Plane		36.5 Plane		45.5 Plane	
	3.5 (102°)	8.0A (270°)	3.5 (102°)	8.0A (270°)	3.5 (102°)	8.0A (270°)	3.5 (102°)	8.0A (270°)	3.5 (102°)	8.0A (270°)	3.5 (102°)	8.0A (270°)	3.5 (102°)	8.0A (270°)
10	0.5	-0.2	-3.1	-2.7	-2.9	-1.0	-3.3	-0.4	-2.9	0.6	-2.7	0.9	-1.8	1.9
30	-4.8	-4.6	-5.8	-5.4	-3.9	-4.0	-3.0	-3.5	-3.0	-3.2	-2.0	-2.2	-1.7	-1.7
40	-3.1	-3.0	-4.7	-4.8	-2.5	-3.2	-2.5	-2.3	-2.6	-2.9	-2.3	-2.1	-2.4	-1.7
50	-4.1	-3.8	-3.7	-3.6	-3.0	-2.2	-3.1	-2.0	-3.4	-2.0	-0.7	-1.3	-2.6	-1.2
60	-3.6	-3.2	-3.0	-2.9	-3.3	-1.3	-2.9	-1.2	-3.3	-0.9	-3.1	-1.0	-1.8	-0.6
70	-2.3	-1.8	-3.7	-2.4	-3.4	-0.7	-3.4	-0.8	-2.7	-0.7	-4.4	0.0	-3.7	0.0
80	-2.2	-1.7	-2.5	-1.3	-3.0	-0.5	-2.7	-0.2	-3.5	0.6	-3.2	0.2	-3.1	0.2
90	-1.1	-0.6	-1.6	-0.3	-1.7	0.6	-2.0	0.3	-2.5	1.3	-2.6	0.7	-2.3	0.5
100	-0.4	0.2	-1.0	0.6	-1.3	1.1	-1.0	1.4	-0.8	1.4	-1.2	1.1	-1.9	0.4
110	0.7	1.5	0.1	1.5	0.1	1.1	0.3	2.2	0.5	2.1	0.5	1.8	0.2	1.4
120	1.8	2.4	2.1	2.6	2.1	2.8	1.7	2.4	1.7	2.4	1.4	1.9	1.7	1.6
130	2.2	1.3	3.2	2.9	3.7	2.7	3.8	2.6	3.3	1.6	3.1	2.0	2.8	0.4
140	2.8	2.4	3.4	2.2	3.3	1.4	2.9	0.3	3.2	-0.1	3.1	-0.4	2.5	-1.9
150	2.4	2.2	2.7	1.7	2.2	-0.7	2.1	-1.7	2.0	-2.6	1.9	-2.8	2.1	-0.9
160	0.8	0.4	2.1	0.9	1.0	-2.8	1.4	-5.1	2.3	-4.8	2.2	-2.9	2.9	-1.4
OACOP	129.0	130.8	131.0	133.8	131.5	134.7	131.6	135.3	132.7	136.1	133.9	137.3	134.5	138.0

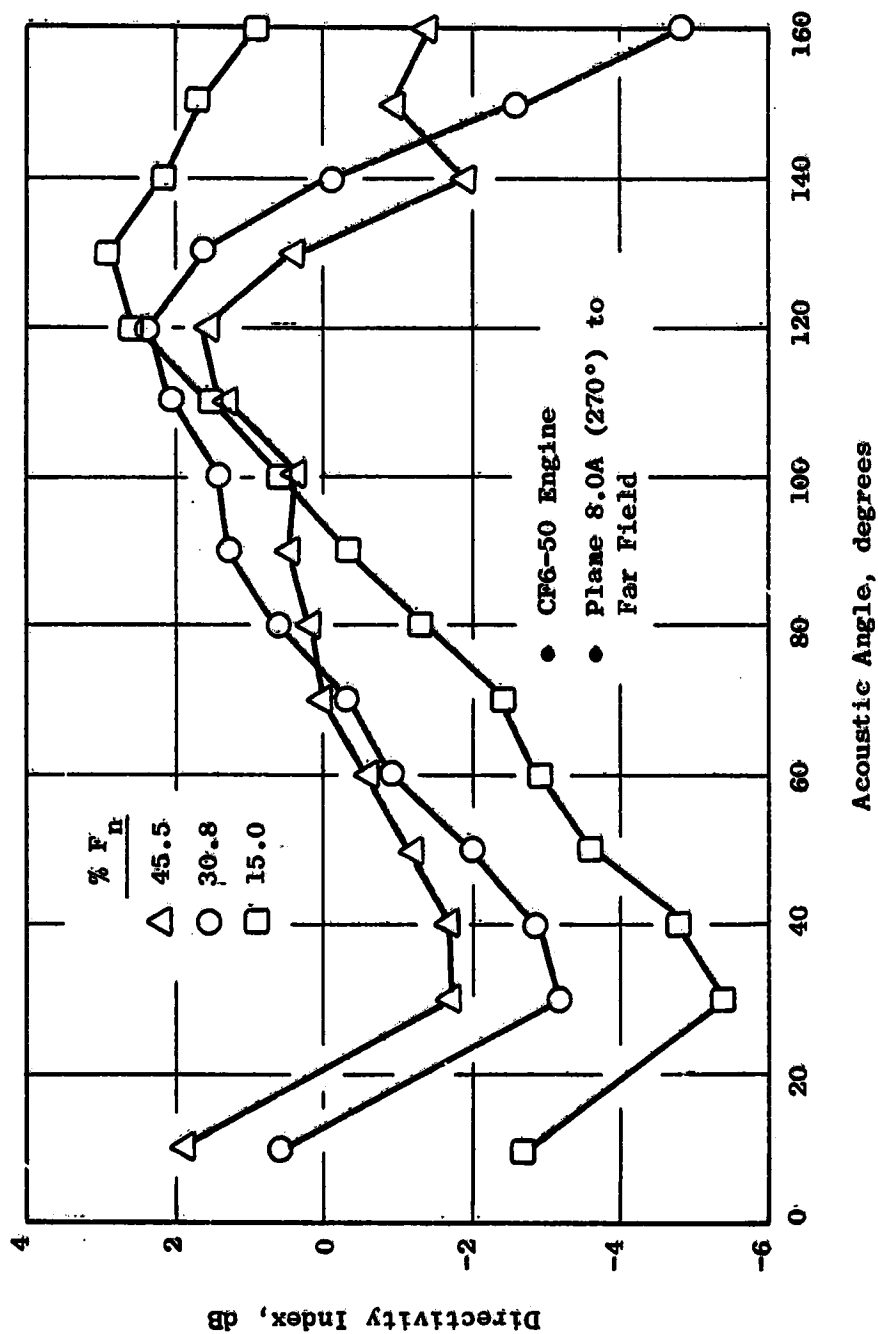


Figure 4.4-9. Directivity Index Comparison From Far-Field Coherent Measurements Relative to Plane 8.0.

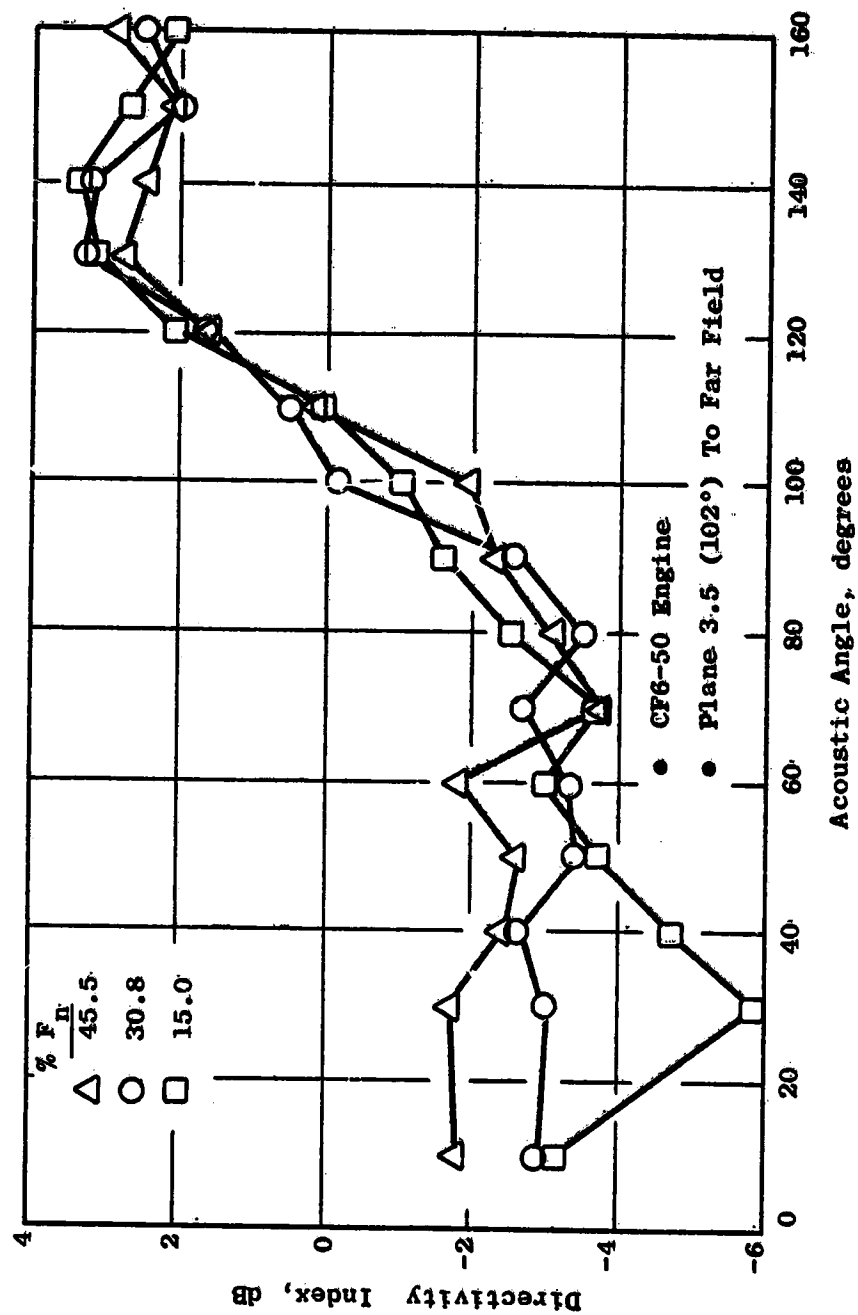


Figure 4.4-10. Directivity Index Comparison from Far-Field Coherent Measurements Relative to Plane 3.5.

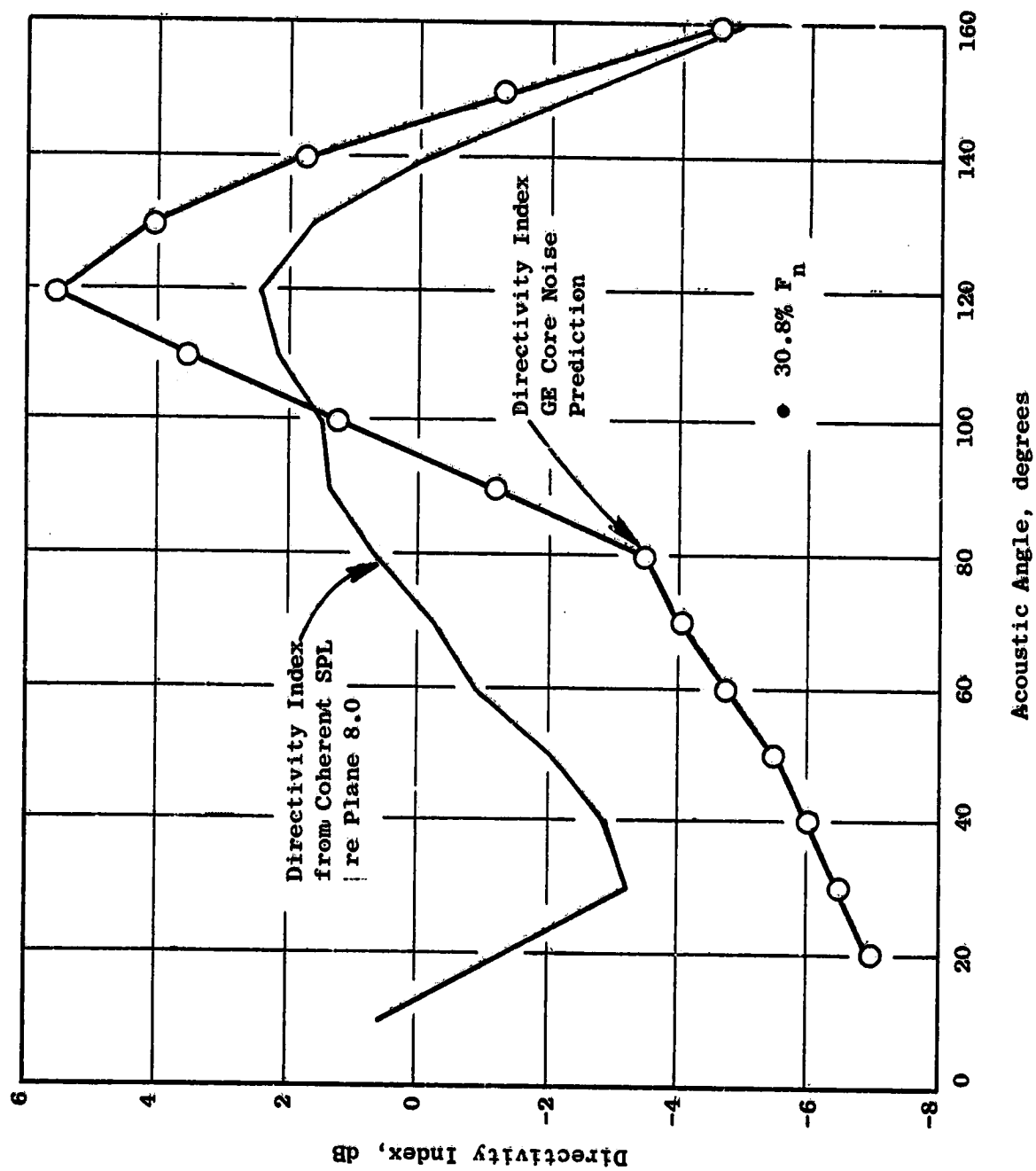


Figure 4.4-11. Directivity Index Comparison Between Coherent Measurements and Predicted Results.

5.0 CONCLUSIONS

The work performed during the execution of this contract has lead to several conclusions and observations from the analysis results. The simultaneous acquisition of a set of fluctuating pressure measurements from engine internal and far-field sensors over the operating range of the CF6-50 high-bypass turbofan engine forms the nucleus of a unique data base for comparison with separate internal and far-field data on this type of aircraft engine system. The following conclusions are based on ordinary coherence analysis which assumes a linear process. If nonlinear processes exist, then the conclusions stated may not be valid.

5.1 OBSERVATIONS ON THE ACQUISITION AND PROCESSING OF MEASUREMENTS

A key factor in the correlation and coherence analysis of these data is the simultaneous acquisition of measurements from internal and far-field sensors. The measurements must be checked for signal polarity in order to properly determine phase information. An impulse signal, such as a blast from a shotgun or horn, etc., recorded simultaneously on all channels, provides a polarity check for far-field microphones that is a considerable time savings. Kulites have to be pressure-checked for signal polarity.

The selection of time-series parameters for data analysis has an influence on the output results. For example, with this set of data, cross-correlations between poorly correlated signals are sensitive to computation parameters. The cross-correlations between internal-to-internal sensors were determined to be best when the frequency bands were restricted to 100-1000 Hz, while the internal-to-external cross-correlations were best when a 100-500-Hz frequency range was used.

5.2 CORE NOISE SPECTRA COMPARISONS WITH ECCP PHASES II AND III RESULTS

Comparisons of the 1/3-octave-band spectral results from the internal measurements obtained on the CF6-50 engine - fitted with the standard production annular combustor with similar engine internal spectra obtained from the ECCP Phase III program with a double annular combustor - indicated a general agreement in spectra levels. Differences were noted in the spectral shapes at nearly all measurement planes within the combustor. However, this was expected since the combustors were quite different in design.

The comparisons of fuel nozzle spectra with the combustor inlet spectra, which were obtained on this program, indicated that the spectral shapes were similar for both measurements and the degree of similarity increased with speed. However, the peak regions did not vary with speed but remain in fixed frequency bands. The internal spectra exhibited a bilobed shape with peaks occurring between 300 to 600 Hz and between 1200 to 1600 Hz. The low frequency peak corresponds to the typical frequency range associated with combustor noises. The fuel system components are the source of several tones

apparent in both the narrowband spectra of the fuel nozzle measurements and in the far-field measurements at the idle condition.

A comparison of the engine data with the ECCP Phase II results from the full-scale duct-rig tests of the CF6-50 standard annular combustor showed the power spectra to be generally similar in shape, especially in the combustor discharge region. The engine levels agreed with the duct rig at the low frequencies (<315 Hz), but were lower than the component data at the higher frequencies for both inlet (~ 14 dB) and discharge (~ 8 dB) planes at the approach power setting. Greater differences were noted at the takeoff condition comparison.

Differences in measurement plane location, instrumentation, the choked turbine nozzle diaphragm in the engine, and the variations in the test conditions - all contribute to the differences in levels apparent between the engine and duct rig.

5.3 APPARENT PRIMARY CORE NOISE SOURCE LOCATION

Cross-correlations between selected pairs of internal sensors were used to identify a probable region within the combustor that appeared to be a primary noise source location. Vectoring of the time delays indicated the apparent location of the primary noise source within the standard production combustor is between Planes 3.5 and 4.0. The analysis indicated that several different groups of frequencies contribute to the sources within the combustor. It is also apparent that these groups of frequencies travel at different directions within the combustor. There is evidence of circumferentially traveling waves similar to those indicated in the ECCP Phase III results.

5.4 TURBINE TRANSMISSION LOSS

The transmission loss across the CF6-50 turbine and exhaust nozzle was determined from the CF6-50 engine internal coherent measurements in terms of Δ dB_{PWL} attenuation. Comparison of the results from the present test with those of a previous test conducted under the ECCP Phase III program showed the CF6-50 core noise attenuations to be generally higher than the ECCP data, especially at frequencies above 160 Hz. The reason for this can be attributed to the low coherence values that occur between the Plane 3.5 (282°) sensor and the core probe, Plane 8.0A (270°), which indicate little signal coherence at Plane 8.0 relative to the combustor.

The theoretical prediction is lower than both the core noise and ECCP attenuations, but the spectral shape is similar. The differences between the data and the theory may be attributed, in part, to the large engine exhaust nozzle duct area changes, potentially producing more attenuation than the simplified production model.

5.5 COHERENCE AND TRANSFER FUNCTION TO FAR FIELD

The coherence and transfer function results were well defined between the planes within the combustor and between the sensors at the core exit plane. However, very low values of the coherence function (<0.1) were observed between the combustor and the core nozzle. The results of the internal to far field proved to give generally low coherence levels (<0.1) except at very low frequencies (<100 Hz). This was especially true of the data relative to the Plane 3.5 (102°) input signal. These low values may be the result of the failure of ordinary coherence calculations in the very complex environment. An evaluation of the results from the ordinary coherence method which assumes a linear relationship between a single input and single output signal may suggest that, for the CF6-50 high-bypass turbofan engine, perhaps a different model would have been more appropriate. Consider the case where multiple signals (of different bands) are transmitted from the internal source to the far field from the engine along different paths (such as the core nozzle exit, the engine sidewall, or the fan nozzle exit) and the far-field receiver is influenced by several additional sources (e.g., the fan, jet, etc.). This case is closer to the actual engine situation. The single input-output model assumption would be an oversimplification of the problem that could lead to erroneous information. A possible means of analyzing such a situation might be through multiple coherence which uses the existing data from groups of internal sensors in combination with the far-field microphones to obtain coherent signals.

5.6 CORE NOZZLE AND COMBUSTOR PWL's

The coherent power level, computed from the measurements obtained from the sound separation probe in the CF6-50 core exhaust duct, agrees with the General Electric core noise prediction and with previous engine test data. This result indicates that valid core noise data can be obtained with duct probe measurements at a single immersion.

The results from the internally generated power levels as determined from the measured pressures in the standard combustor of the CF6-50 engine match the simplified component prediction defined from ECCP Phase II work.

5.7 COHERENT OUTPUT POWER OBSERVATIONS

The coherent power in the far field appears to be more clearly defined by the set of far-field coherent spectra determined relative to the core nozzle discharge Plane 8.0 rather than Plane 3.5 in the combustor. And even with this distinction, the far-field coherent power level obtained from the ordinary coherence procedure appears to be questionable with this engine, due to the level of coherence at many of the microphone locations. If this set of data was processed through a multiple coherence procedure rather than one that employs a single input/single output model, perhaps higher coherence levels would be achieved. The directivity indices computed from these results might also give a better comparison with the prediction.

APPENDIX A
COHERENCE FUNCTIONS AND TRANSFER FUNCTIONS FOR
INTERNAL AND FAR-FIELD SENSORS

Appendix A contains the ordinary coherence functions and transfer functions for the data acquired under this program. The transfer function is expressed as gain and phase. Time delays due to acoustic wave propagation were removed from the data. Far-field transfer functions had the loss due to spherical divergence removed. The transfer gain displayed represents the loss in the far field due to other causes (nonlinearity, multiple sources, etc.).

The data are presented in two sets: internal and internal to far field. The internal results are presented in Part A for the following pairs of internal sensors:

- Plane 3.0 (16°) to 3.5 (42°).
- Plane 3.5 (102°) to 4.0 (92°)
- Plane 3.5 (282°) to 8.0A (270°)
- Plane 8.0A (270°) to 8.0B (270°)
- Fuel nozzle (42°) to 3.5 (42°)
- Fuel nozzle (102°) to 3.5 (102°)

The far-field microphones (15) paired with the Plane 3.5 (102°) and Plane 8.0A (270°) sensors are presented in Part B of this appendix. All of the results presented are for seven power settings of the CF6-50 engine and include percent net thrust points of 3.8, 15.0, 22.8, 26.7, 30.8, 36.5, and 45.5.

The analysis was conducted over a frequency range of 0 to 1000 Hz with a data bandwidth of 2.5 Hz, a 2048 block size, 100 averages, and a total record time of 40 seconds.

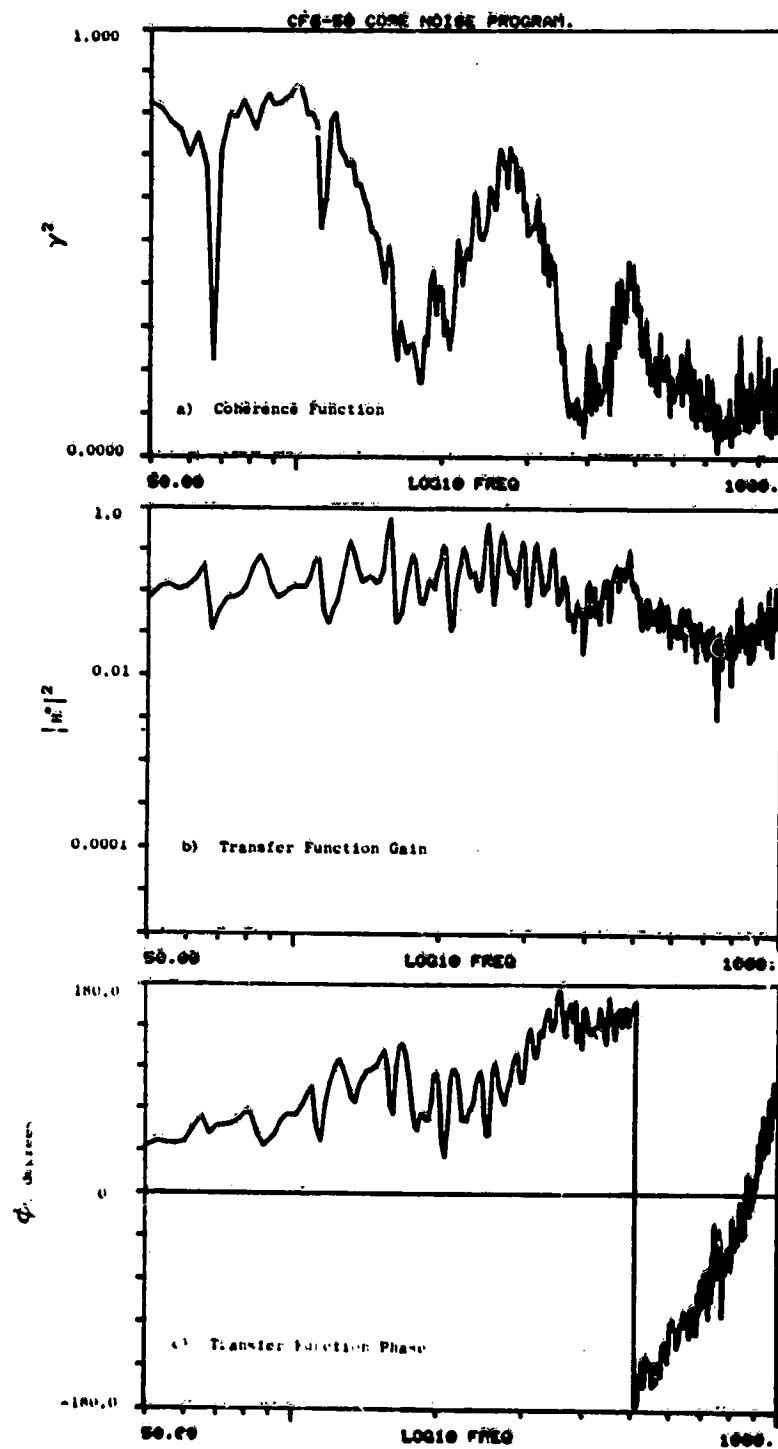


Figure A-1. Coherence and Transfer Functions for Plane 3.0 (16°) to Plane 3.5 (42°) at 3.8% Thrust.

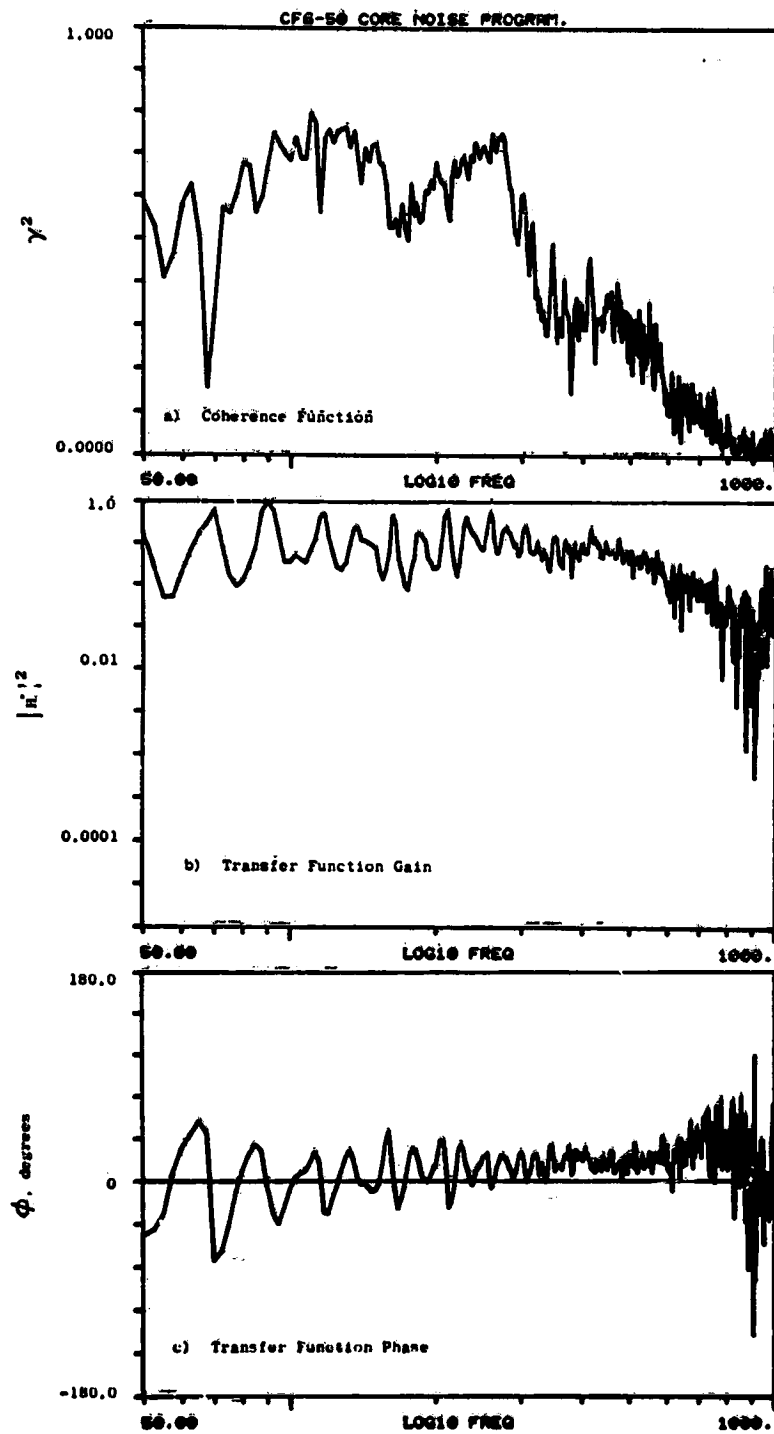


Figure A-2. Coherence and Transfer Functions for Plane 3.5 (102°) to Plane 4.0 (92°) at 3.8% Thrust.

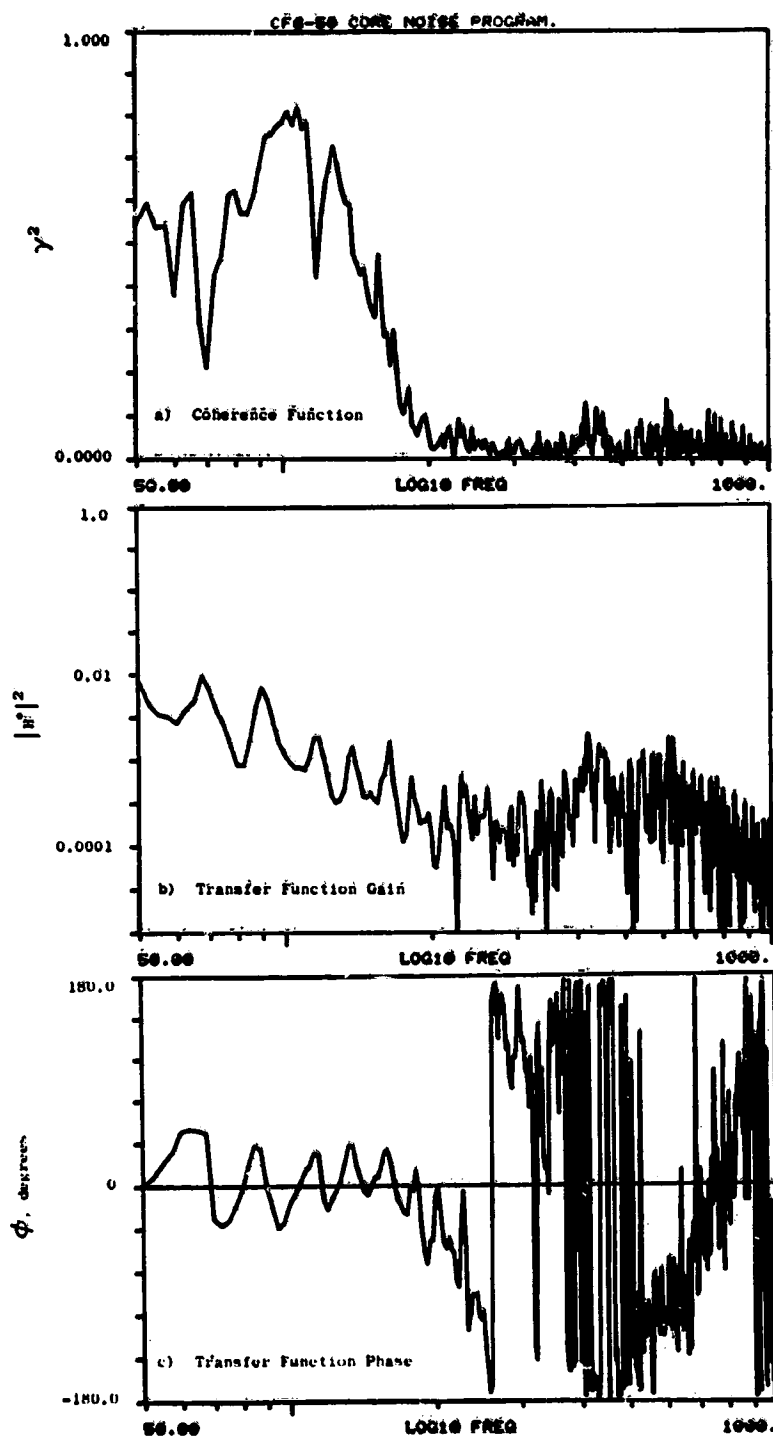


Figure A-3. Coherence and Transfer Functions for Plane 3.5 (282°) to Plane 8.0A (270°) at 9.8% Thrust.

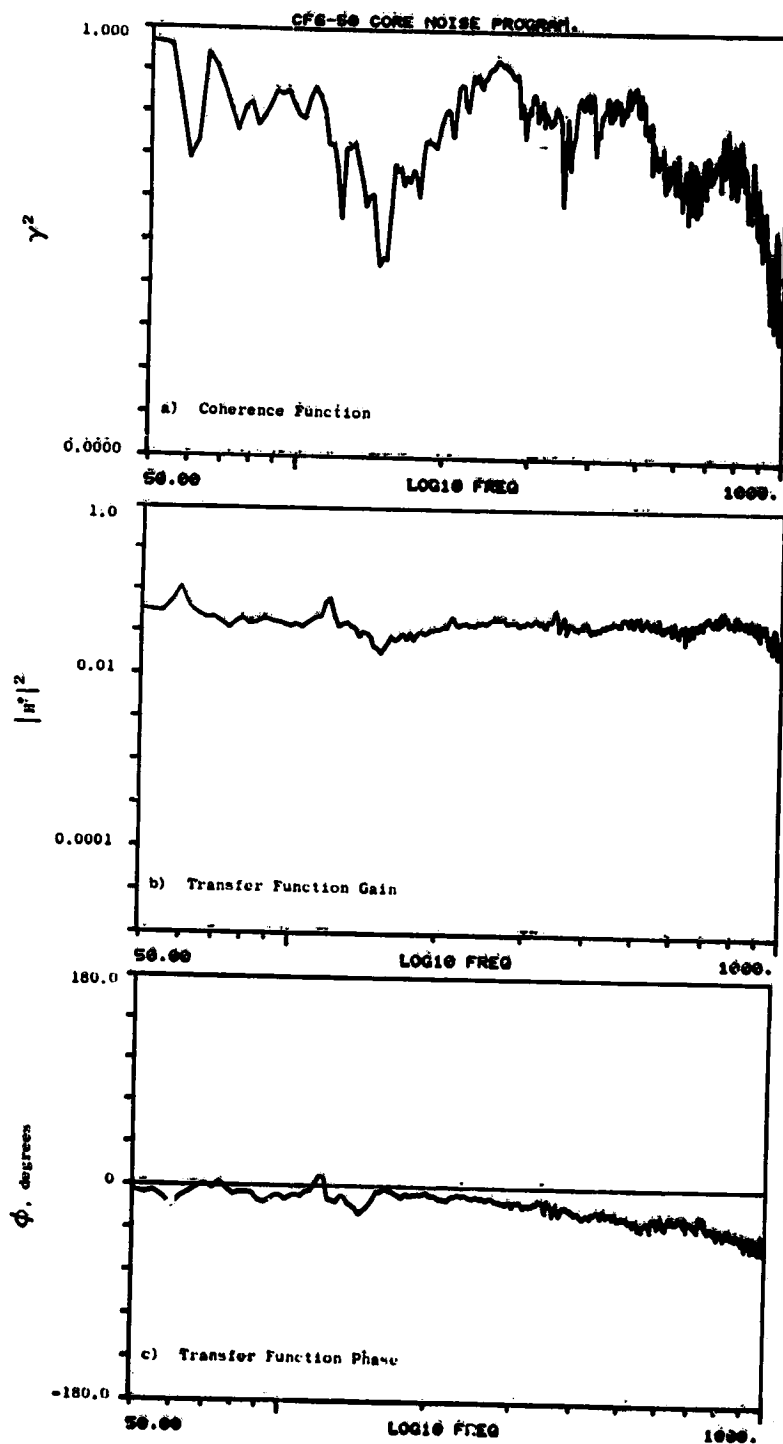


Figure A-4. Coherence and Transfer Functions for Plane 8.0A to Plane 8.0B (270°) at 3.8% Thrust.

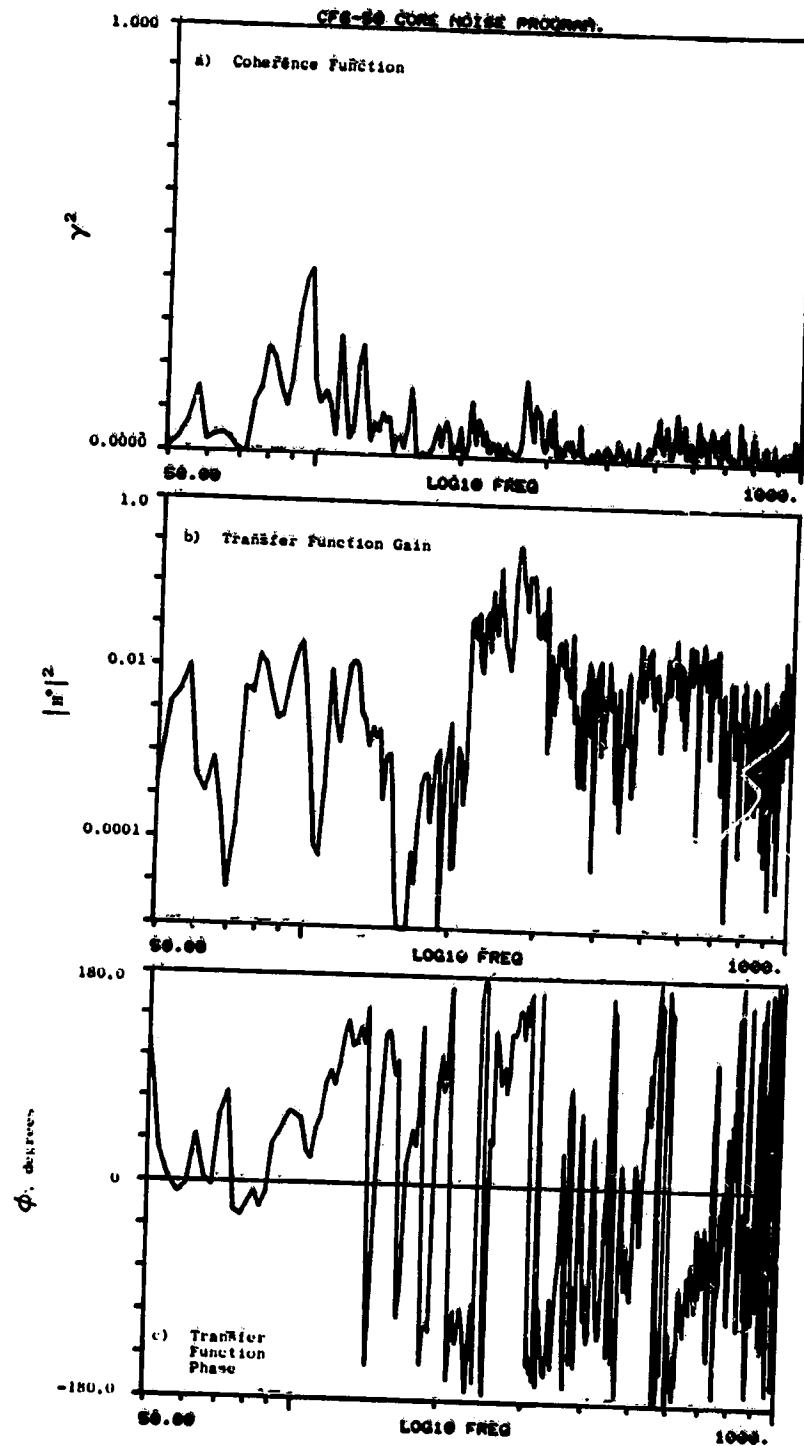


Figure A-5. Coherence and Transfer Functions for Fuel Nozzle (42°) to Plane 3.5 (42°) at 3.8% Thrust.

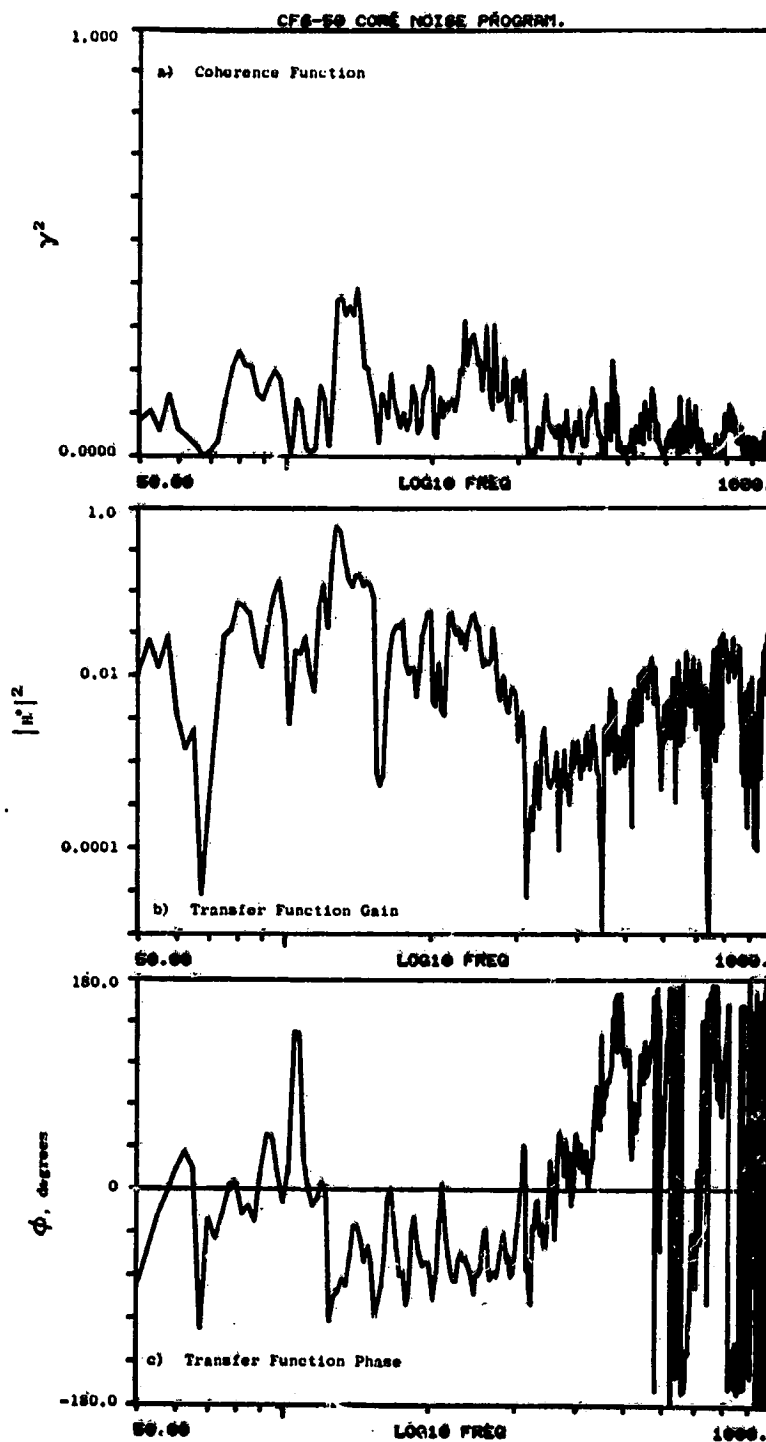


Figure A-6. Coherence and Transfer Functions for Fuel Nozzle (102°) to Plane 3.5 (102°) at 3.8% Thrust.

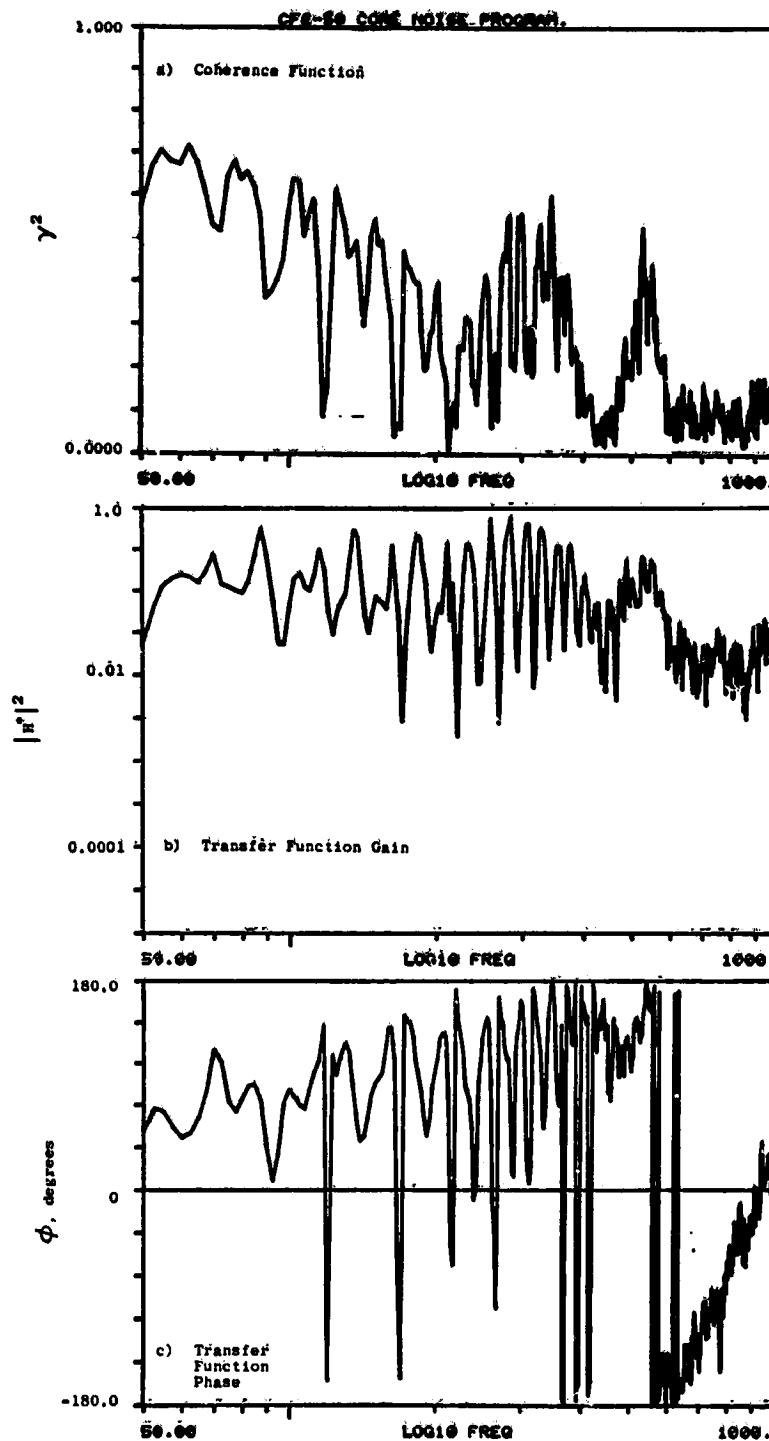


Figure A-7. Coherence and Transfer Functions for Plane 3.0 (16°) to Plane 3.5 (42°) at 15.0% Thrust.

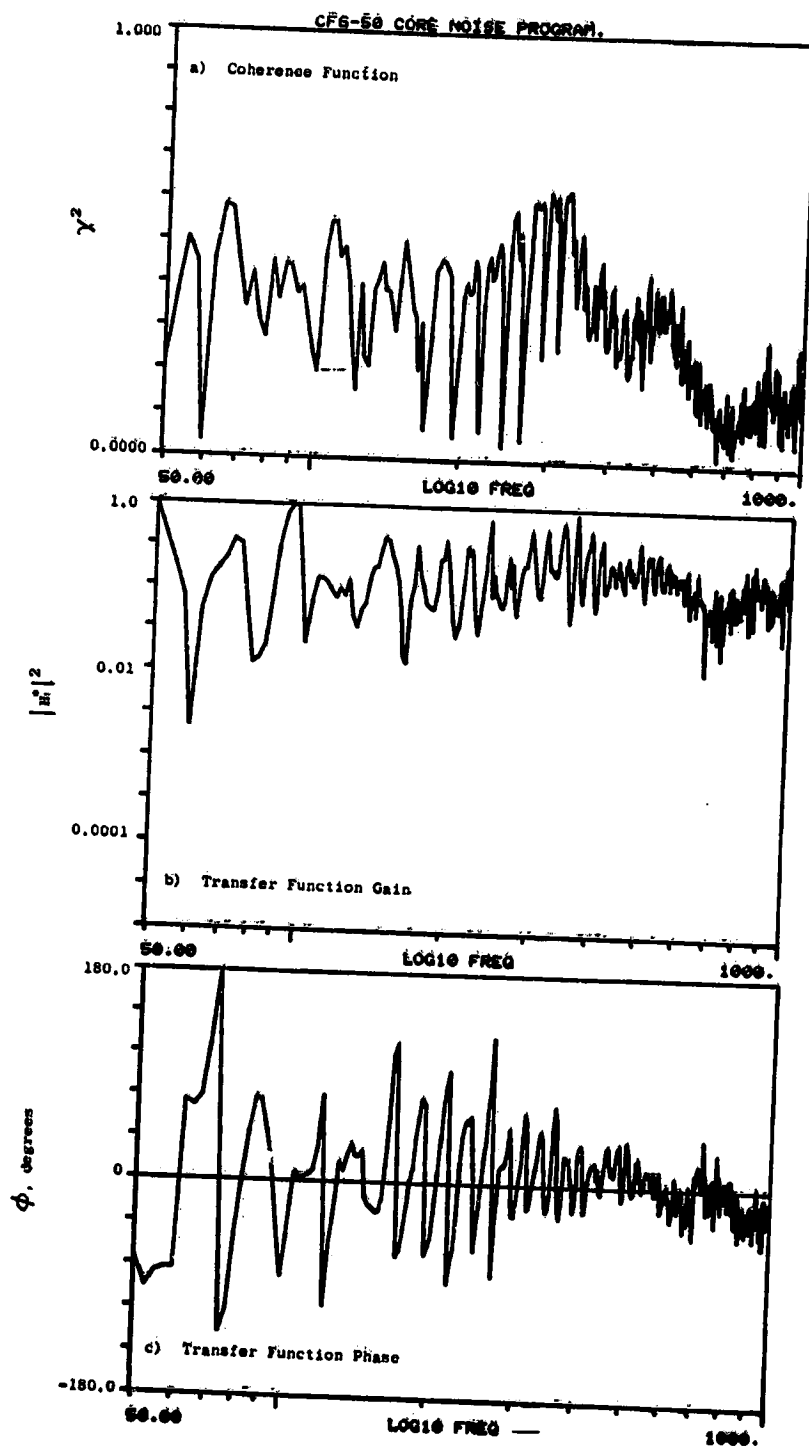


Figure A-8. Coherence and Transfer Functions for Plane 3.5 (102°) to Plane 4.0 (92°) at 15.0% Thrust.

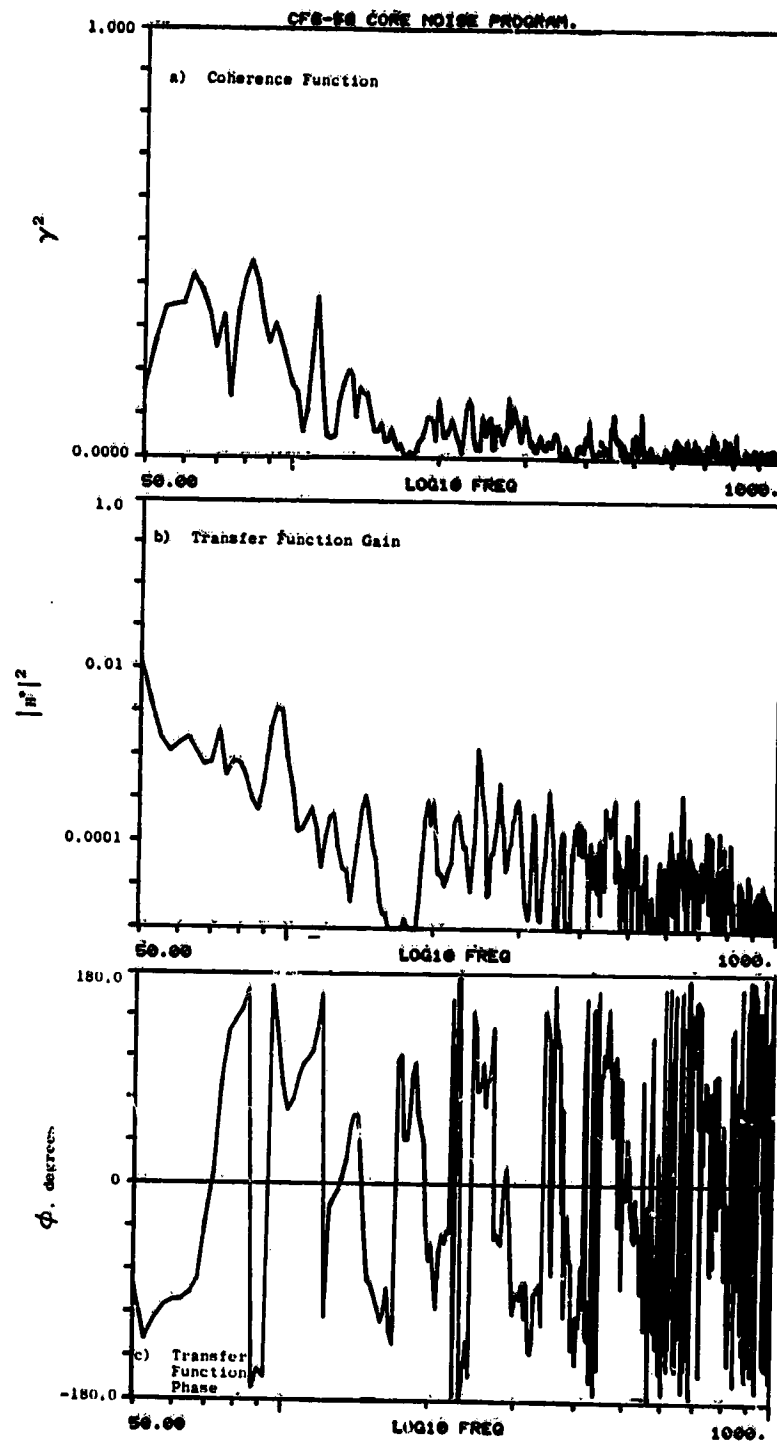


Figure A-9. Coherence and Transfer Functions for Plane 3.5 (282°) to Plane 8.0A (270°) at 15.0% Thrust.

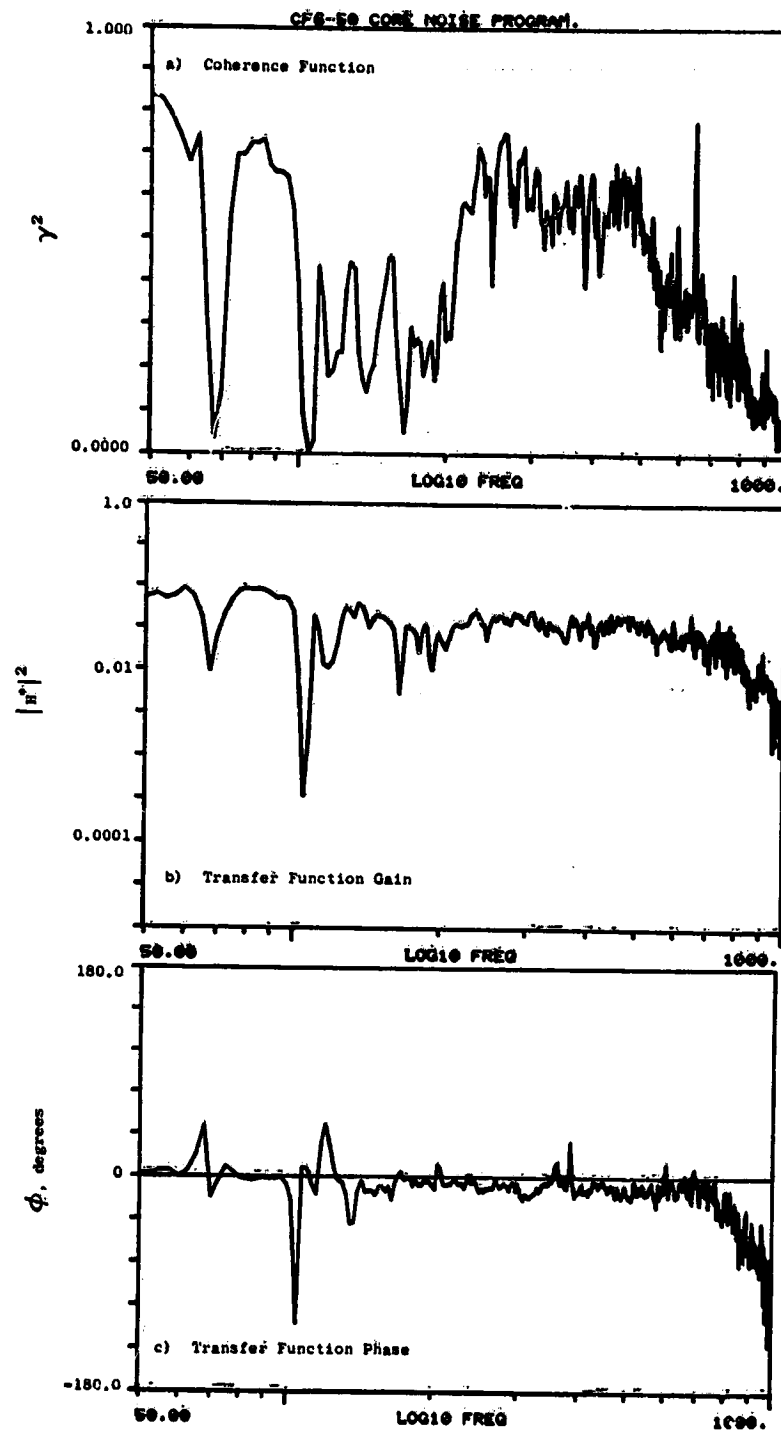


Figure A-10. Coherence and Transfer Functions for Plane 8.0A to Plane 8.0B (270°) at 15.0% Thrust.

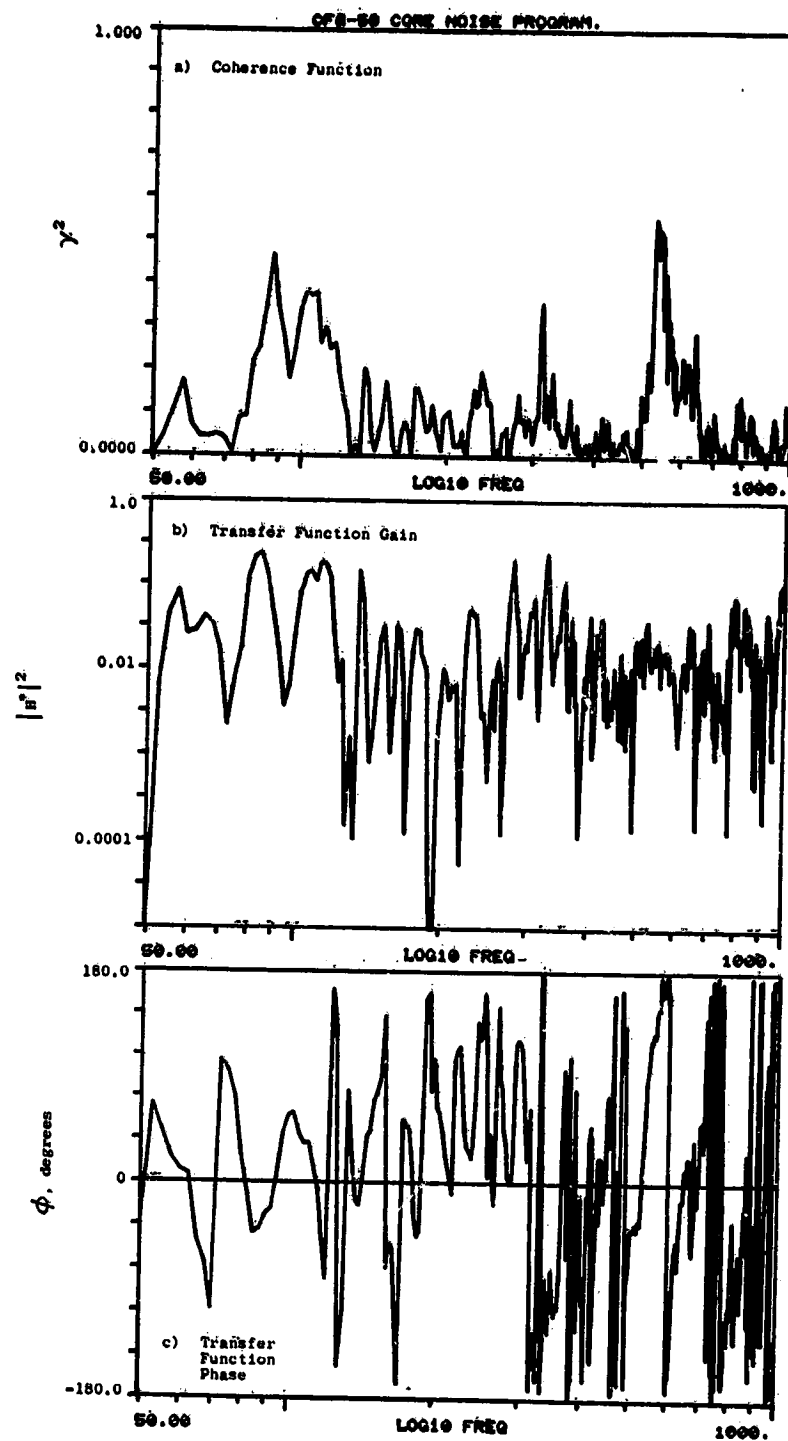


Figure A-11. Coherence and Transfer Functions for Fuel Nozzle (42°) to Plane 3.5 (42°) at 15.0% Thrust.

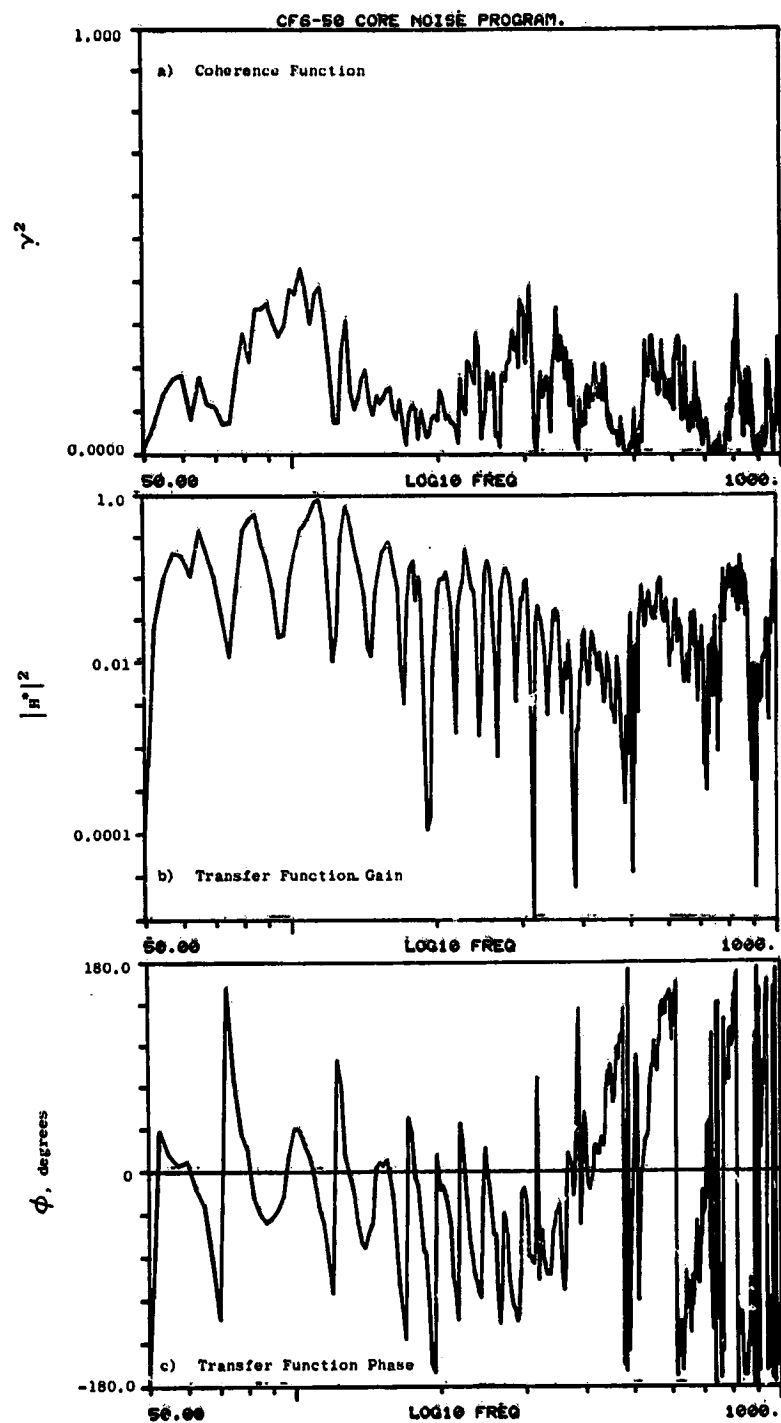


Figure A-12. Coherence and Transfer Functions for Fuel Nozzle (102°) to Plane 3.5 (102°) at 15.0% Thrust.

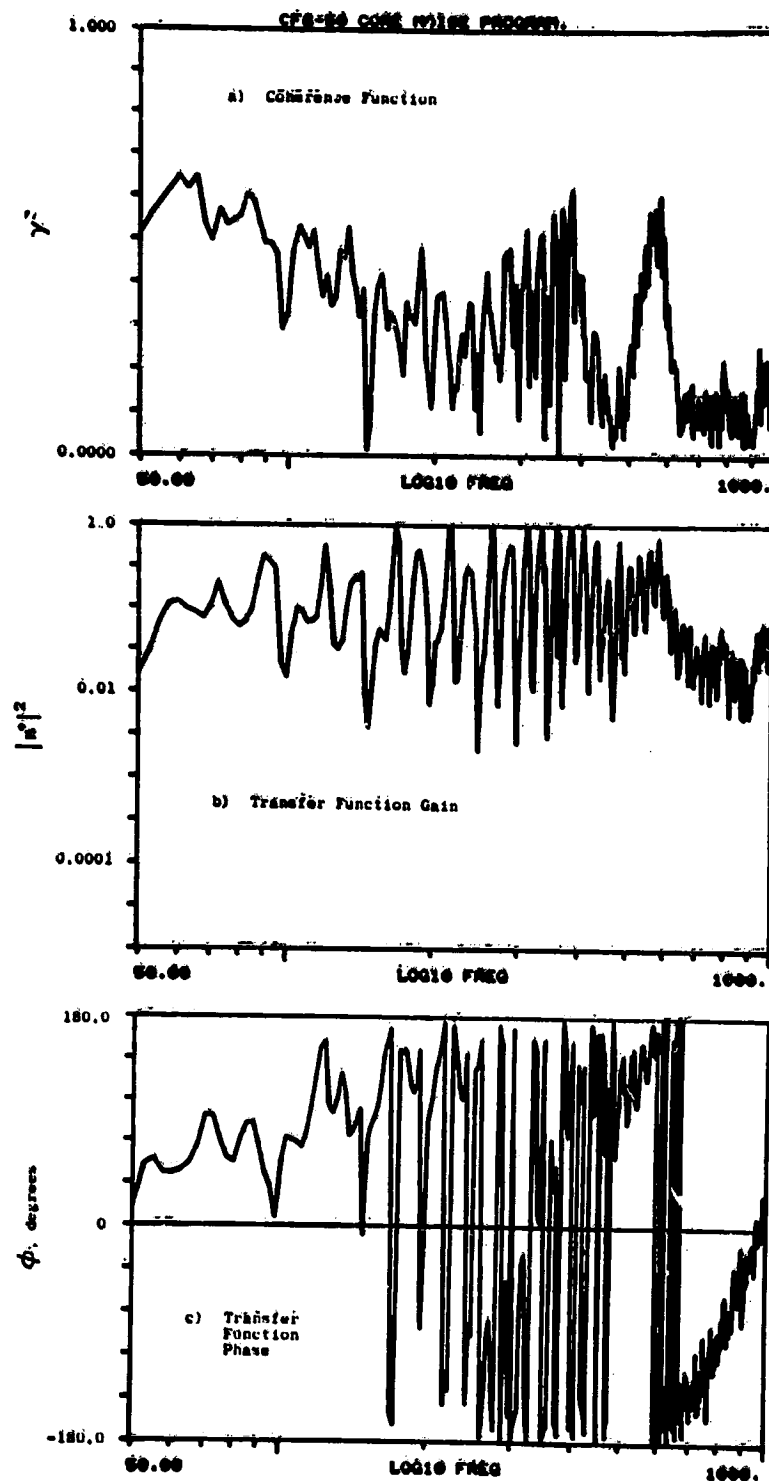


Figure A-13. Coherence and Transfer Functions for Plane 3.0 (16°) to Plane 3.5 (42°) at 22.8% Thrust.

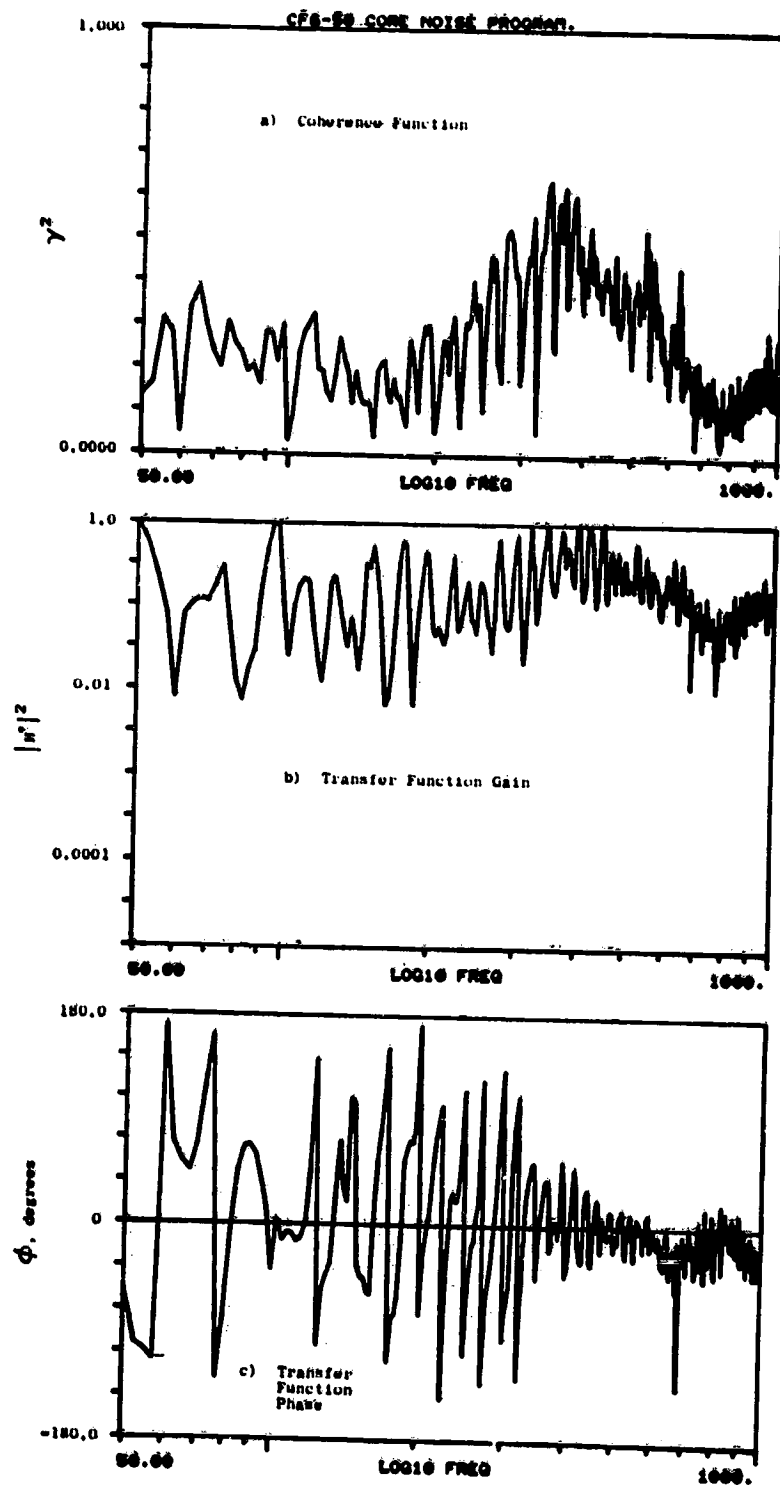


Figure A-14. Coherence and Transfer Functions for Plane 3.5 (102°) to Plane 4.0 (92°) at 22.8% Thrust.

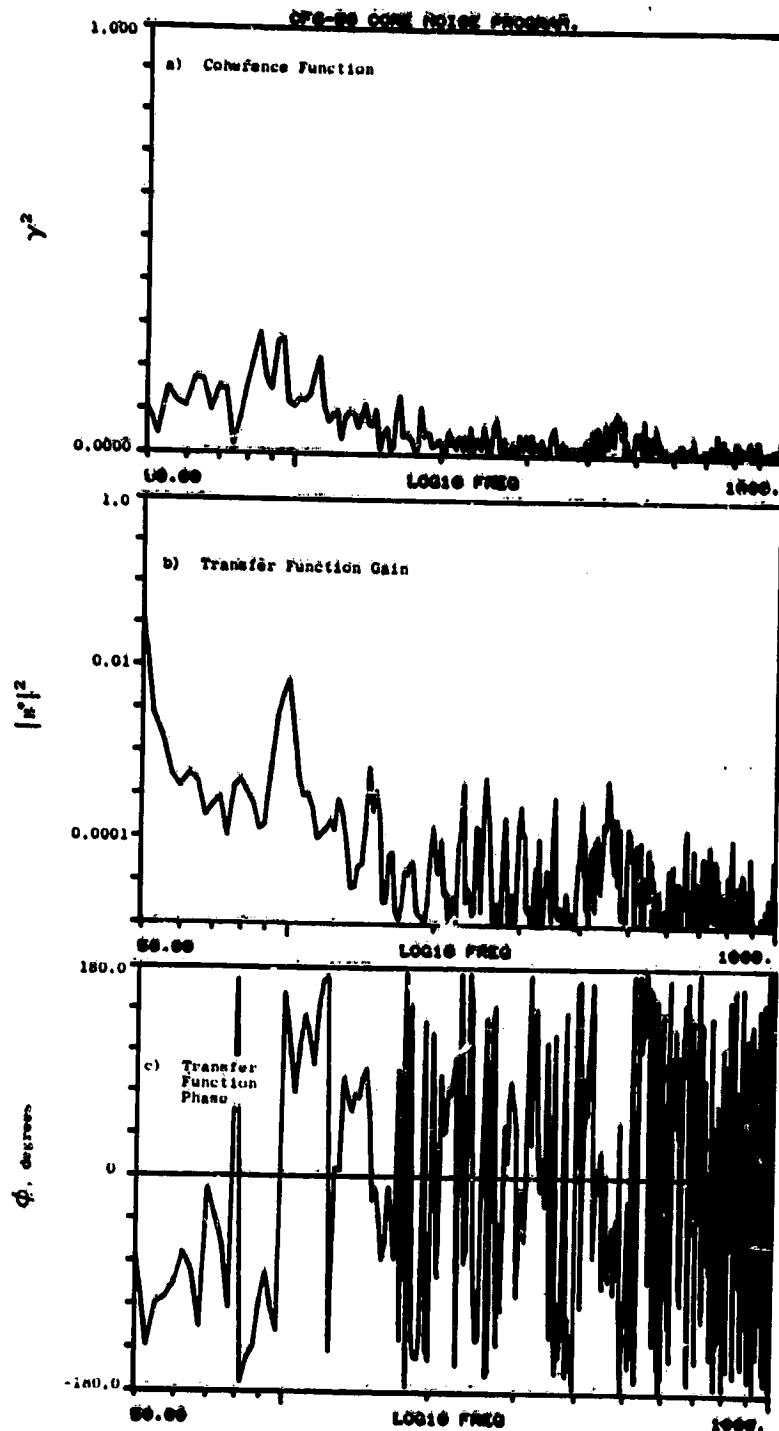


Figure A-15. Coherence and Transfer Functions for Plane 3.5 (282°) to Plane 8.0A (270°) at 22.8% Thrust.

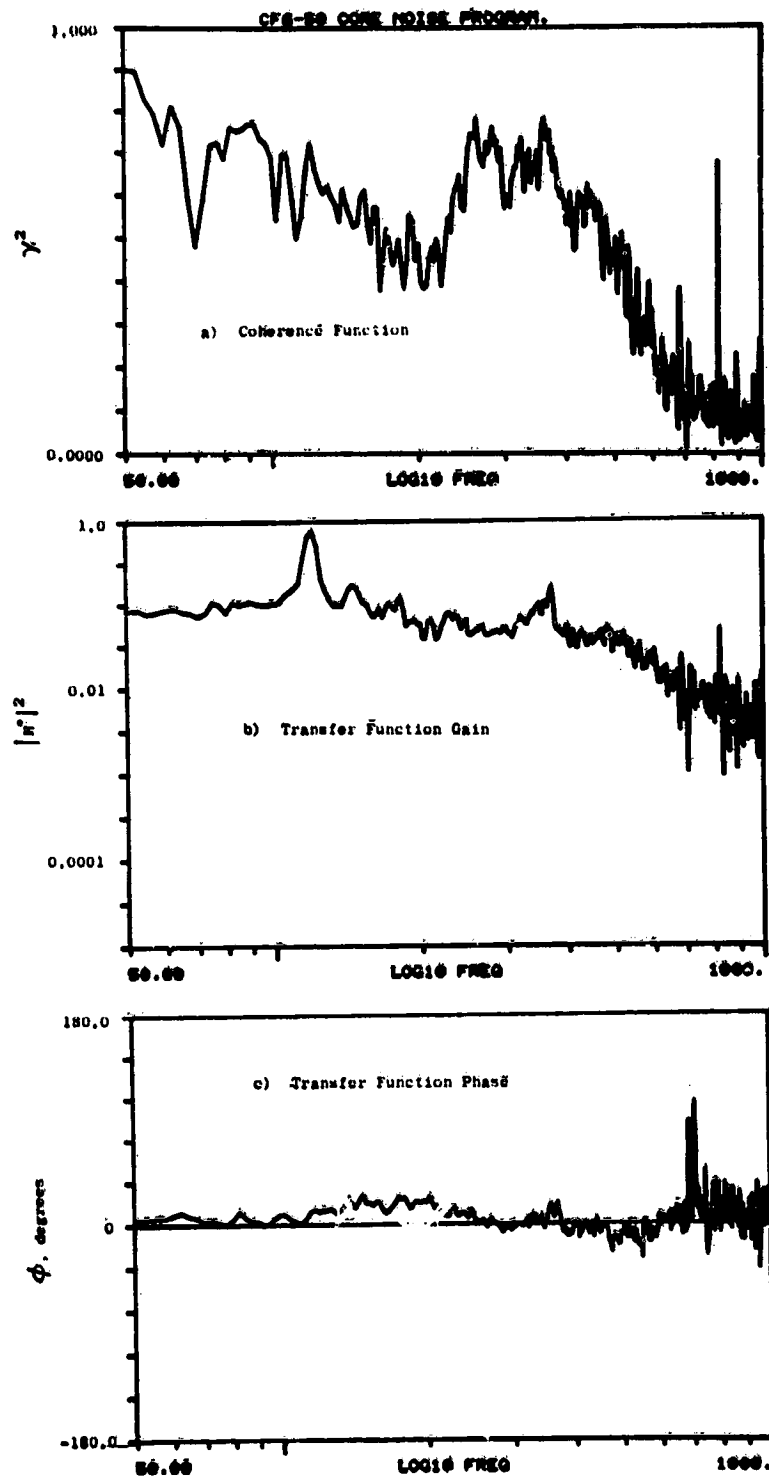


Figure A-16. Coherence and Transfer Functions
for Plane 8.0A to Plane 8.0B
(270°) at 22.8% Thrust.

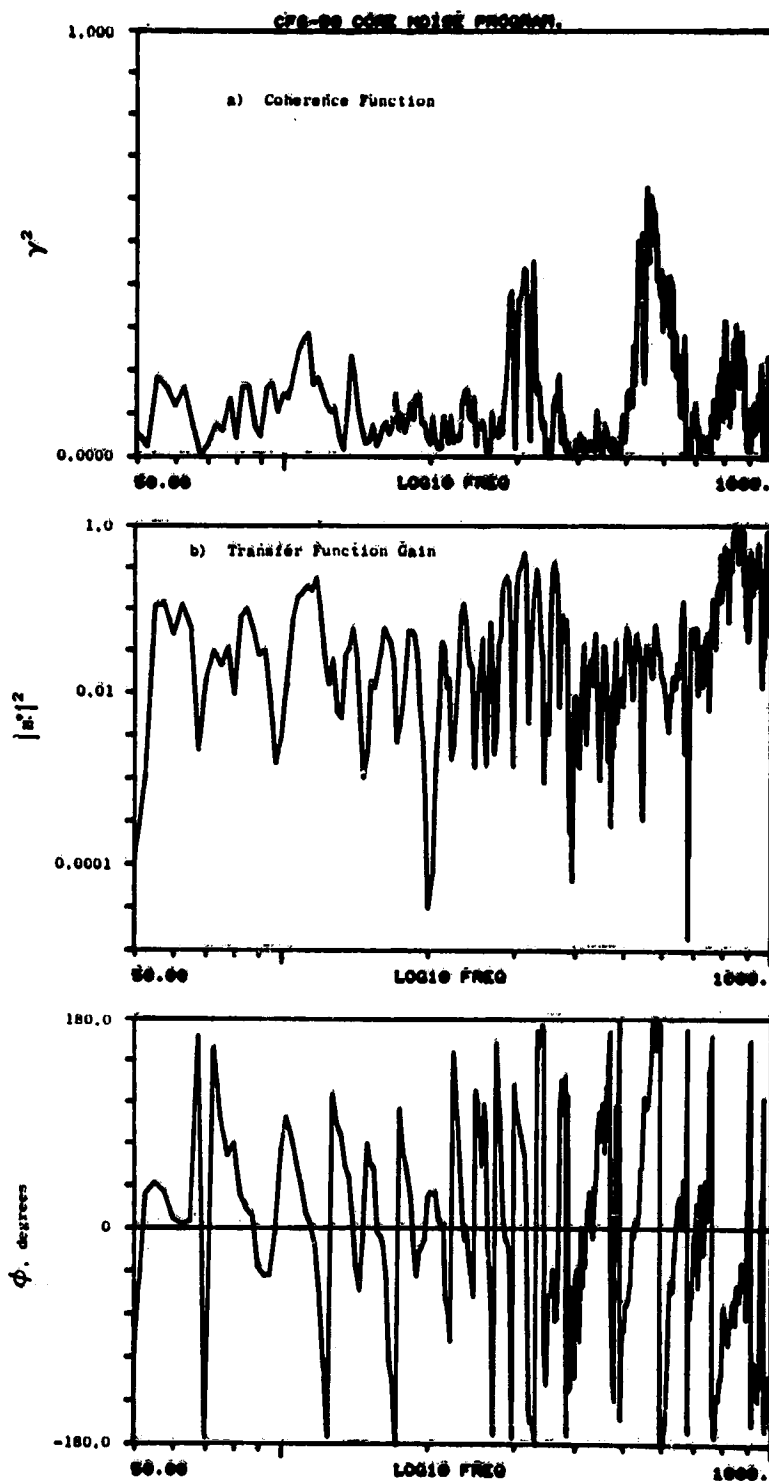


Figure A-17. Coherence and Transfer Functions for Fuel Nozzle (42°) to Plane 3.5 (42°) at 22.8% Thrust.

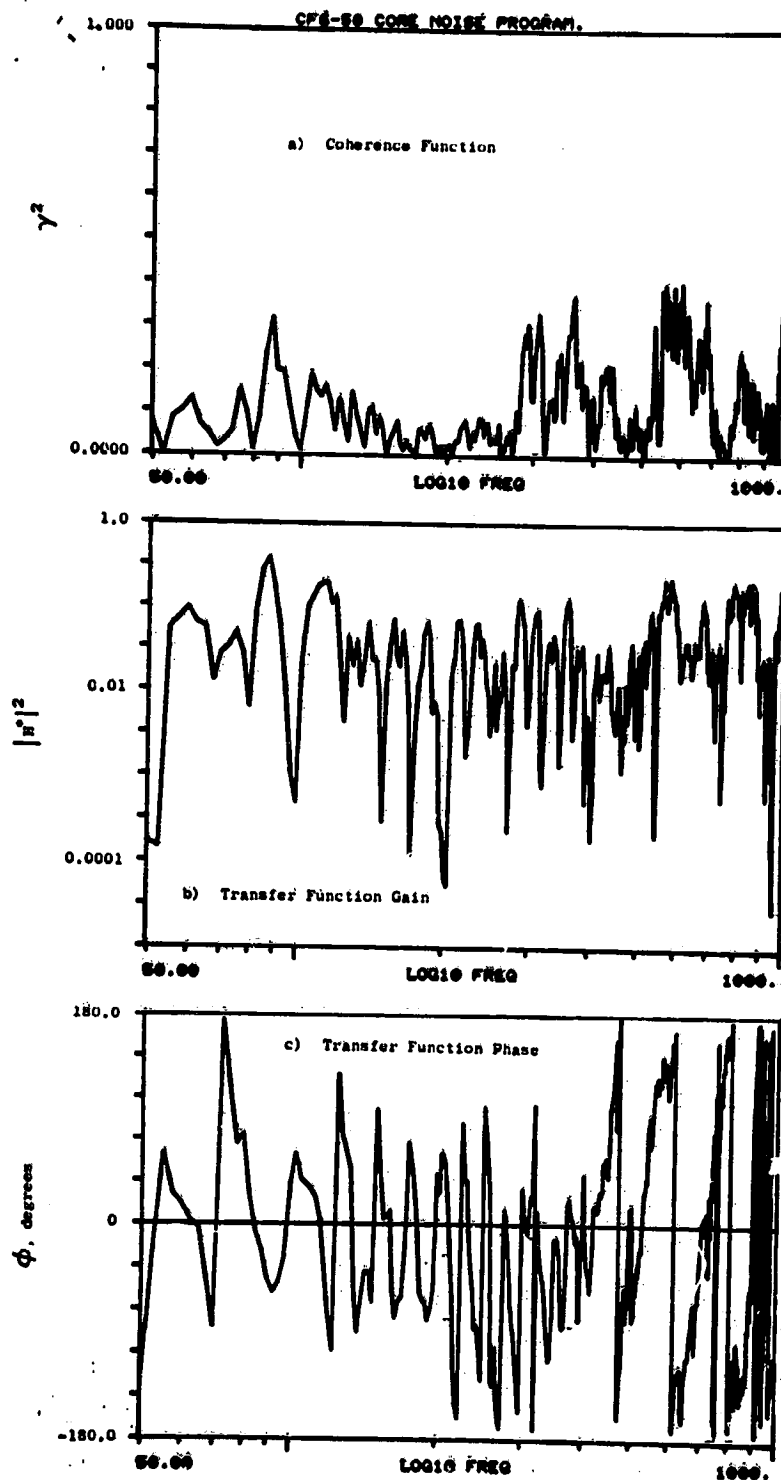


Figure A-18. Coherence and Transfer Functions for Fuel Nozzle (102°) to Plane 3.5 (102°) at 22.8% Thrust.

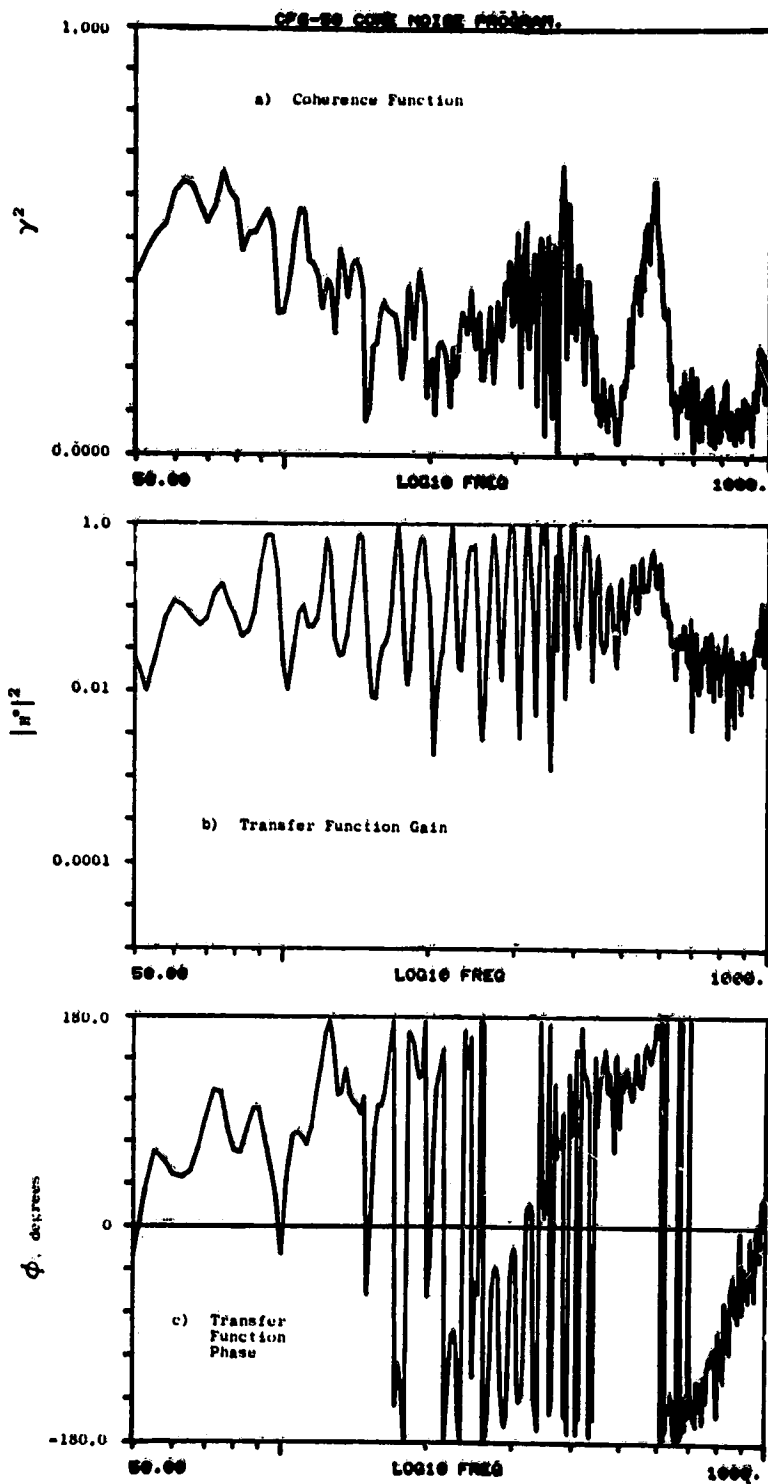


Figure A-19. Coherence and Transfer Functions for Plane 3.0 (16°) to Plane 3.5 (42°) at 26.7% Thrust.

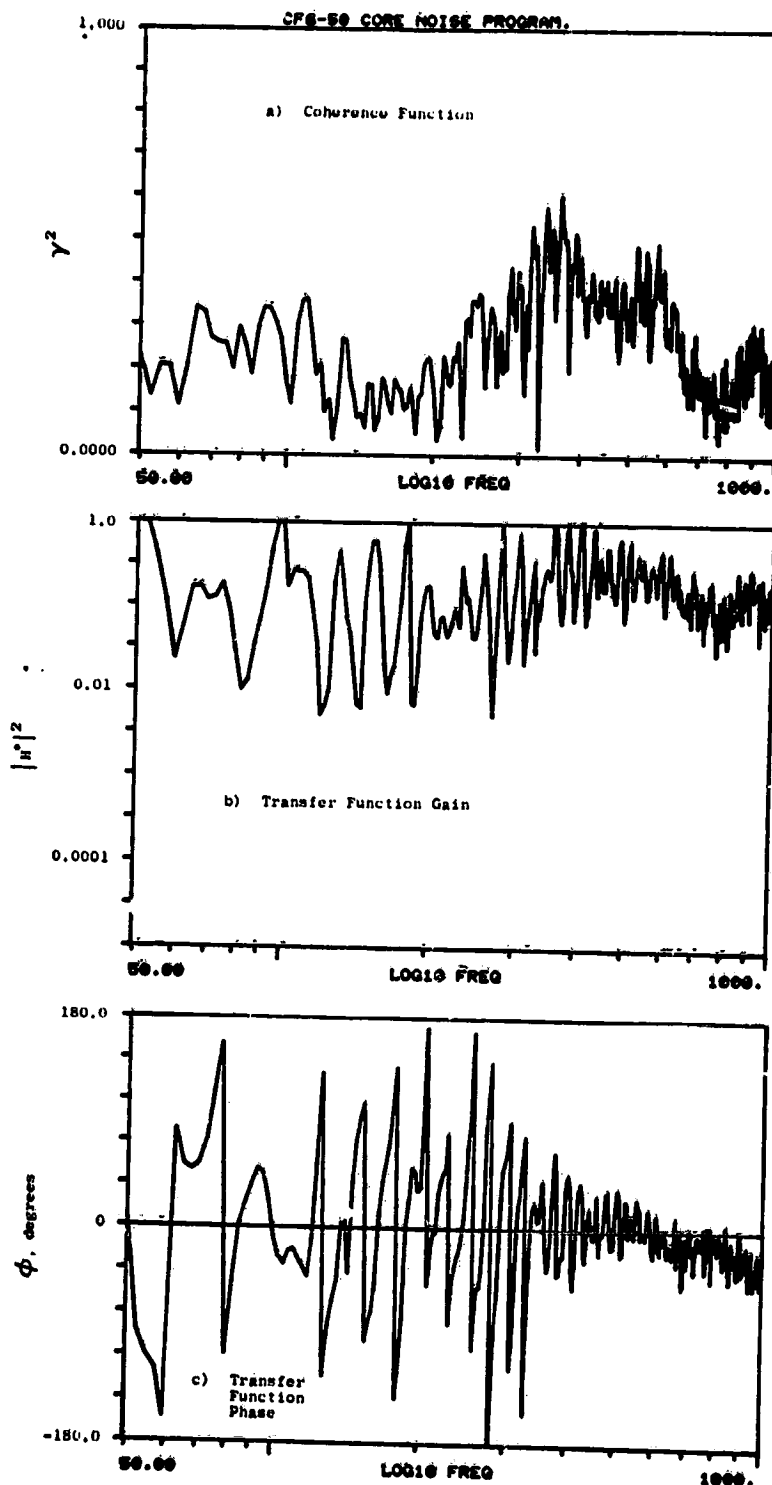


Figure A-20. Coherence and Transfer Functions for Plane 3.5 (102°) to Plane 4.0 (92°) at 26.7% Thrust.

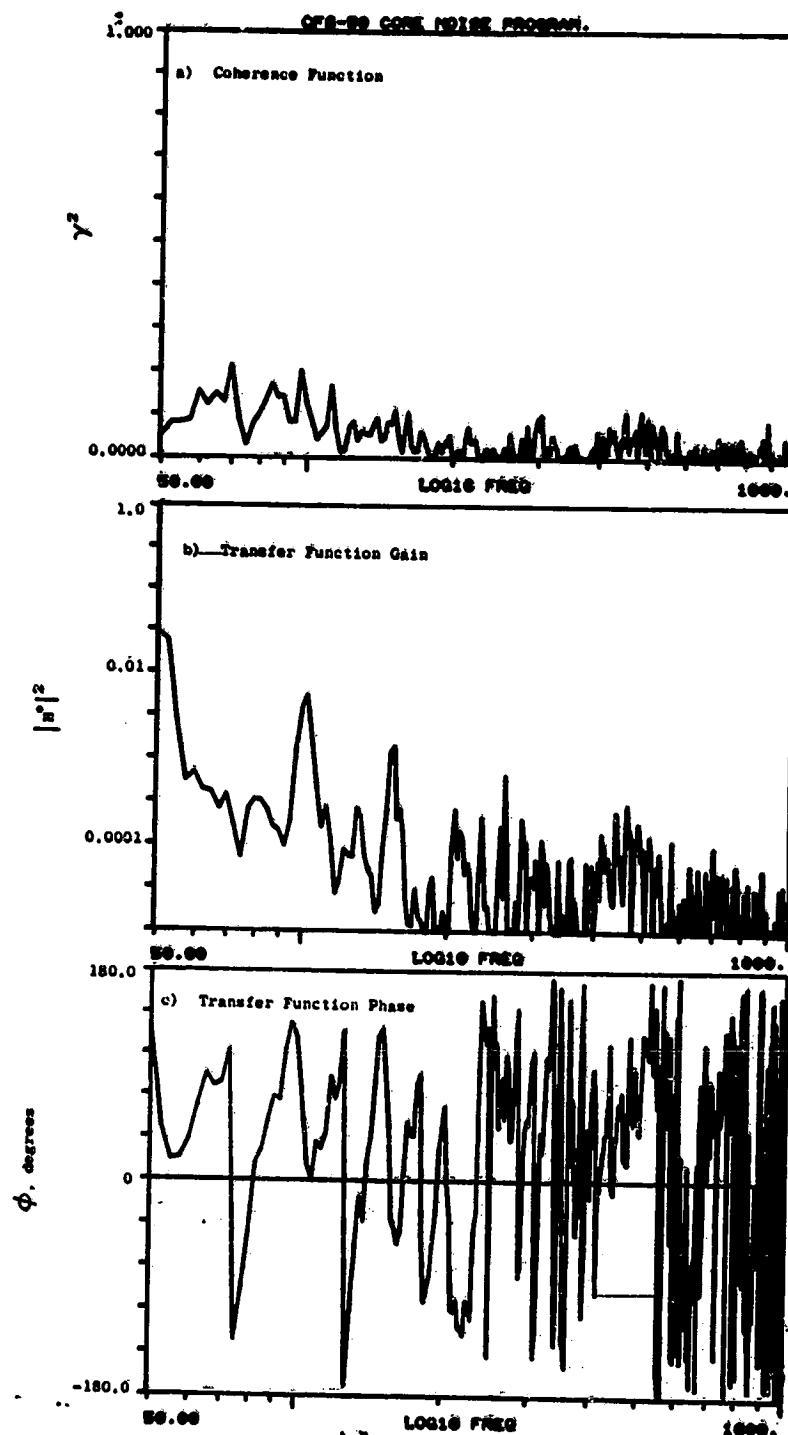


Figure A-21. Coherence and Transfer Functions for Plane 3.5 (282°) to Plane 8.0A (270°) at 26.7% Thrust.

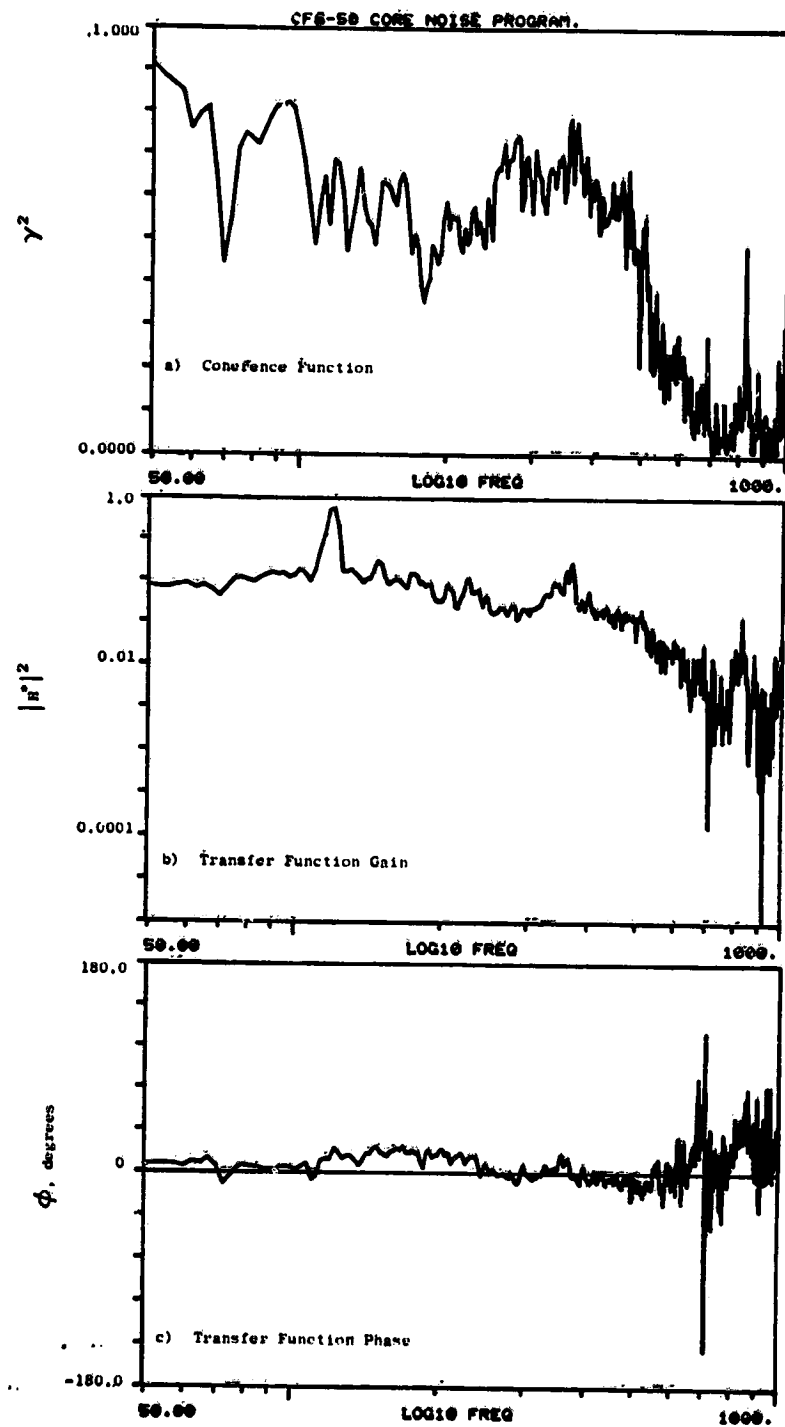


Figure A-22. Coherence and Transfer Functions
for Plane 8.0A to Plane 8.0B
(270°) at 26.7 Thrust.

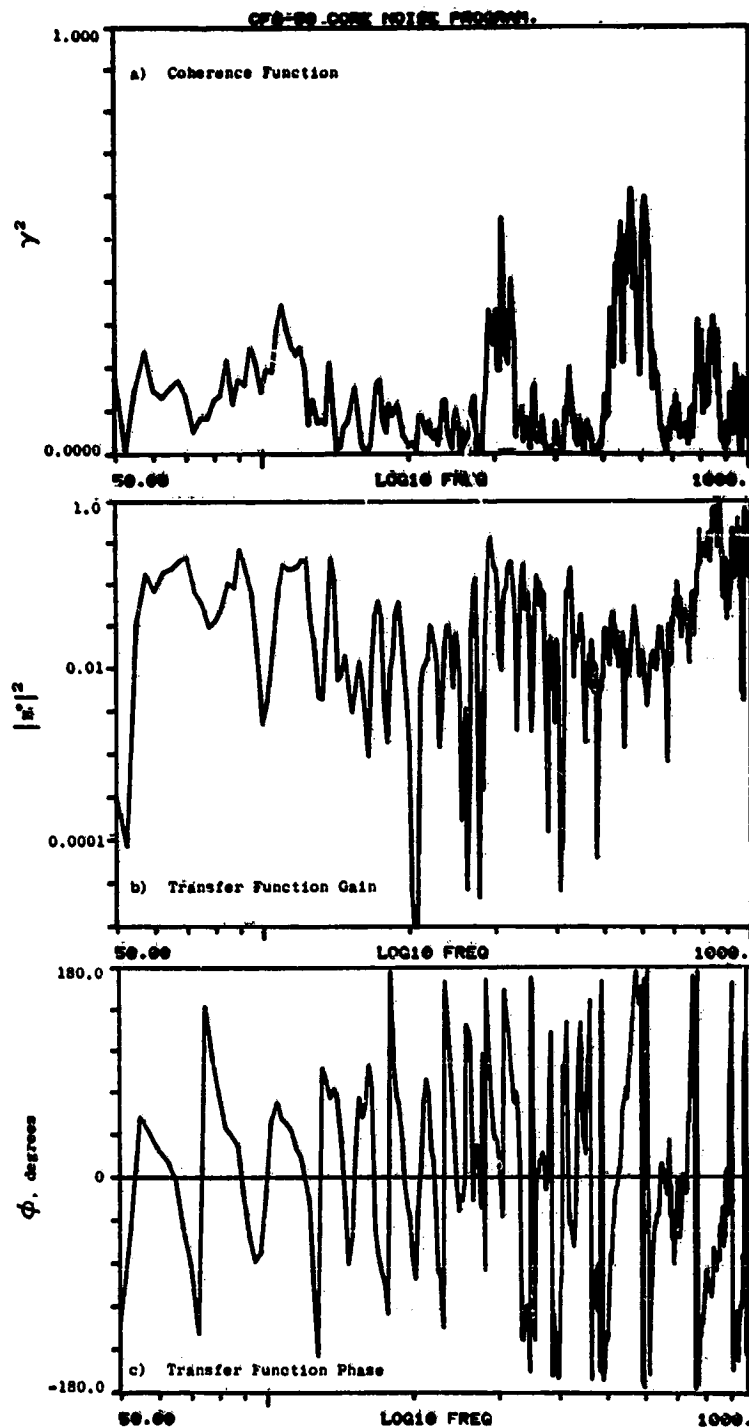


Figure A-23. Coherence and Transfer Functions for Fuel Nozzle (42°) to Plane 3.5 (42°) at 26.7% Thrust.

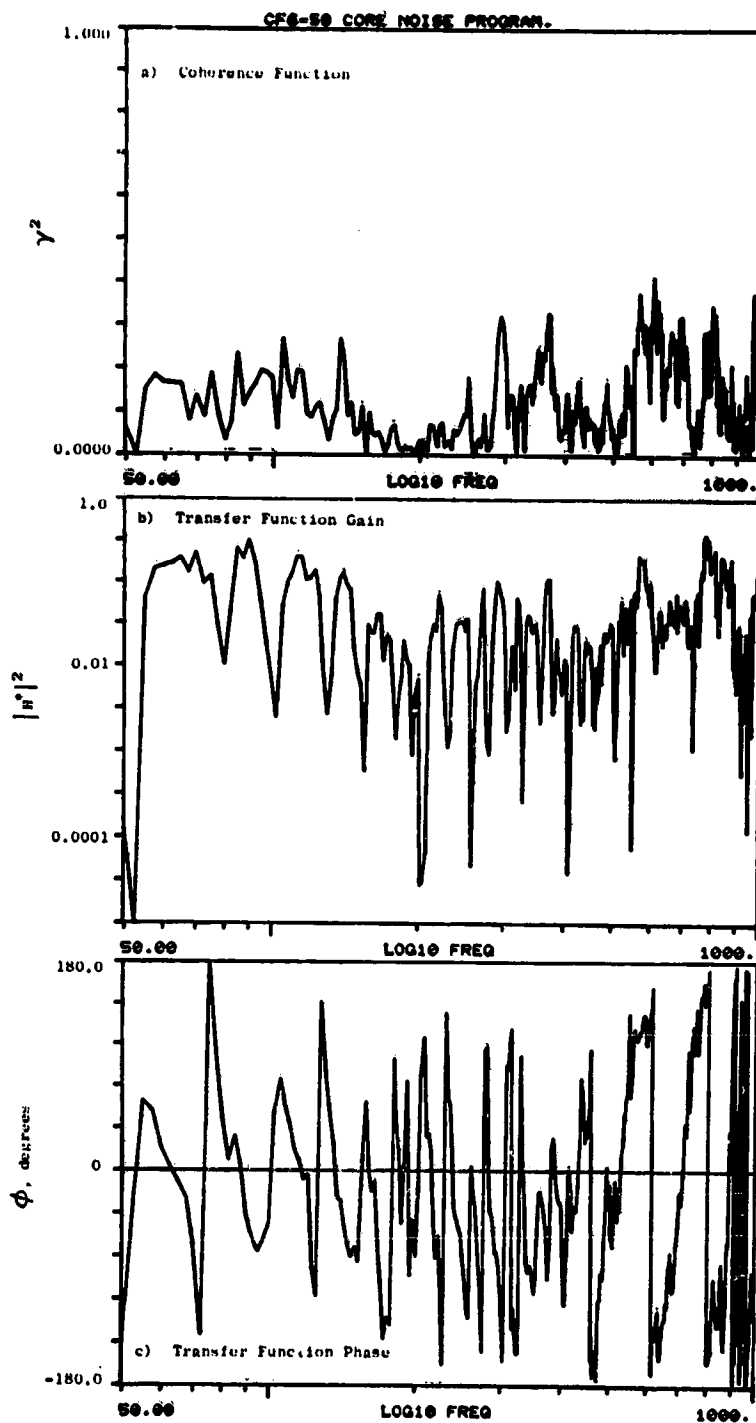


Figure A-24. Coherence and Transfer Functions for Fuel Nozzle (102°) to Plane 3.5 (102°) at 26.7% Thrust.

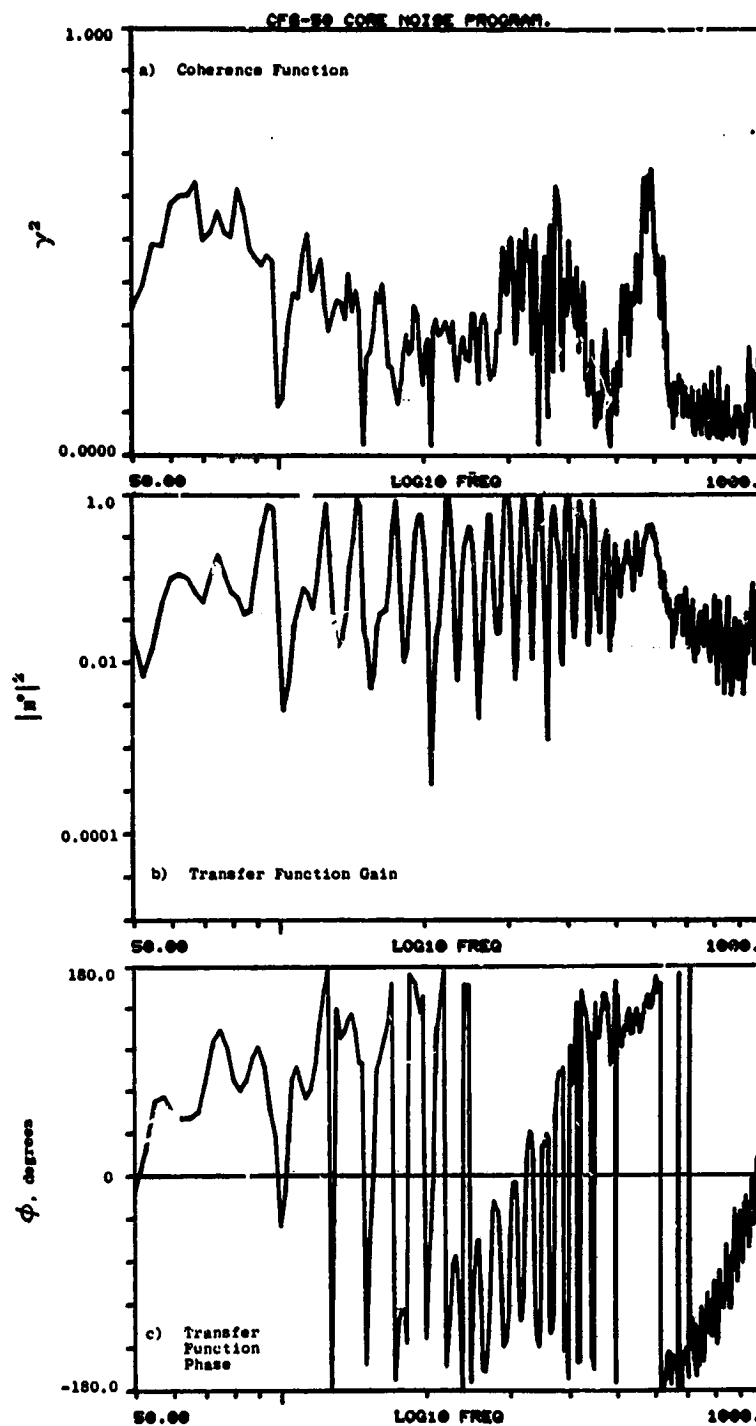


Figure A-25. Coherence and Transfer Functions for Plane 3.0 (16°) to Plane 3.5 (42°) at 30.8% Thrust.

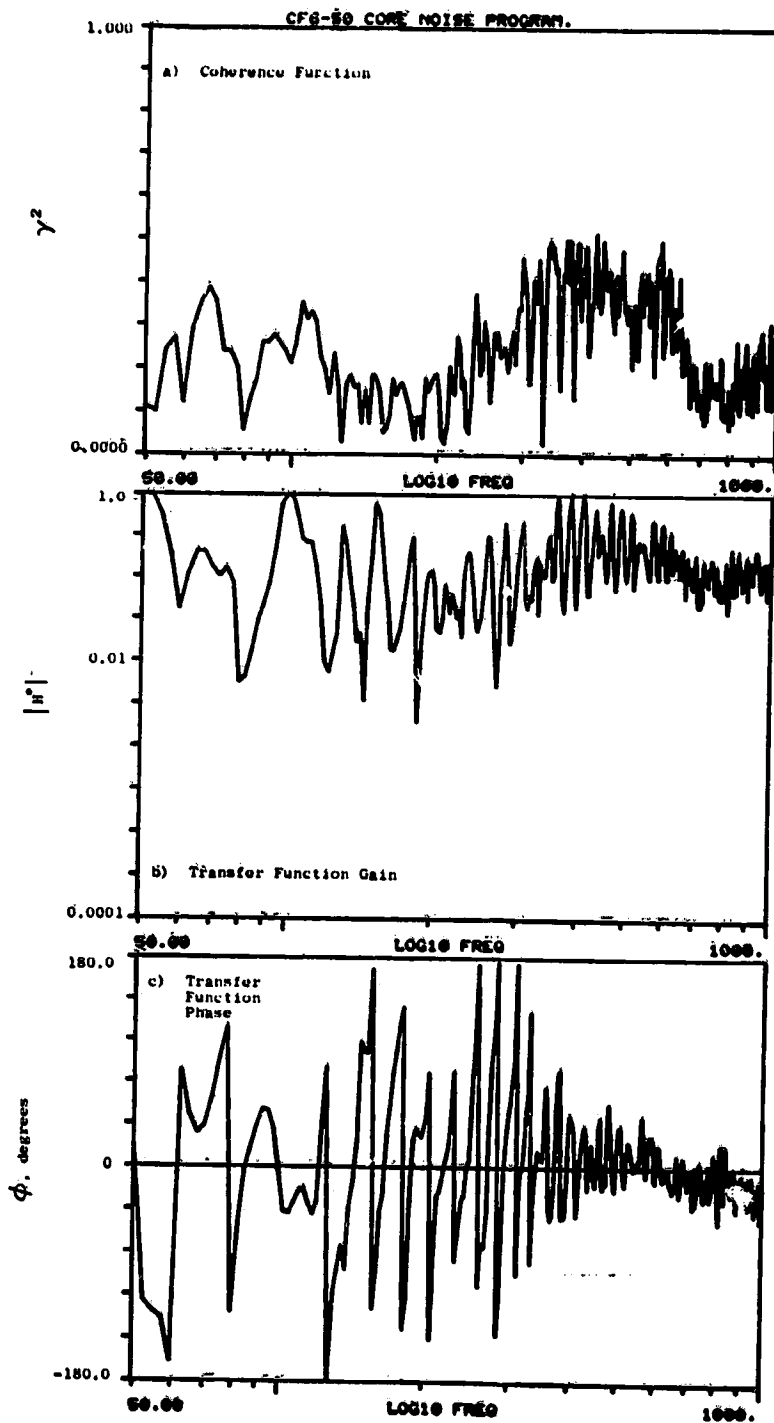


Figure A-26. Coherence and Transfer Functions for Plane 3.5 (102°) to Plane 4.0 (92°) at 30.8% Thrust.

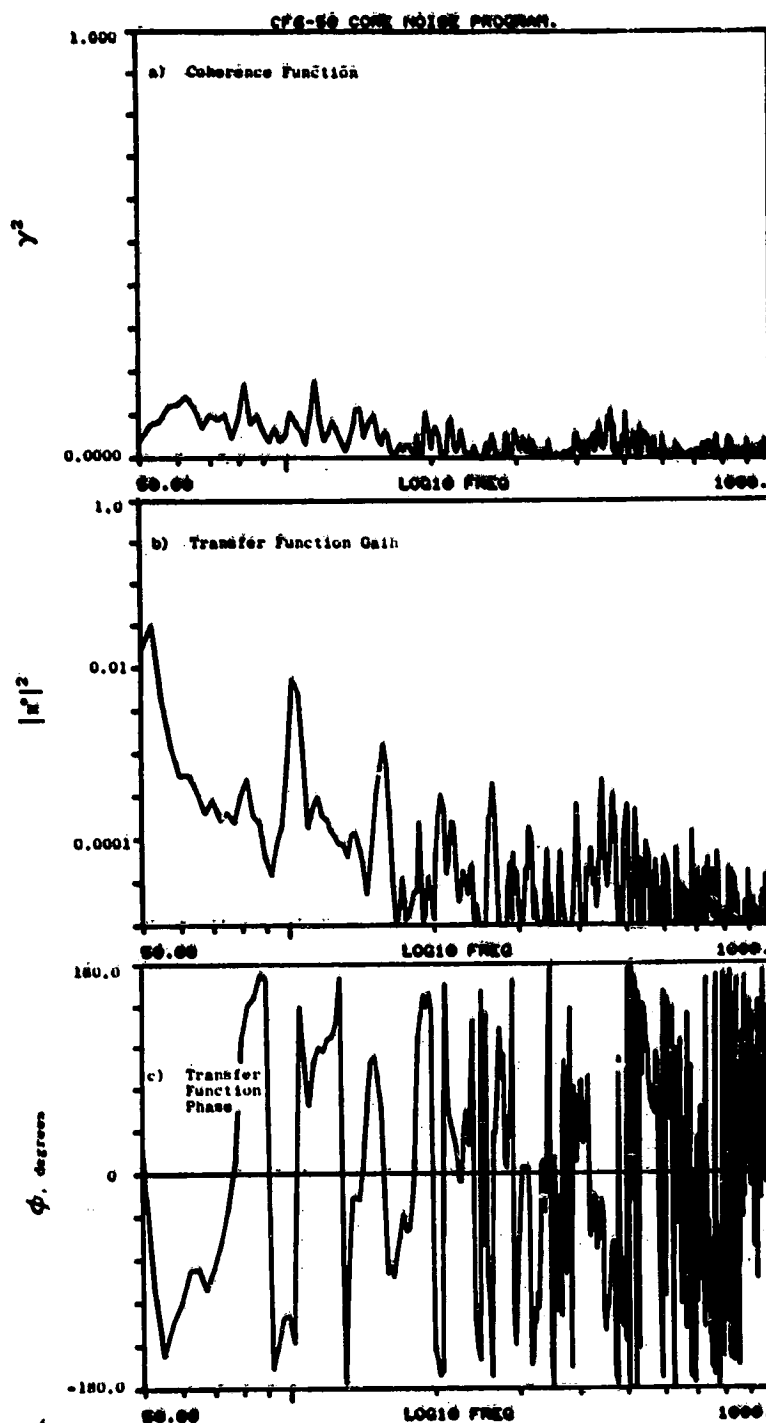


Figure A-27. Coherence and Transfer Functions for Plane 3.5 (282°) to Plane 8.0A (270°) at 30.8% Thrust.

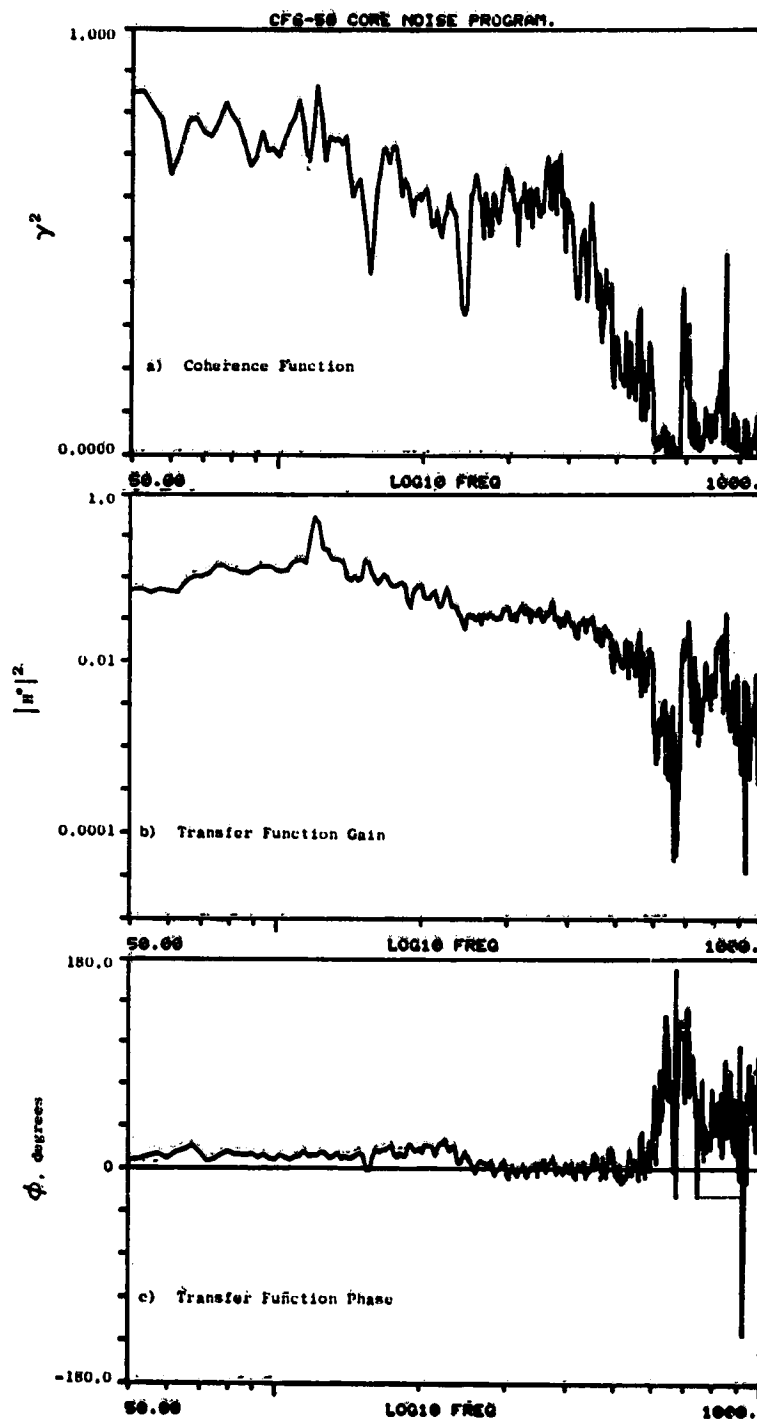


Figure A-28. Coherence and Transfer Functions for Plane 8.0A to Plane 8.0B (270°) at 30.8% Thrust.

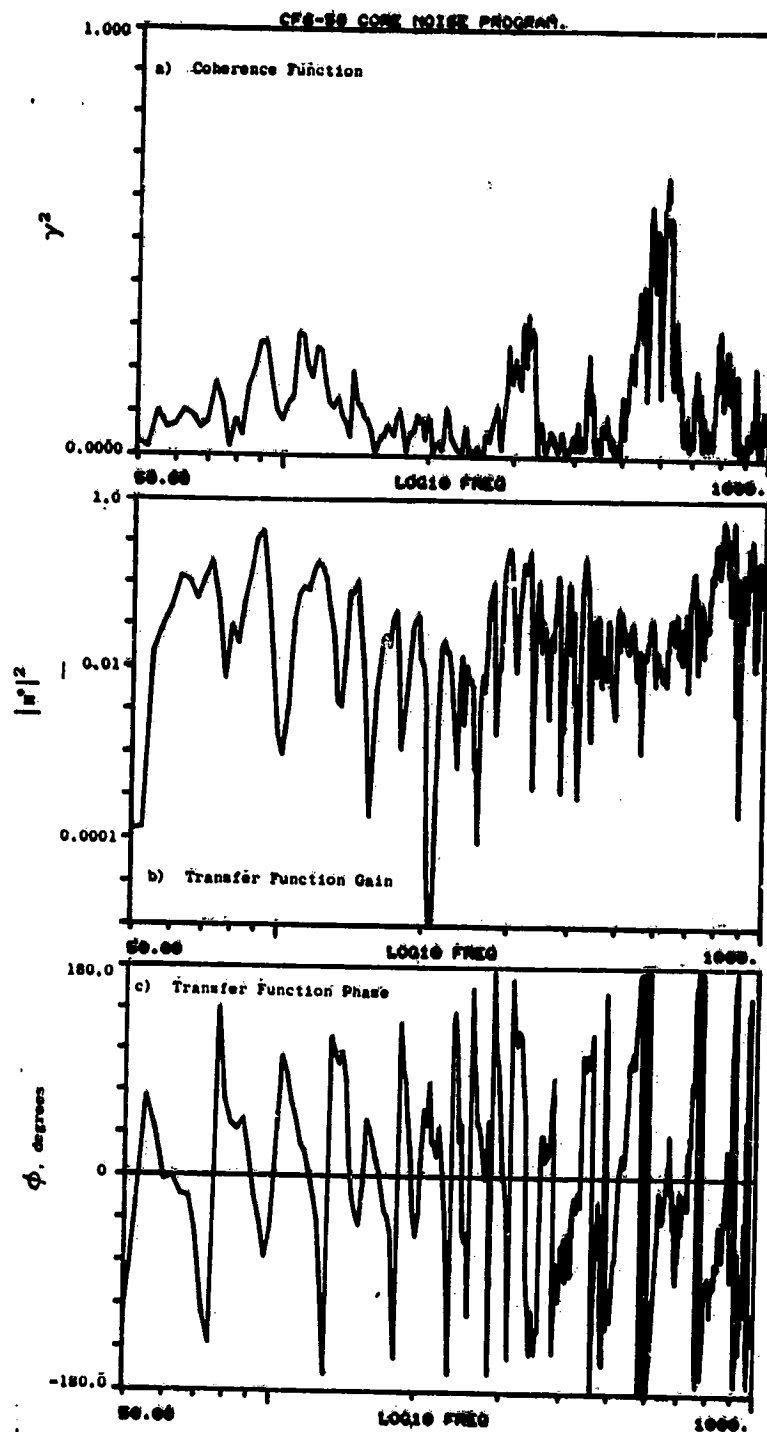


Figure A-29. Coherence and Transfer Functions for Fuel Nozzle (42°) to Plane 3.5 (42°) at 30.8% Thrust.

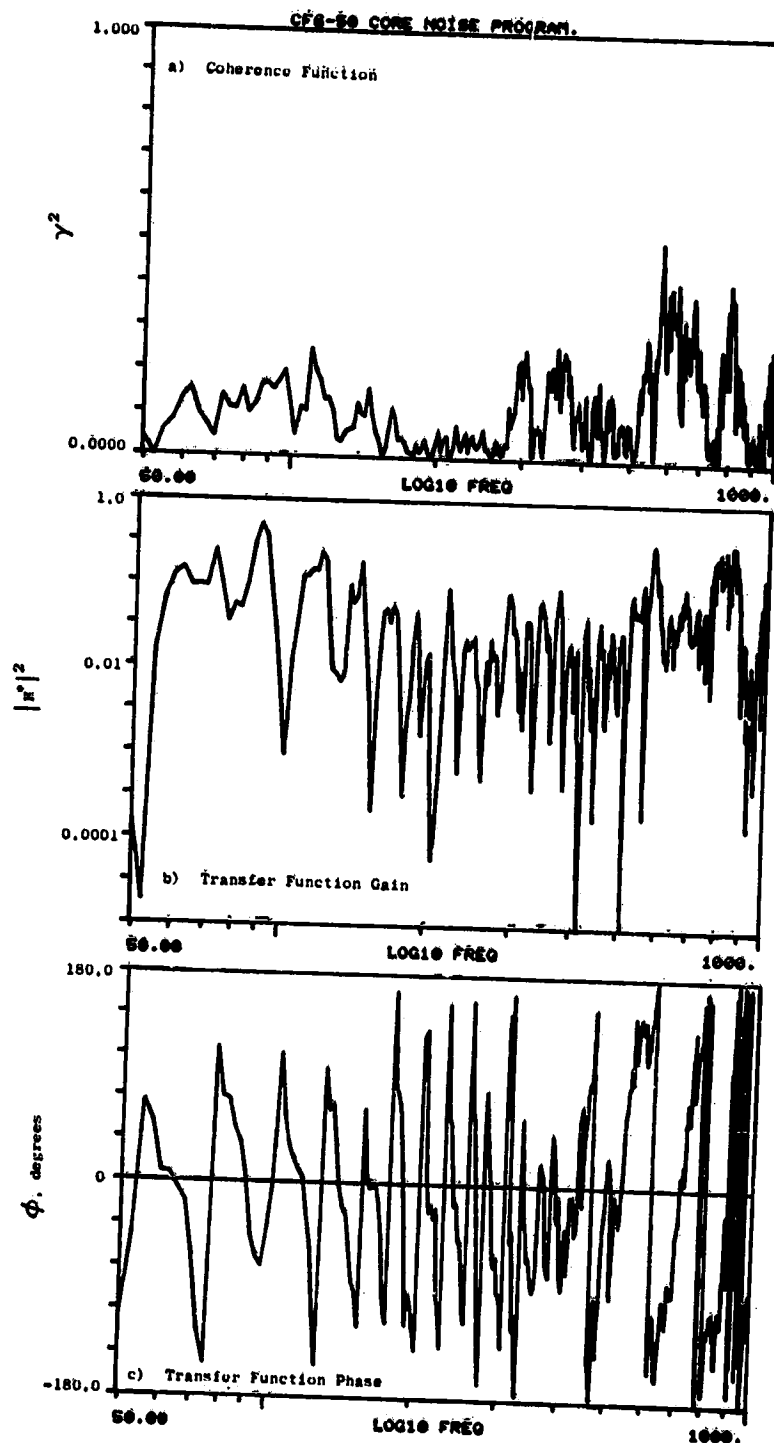


Figure A-30. Coherence and Transfer Functions for Fuel Nozzle (102°) to Plane 3.5 (102°) at 30.8% Thrust.

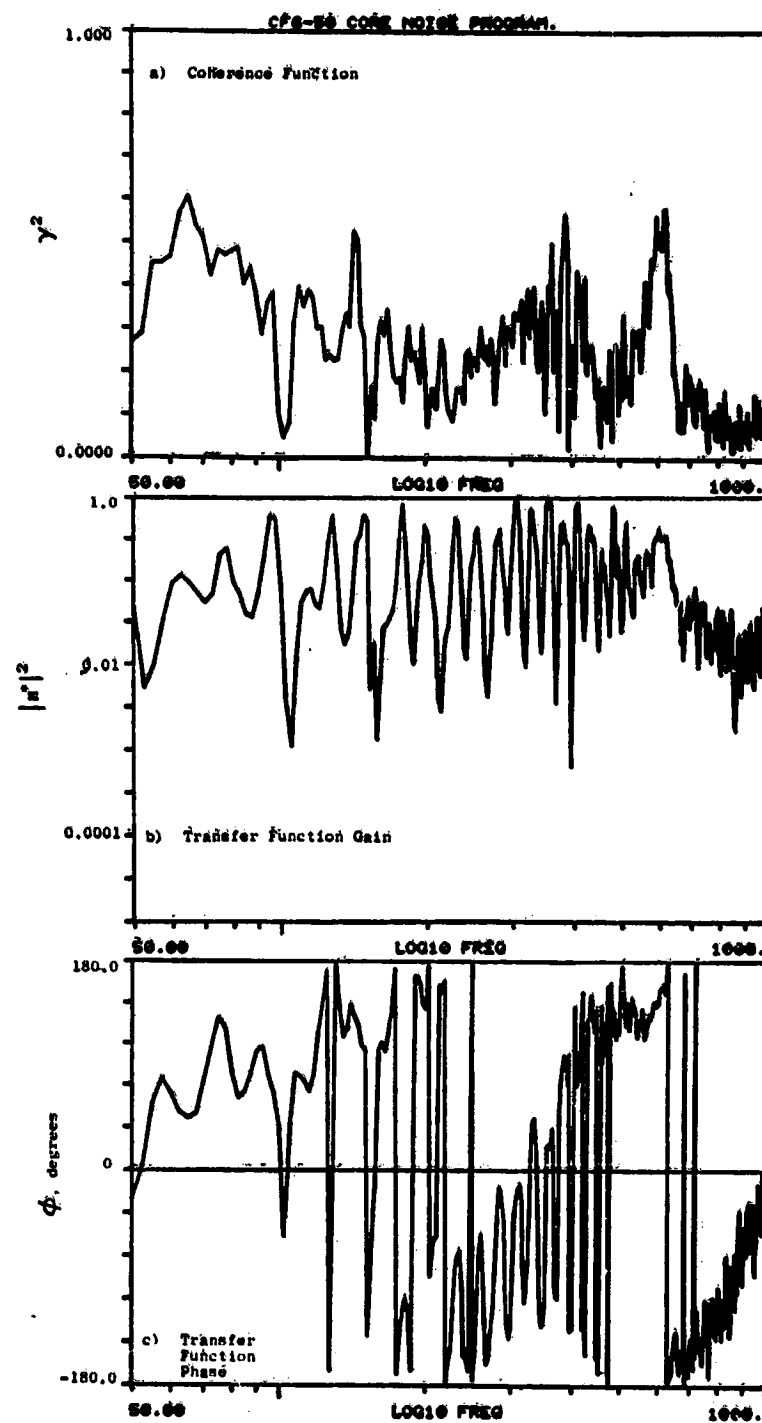


Figure A-31. Coherence and Transfer Functions for Plane 3.0 (16°) to Plane 3.5 (42°) at 36.5% Thrust.

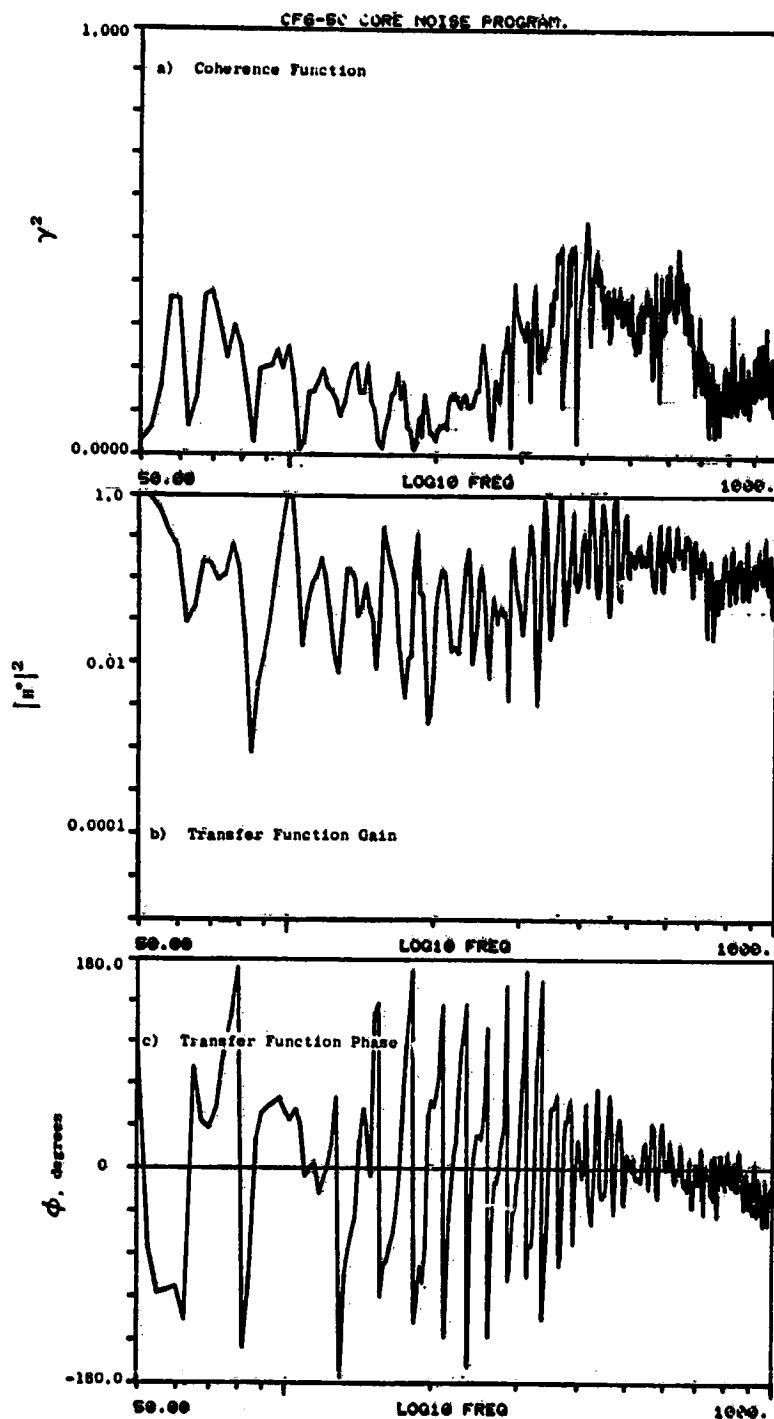


Figure A-32. Coherence and Transfer Functions for Plane 3.5 (102°) to Plane 4.0 (92°) at 36.5% Thrust.

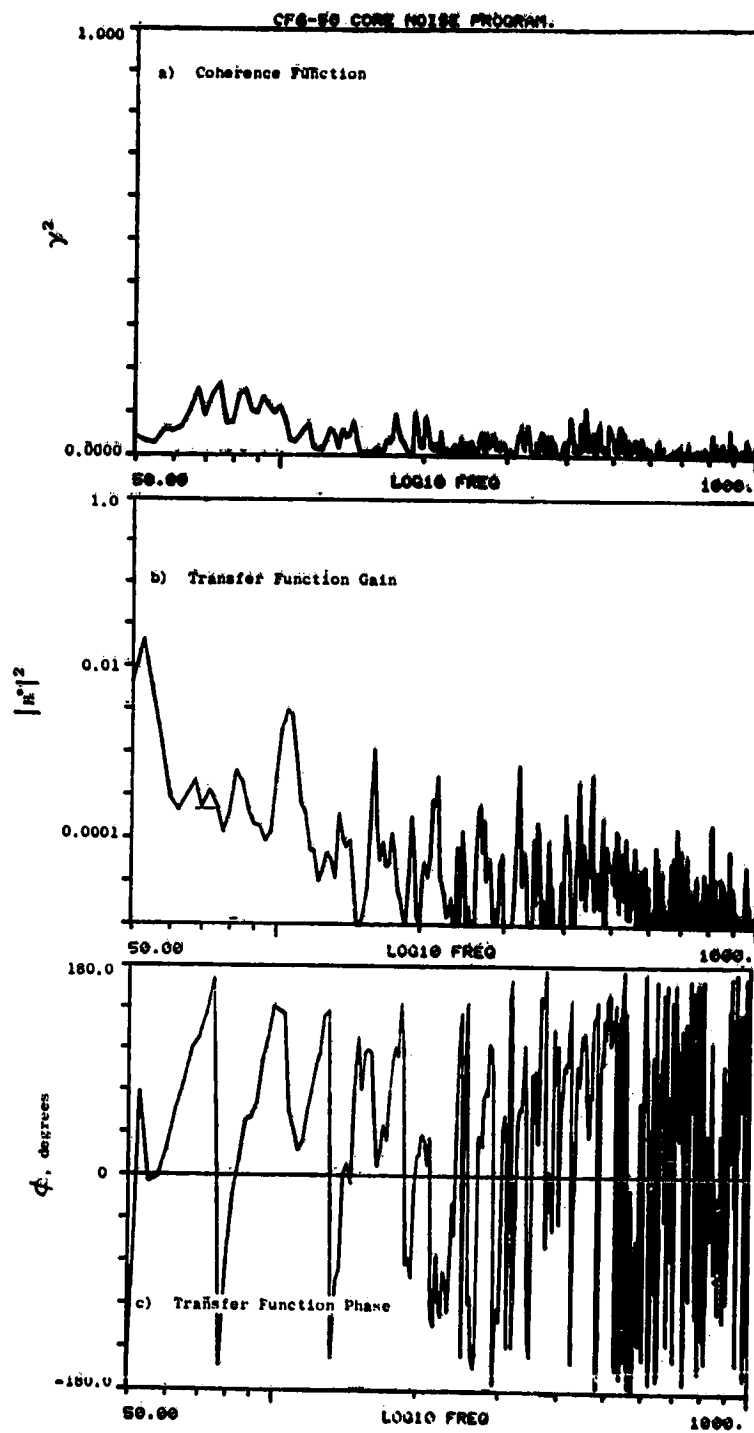


Figure A-33. Coherence and Transfer Functions for Plane 3.5 (282°) to Plane 8.0A (270°) at 36.5% Thrust.

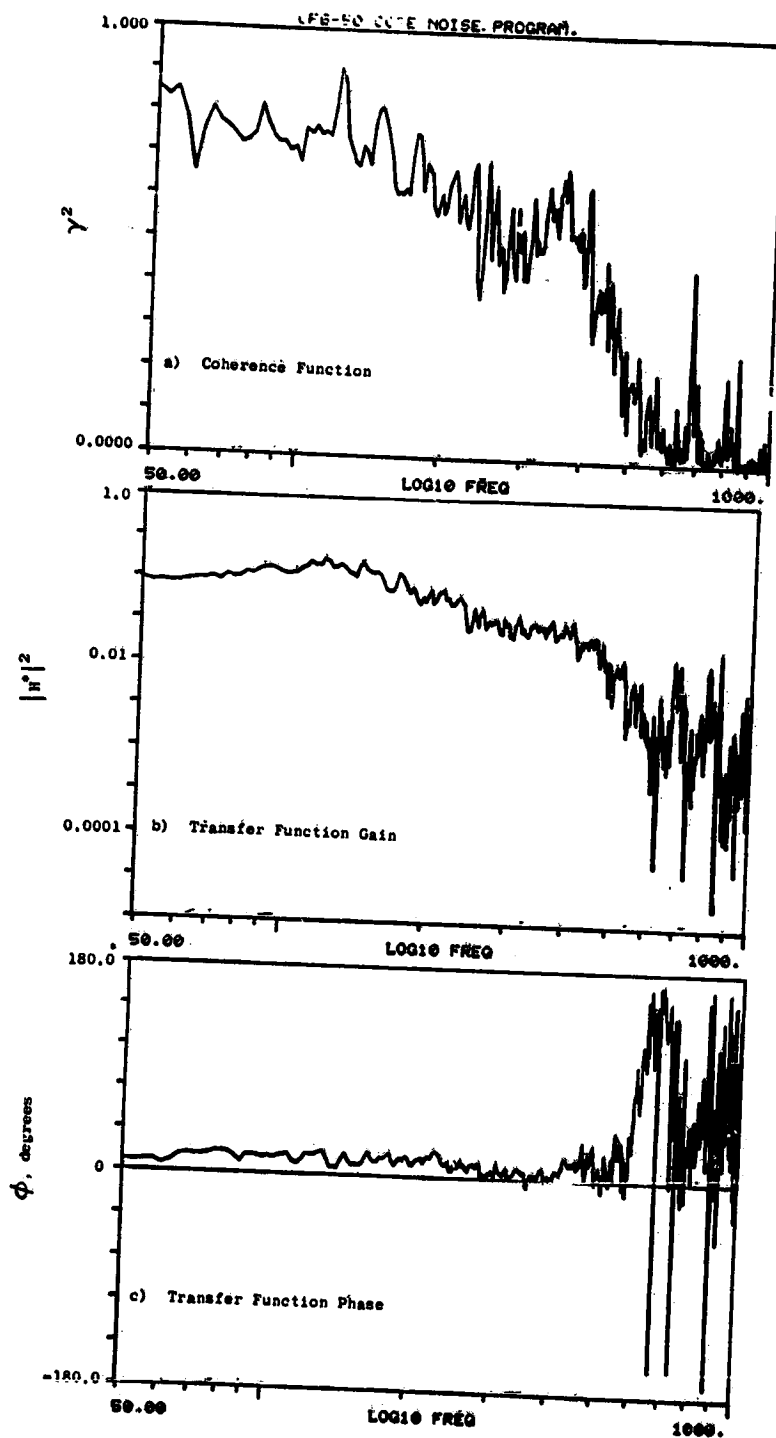


Figure A-34. Coherence and Transfer Functions
for Plane 8.0A to Plane 8.0B
(270°) at 36.5% Thrust.

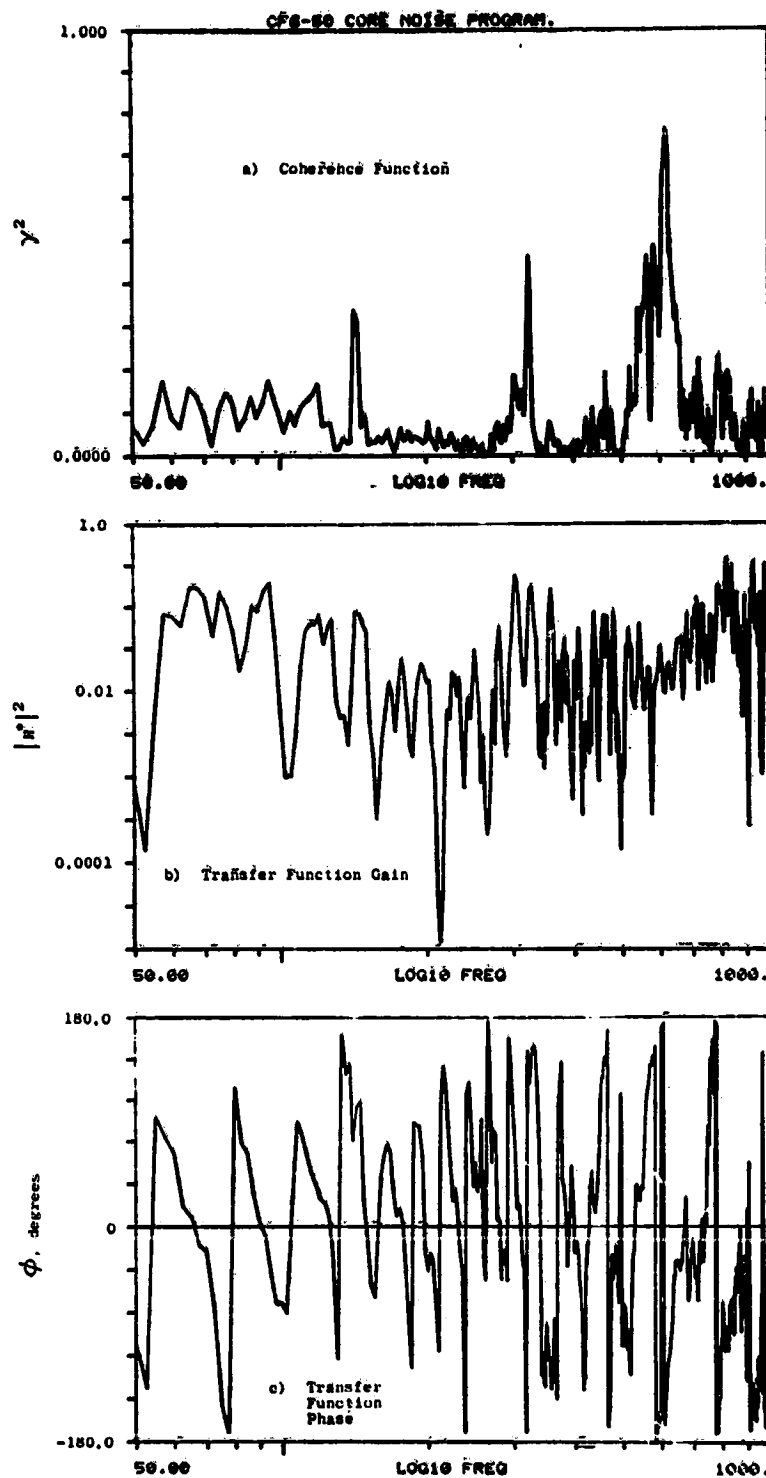


Figure A-35. Coherence and Transfer Functions for Fuel Nozzle (42°) to Plane 3.5 (42°) at 36.5% Thrust.

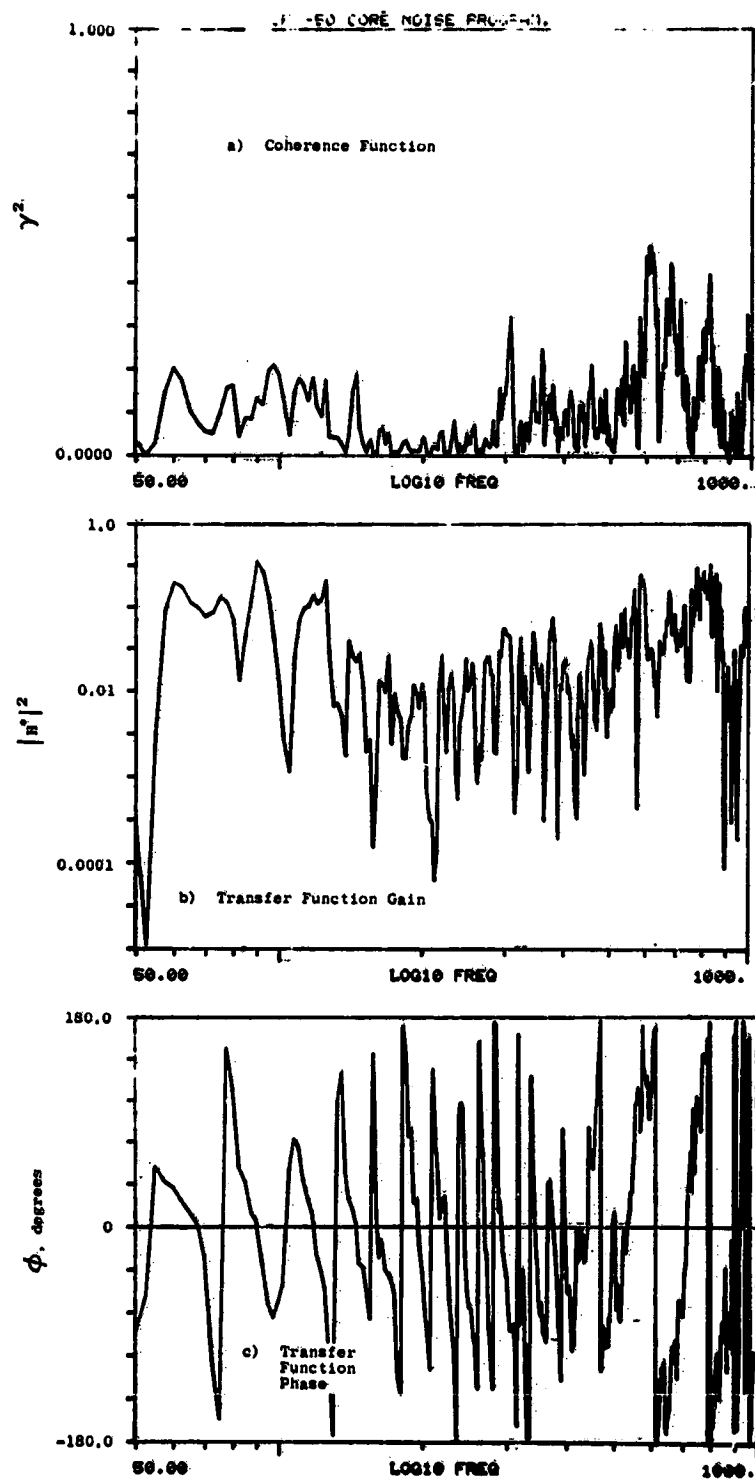


Figure A-36. Coherence and Transfer Functions for Fuel Nozzle (102°) to Plane 3.5 (102°) at 36.5% Thrust.

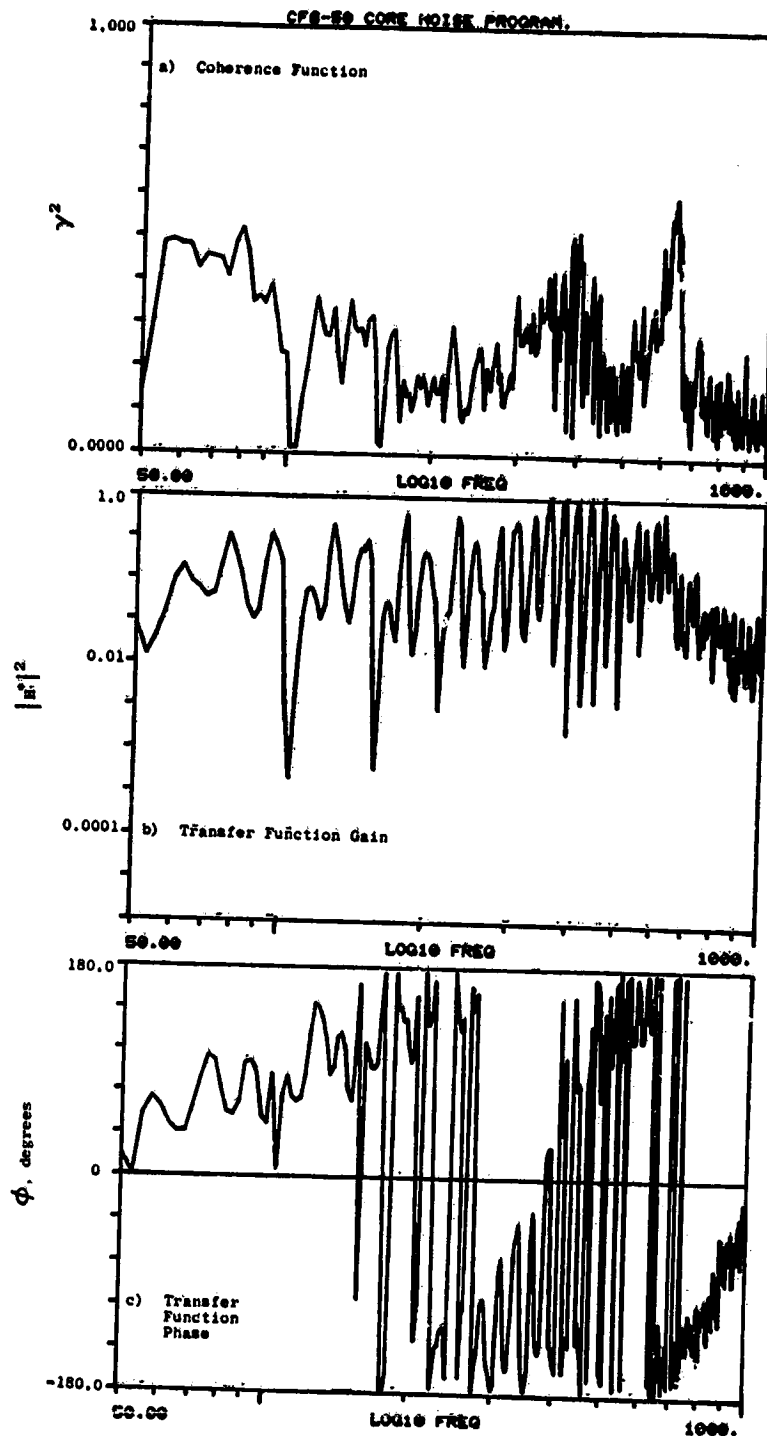


Figure A-37. Coherence and Transfer Functions for Plane 3.0 (16°) to Plane 3.5 (42°) at 45.5% Thrust.

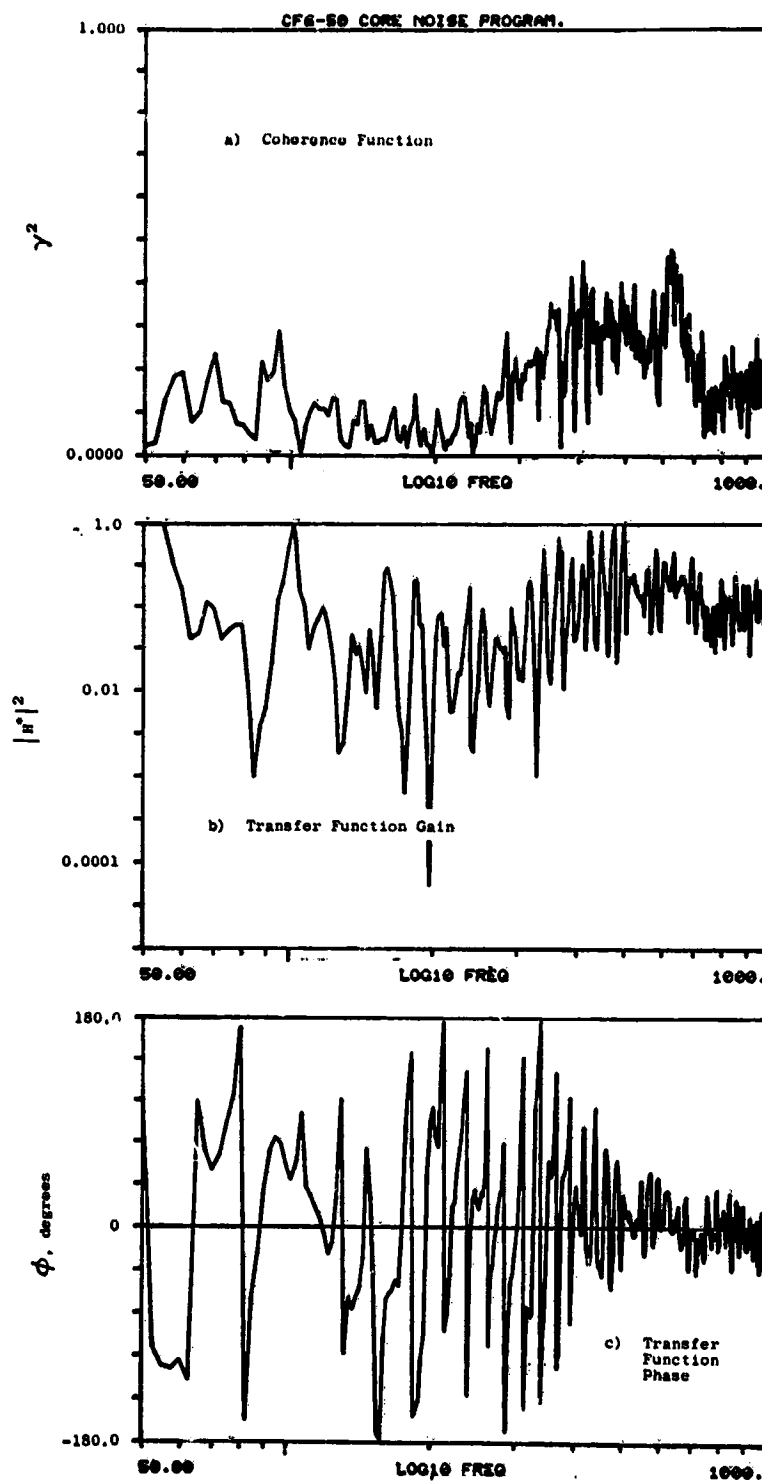


Figure A-38. Coherence and Transfer Functions for Plane 3.5 (102°) to Plane 4.0 (92°) at 45.5% Thrust.

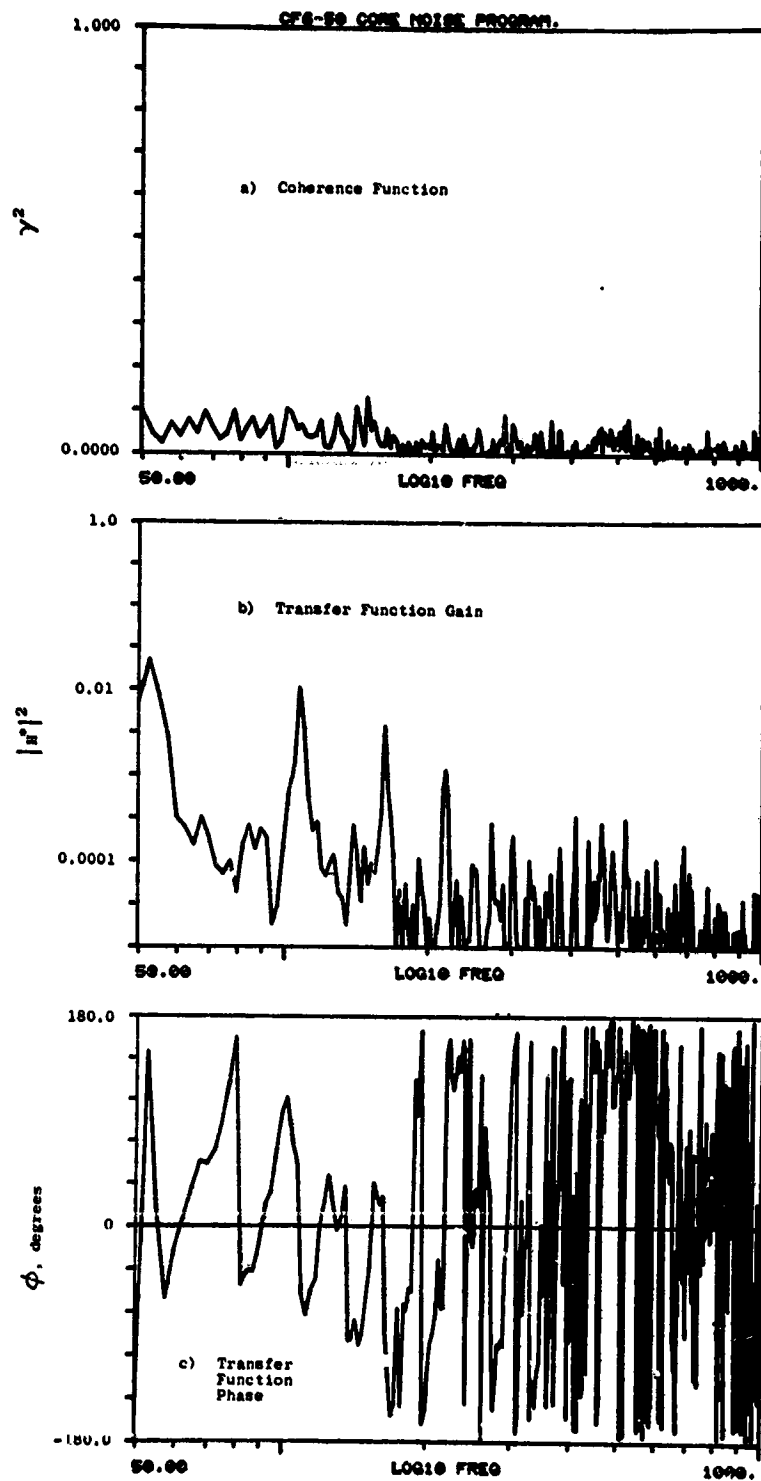


Figure A-39. Coherence and Transfer Functions for Plane 3.5 (282°) to Plane 8.0A (270°) at 45.5% Thrust.

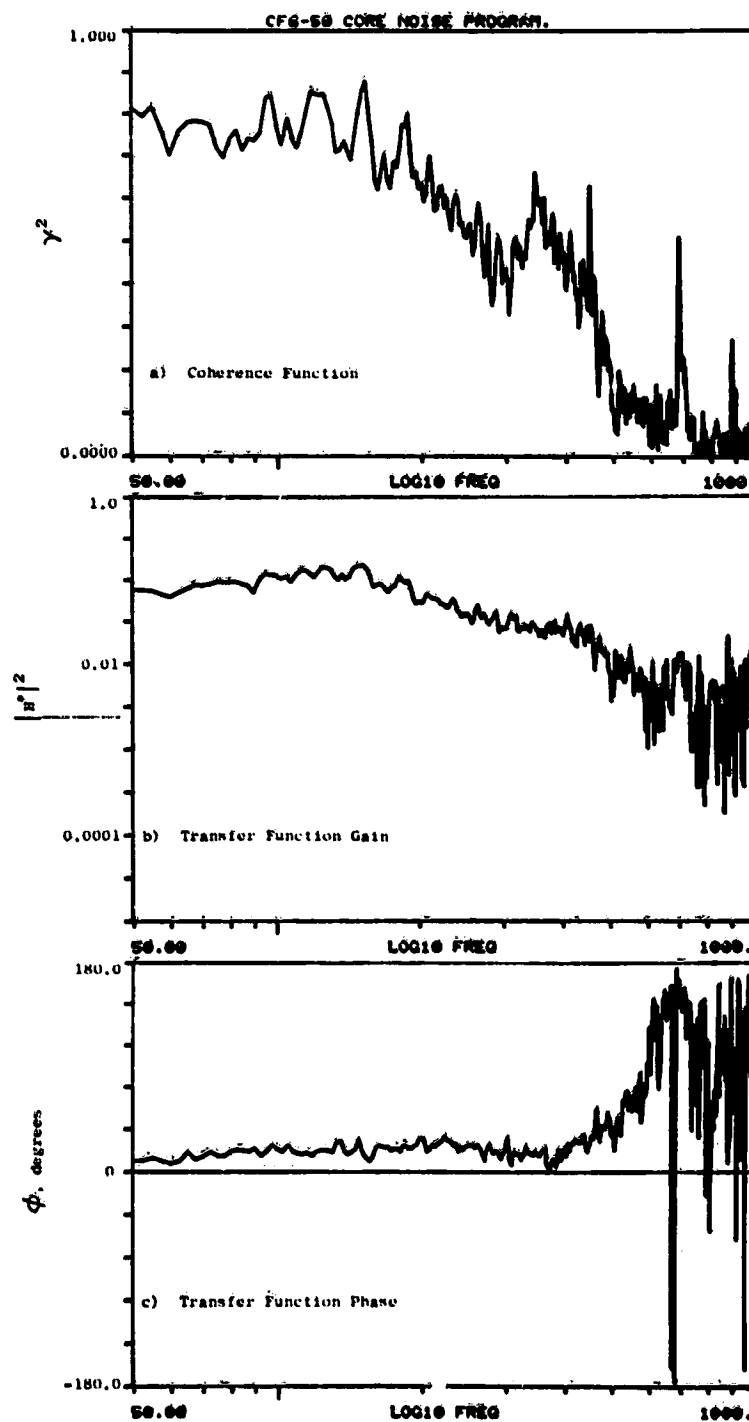


Figure A-40. Coherence and Transfer Functions for Plane 8.0A to Plane 8.0B (270°) at 45.5% Thrust.

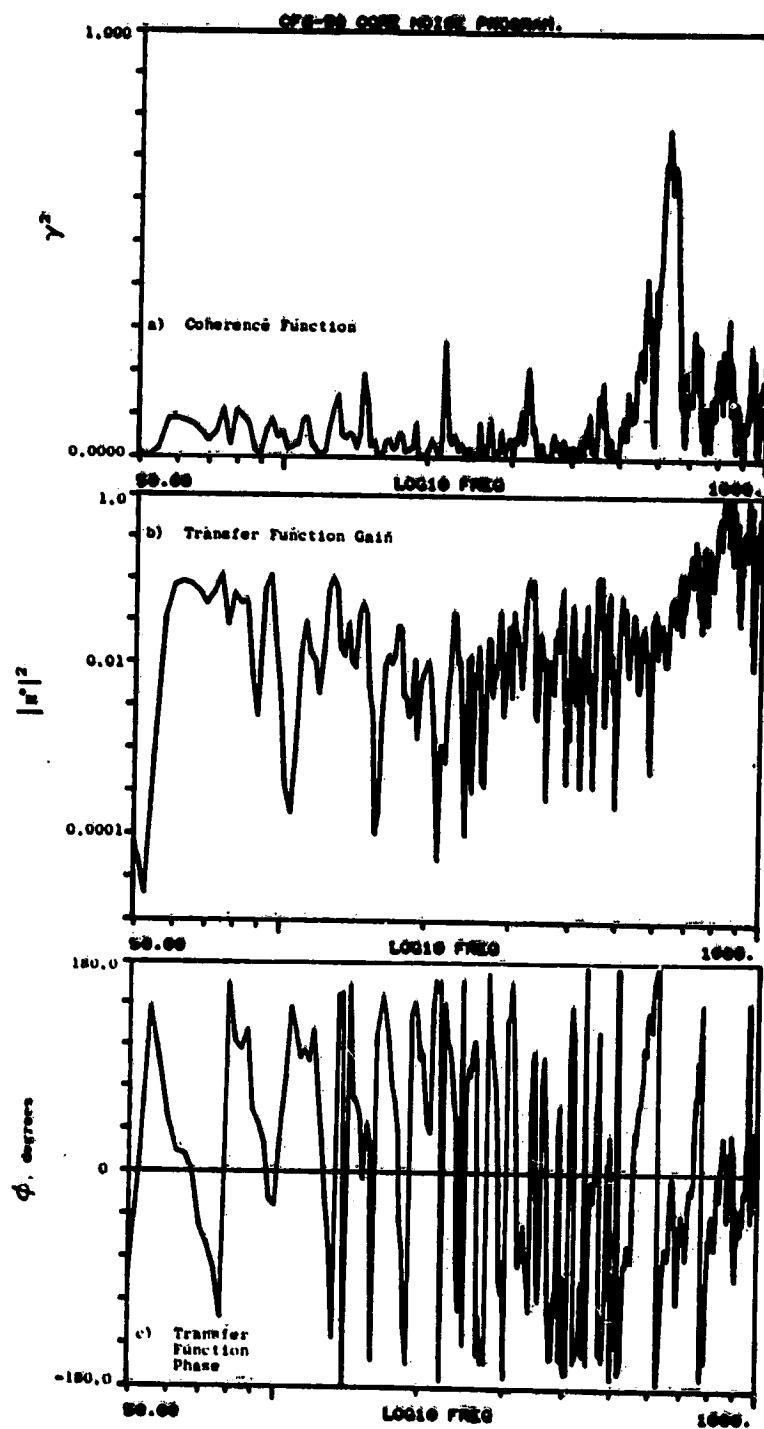


Figure A-41. Coherence and Transfer Functions for Fuel Nozzle (42°) to Plane 3.5 (42°) at 45.5% Thrust.

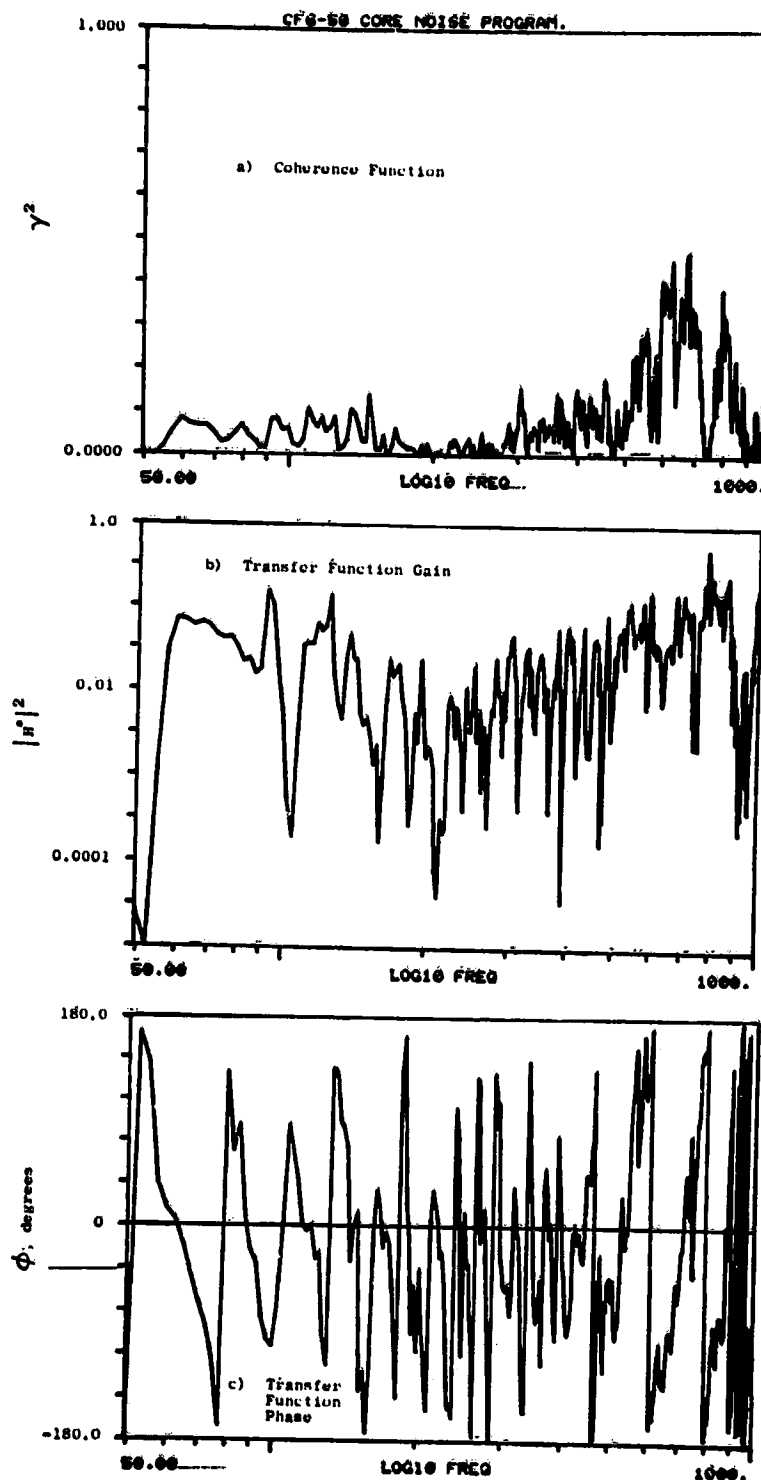


Figure A-42. Coherence and Transfer Functions for Fuel Nozzle (102°) to Plane 3.5 (102°) at 45.5% Thrust.

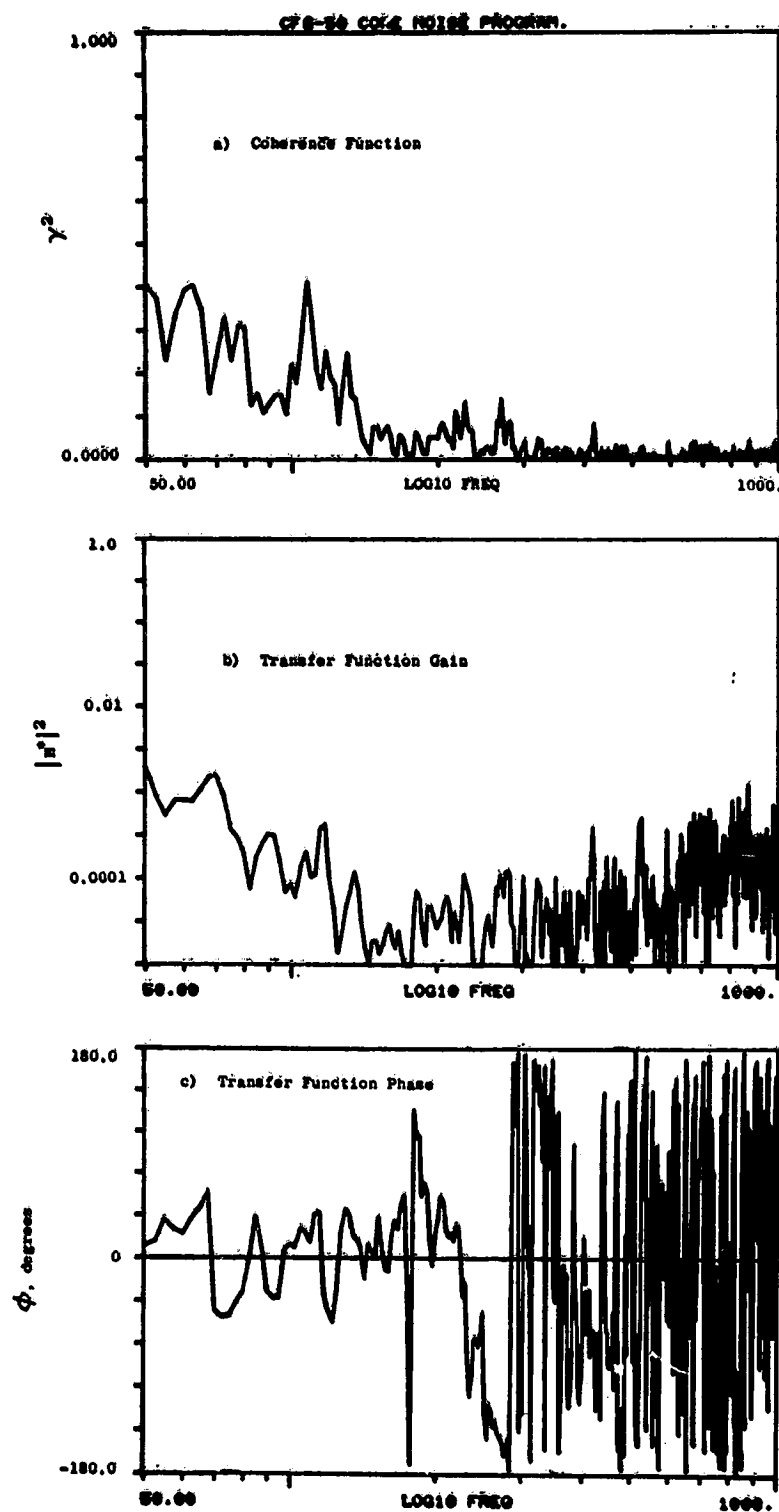


Figure A-43. Coherence and Transfer Functions for Plane 3.5 (102°) to 10° Farfield Microphone at 3.8% Thrust.

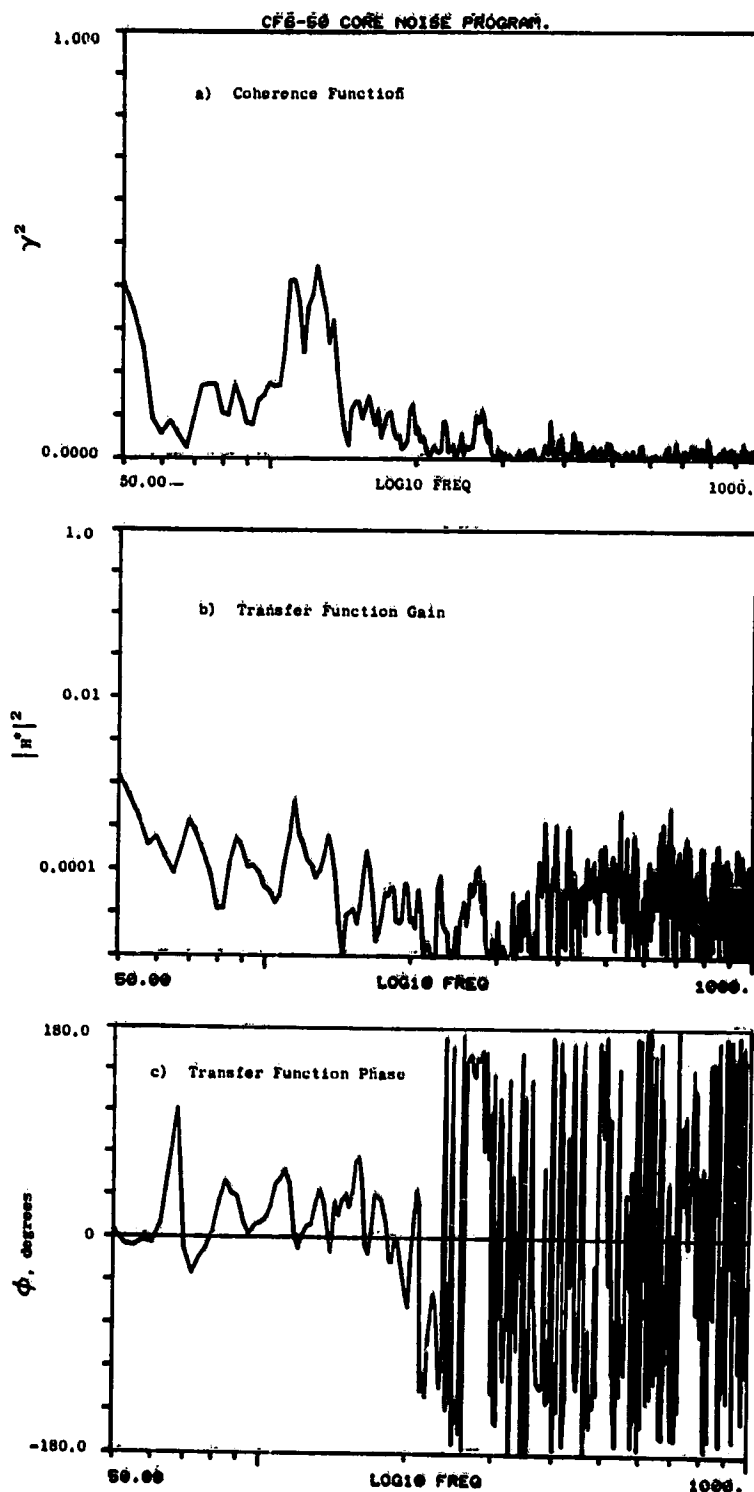


Figure A-44. Coherence and Transfer Functions for Plane 3.5 (102°) to 30° Farfield Microphone at 3.8% Thrust.

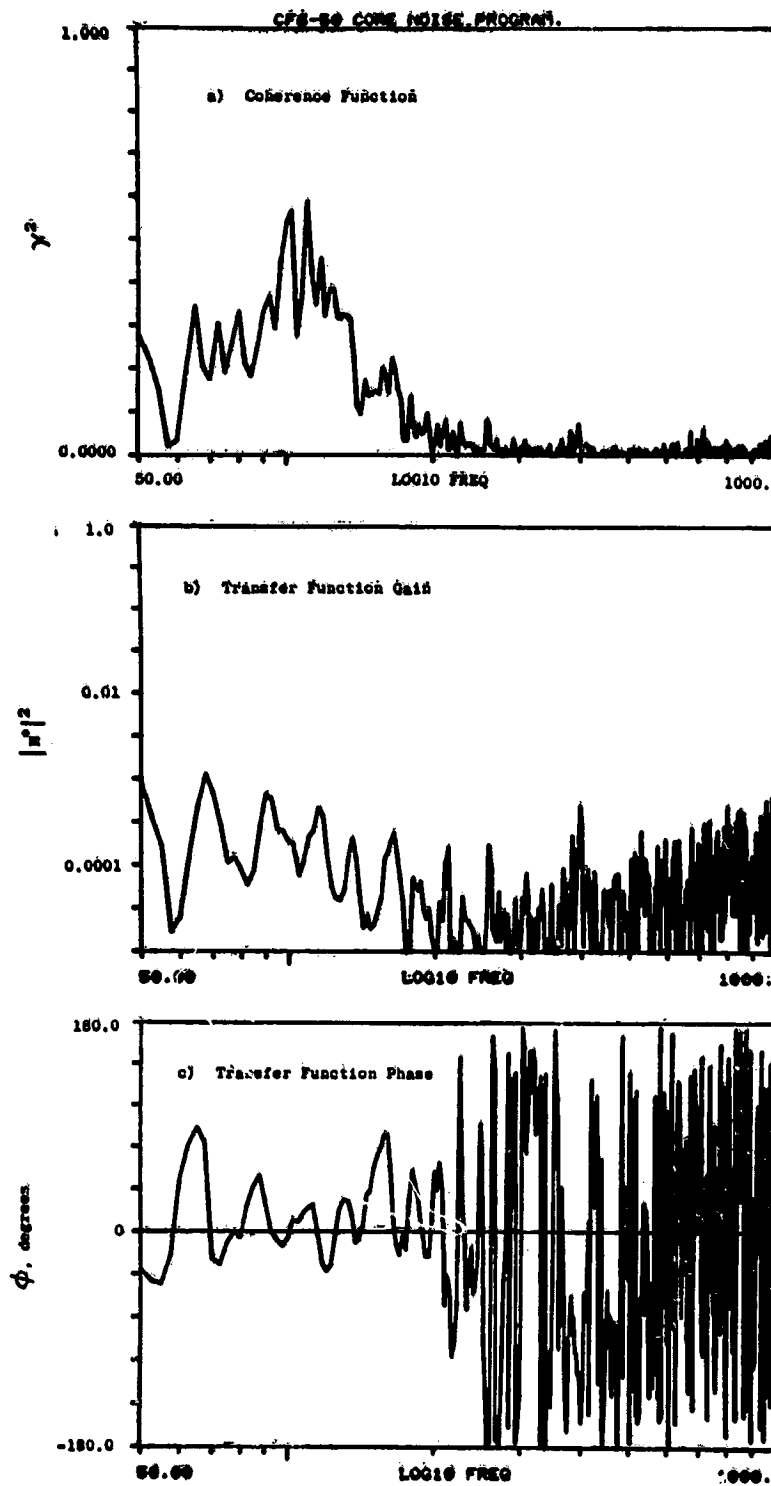


Figure A-45. Coherence and Transfer Functions for Plane 3.5 (102°) to 40° Farfield Microphone at 3.8% Thrust.

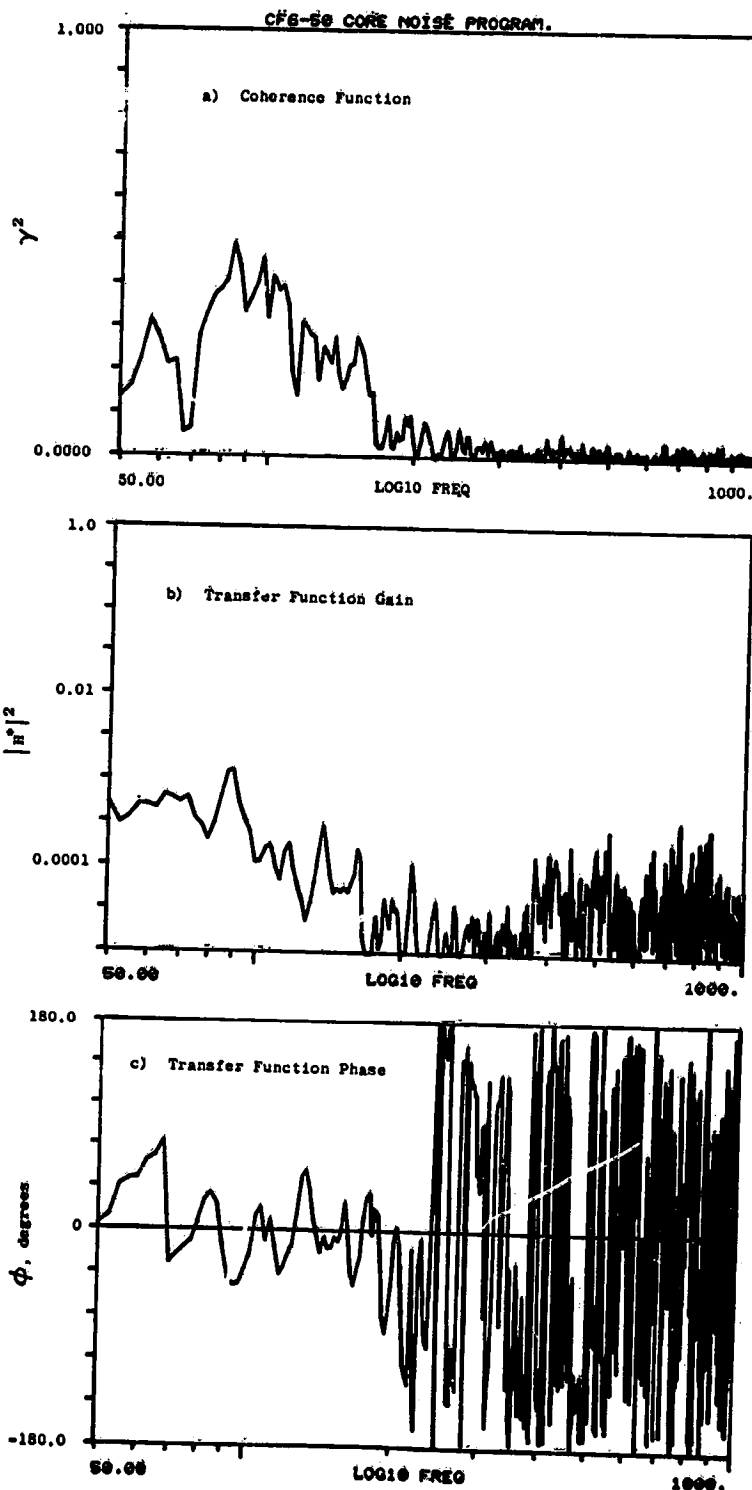


Figure A-46. Coherence and Transfer Functions for Plane 3.5 (102°) to 50° Farfield Microphone at 3.8% Thrust.

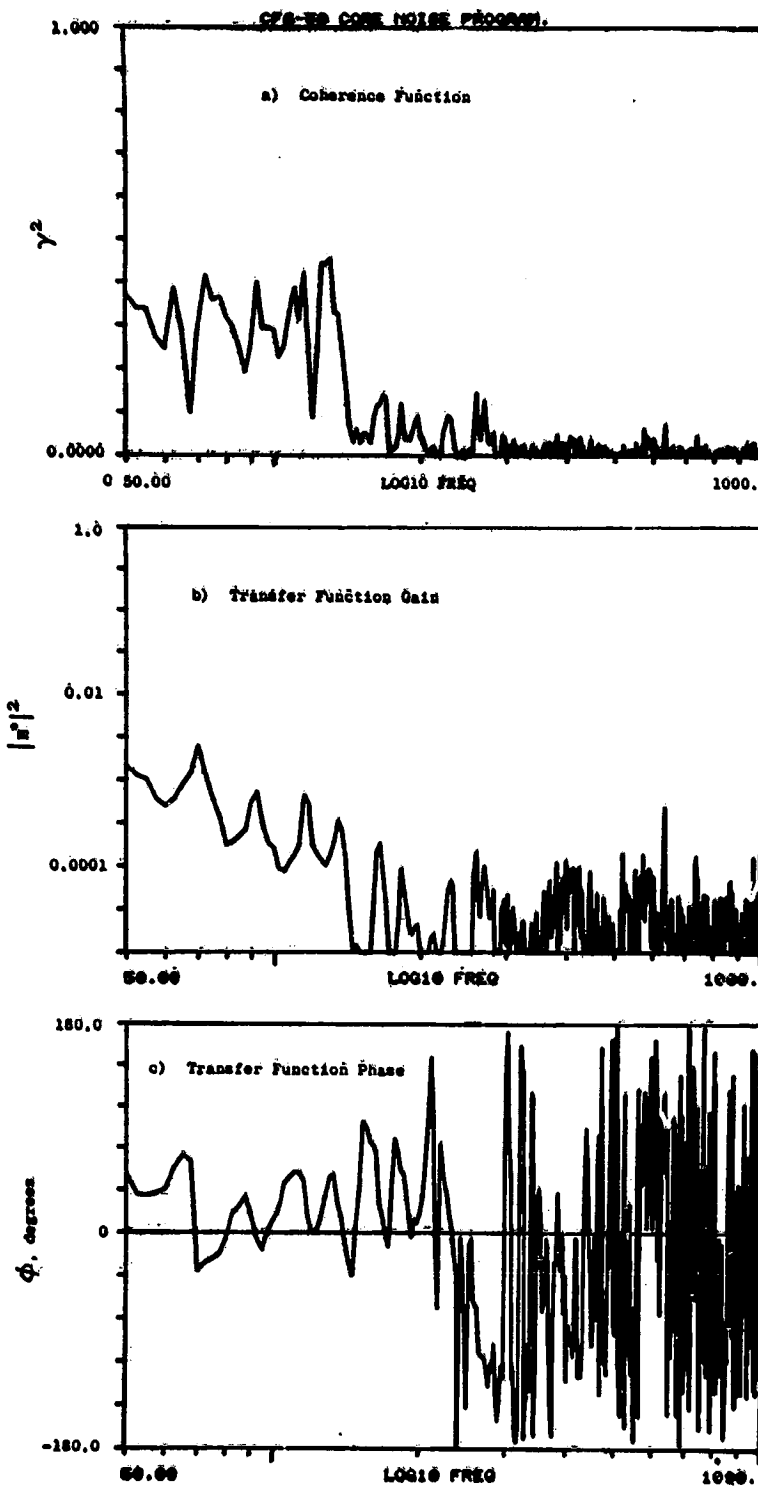


Figure A-47. Coherence and Transfer Functions for Plane 3.5 (102°) to 60° Farfield Microphone at 3.8% Thrust.

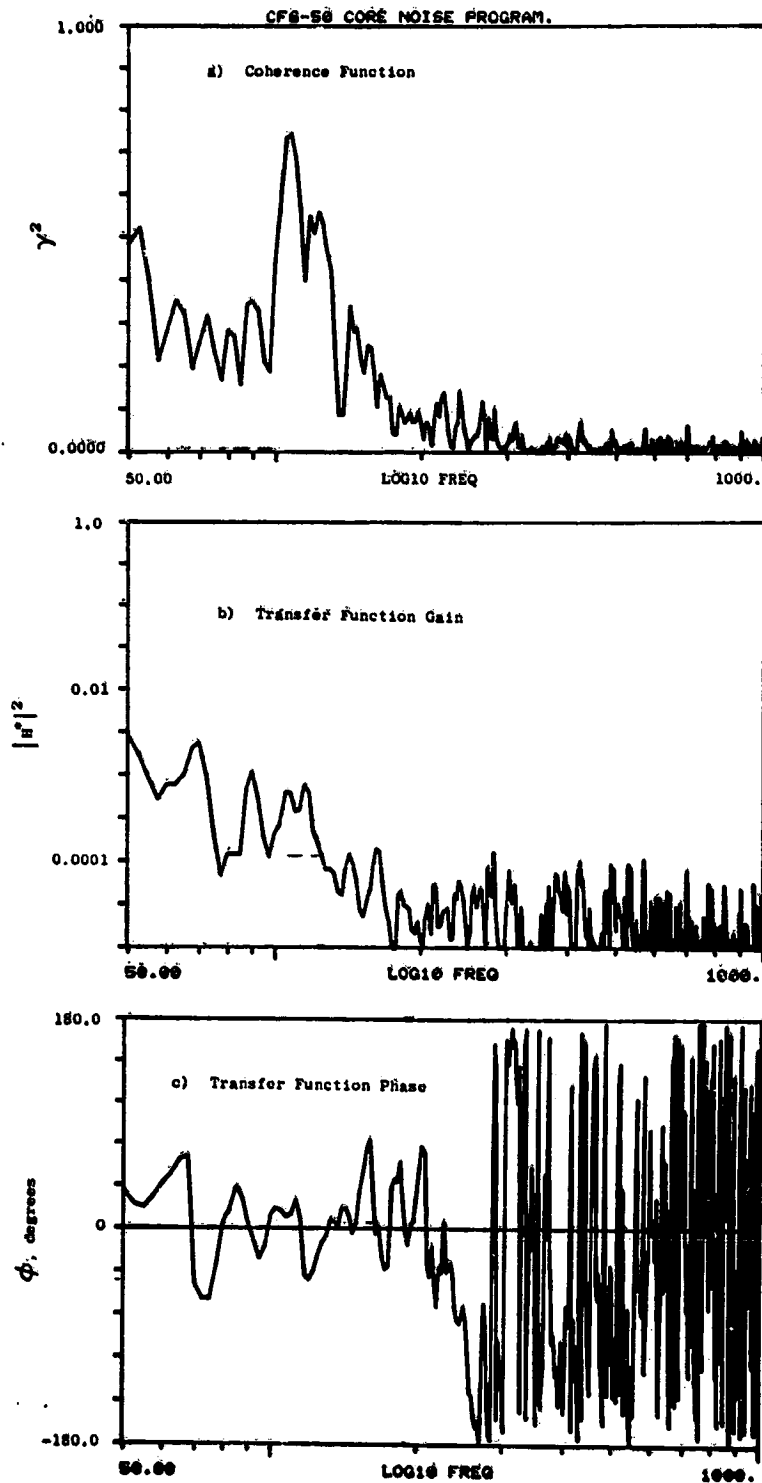


Figure A-48. Coherence and Transfer Functions for Plane 3.5 (102°) to 70° Farfield Microphone at 3.8% Thrust.

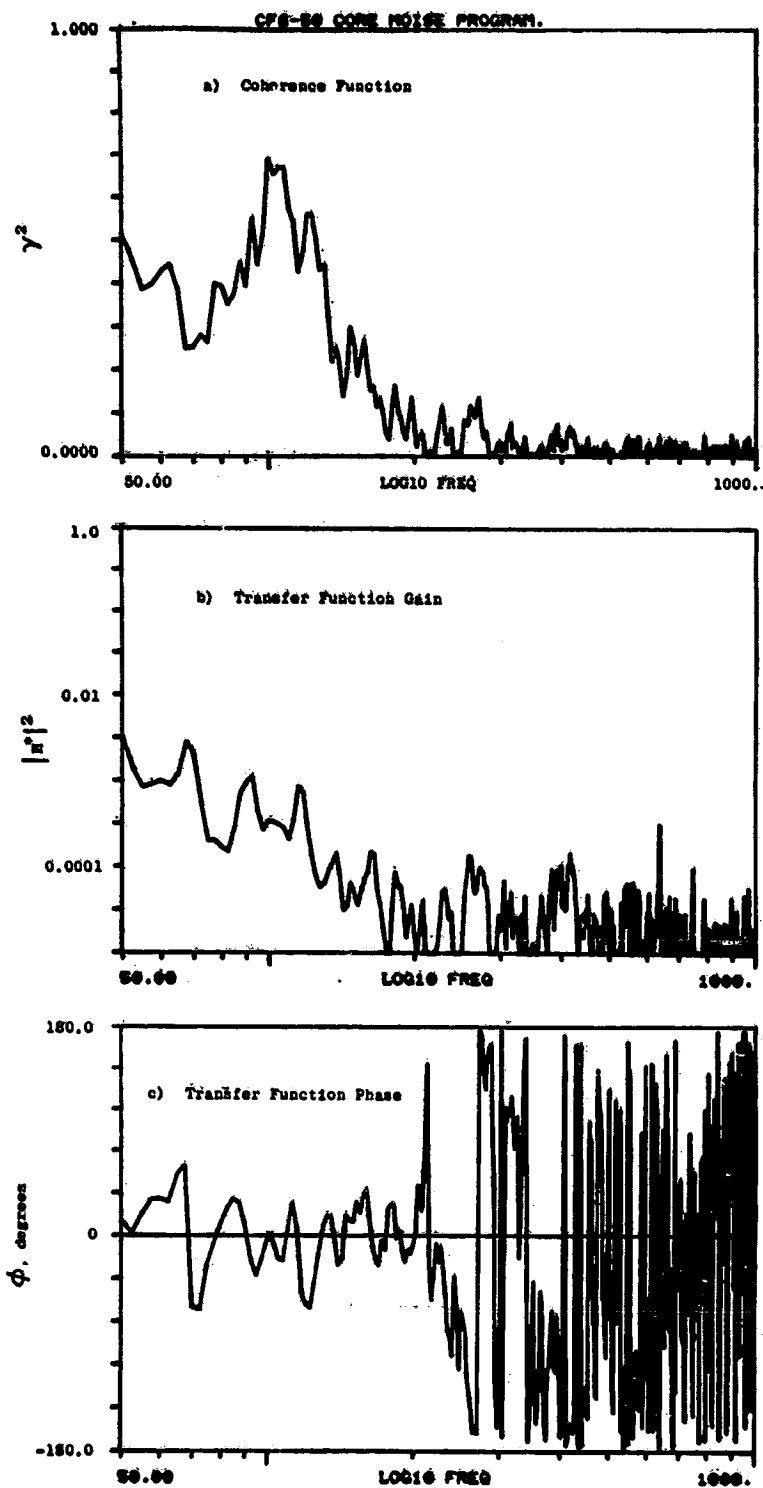


Figure A-49. Coherence and Transfer Functions for Plane 3.5 (102°) to 80° Farfield Microphone at 3.8% Thrust.

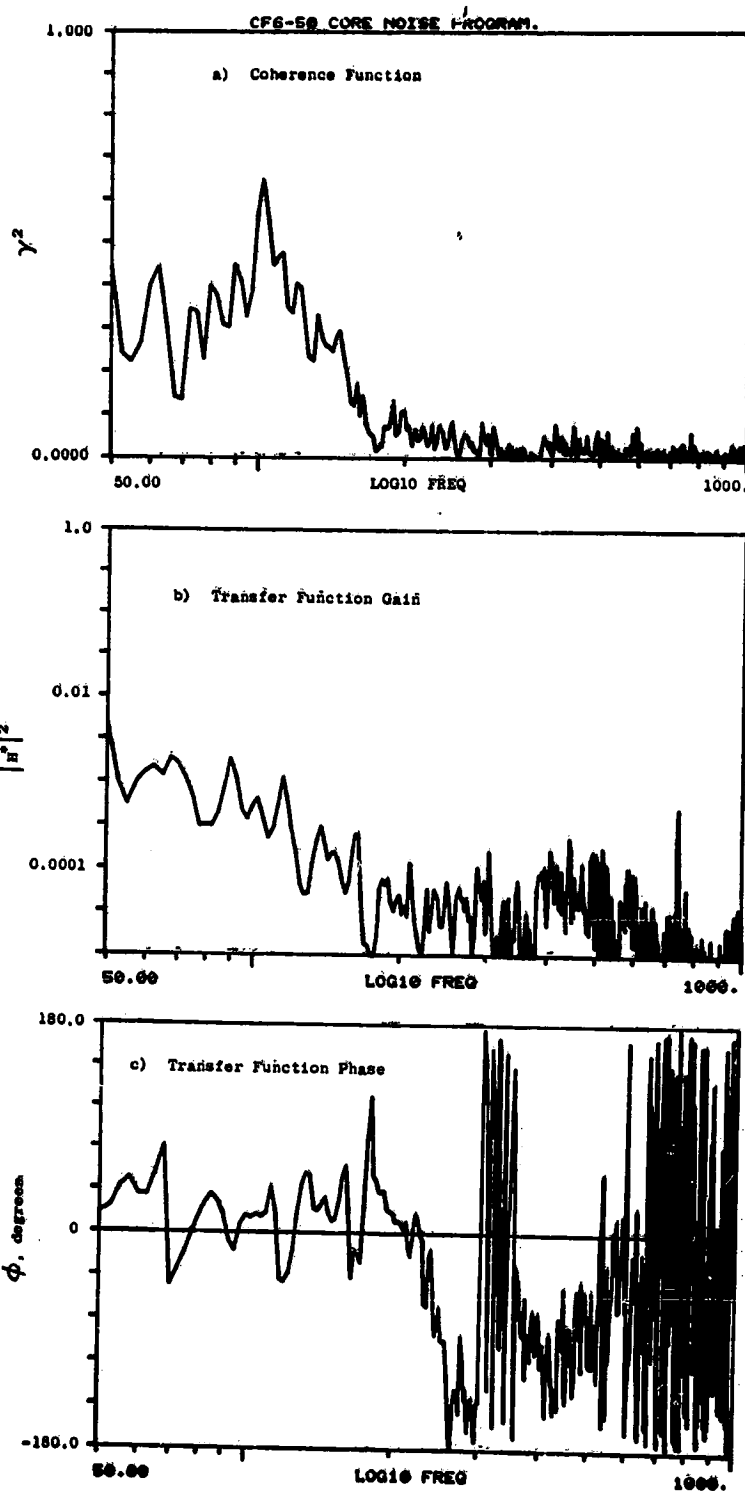


Figure A-50. Coherence and Transfer Functions for Plane 3.5 (102°) to 90° Farfield Microphone at 3.8% Thrust.

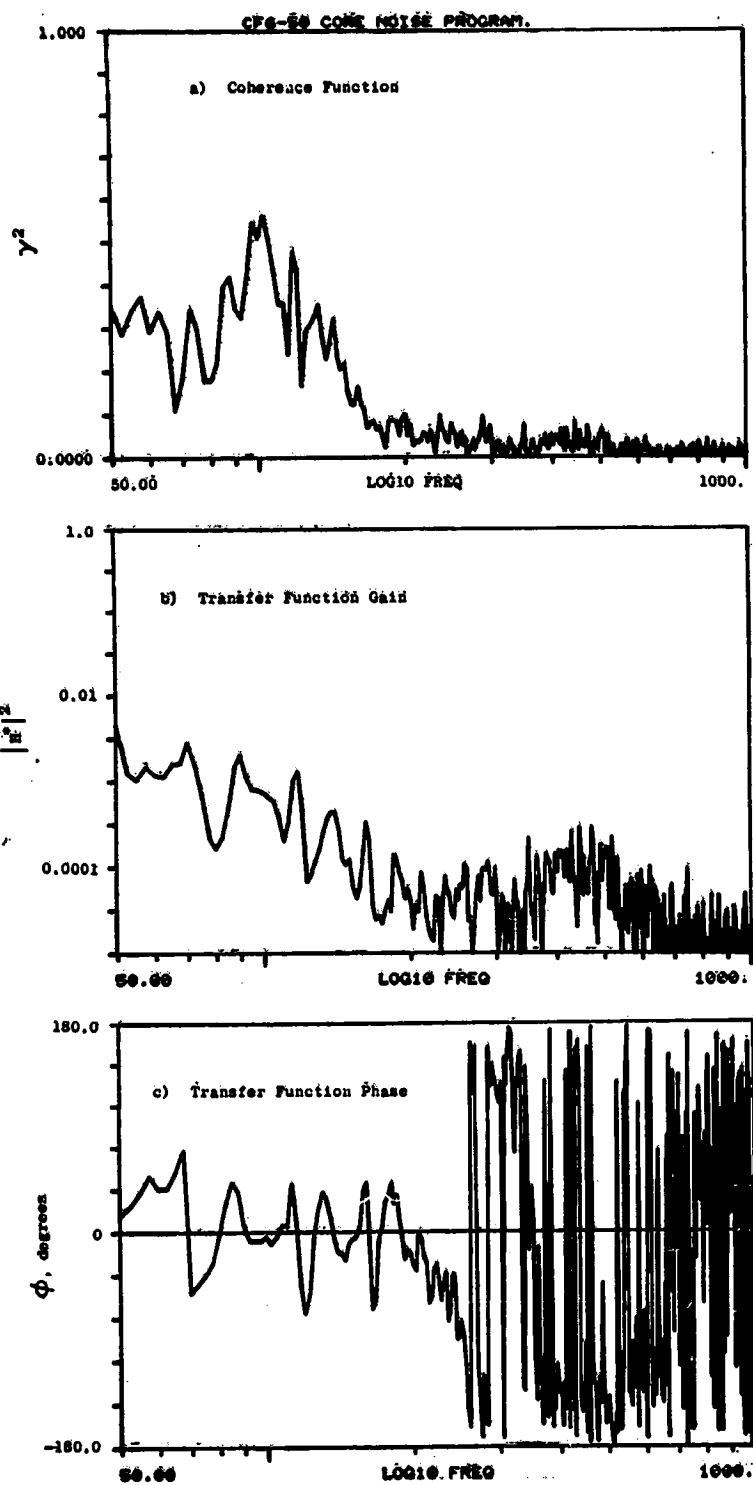


Figure A-51. Coherence and Transfer Functions for Plane 3.5 (102°) to 100° Farfield Microphone at 3.8% Thrust.

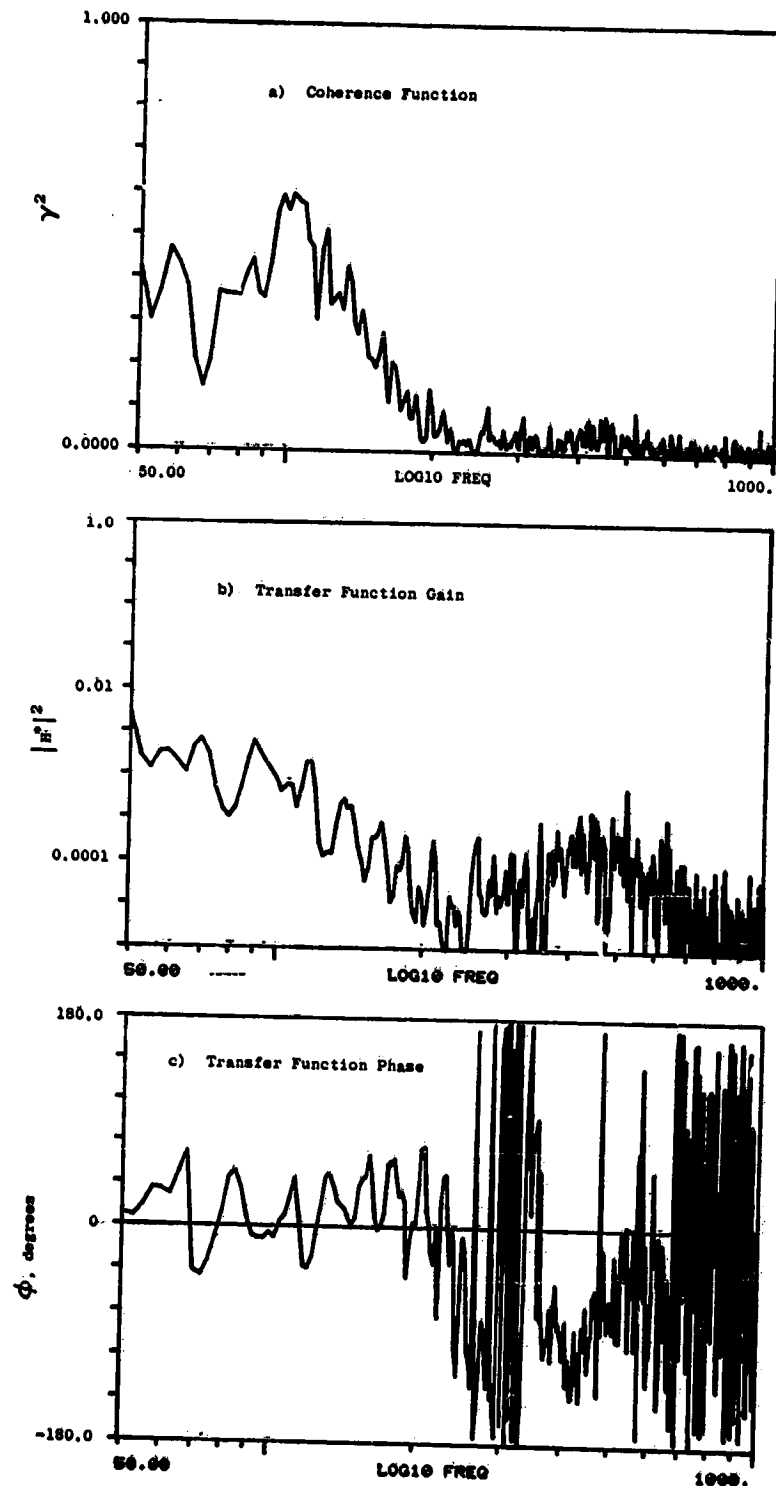


Figure A-52. Coherence and Transfer Functions for Plane 3.5 (102°) to 110° Farfield Microphone at 3.8% Thrust.

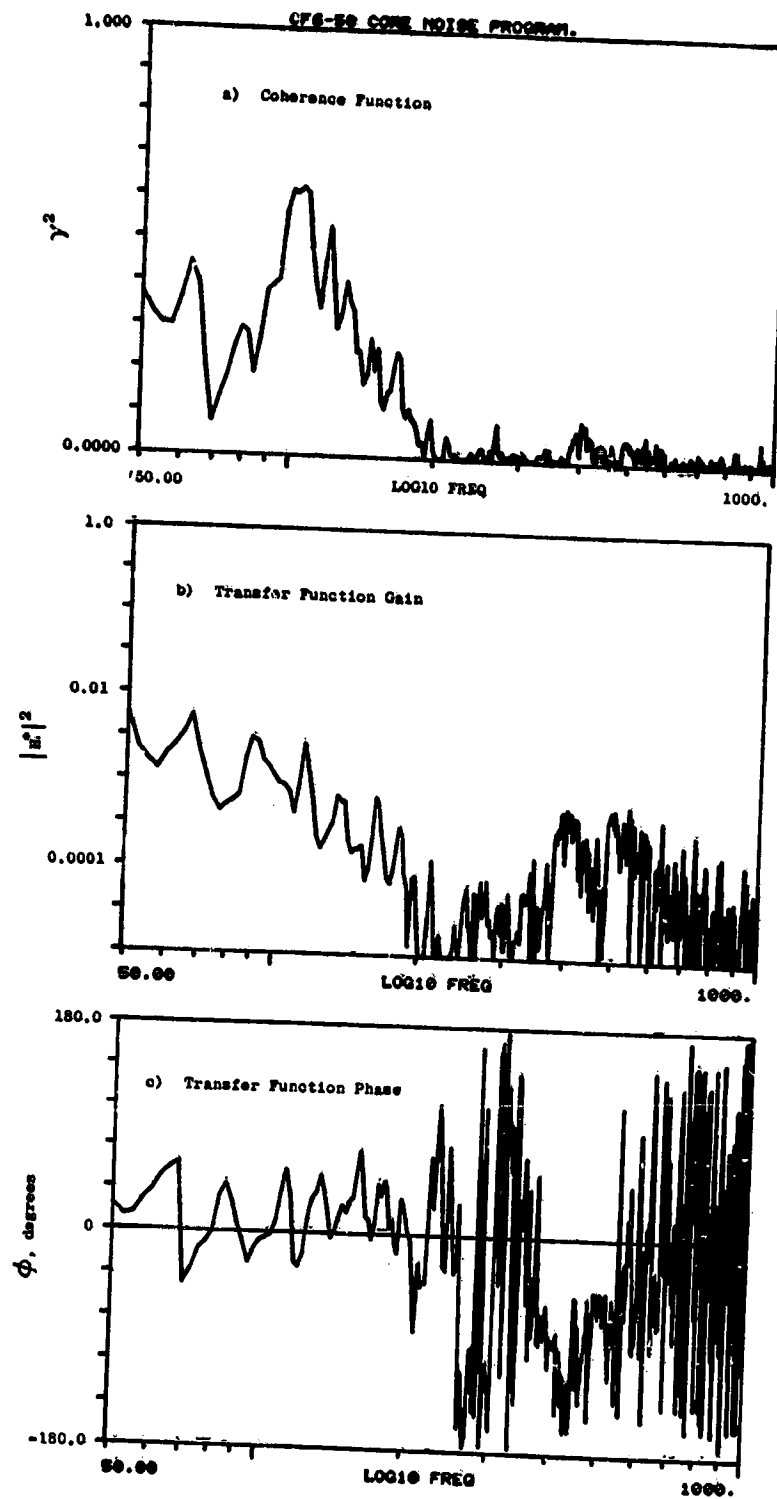


Figure A-53. Coherence and Transfer Functions for Plane 3.5 (102°) to 120° Farfield Microphone at 3.8% Thrust.

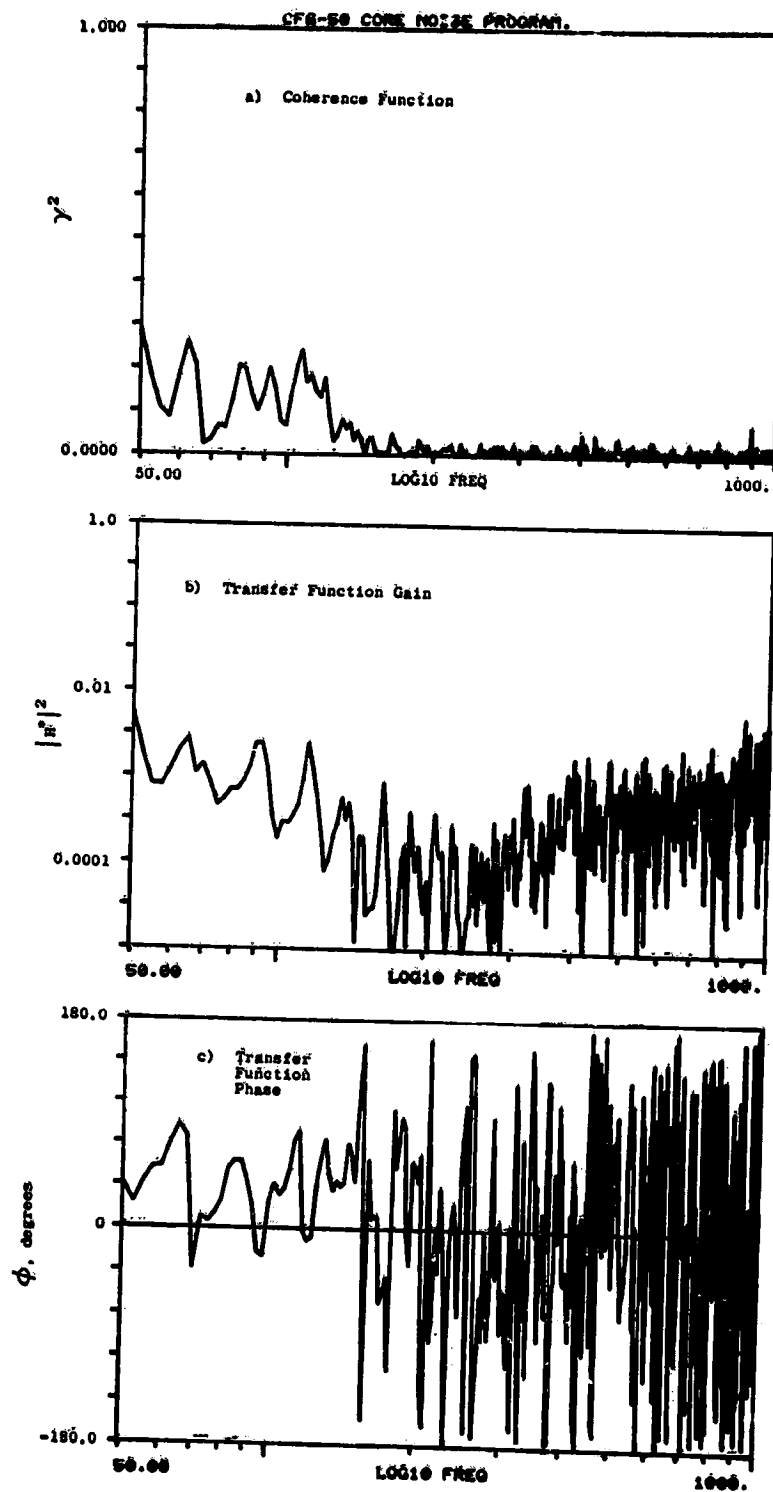


Figure A-54. Coherence and Transfer Functions for Plane 3.5 (102° to 130° Farfield Microphone at 3.8% Thrust.

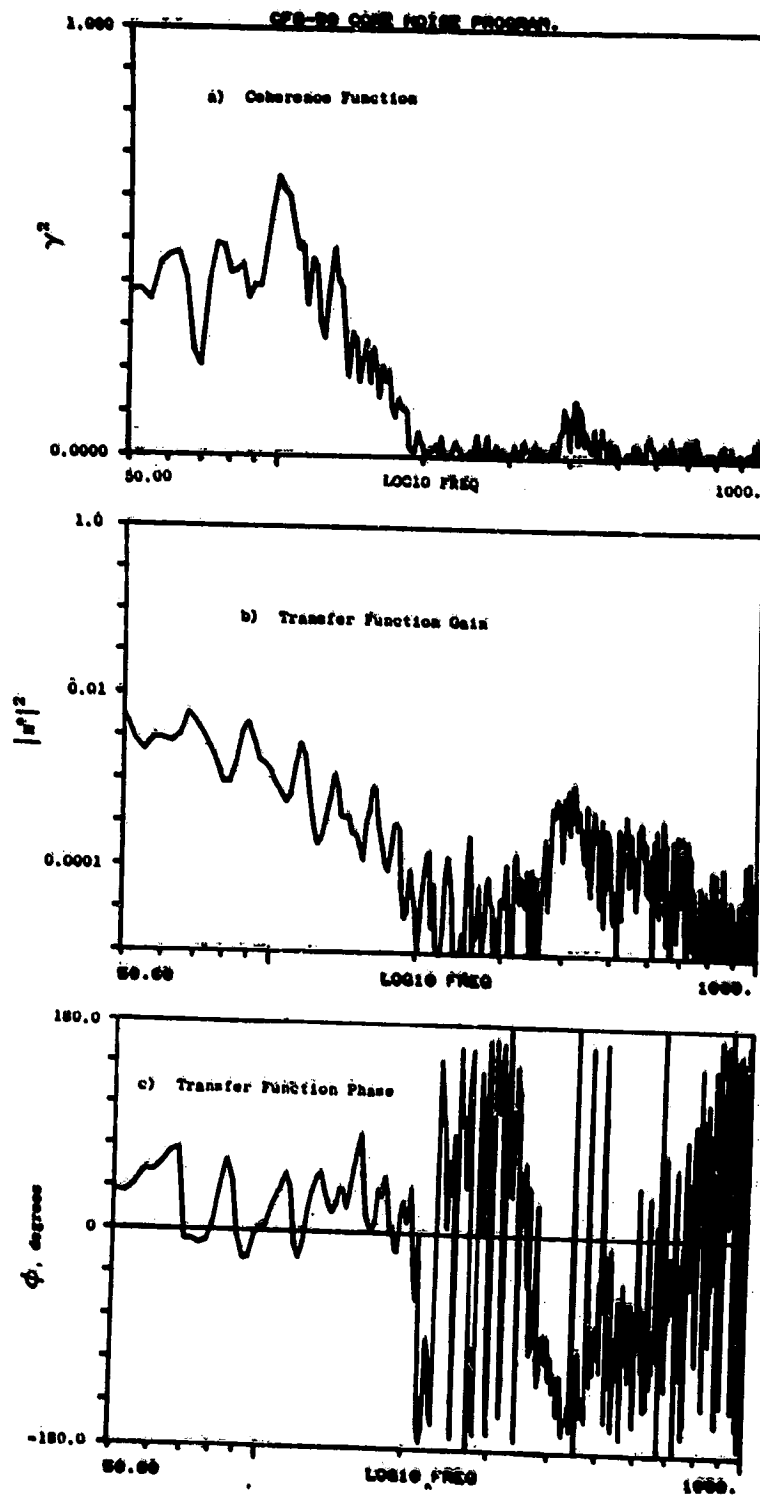


Figure A-55. Coherence and Transfer Functions for Plane 3.5 (102°) to 140° Farfield Microphone at 3.8% Thrust.

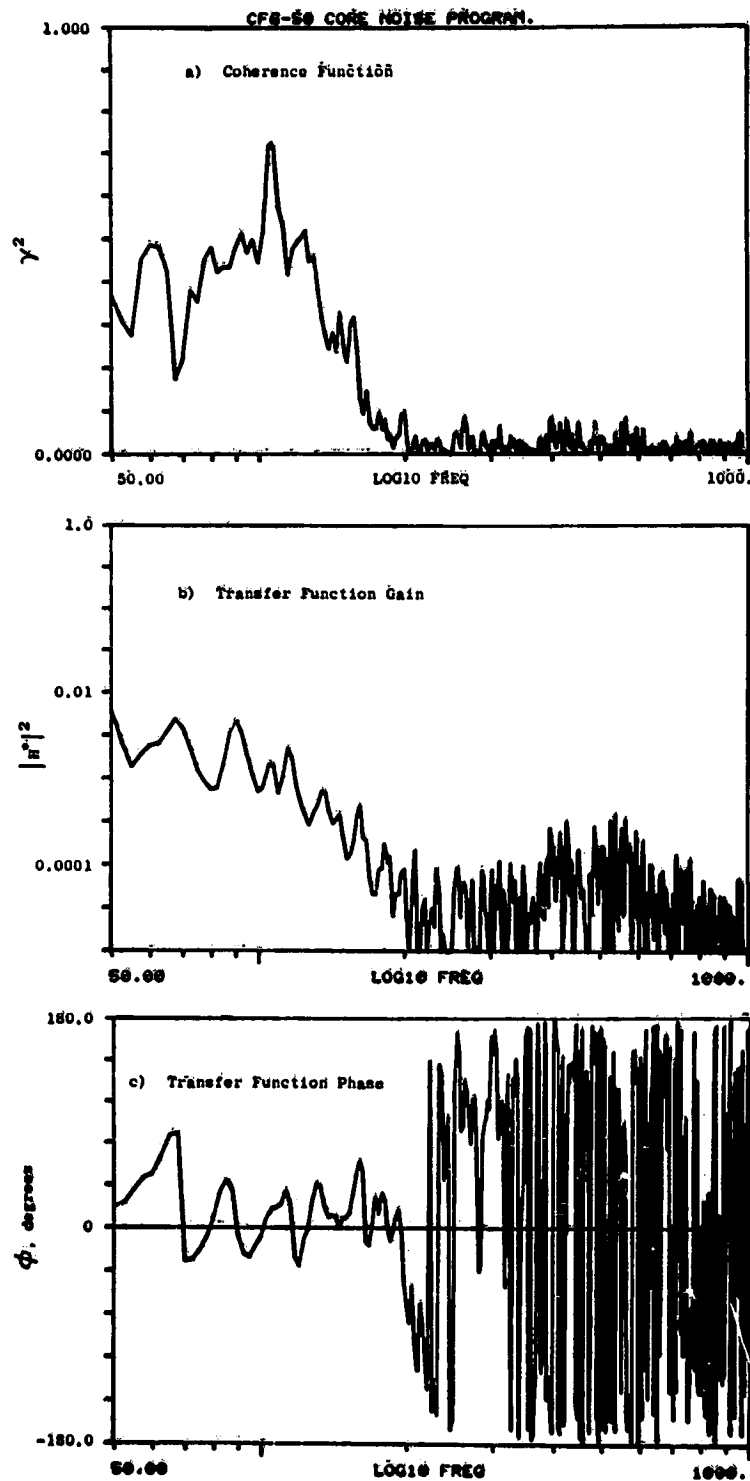


Figure A-56. Coherence and Transfer Functions for Plane 3.5 (102°) to 150° Farfield Microphone at 3.8% Thrust.

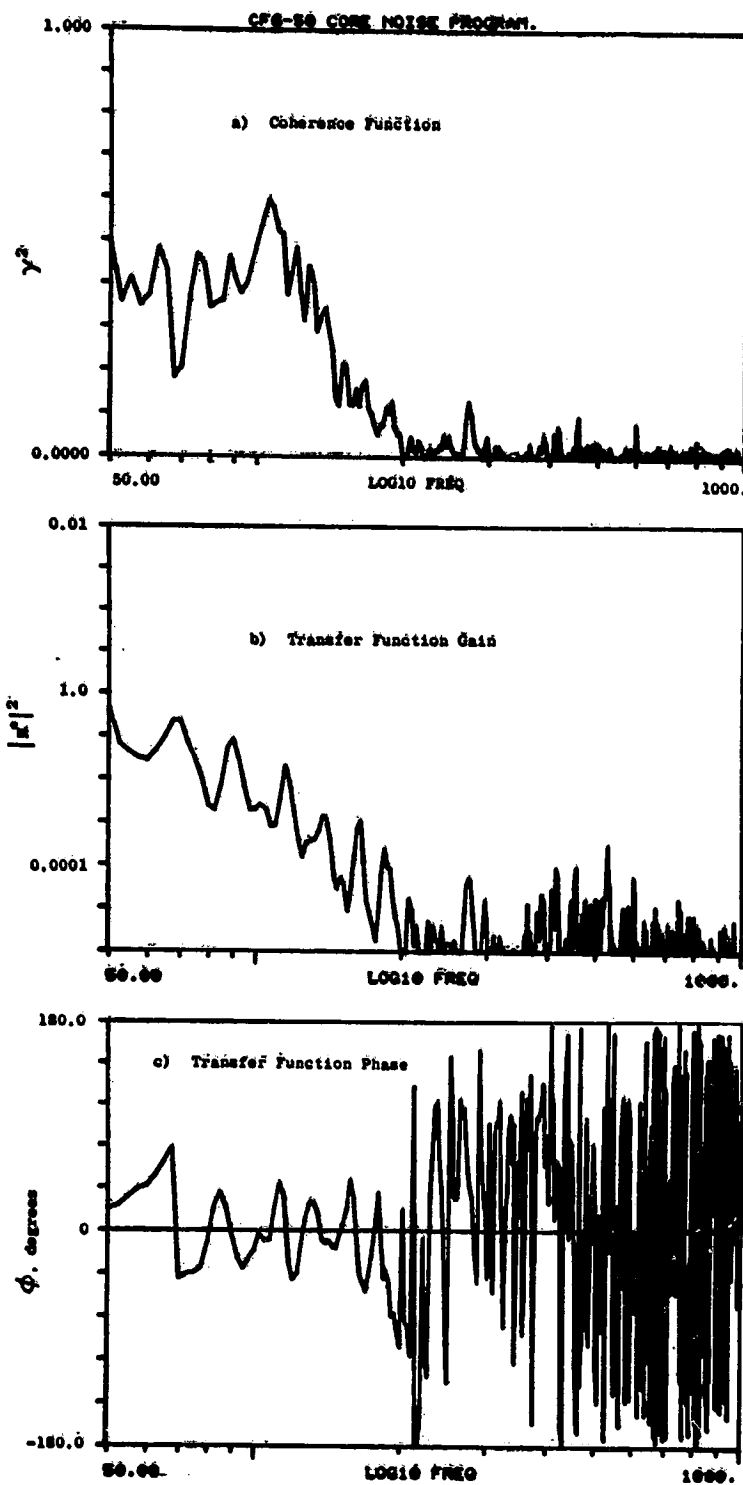


Figure A-57. Coherence and Transfer Functions for Plane 3.5 (102°) to 160° Farfield Microphone at 3.8% Thrust.

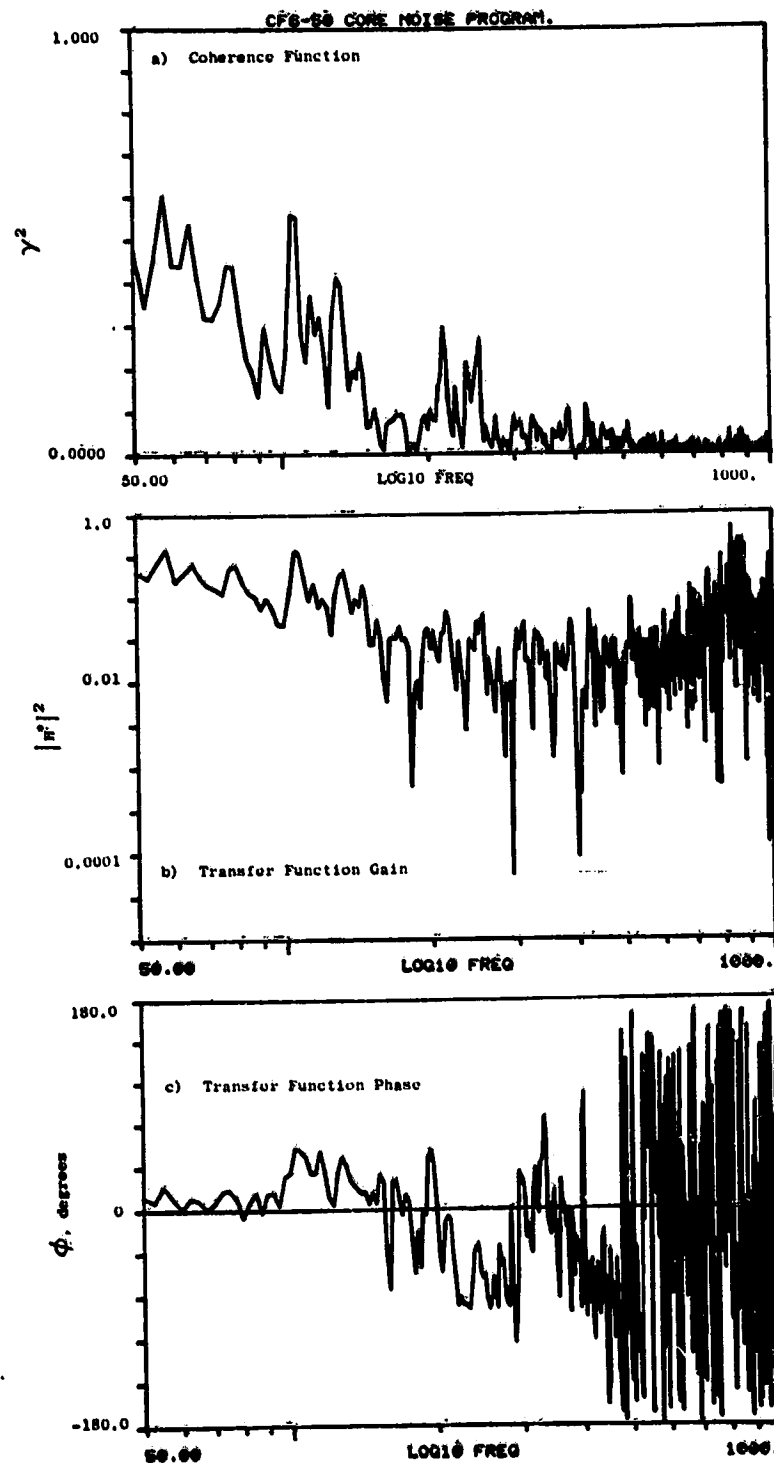


Figure A-58. Coherence and Transfer Functions for Plane 8.0A (270°) to 10° Farfield Microphone at 3.8% Thrust.

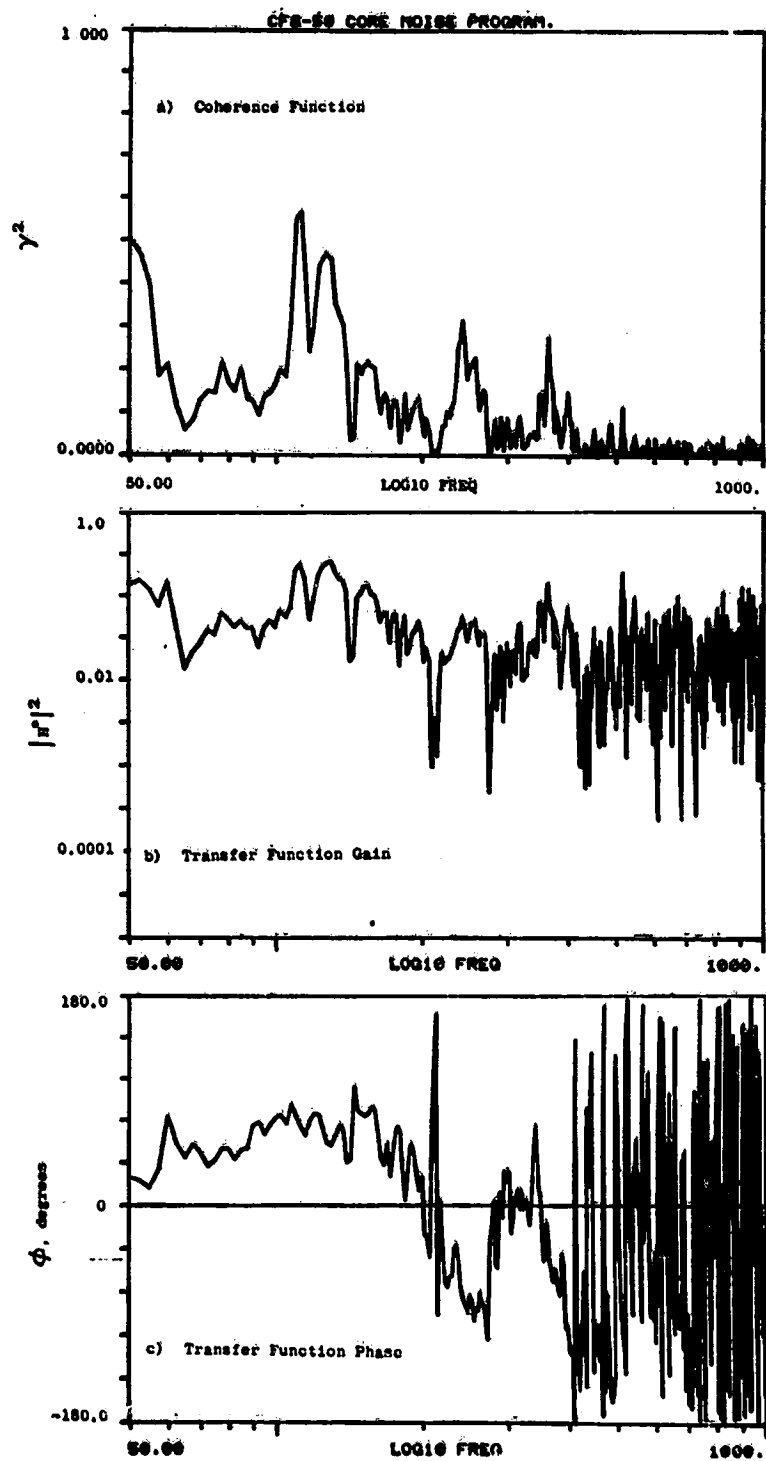


Figure A-59. Coherence and Transfer Functions for Plane 8.0A (270°) to 30° Farfield Microphone at 3.8% Thrust.

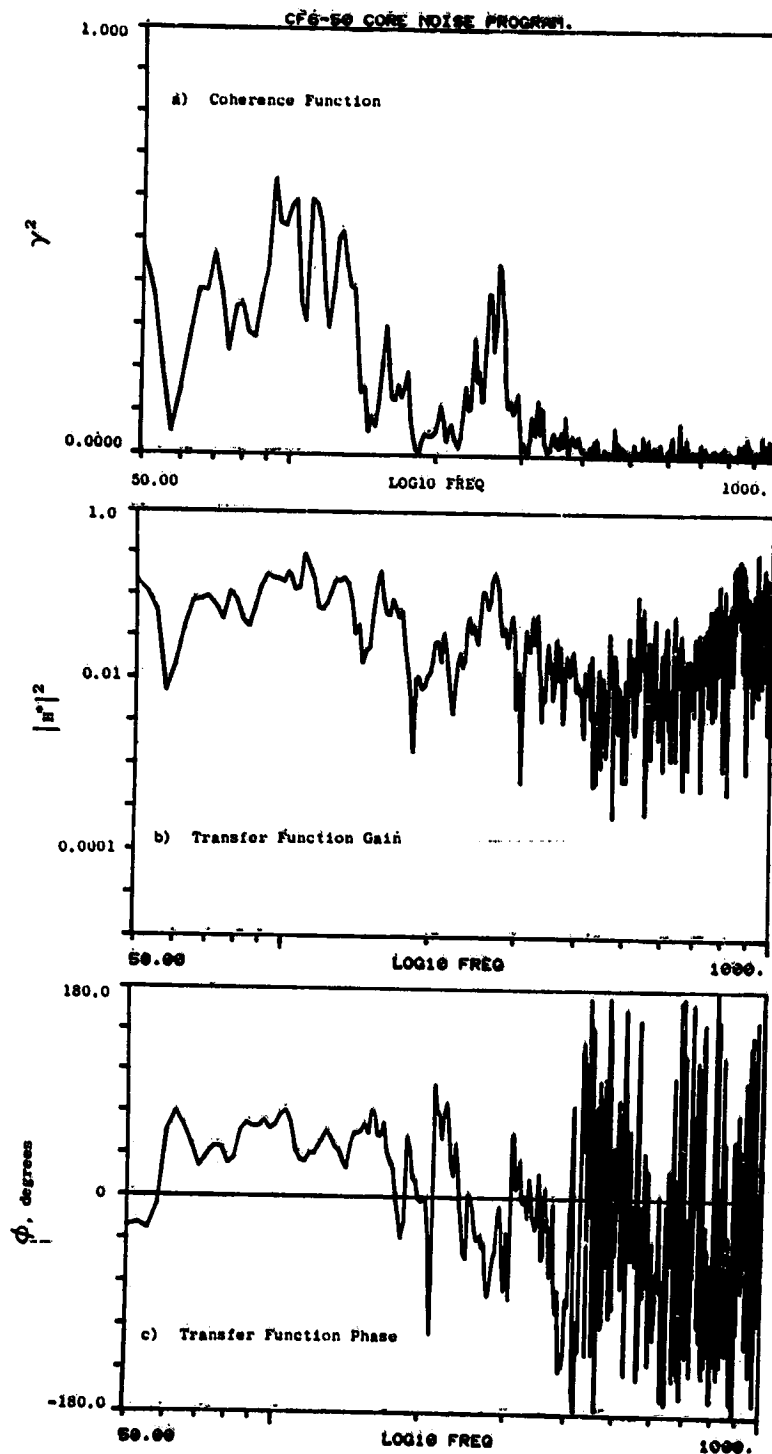


Figure A-60. Coherence and Transfer Functions for Plane 8.0A (270°) to 40° Farfield Microphone at 3.8% Thrust.

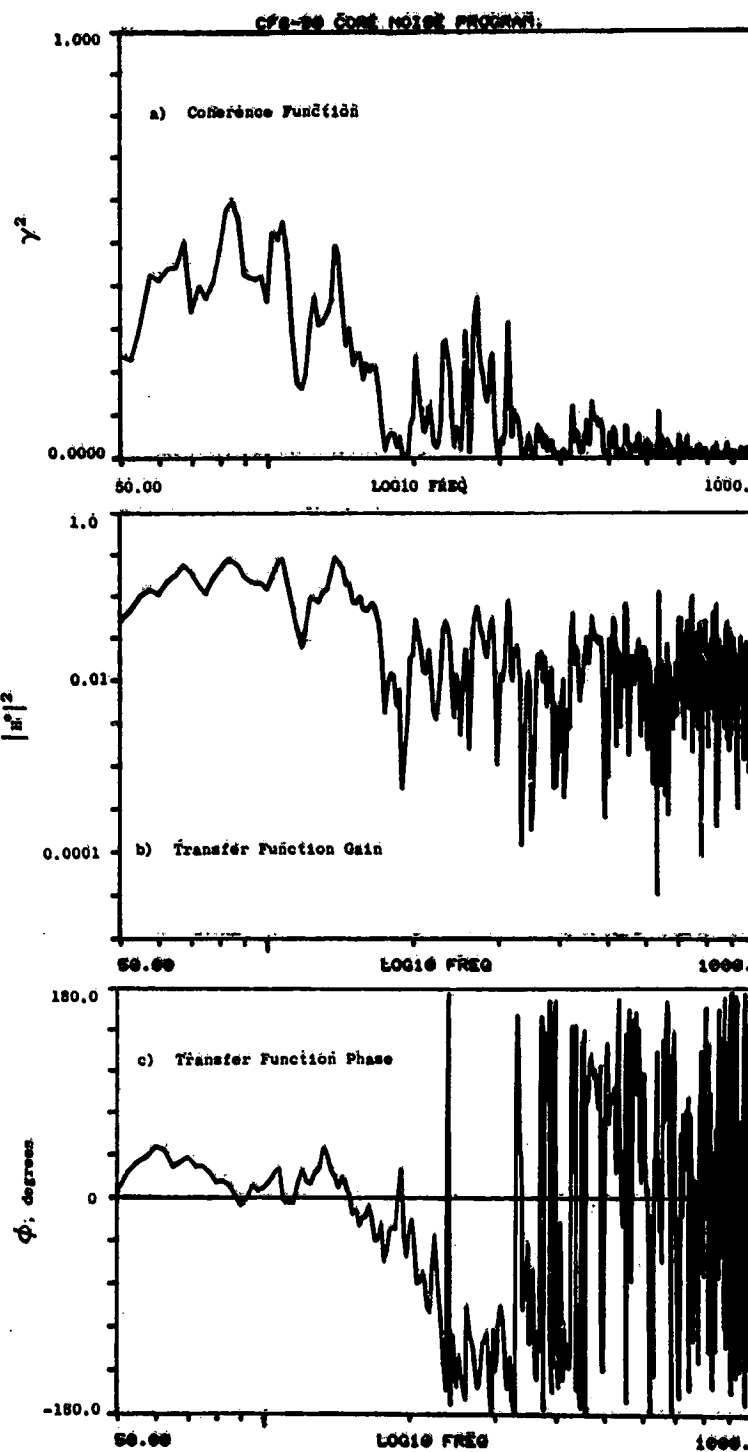


Figure A-61. Coherence and Transfer Functions for Plane 8.0A (270°) to 50° Farfield Microphone at 3.8% Thrust.

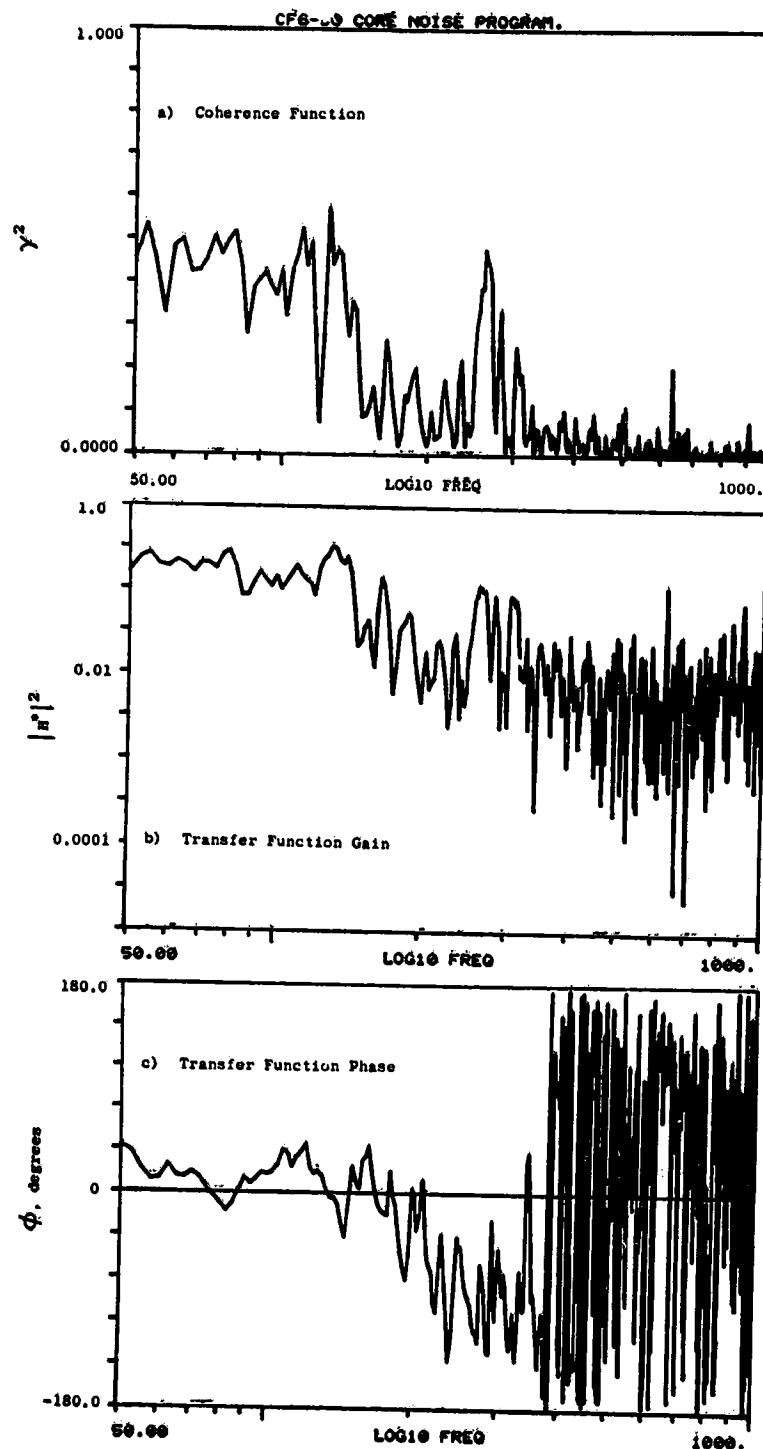


Figure A-62. Coherence and Transfer Functions for Plane 8.0A (270°) to 60° Farfield Microphone at 3.8% Thrust.

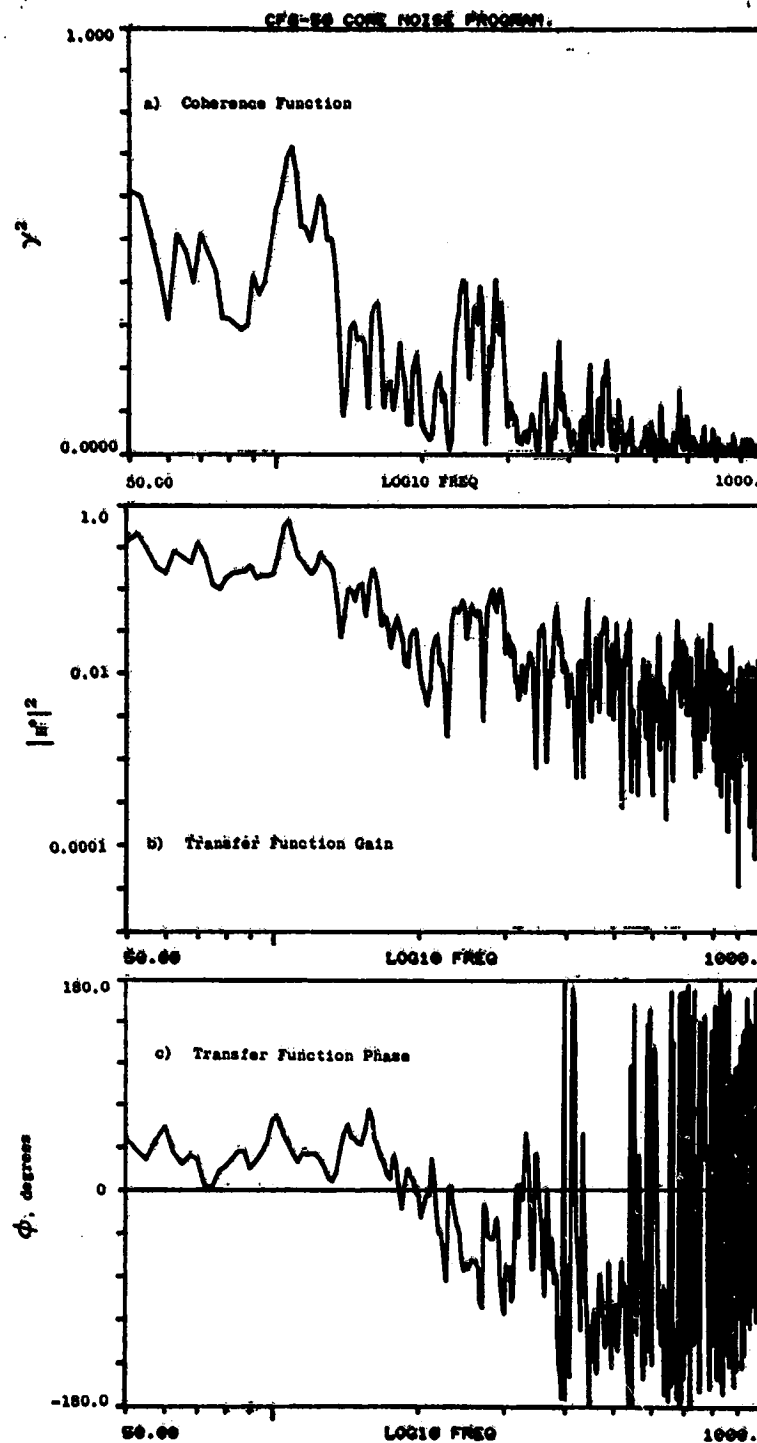


Figure A-63. Coherence and Transfer Functions for Plane 8.0A (270°) to 70° Farfield Microphone at 3.8% Thrust.

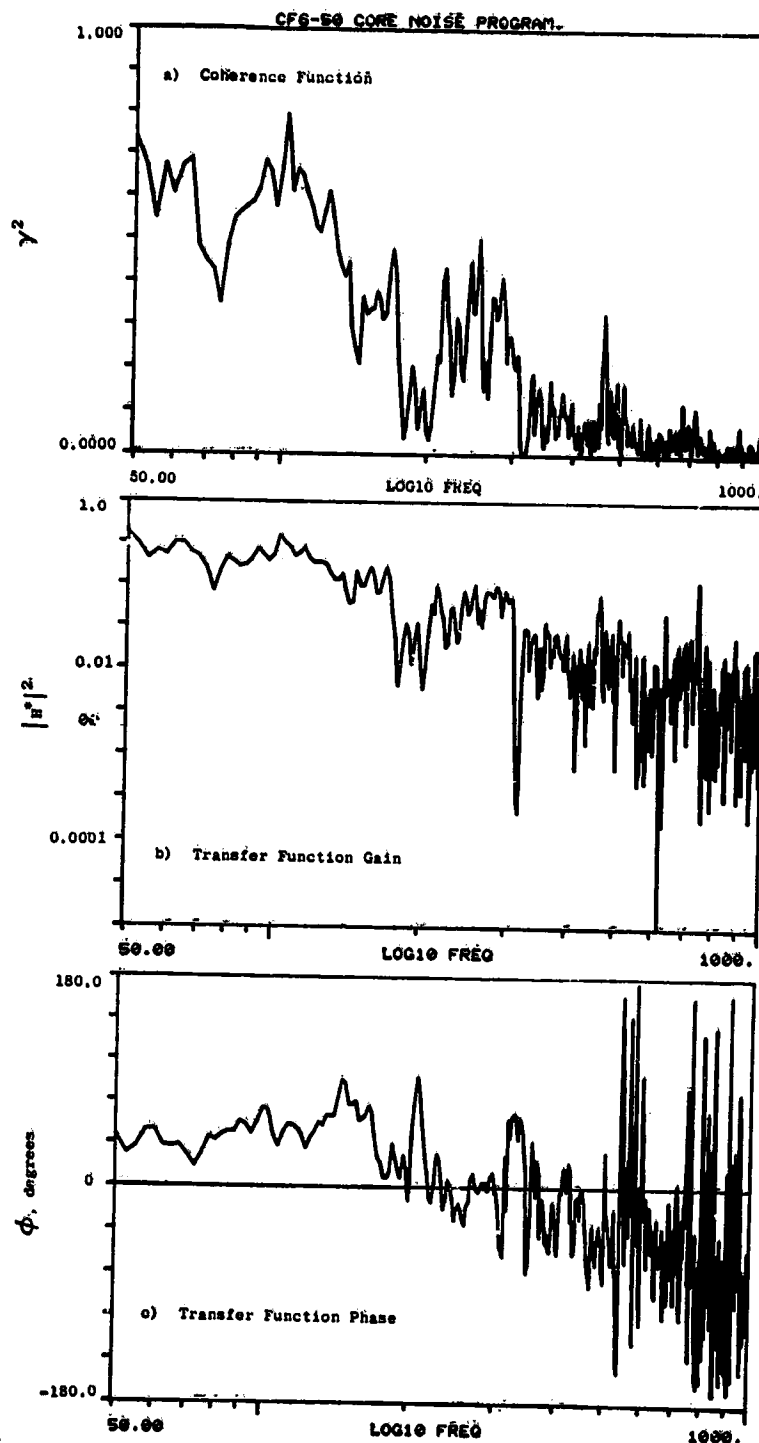


Figure A-64. Coherence and Transfer Functions for Plane 8.0A (270°) to 80° Farfield Microphone at 3.8% Thrust.

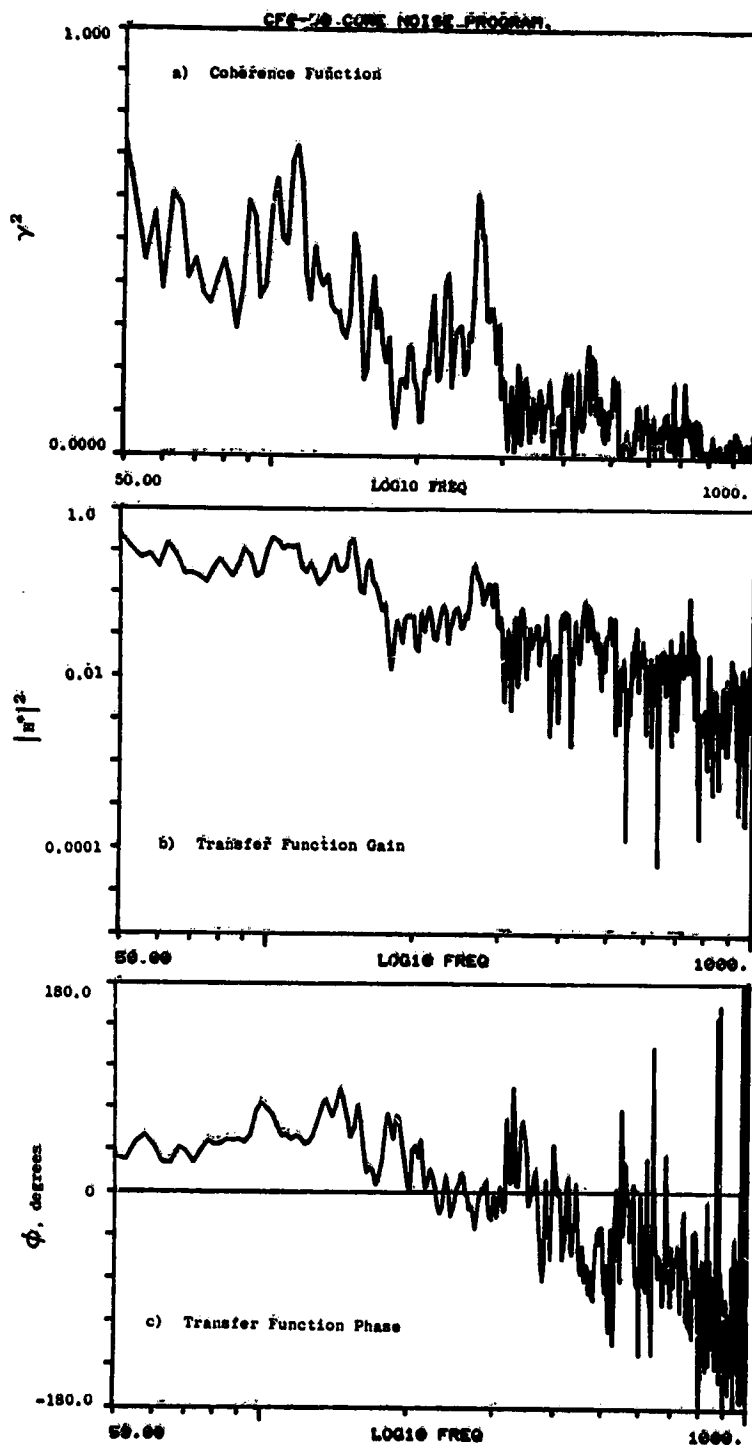


Figure A-65. Coherence and Transfer Functions for Plané 8.0A (270°) to 90° Farfield Microphone at 3.8% Thrust.

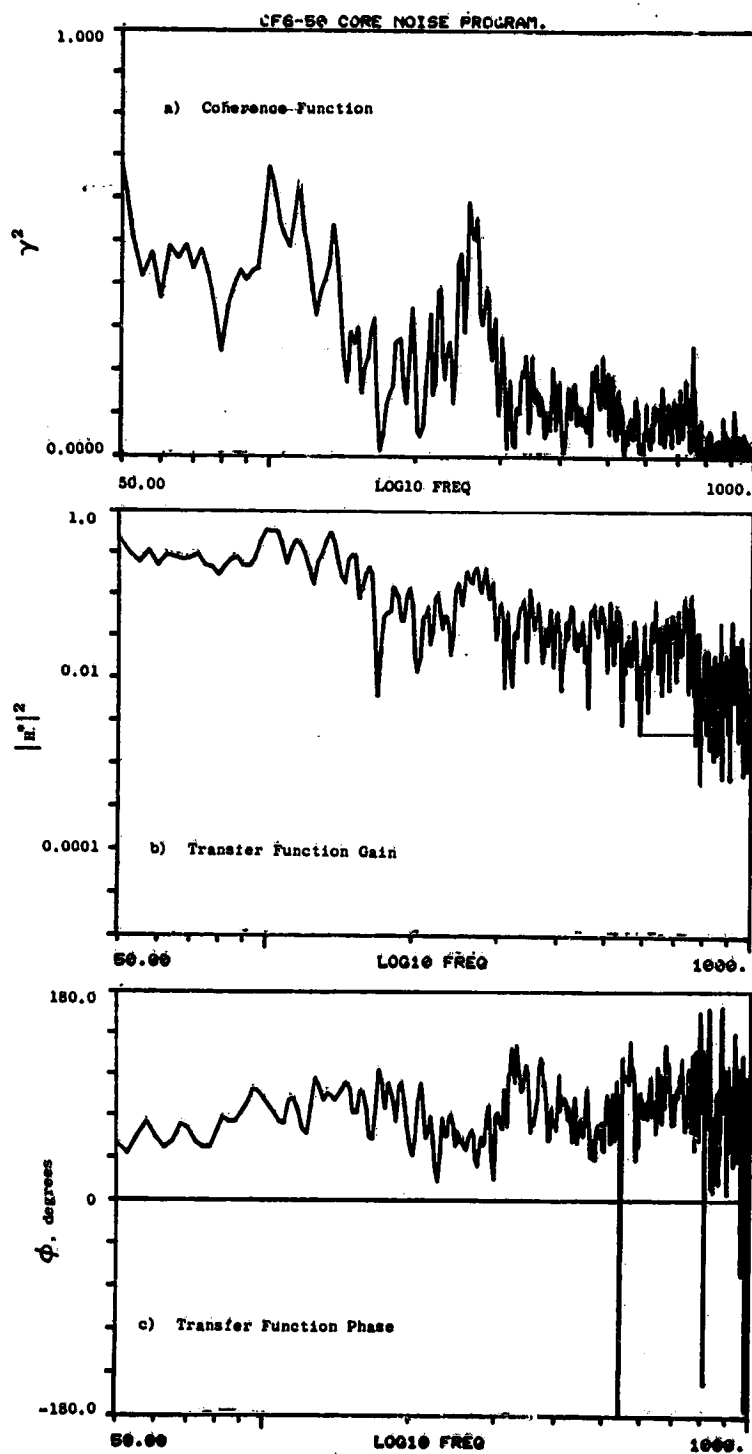


Figure A-66. Coherence and Transfer Functions for Plane 8.0A (270°) to 100° Farfield Microphone at 3.8% Thrust.

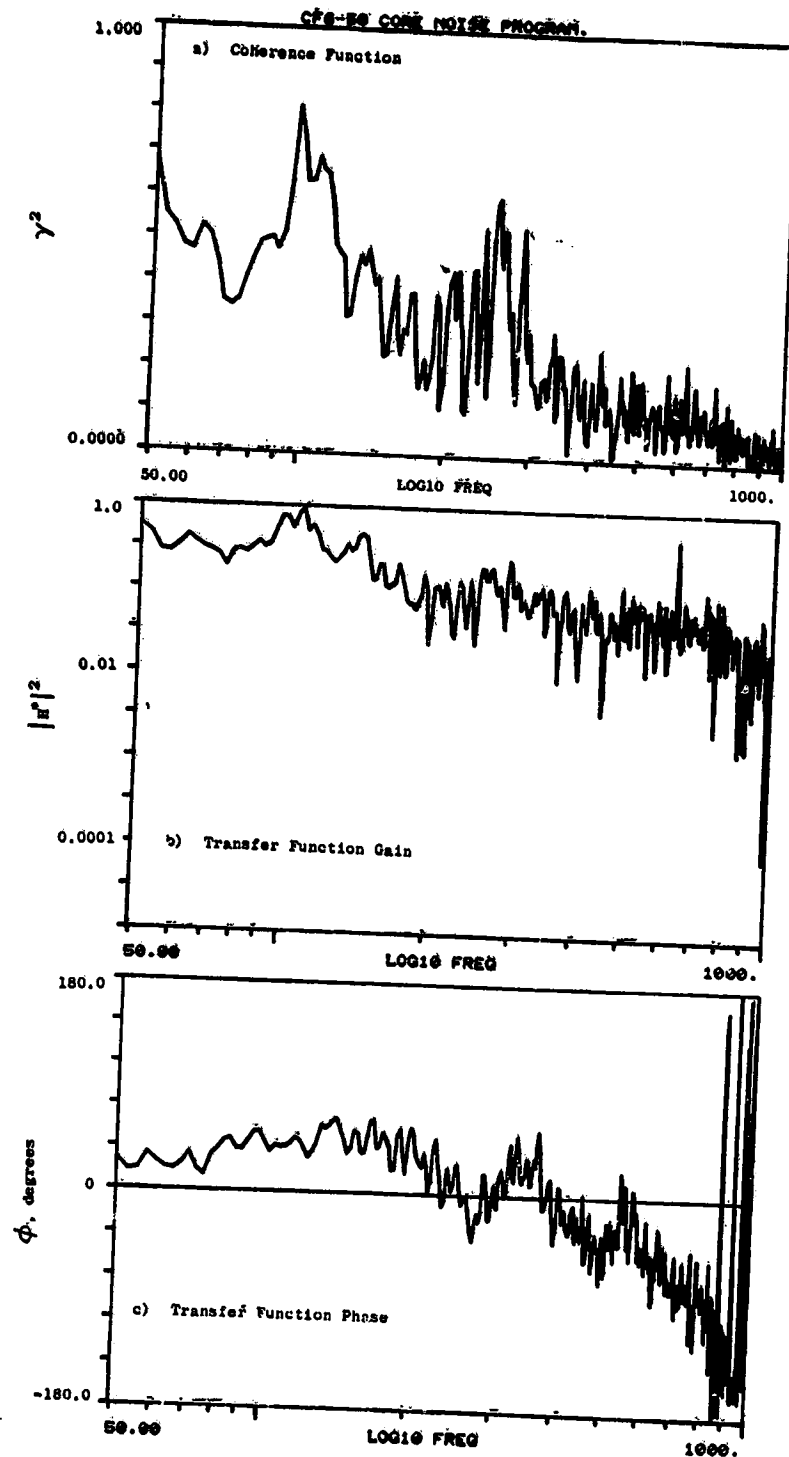


Figure A-67. Coherence and Transfer Functions for Plane 8.0A (270°) to 110° Farfield Microphone at 3.8% Thrust.

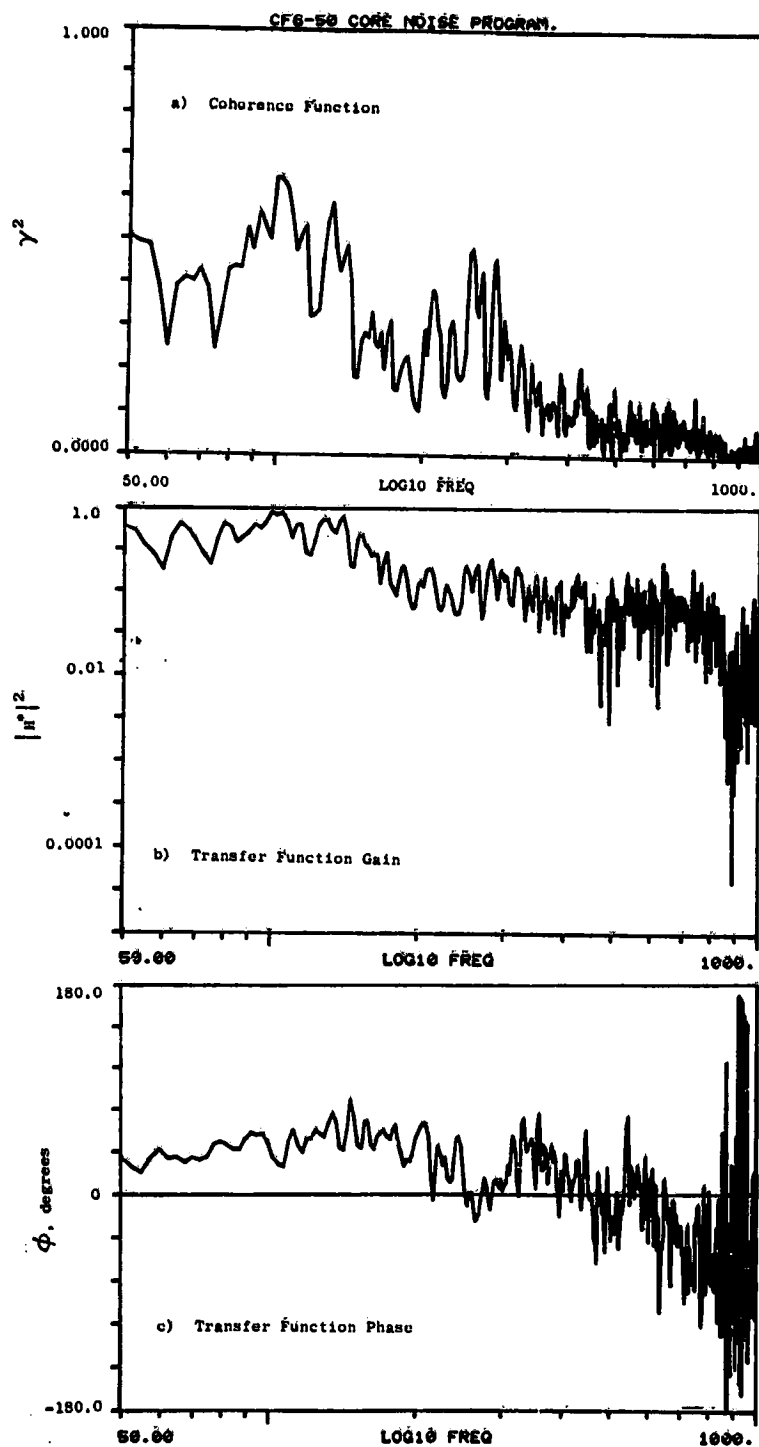


Figure A-68. Coherence and Transfer Functions for Plane 8.0A (270°) to 120° Farfield Microphone at 3.8% Thrust.

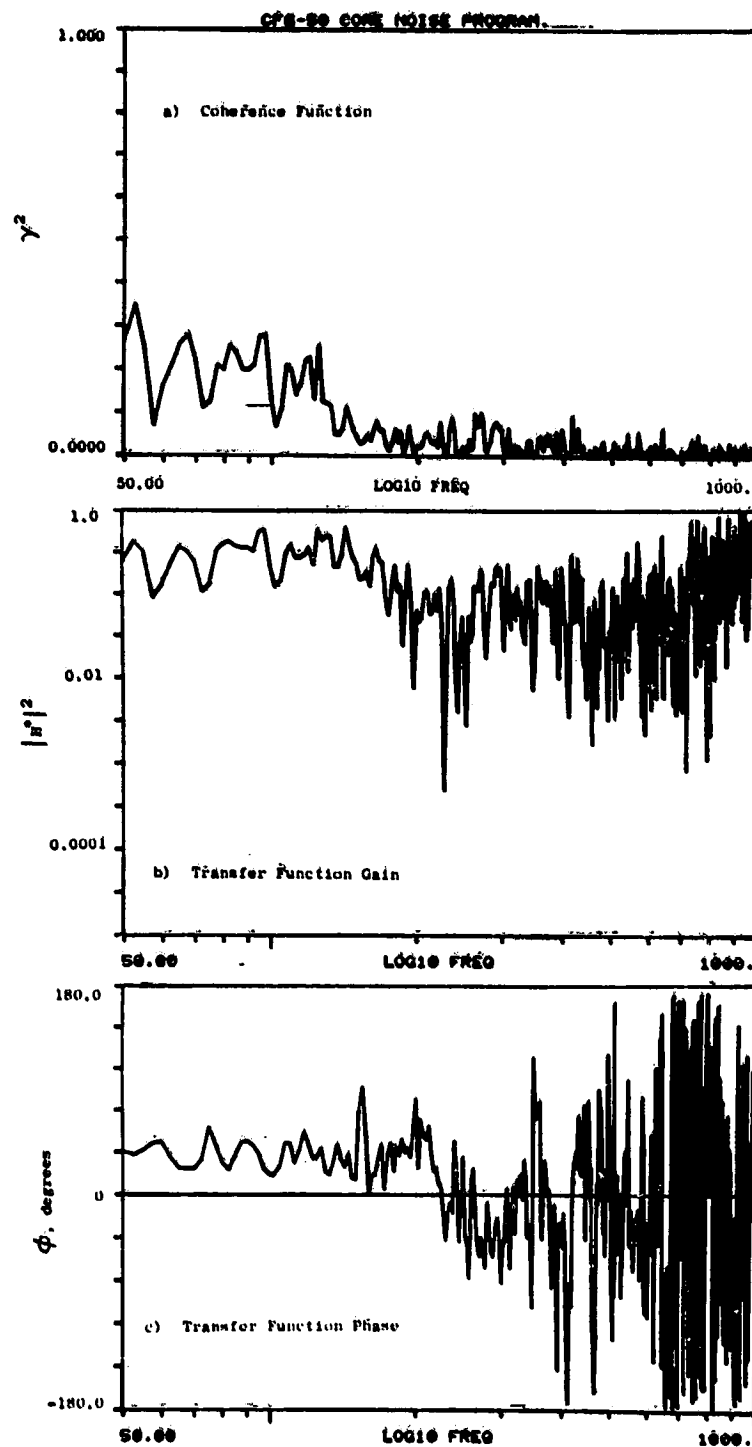


Figure A-69. Coherence and Transfer Functions for Plane 8.0A (27[°]) to 130[°] Farfield Microphone at 3.8% Thrust.

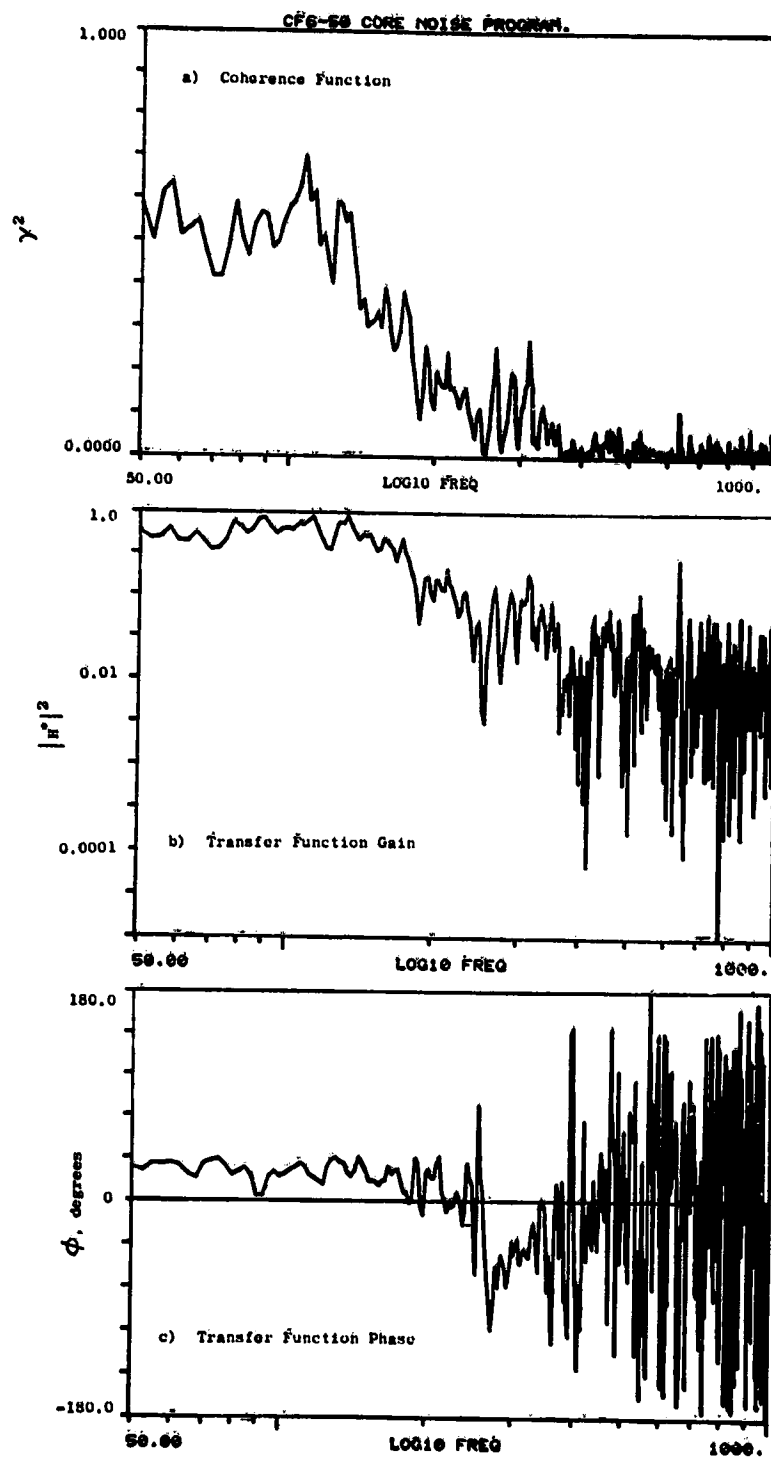


Figure A-70. Coherence and Transfer Functions for Plane 8.0A (270°) to 140° Farfield Microphone at 3.8% Thrust.

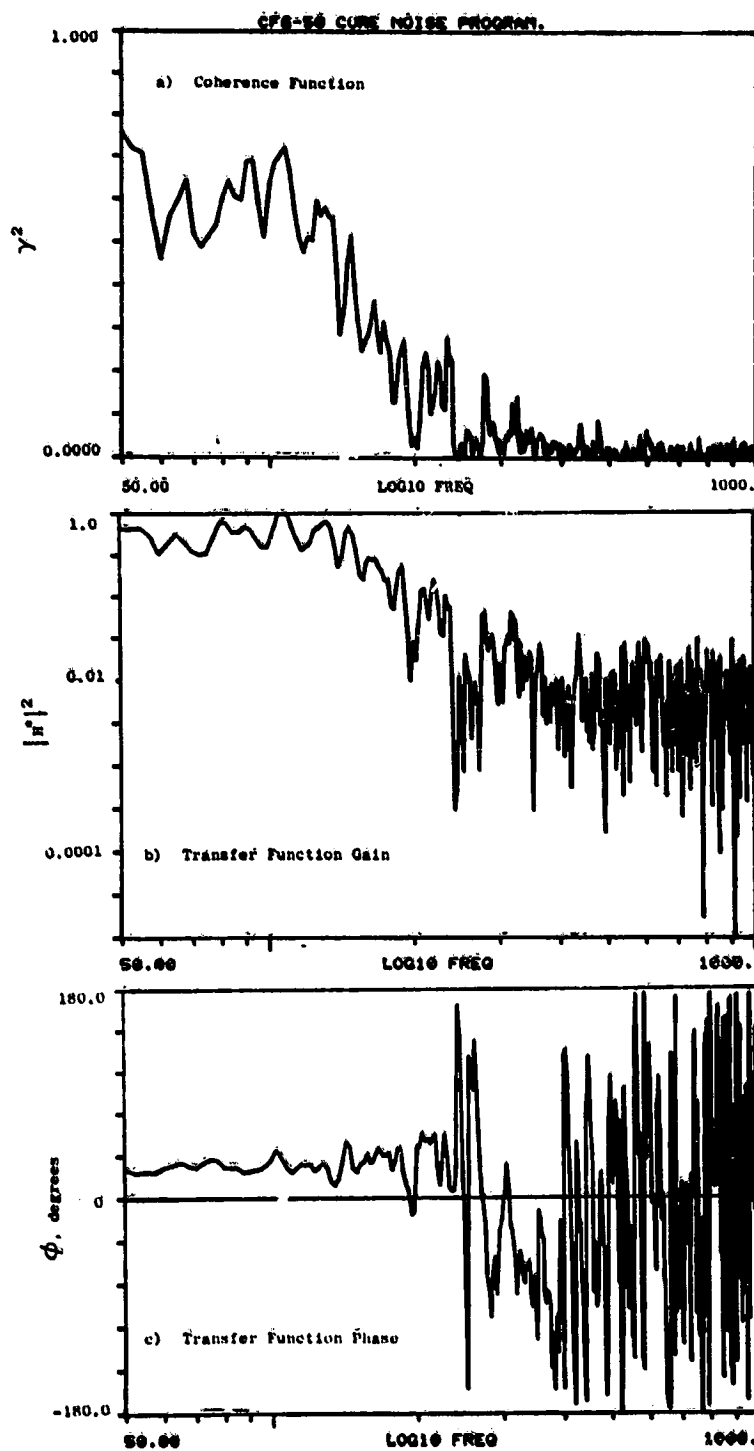


Figure A-71. Coherence and Transfer Functions for Plane 8.0A (270°) to 150° Farfield Microphone at 3.8% Thrust.

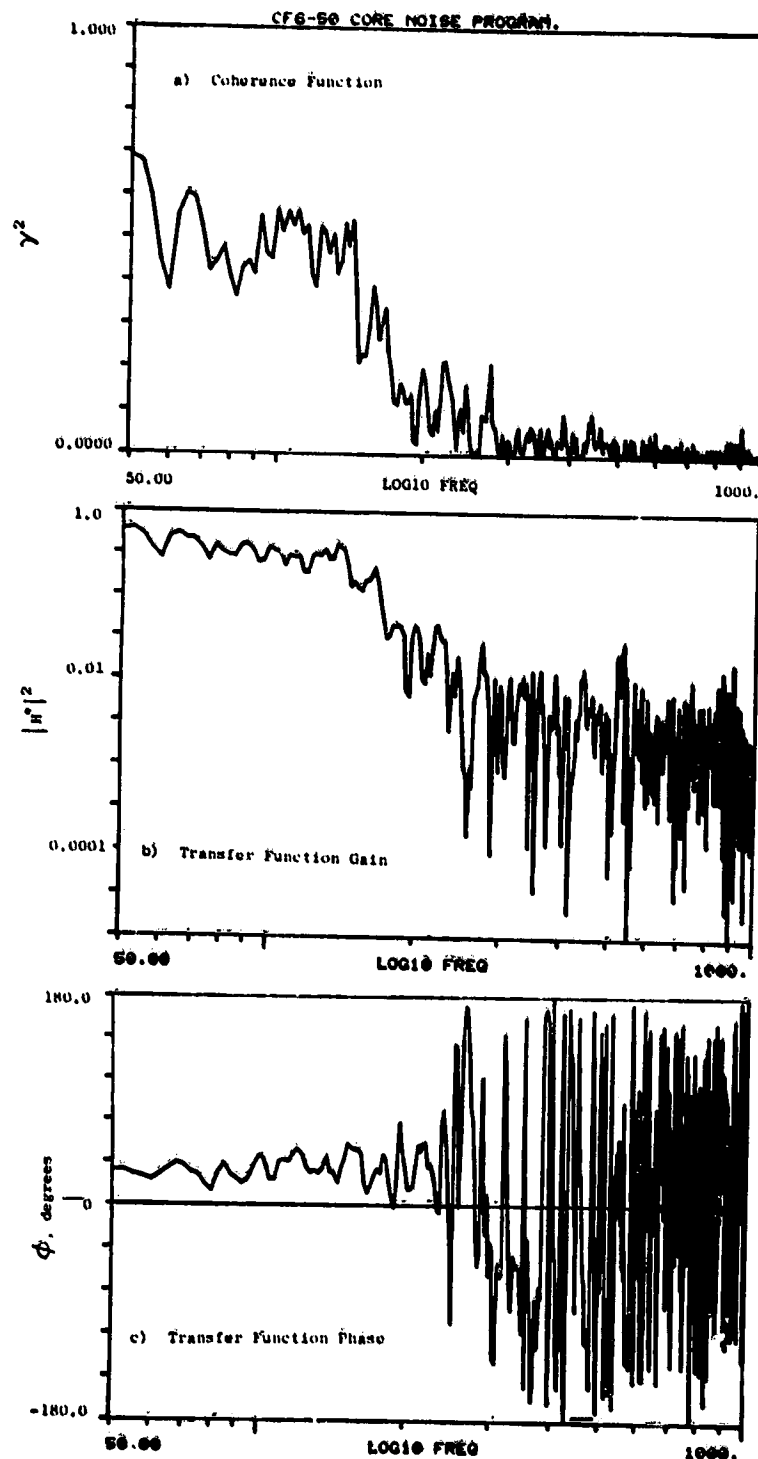


Figure A-72. Coherence and Transfer Functions for Plane 8.0A (270°) to 160° Farfield Microphone at 3.8% Thrust.

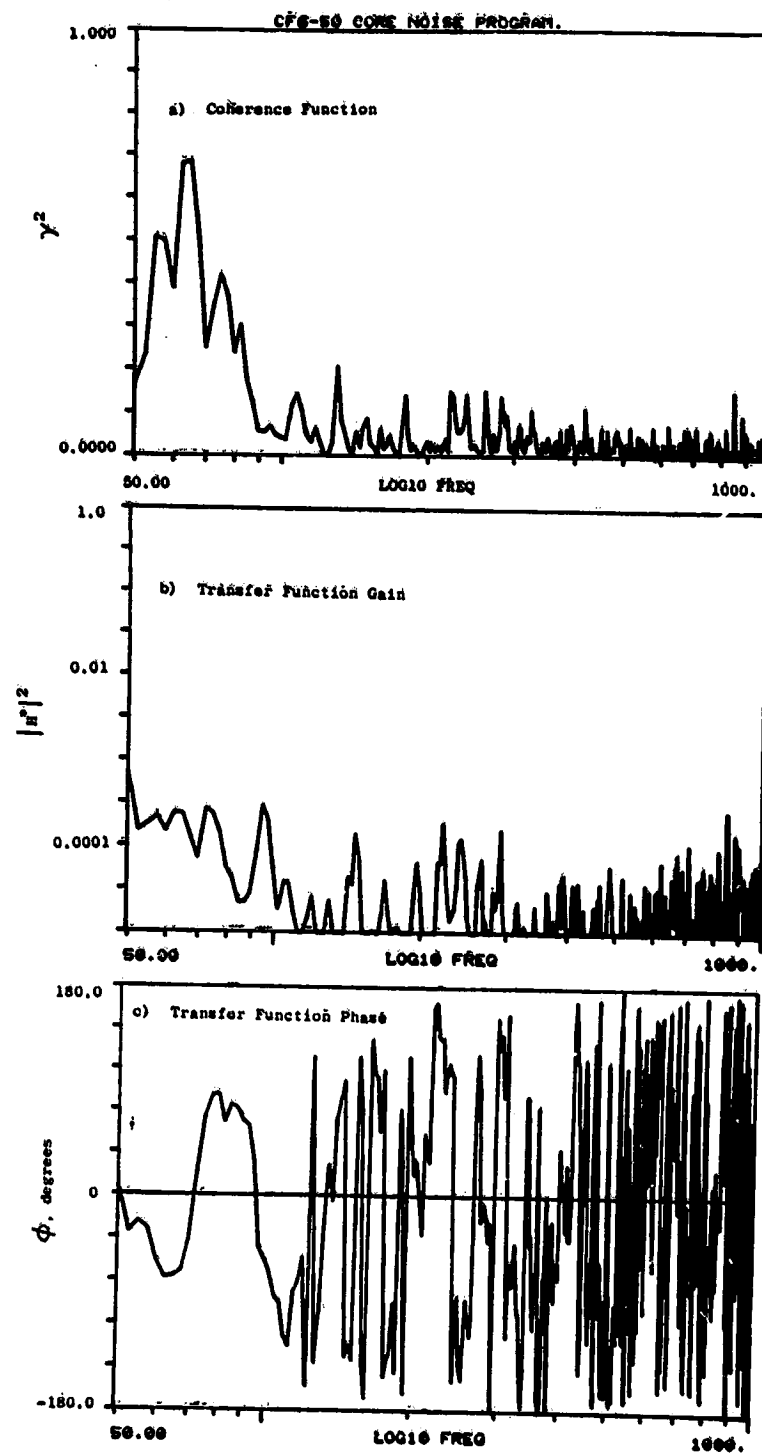


Figure A-73. Coherence and Transfer Functions for Plane 3.5 (102°) to 10° Farfield Microphone at 15% Thrust.

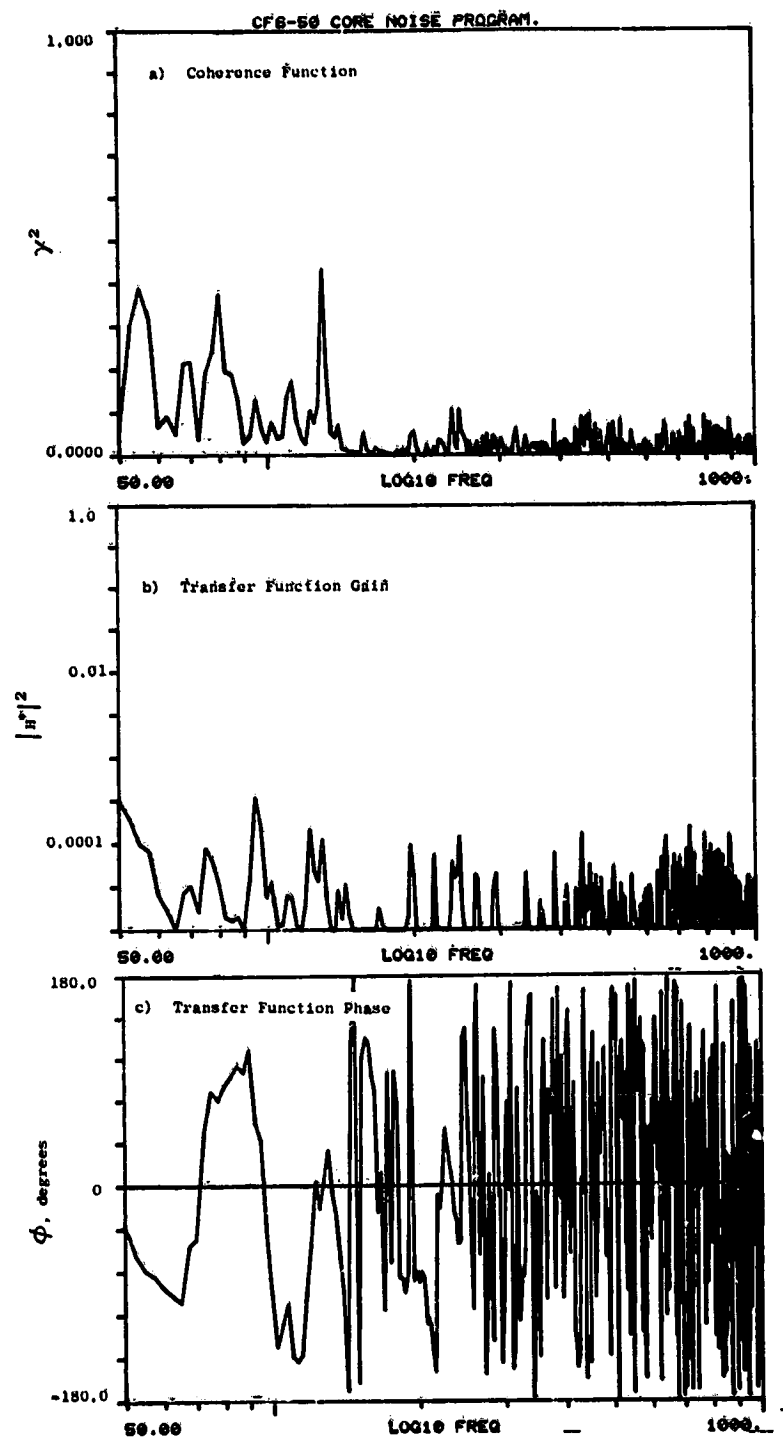


Figure A-74. Coherence and Transfer Functions for Plane 3.5 (102°) to 30° Farfield Microphone at 15% Thrust.

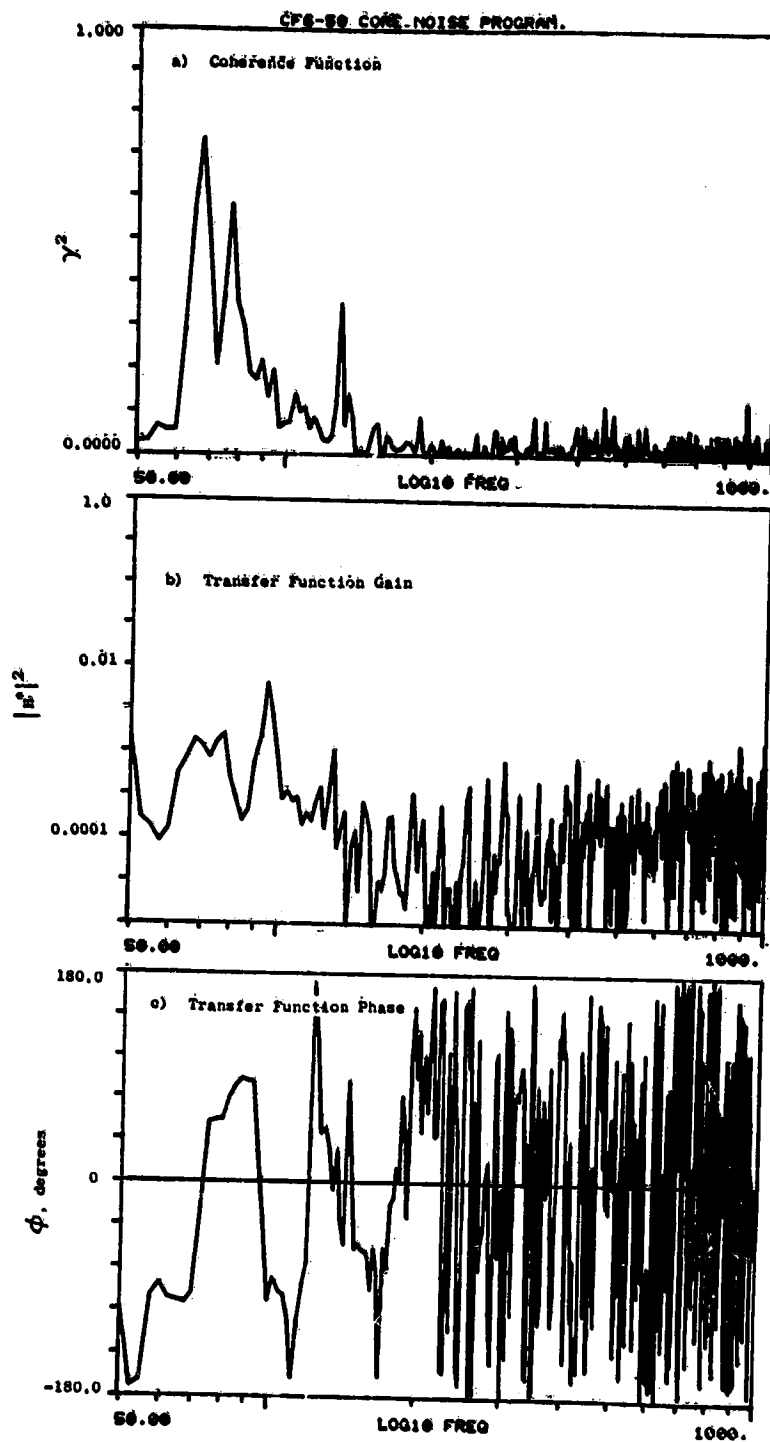


Figure A-75. Coherence and Transfer Functions for Plane 3.5 (102°) to 40° Farfield Microphone at 15% Thrust.

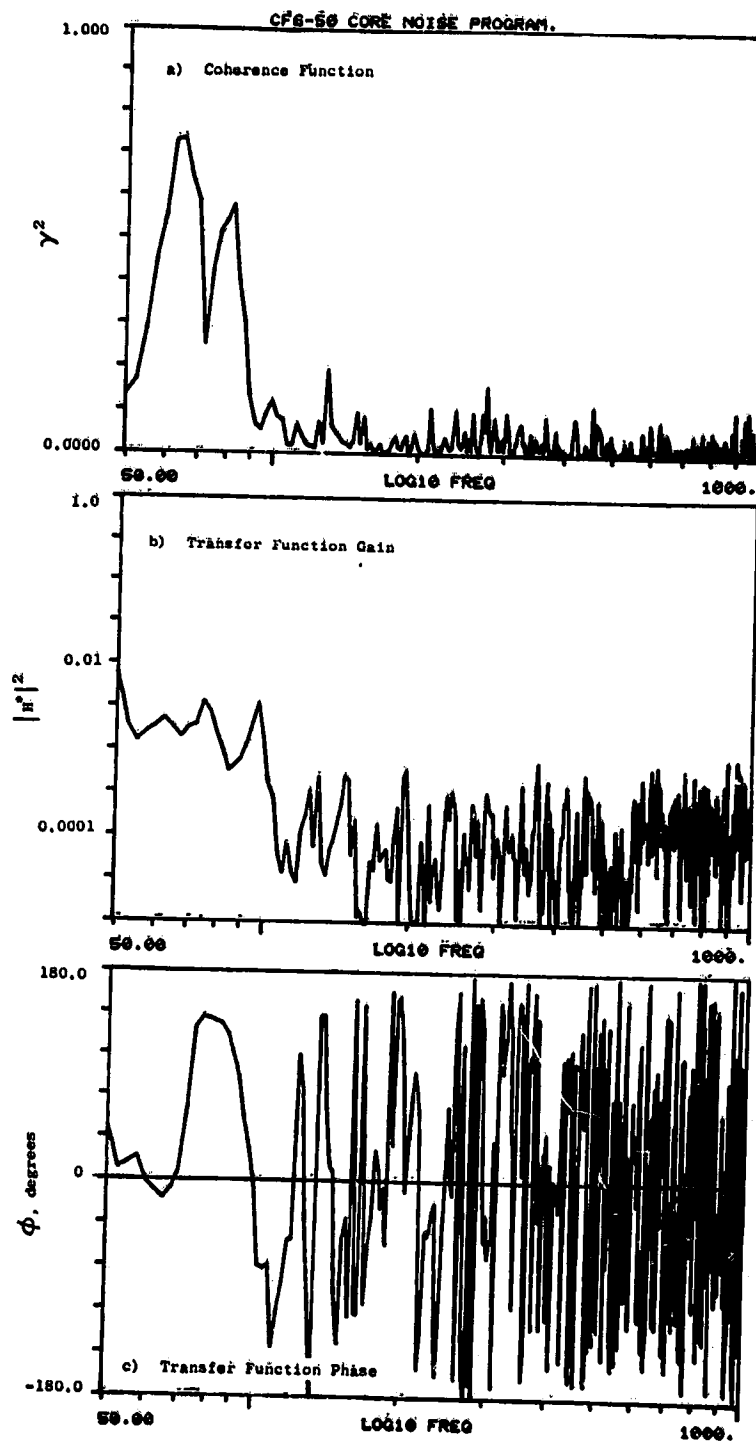


Figure A-76. Coherence and Transfer Functions for Plane 3.5 (102°) to 50° Farfield Microphone at 15% Thrust.

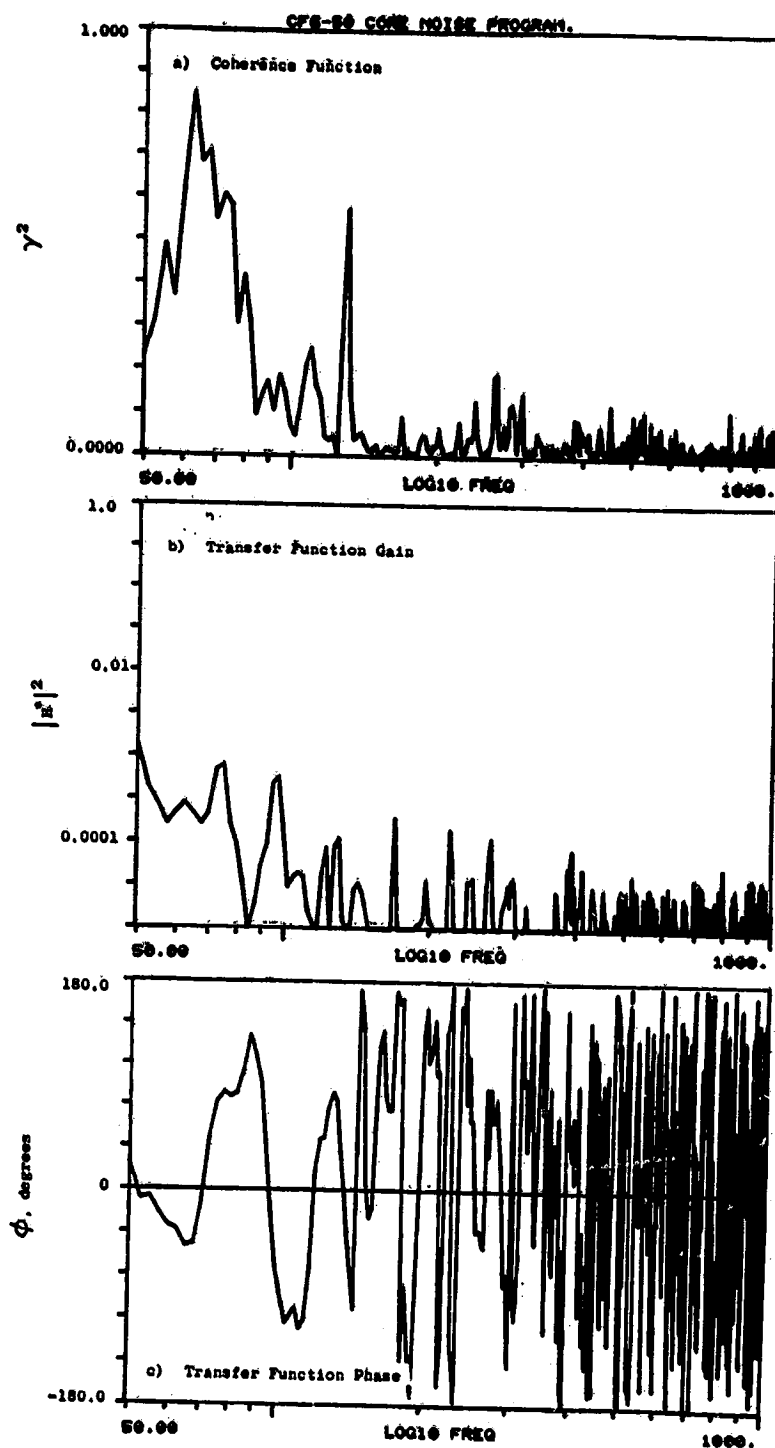


Figure A-77. Coherence and Transfer Functions for Plane 3.5 (102°) to 60° Farfield Microphone at 15% Thrust.

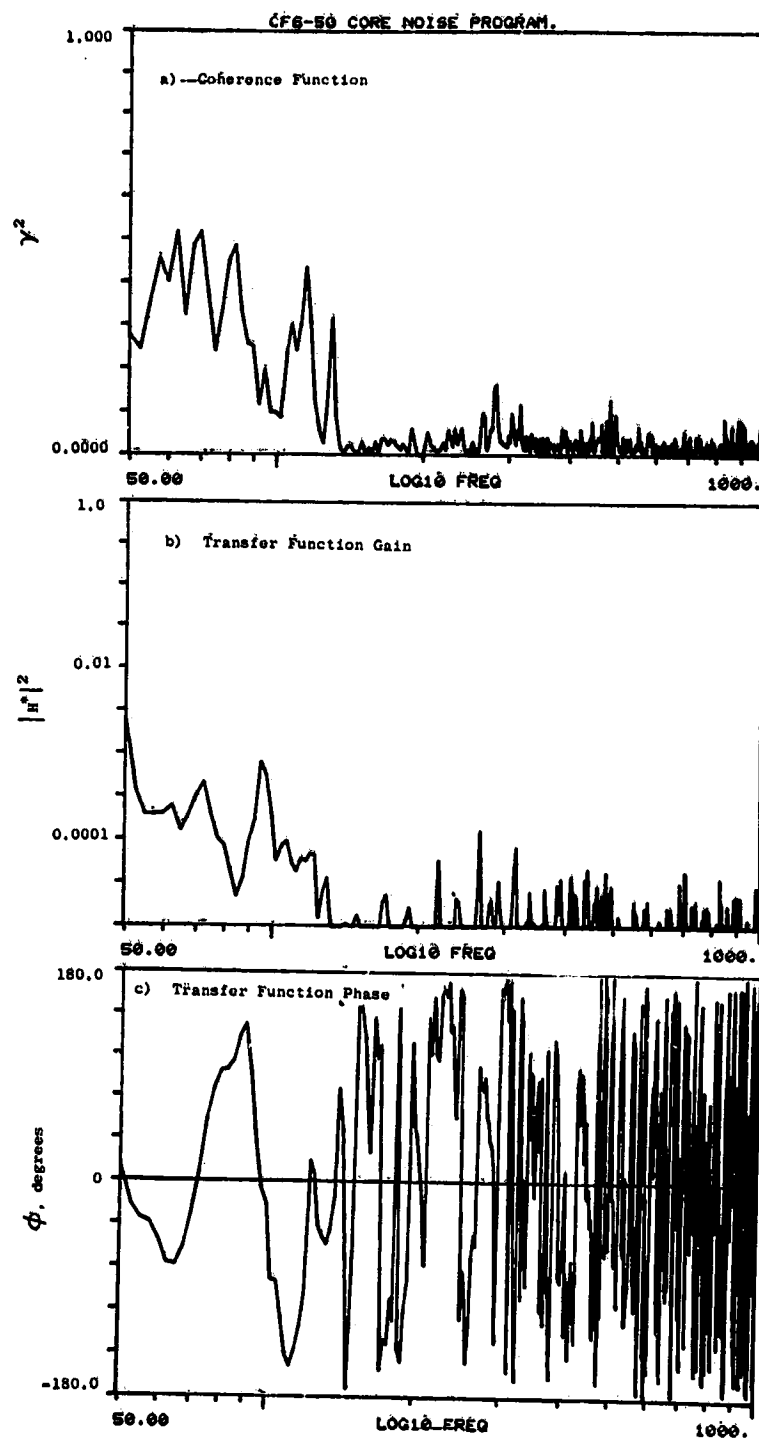


Figure A-78. Coherence and Transfer Functions for Plane 3.5 (102°) to 70° Farfield Microphone at 15% Thrust.

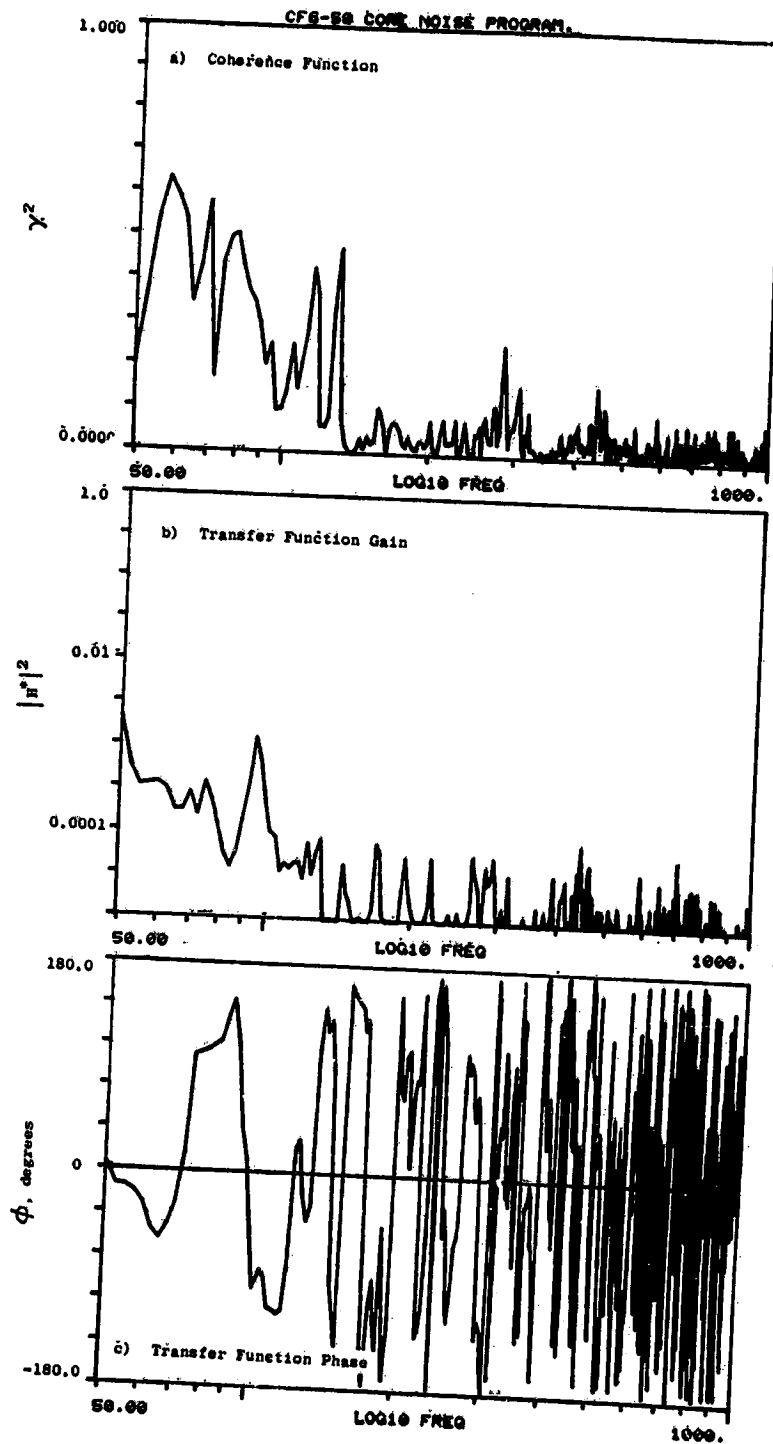


Figure A-79. Coherence and Transfer Functions for Plane 3.5 (102°) to 80° Farfield Microphone at 15% Thrust.

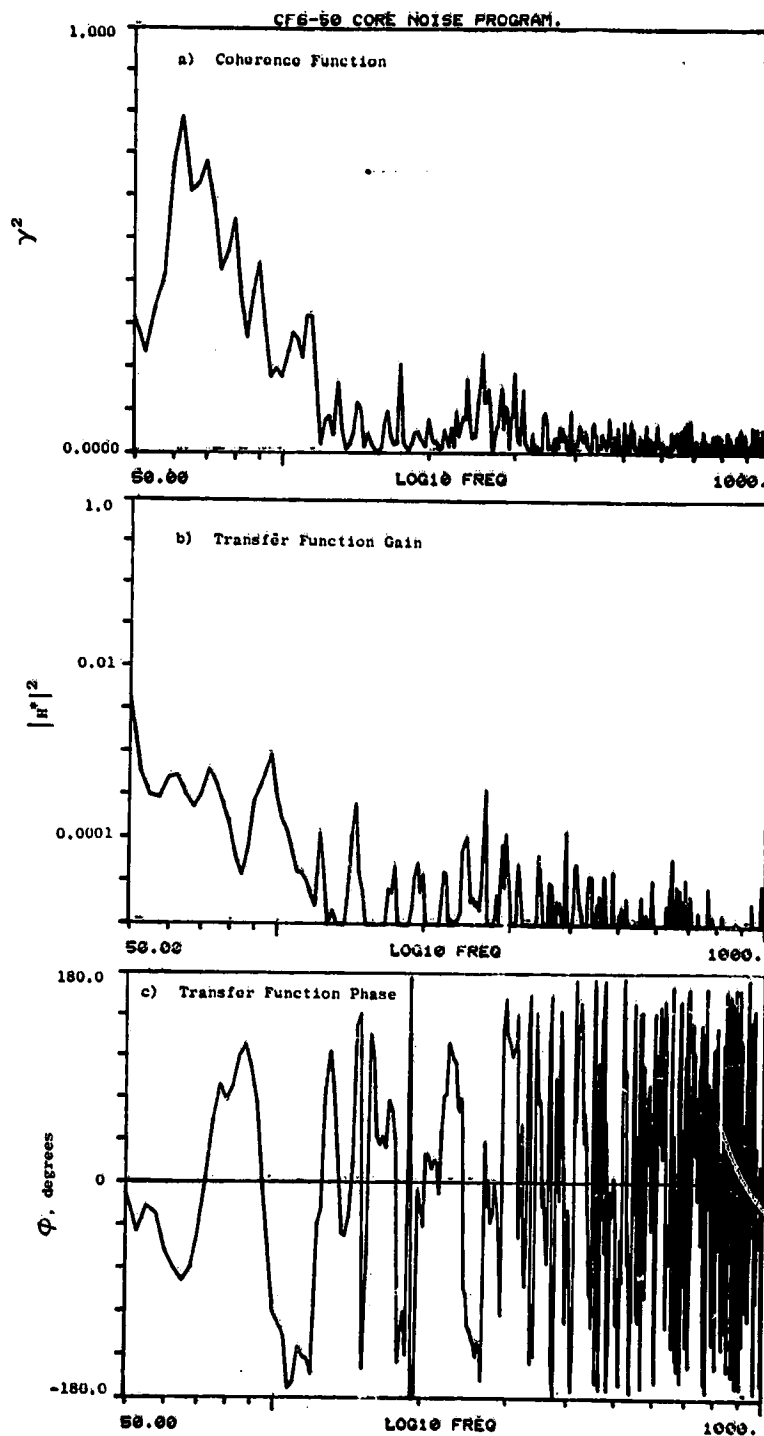


Figure A-80. Coherence and Transfer Functions for Plane 3.5 (102°) to 90° Farfield Microphone at 15% Thrust.

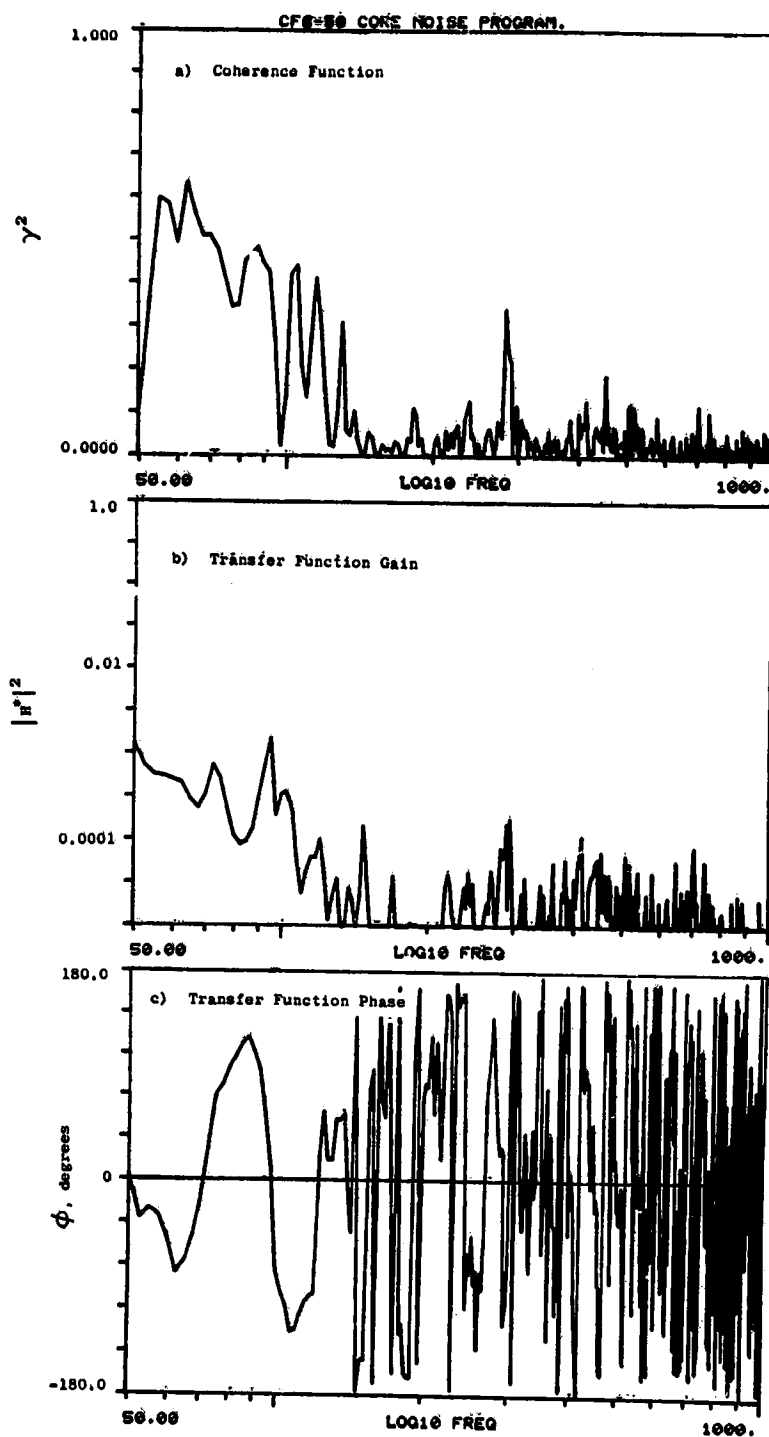


Figure A-81. Coherence and Transfer Functions for Plane 3.5 (102°) to 100° Farfield Microphone at 15% Thrust.

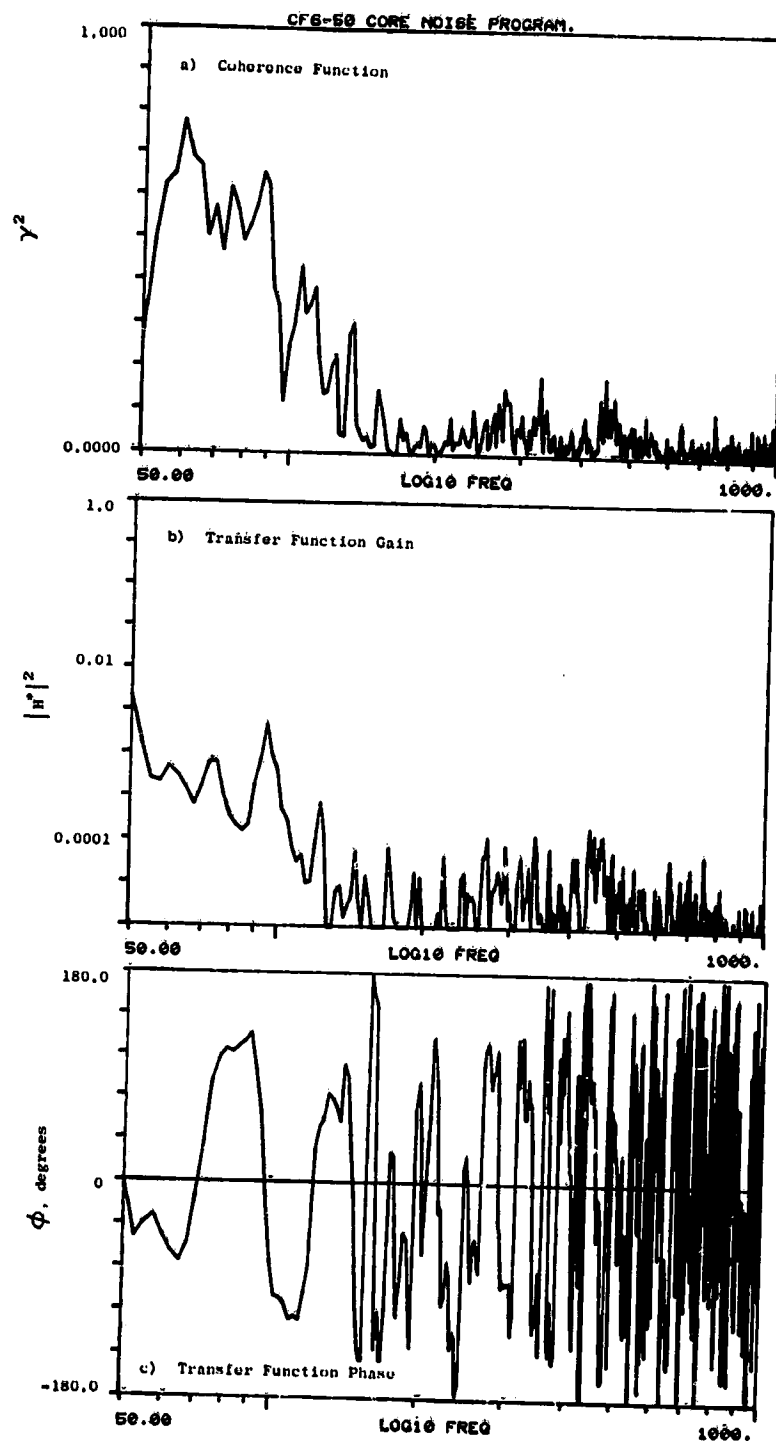


Figure A-82. Coherence and Transfer Functions for Plane 3.5 (102°) to 110° Farfield Microphone at 15% Thrust.

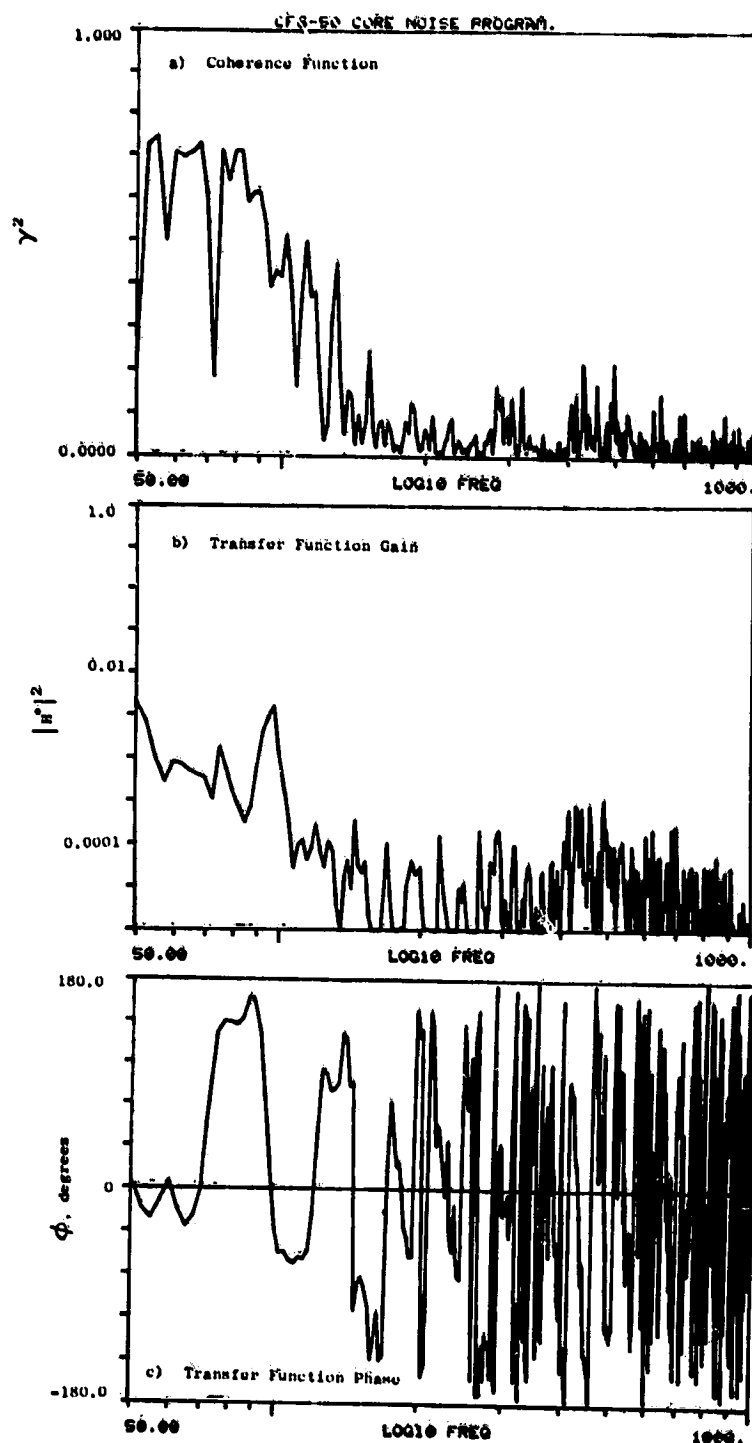


Figure A-83. Coherence and Transfer Functions for Plane 3.5 (102°) to 120° Farfield Microphone at 15% Thrust.

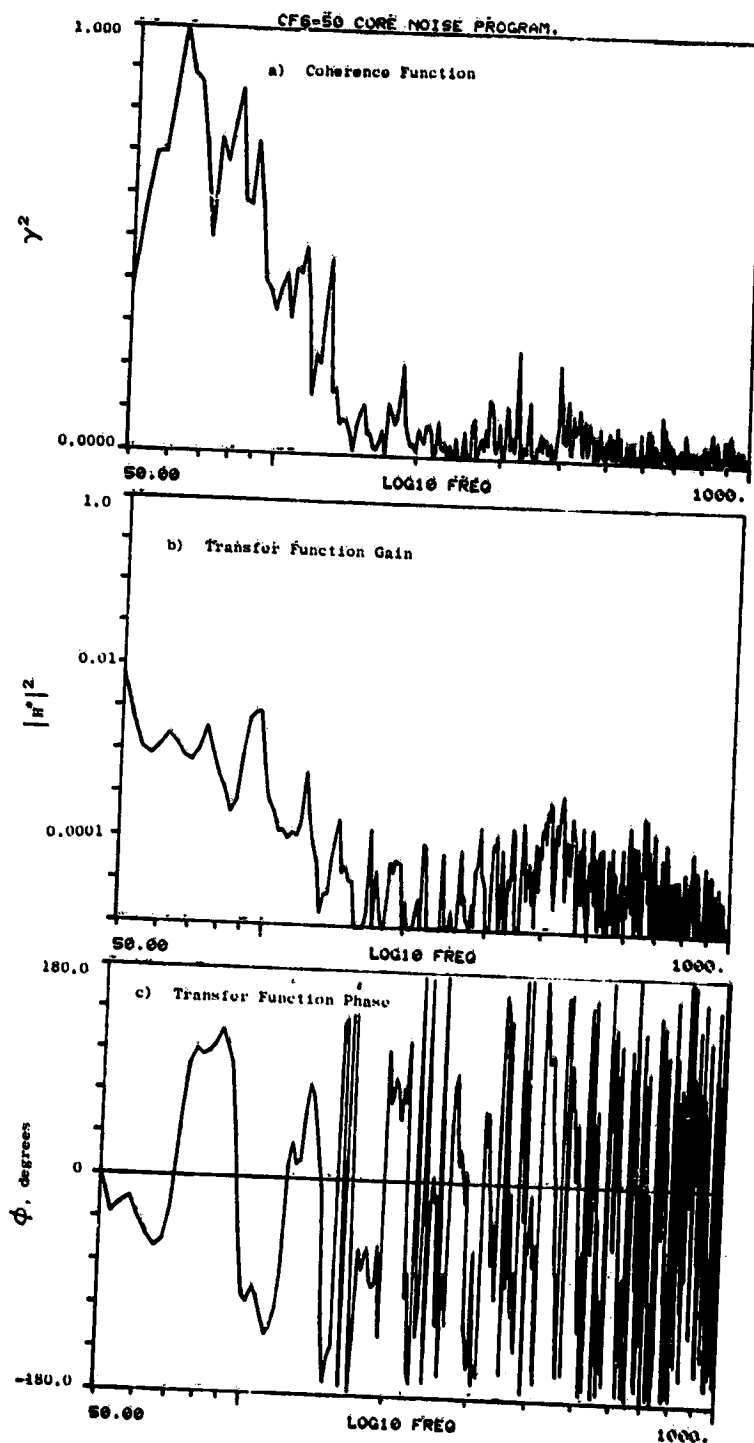


Figure A-84. Coherence and Transfer Functions for Plane 3.5 (102°) to 130° Farfield Microphone at 15% Thrust.

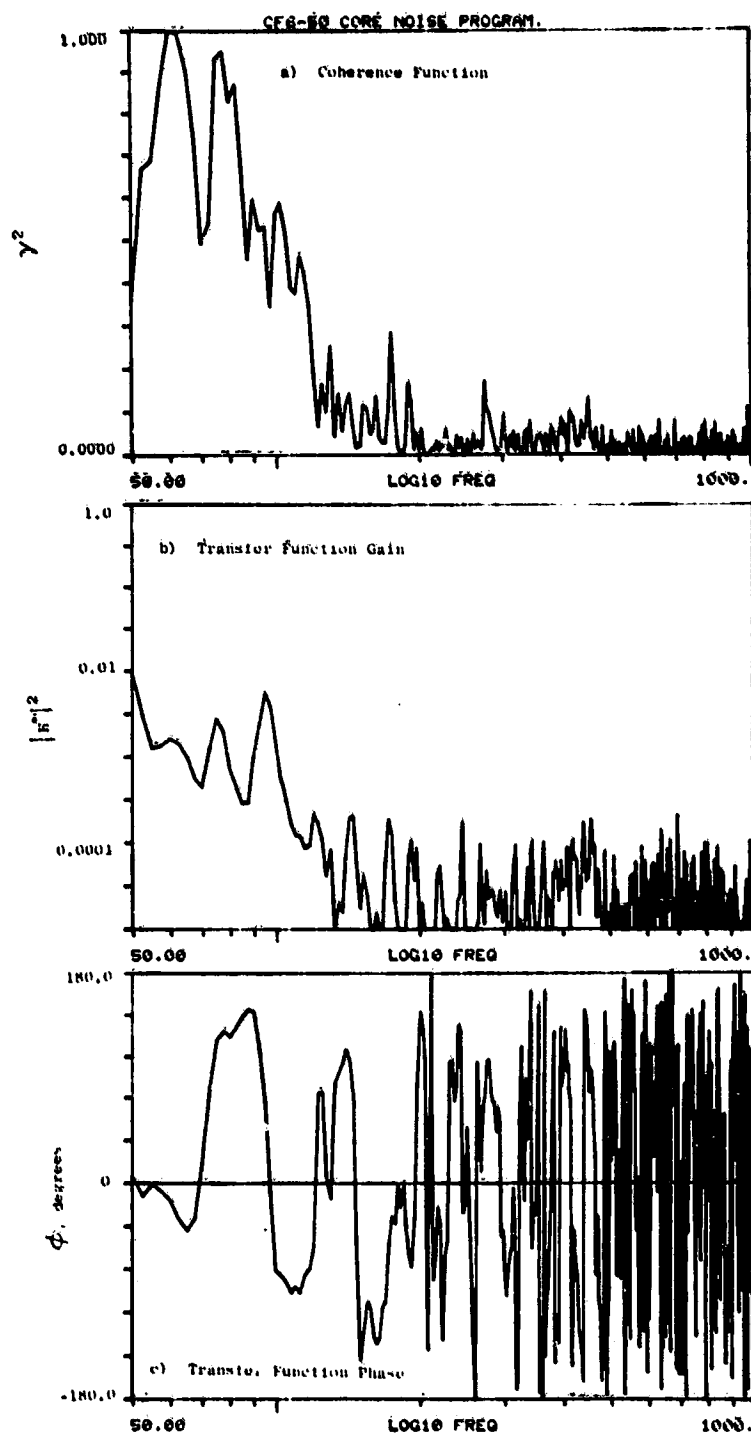


Figure A-85. Coherence and Transfer Functions for Plane 3.5 (102°) to 140° Farfield Microphone at 15% Thrust.

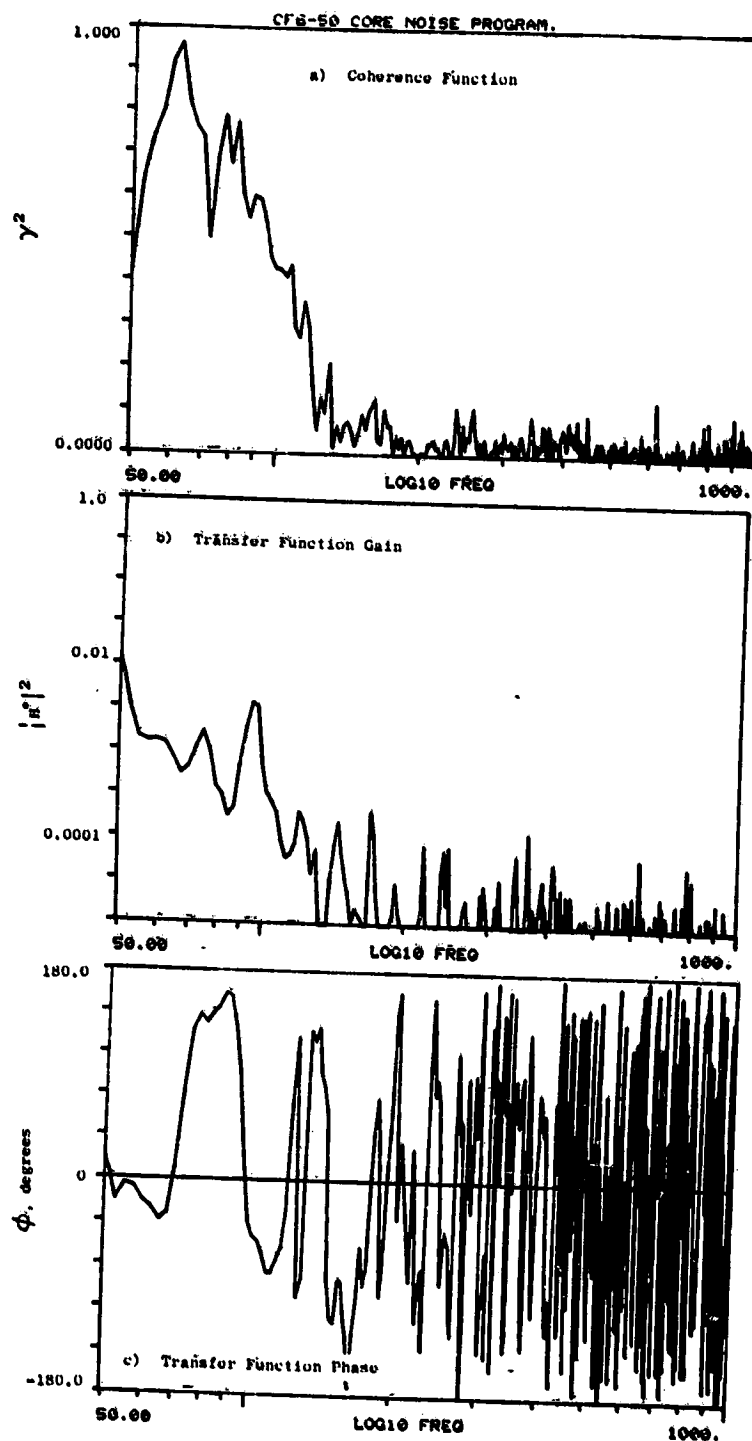


Figure A-86. Coherence and Transfer Functions for Plane 3.5 (102°) to 150° Farfield Microphone at 15% Thrust.

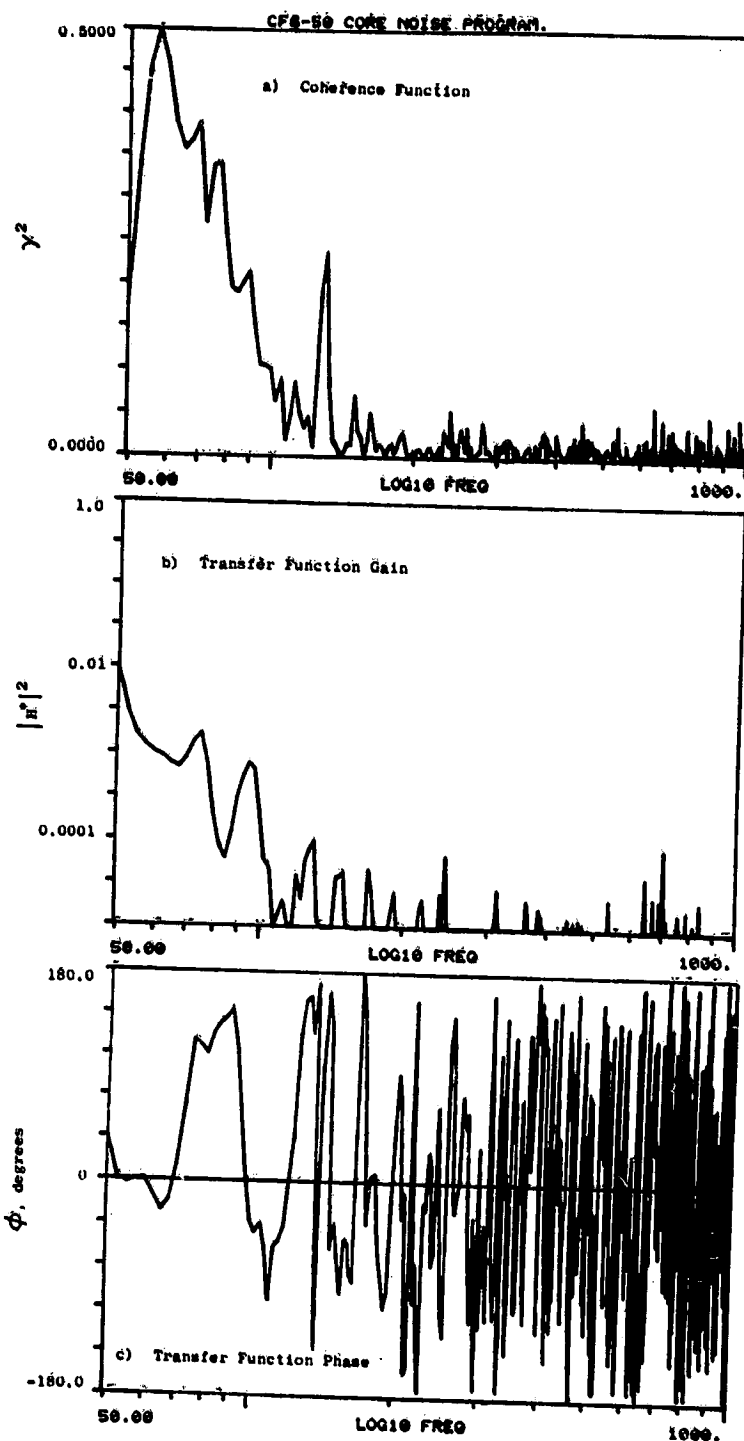


Figure A-87. Coherence and Transfer Functions for Plane 3.5 (102°) to 160° Farfield Microphone at 15% Thrust.

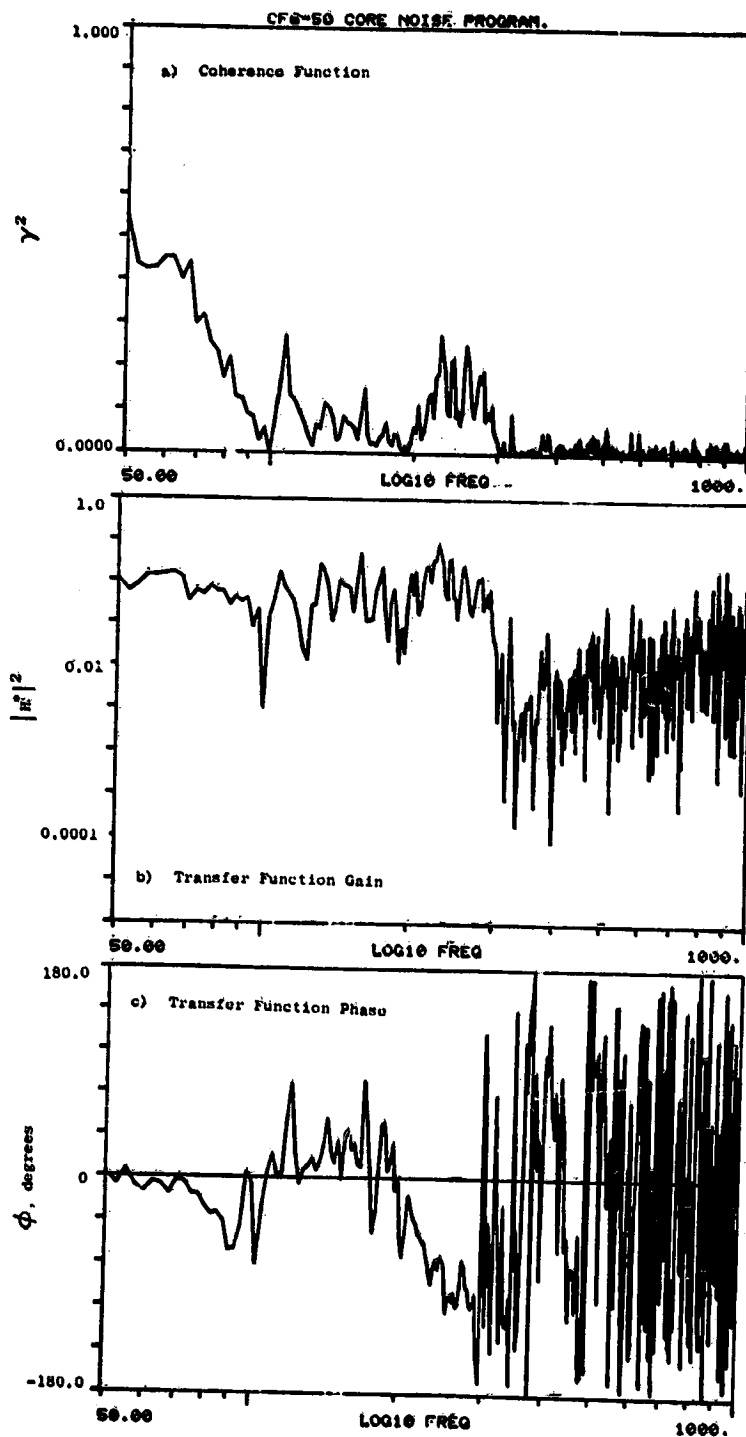


Figure A-88. Coherence and Transfer Functions for Plane 8.0A (270°) to 10° Farfield Microphone at 15% Thrust.

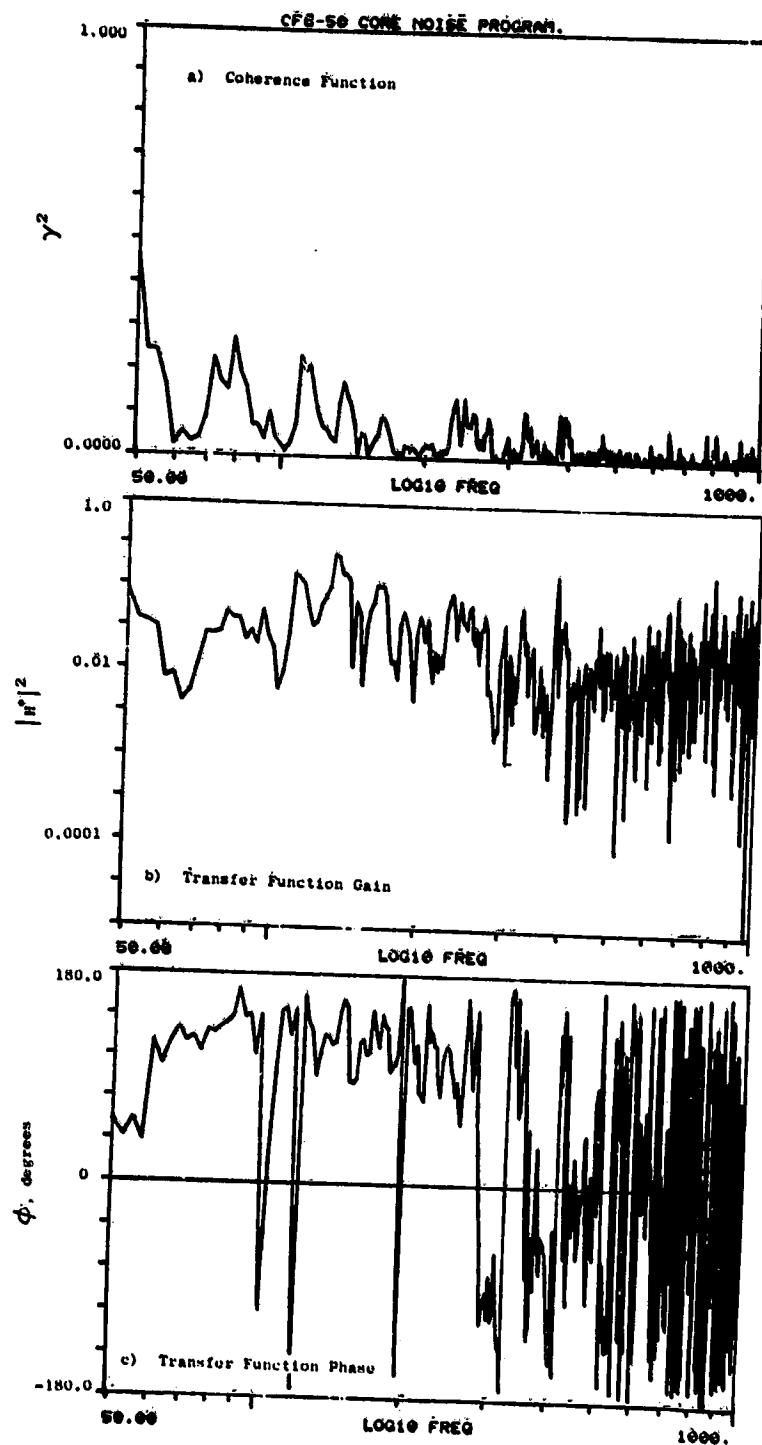


Figure A-89. Coherence and Transfer Functions for Plane 8.0A (270°) to 30° Farfield Microphone at 15% Thrust.

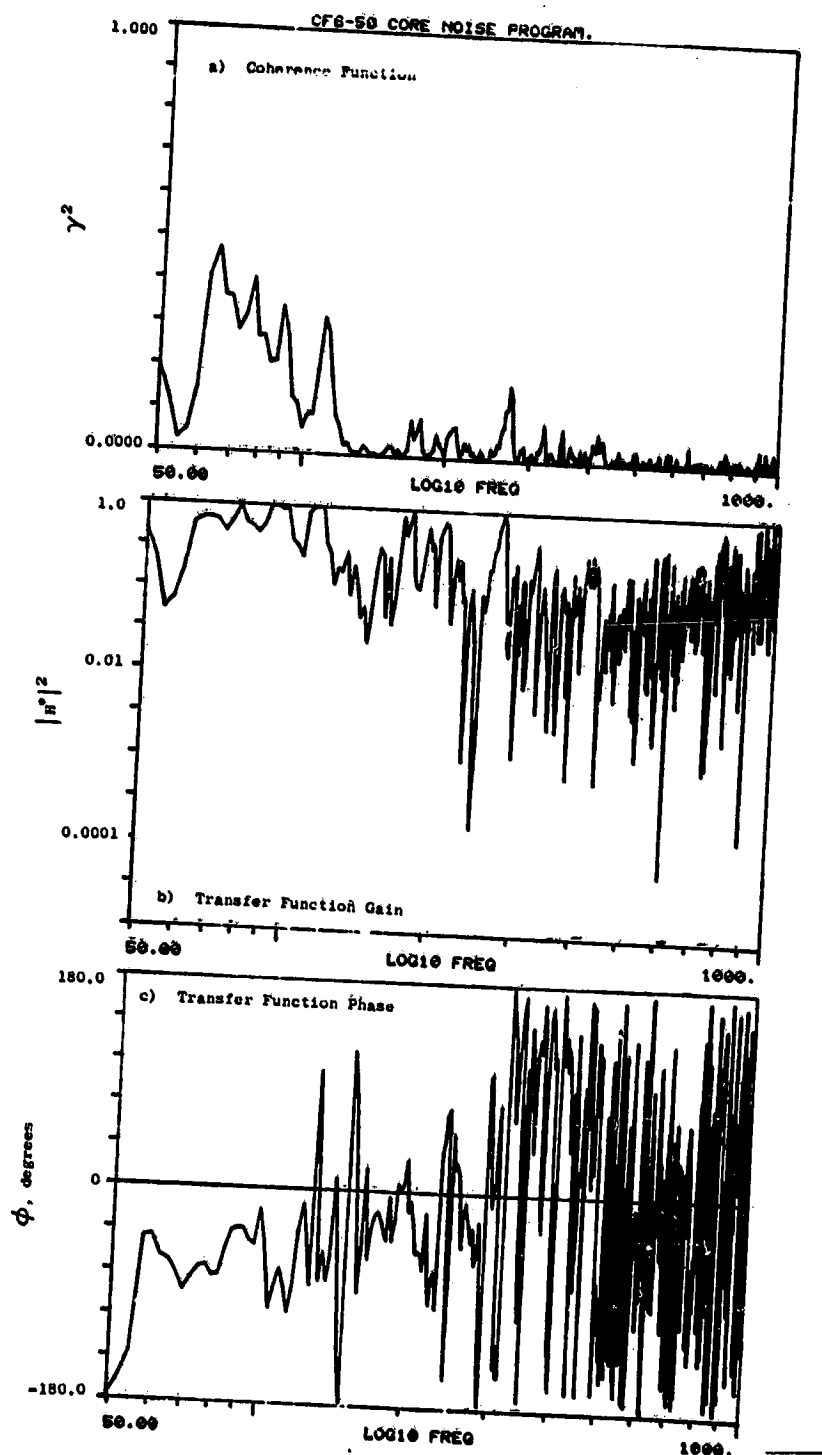


Figure A-90. Coherence and Transfer Functions for Plane 8.0A (270°) to 40° Farfield Microphone at 15% Thrust.

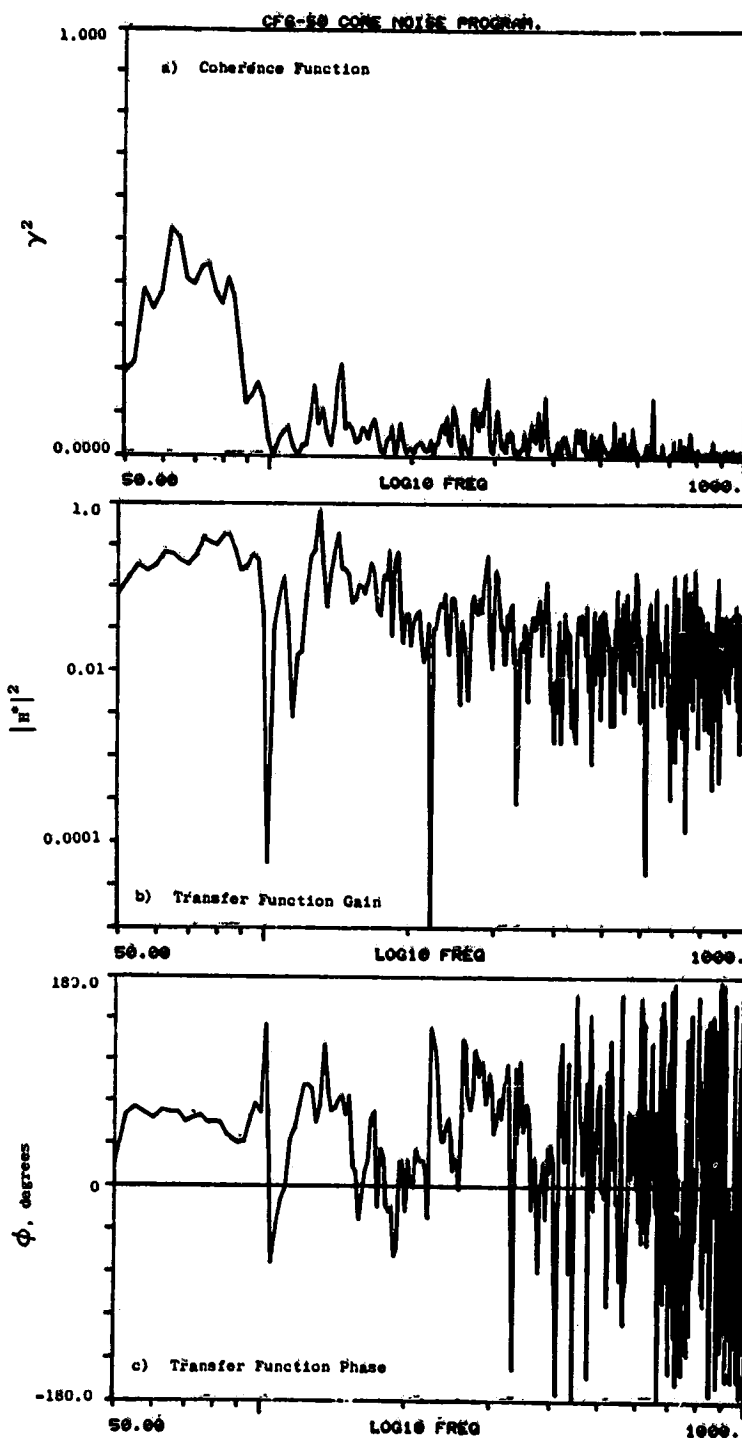


Figure A-91. Coherence and Transfer Functions for Plane 8.0A (270°) to 50° Farfield Microphone at 15% Thrust.

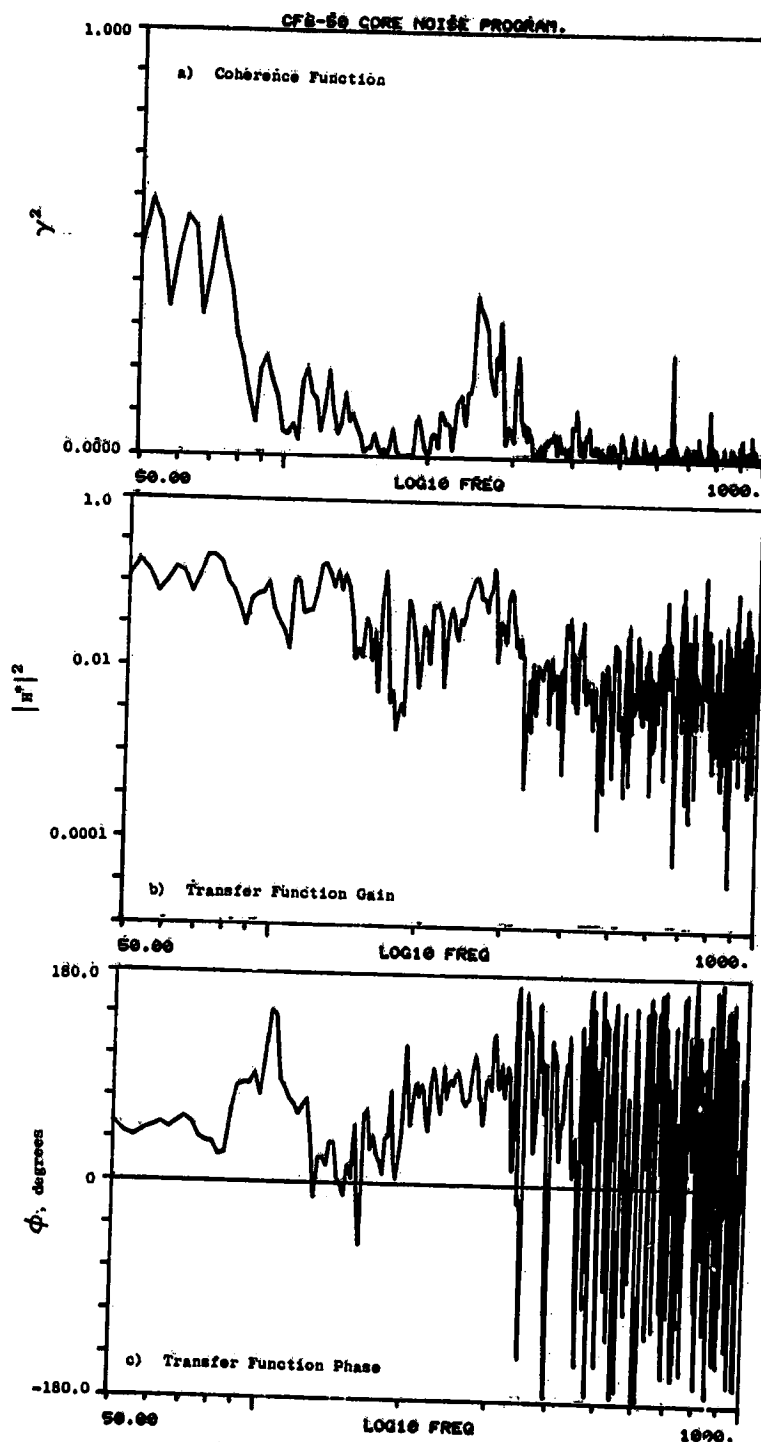


Figure A-92. Coherence and Transfer Functions for Plane 8.0A (270°) to 60° Farfield Microphone at 15% Thrust.

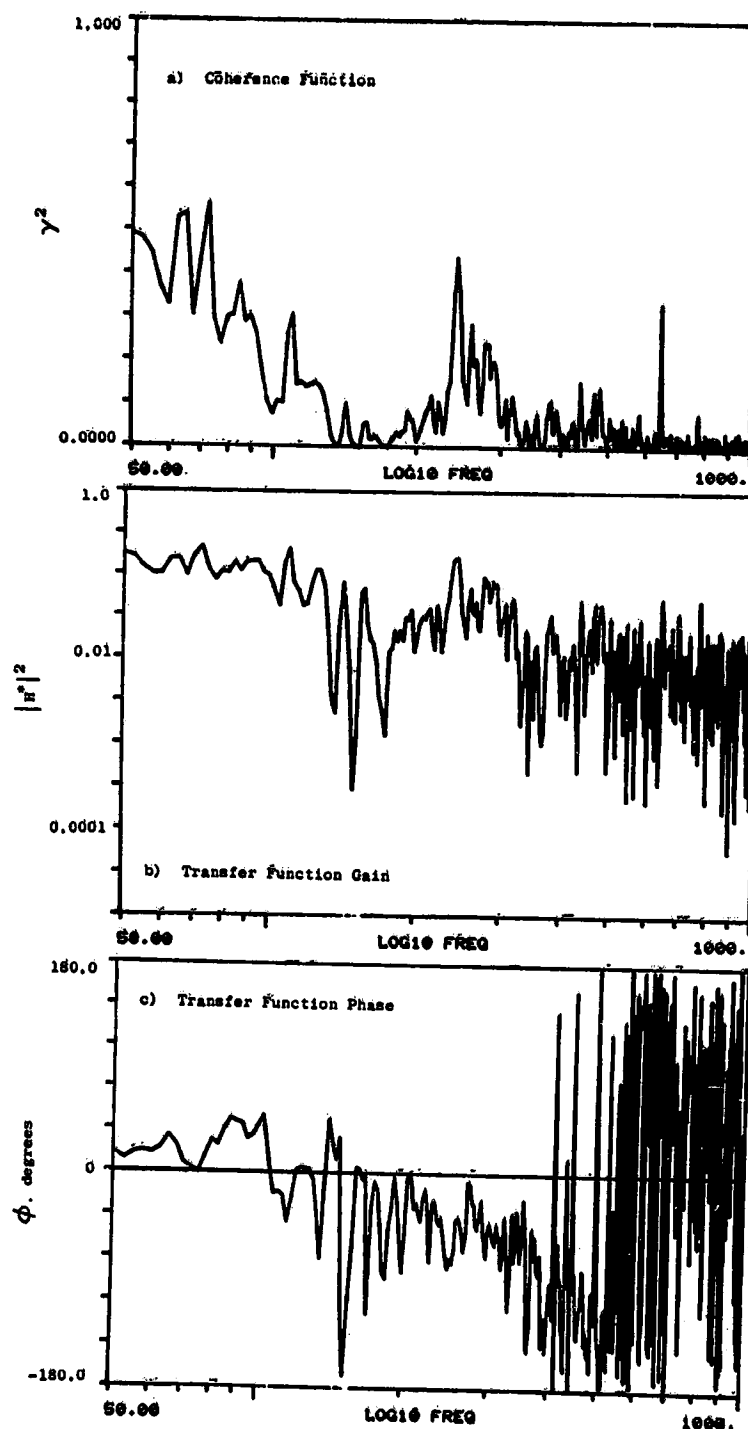


Figure A-93. Coherence and Transfer Functions for Plane 8.0A (270°) to 70° Farfield Microphone at 15% Thrust.

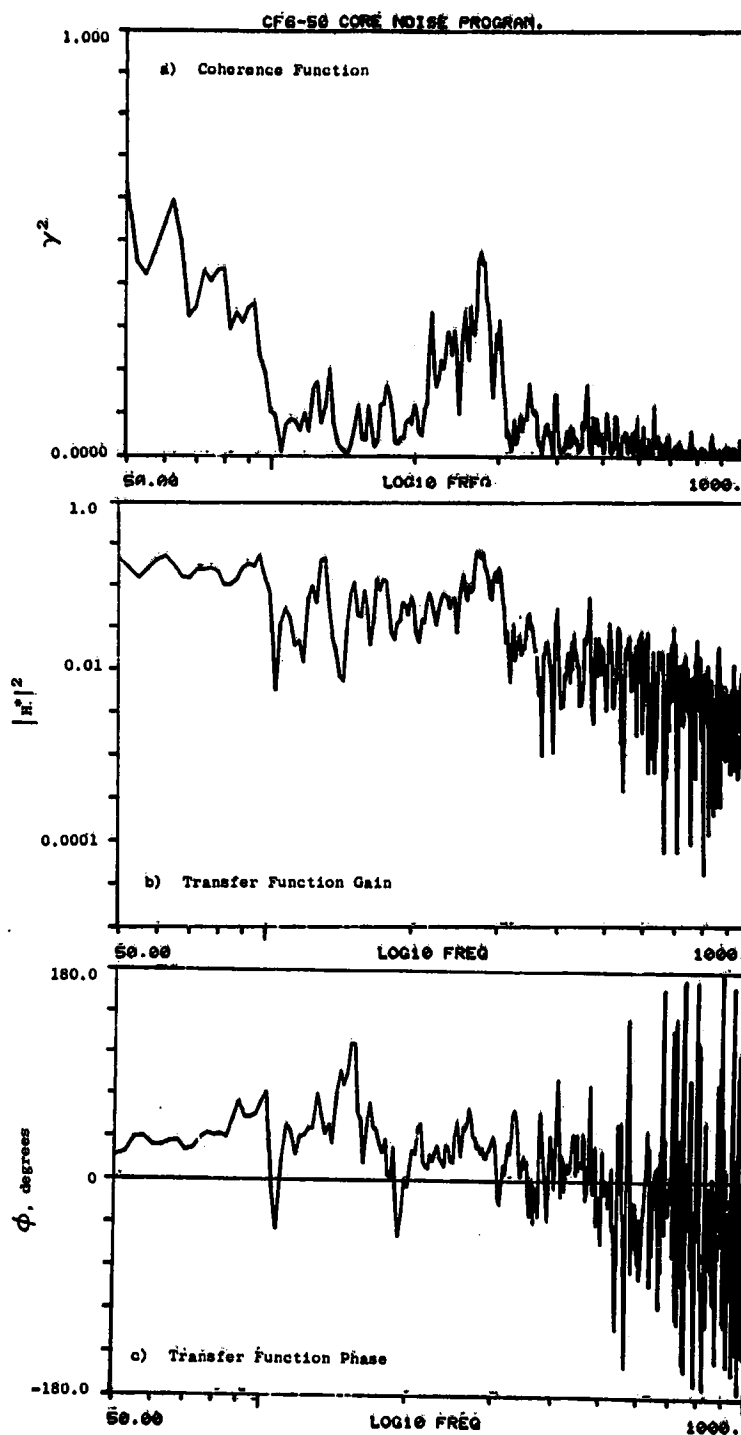


Figure A-94. Coherence and Transfer Functions for Plane 8.0A (270°) to 80° Farfield Microphone at 15% Thrust.

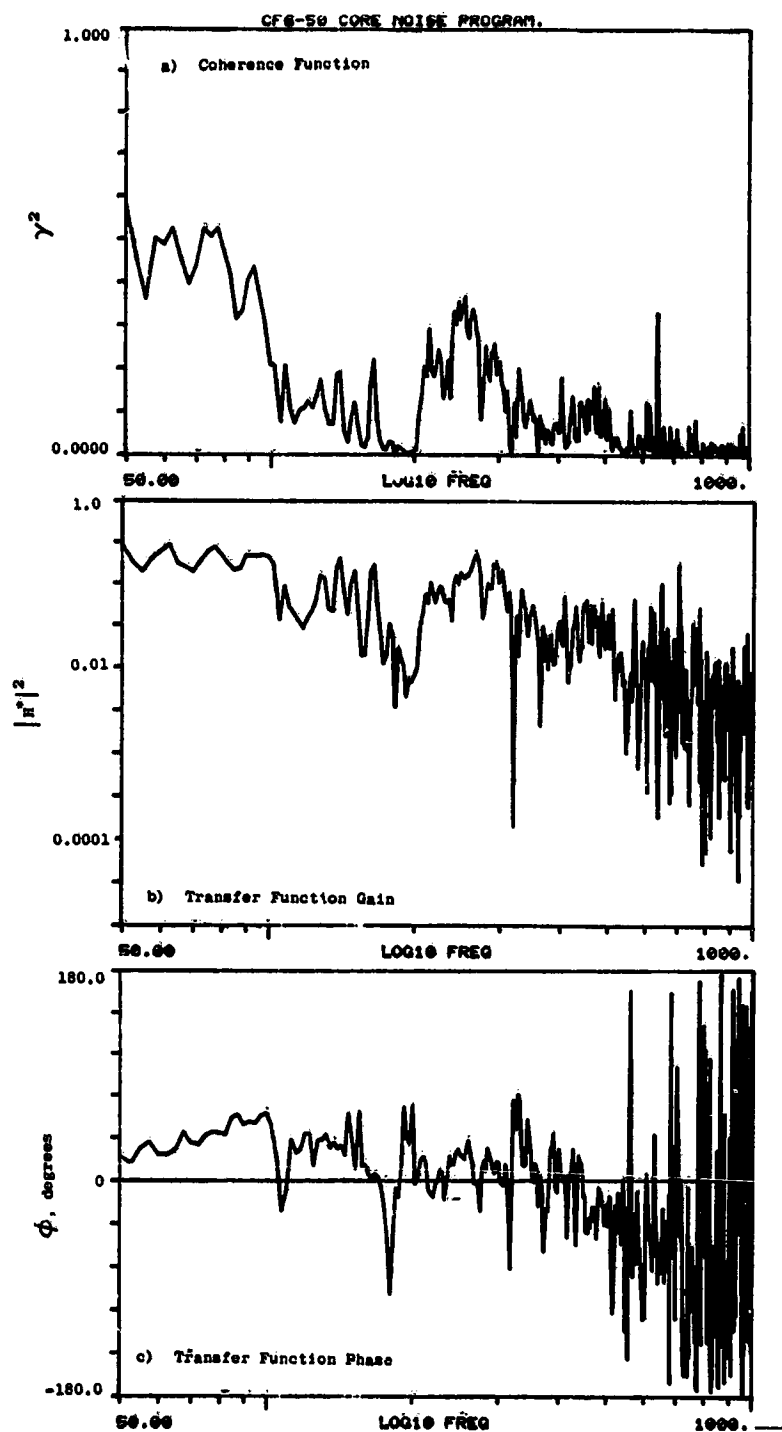


Figure A-95. Coherence and Transfer Functions for Plane 8.0A (270°) to 90° Farfield Microphone at 15% Thrust.

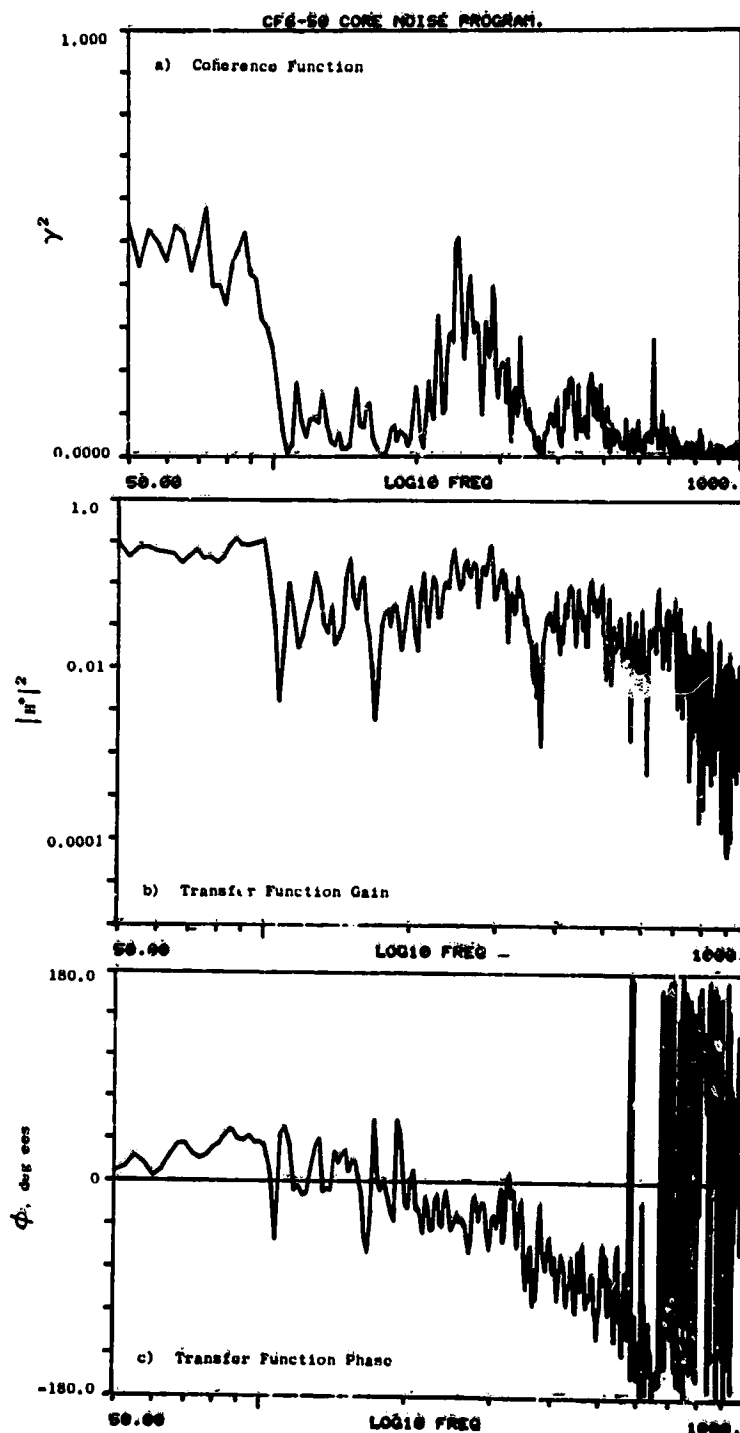


Figure A-96. Coherence and Transfer Functions for Plane 8.0A (270°) to 100° Farfield Microphone at 15% Thrust.

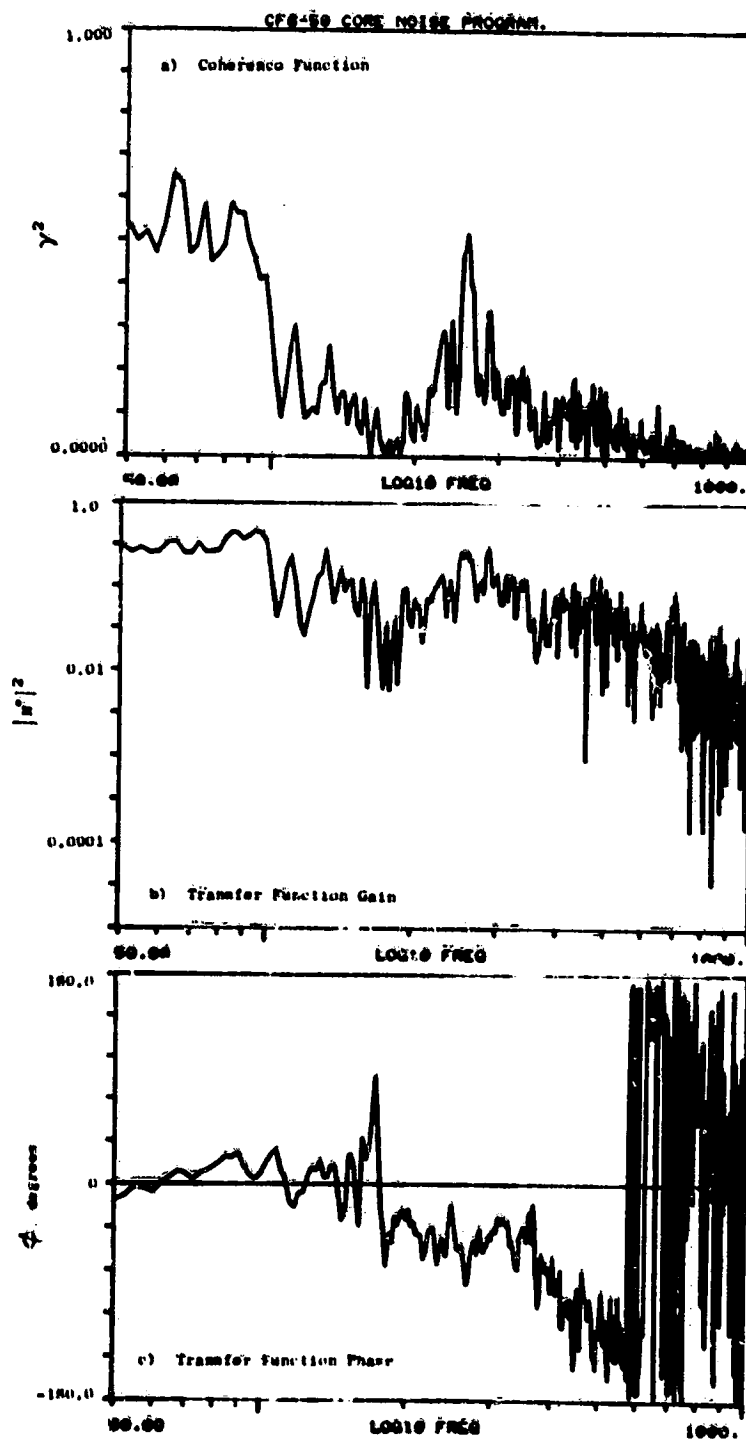


Figure A-97. Coherence and Transfer Functions for Plane 8.0A (270°) to 110° Farfield Microphone at 15% Thrust.

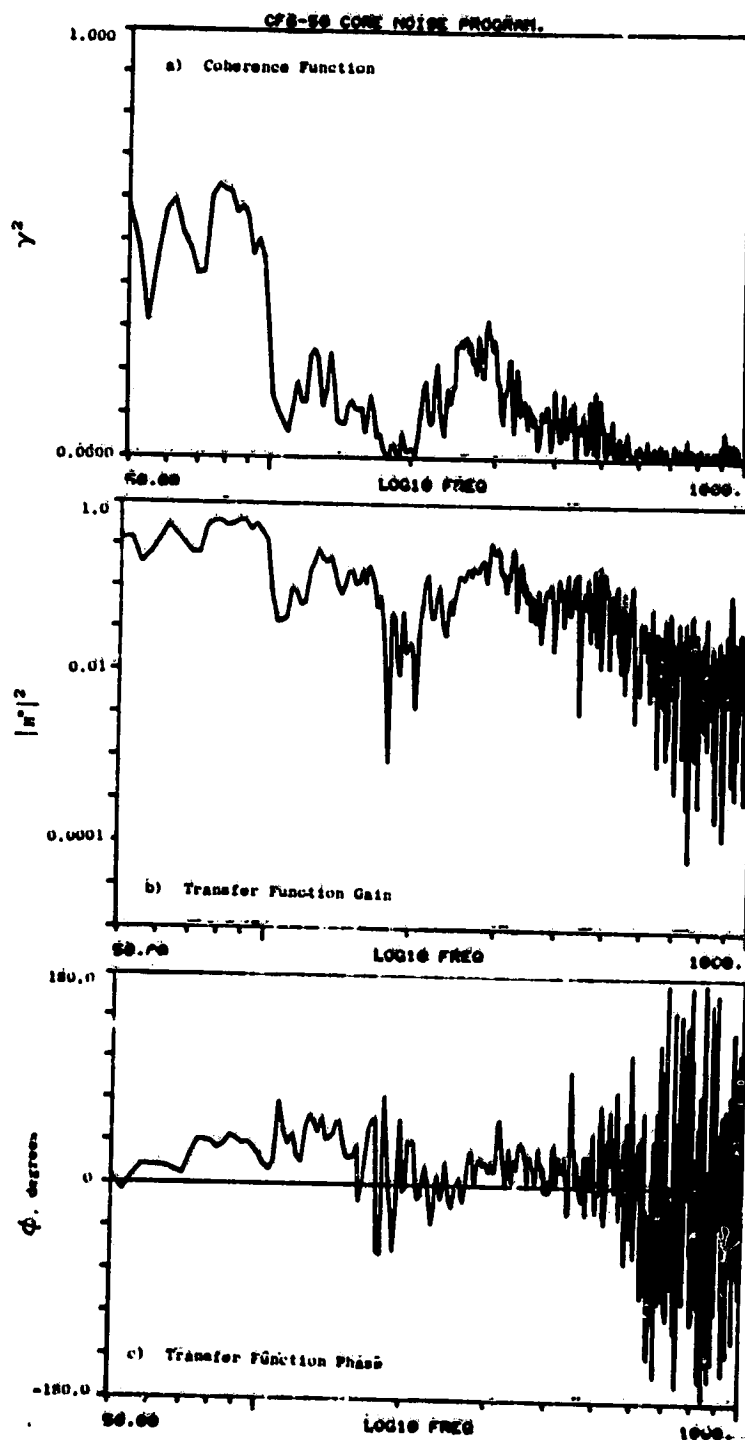


Figure A-98. Coherence and Transfer Functions for Plane 8.0A (270°) to 120° Farfield Microphone at 15% Thrust.

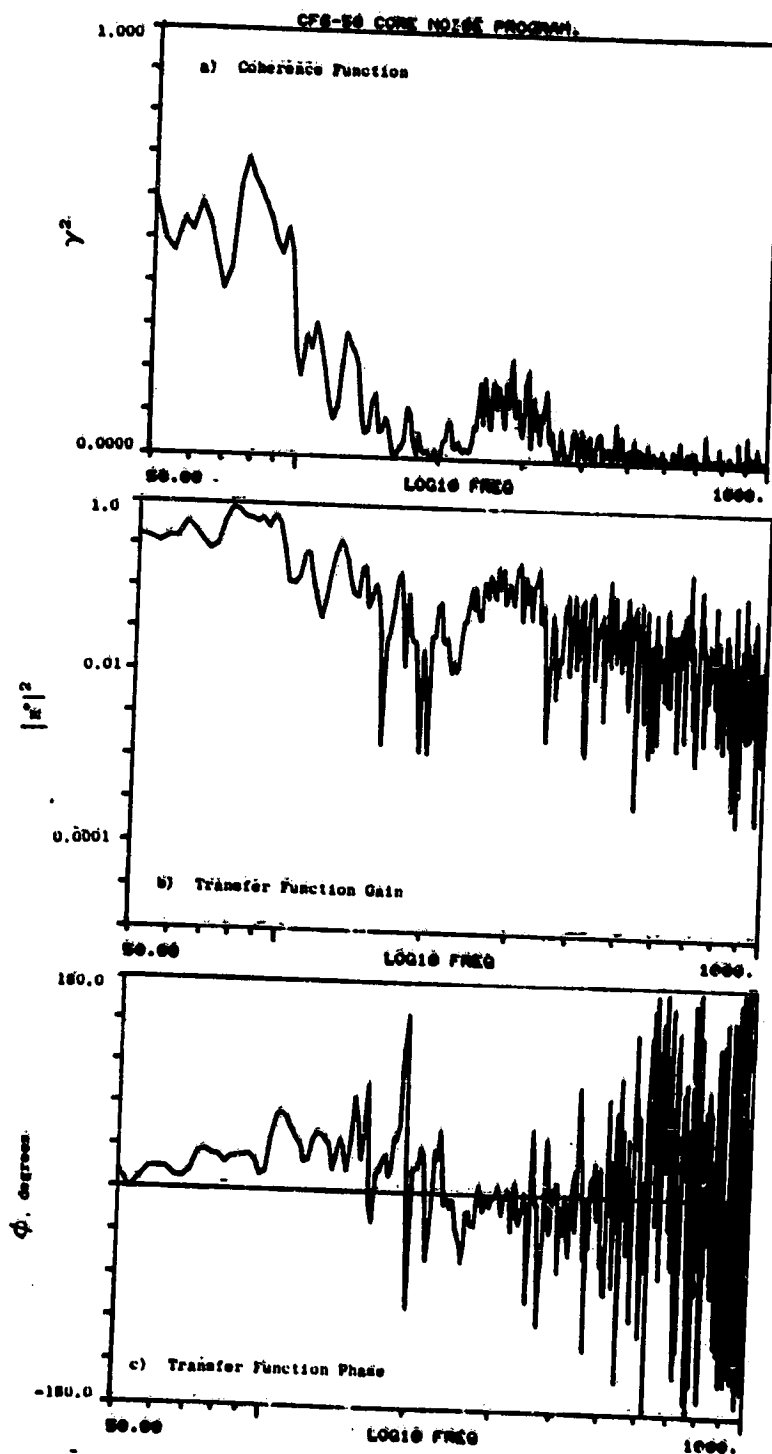


Figure A-99. Coherence and Transfer Functions for Plane 8.0A (270°)
to 130° Farfield Microphone at 15% Thrust.

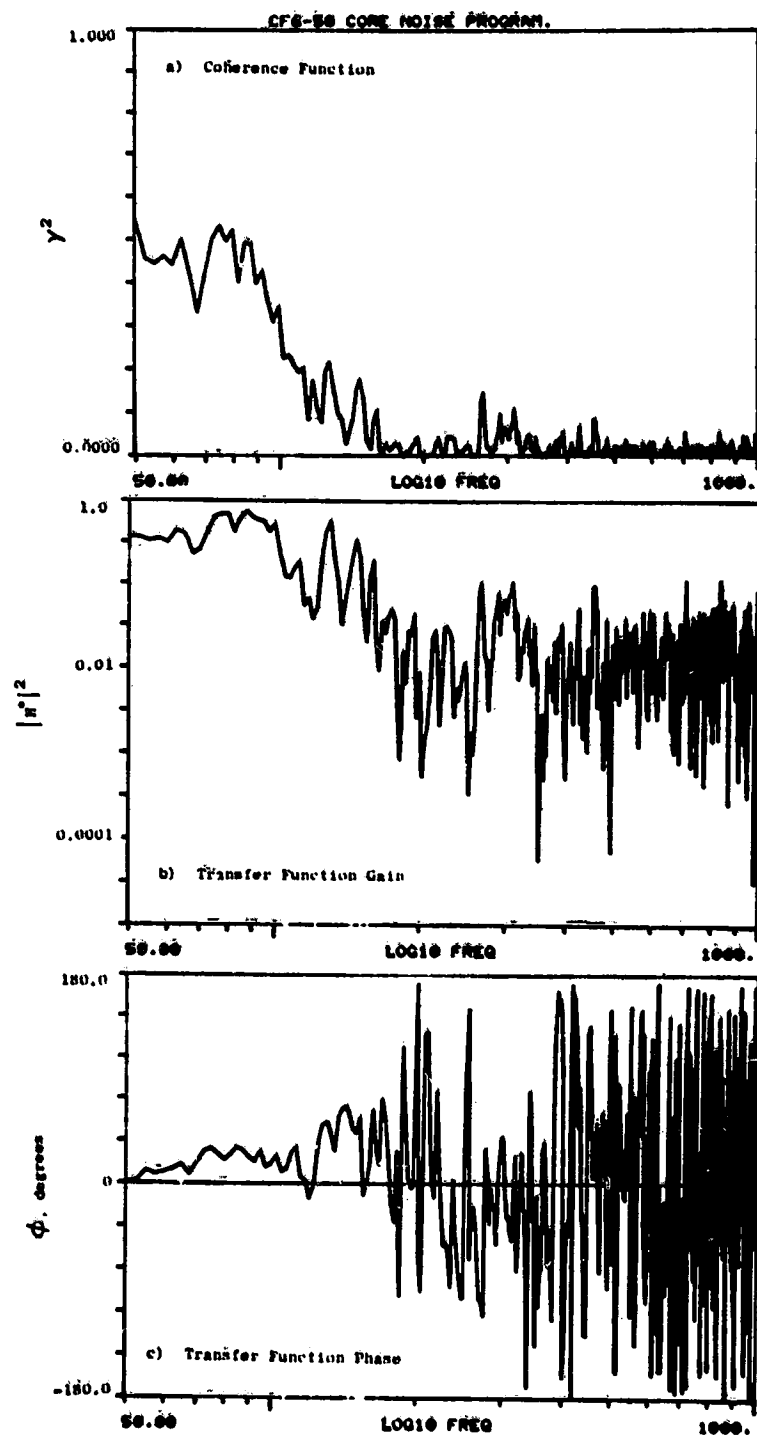


Figure A-100. Coherence and Transfer Functions for Plane 8.0A (270°) to 140° Farfield Microphone at 15% Thrust.

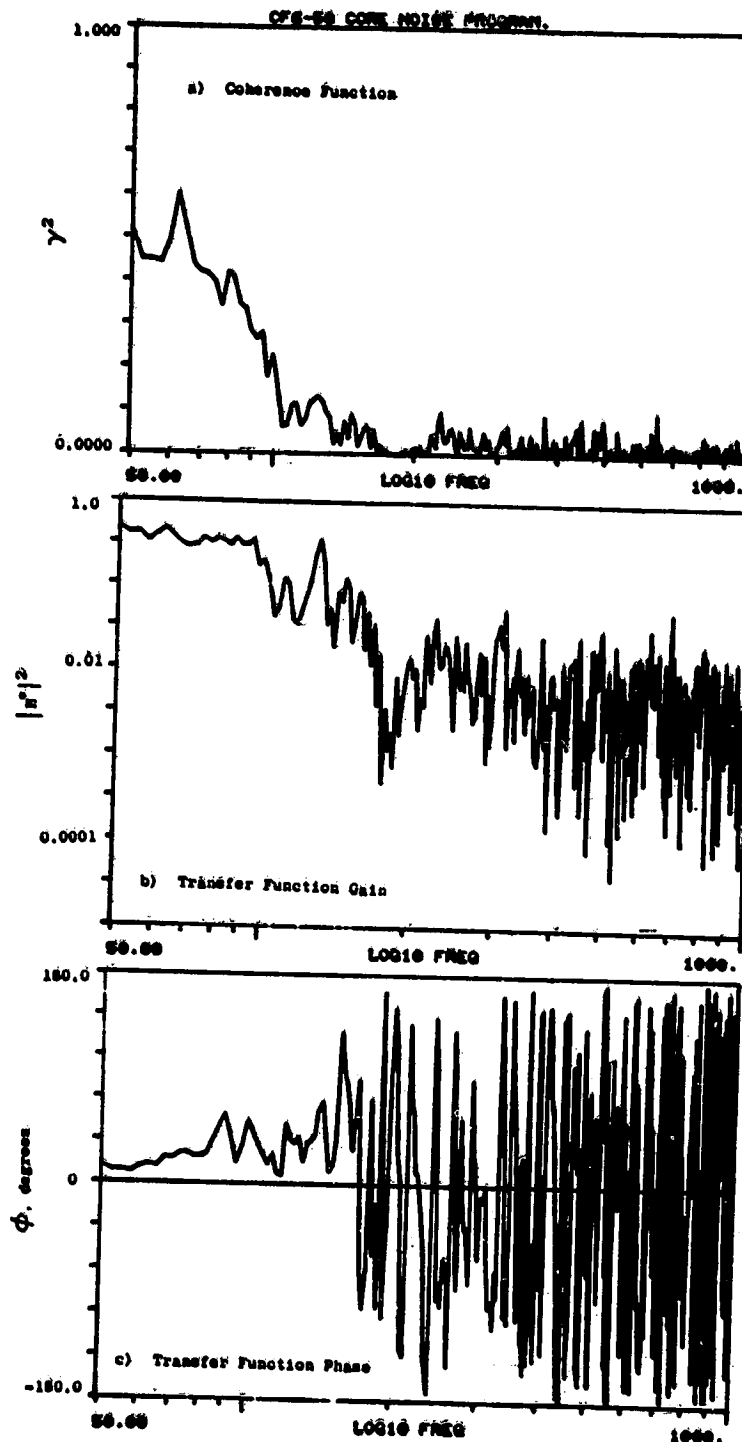


Figure A-101. Coherence and Transfer Functions for Plane 8.0A (270°) to 150° Farfield Microphone at 15% Thrust.

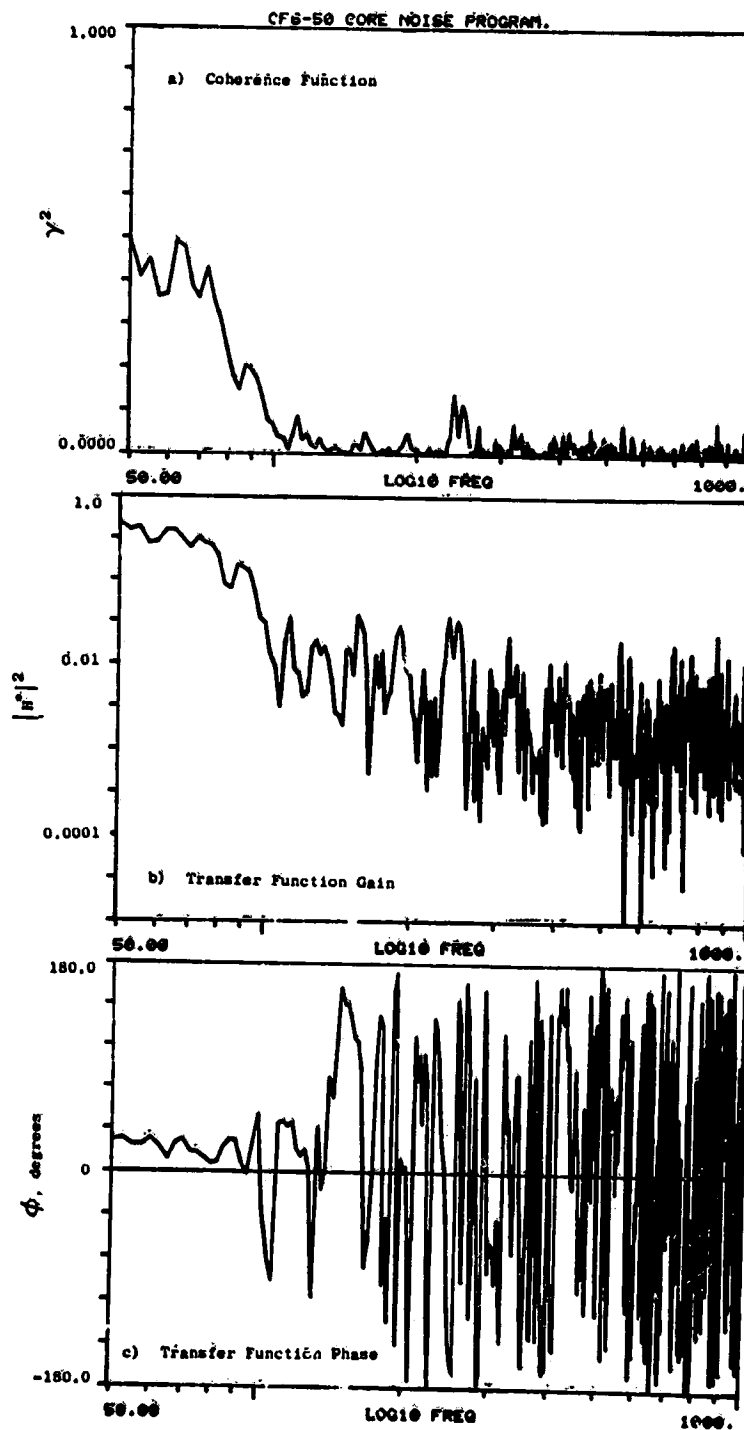


Figure A-102. Coherence and Transfer Functions for Plane 8.0A (270°) to 160° Farfield Microphone at 15% Thrust.

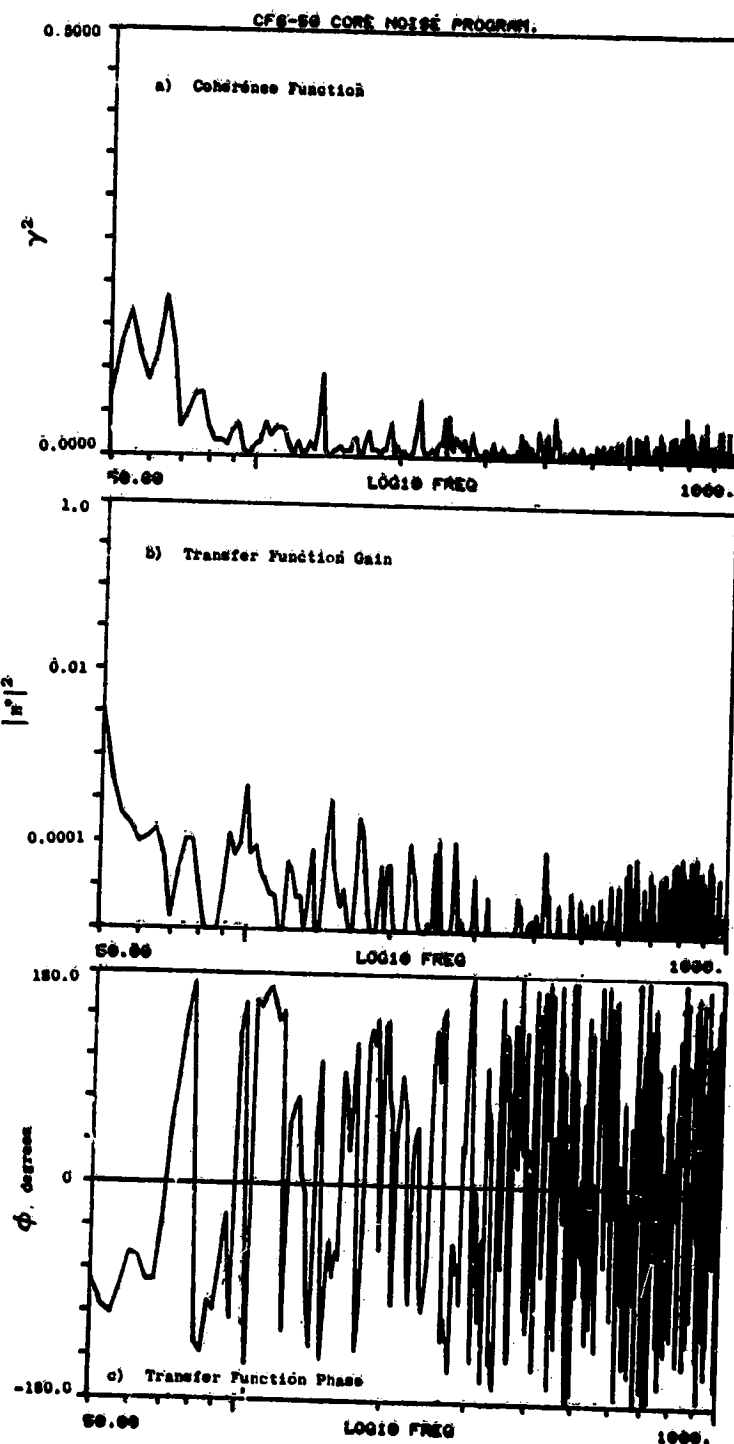


Figure A-103. Coherence and Transfer Functions for Plane 3.5 (102°) to 10° Farfield Microphone : 22.8% Thrust.

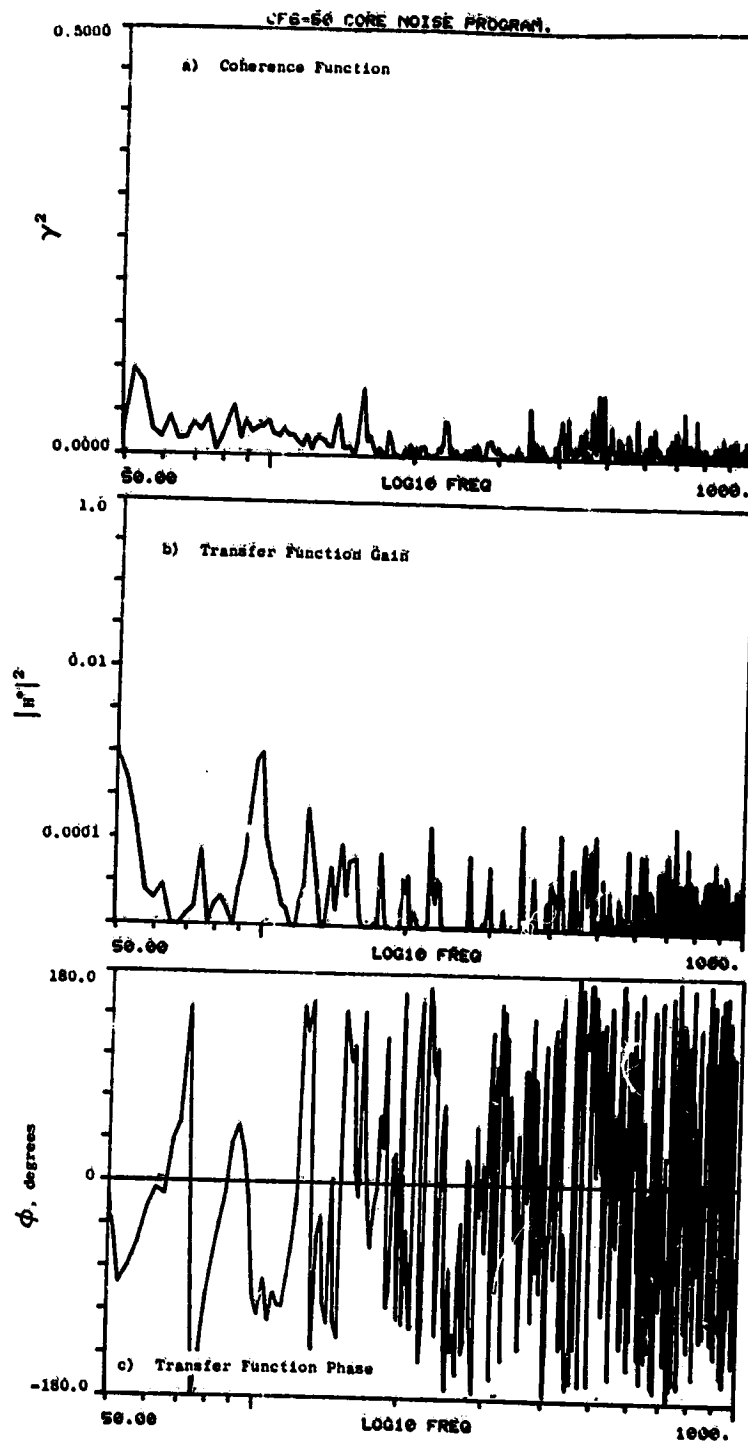


Figure A-104. Coherence and Transfer Functions for Plane 3.5 (102°) to 30° Farfield Microphone at 22.8% Thrust.

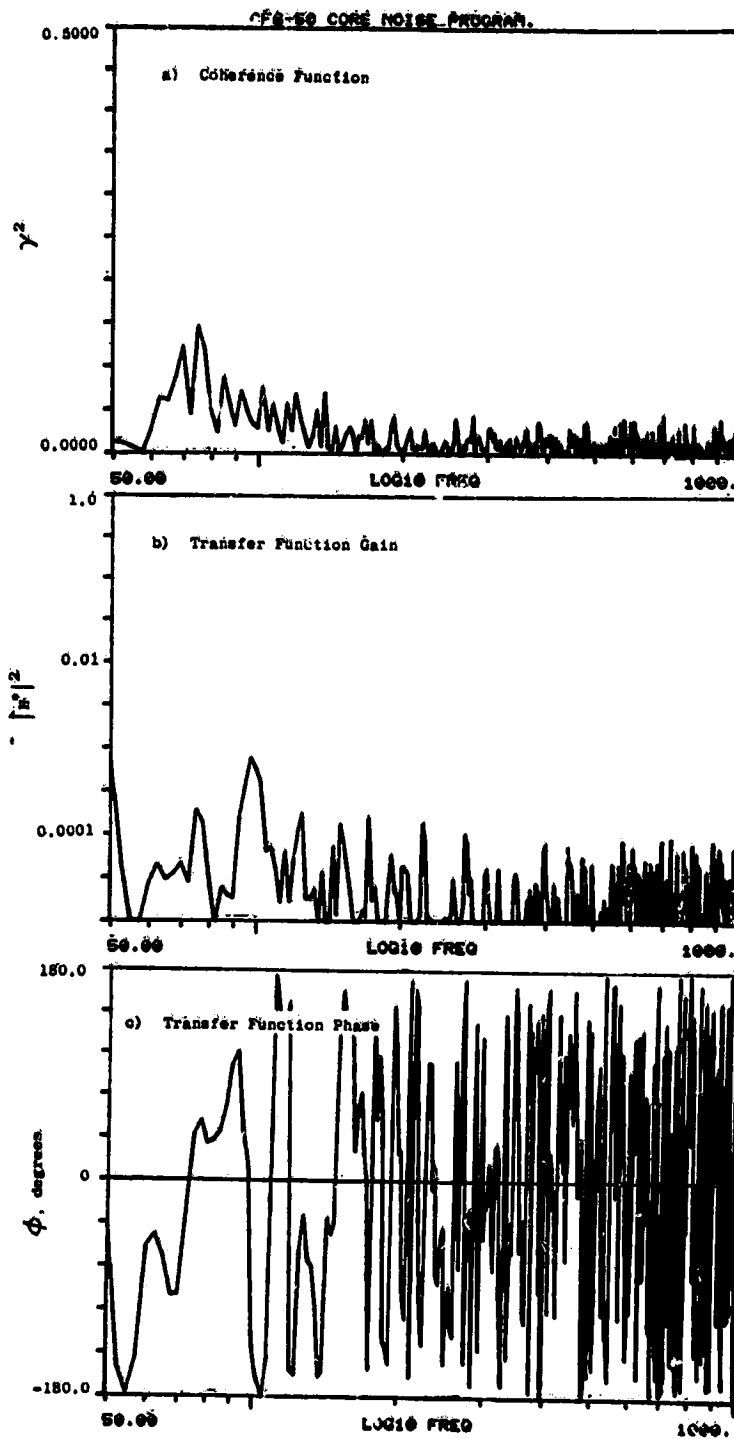


Figure A-105. Coherence and Transfer Functions for Plane 3.5 (102°) to 40° Farfield Microphone at 22.8% Thrust.

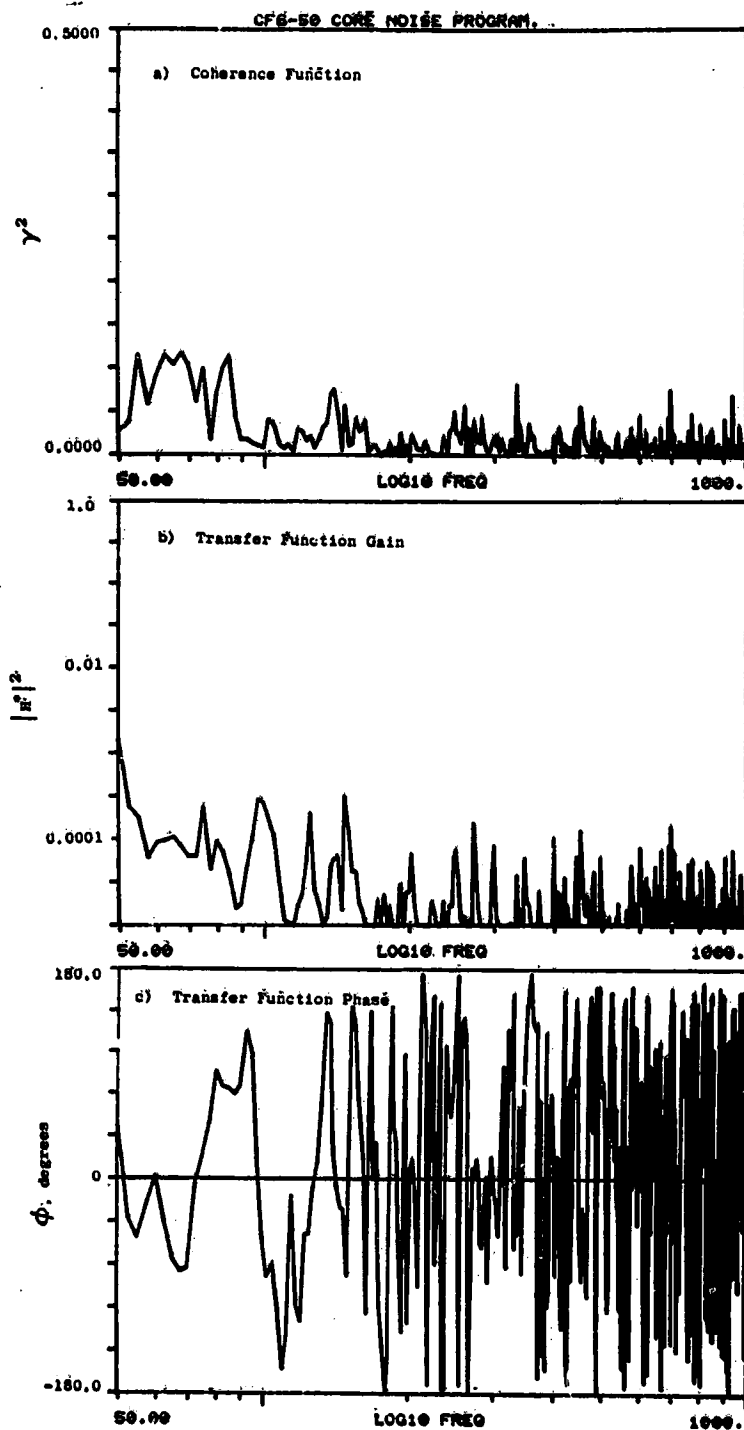


Figure A-106. Coherence and Transfer Functions for Plane 3.5 (102°) to 50° Farfield Microphone at 22.8% Thrust.

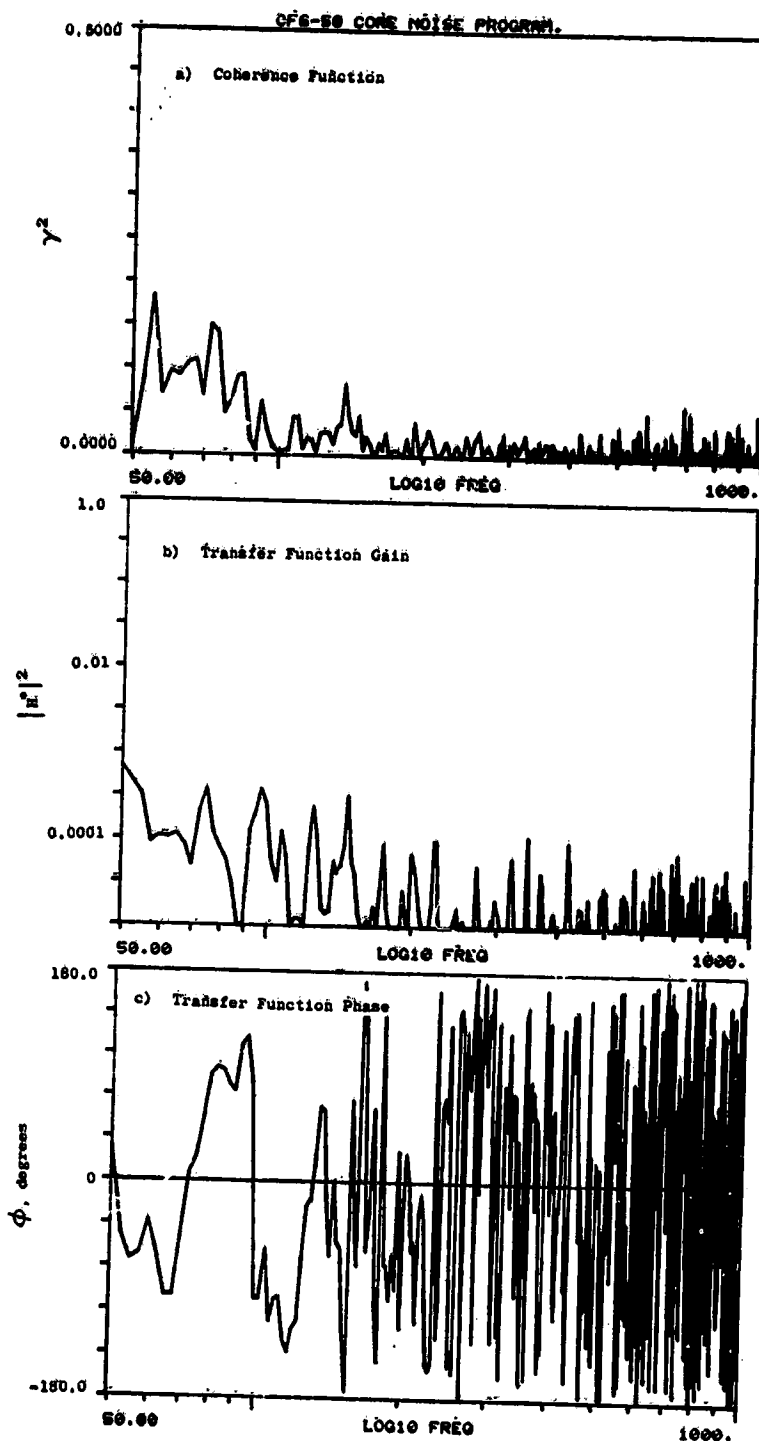


Figure A-107. Coherence and Transfer Functions for Plane 3.5 (102°) to 60° Farfield Microphone at 22.8% Thrust.

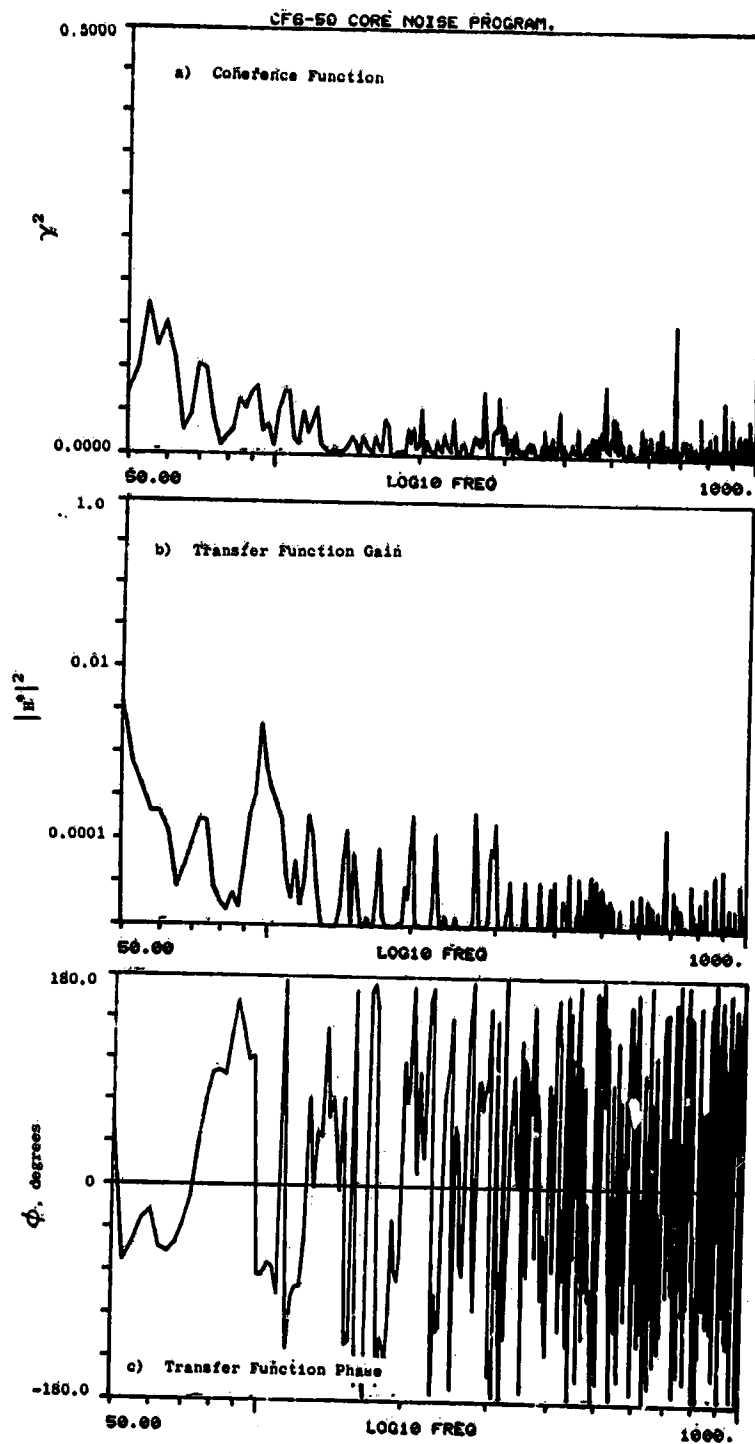


Figure A-108. Coherence and Transfer Functions for Plane 3.5 (102°) to 70° Farfield Microphone at 22.8% Thrust.

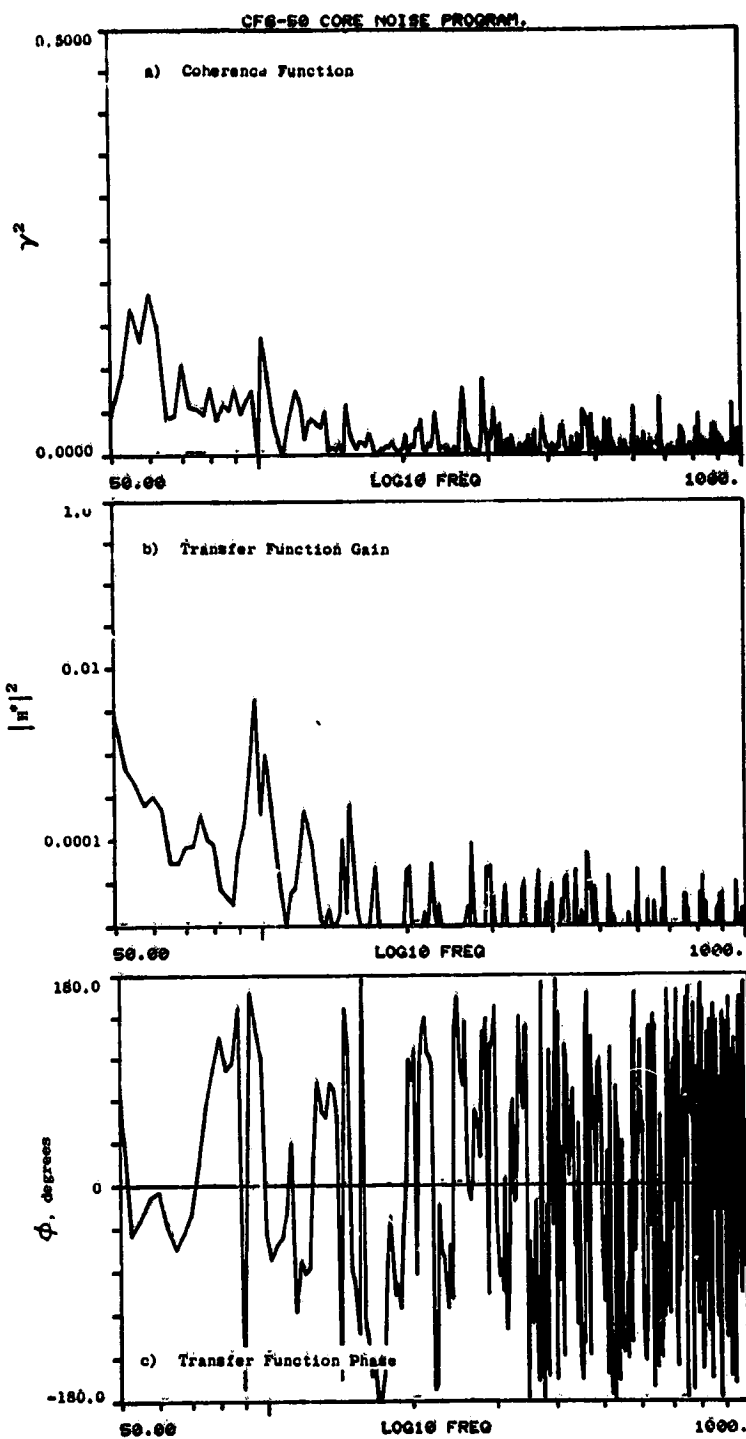


Figure A-109. Coherence and Transfer Functions for Plane 3.5 (102°) to 80° Farfield Microphone at 22.8% Thrust.

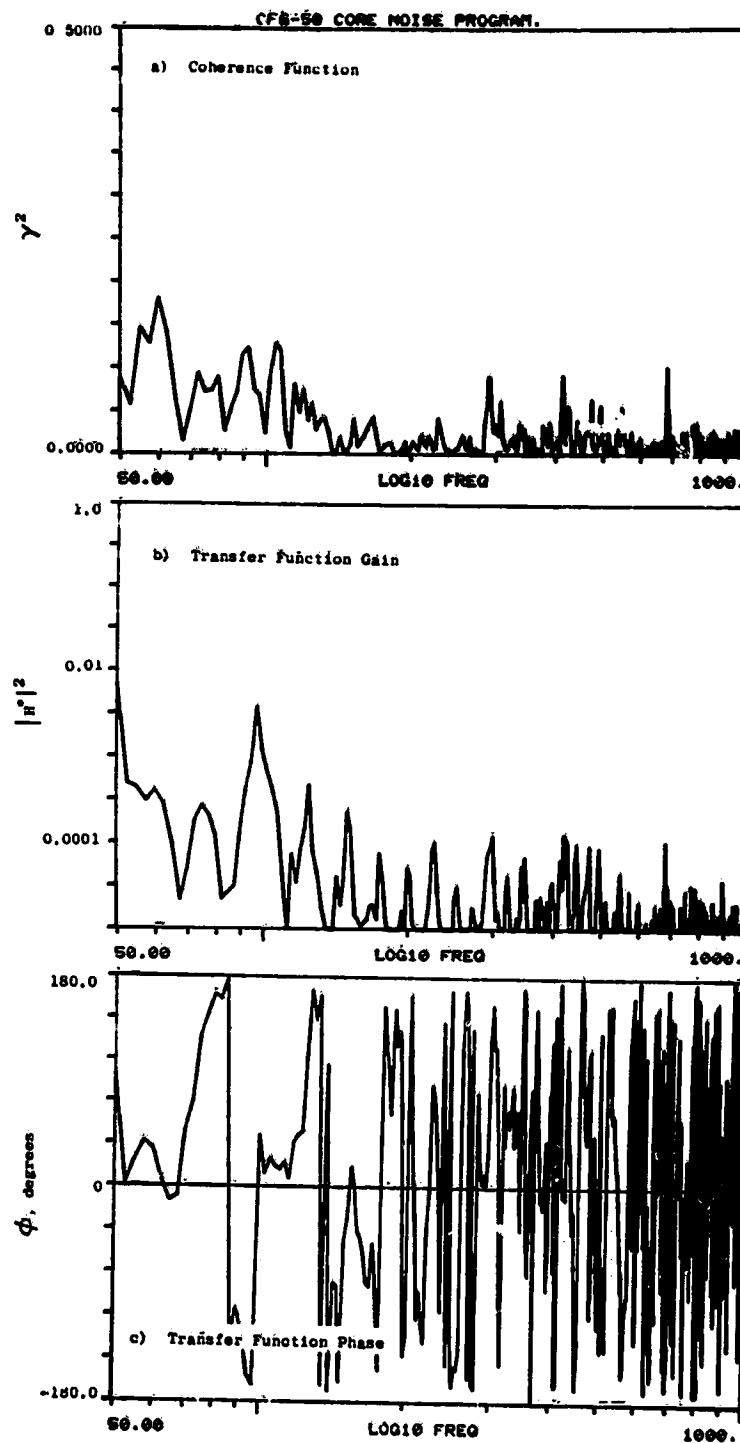


Figure A-110. Coherence and Transfer Functions for Plane 3.5 (102°) to 90° Farfield Microphone at 22.8% Thrust.

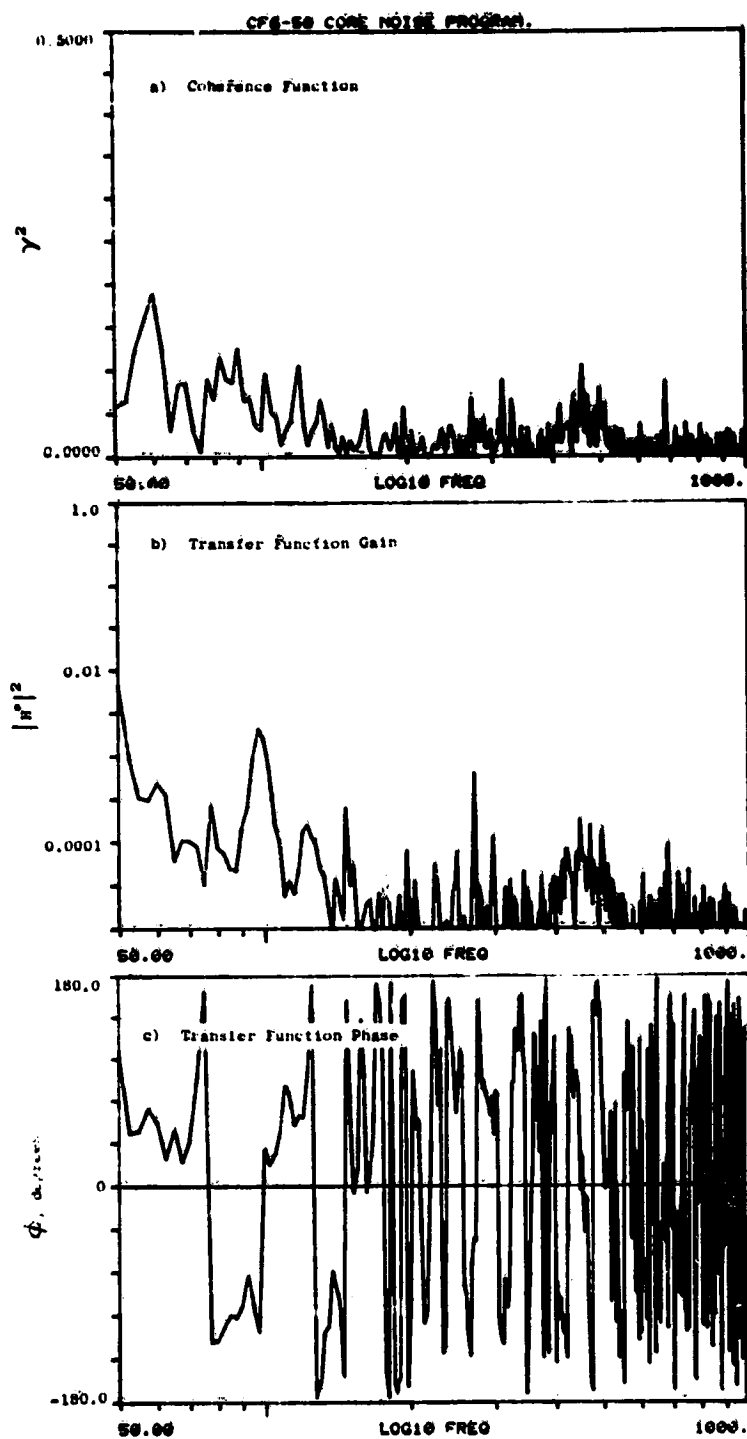


Figure A-111. Coherence and Transfer Functions for Plane 3.5 (102°) to 100° Farfield Microphone at 22.8% Thrust.

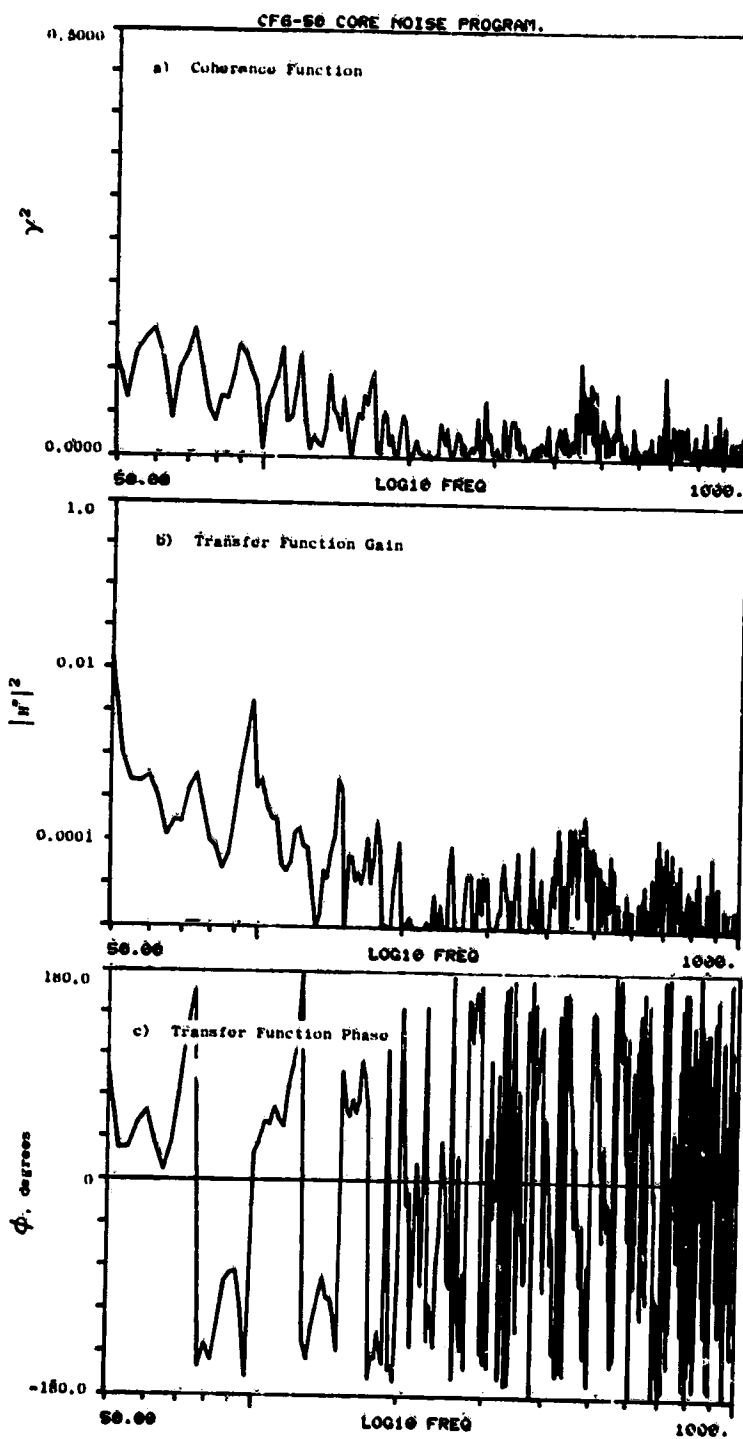


Figure A-112. Coherence and Transfer Functions for Plane 3.5 (102°) to 110° Farfield Microphone at 22.8% Thrust.

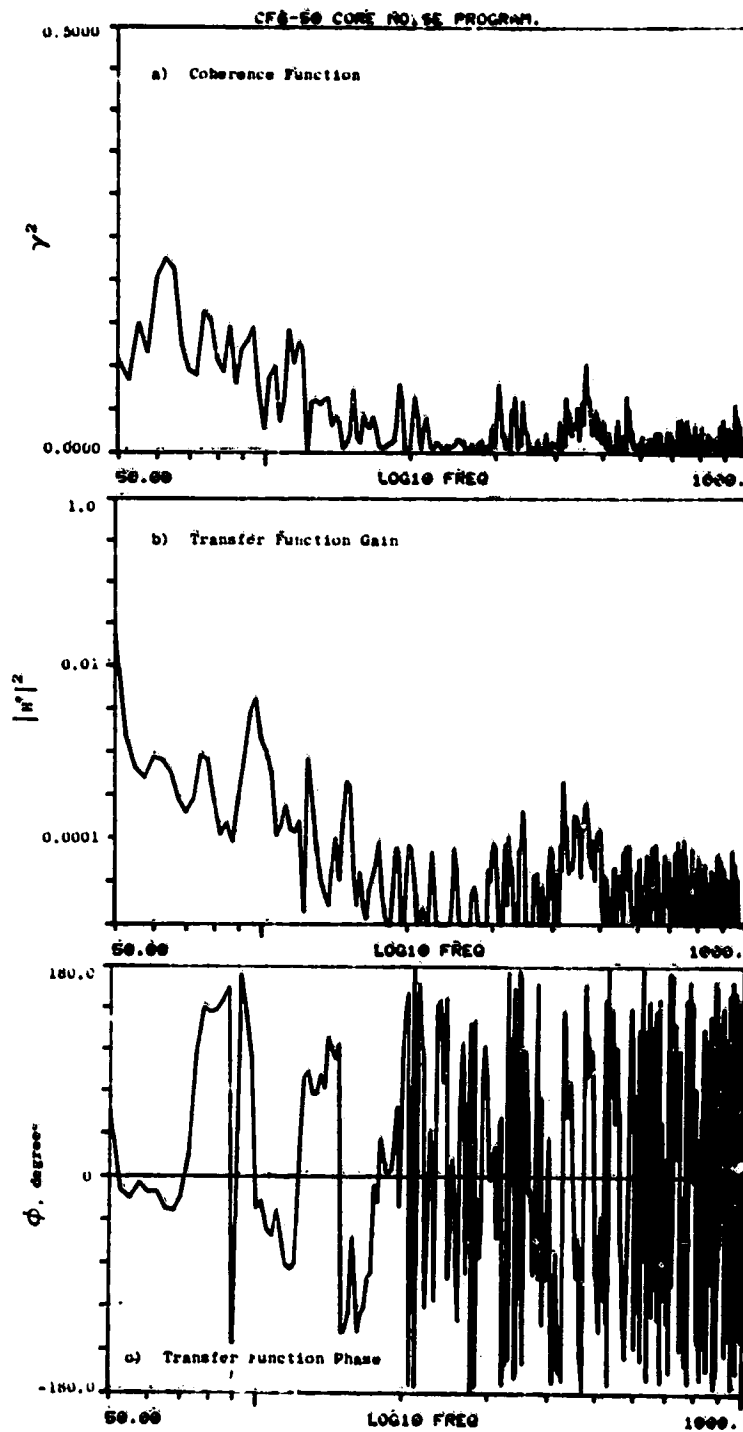


Figure A-113. Coherence and Transfer Functions for Plane 3.5 (102^{U}) to 120° Farfield Microphone at 22.8% Thrust.

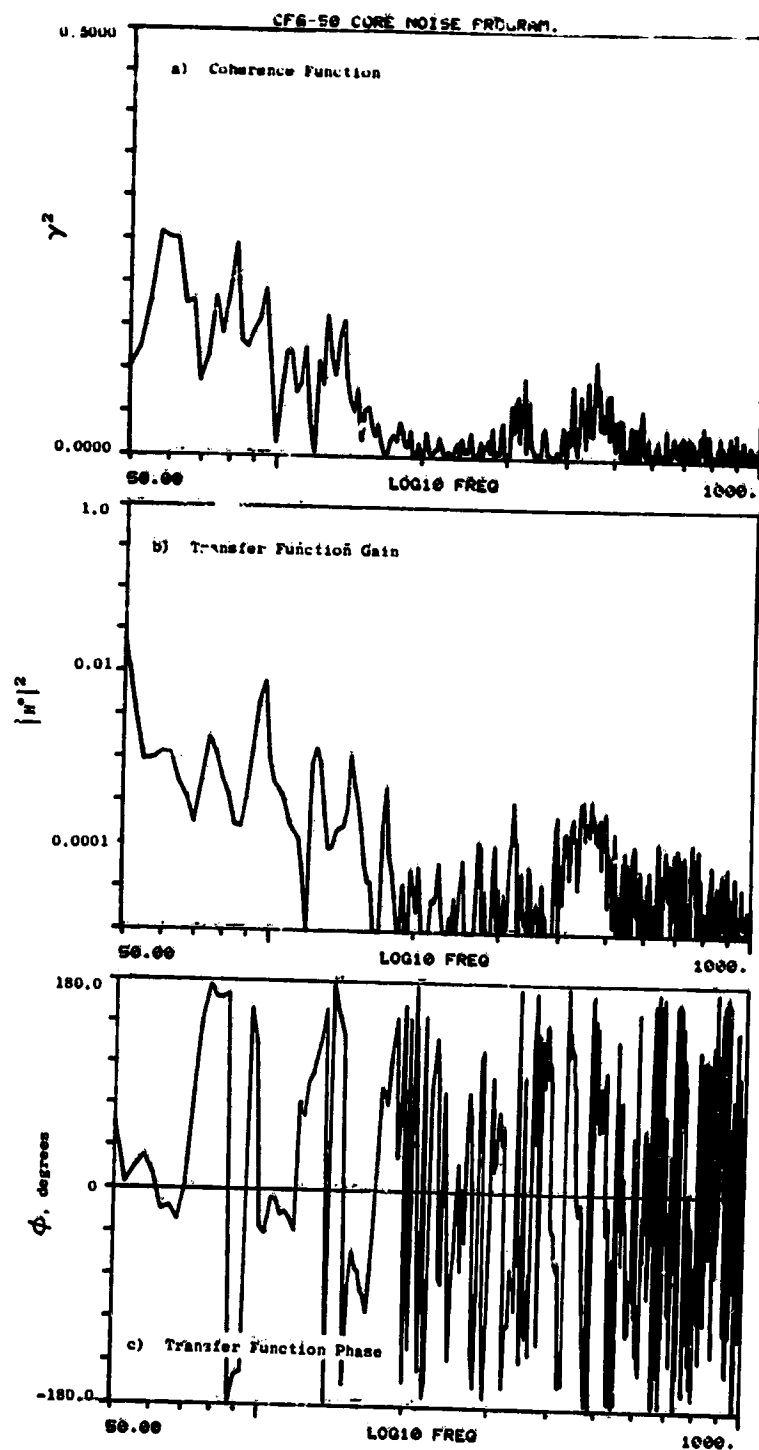


Figure A-114. Coherence and Transfer Functions for Plane 3.5 (102°) to 130° Farfield Microphone at 22.8% Thrust.

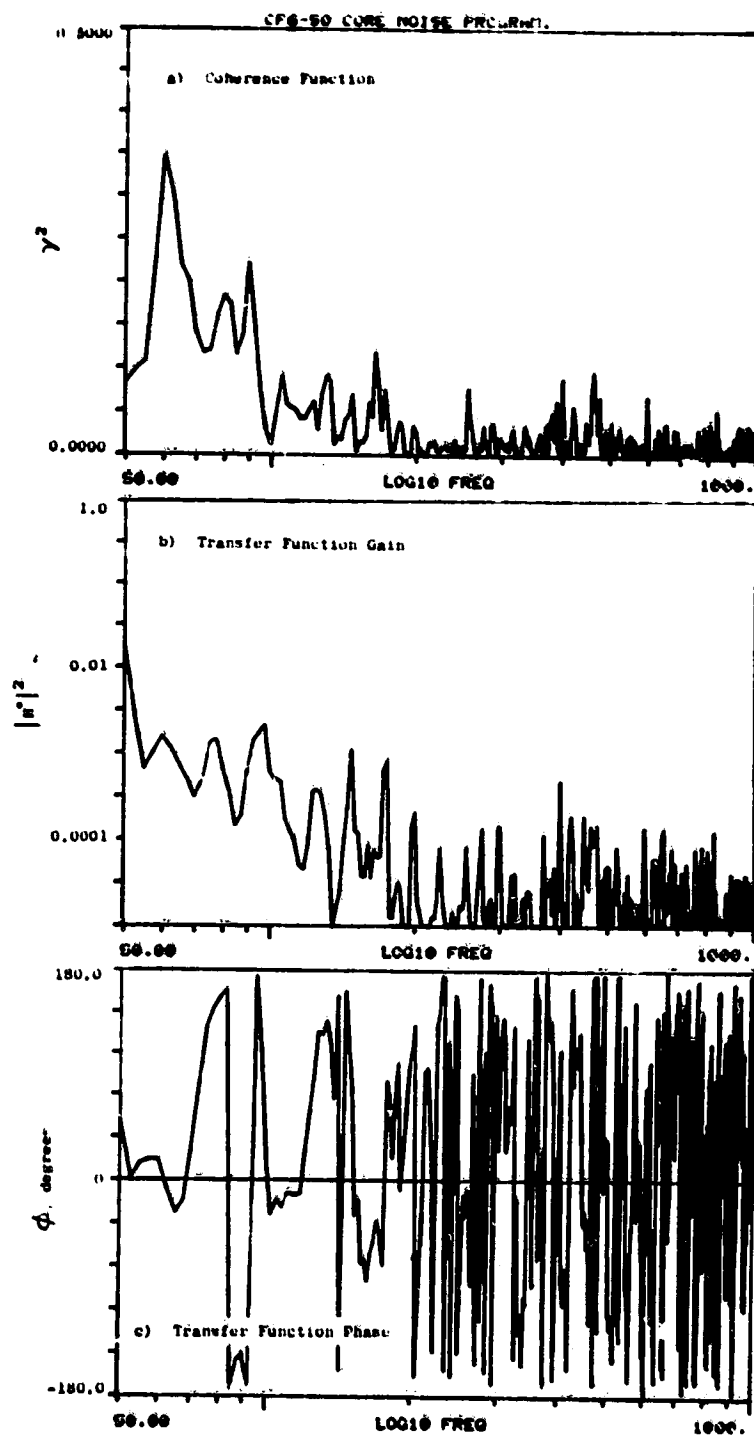


Figure A-115. Coherence and Transfer Functions for Plane 3.5 ($102''$) to 140° Farfield Microphone at 22.8% Thrust.

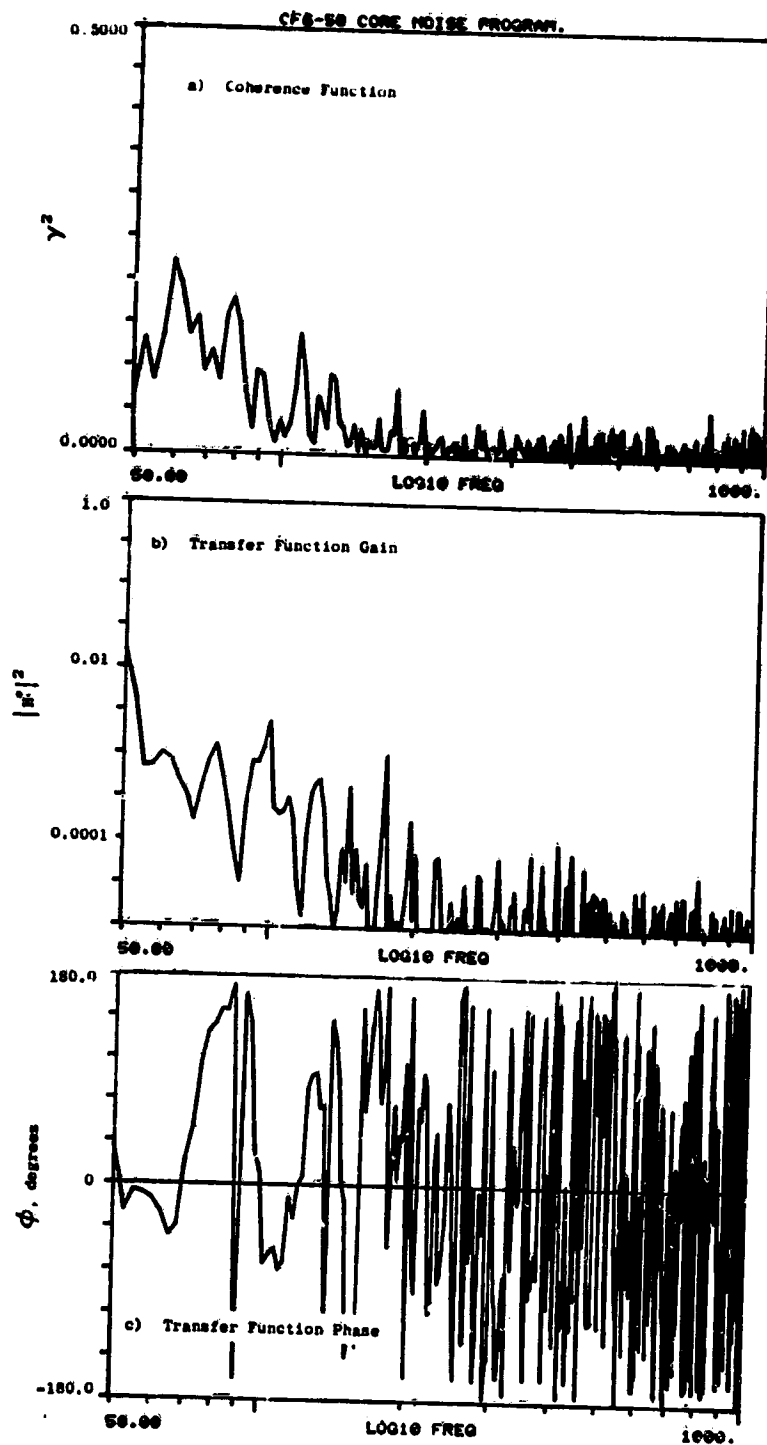


Figure A-116. Coherence and Transfer Functions for Plane 3.5 (102°) to 150° Farfield Microphone at 22.8% Thrust.

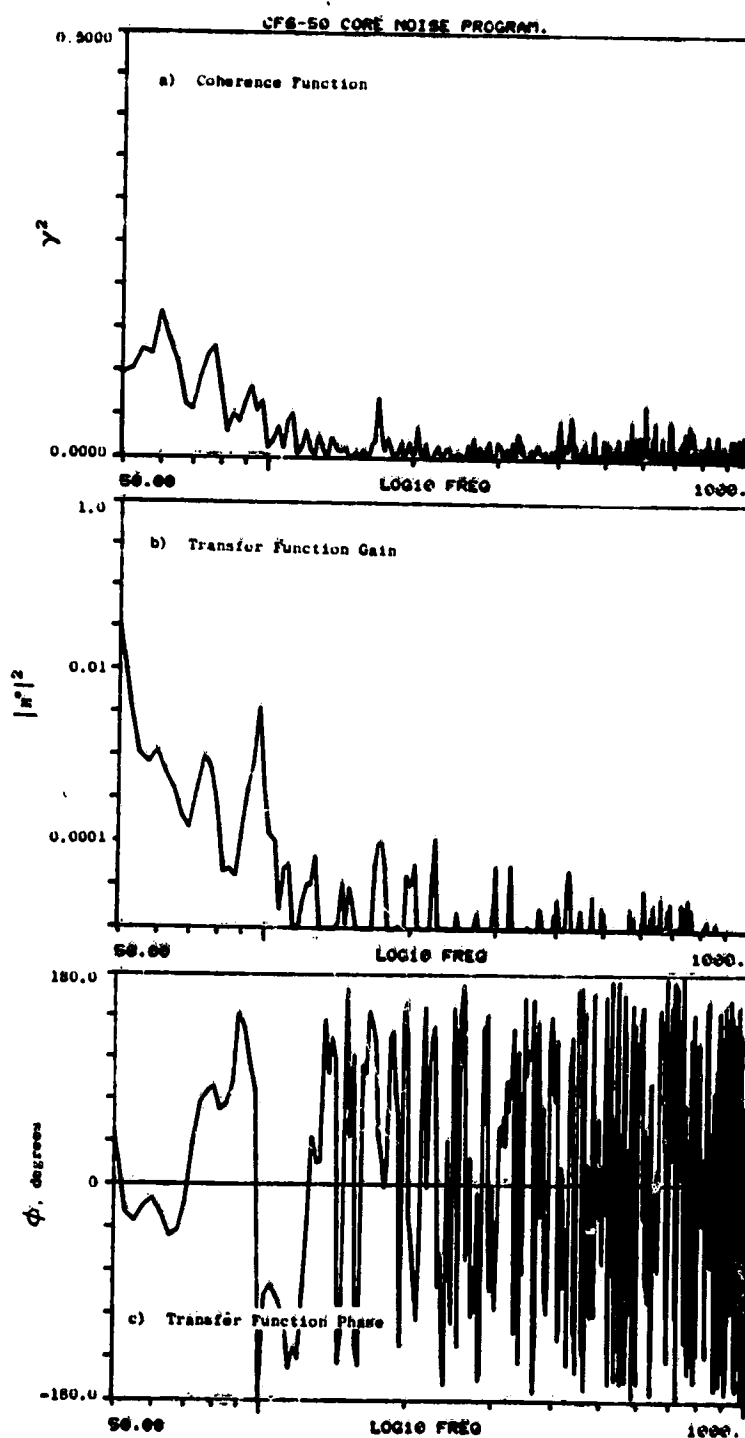


Figure A-117. Coherence and Transfer Functions for Plane 3.5 (102°) to 160° Farfield Microphone at 22.8% Thrust.

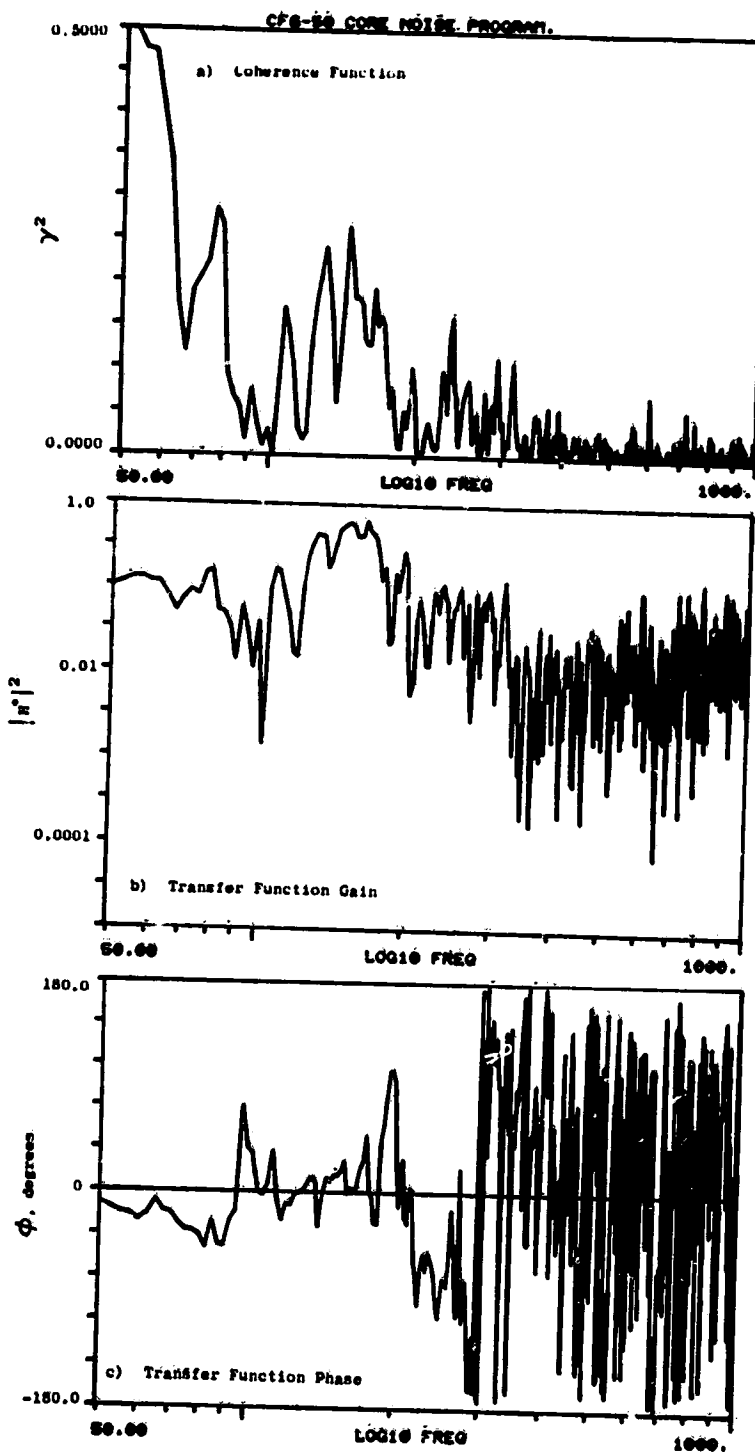


Figure A-118. Coherence and Transfer Functions for Plane 8.0A (270°) to 10° Farfield Microphone at 22.8% Thrust.

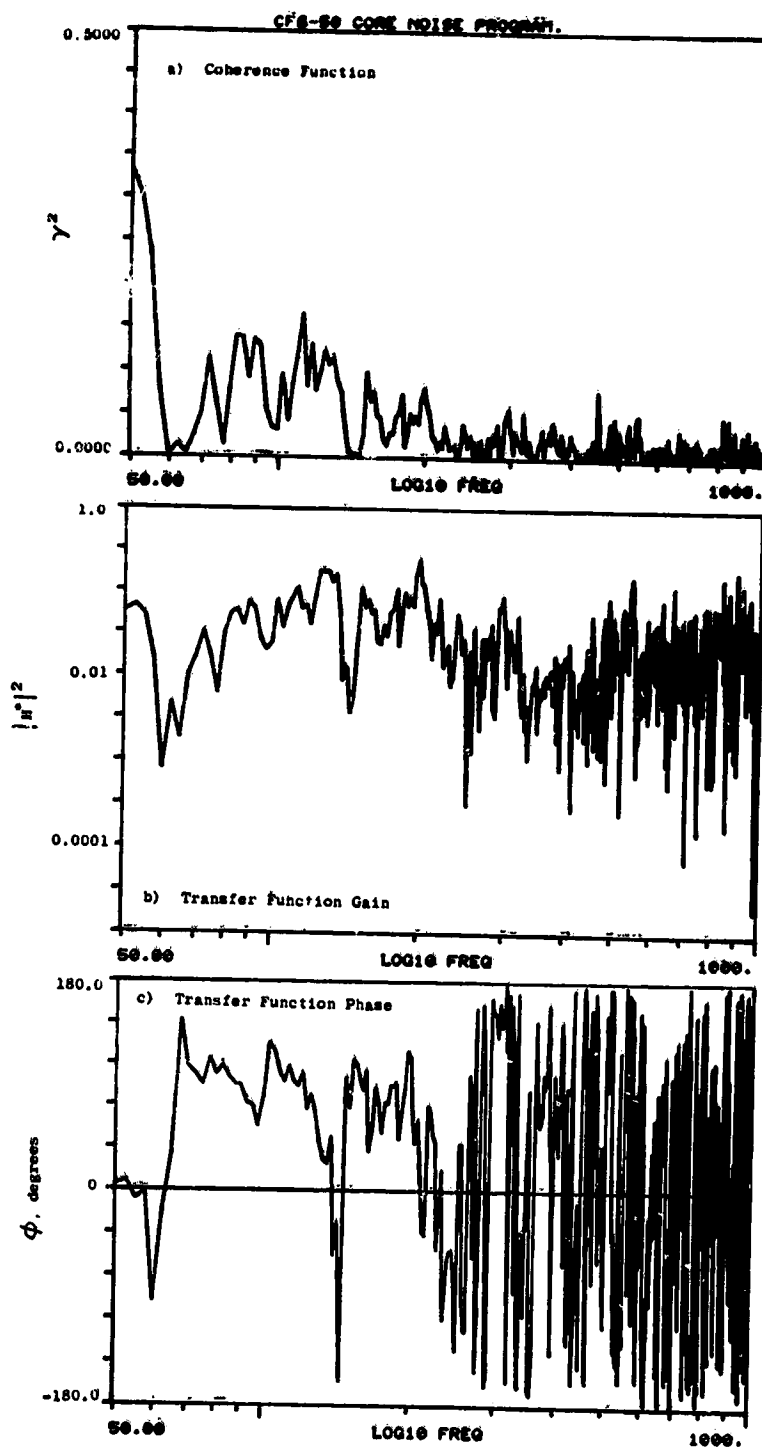


Figure A-119. Coherence and Transfer Functions for Plane 8.0A (270°) to 30° Farfield Microphone at 22.8% Thrust.

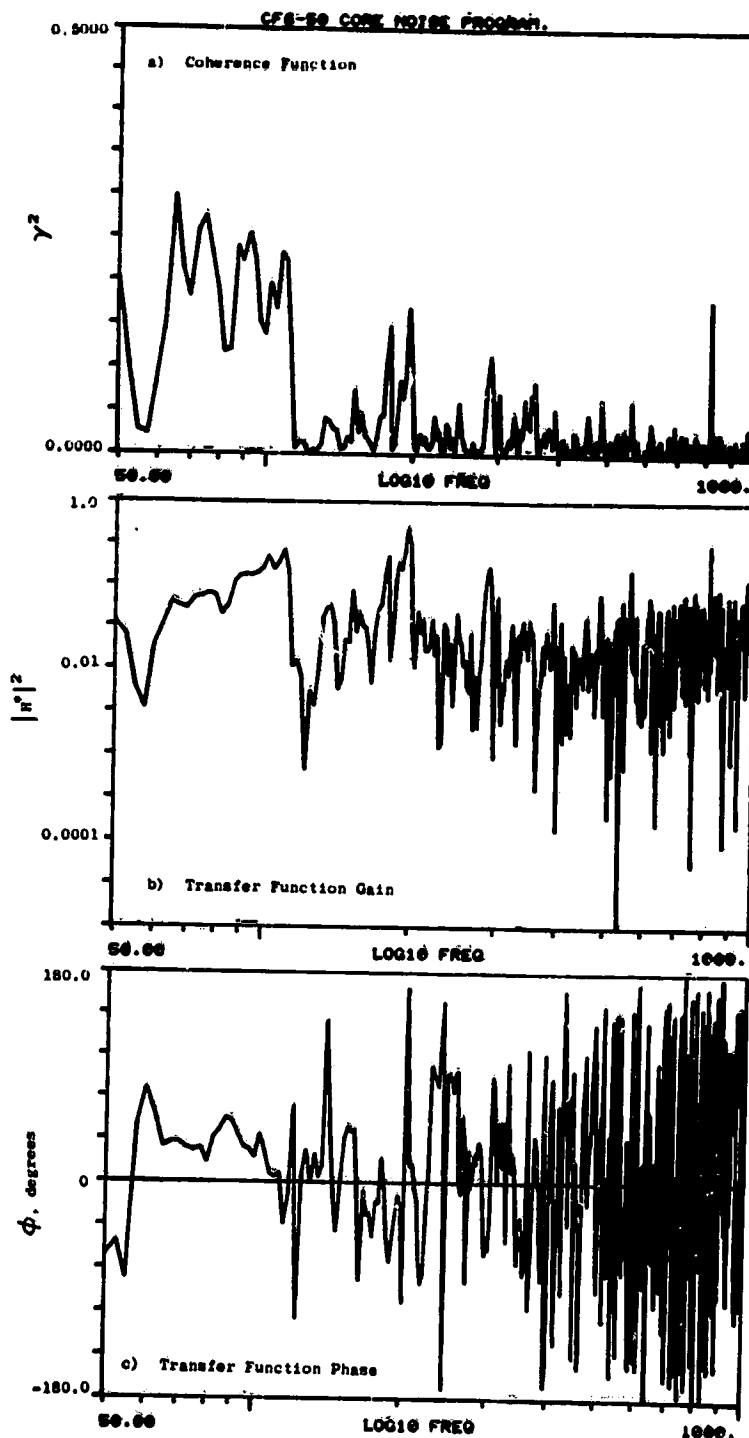


Figure A-120. Coherence and Transfer Functions for Plane 8.0A (270°) to 40° Farfield Microphone at 22.8% Thrust.

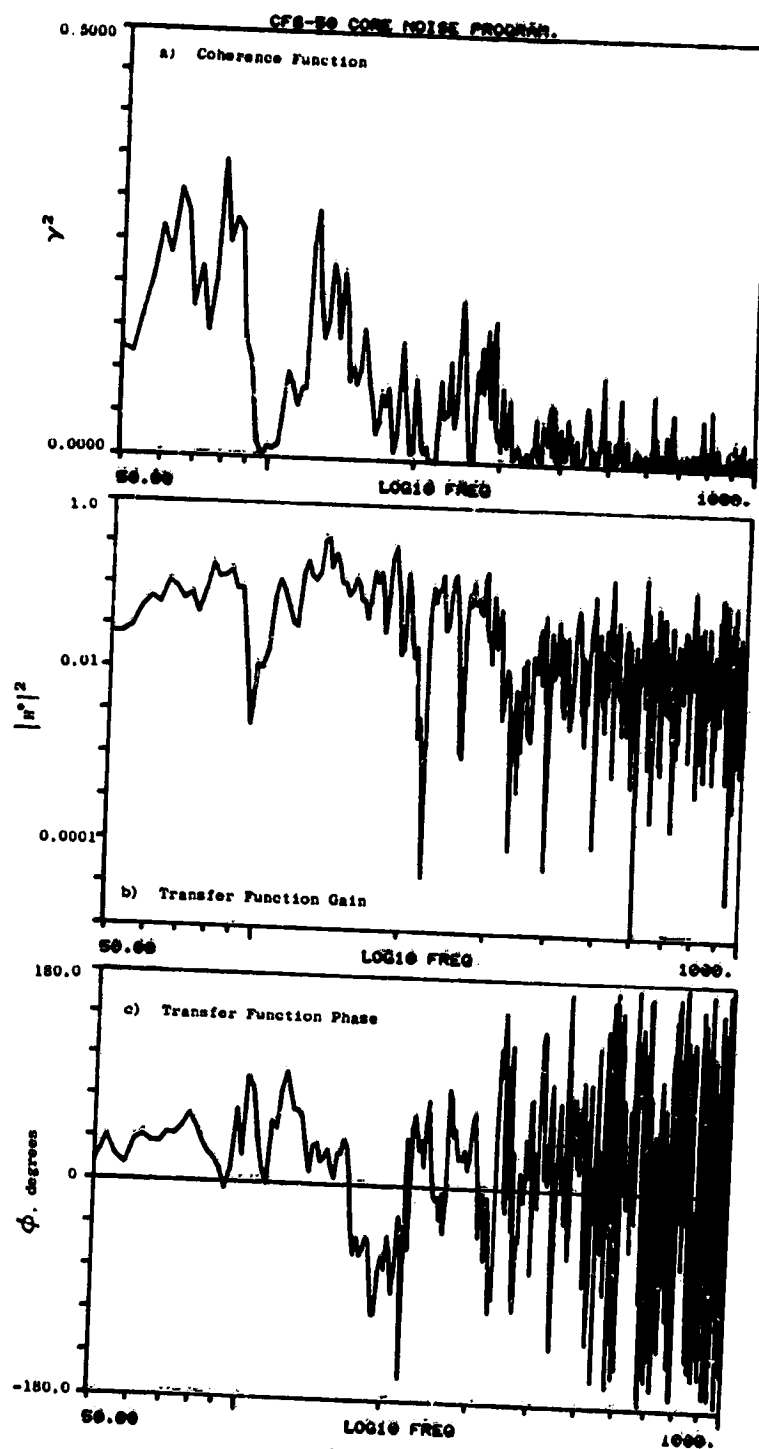


Figure A-121. Coherence and Transfer Functions for Plane 8.0A (270°) to 50° Farfield Microphone at 22.8% Thrust.

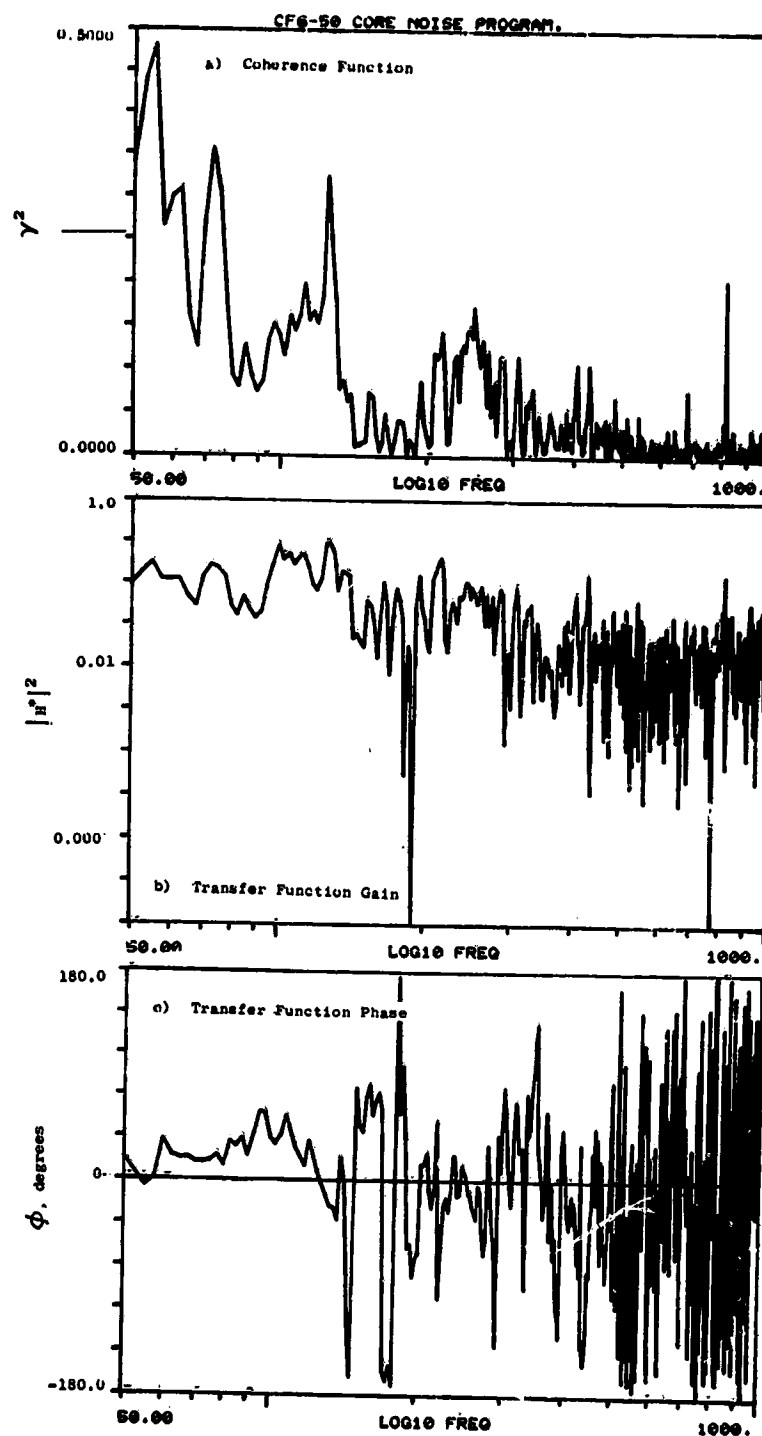


Figure A-122. Coherence and Transfer Functions for Plane 8.0A (270°) to 60° Farfield Microphone at 22.8% Thrust.

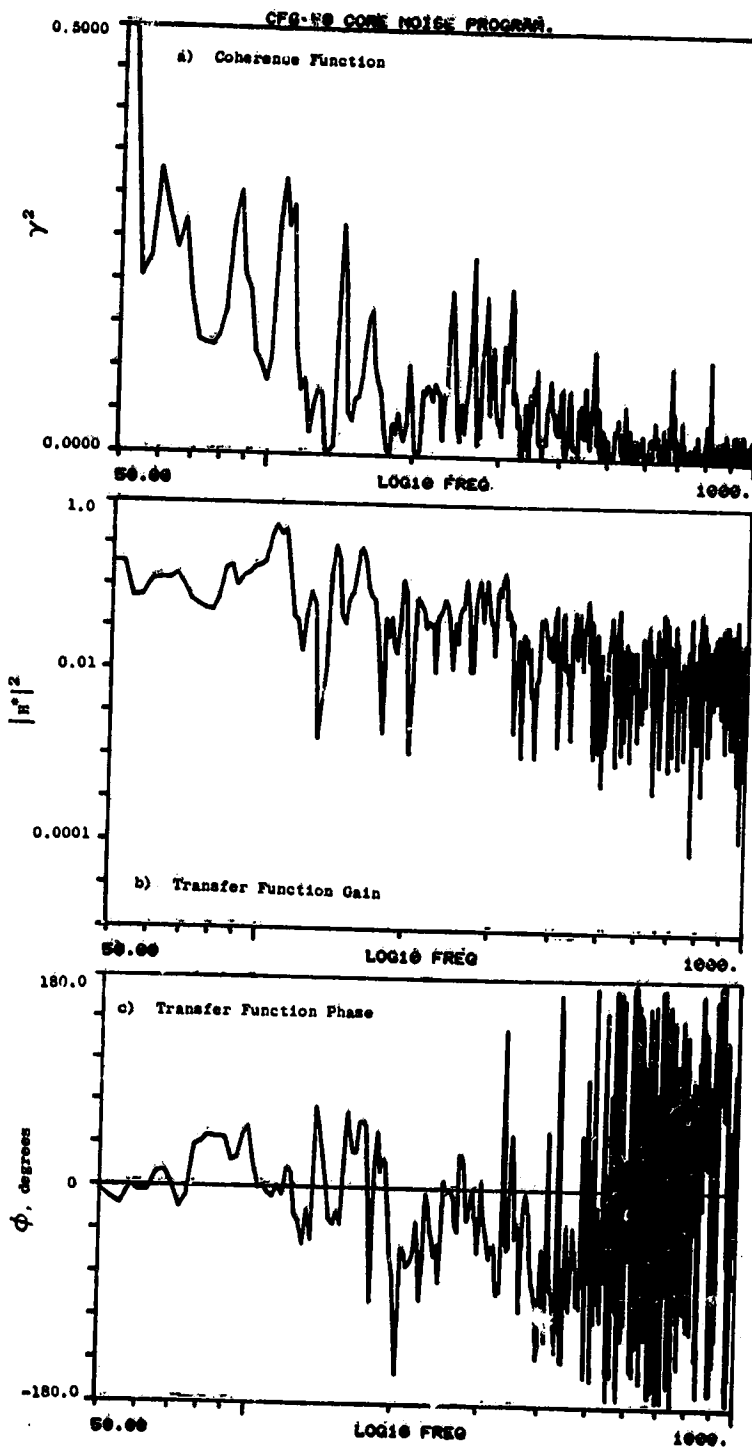


Figure A-123. Coherence and Transfer Functions for Plane 8.0A (270°) to 70° Farfield Microphone at 22.8% Thrust.

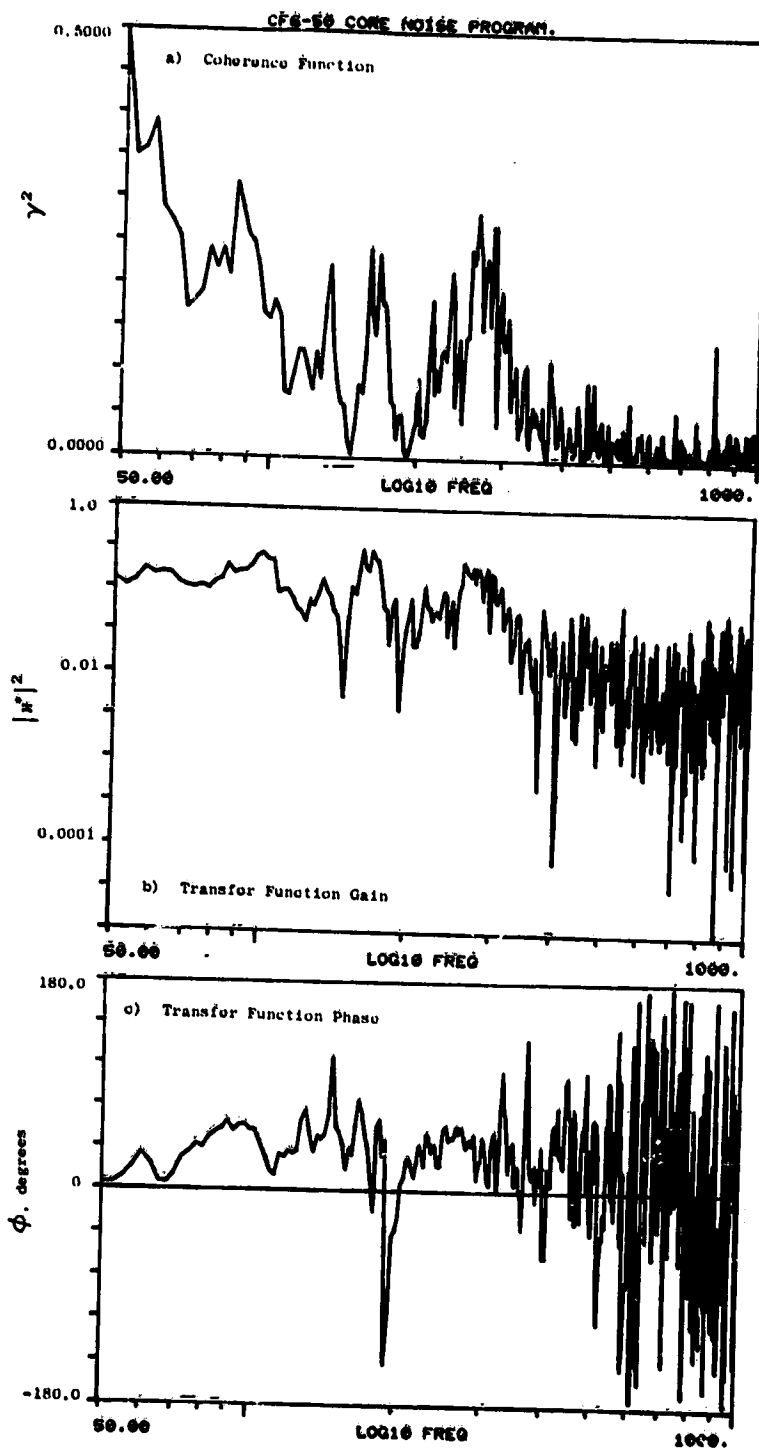


Figure A-124. Coherence and Transfer Functions for Plane 8.0A (270°) to 80° Farfield Microphone at 22.8% Thrust.

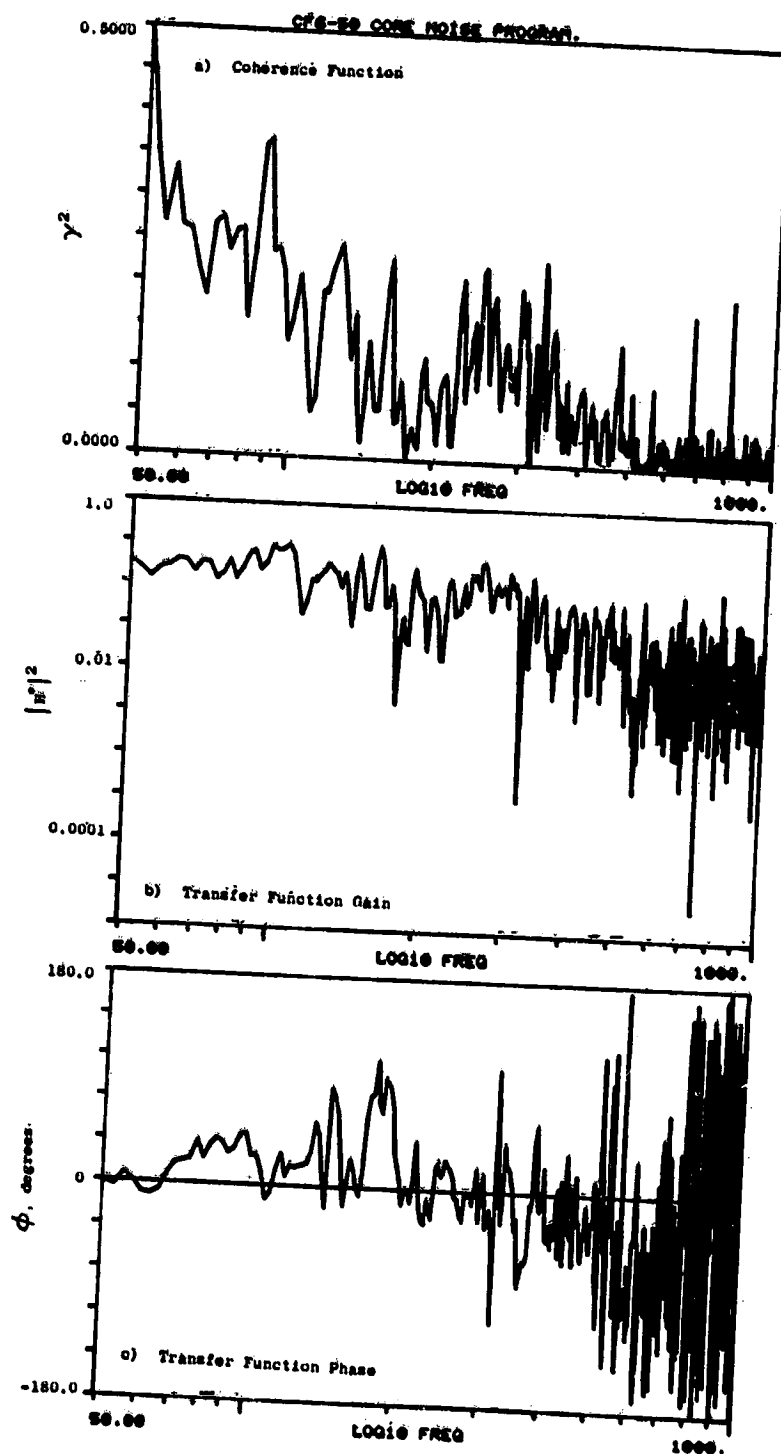


Figure A-125. Coherence and Transfer Functions for Plane 8.0A (270°) to 90° Farfield Microphone at 22.8% Thrust.

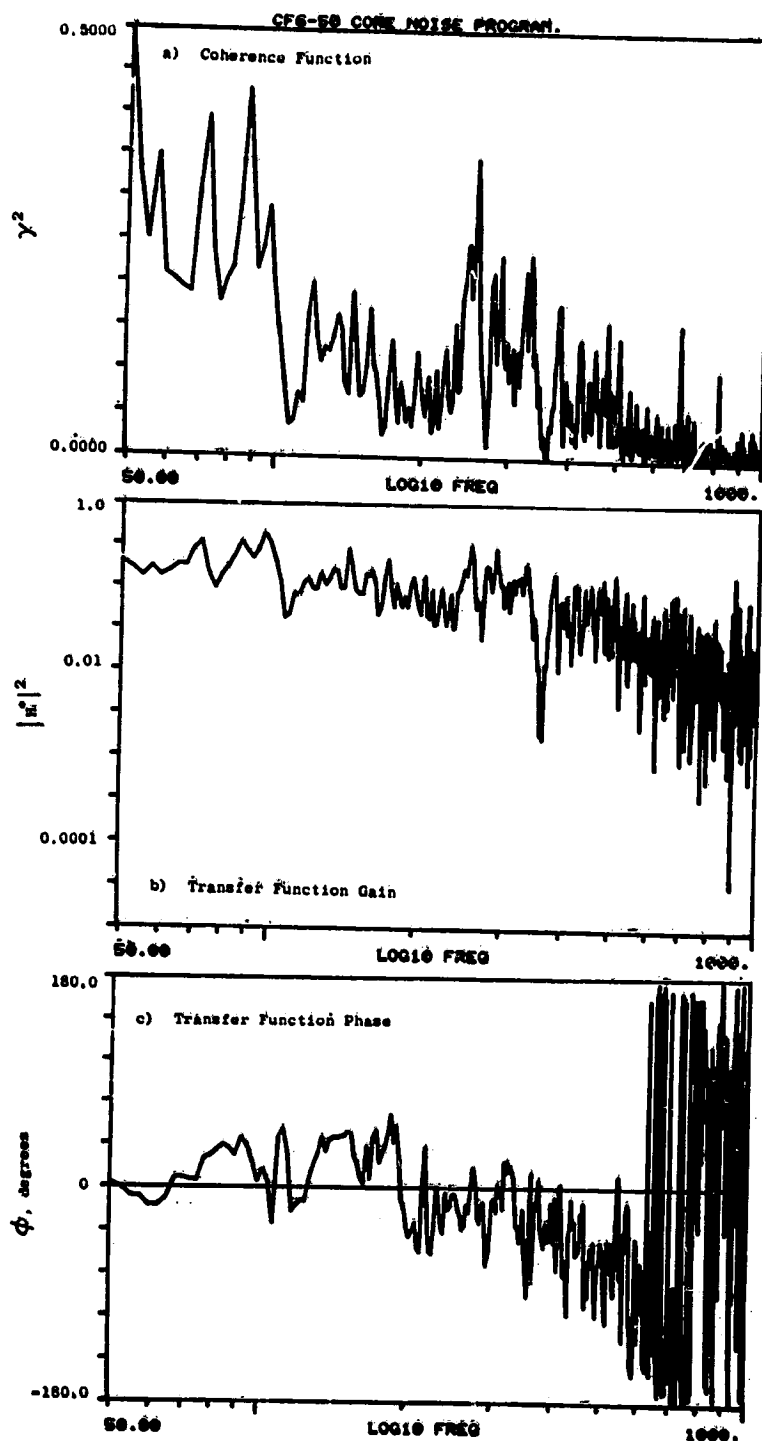


Figure A-126. Coherence and Transfer Functions for Plane 8.0A (270°) to 100° Farfield Microphone at 22.8% Thrust.

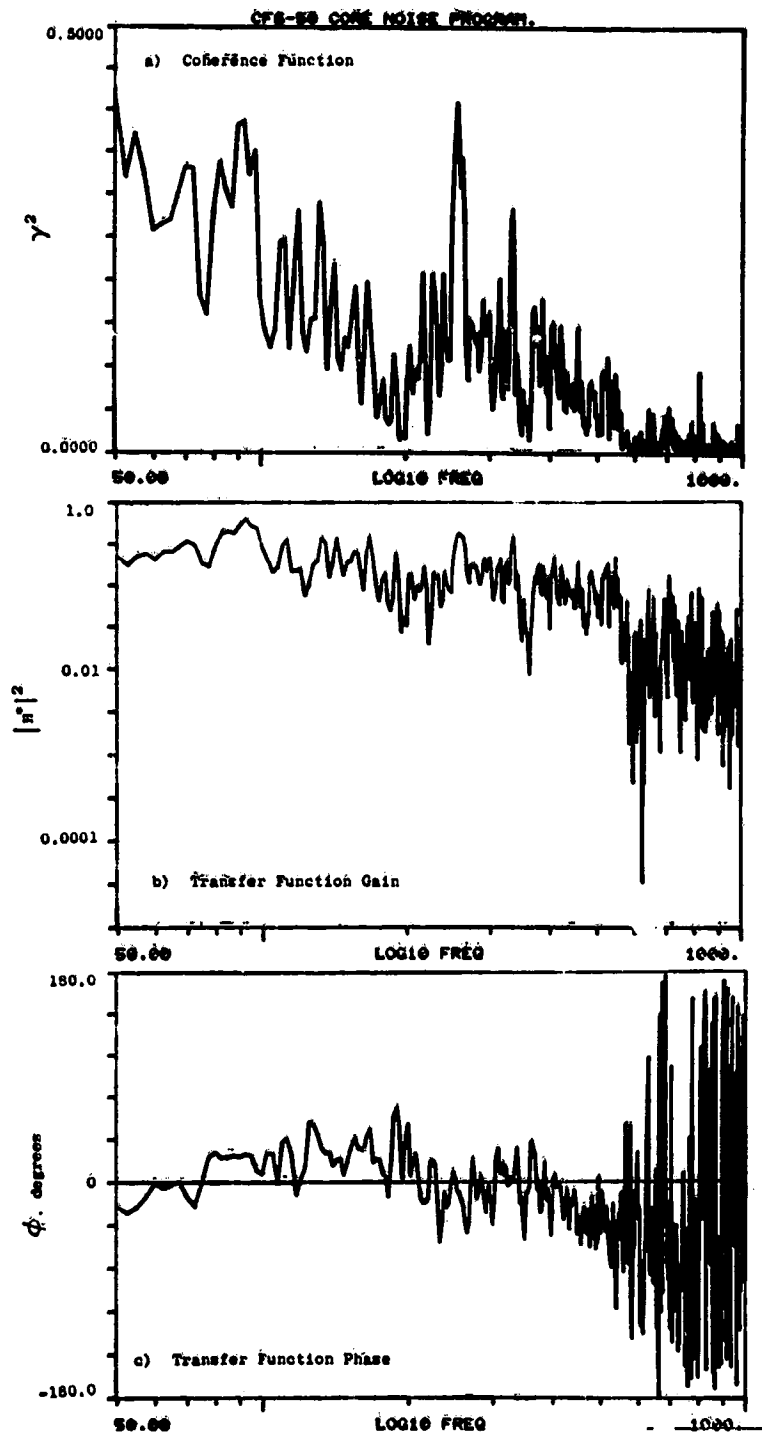


Figure A-127. Coherence and Transfer Functions for Plane 8.0A (270°) to 110° Farfield Microphone at 22.8% Thrust.

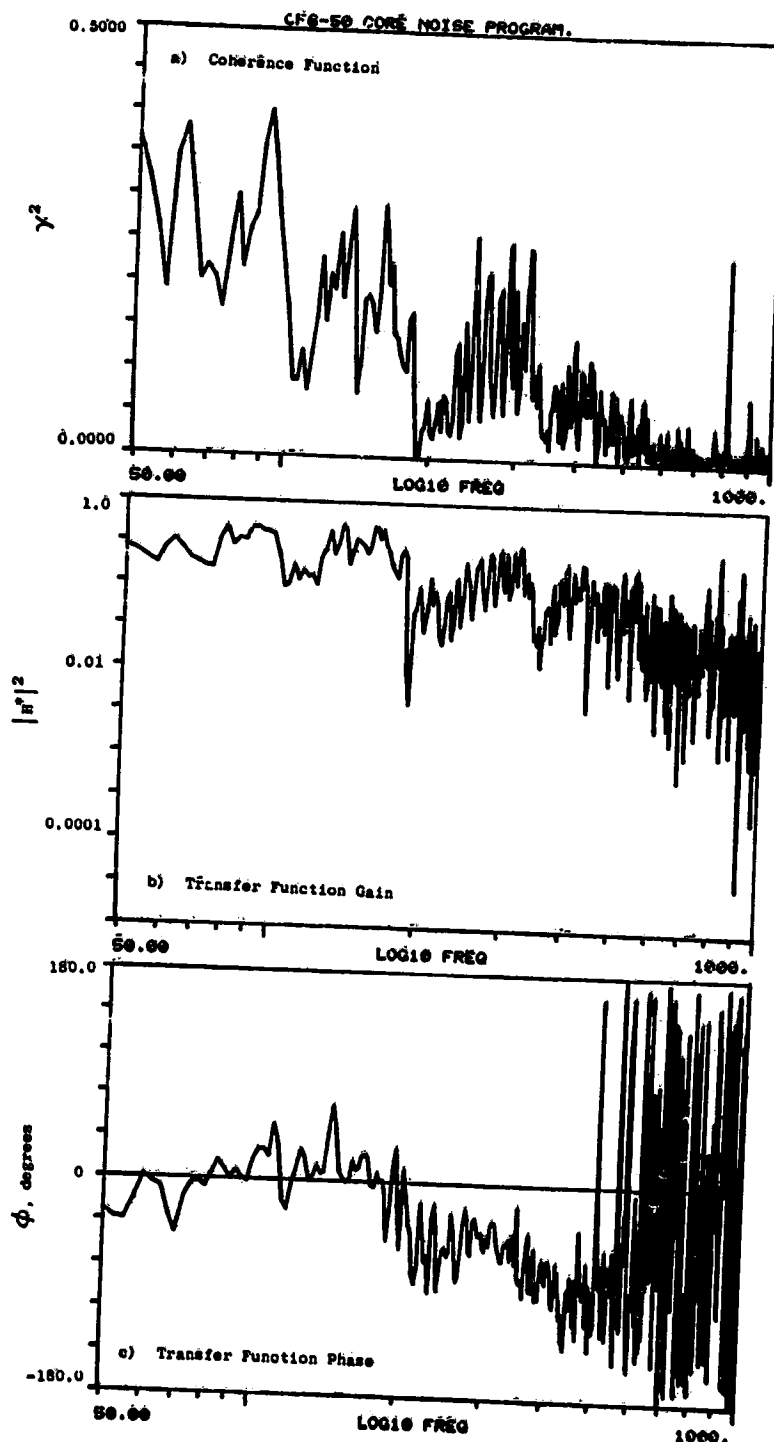


Figure A-128. Coherence and Transfer Functions for Plane 8.0A (270°) to 120° Farfield Microphone at 22.8% Thrust.

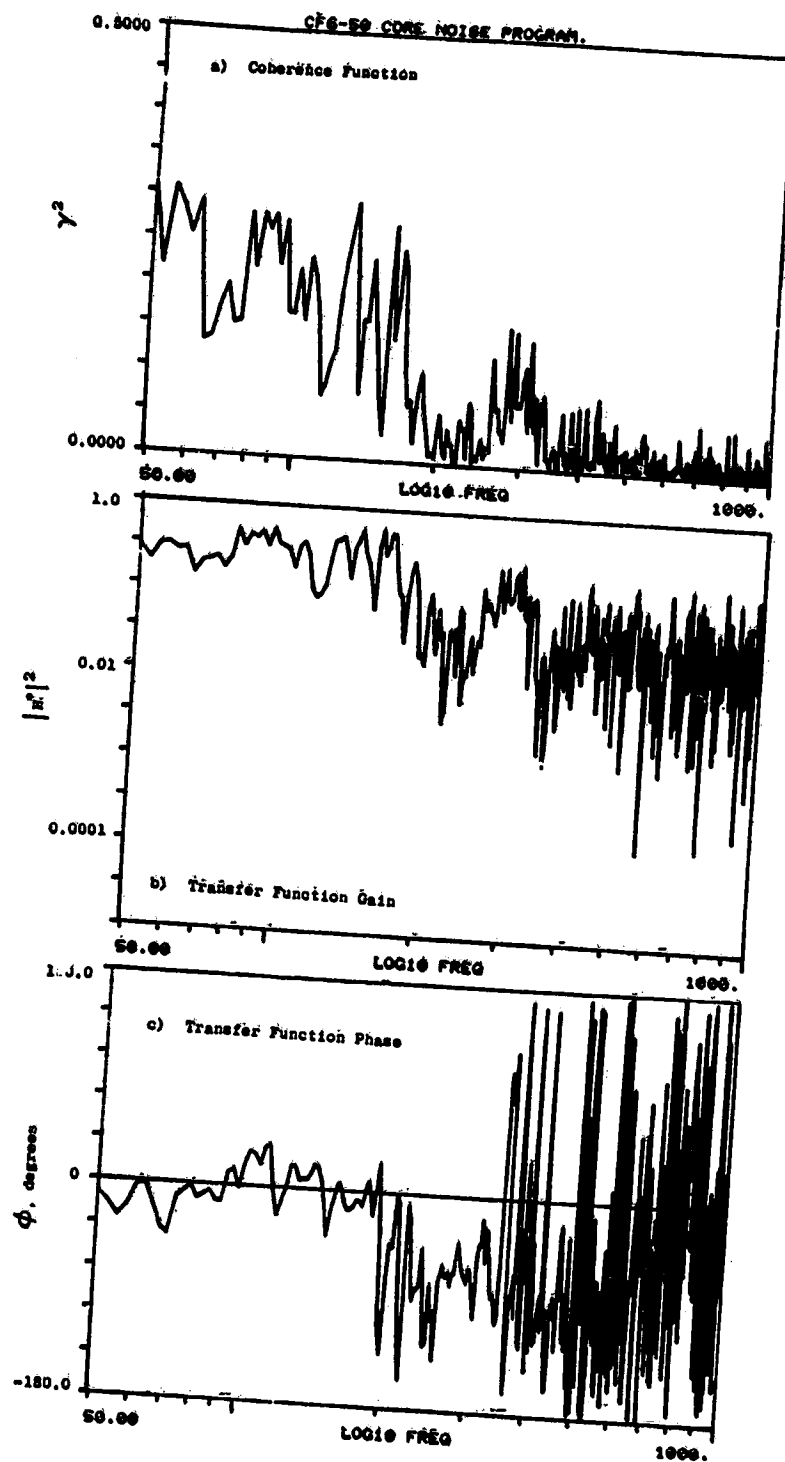


Figure A-129. Coherence and Transfer Functions for Plane 8.0A (270°) to 130° Farfield Microphone at 22.8% Thrust.

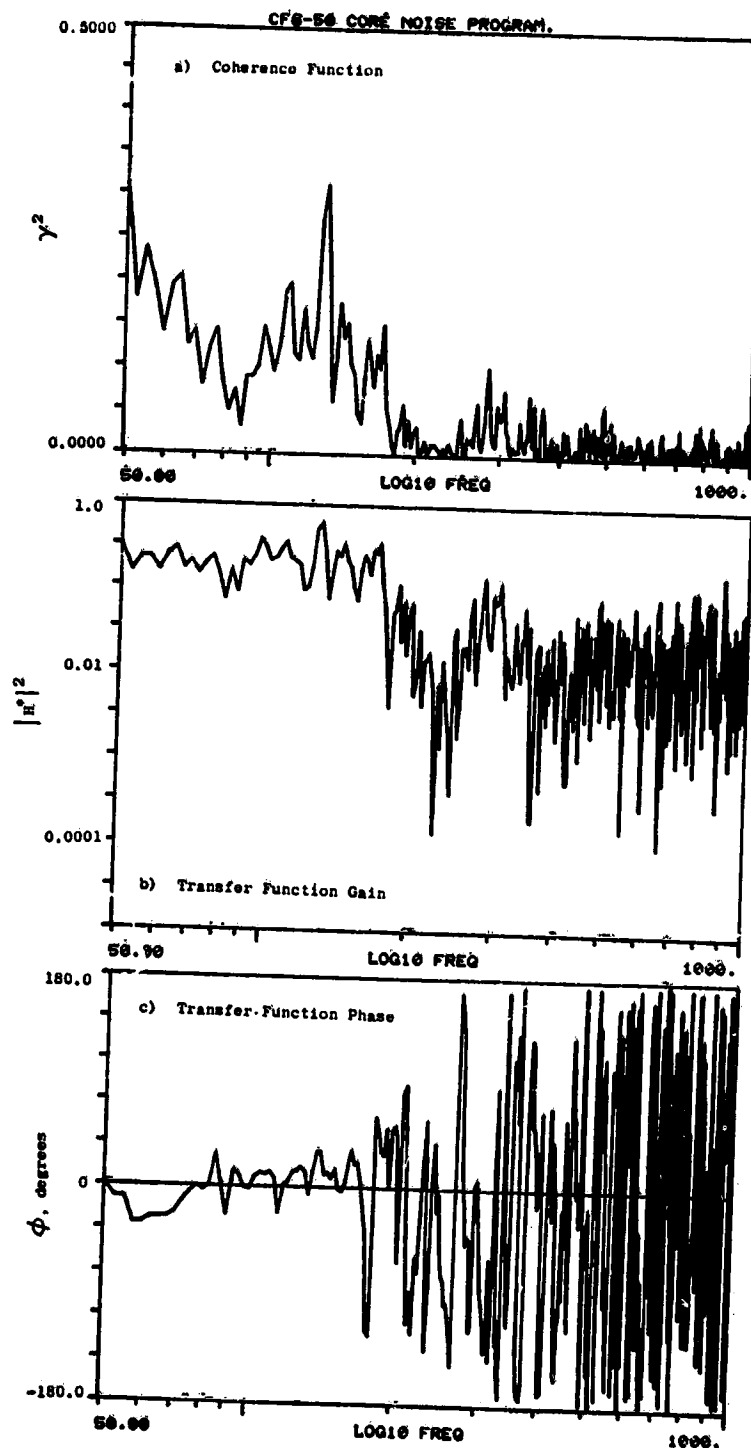


Figure A-130. Coherence and Transfer Functions for Plane 8.0A (270°) to 140° Farfield Microphone at 22.8% Thrust.

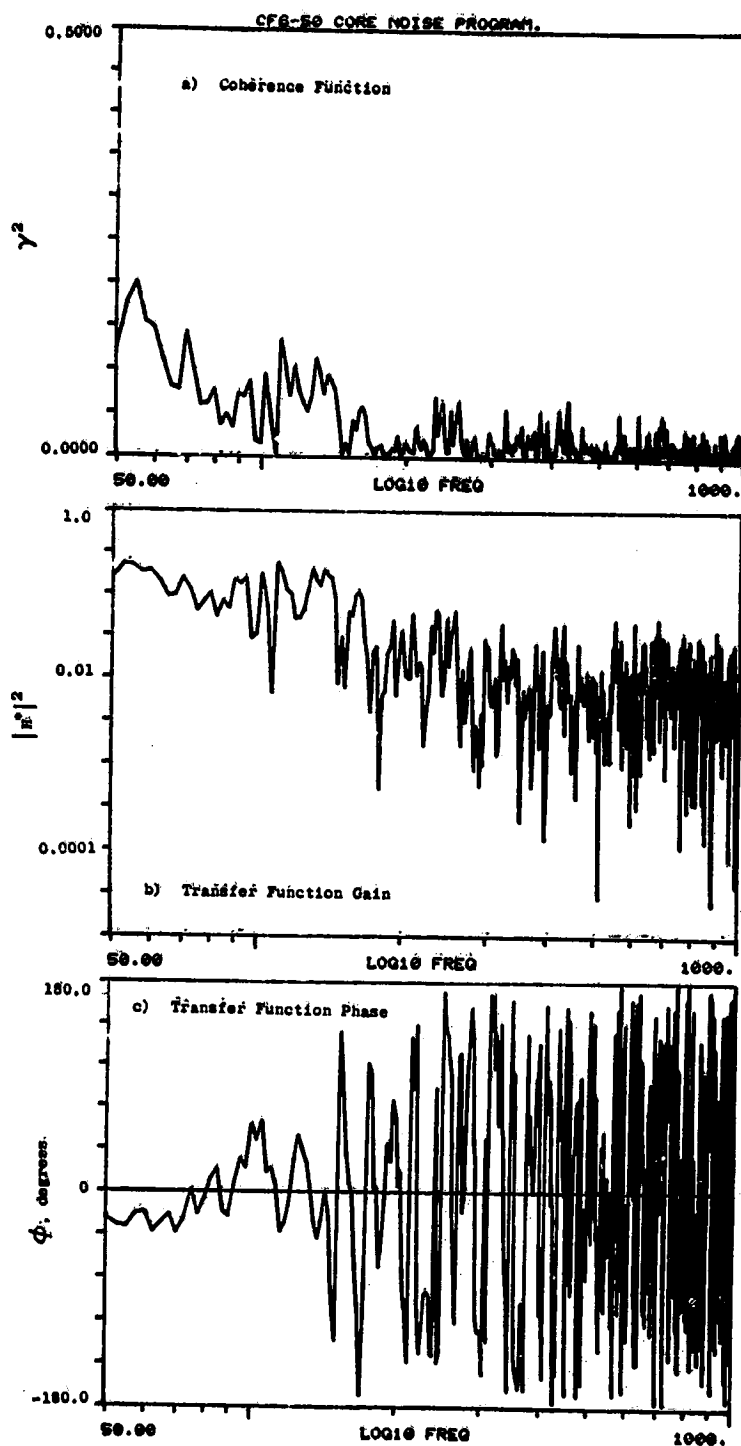


Figure A-131. Coherence and Transfer Functions for Plane 8.0A (270°) to 150° Farfield Microphone at 22.8% Thrust.

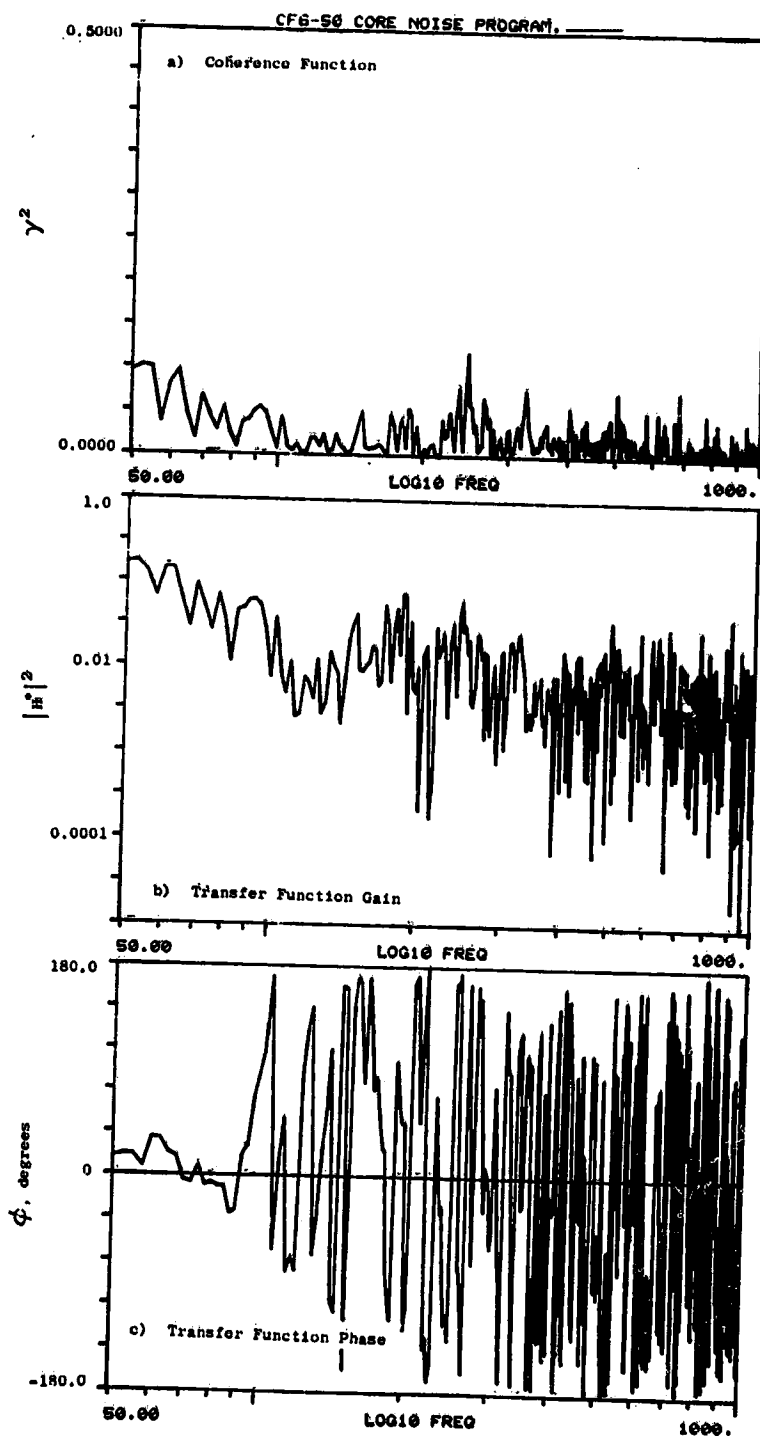


Figure A-132. Coherence and Transfer Functions for Plane 8.0A (270°) to 160° Farfield Microphone at 22.8% Thrust.

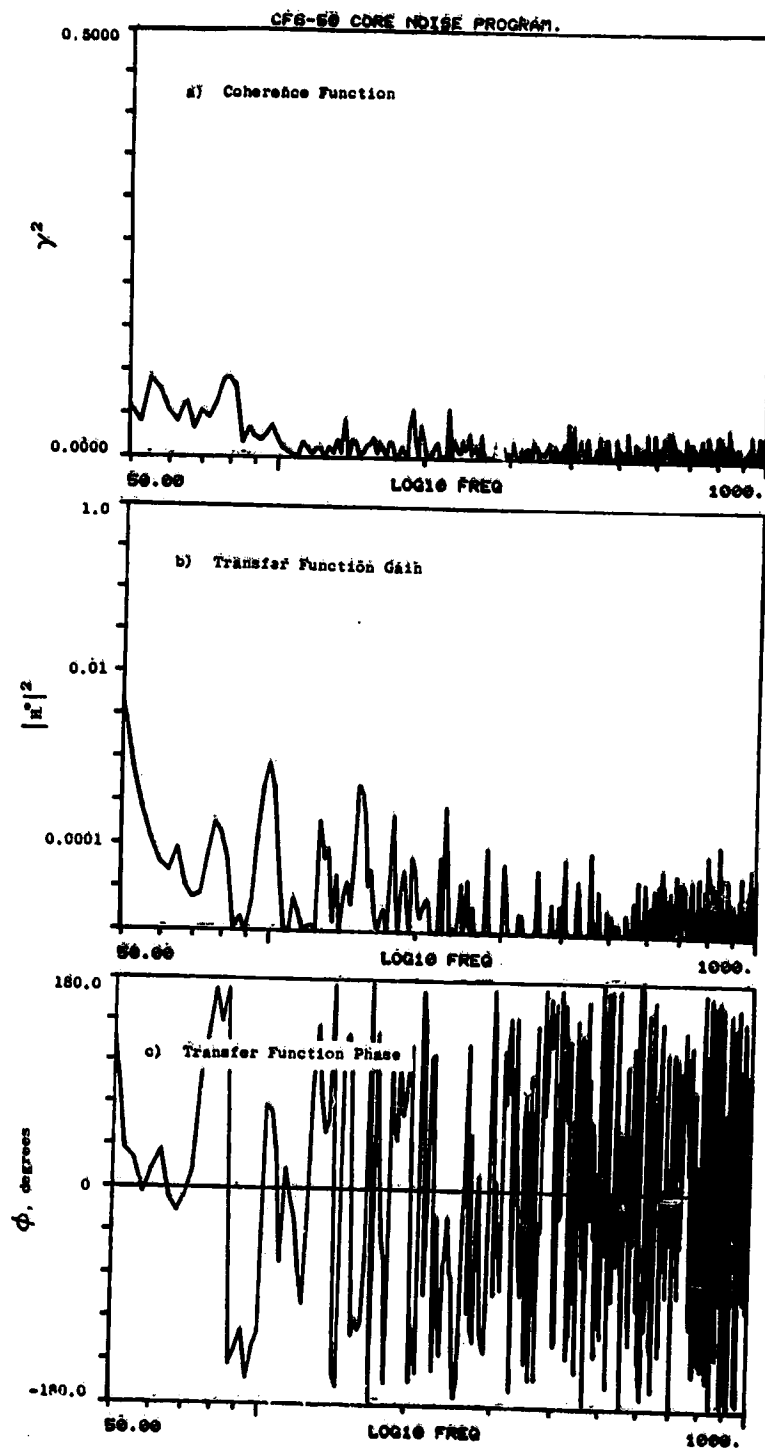


Figure A-133. Coherence and Transfer Functions for Plane 3.5 (102°) to 10° Farfield Microphone at 26.7% Thrust.

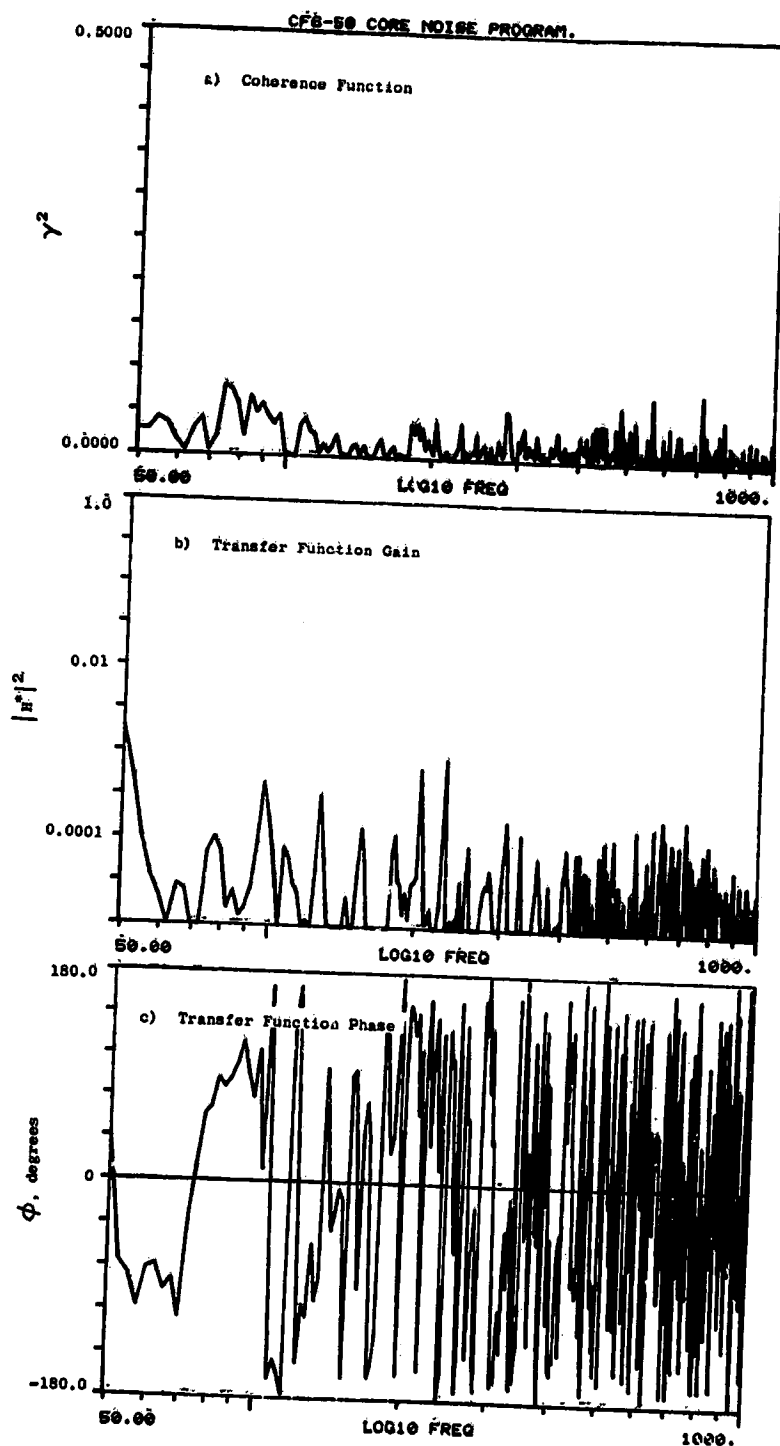


Figure A-134. Coherence and Transfer Functions for Plane 3.5 (102°) to 30° Farfield Microphone at 26.7% Thrust.

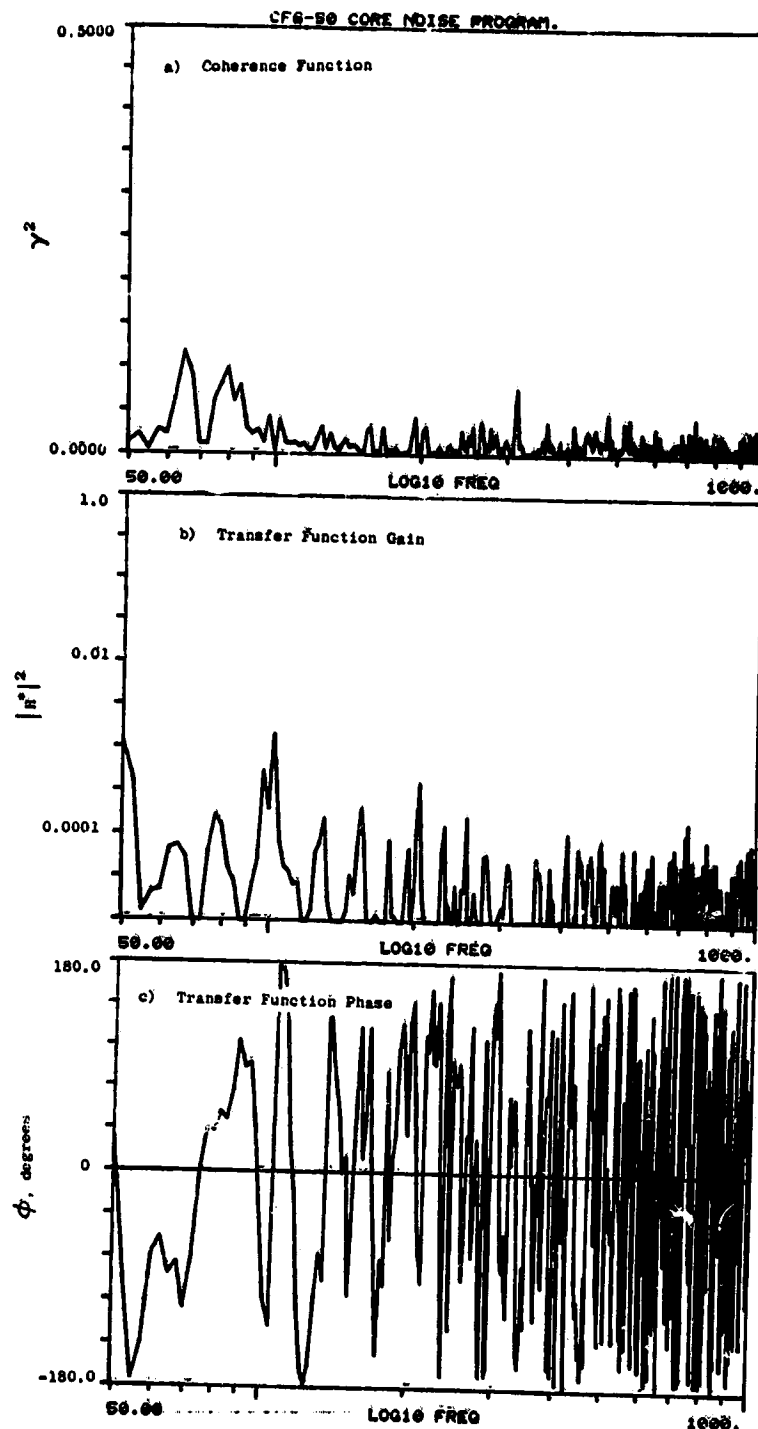


Figure A-135. Coherence and Transfer Functions for Plane 3.5 (102°) to 40° Farfield Microphone at 26.7% Thrust.

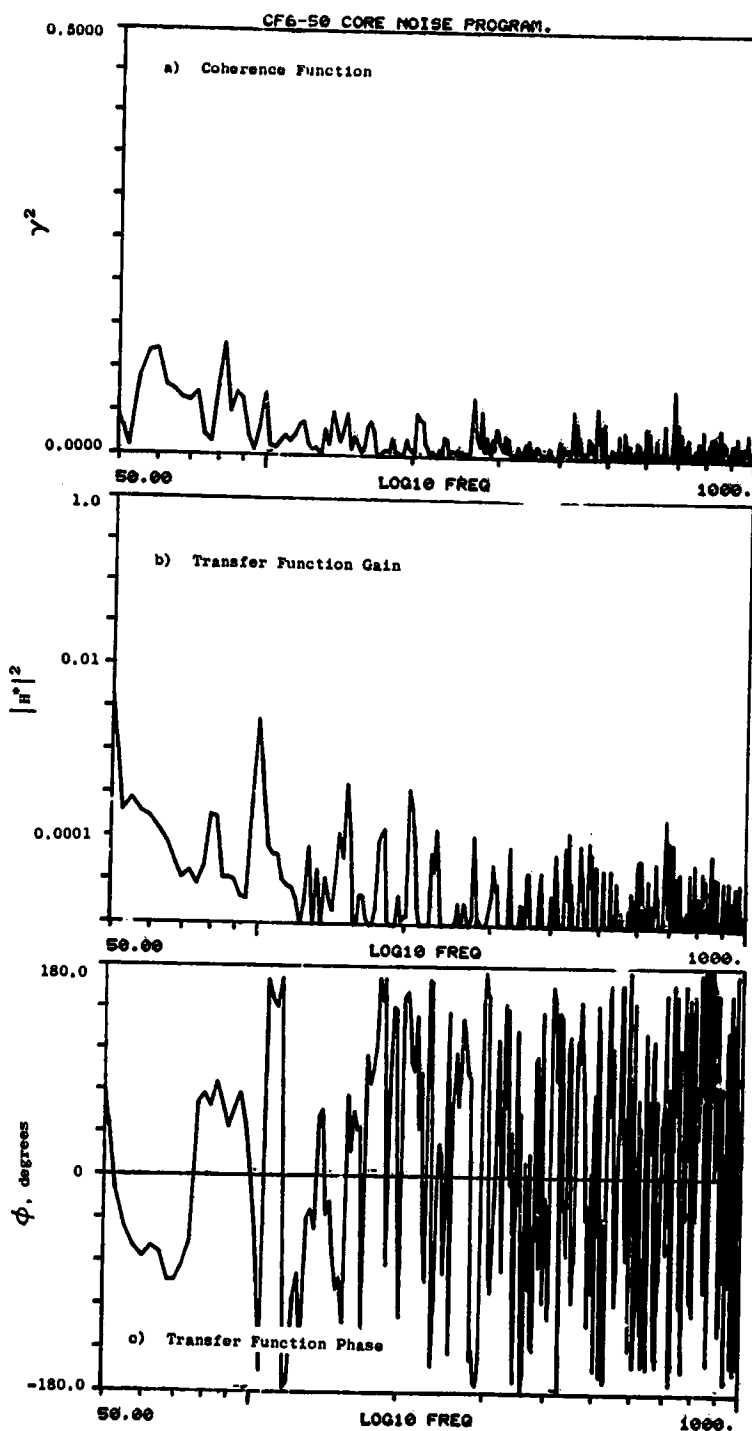


Figure A-136. Coherence and Transfer Functions for Plane 3.5 (102°) to 50° Farfield Microphone at 26.7% Thrust.-----

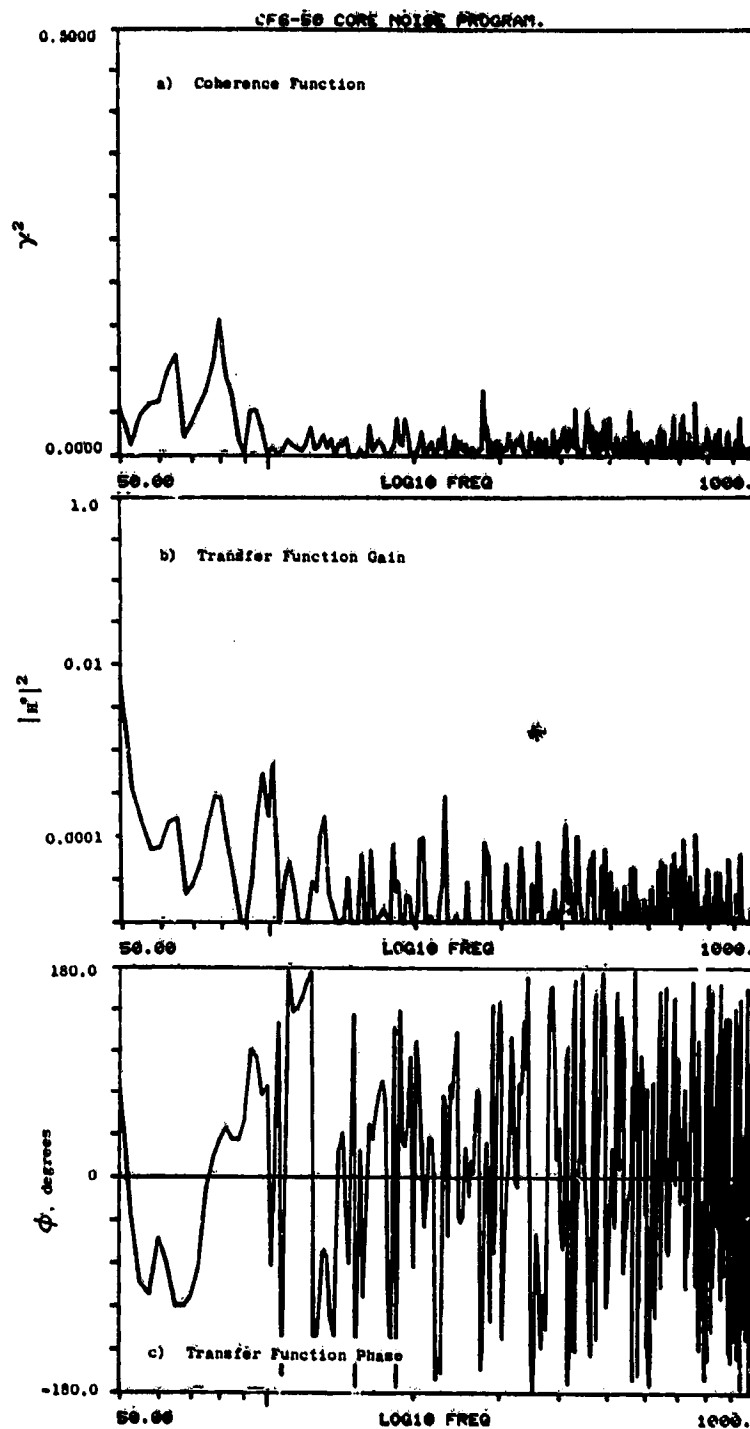


Figure A-137. Coherence and Transfer Functions for Plane 3.5 (102°) to 60° Farfield Microphone at 26.7% Thrust.

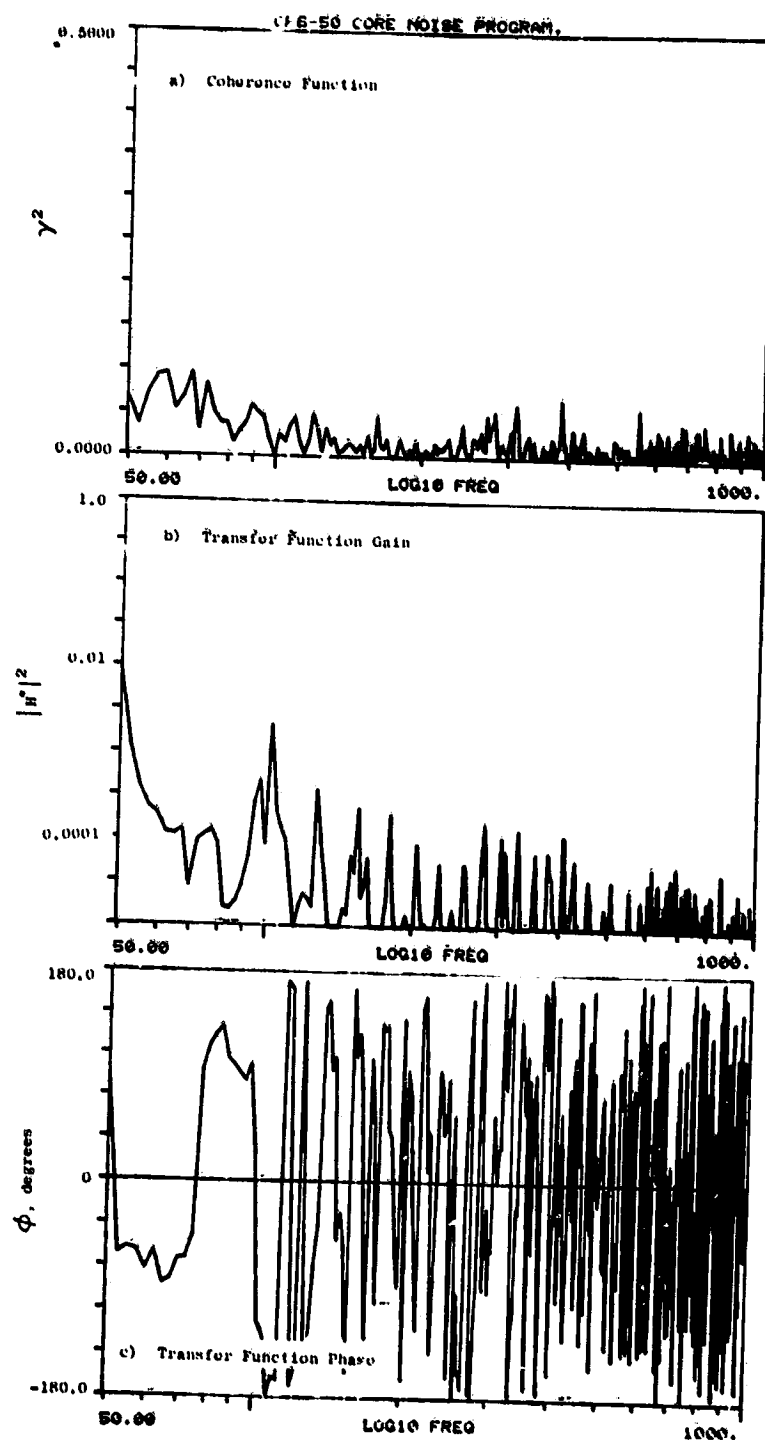


Figure A-138. Coherence and Transfer Functions for Plane 3.5 (102°) to 70° Farfield Microphone at 26.7% Thrust.

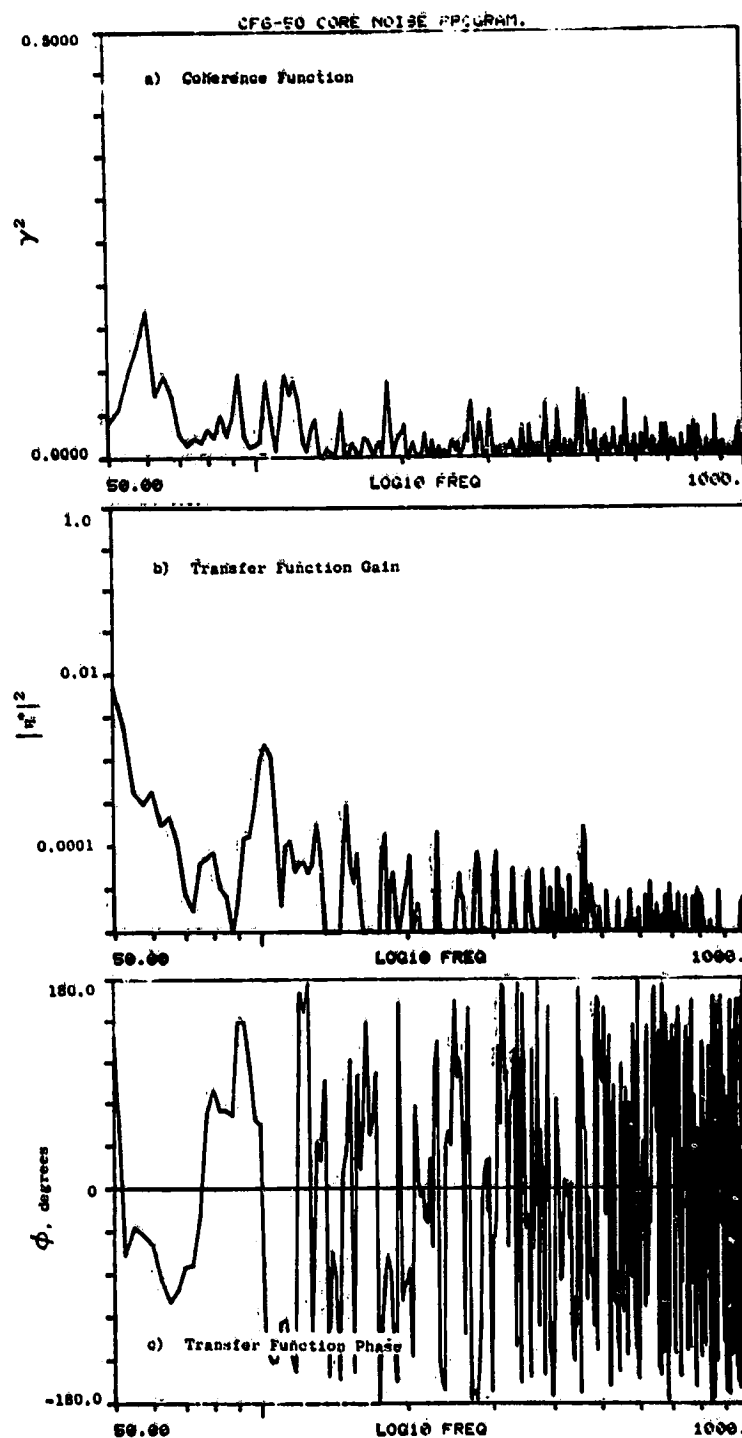


Figure A-139. Coherence and Transfer Functions for Plane 3.5 (102°) to 80° Farfield Microphone at 26.7% Thrust.

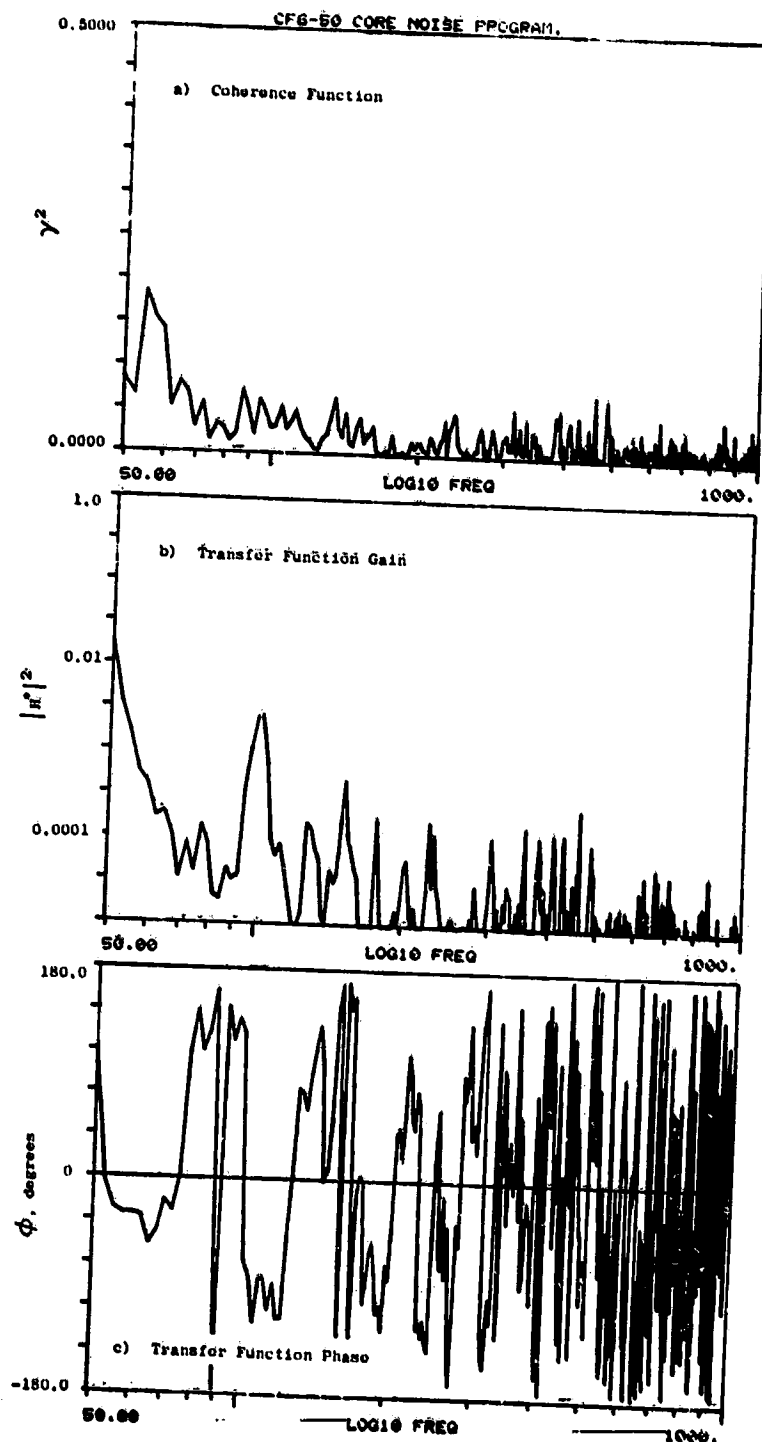


Figure A-140. Coherence and Transfer Functions for Plane 3.5 (102°) to 90° Farfield Microphone at 26.7% Thrust.

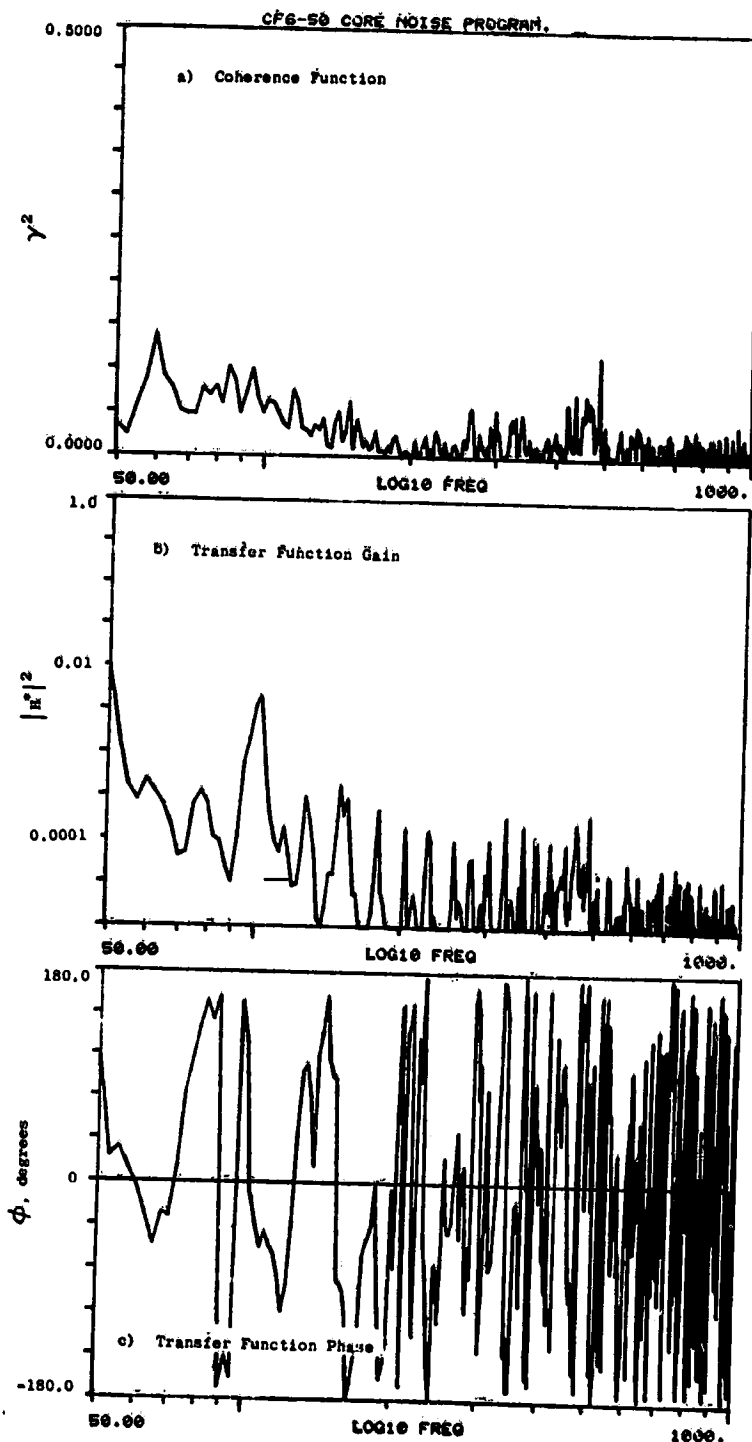


Figure A-141. Coherence and Transfer Functions for Plane 3.5 (102°) to 100° Farfield Microphone at 26.7% Thrust.

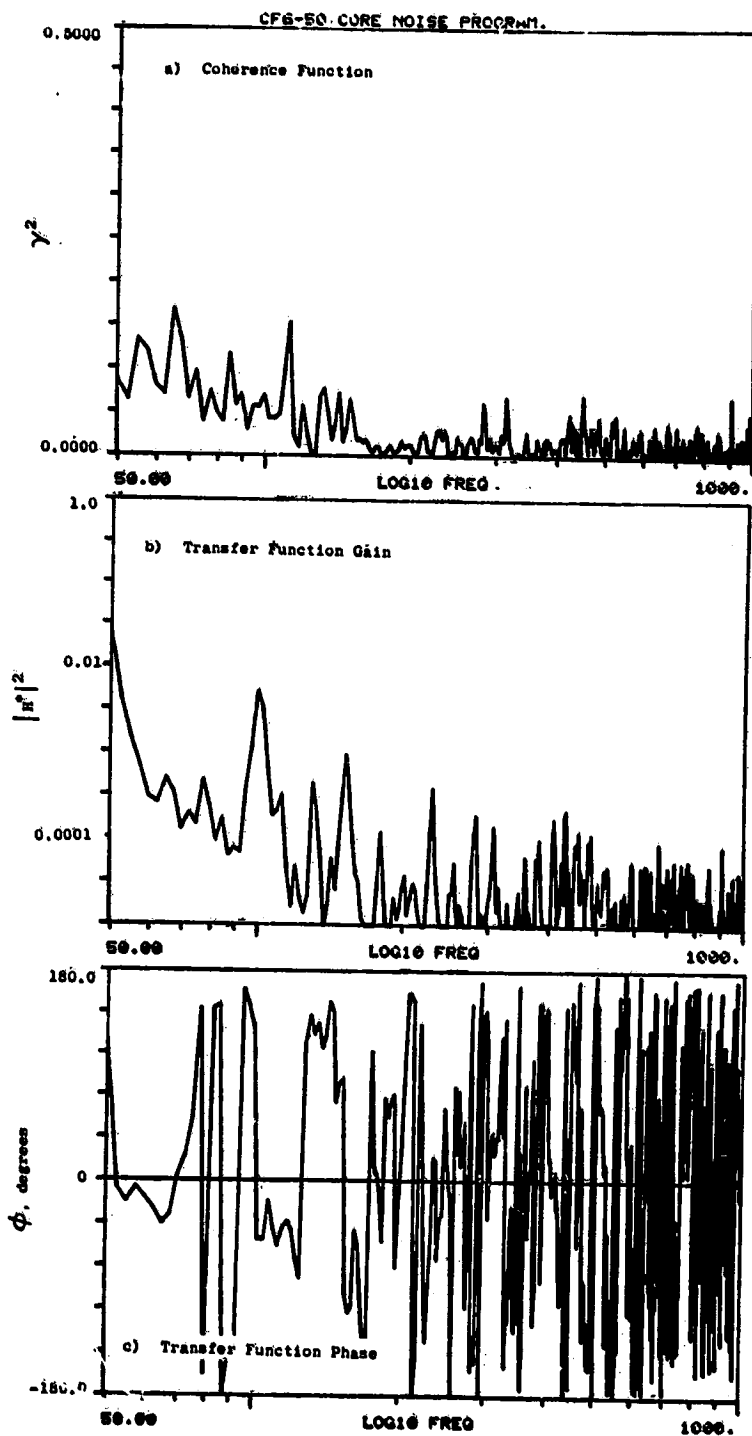


Figure A-142. Coherence and Transfer Functions for Plane 3.5 (102°) to 110° Farfield Microphone at 26.7% Thrust.

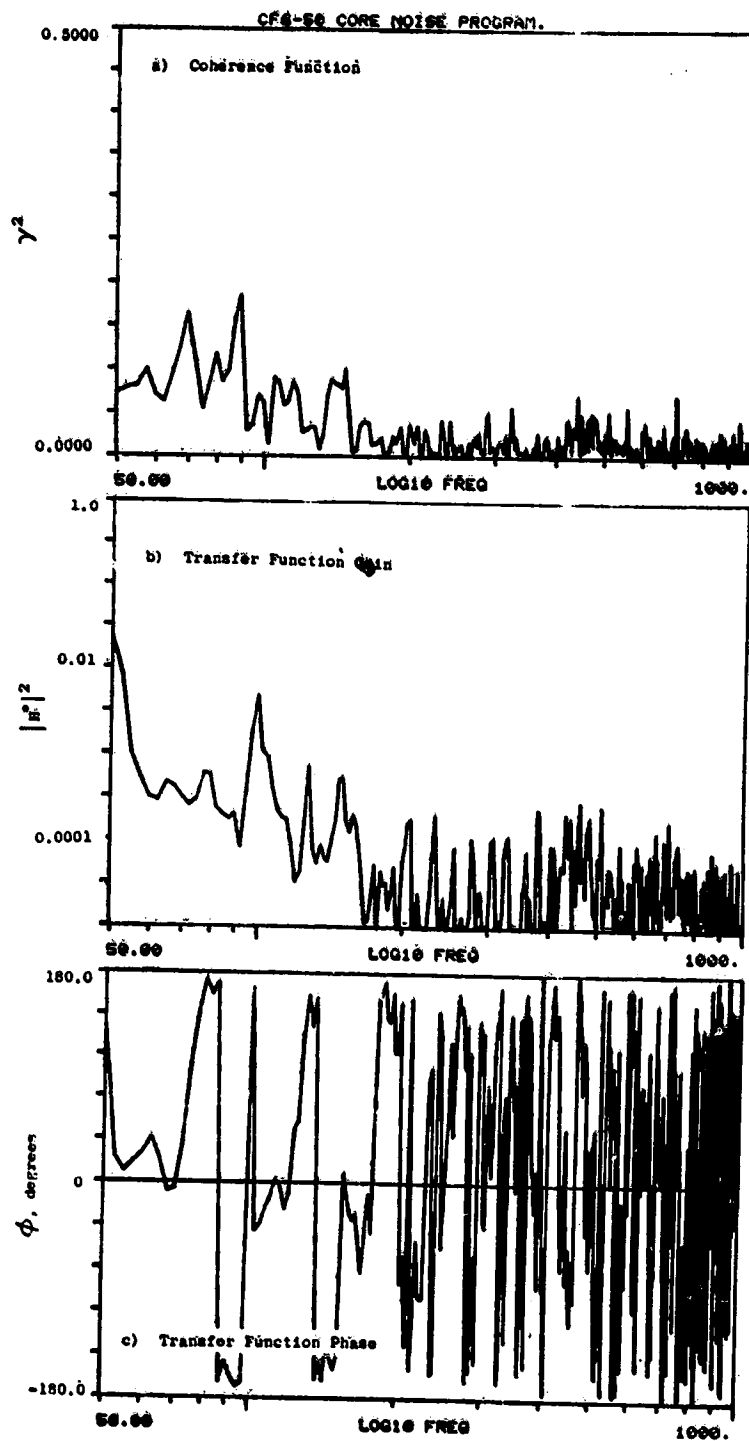


Figure A-143. Coherence and Transfer Functions for Plane 3.5 (102°) to 120° Farfield Microphone at 26.7% Thrust.

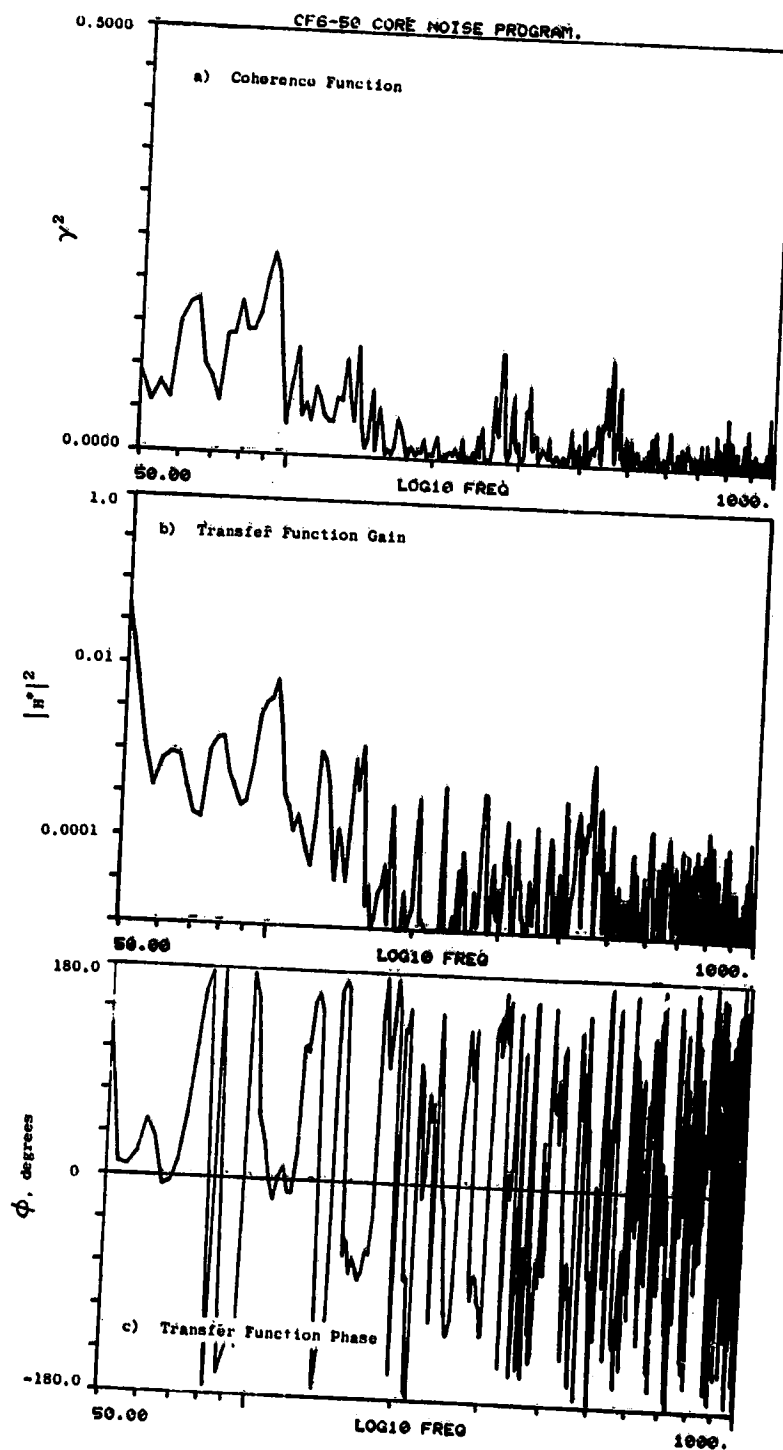


Figure A-144. Coherence and Transfer Functions for Plane 3.5 (102°) to 130° Farfield Microphone at 26.7% Thrust.

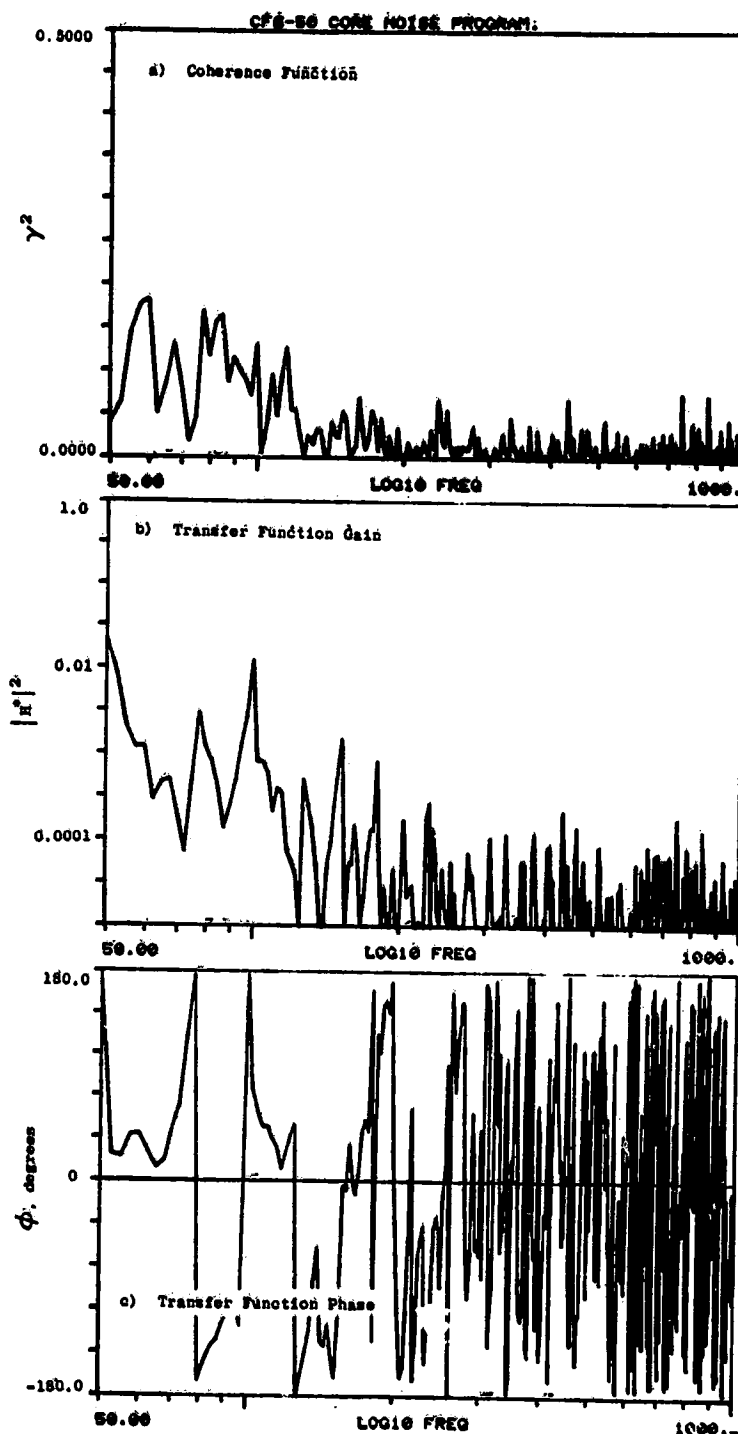


Figure A-145. Coherence and Transfer Functions for Plane 3.5 (102°) to 140° Farfield Microphone at 26.7% Thrust.

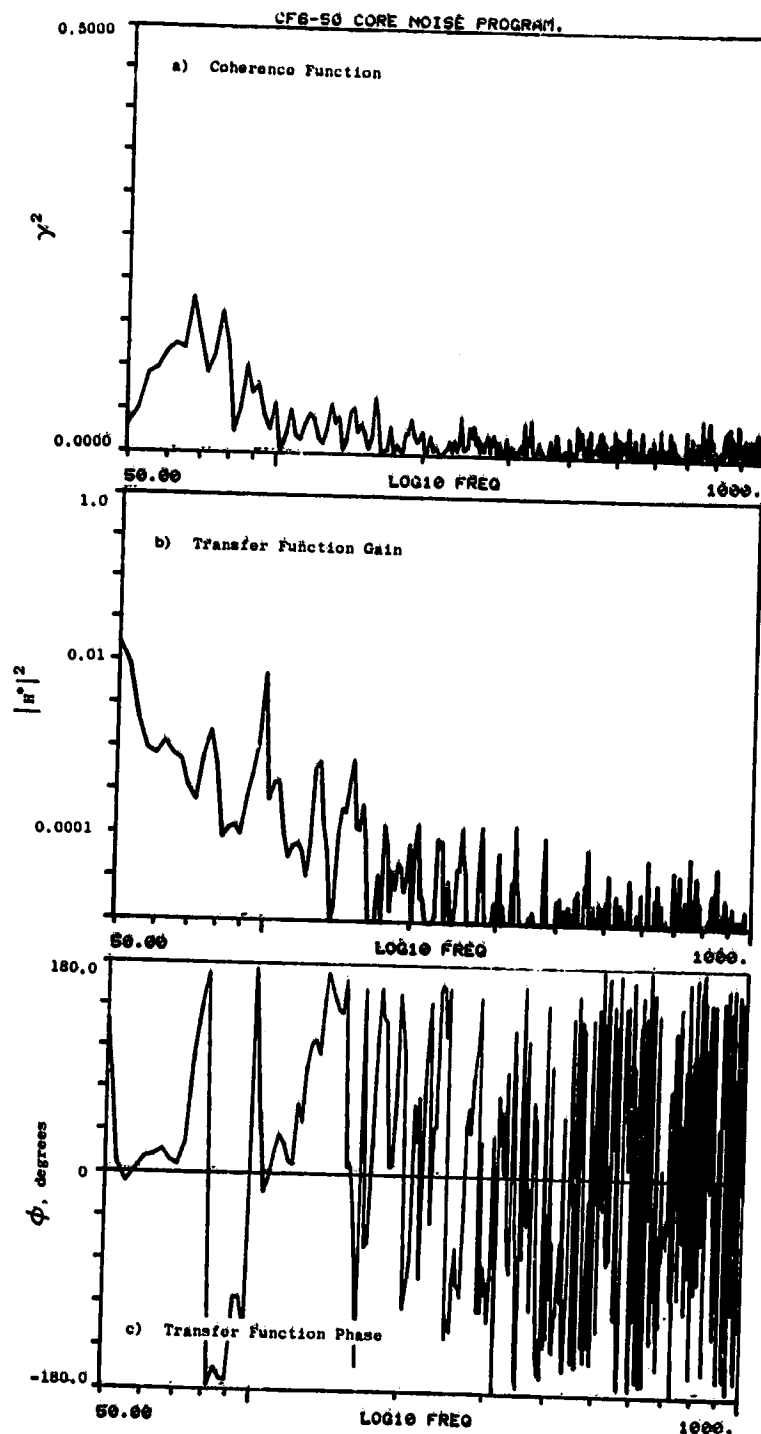


Figure A-146. Coherence and Transfer Functions for Plane 3.5 (102°) to 150° Farfield Microphone at 26.7% Thrust.

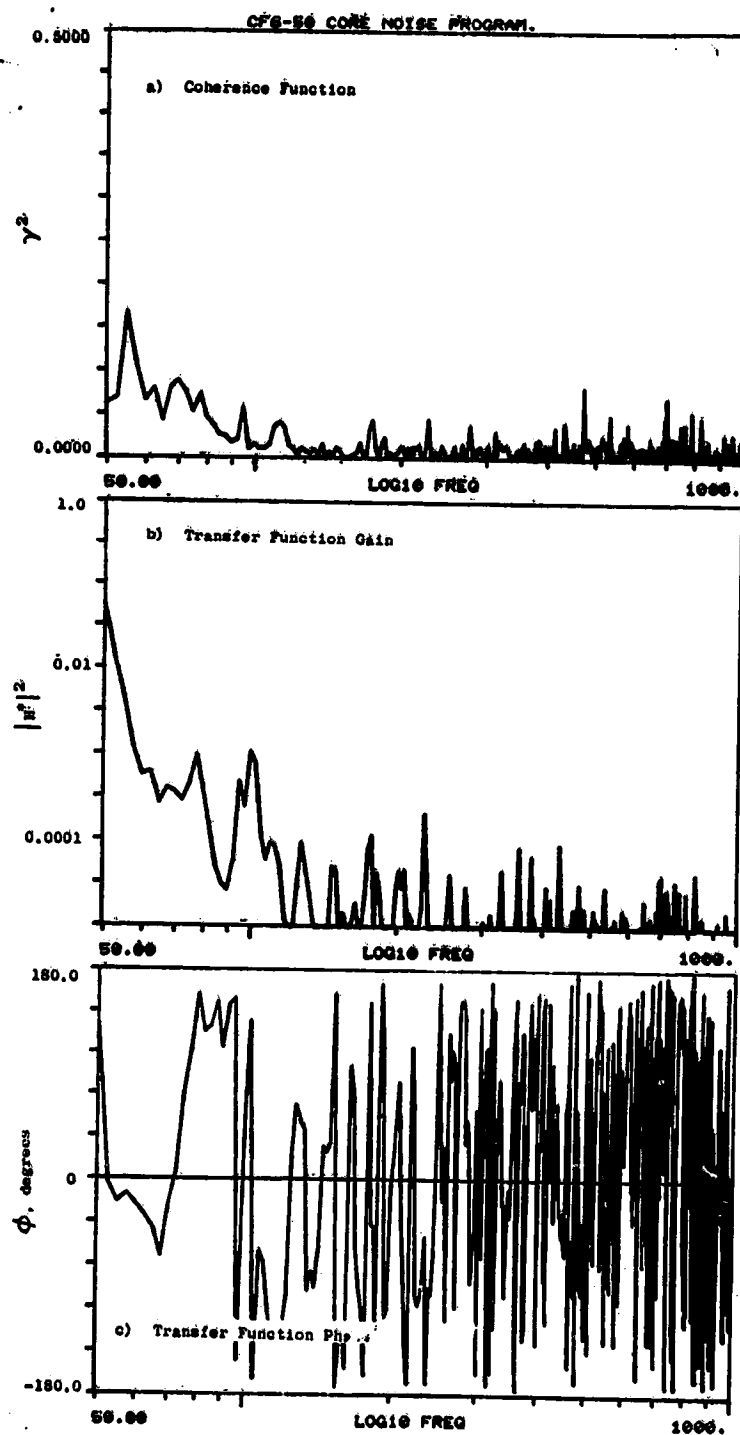


Figure A-147. Coherence and Transfer Functions for Plane 3.5 (102°) to 160° Farfield Microphone at 26.7% Thrust.

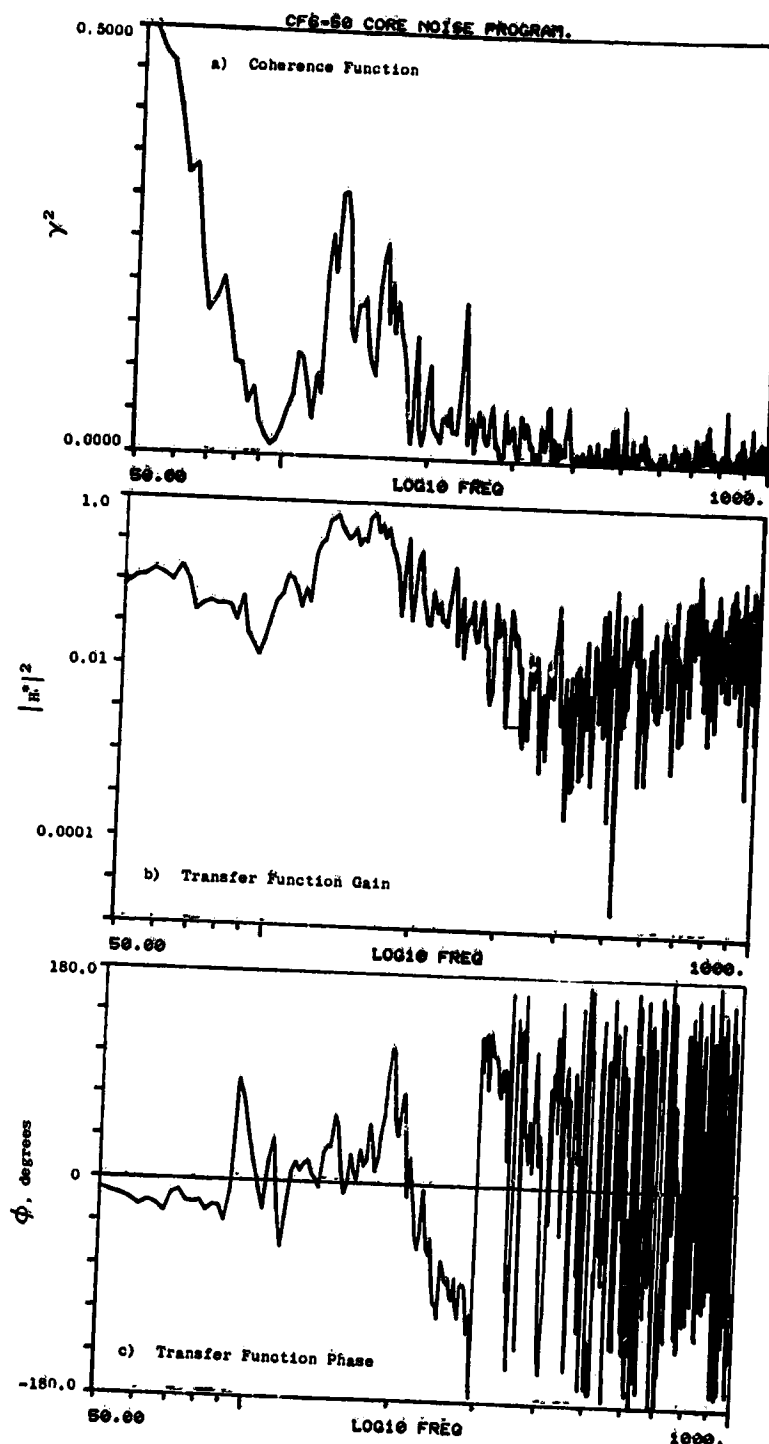


Figure A-148. Coherence and Transfer Functions for Plane 8.0A (270°) to 10° Farfield Microphone at 26.7% Thrust.

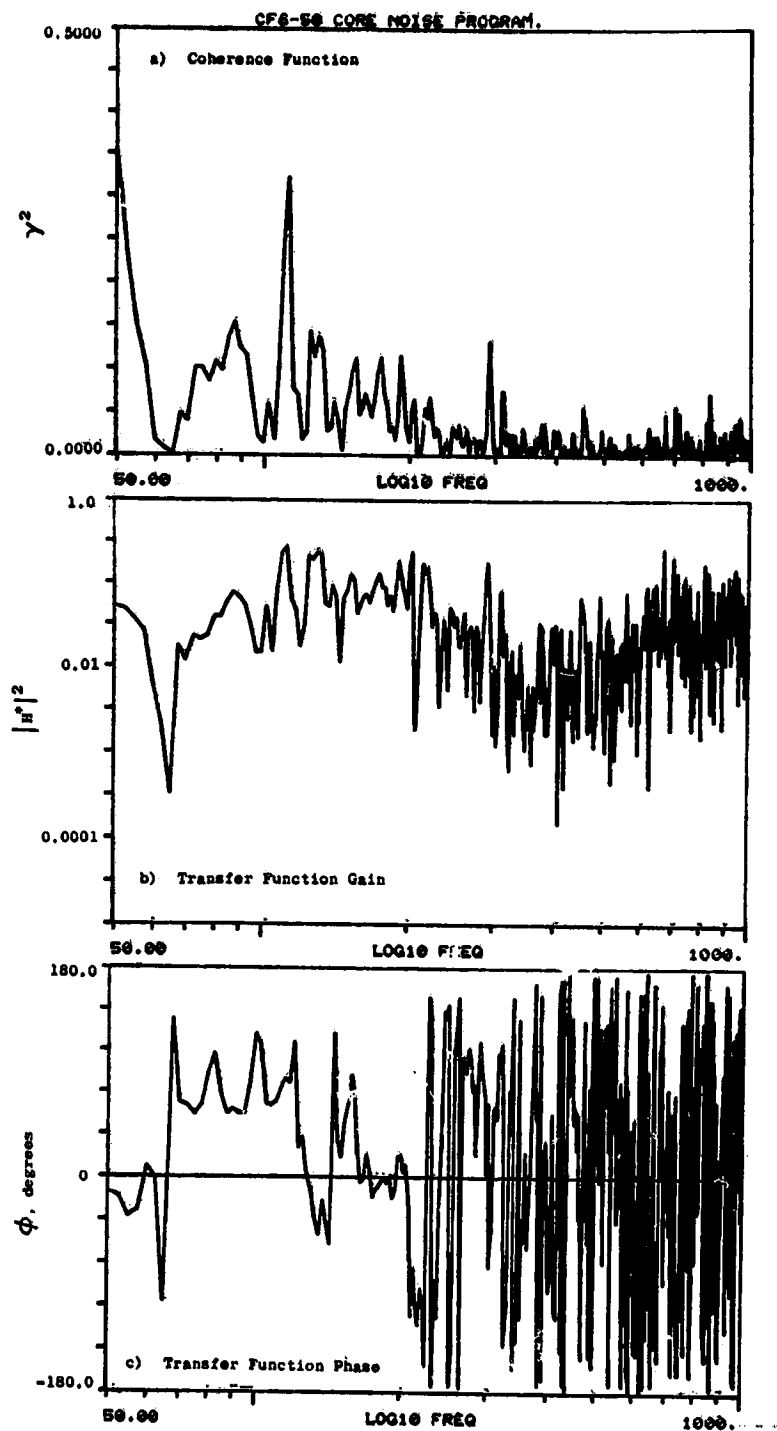


Figure A-149. Coherence and Transfer Functions for Plane 8.0A (270°) to 30° Farfield Microphone at 26.7% Thrust.

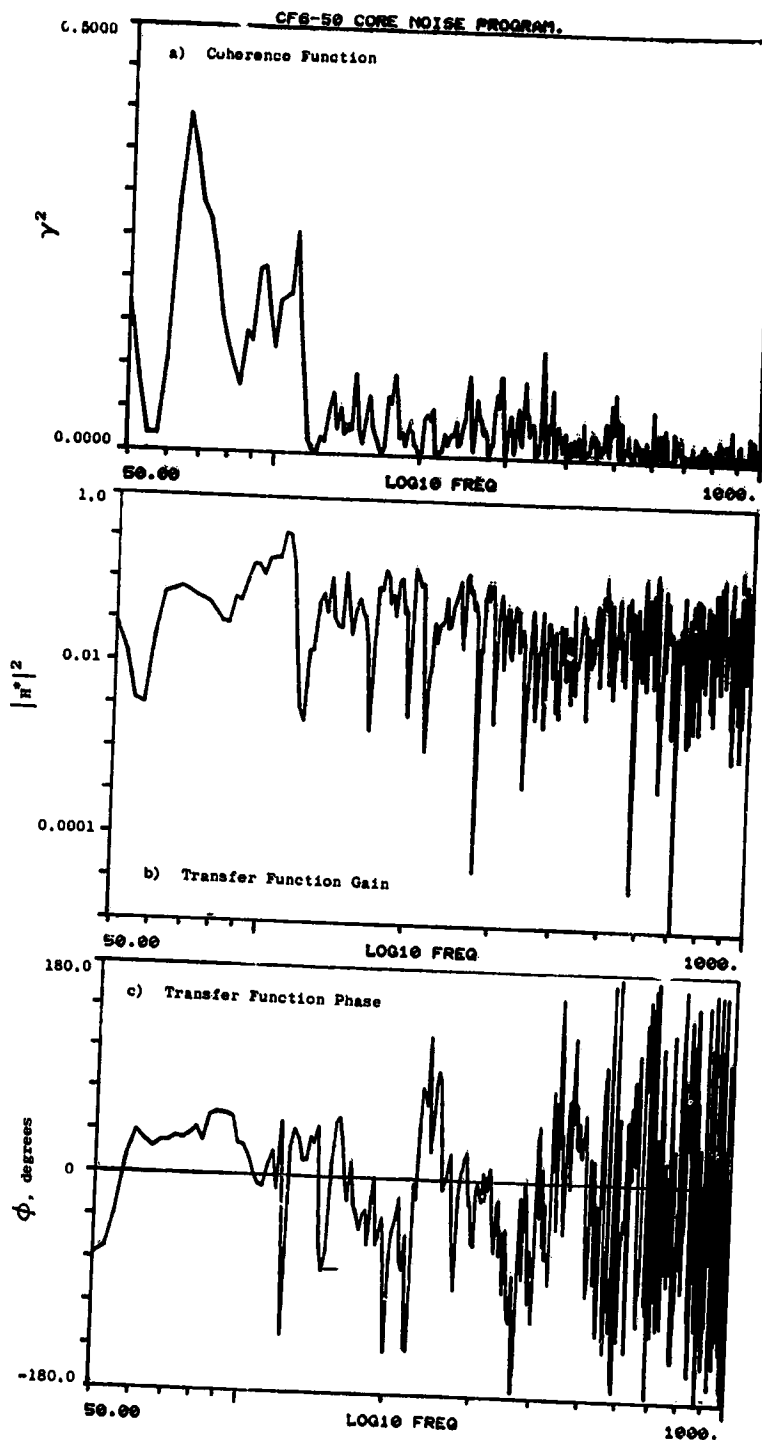


Figure A-150. Coherence and Transfer Functions for Plane 8.0A (270°) to 40° Farfield Microphone at 26.7% Thrust.

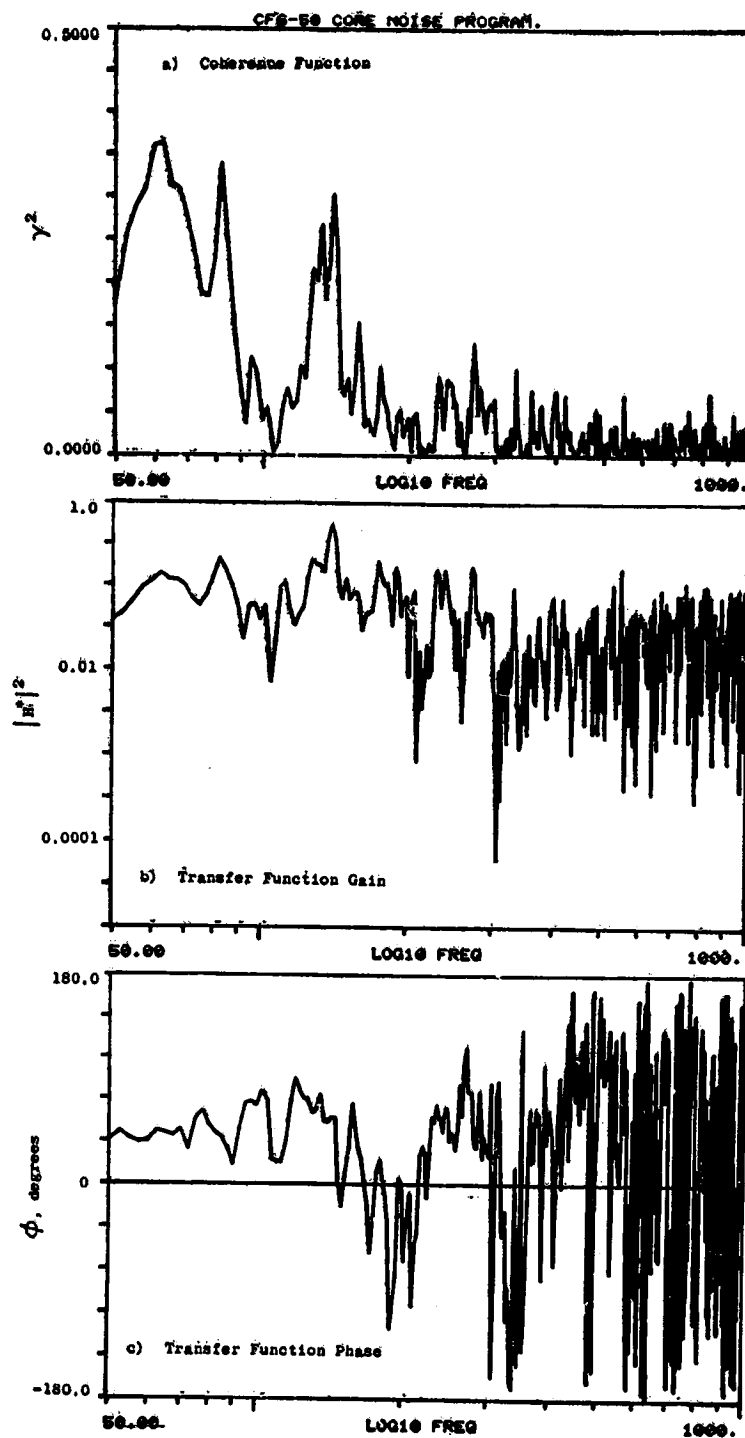


Figure A-151. Coherence and Transfer Functions for Plane 8.0A (270°) to 50° Farfield Microphone at 26.7% Thrust.

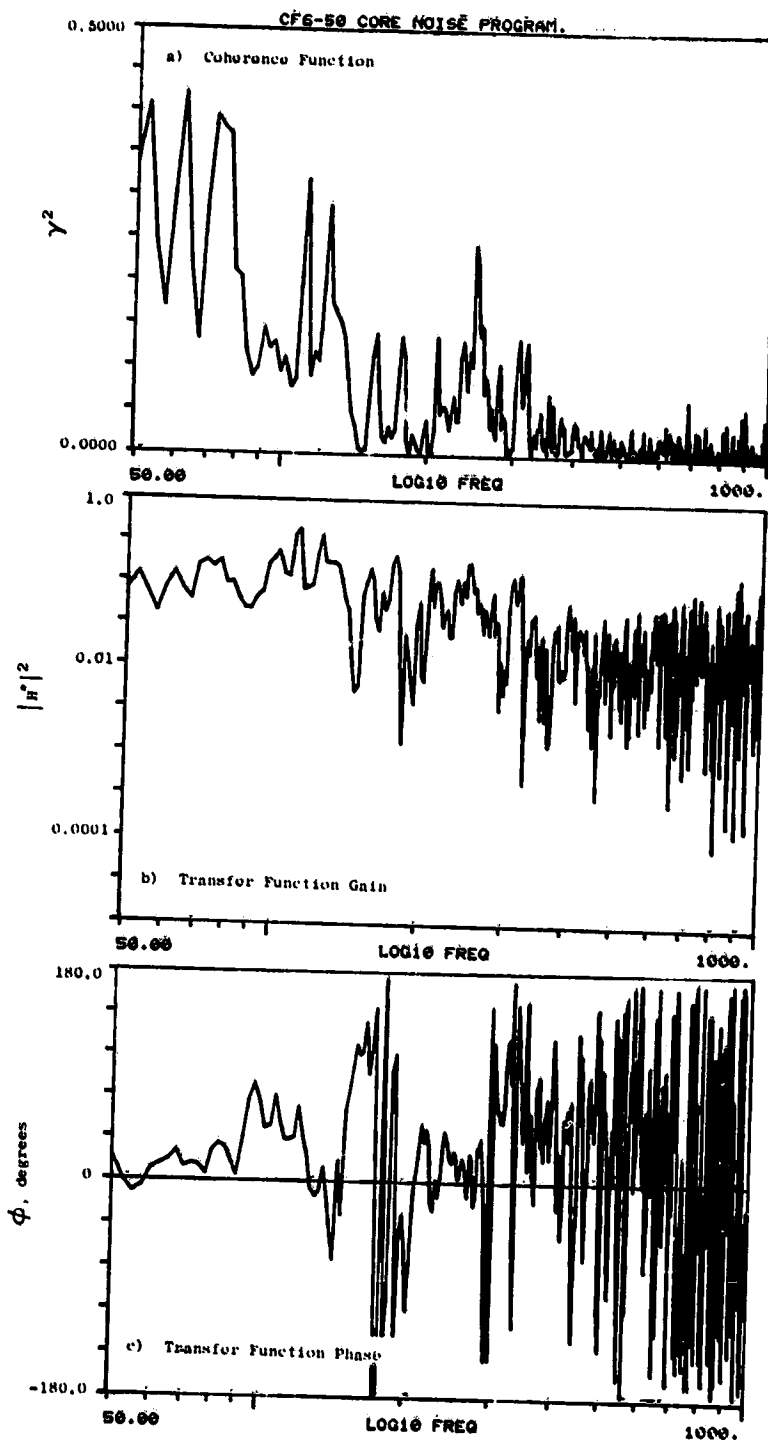


Figure A-152. Coherence and Transfer Functions for Plane 8.0A (270°) to 60° Farfield Microphone at 26.7% Thrust.

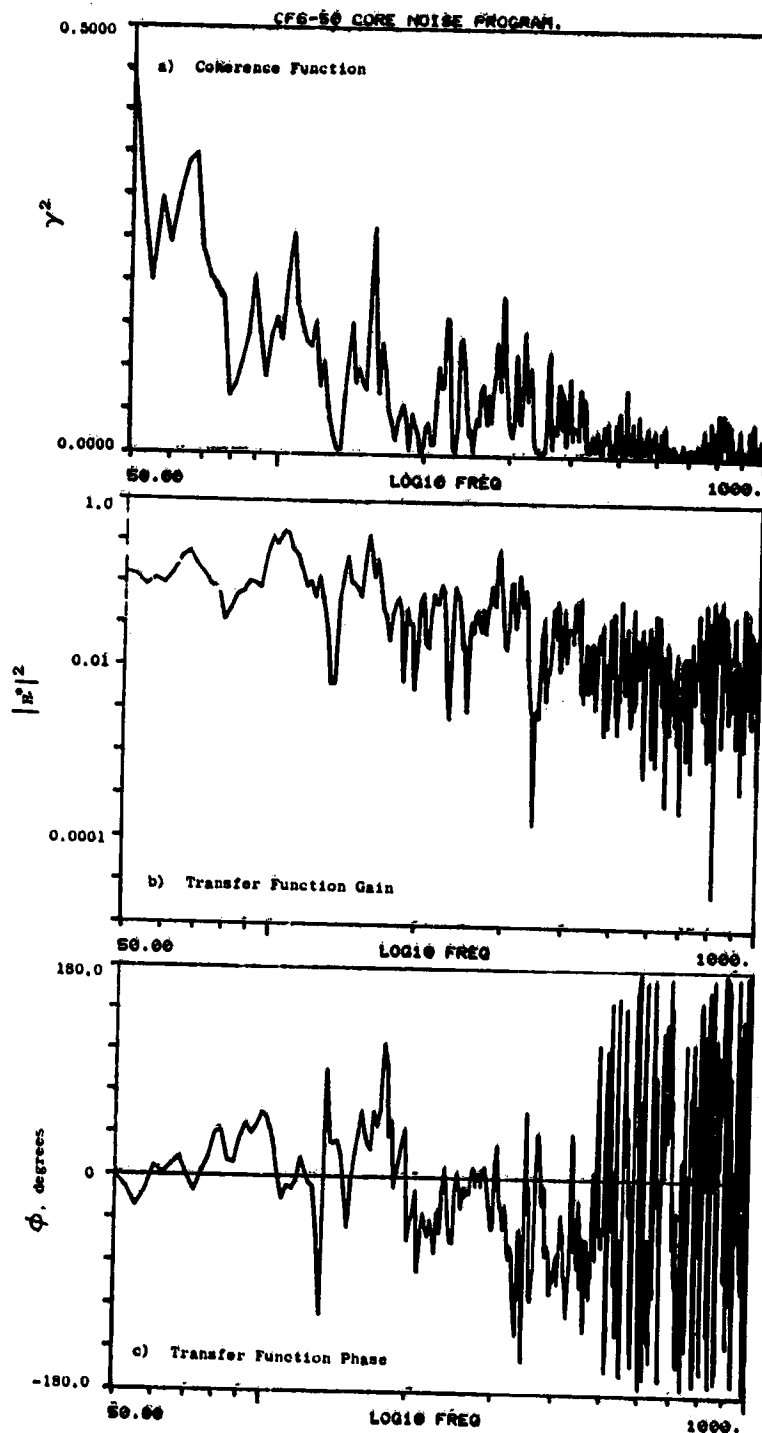


Figure A-153. Coherence and Transfer Functions for Plane 8.0A (270°) to 70° Farfield Microphone at 26.7% Thrust.

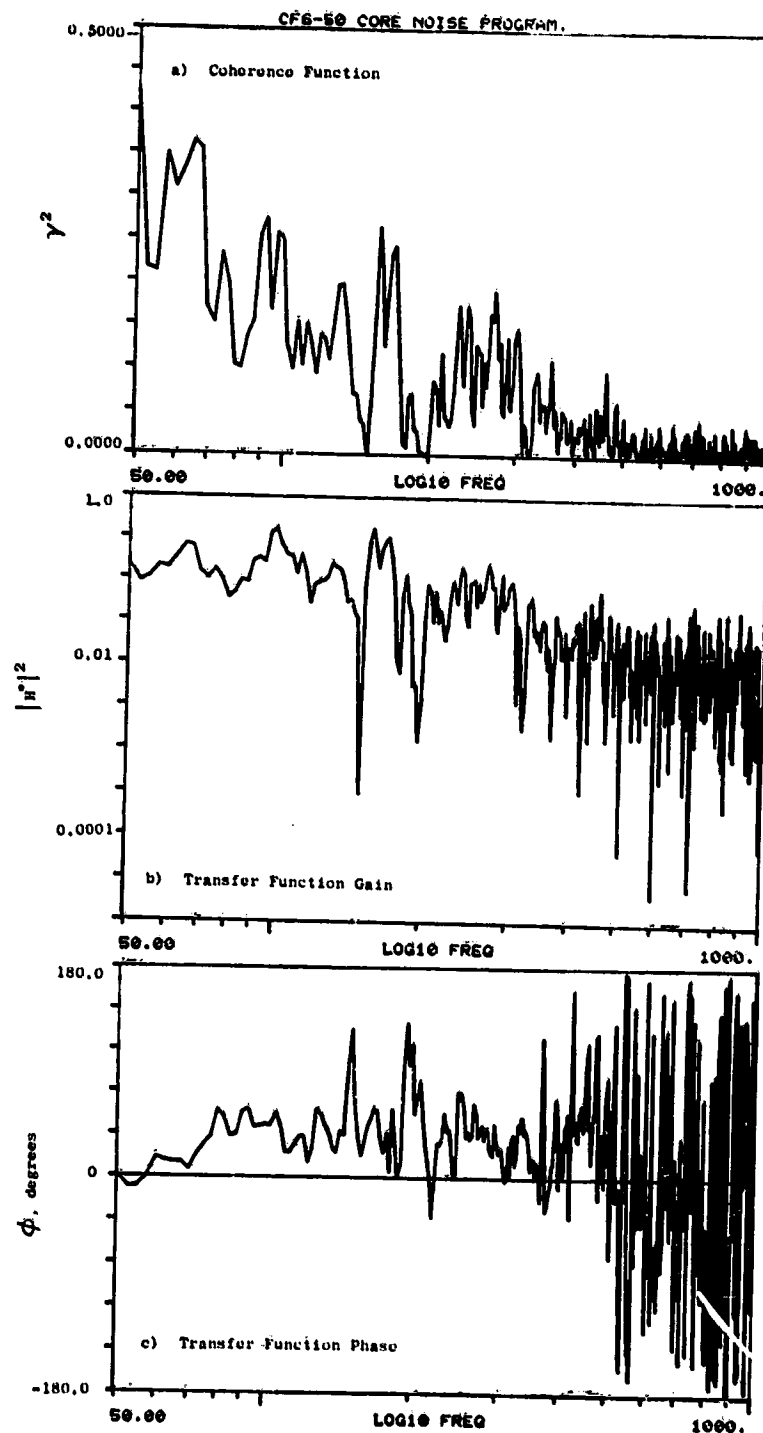


Figure A-154. Coherence and Transfer Functions for Plane 8.0A (270°) to 80° Farfield Microphone at 26.7% Thrust.

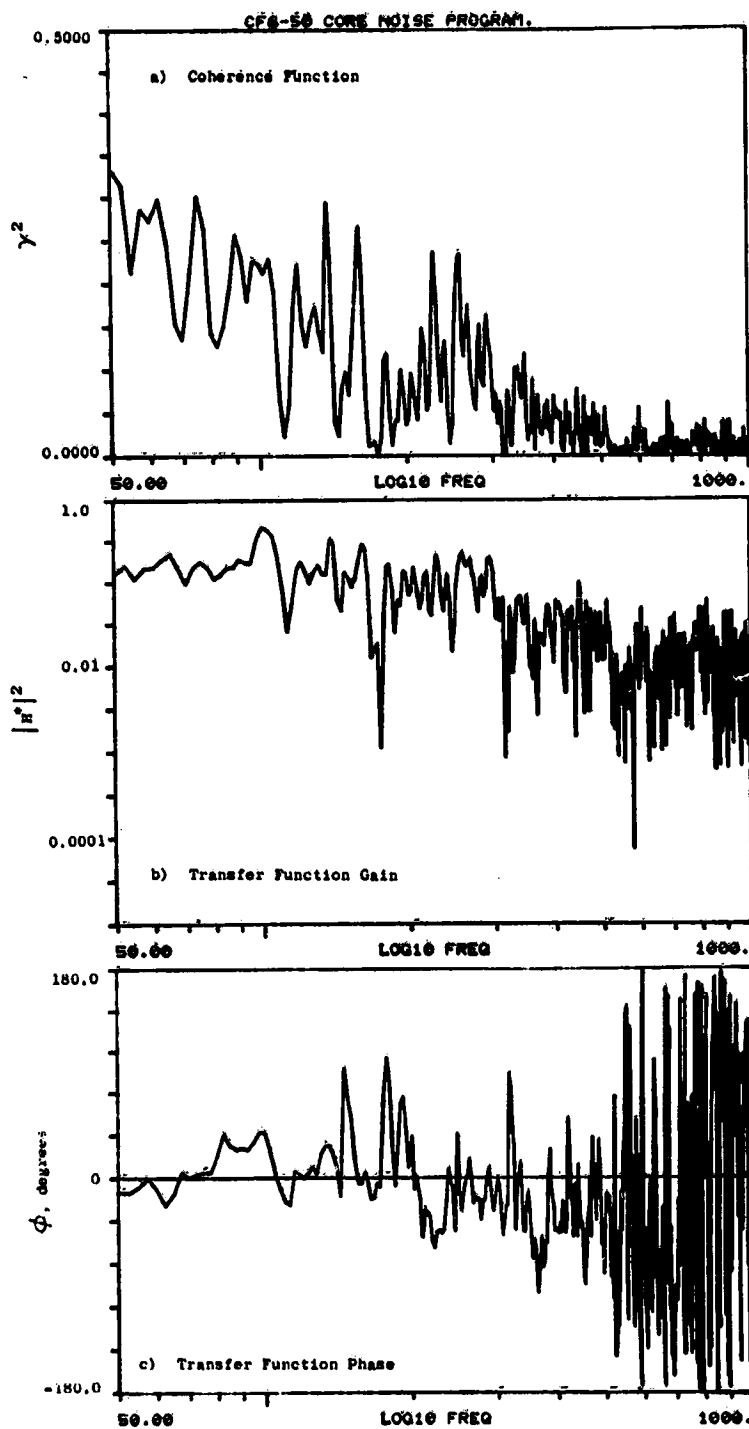


Figure A-155. Coherence and Transfer Functions for Plane 8.0A (270°) to 90° Farfield Microphone at 26.7% Thrust.

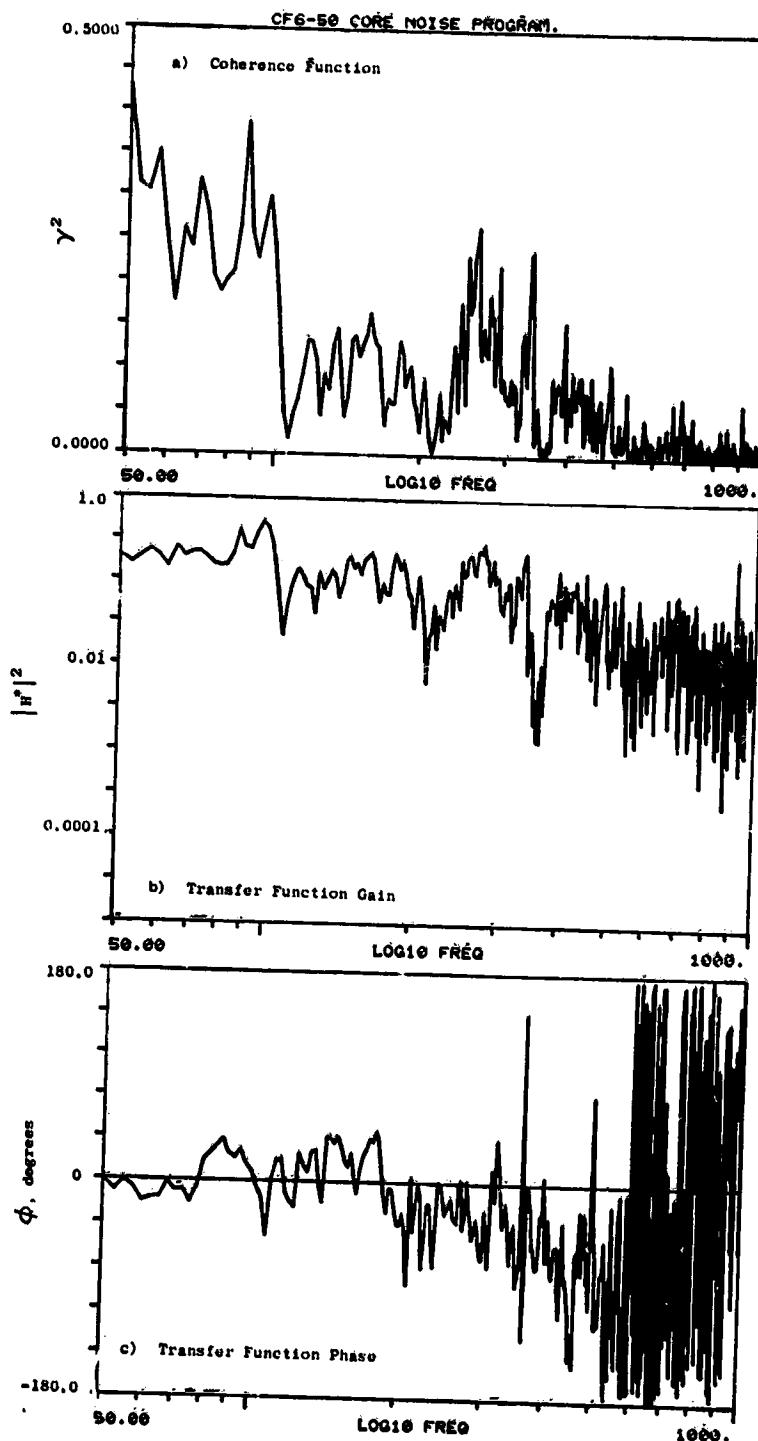


Figure A-156. Coherence and Transfer Functions for Plane 8.0A (270°) to 100° Farfield Microphone at 26.7% Thrust.

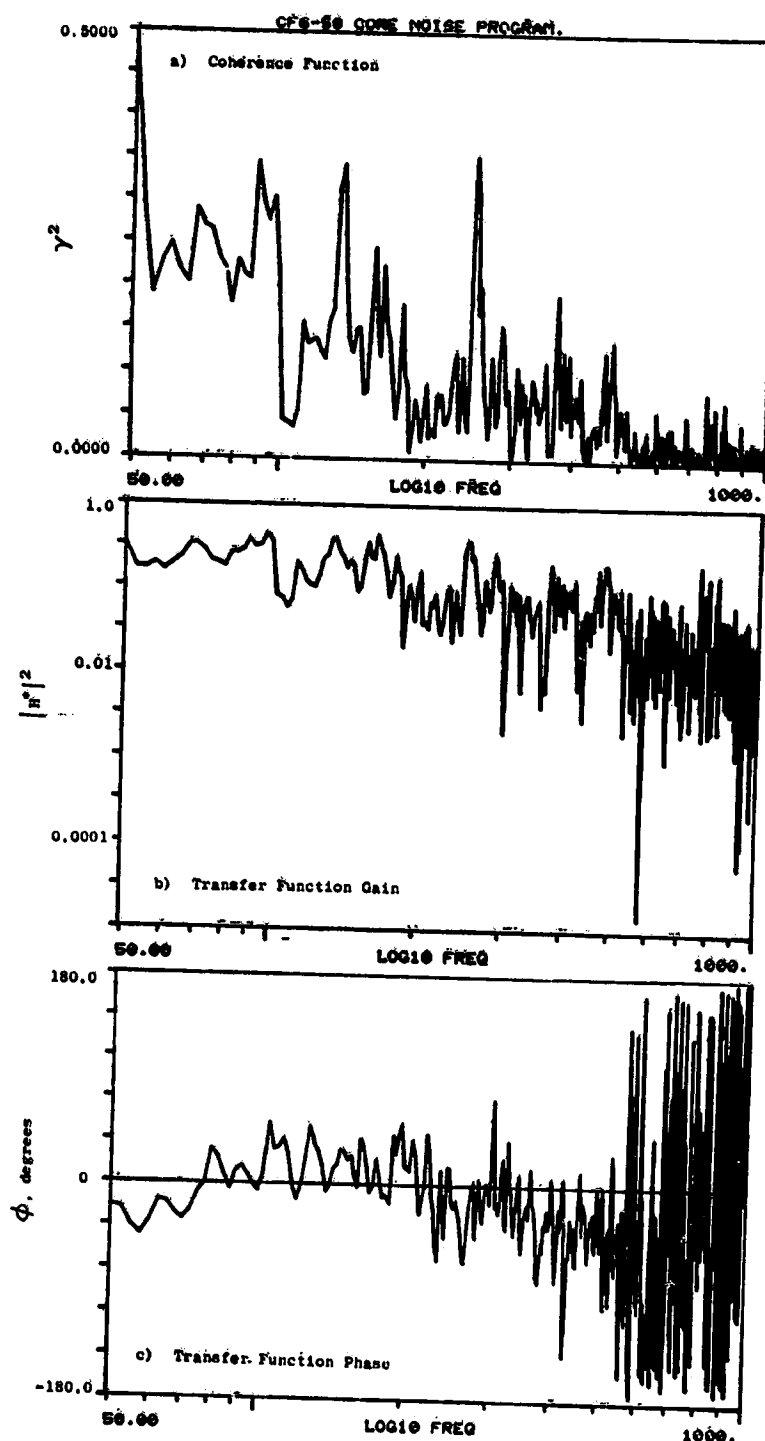


Figure A-157. Coherence and Transfer Functions for Plane 8.0A (270°) to 110° Farfield Microphone at 26.7% Thrust.

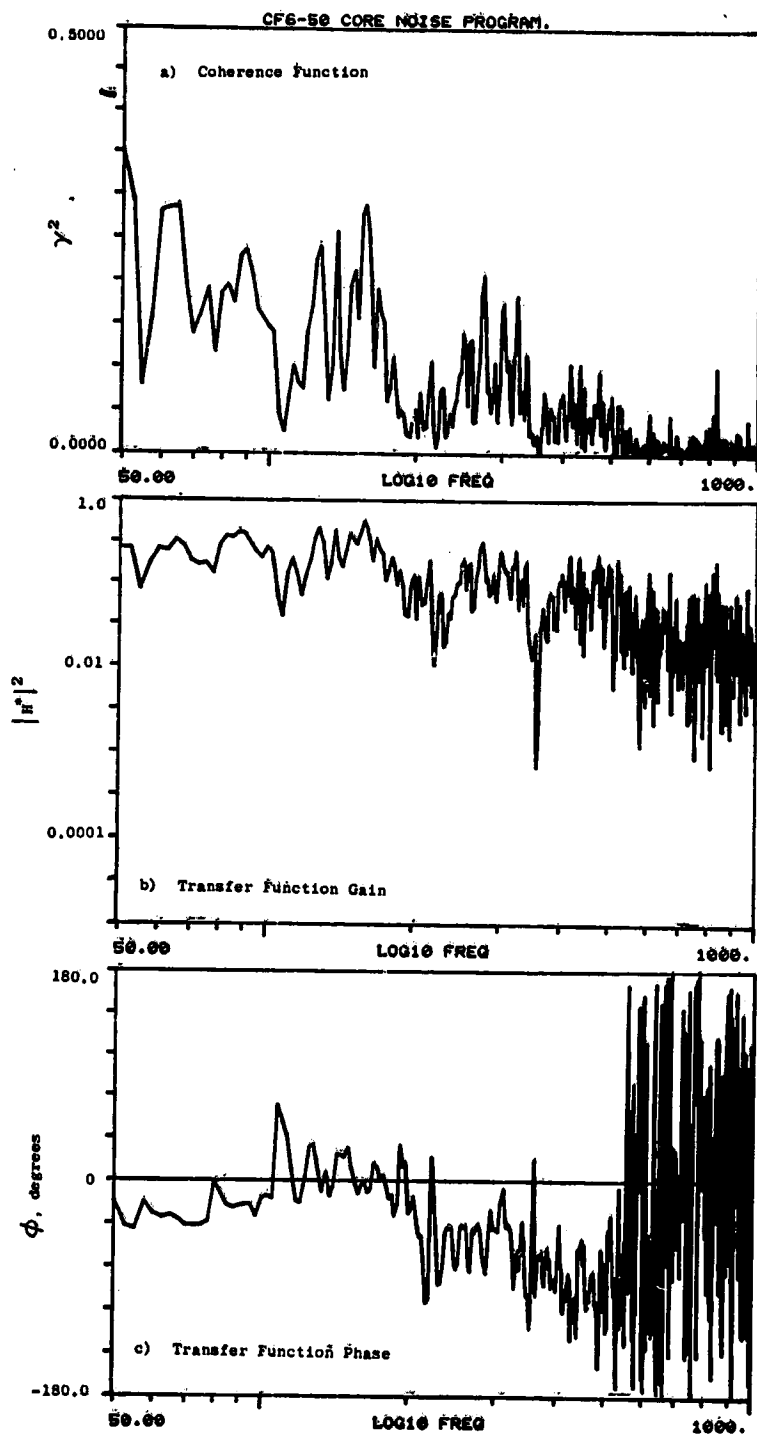


Figure A-158. Coherence and Transfer Functions for Plane 8.0A (270°) to 120° Farfield Microphone at 26.7% Thrust.

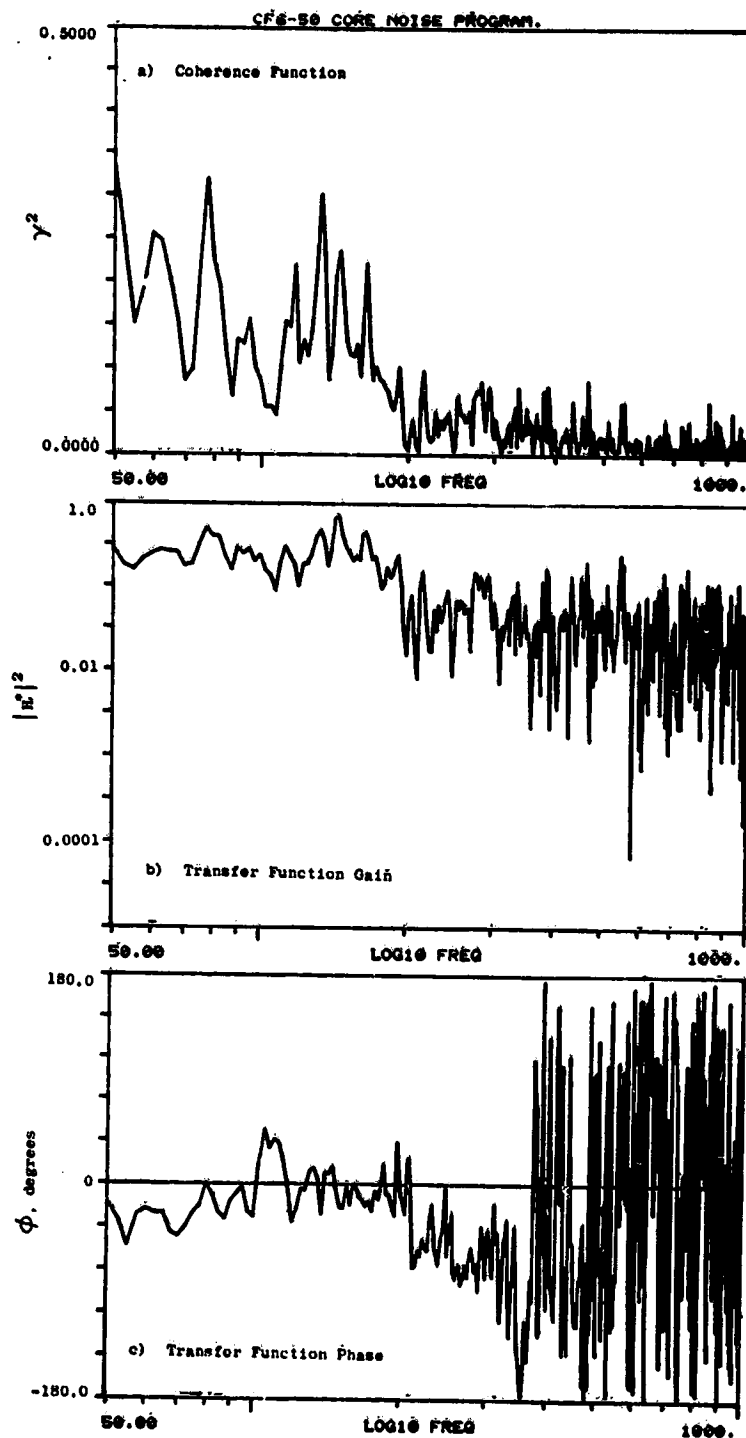


Figure A-159. Coherence and Transfer Functions for Plane 8.0A (270°) to 130° Farfield Microphone at 26.7% Thrust.

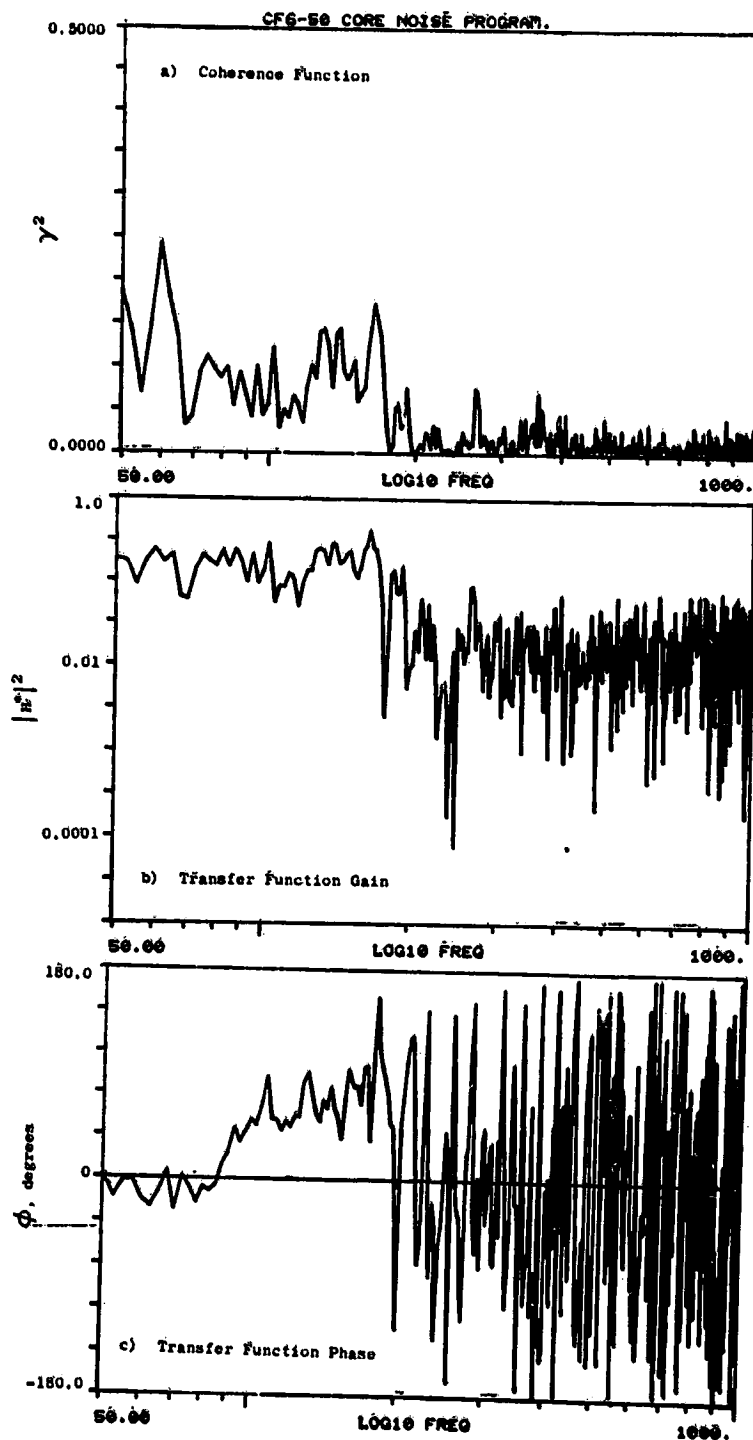


Figure A-160. Coherence and Transfer Functions for Plane 8.0A (270°) to 140° Farfield Microphone at 26.7% Thrust.

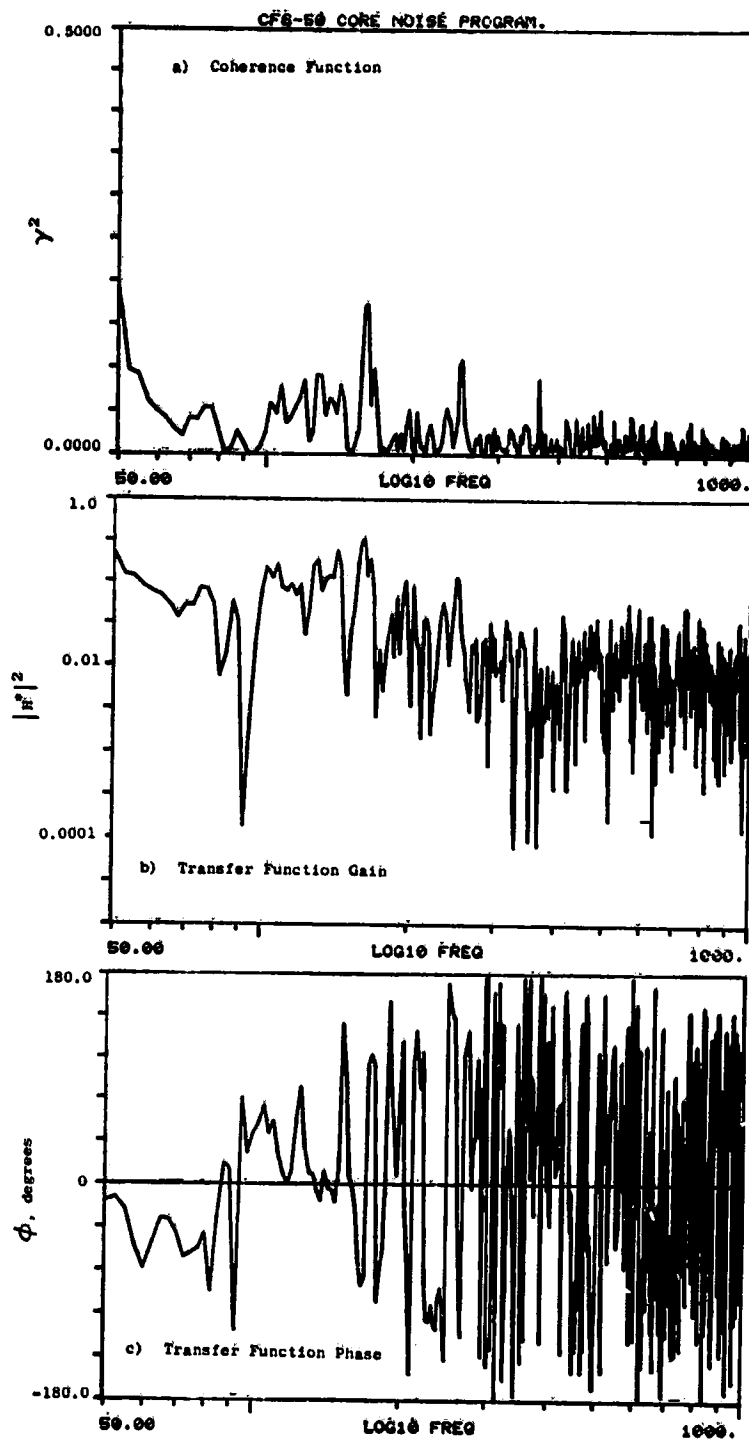


Figure A-161. Coherence and Transfer Functions for Plane 8.0A (270°) to 150° Farfield Microphone at 26.7% Thrust.

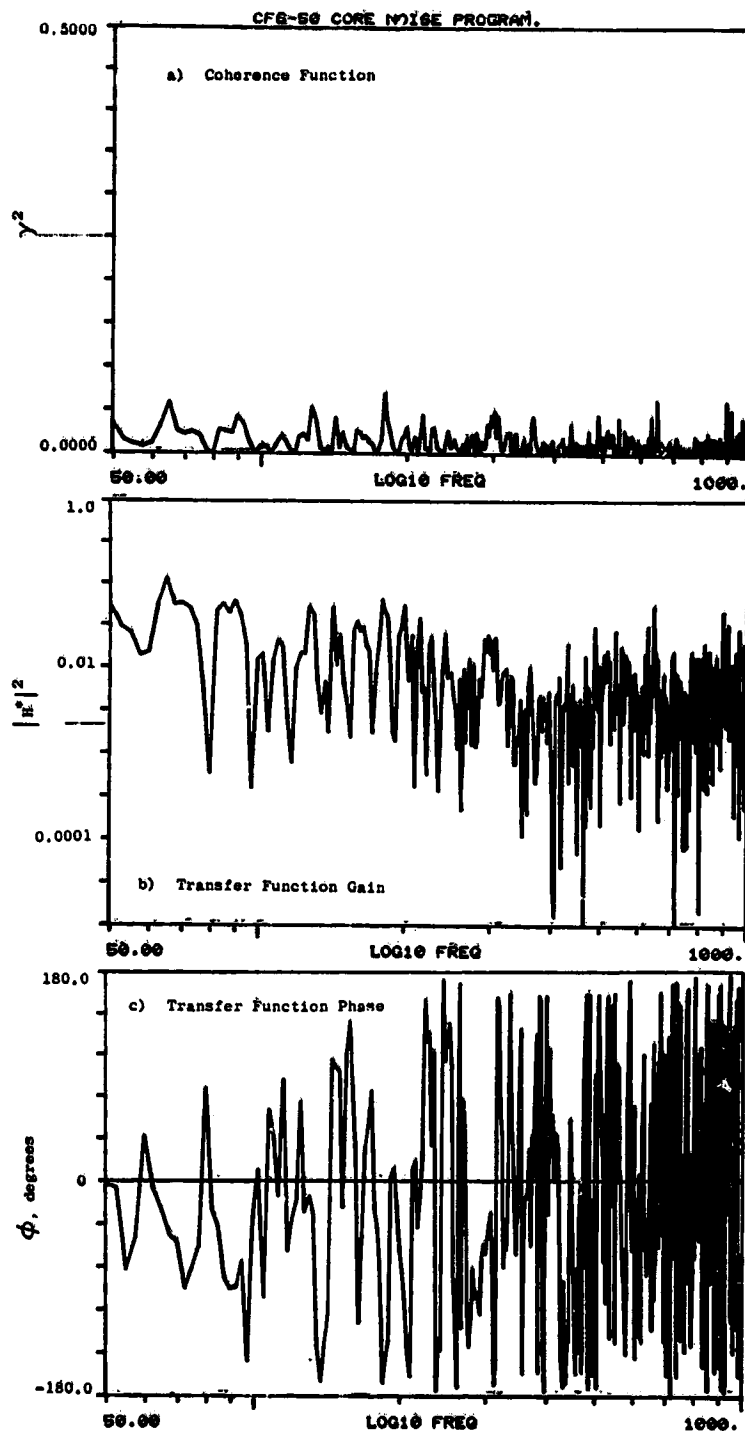


Figure A-162. Coherence and Transfer Functions for Plane 8.0A (270°) to 160° Farfield Microphone at 26.7% Thrust.

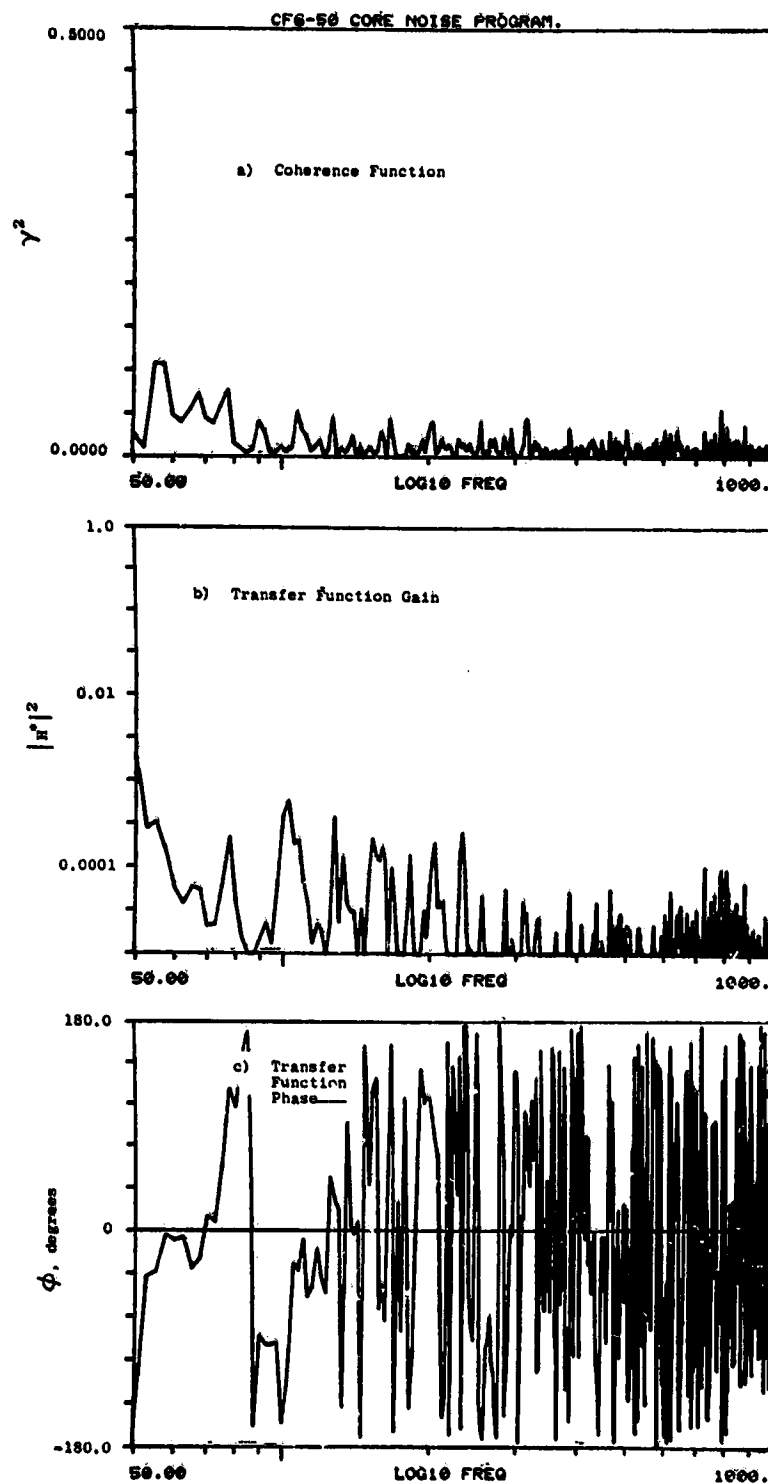


Figure A-163. Coherence and Transfer Functions for Plane 3.5 (102°) to 10° Farfield Microphone at 30.8% Thrust.

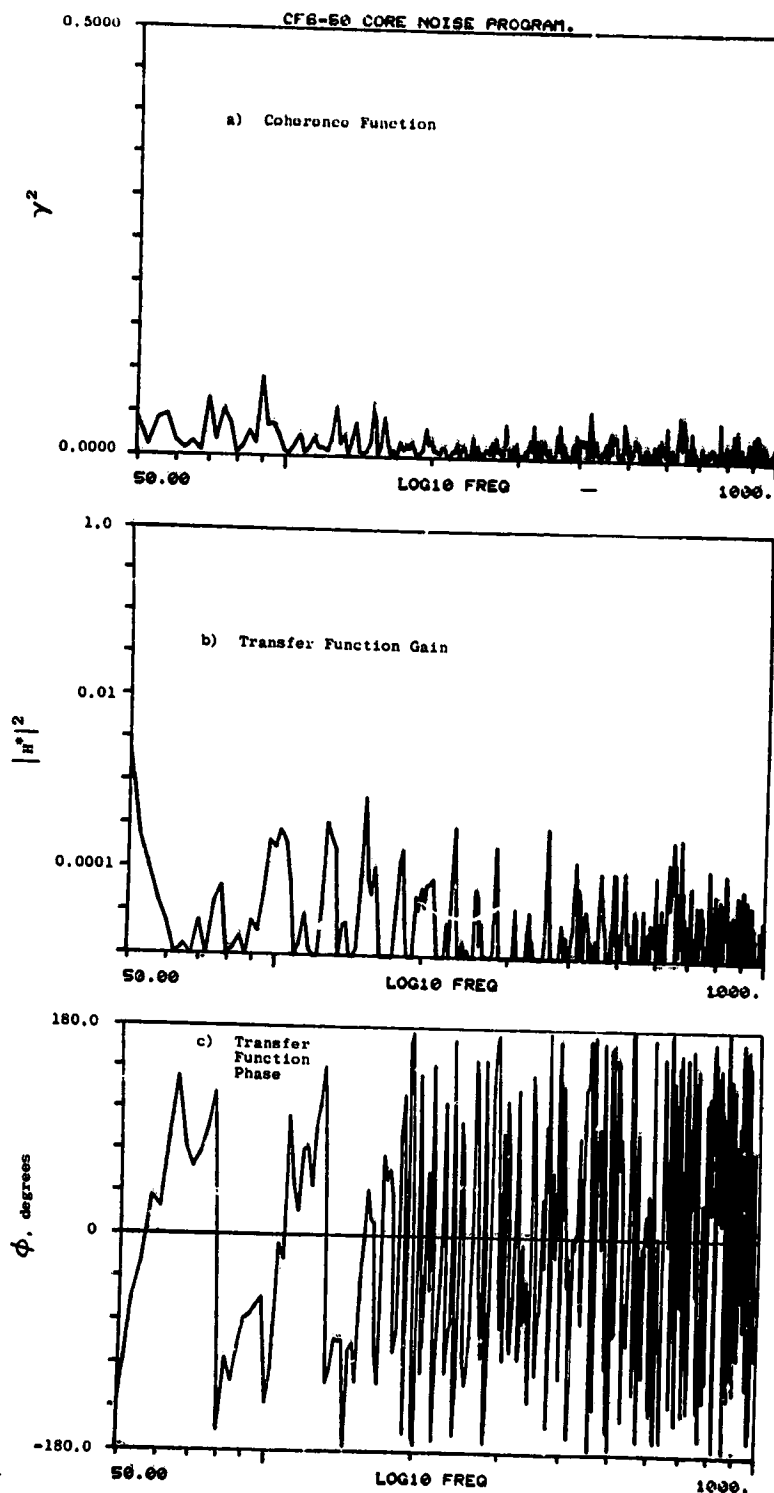


Figure A-164. Coherence and Transfer Functions for Plane 3.5 (102°) to 30° Farfield Microphone at 30.8% Thrust.

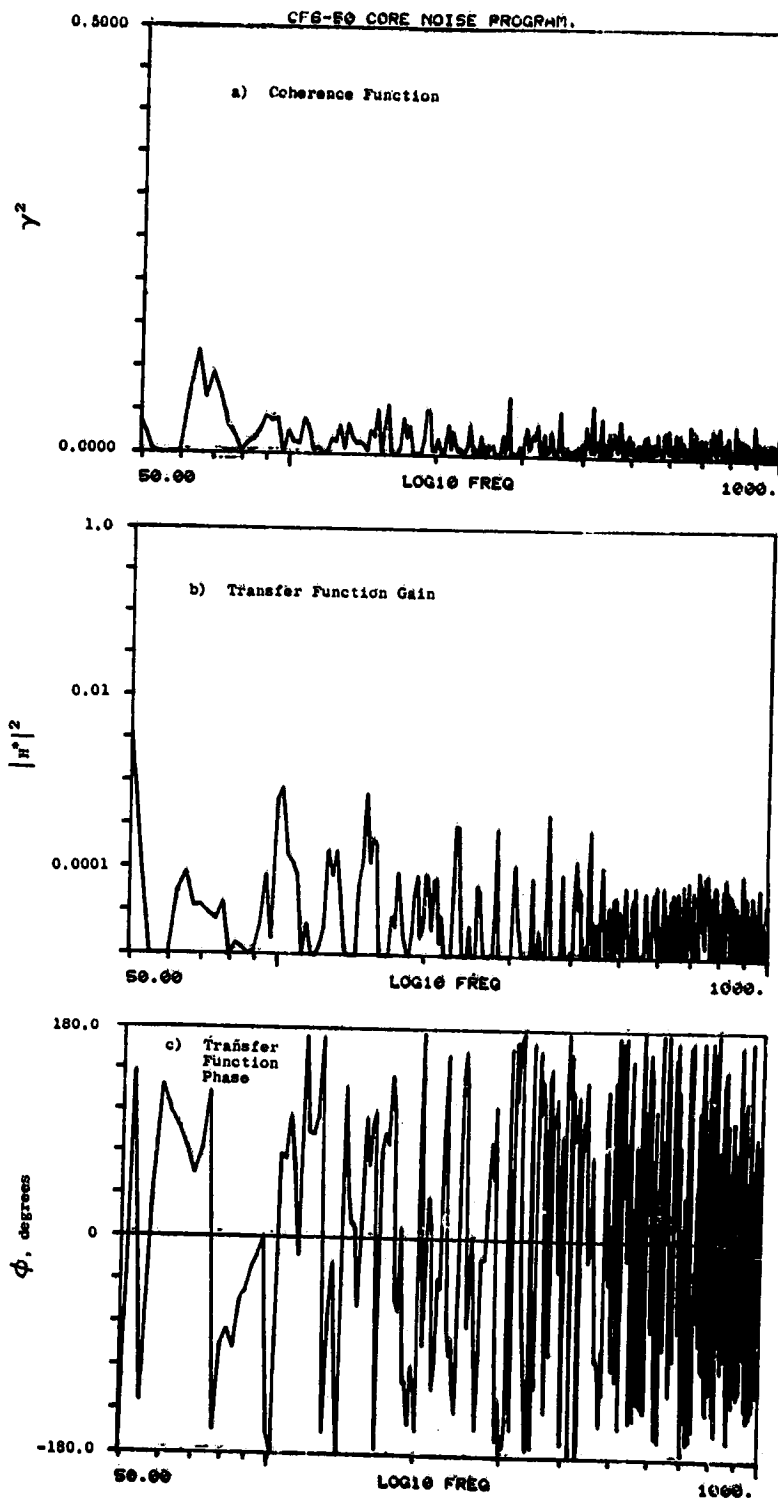


Figure A-165. Coherence and Transfer Functions for Plane 3.5 (102°) to 40° Farfield Microphone at 30.8% Thrust.

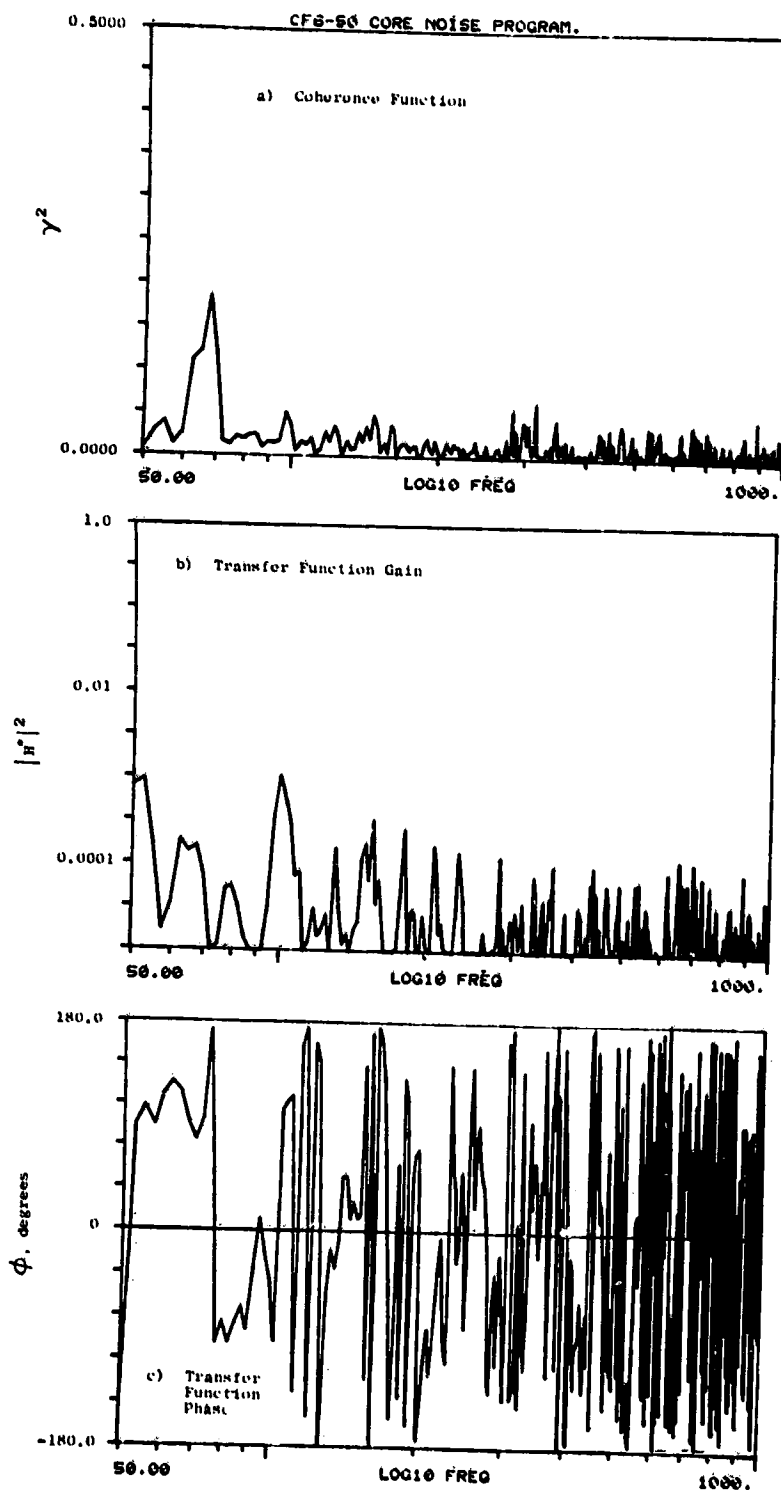


Figure A-166. Coherence and Transfer Functions for Plane 3.5 (102°) to 50° Farfield Microphone at 30.8% Thrust.

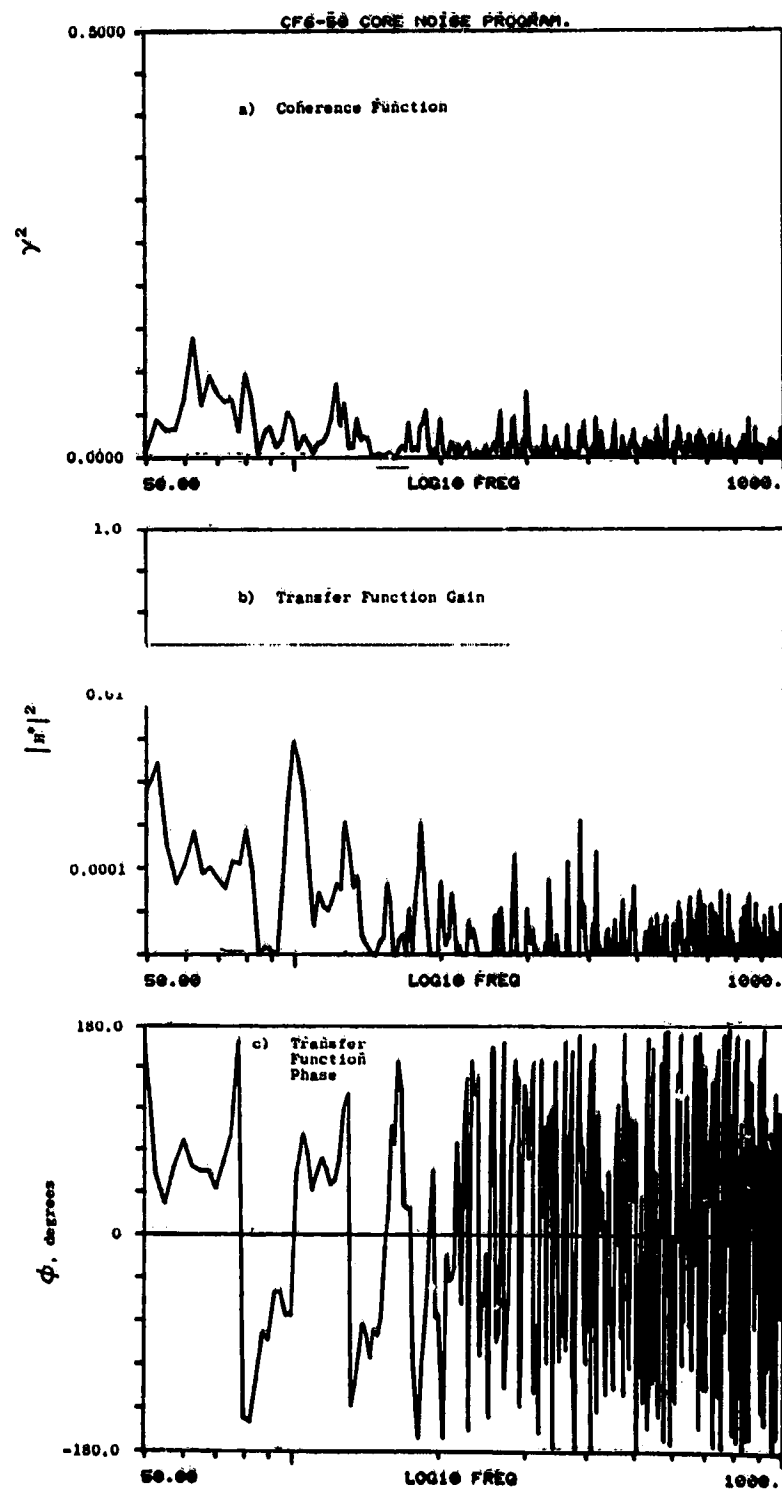


Figure A-167. Coherence and Transfer Functions for Plane 3.5 (102°) to 60° Farfield Microphone at 30.8% Thrust.

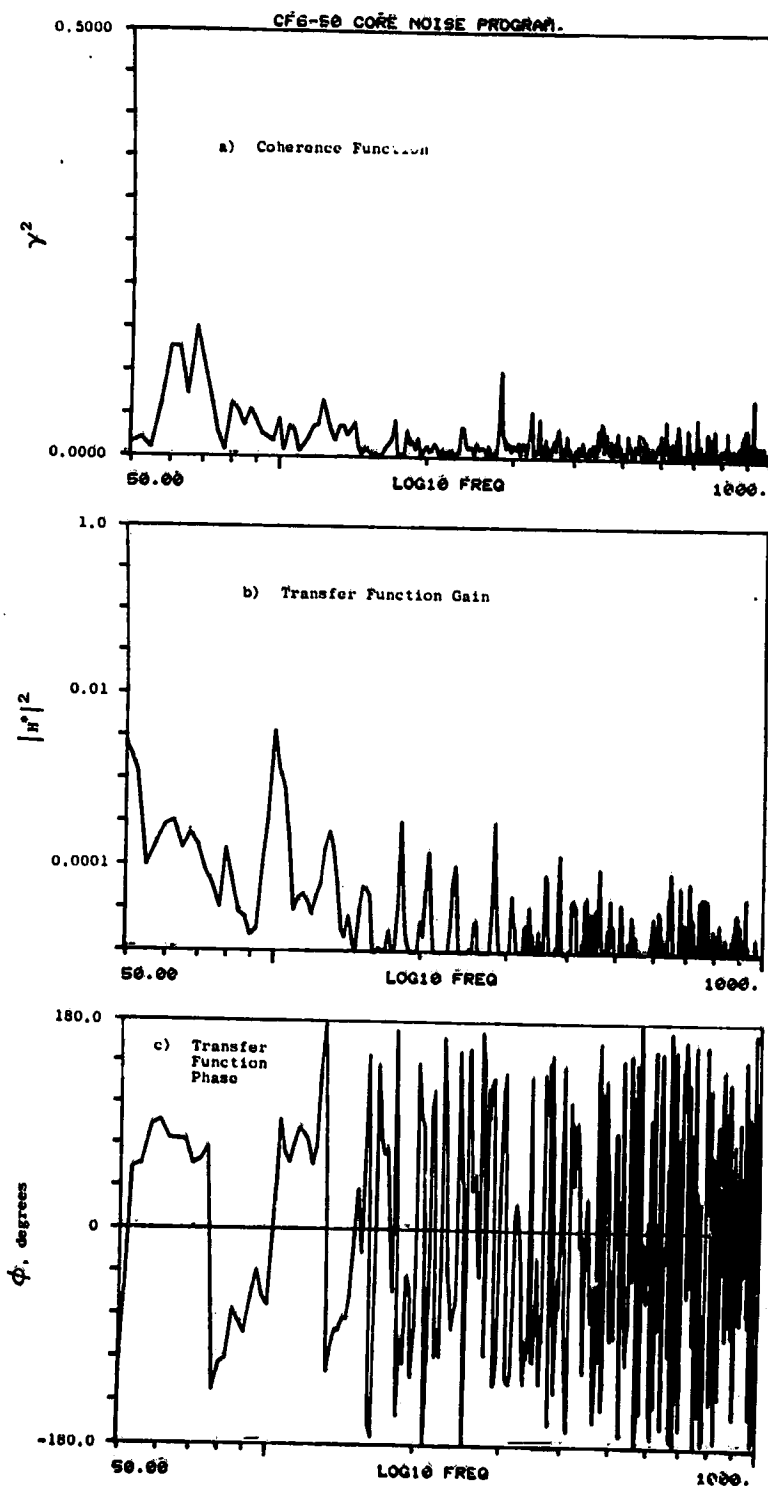


Figure A-168. Coherence and Transfer Functions for Plane 3.5 (102°) to 70° Farfield Microphone at 30.8% Thrust.

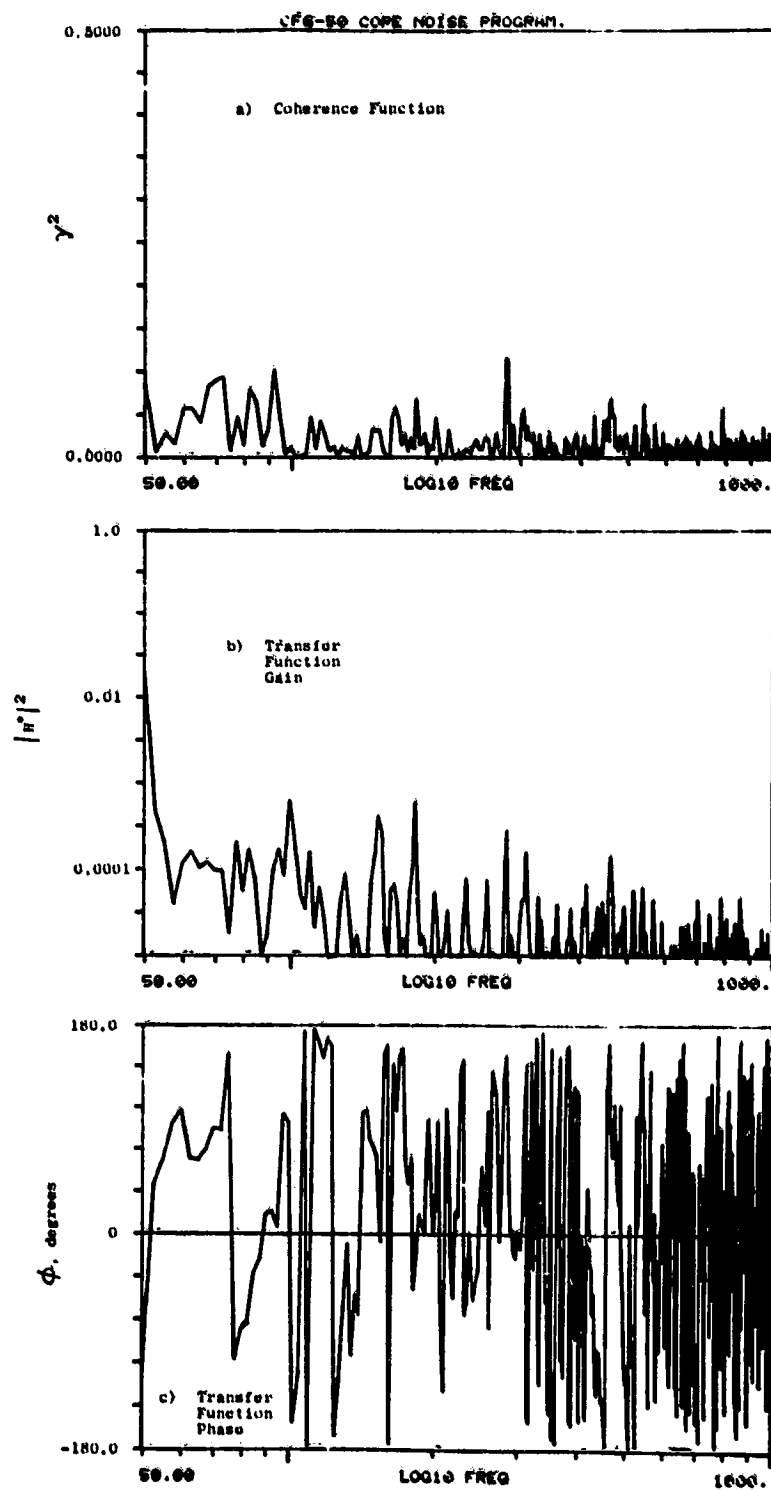


Figure A-169. Coherence and Transfer Functions for Plane 3.5 (102°) to 80° Farfield Microphone at 30.8% Thrust.

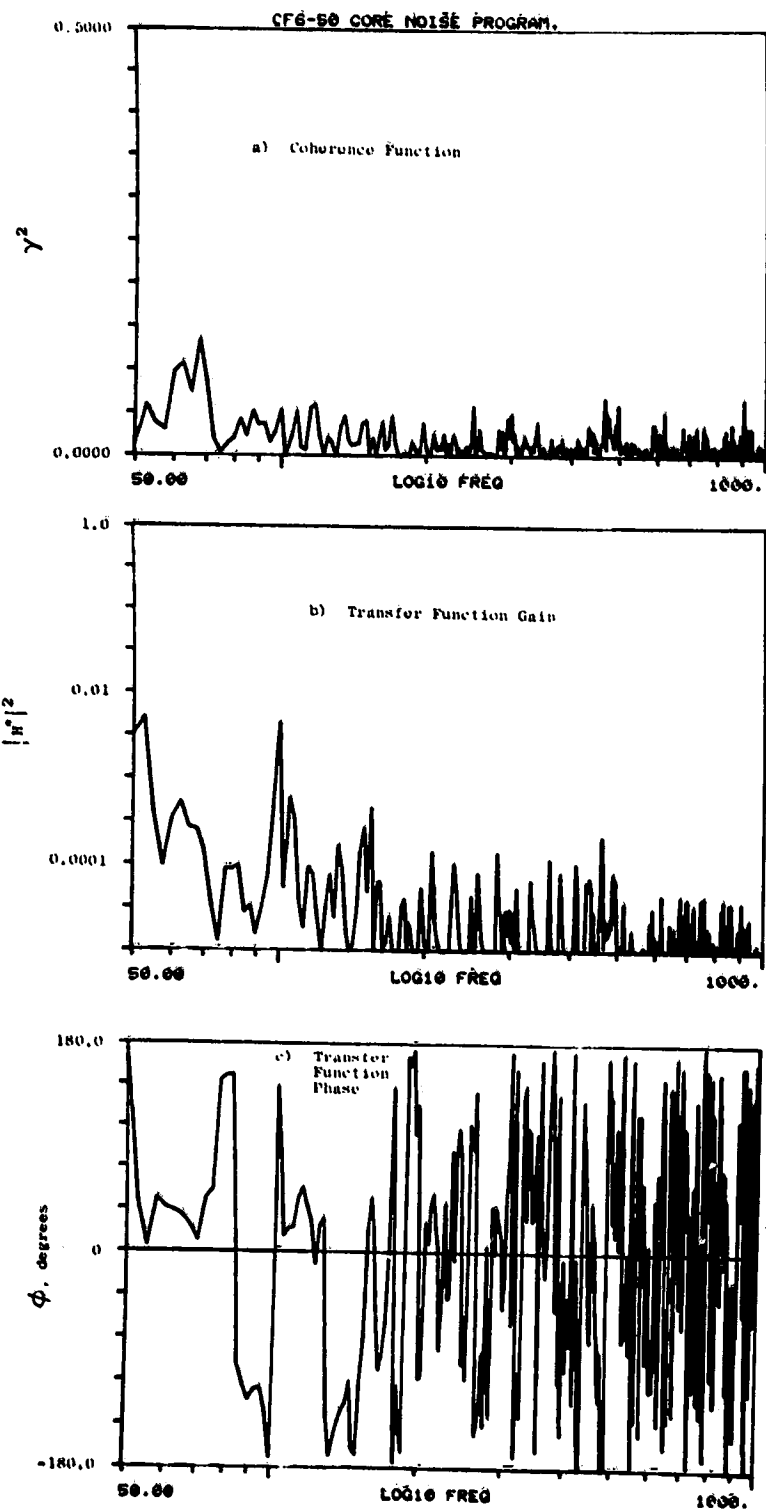


Figure A-170. Coherence and Transfer Functions for Plane 3.5 (102°) to 90° Farfield Microphone at 30.8% Thrust.

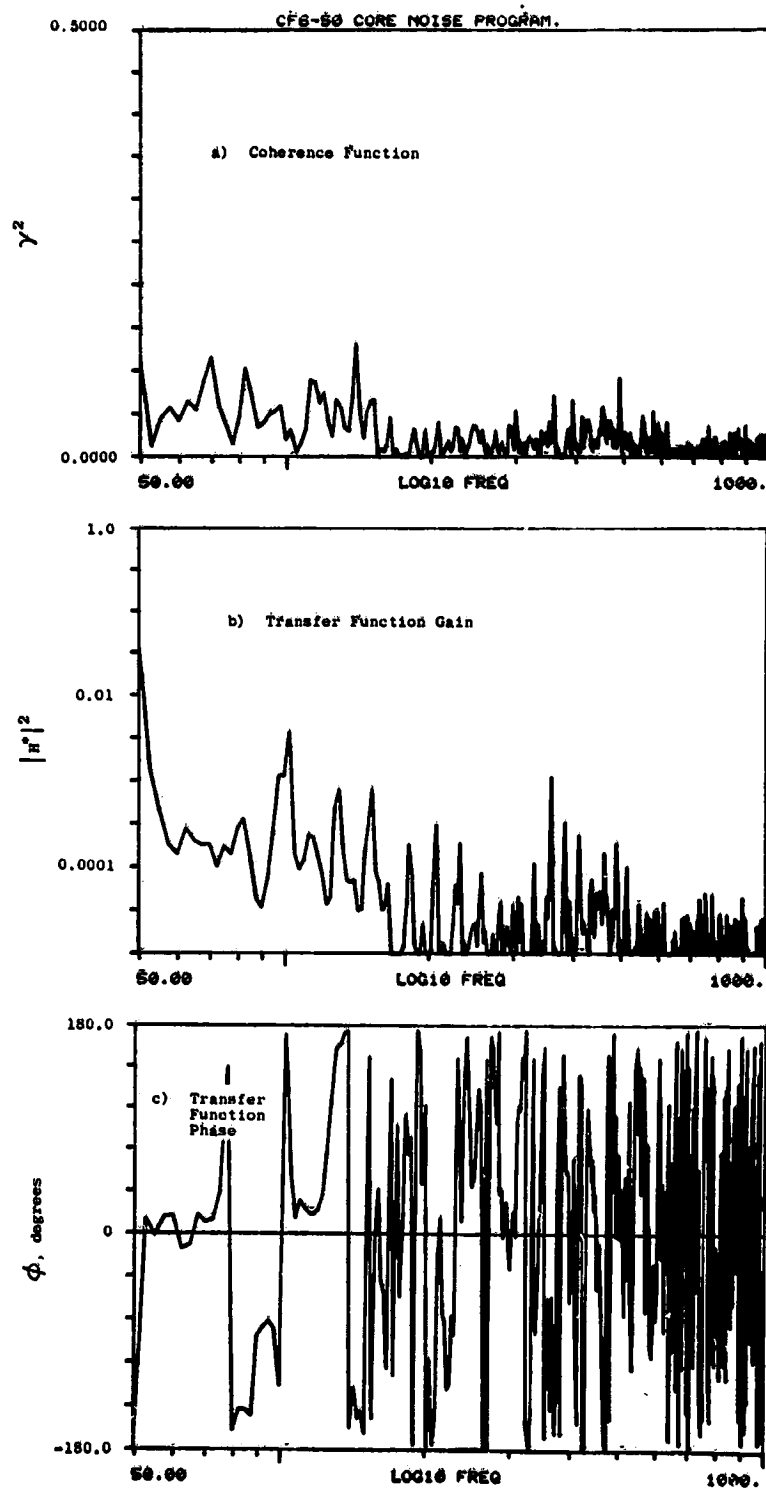


Figure A-171. Coherence and Transfer Functions for Plane 3.5 (102°) to 100° Farfield Microphone at 30.8% Thrust.

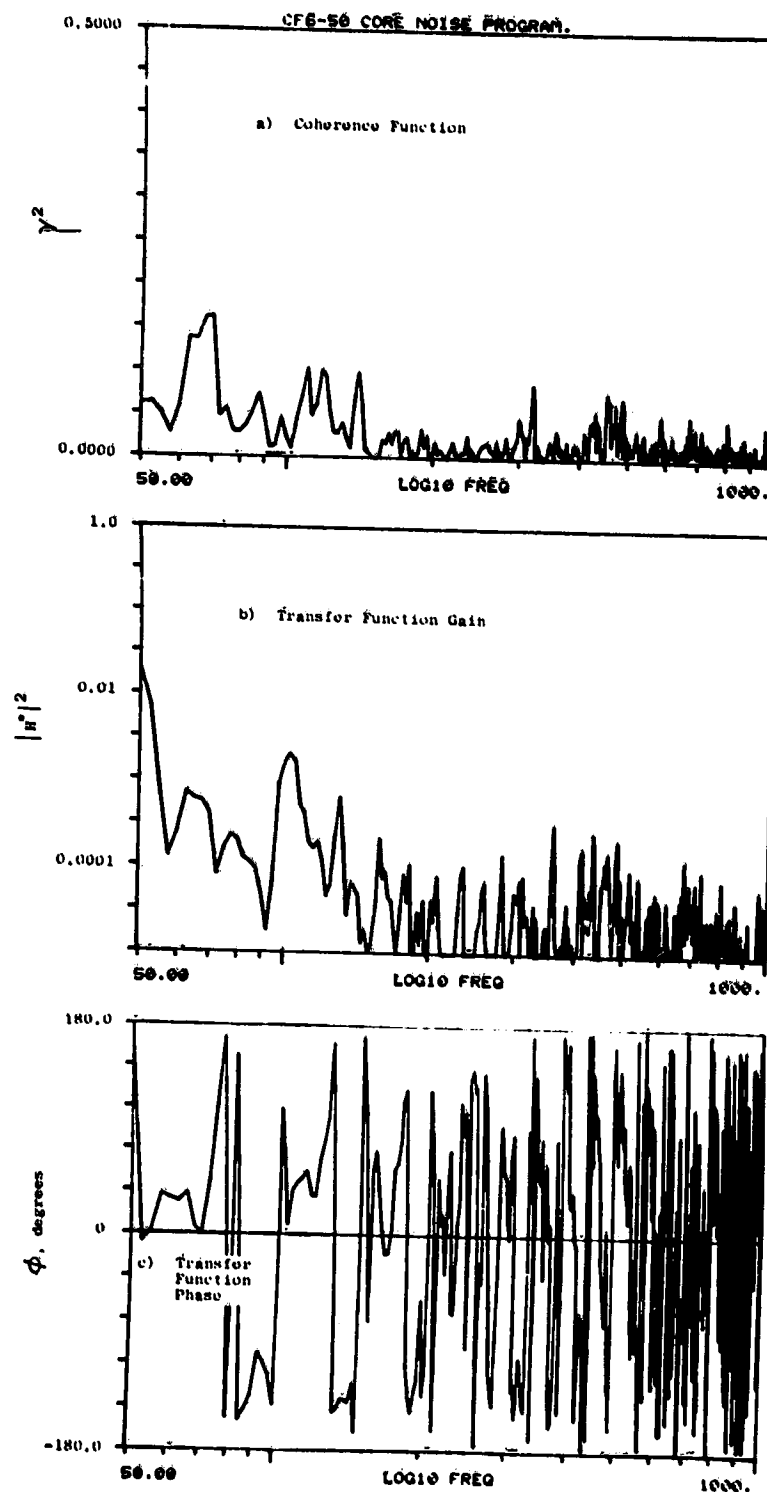


Figure A-172. Coherence and Transfer Functions for Plane 3.5 (102°) to 110° Farfield Microphone at 30.8% Thrust.

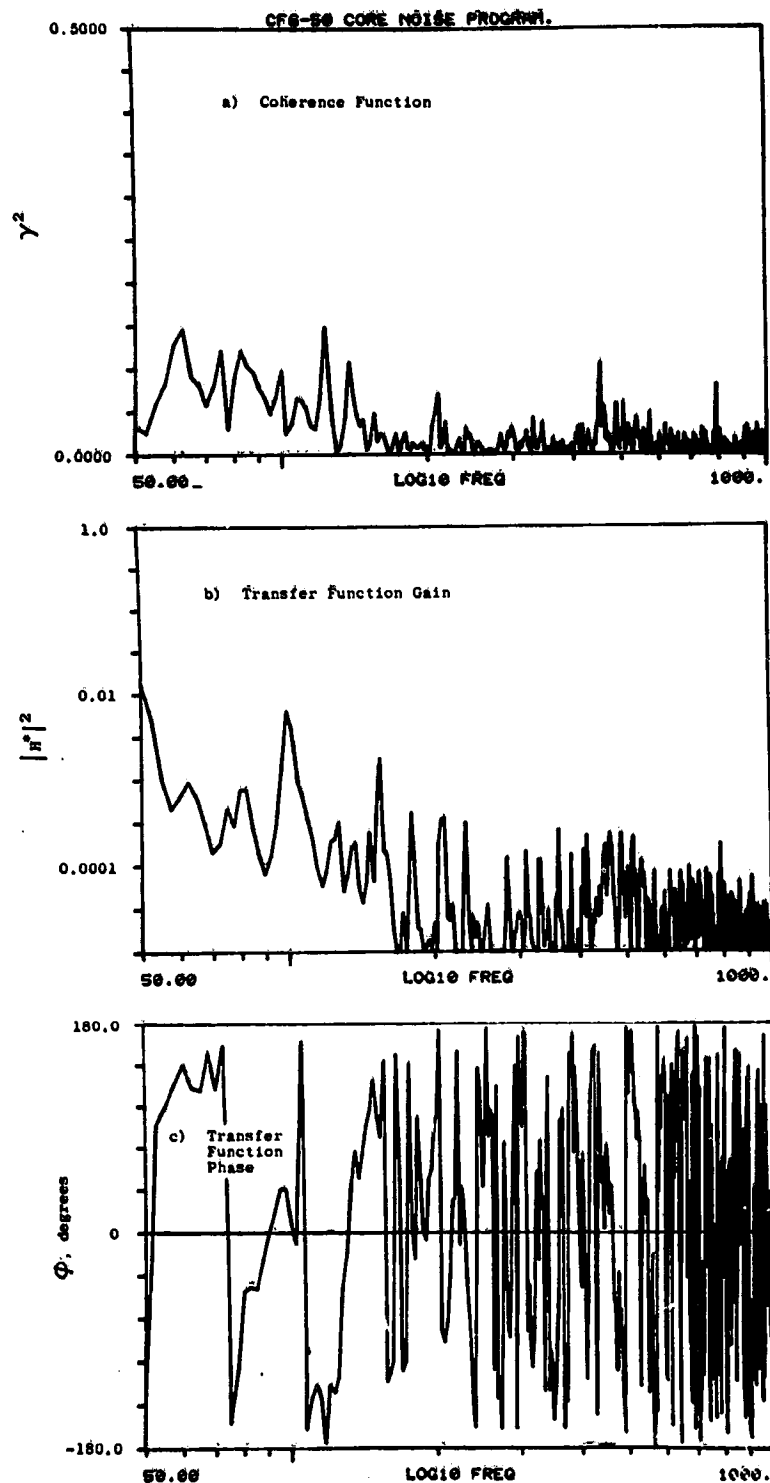


Figure A-173. Coherence and Transfer Functions for Plane 3.5 (102°) to 120° Farfield Microphone at 30.8% Thrust.

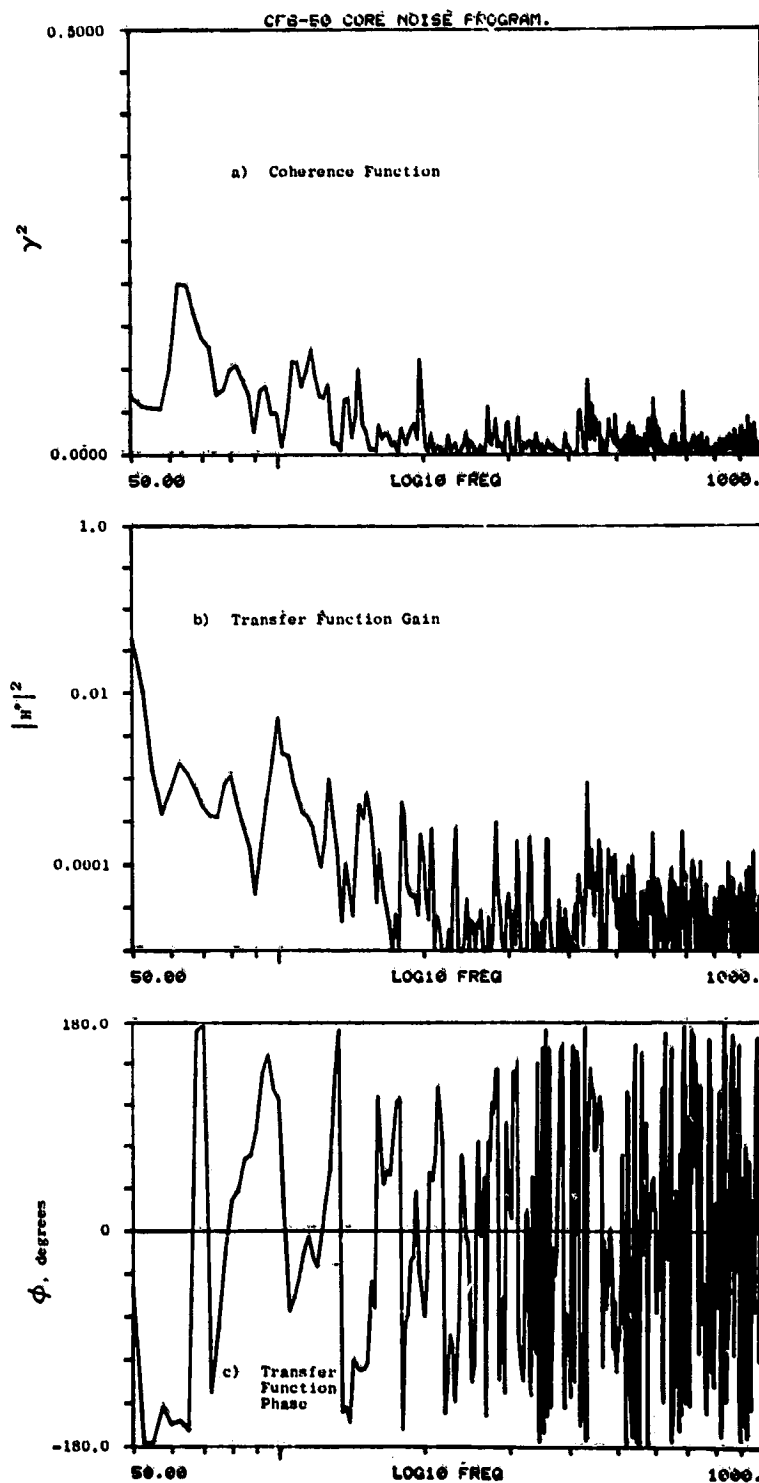


Figure A-174. Coherence and Transfer Functions for Plane 3.5 (102° to 130° Farfield Microphone at 30.8% Thrust.

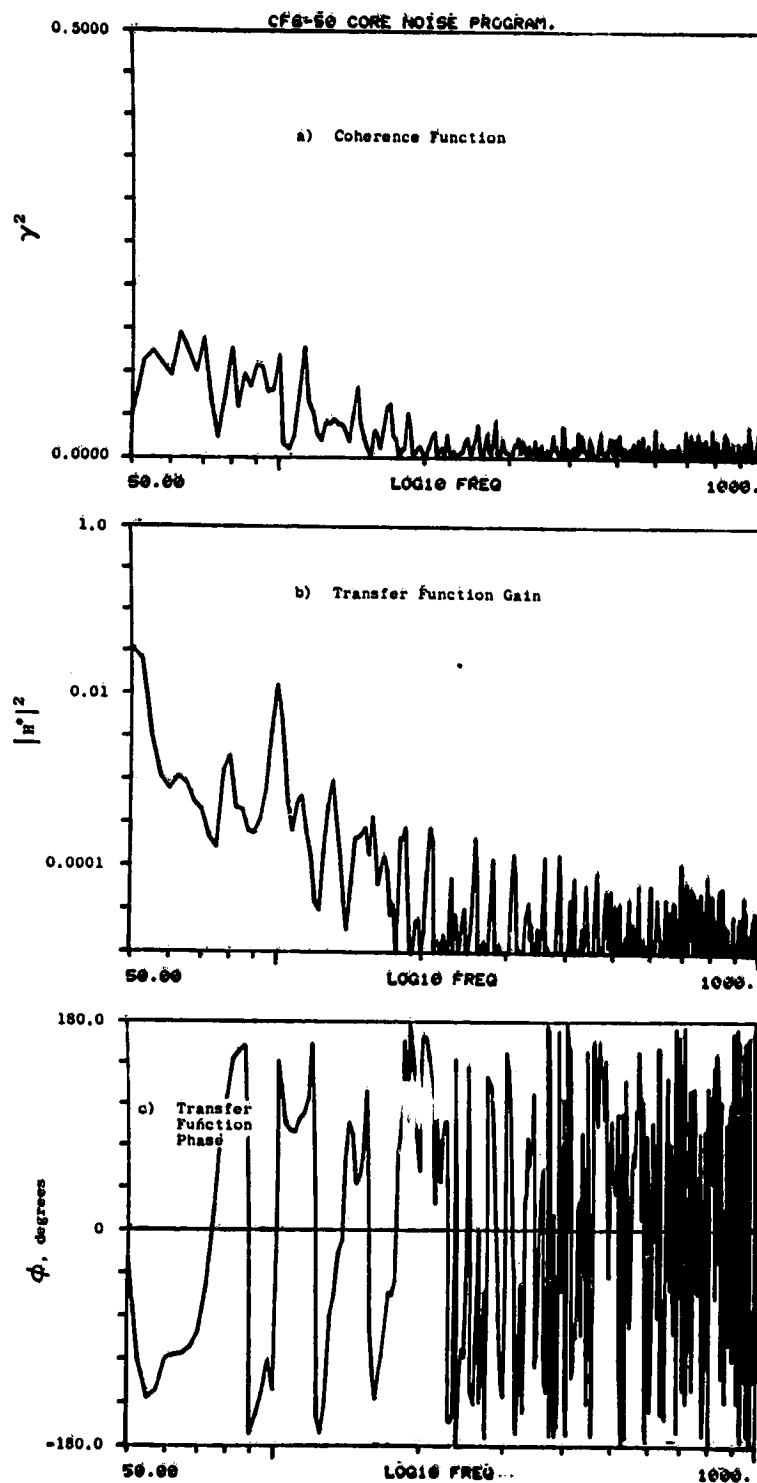


Figure A-175. Coherence and Transfer Functions for Plane 3.5 (102° to 140° Farfield Microphone at 30.8% Thrust.

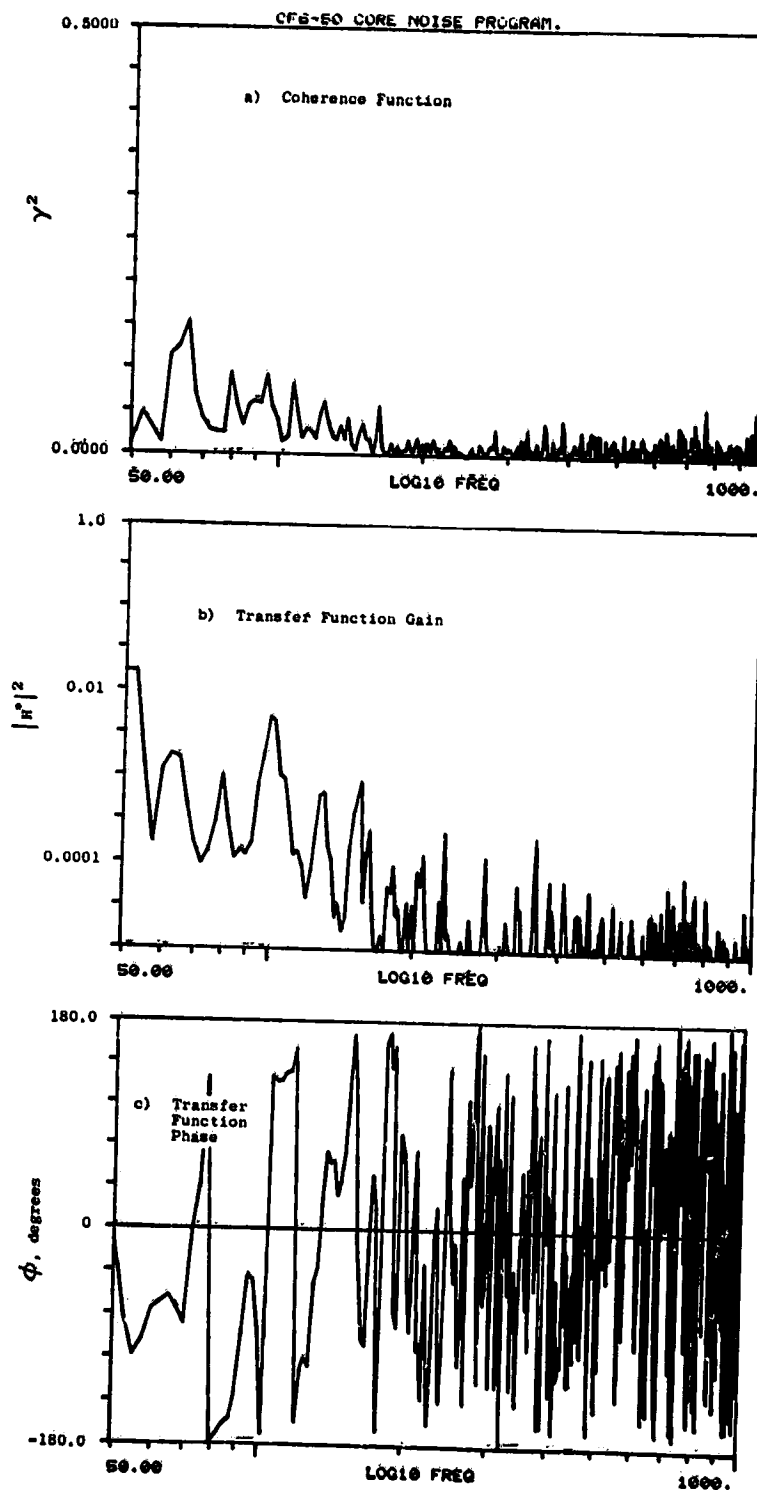


Figure A-176. Coherence and Transfer Functions for Plane 3.5 (102°) to 150° Farfield Microphone at 30.8% Thrust.

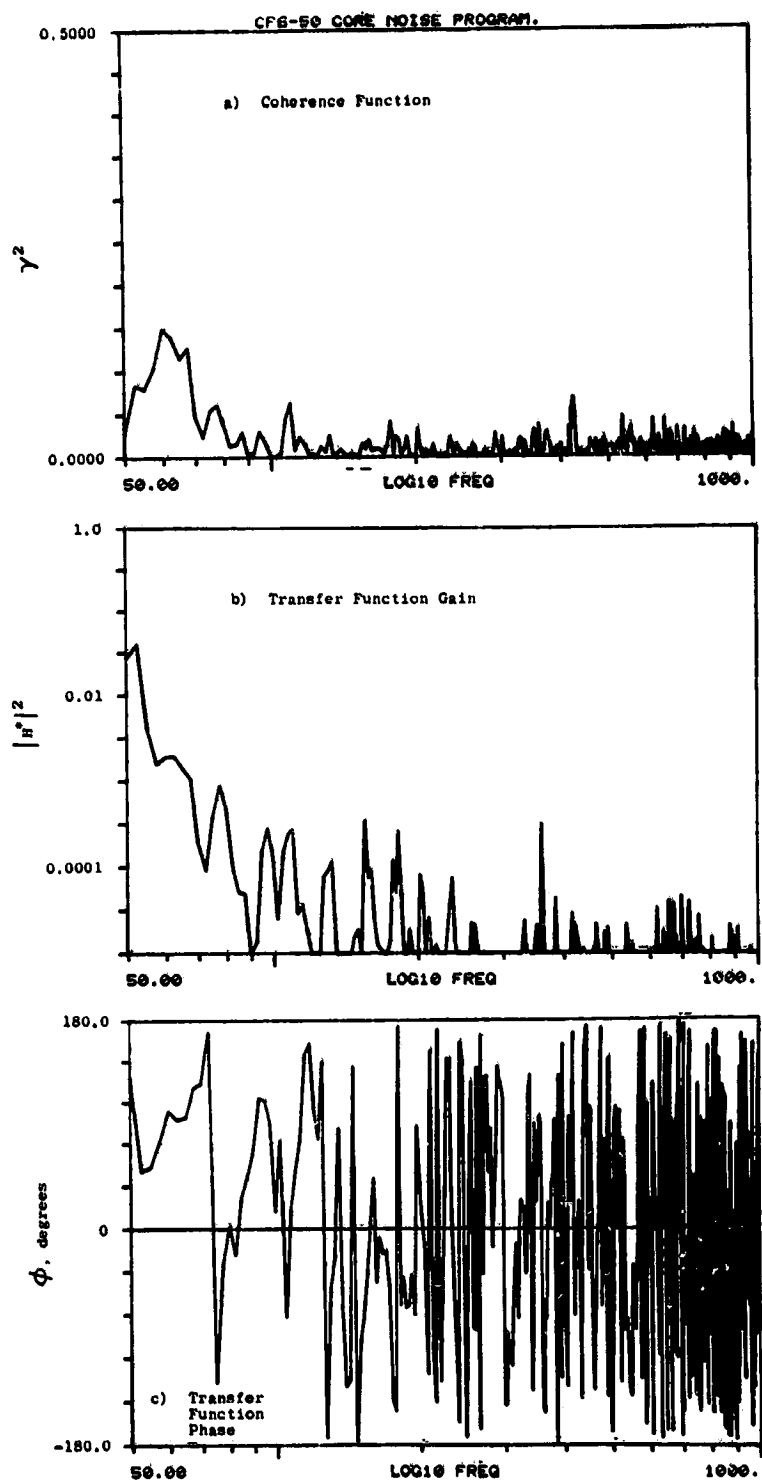


Figure A-177. Coherence and Transfer Functions for Plane 3.5 (102°) to 160° Farfield Microphone at 30.8% Thrust.

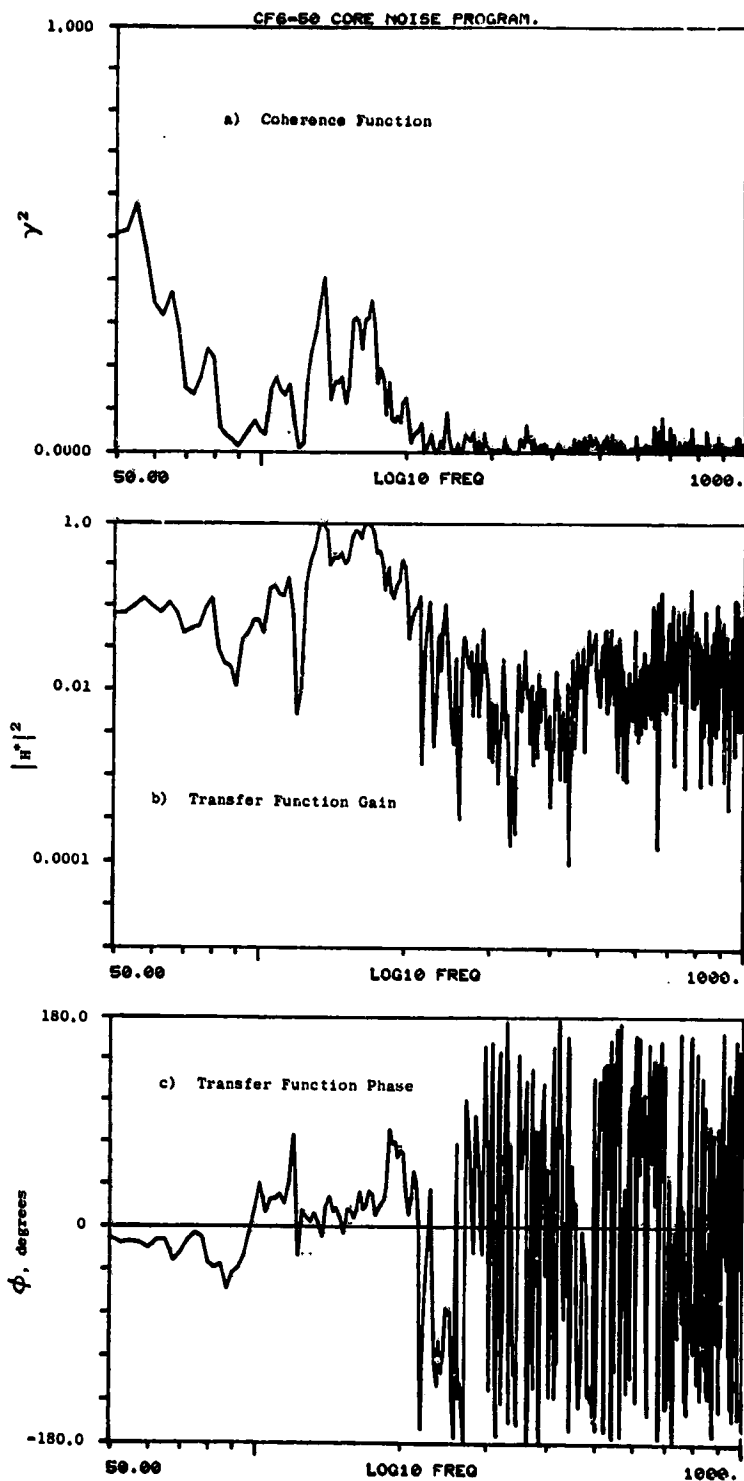


Figure A-178. Coherence and Transfer Functions
for Plane 8.0A (270°) to 10°
Farfield Microphone at 30.8% Thrust.

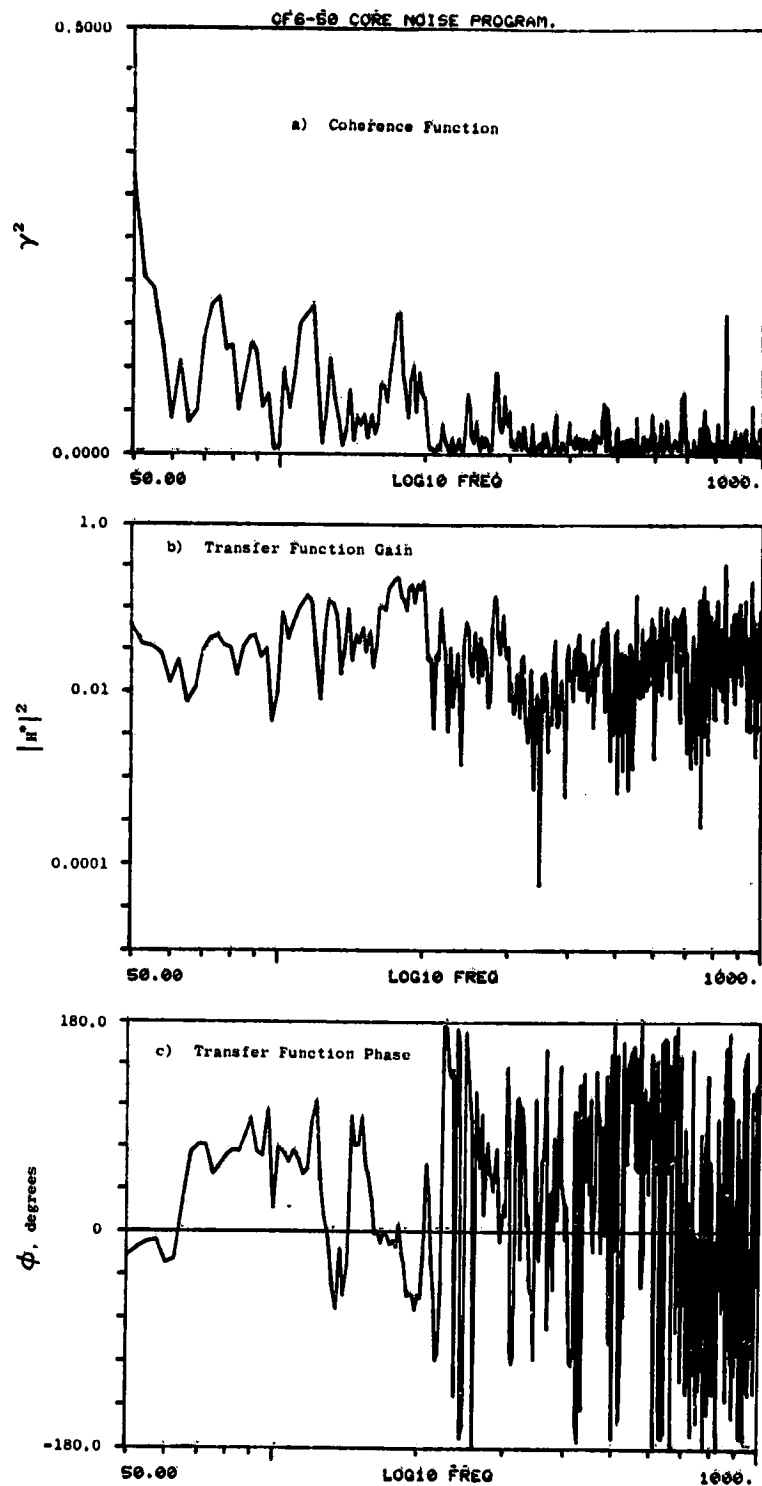


Figure A-179. Coherence and Transfer Functions
for Plane 8.0A (270°) to 30°
Farfield Microphone at 30.8% Thrust.

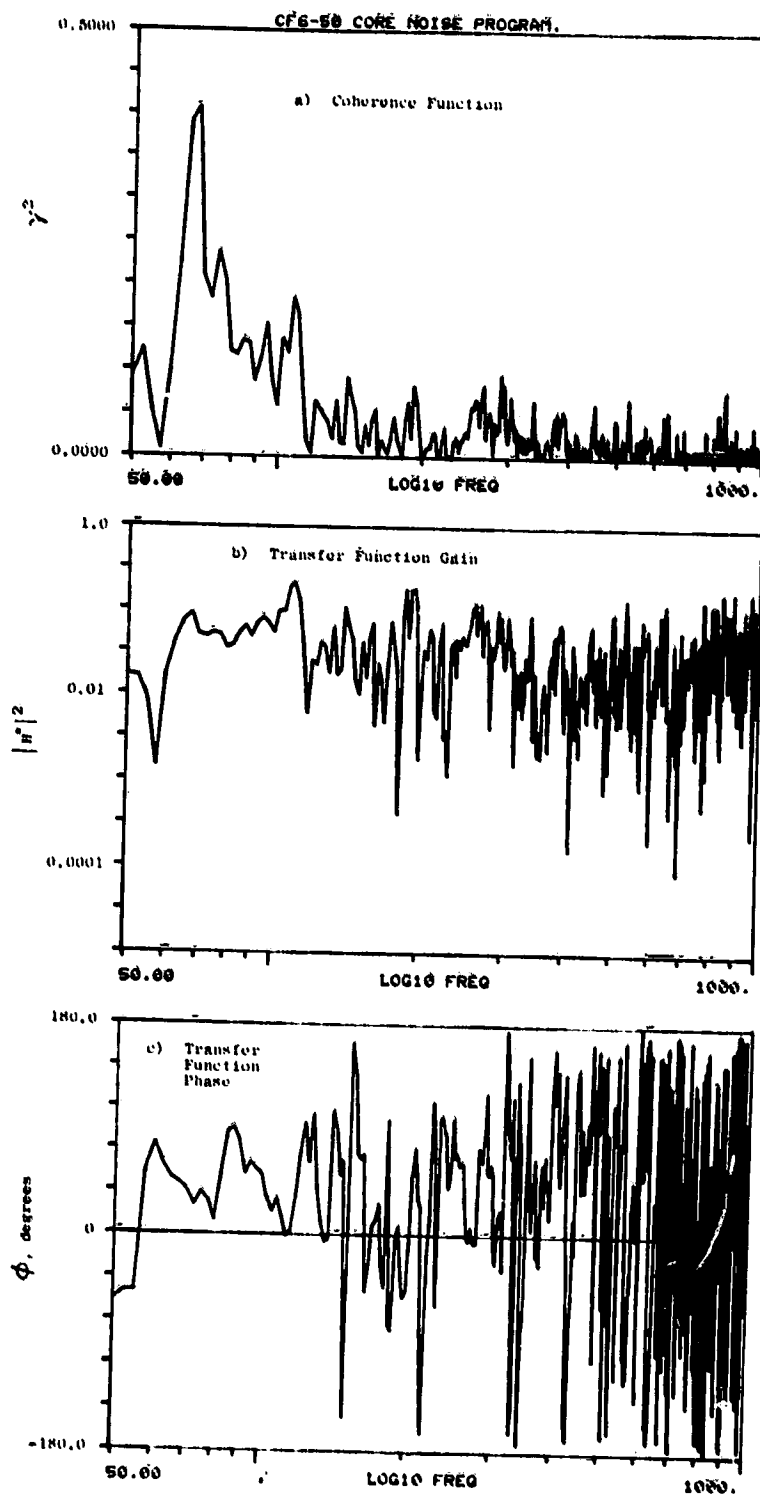


Figure A-180. Coherence and Transfer Functions for Plane 8.0A (270°) to 40° Farfield Microphone at 30.8% Thrust.

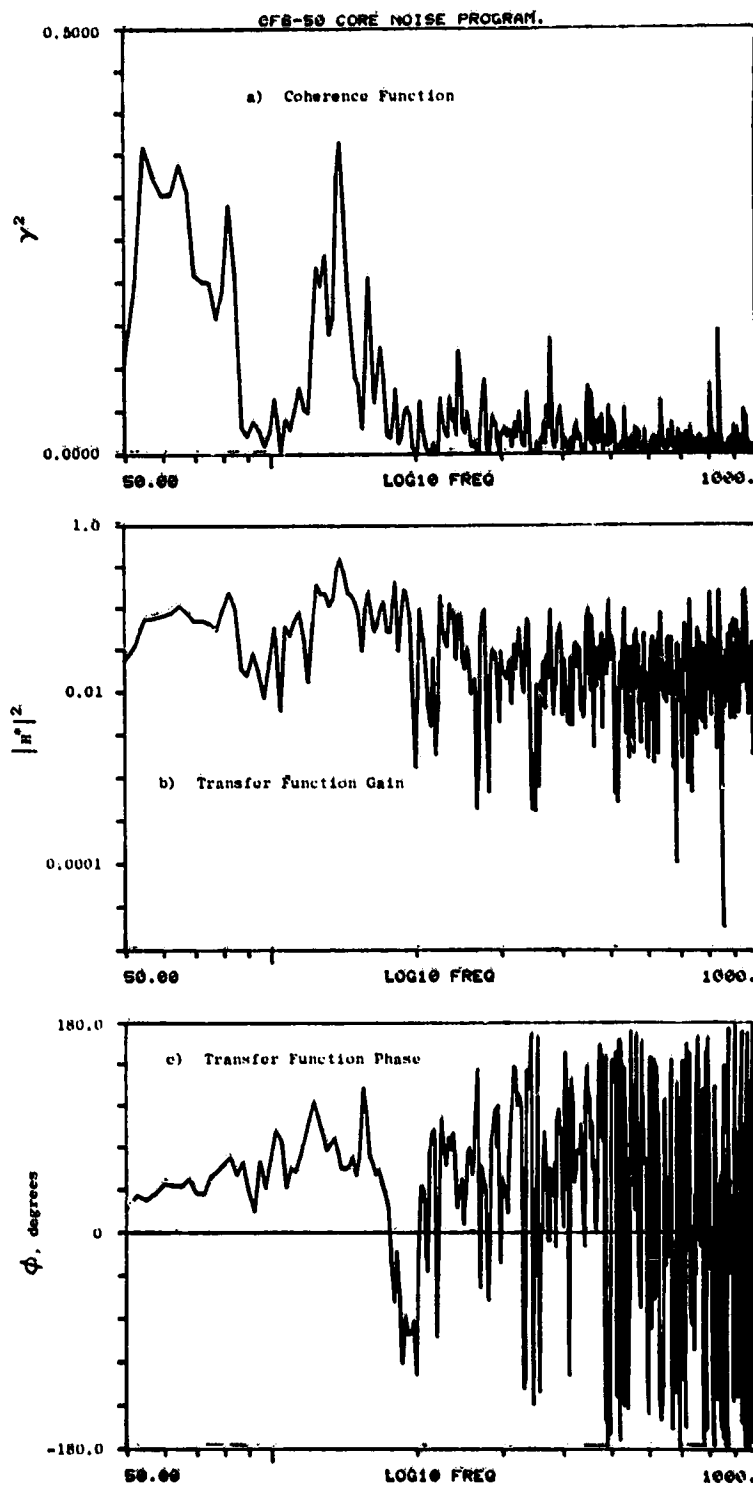


Figure A-181. Coherence and Transfer Functions
for Plane 8.0A (270°) to 50°
Farfield Microphone at 30.8% Thrust.

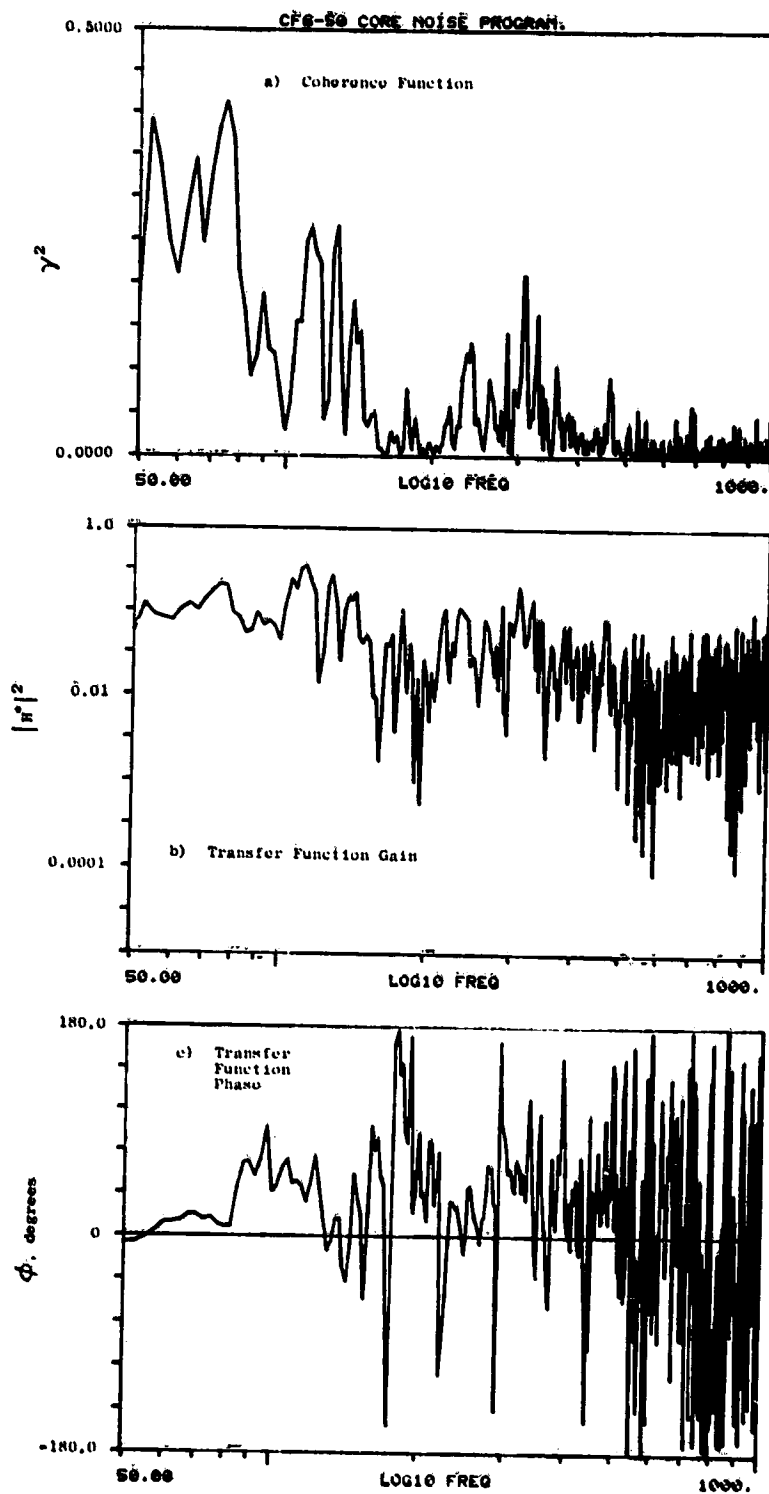


Figure A-182. Coherence and Transfer Functions for Plane 8.0A (270°) to 60° Farfield Microphone at 30.8% Thrust.

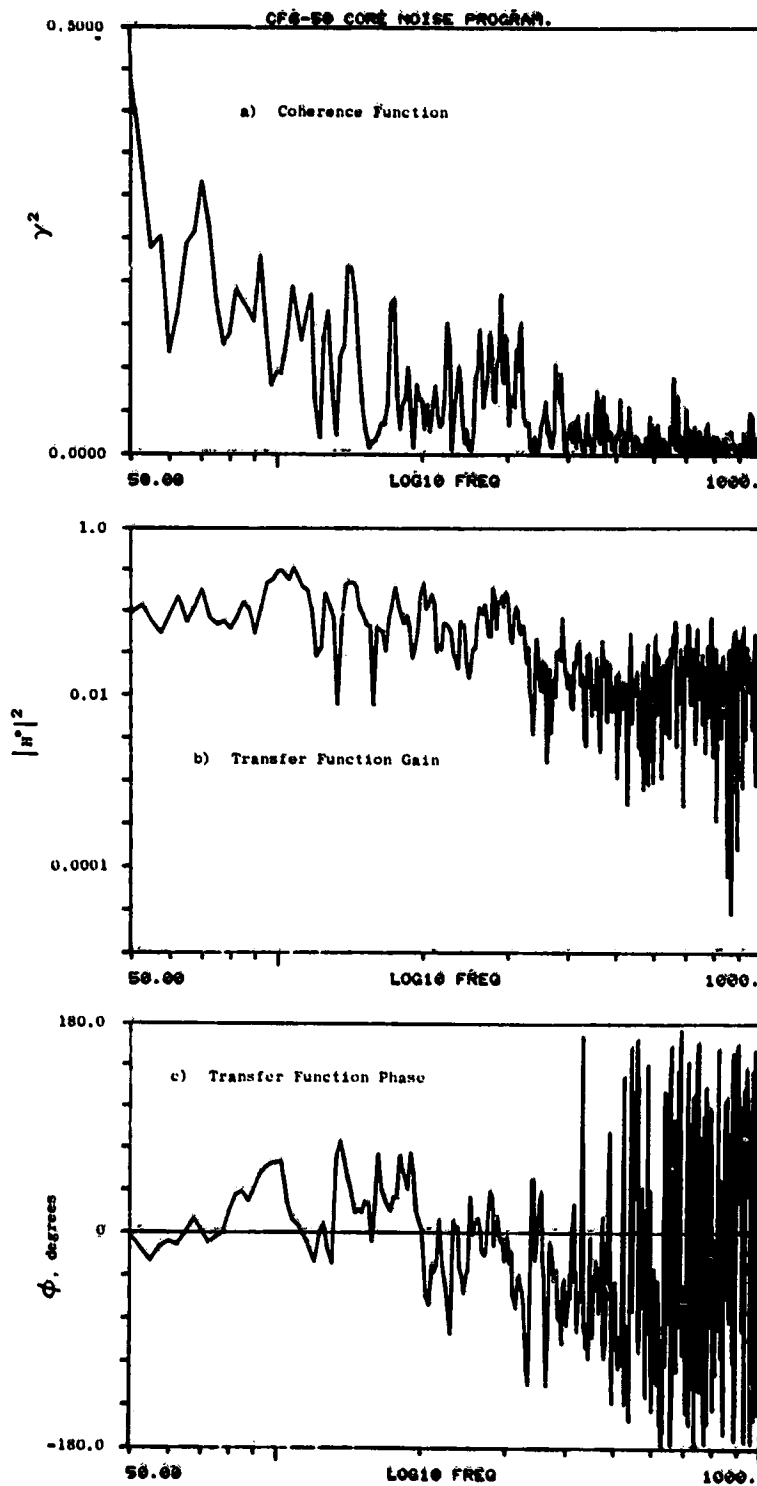


Figure A-183. Coherence and Transfer Functions
for Plane 8.0A (270°) to 70°
Farfield Microphone at 30.8% Thrust.

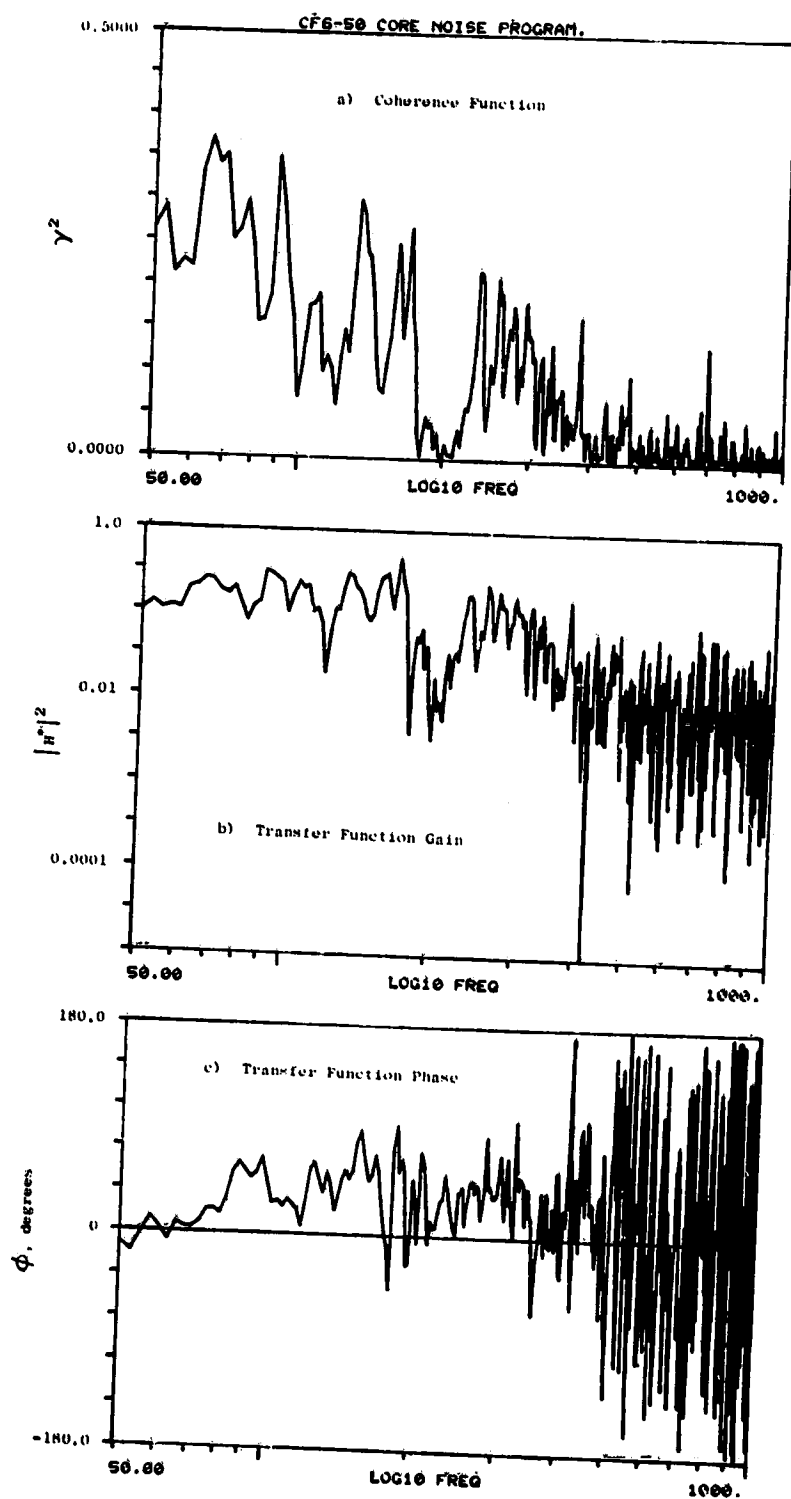


Figure A-184. Coherence and Transfer Functions for Plane 8.0A (270°) to 80° Farfield Microphone at 30.8% Thrust.

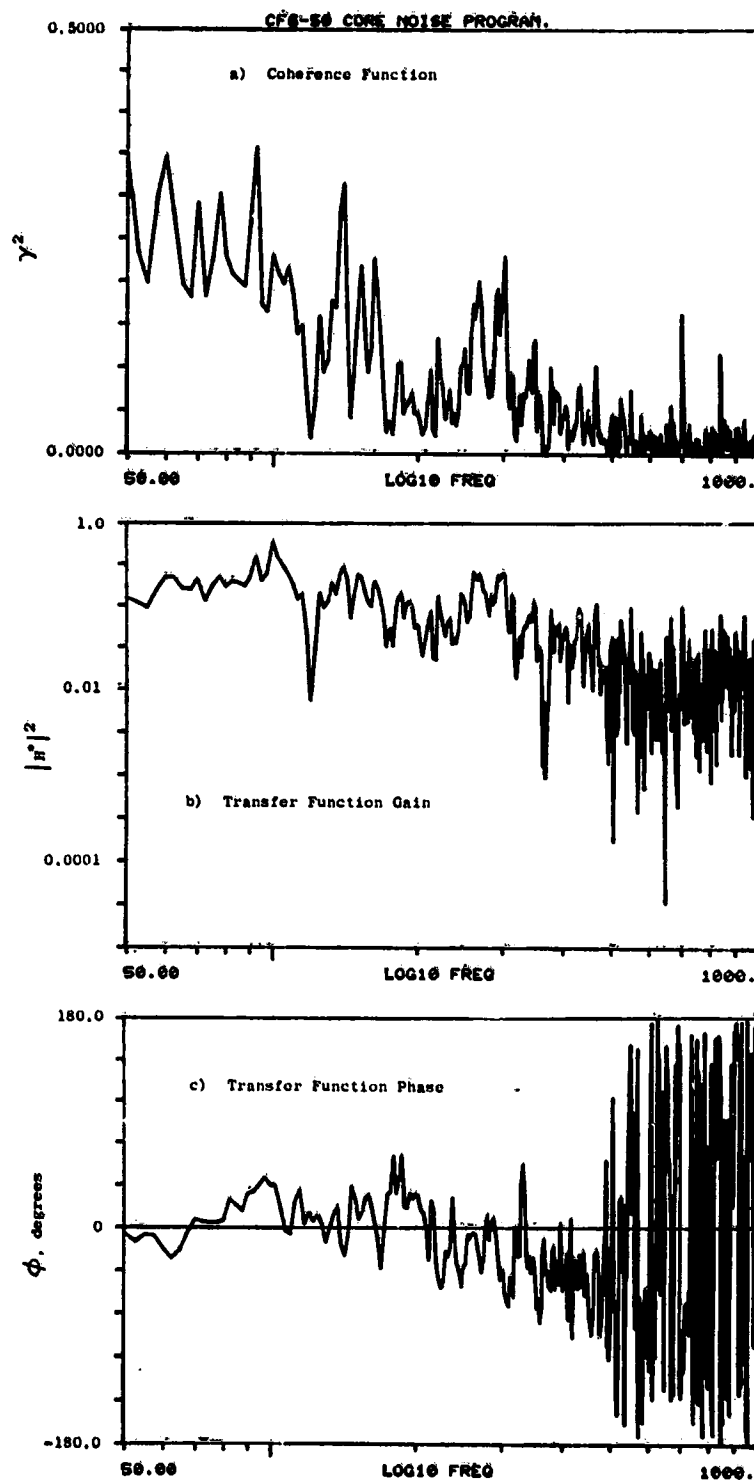


Figure A-185. Coherence and Transfer Functions
for Plane 8.0A (270°) to 90°
Farfield Microphone at 30.8% Thrust.

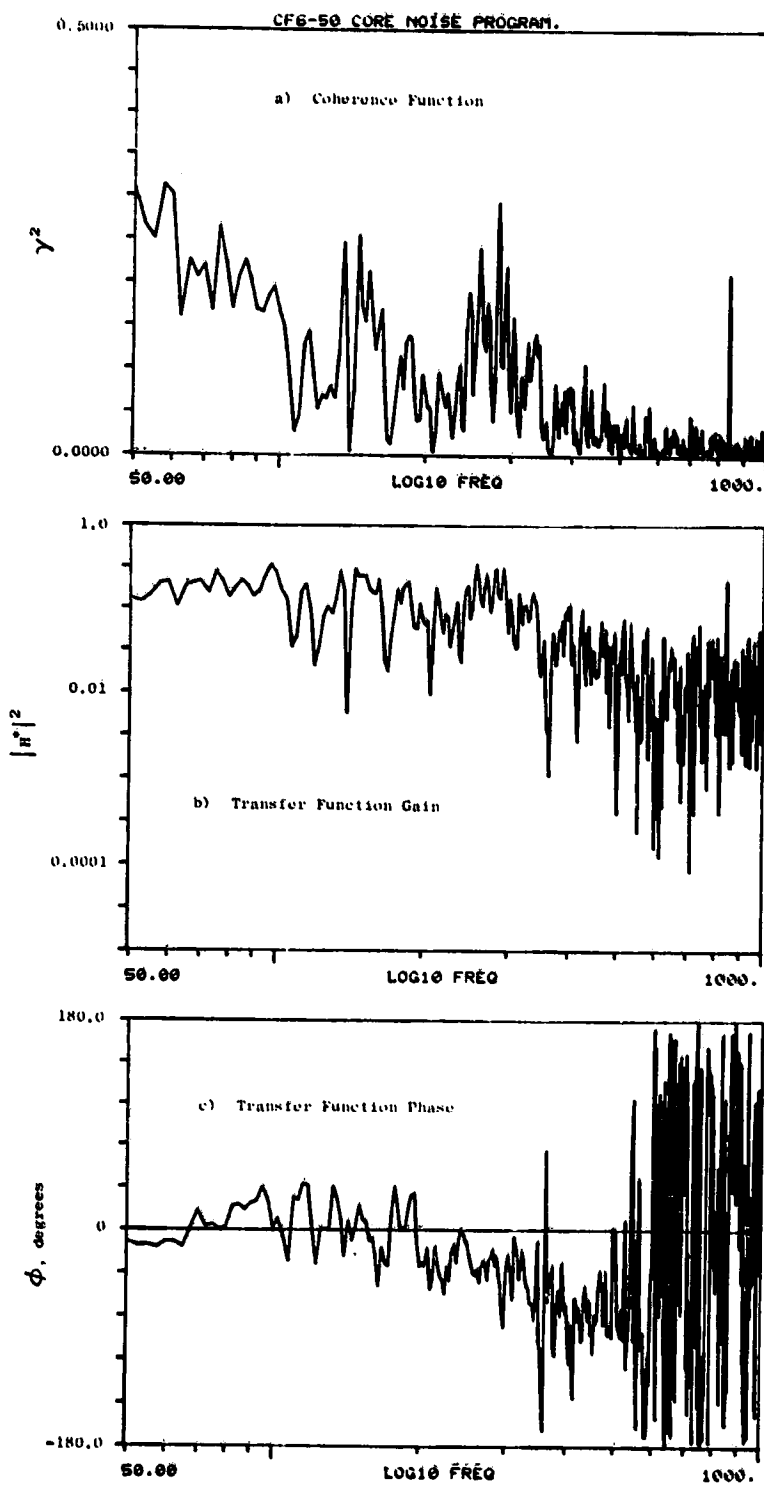


Figure A-186. Coherence and Transfer Functions
for Plane 8.0A (270°) to 100°
Farfield Microphone at 30.8% Thrust.

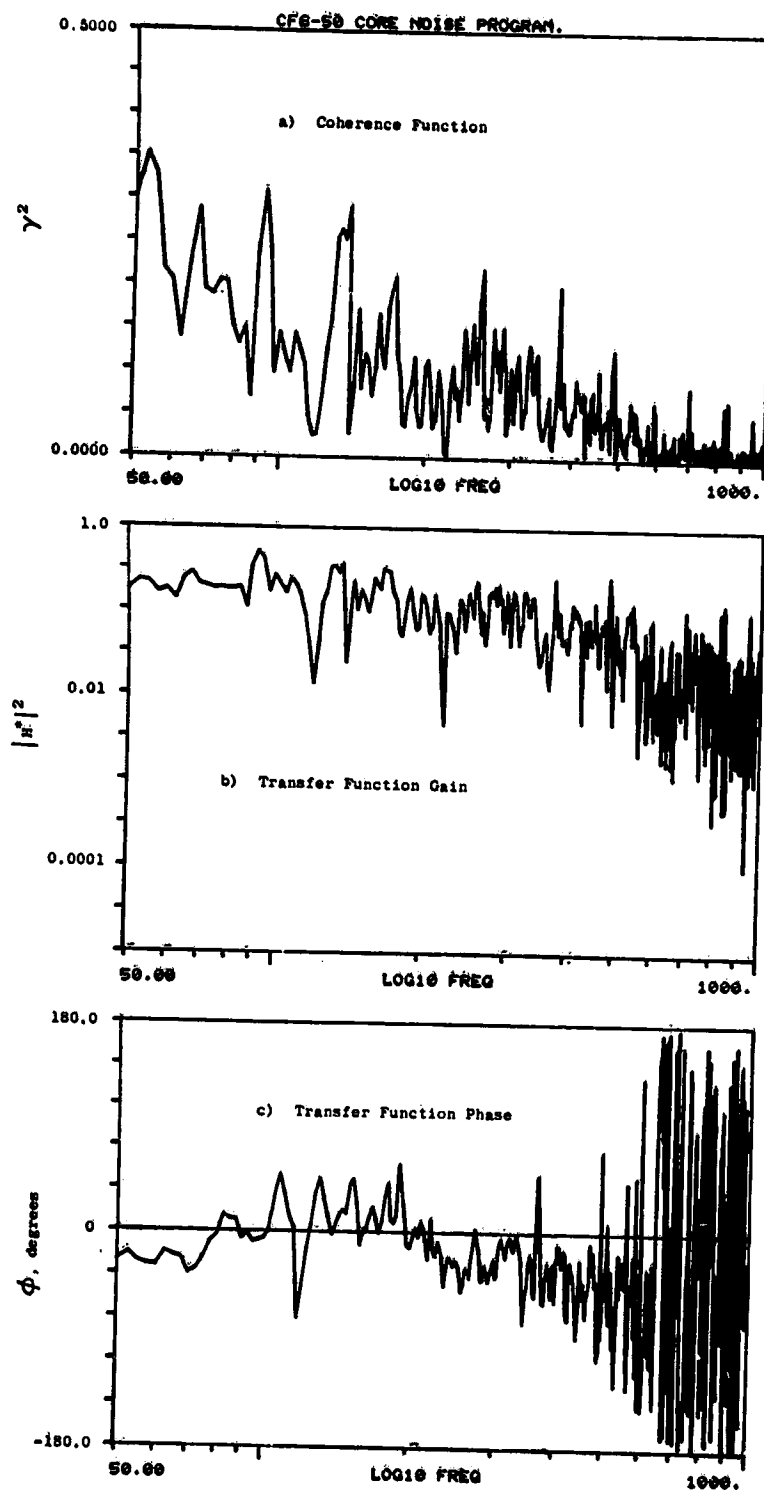


Figure A-187. Coherence and Transfer Functions
for Plane 8.0A (270°) to 110°
Farfield Microphone at 30.8% Thrust.

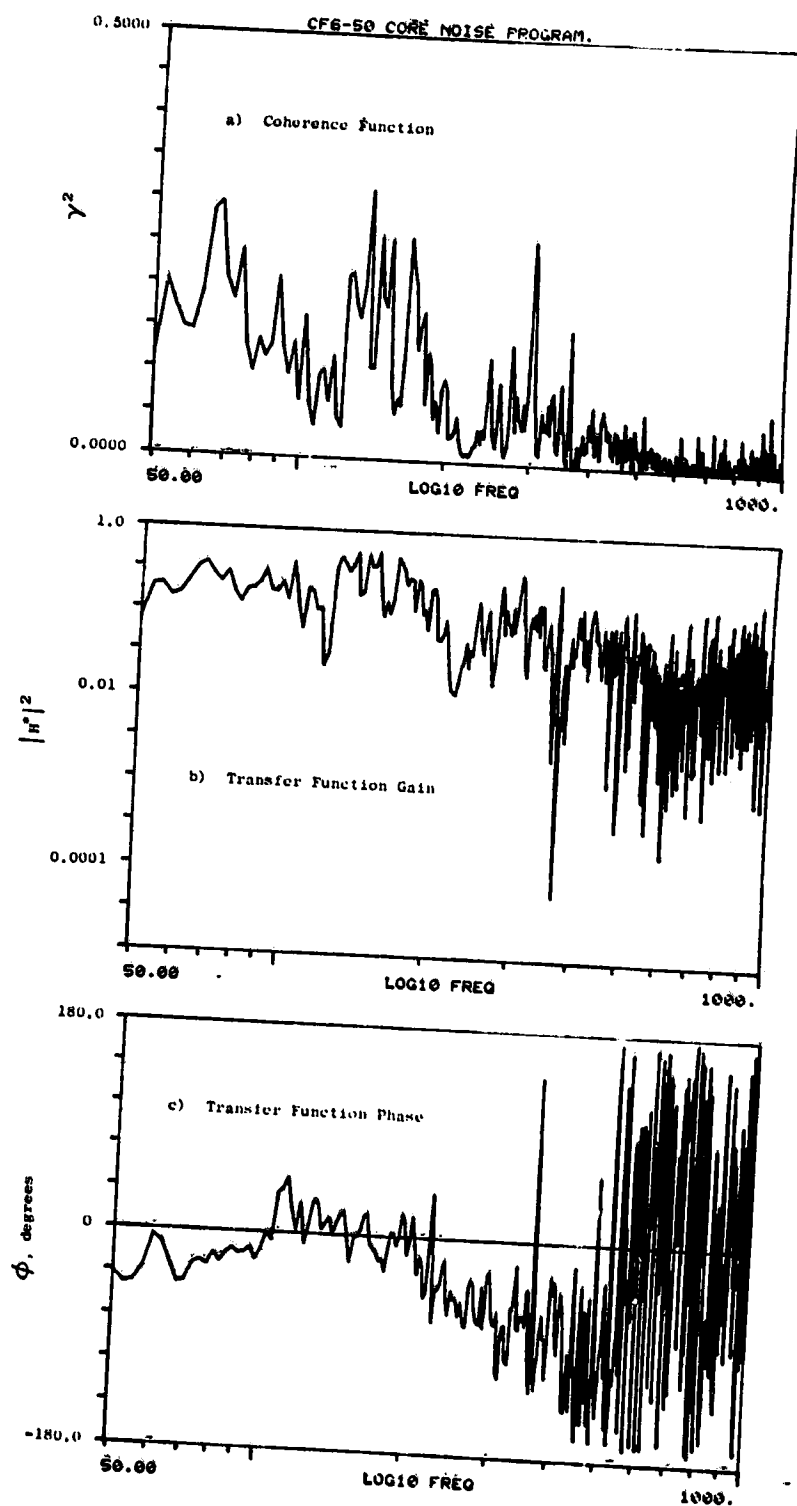


Figure A-188. Coherence and Transfer Functions
for Plane 8.0A (270°) to 120°
Farfield Microphone at 30.8% Thrust.

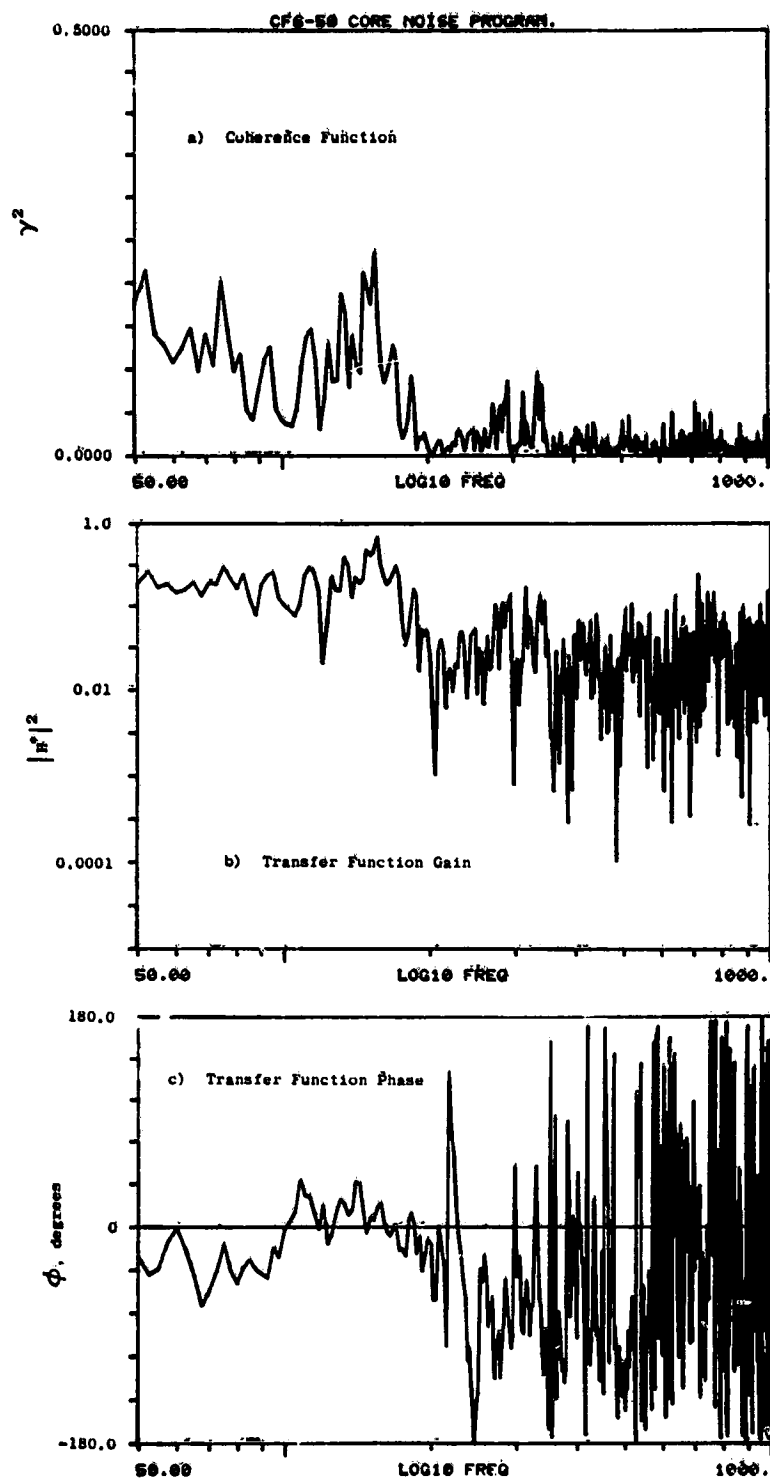


Figure A-189. Coherence and Transfer Functions
for Plane 8.0A (270°) to 130°-
Farfield Microphone at 30.8% Thrust.

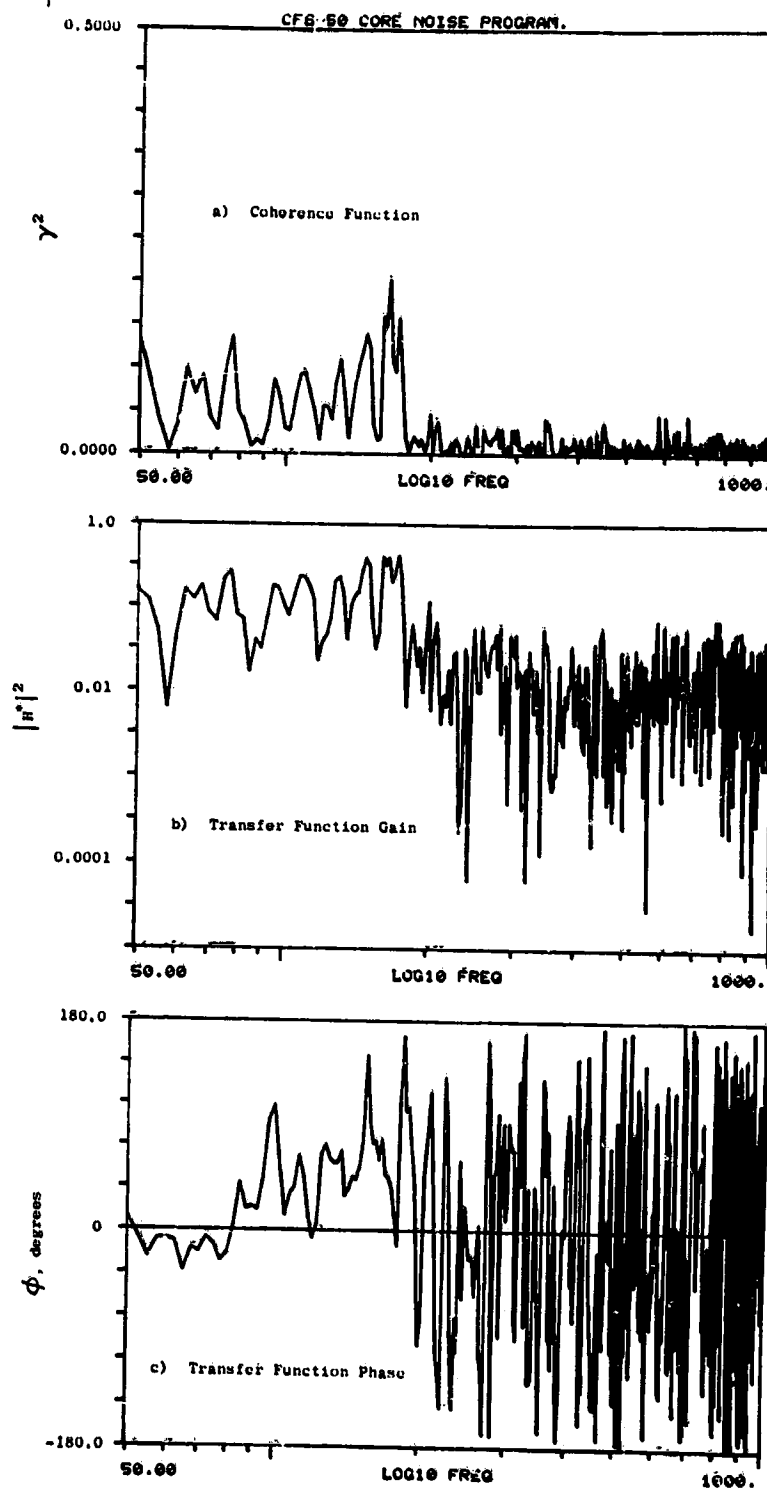


Figure A-190. Coherence and Transfer Functions for Plane 8.0A (270°) to 140° Farfield Microphone at 30.8% Thrust.

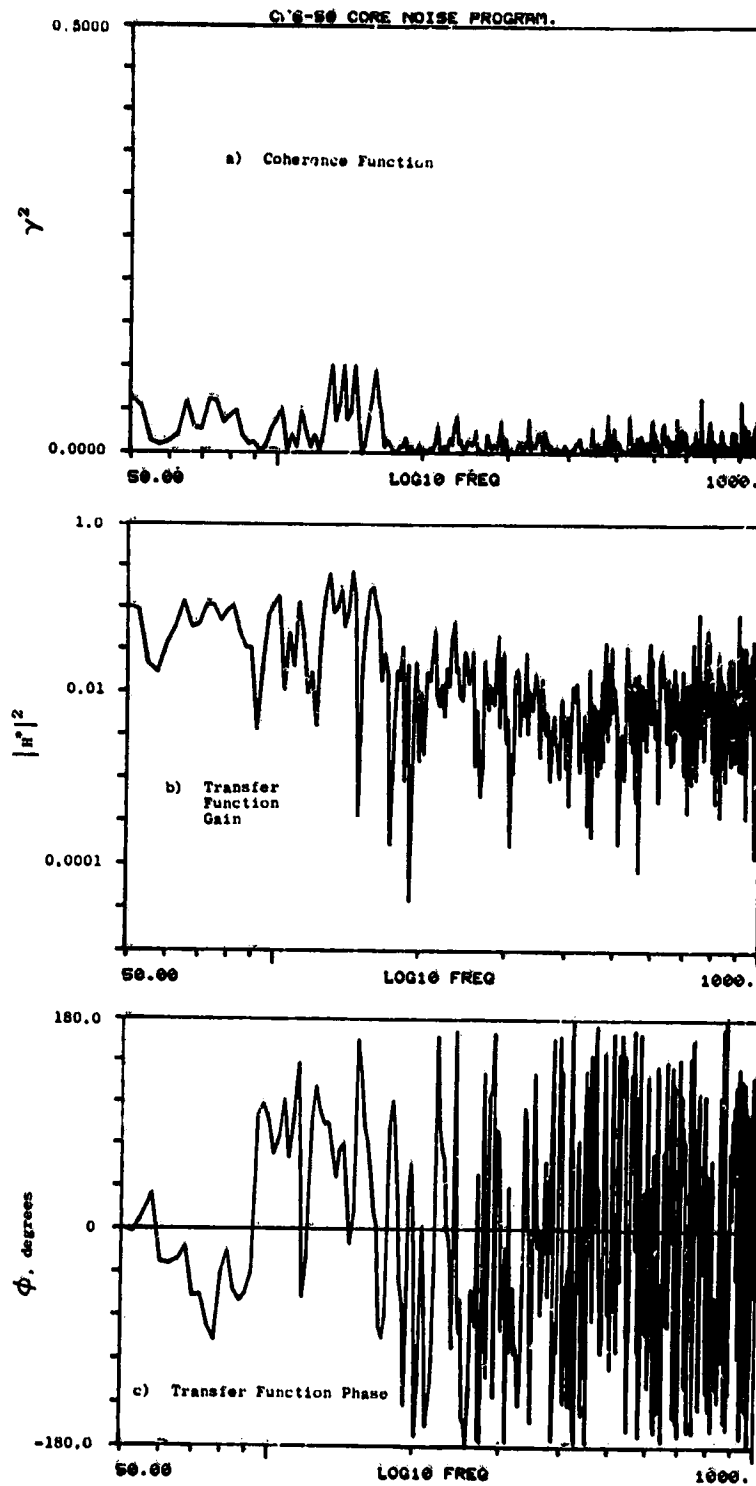


Figure A-191. Coherence and Transfer Functions for Plane 8.0A (270°) to 150° Farfield Microphone at 30.8% Thrust.

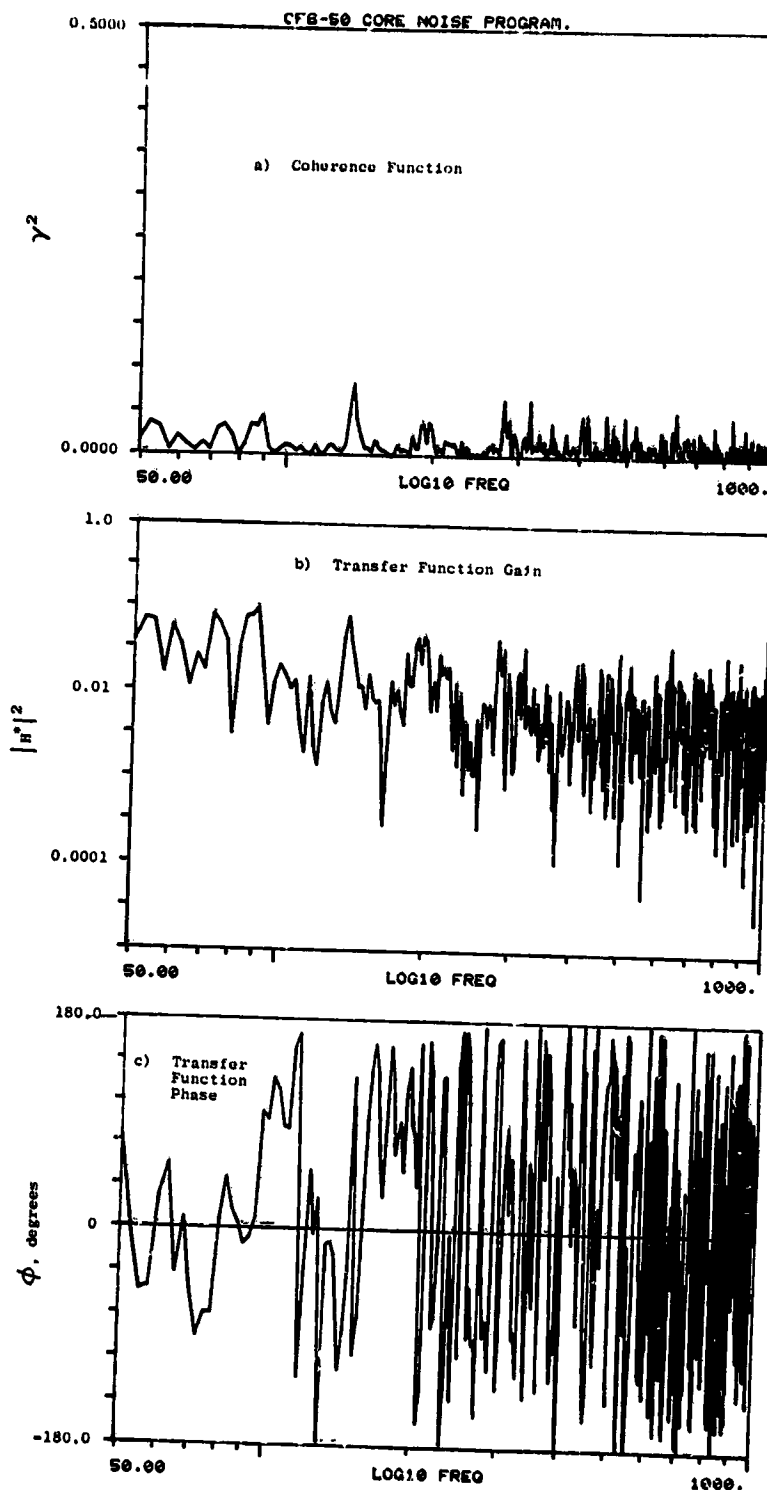


Figure A-192. Coherence and Transfer Functions
for Plane 8.0A (270°) to 160°
Farfield Microphone at 30.8% Thrust.

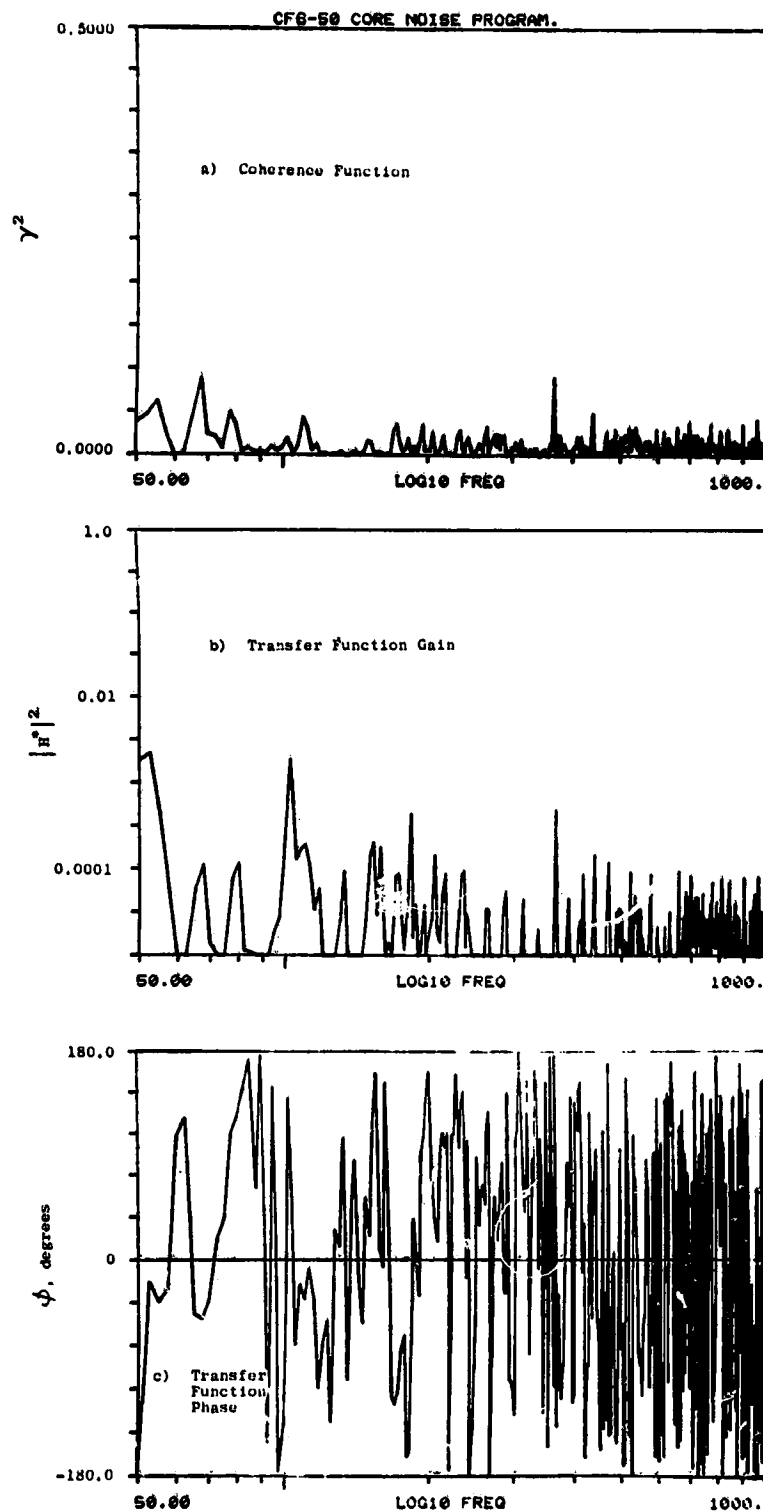


Figure A-193. Coherence and Transfer Functions for Plane 3.5 (102°) to 10° Farfield Microphone at 36.5% Thrust.

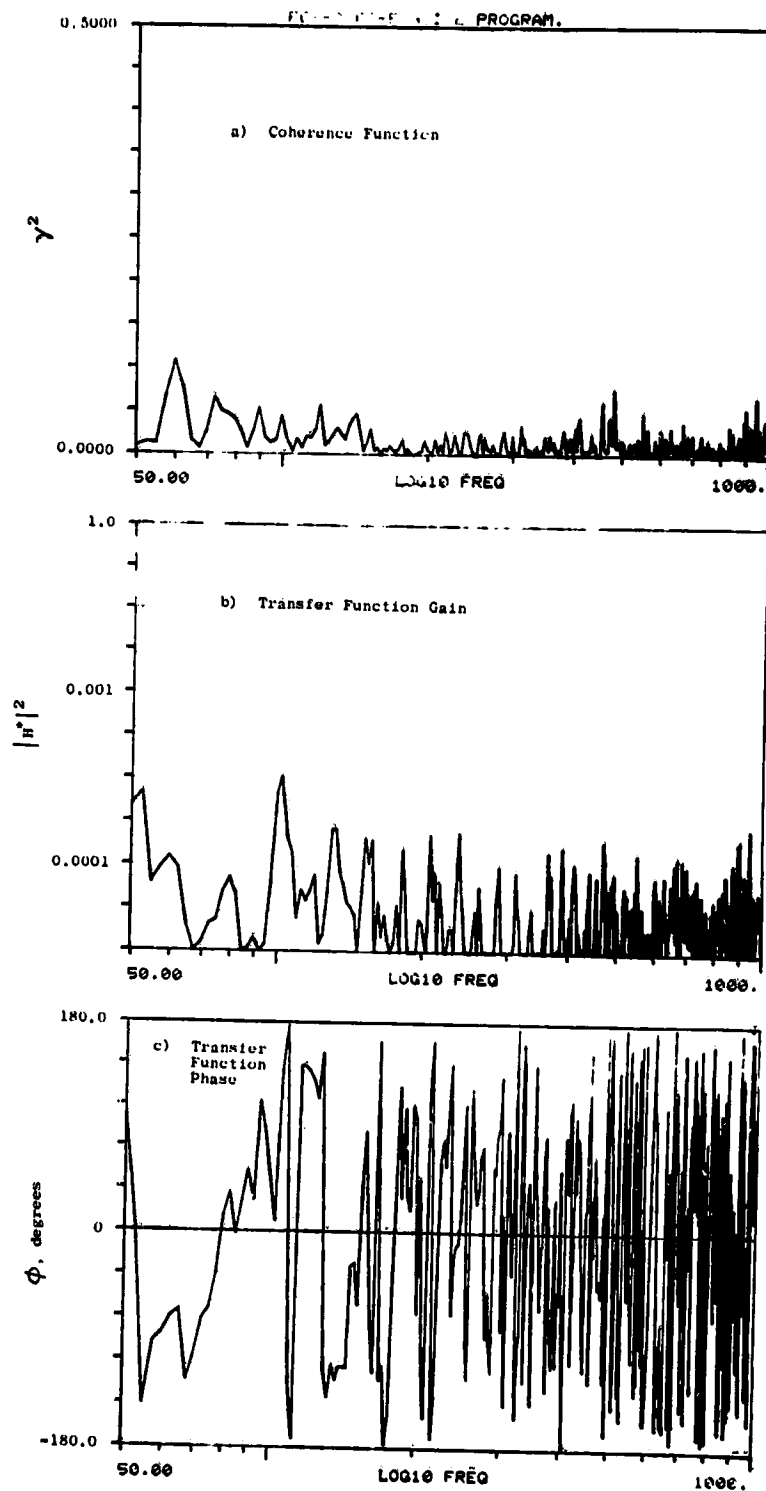


Figure A-194. Coherence and Transfer Functions for Plane 3.5 (102°) to 30° Farfield Microphone at 36.5% Thrust.

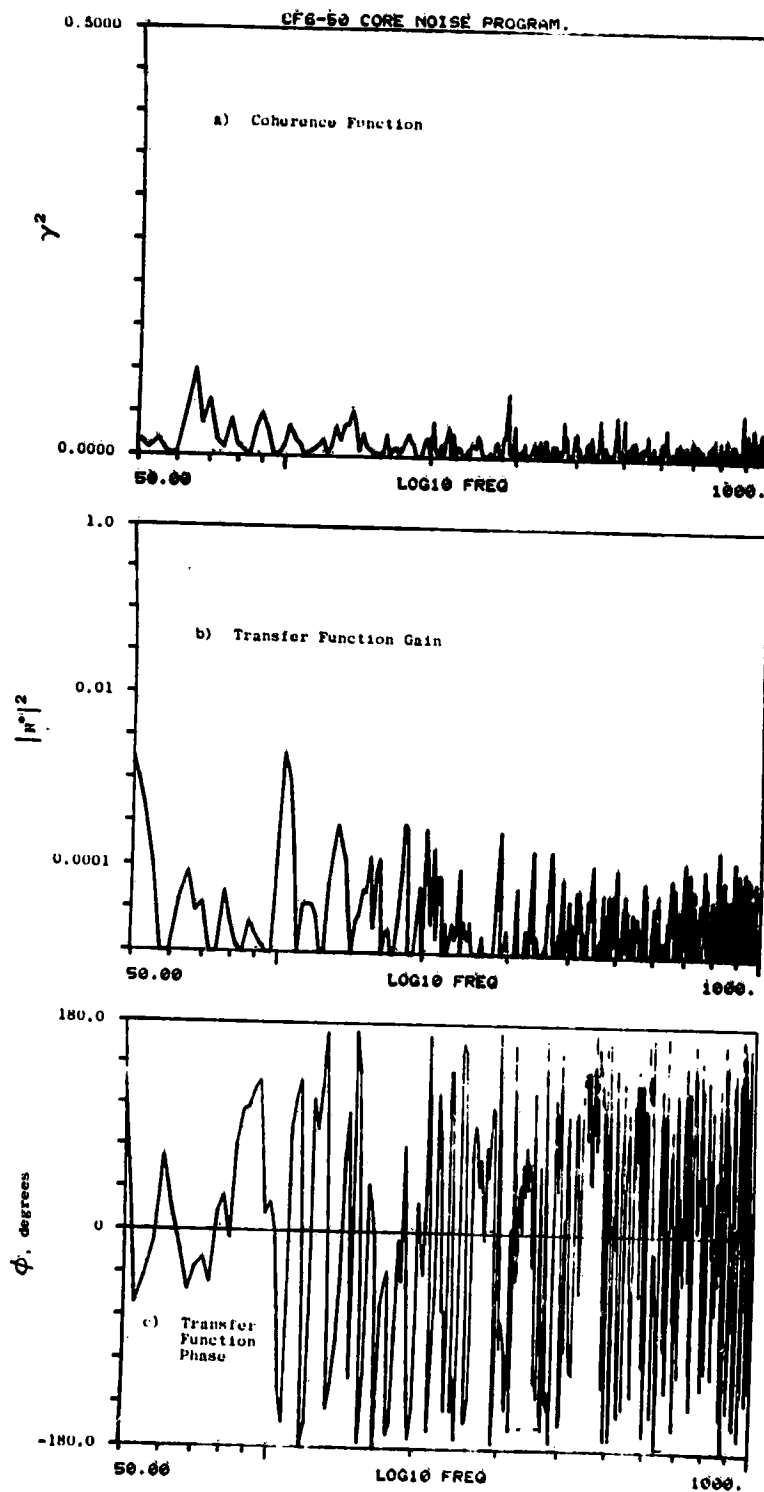


Figure A-195. Coherence and Transfer Functions for Plane 3.5 (102°) to 40° Farfield Microphone at 36.5% Thrust.

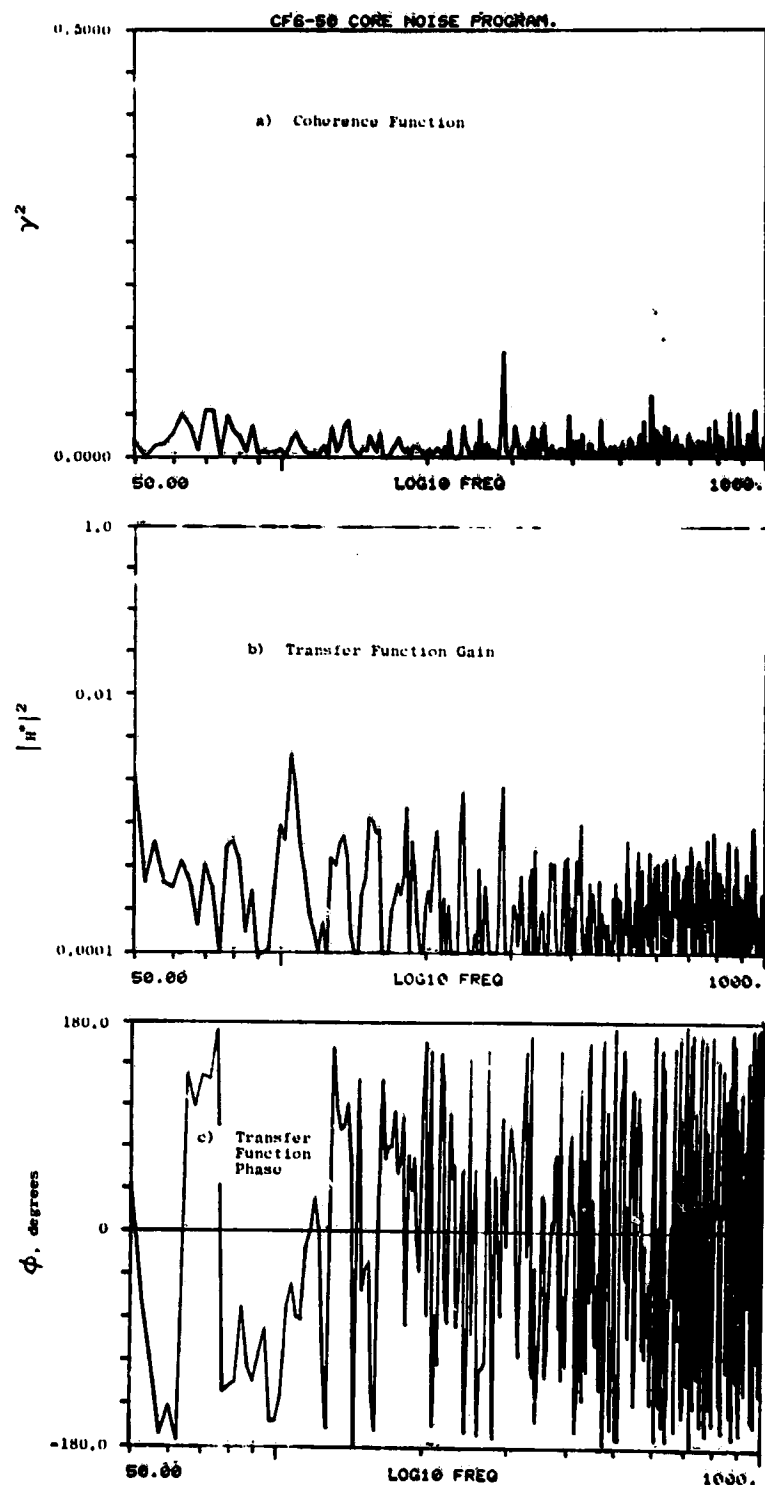


Figure A-196. Coherence and Transfer Functions for Plane 3.5 (102°) to 50° Farfield Microphone at 36.5% Thrust.

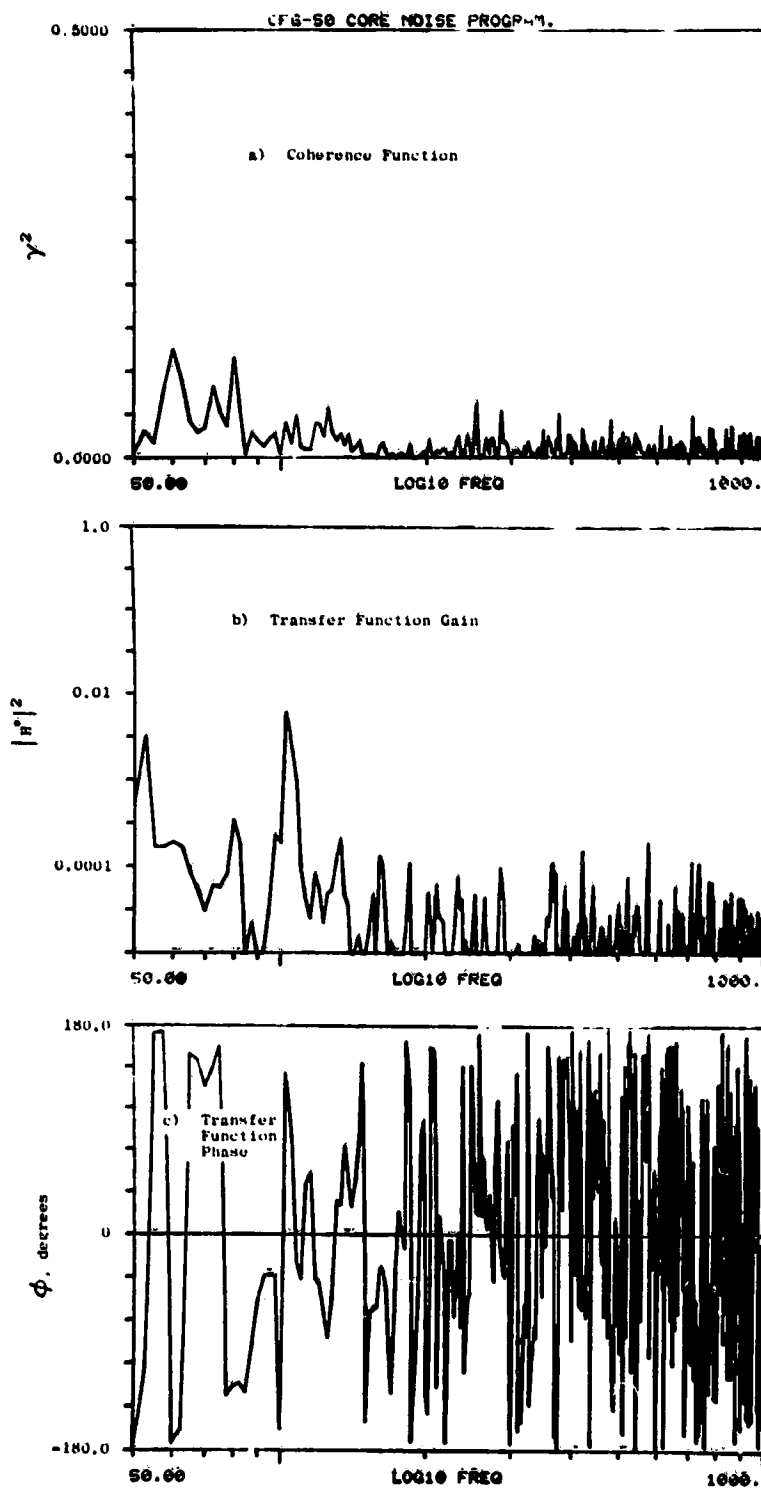


Figure A-197. Coherence and Transfer Functions for Plane 3.5 (102°) to 60° Farfield Microphone at 36.5% Thrust.

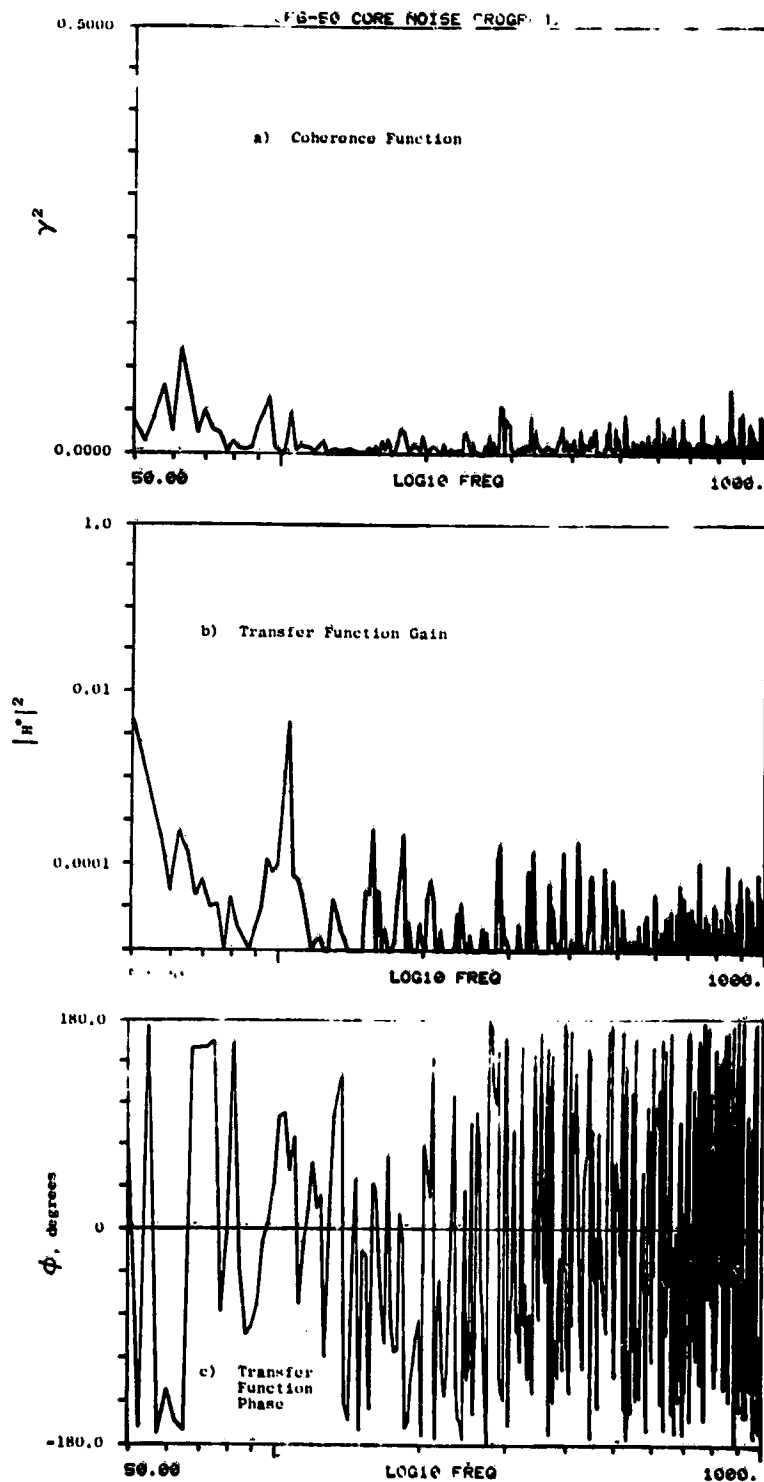


Figure A-198. Coherence and Transfer Functions for Plane 3.5 (102°) to 70° Farfield Microphone at 36.5% Thrust.

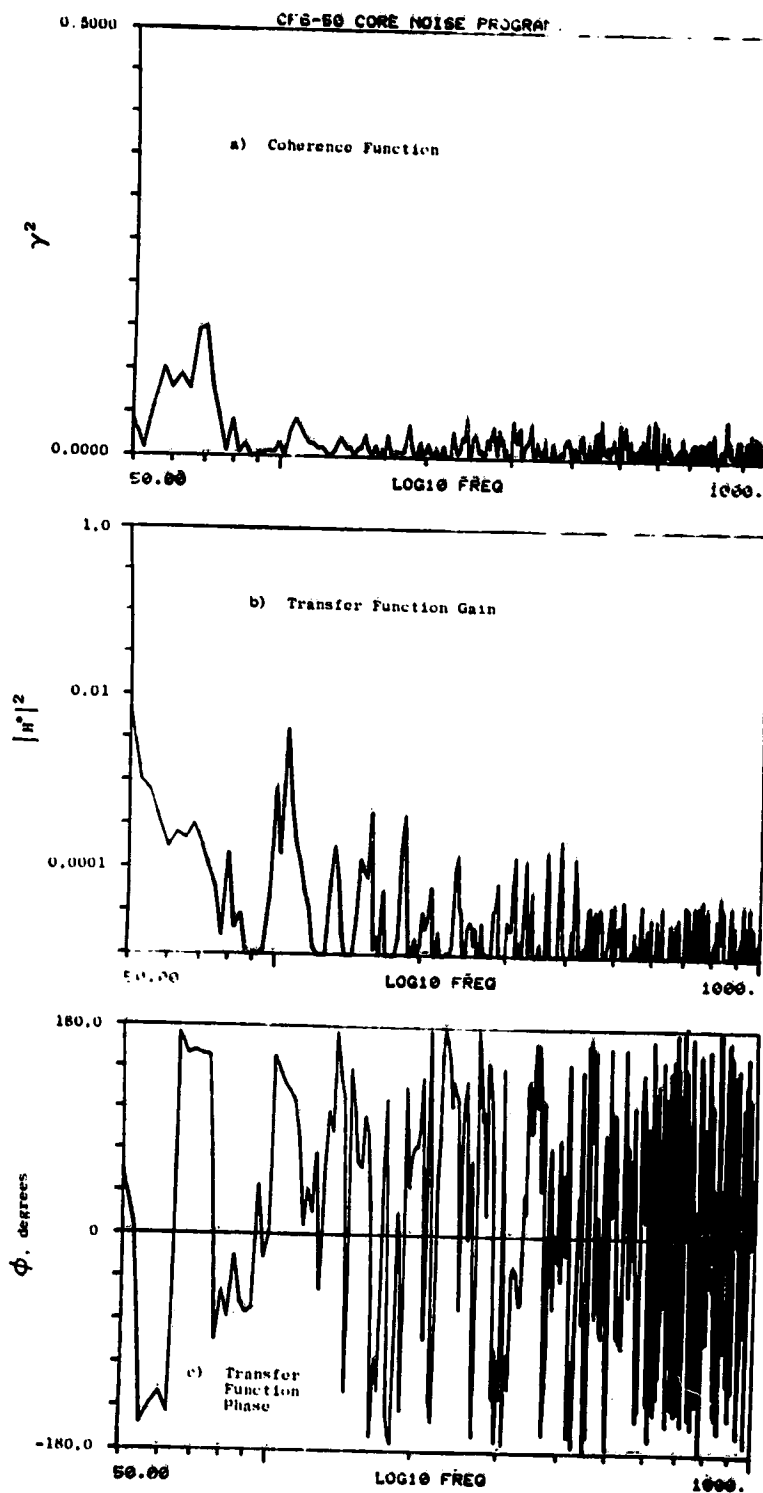


Figure A-199. Coherence and Transfer Functions for Plane 3.5 (102°) to 80° Farfield Microphone at 36.5% Thrust.

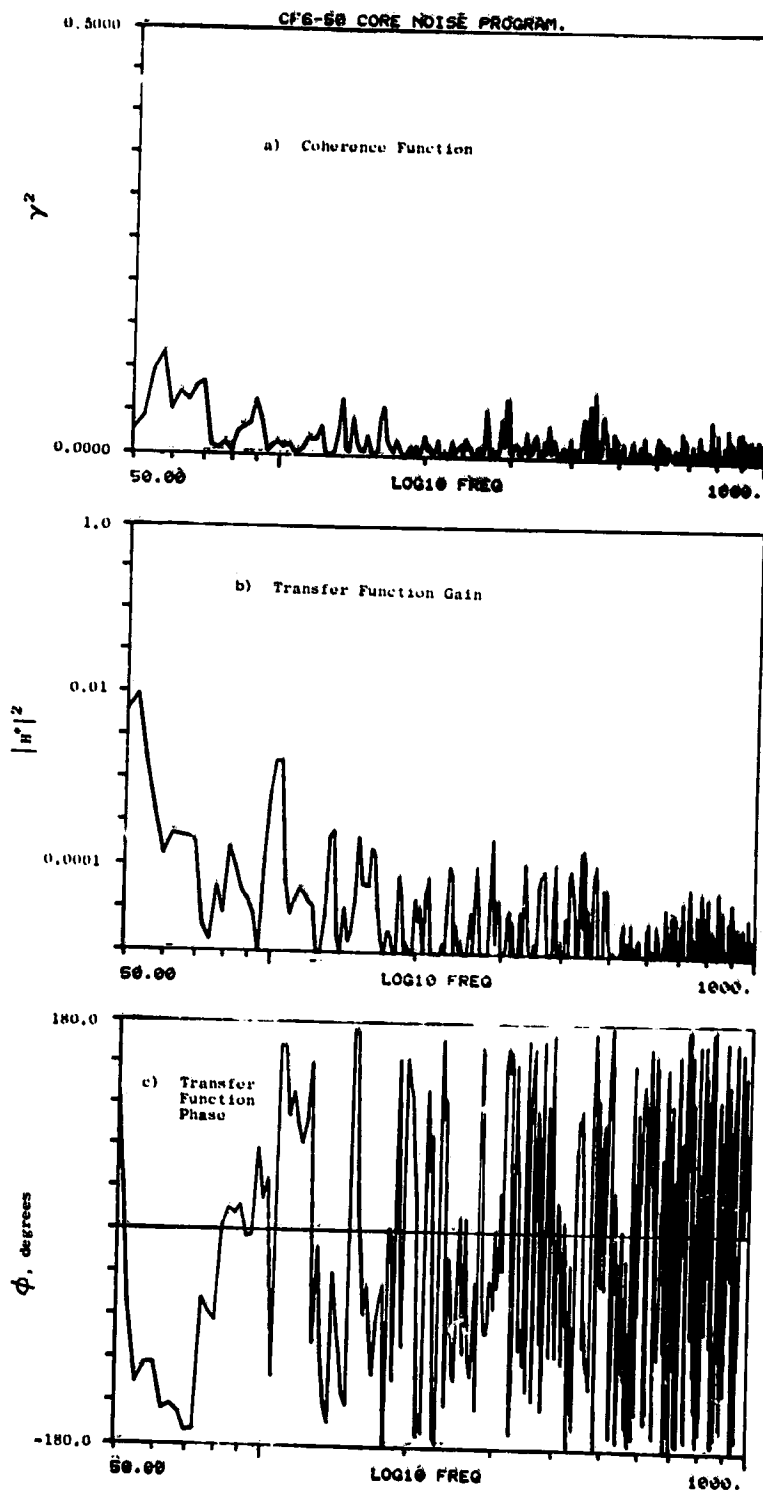


Figure A-200. Coherence and Transfer Functions for Plane 3.5 (102°) to 90° Farfield Microphone at 36.5% Thrust.

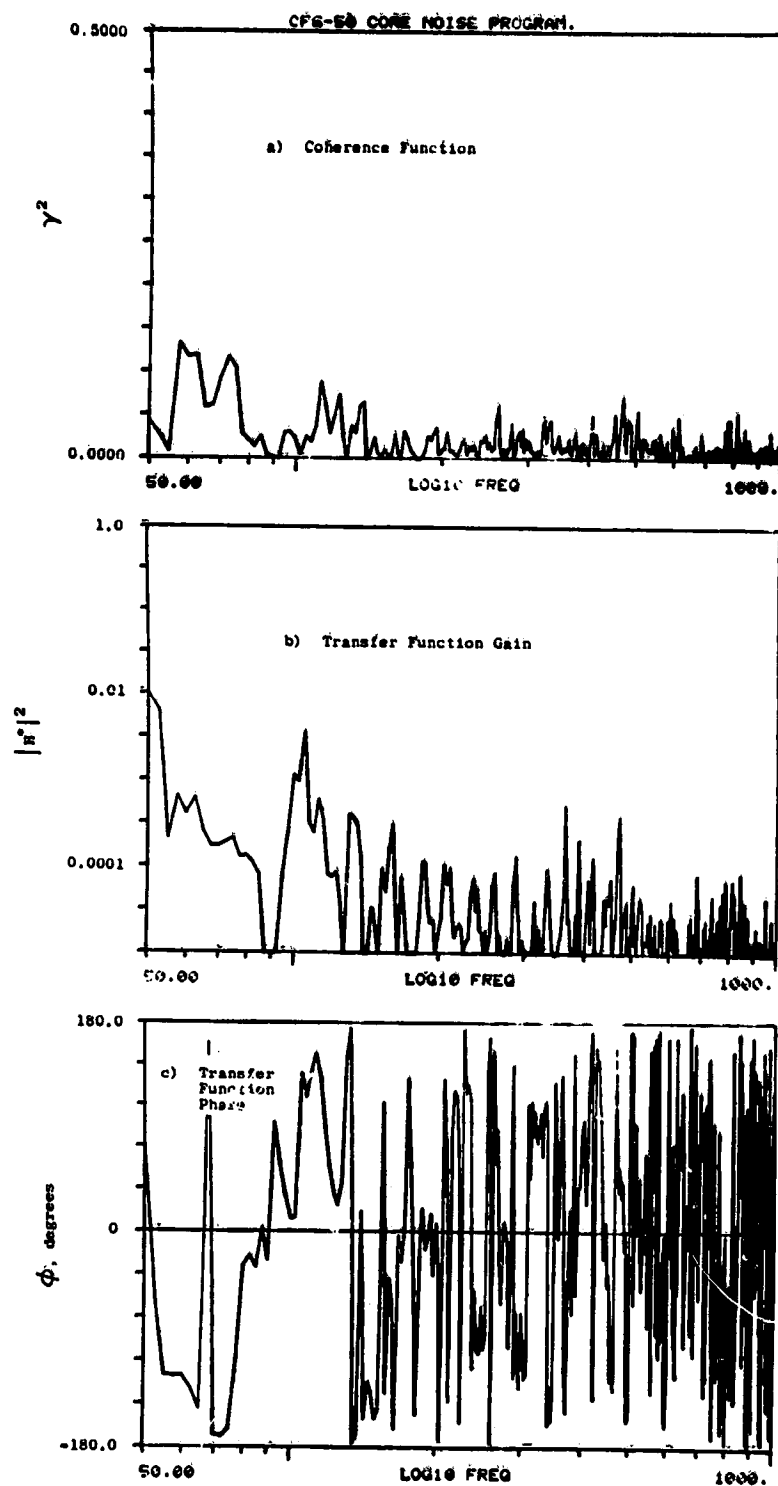


Figure A-201. Coherence and Transfer Functions for Plane 3.5 (102°) to 100° Farfield . Microphone at 36.5% Thrust.

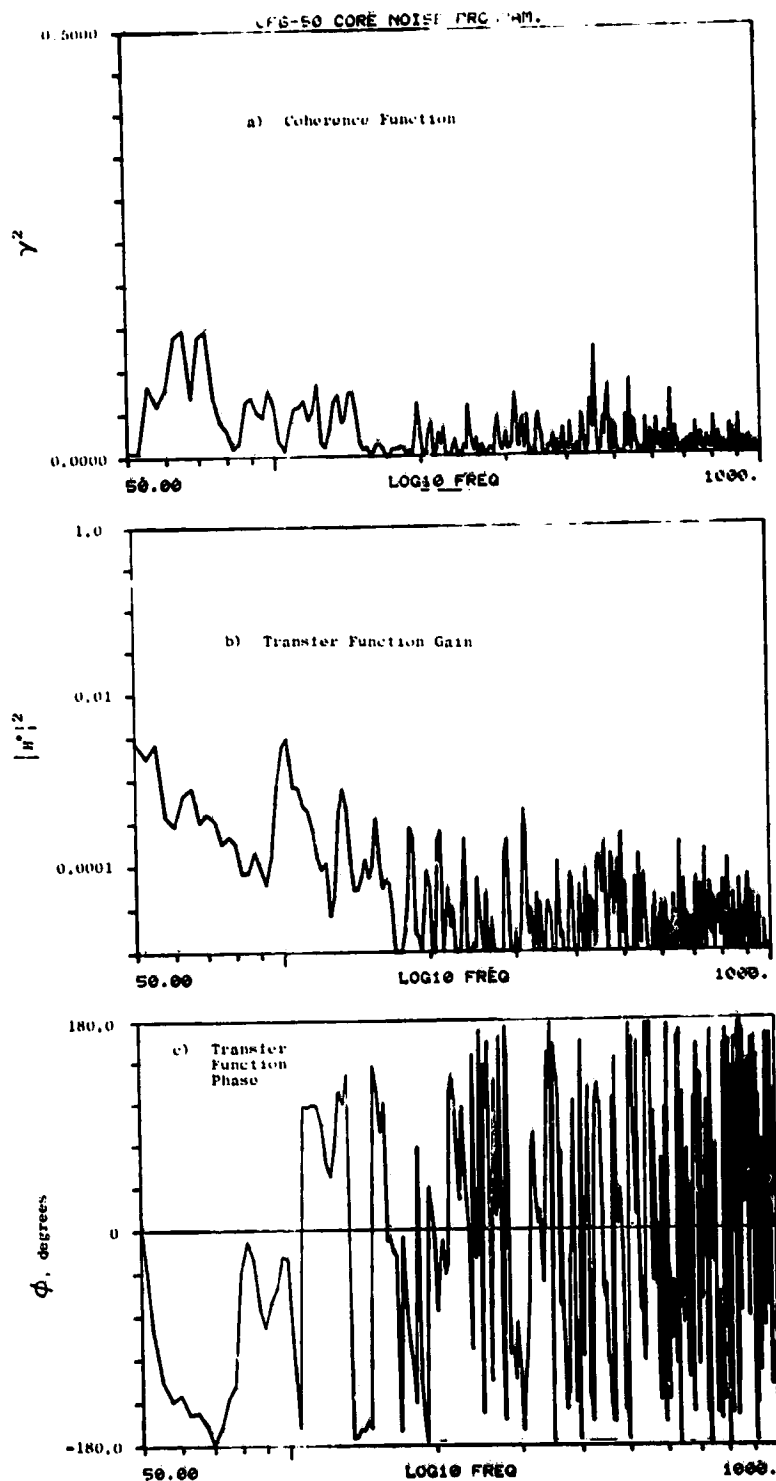


Figure A-202. Coherence and Transfer Functions for Plane 3.5 (102°) to 110° Farfield Microphone at 36.5% Thrust.

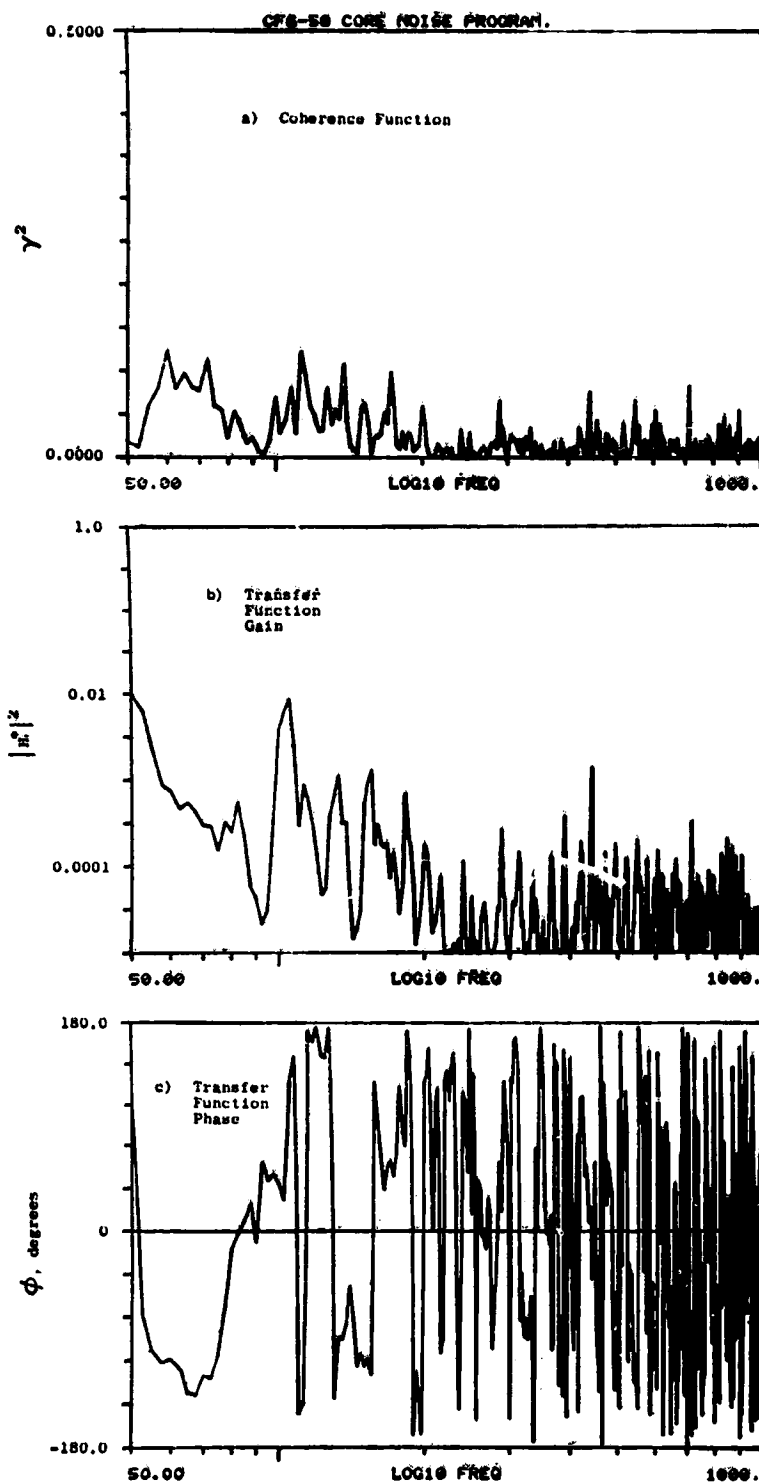


Figure A-203. Coherence and Transfer Functions for Plane 3.5 (102°) to 120° Farfield Microphone at 36.5% Thrust.

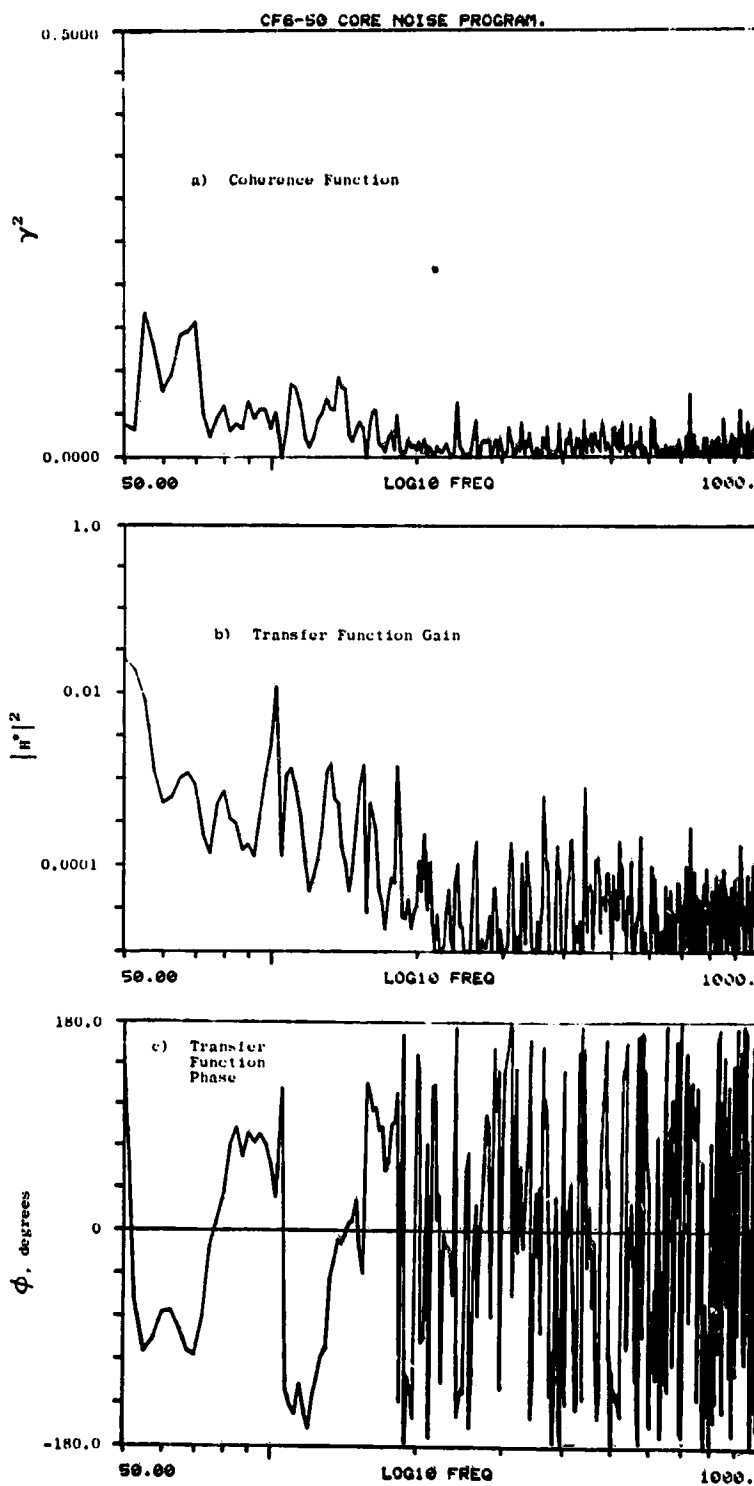


Figure A-204. Coherence and Transfer Functions for Plane 3.5 (102°) to 130° Farfield Microphone at 36.5% Thrust.

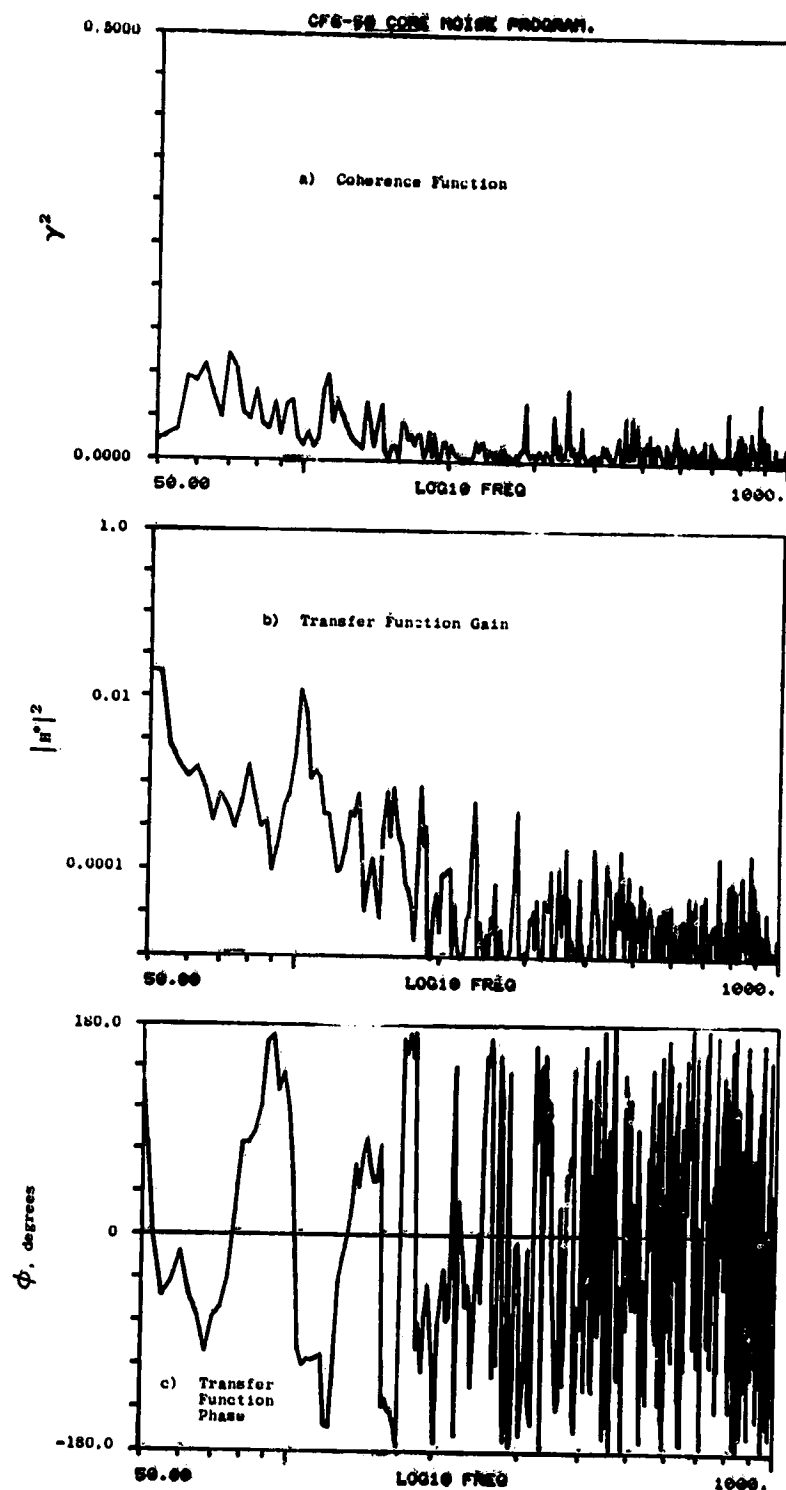


Figure A-205. Coherence and Transfer Functions for Plane 3.5 (102° to 140° Farfield Microphone at 36.5% Thrust.

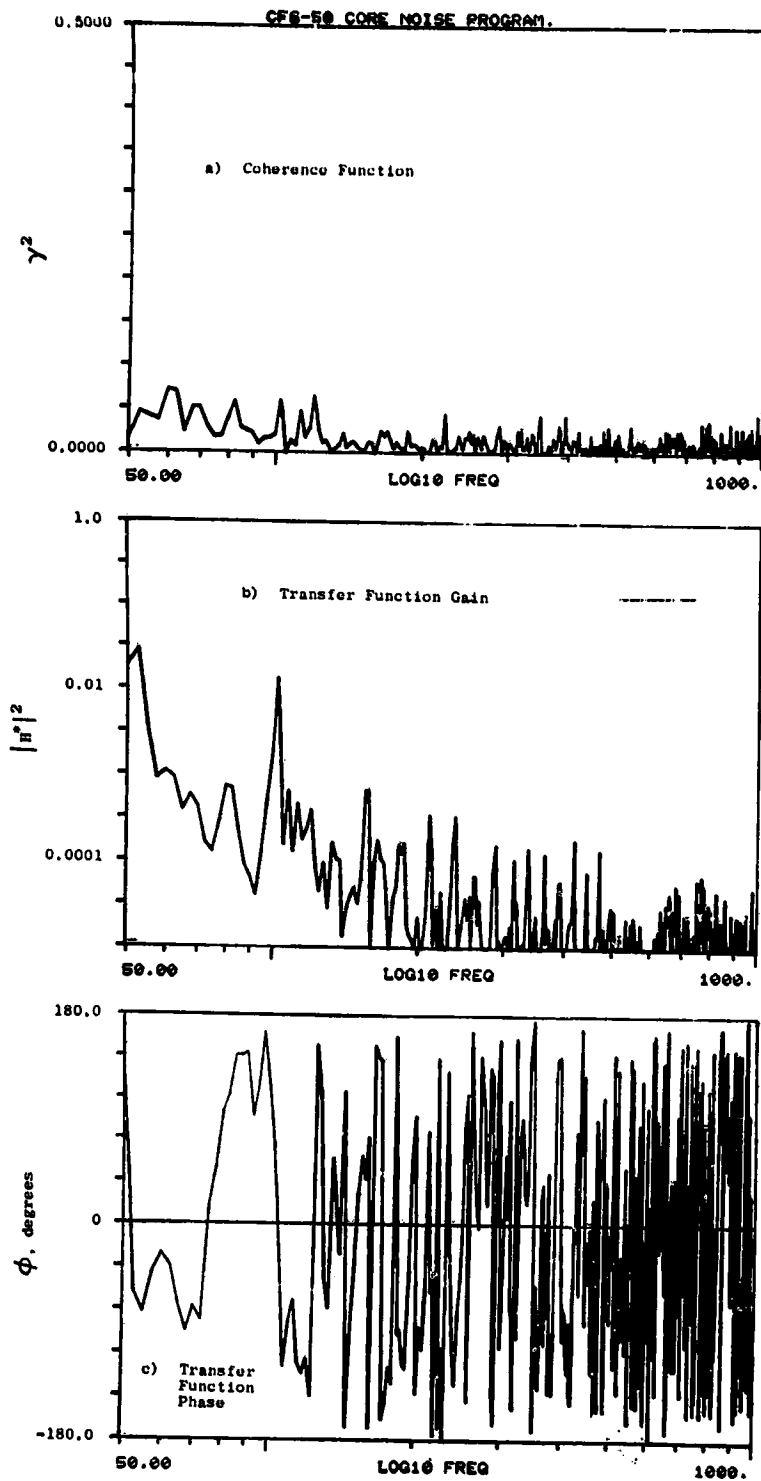


Figure A-206. Coherence and Transfer Functions for Plane 3.5 (102°) to 150° Farfield Microphone at 36.5% Thrust.

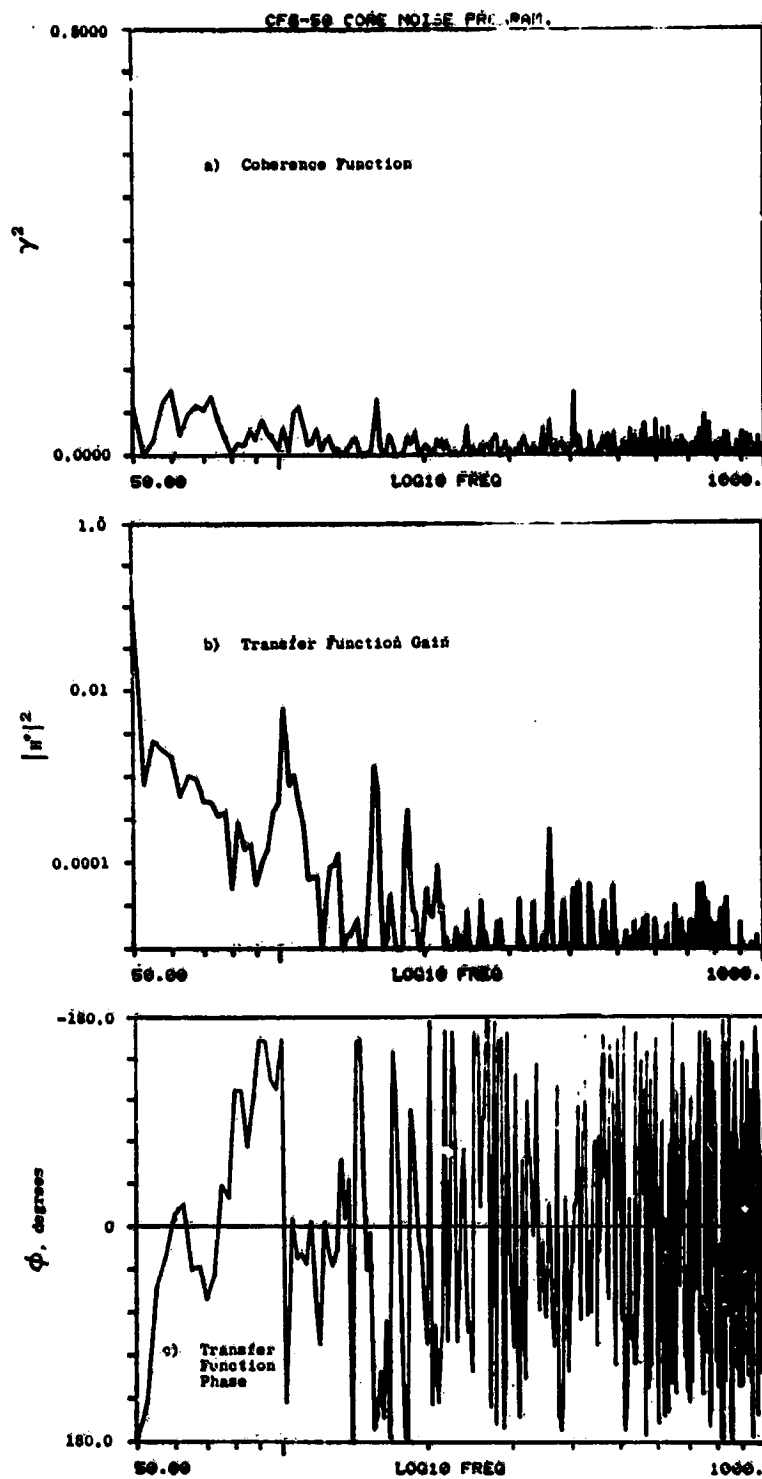


Figure A-207. Coherence and Transfer Functions for Plane 3.5 (102°) to 160° Farfield Microphone at 36.5% Thrust.

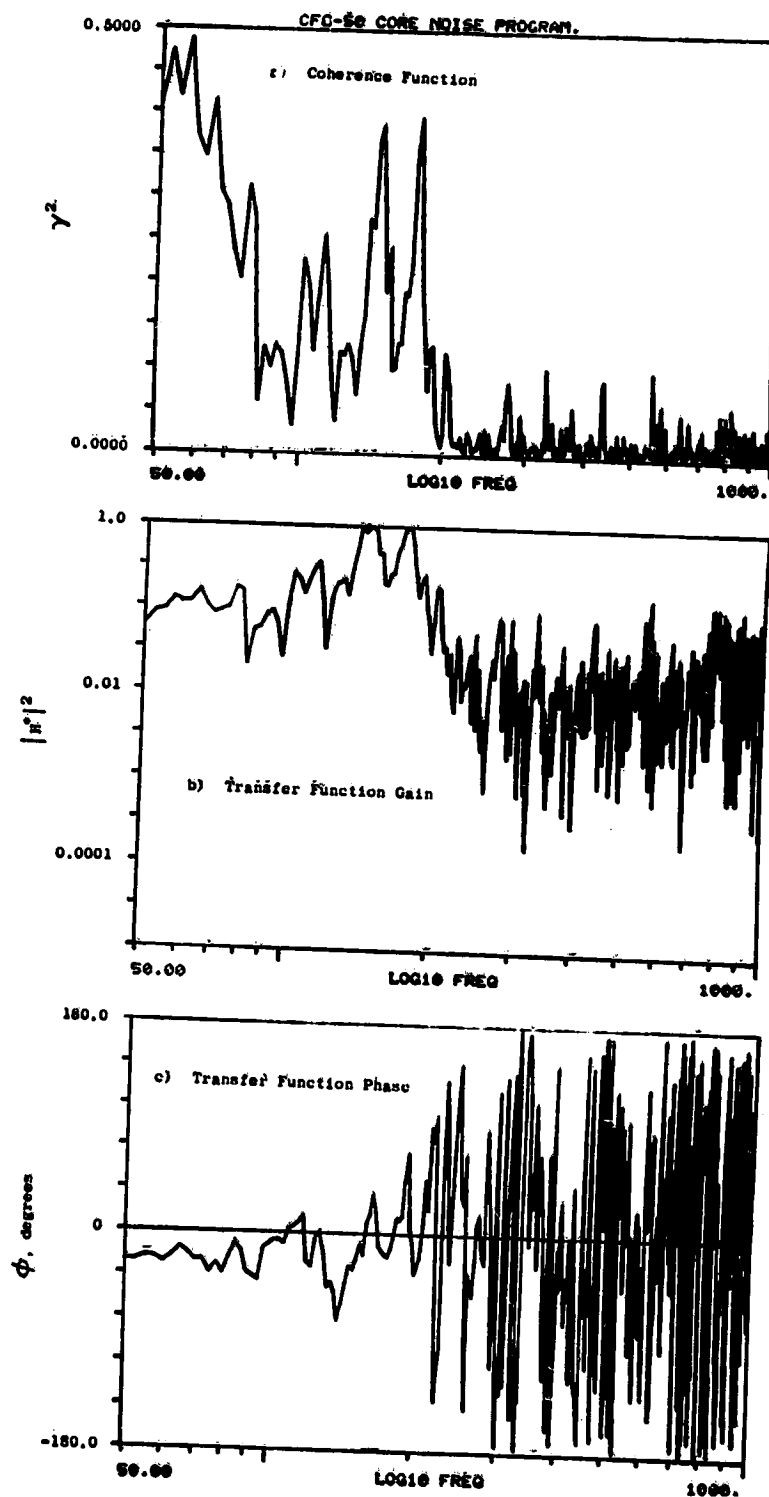


Figure A-208. Coherence and Transfer Functions for Plane 8.0A (270°) to 10° Farfield Microphone at 36.5% Thrust.

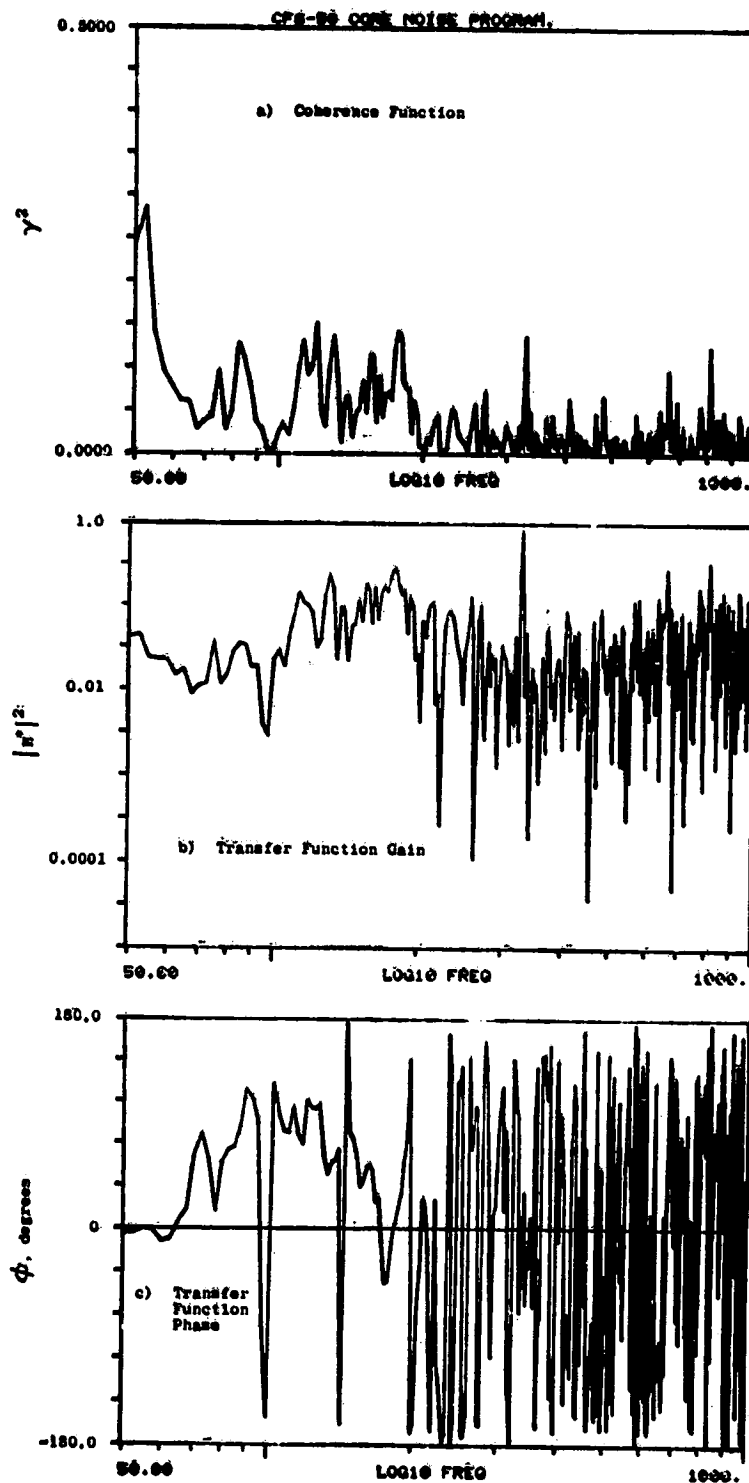


Figure A-209. Coherence and Transfer Functions
for Plane 8.0A (270°) to 30°
Farfield Microphone at 36.5% Thrust.

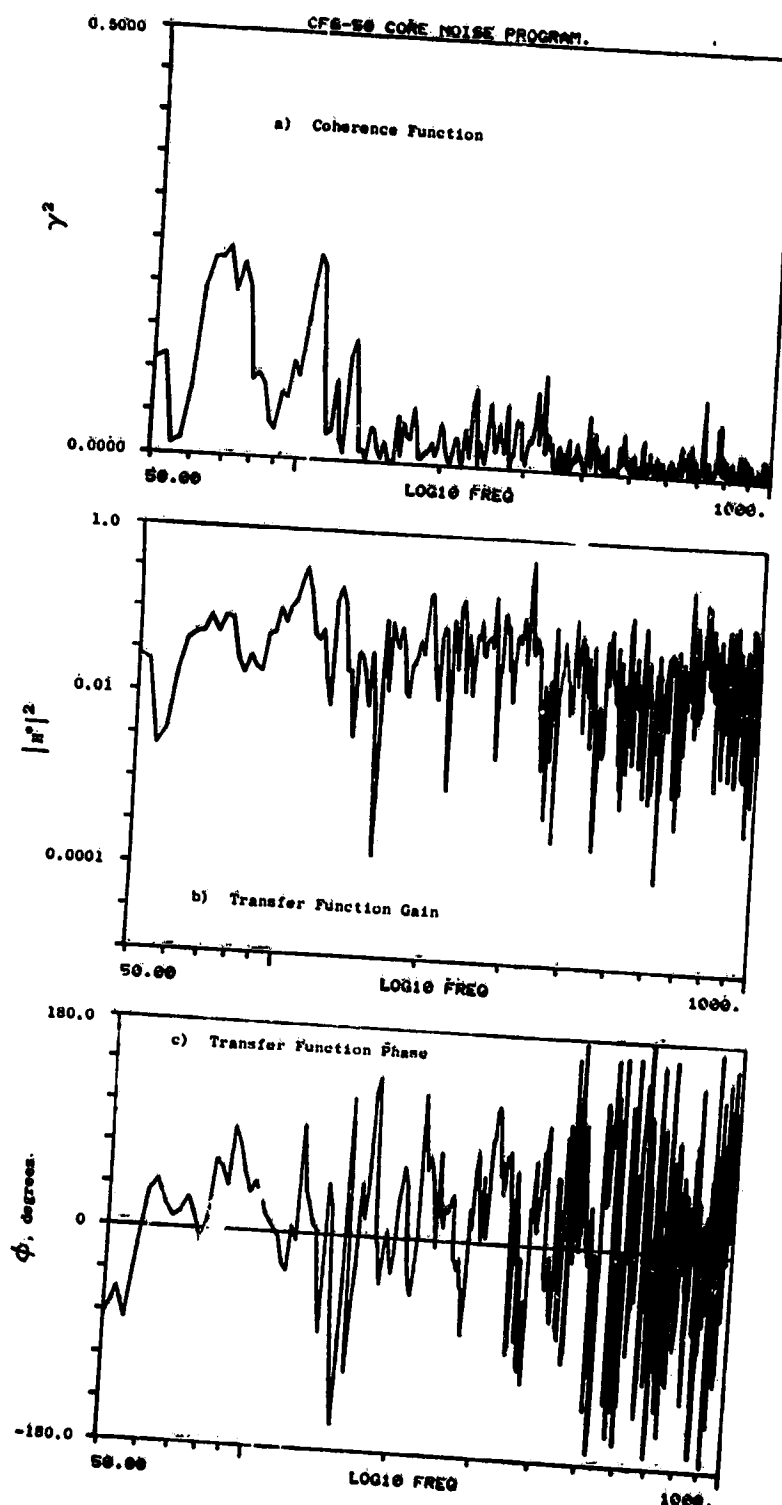


Figure A-210. Coherence and Transfer Functions for Plane 8.0A (270°) to 40° Farfield Microphone at 36.5% Thrust.

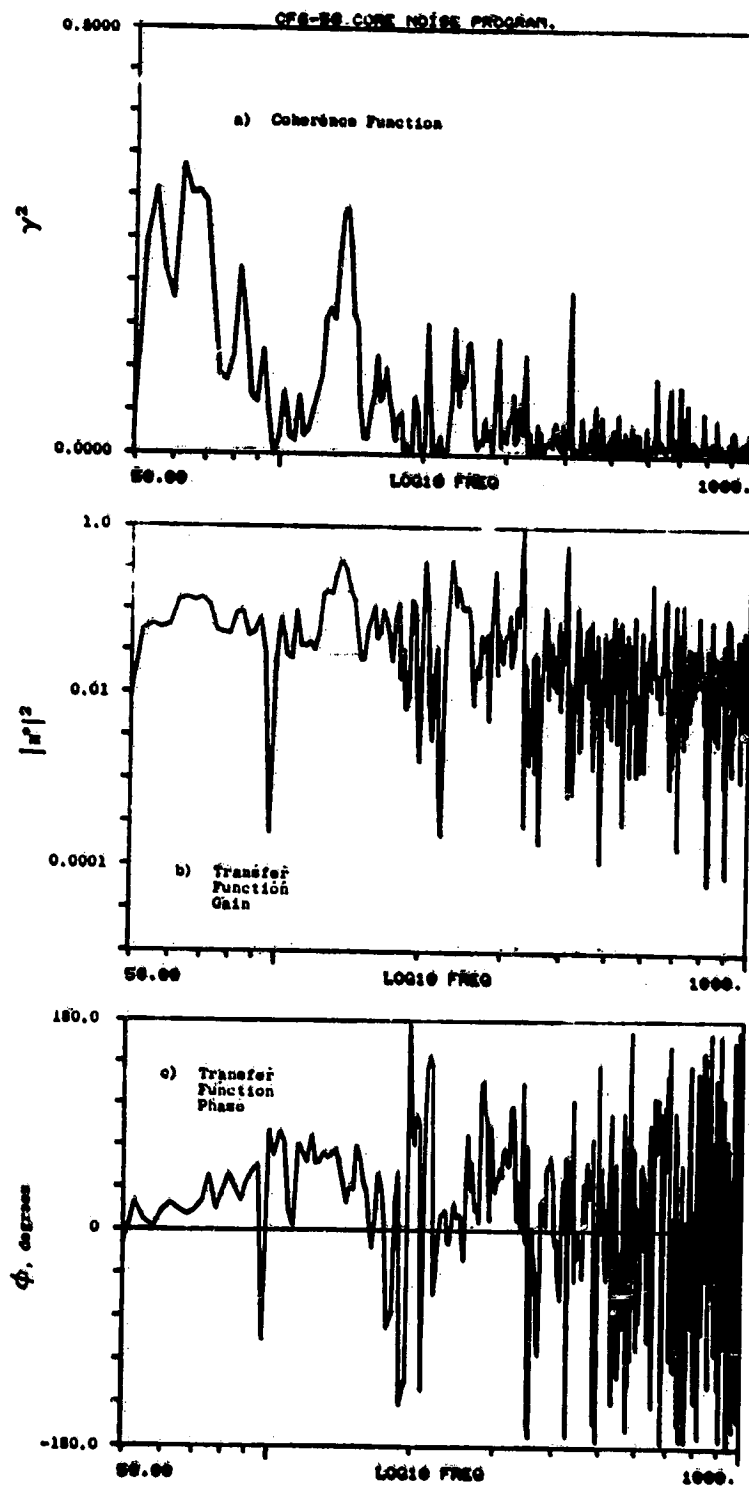


Figure A-211. Coherence and Transfer Functions for Plane 8.0A (270°) to 50° Farfield Microphone at 36.5% Thrust.

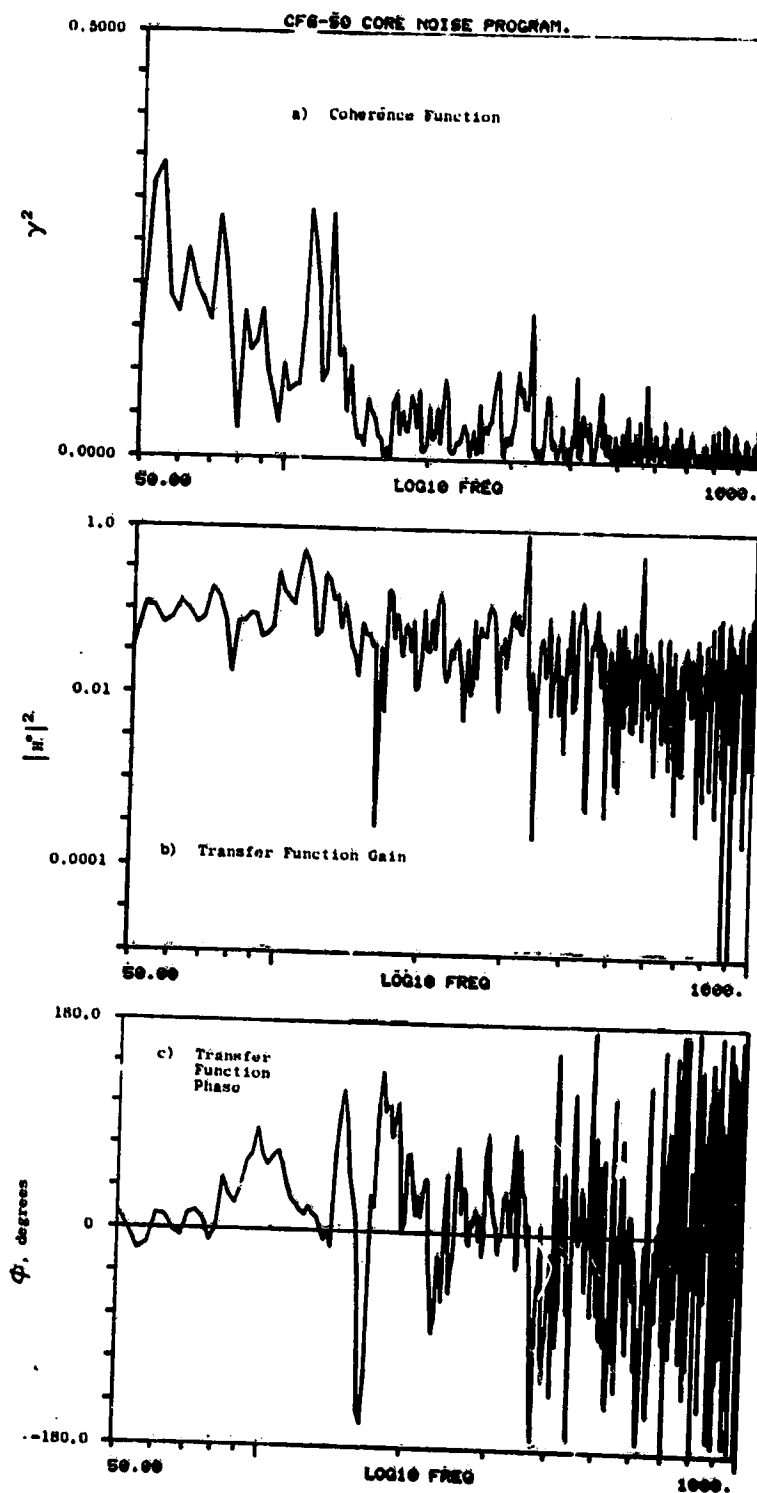


Figure A-212. Coherence and Transfer Functions
for Plane 8.0A (270°) to 60°
Farfield Microphone at 36.5% Thrust.

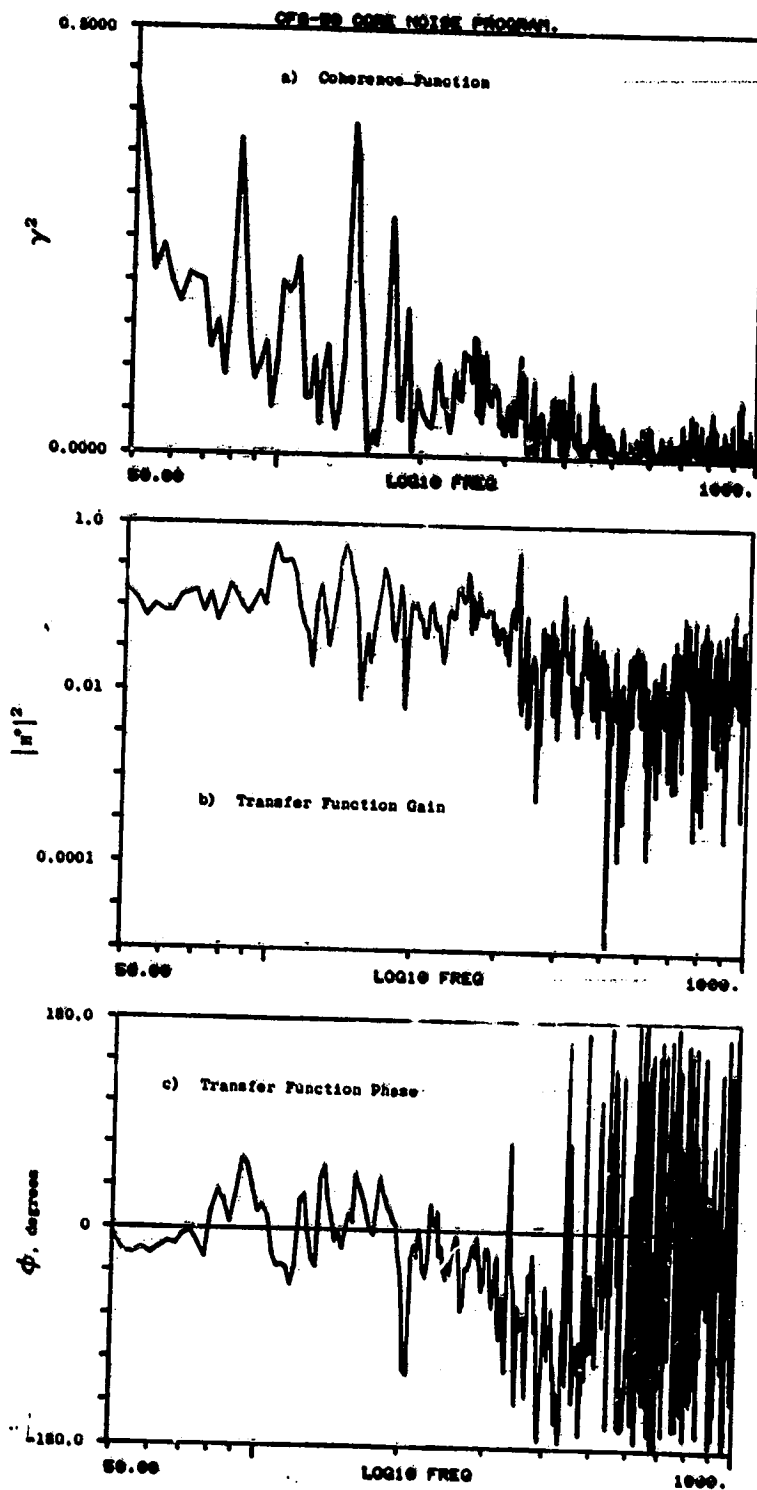


Figure A-213. Coherence and Transfer Functions
for Plane 8.0A (270°) to 70°
Farfield Microphone at 36.5% Thrust.

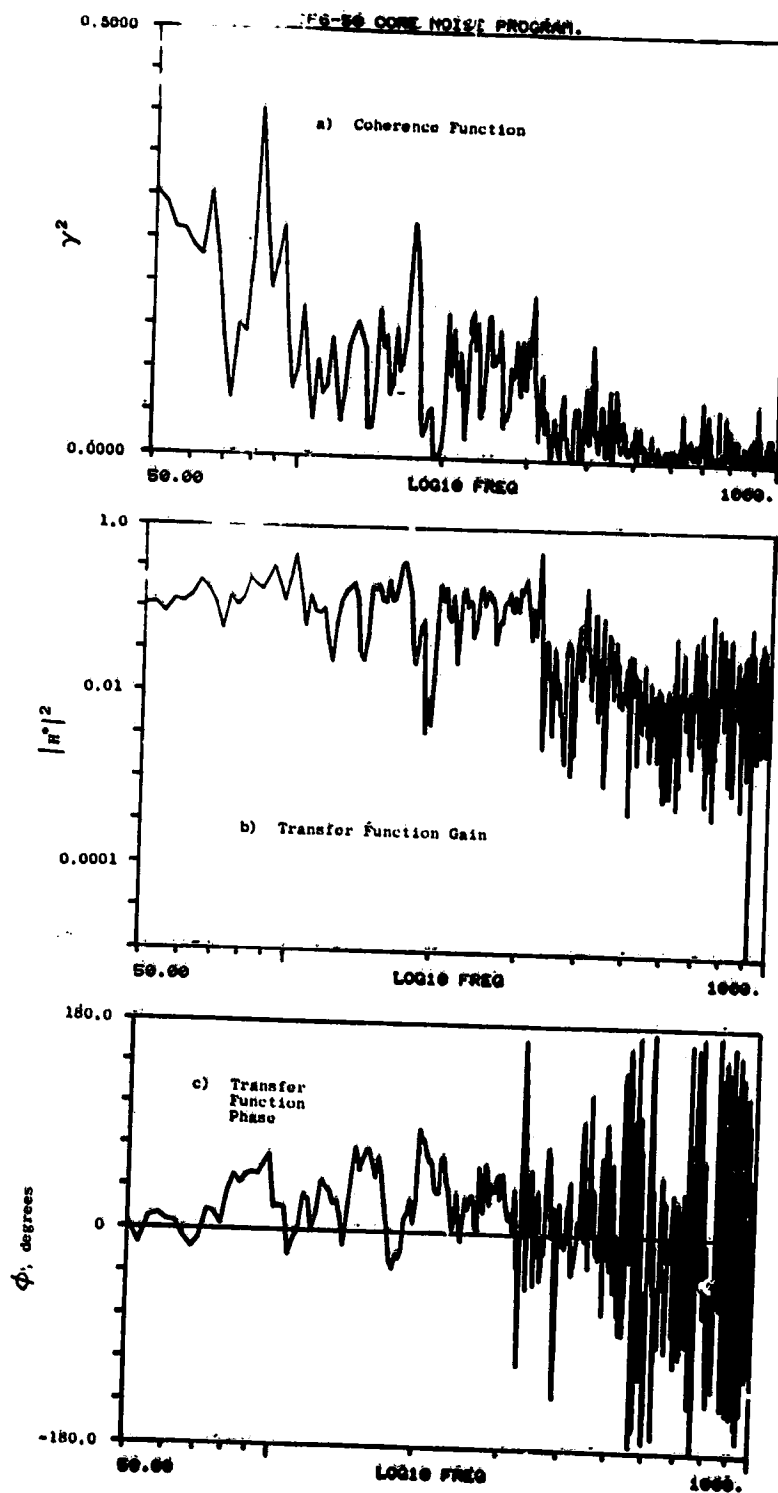


Figure A-214. Coherence and Transfer Functions for Plane 8.0A (270°) to 80° Farfield Microphone at 36.5% Thrust.

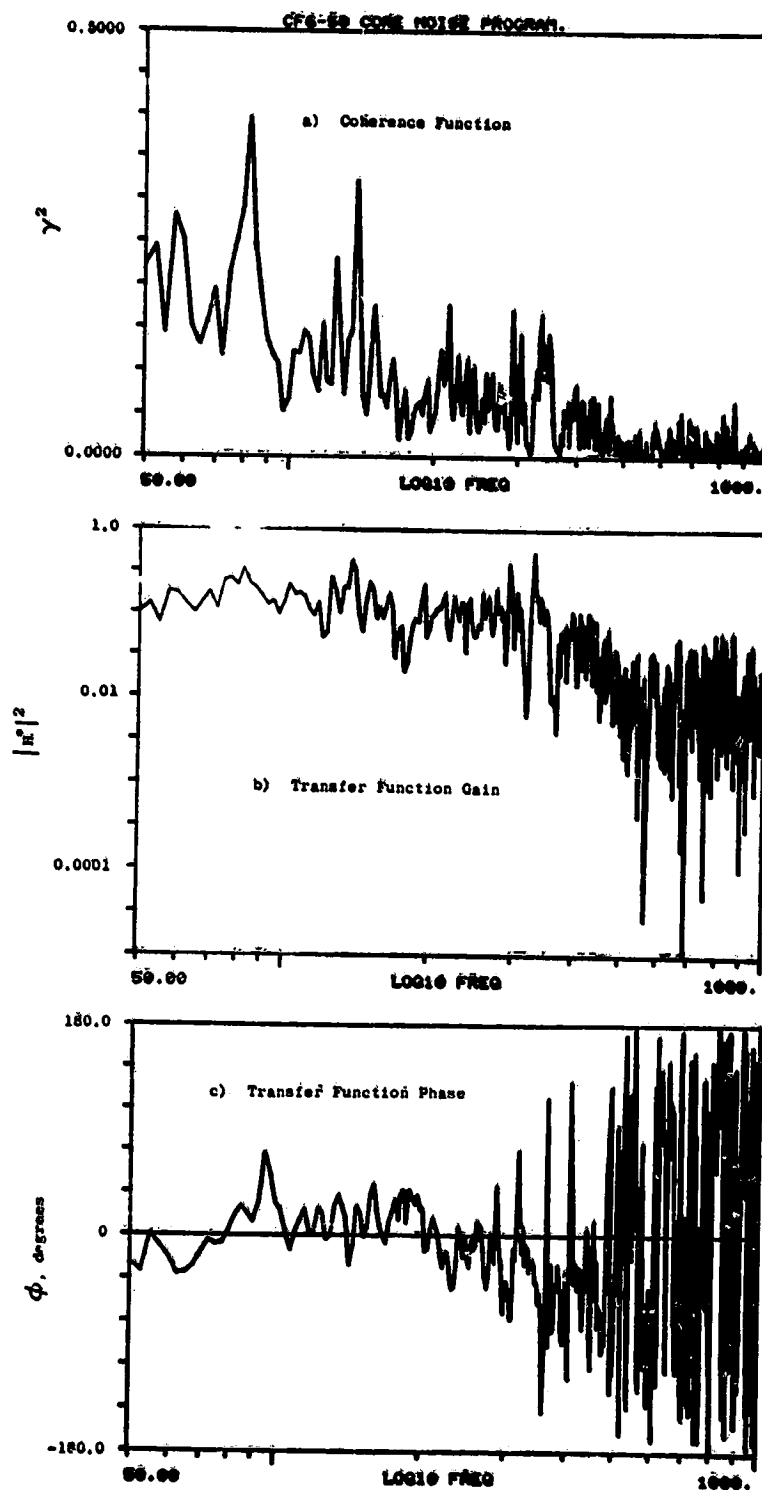


Figure A-215. Coherence and Transfer Functions
for Plane 8.0A (270°) to 90°
Farfield Microphone at 36.5% Thrust.

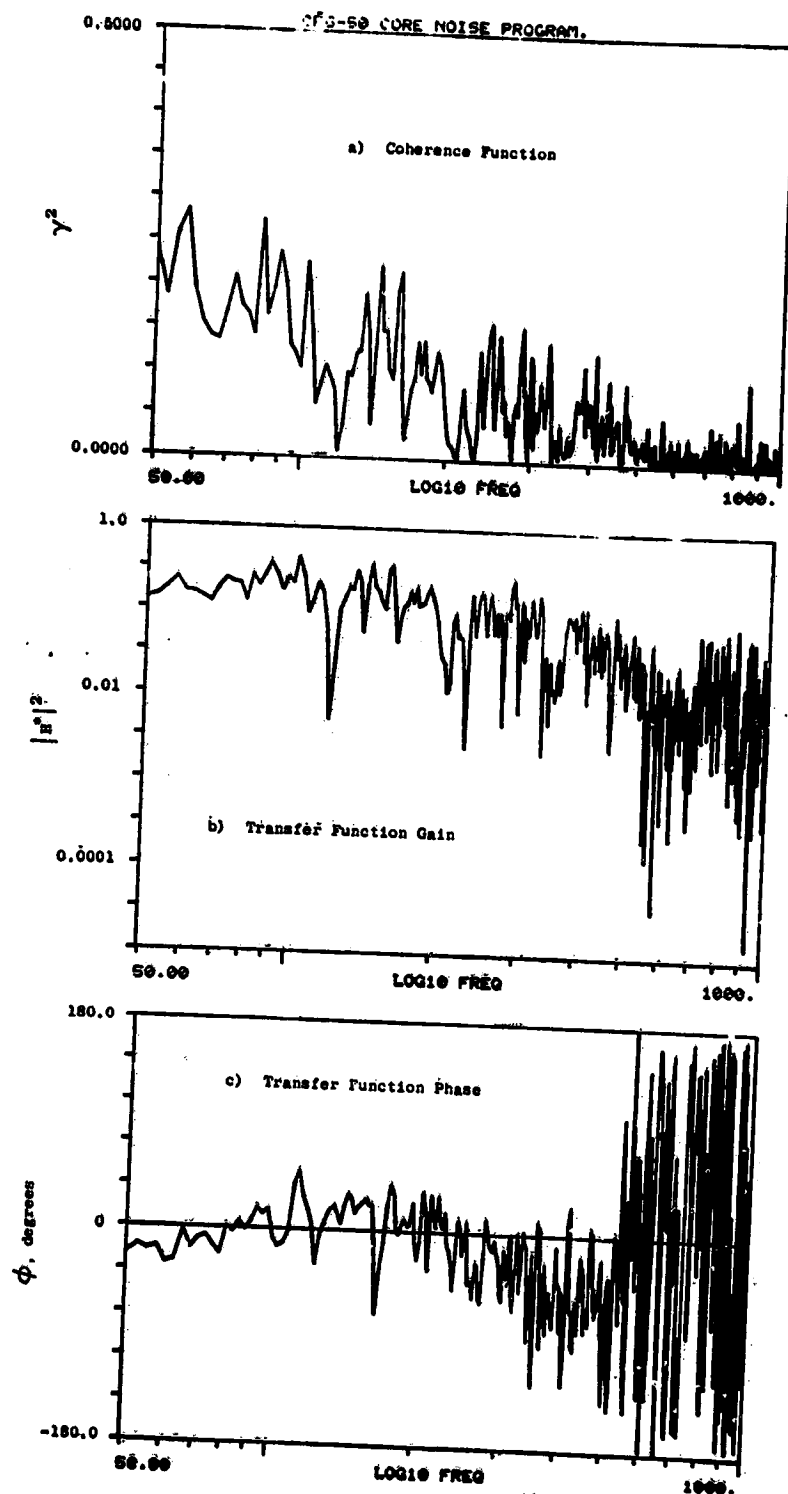


Figure A-216. Coherence and Transfer Functions
for Plane 8.0A (270°) to 100°
Farfield Microphone at 36.5% Thrust.

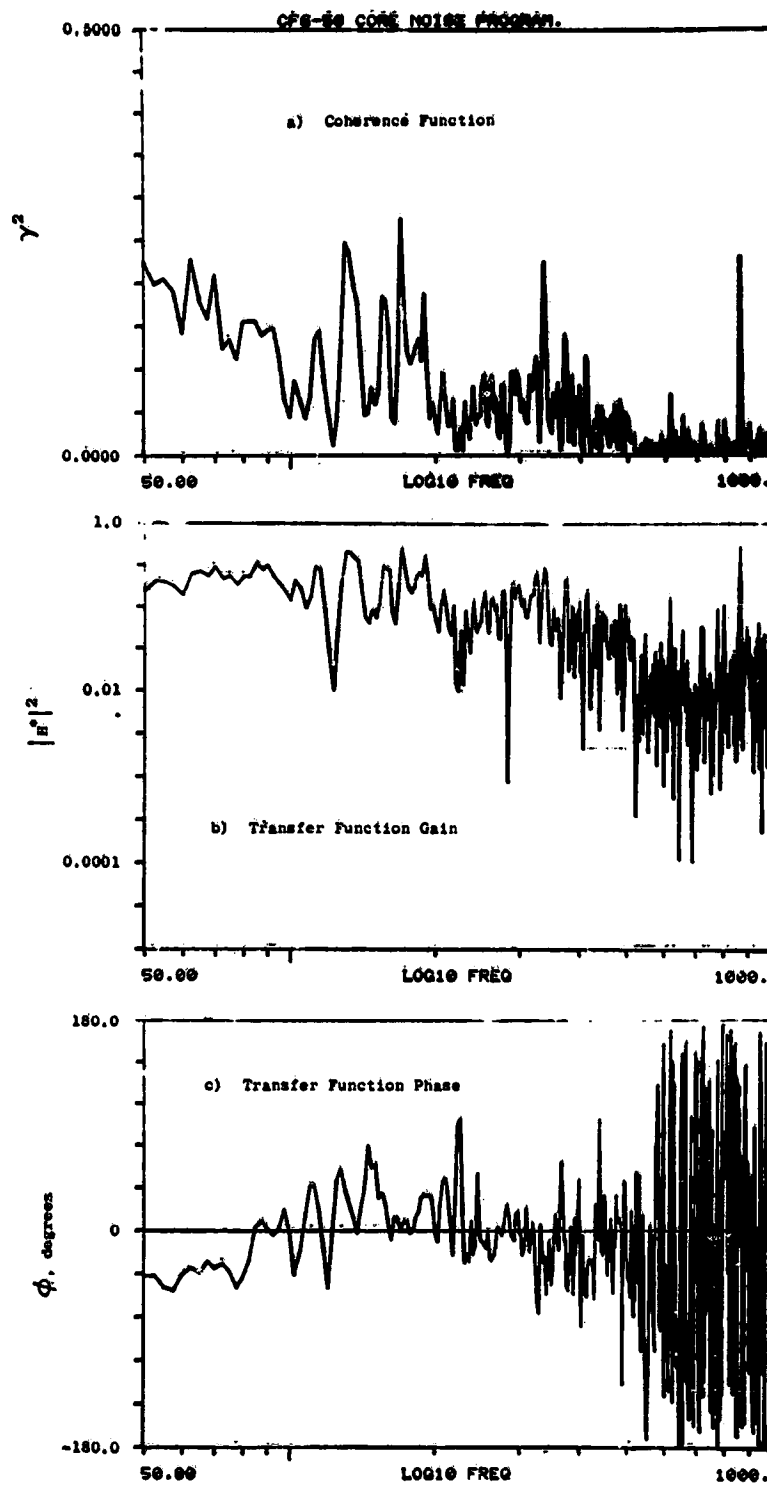


Figure A-217. Coherence and Transfer Functions for Plane 8.0A (270°) to 110° Farfield Microphone at 36.5% Thrust.

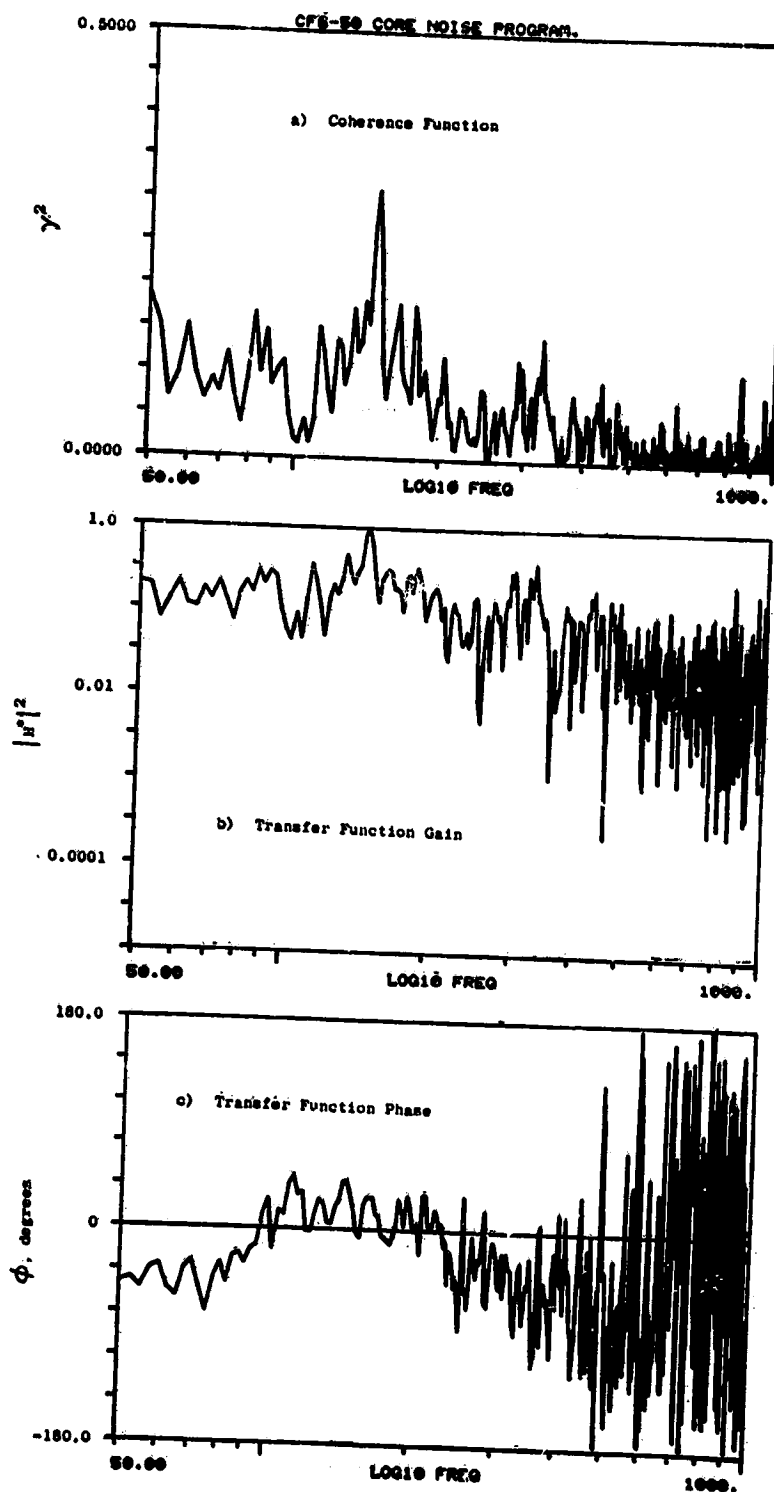


Figure A-218. Coherence and Transfer Functions
for Plane 8.0A (270°) to 120°
Farfield Microphone at 36.5% Thrust.

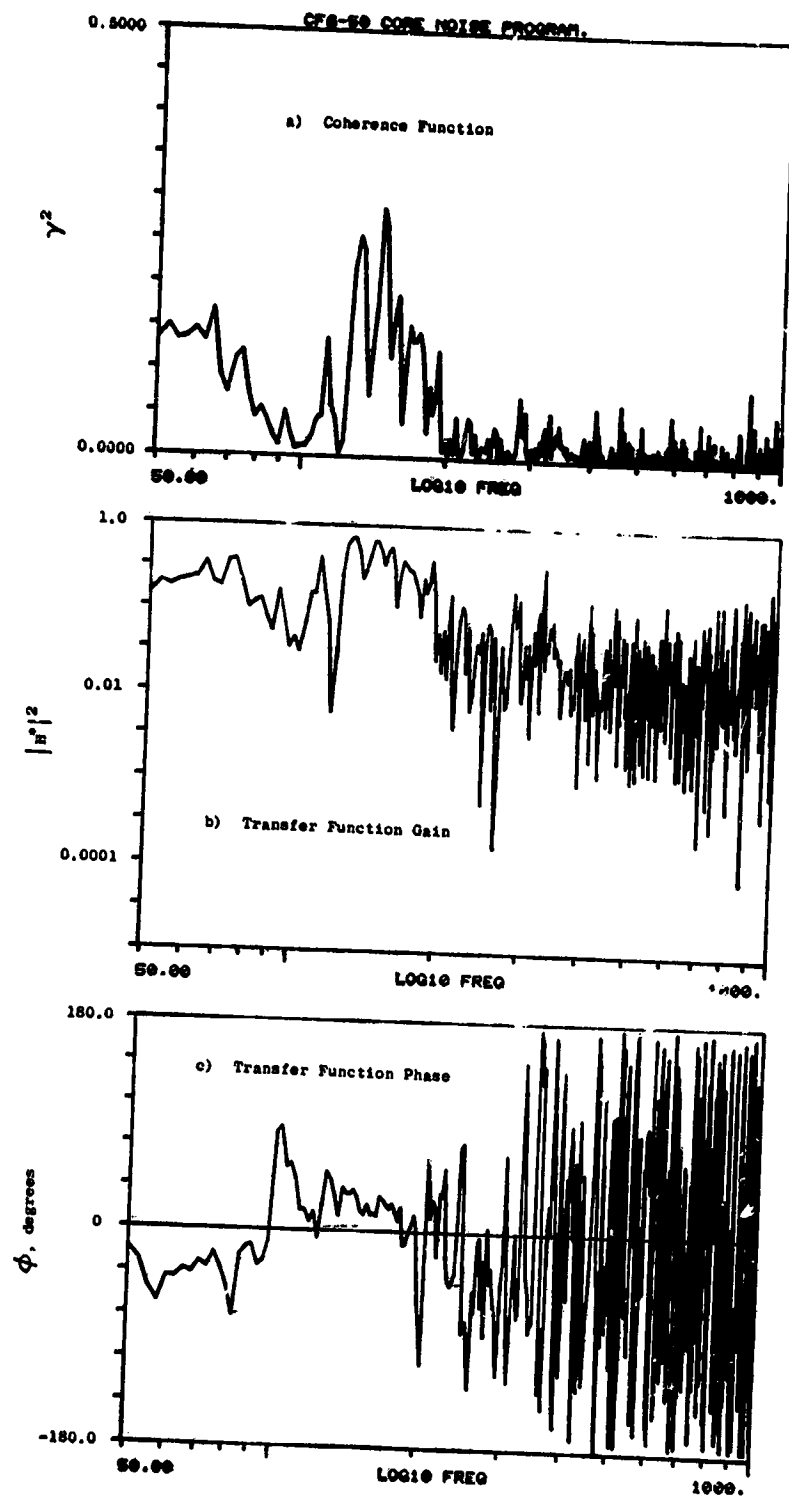


Figure A-219. Coherence and Transfer Functions for Plane 8.0A (270°) to 130° Farfield Microphone at 36.5% Thrust.

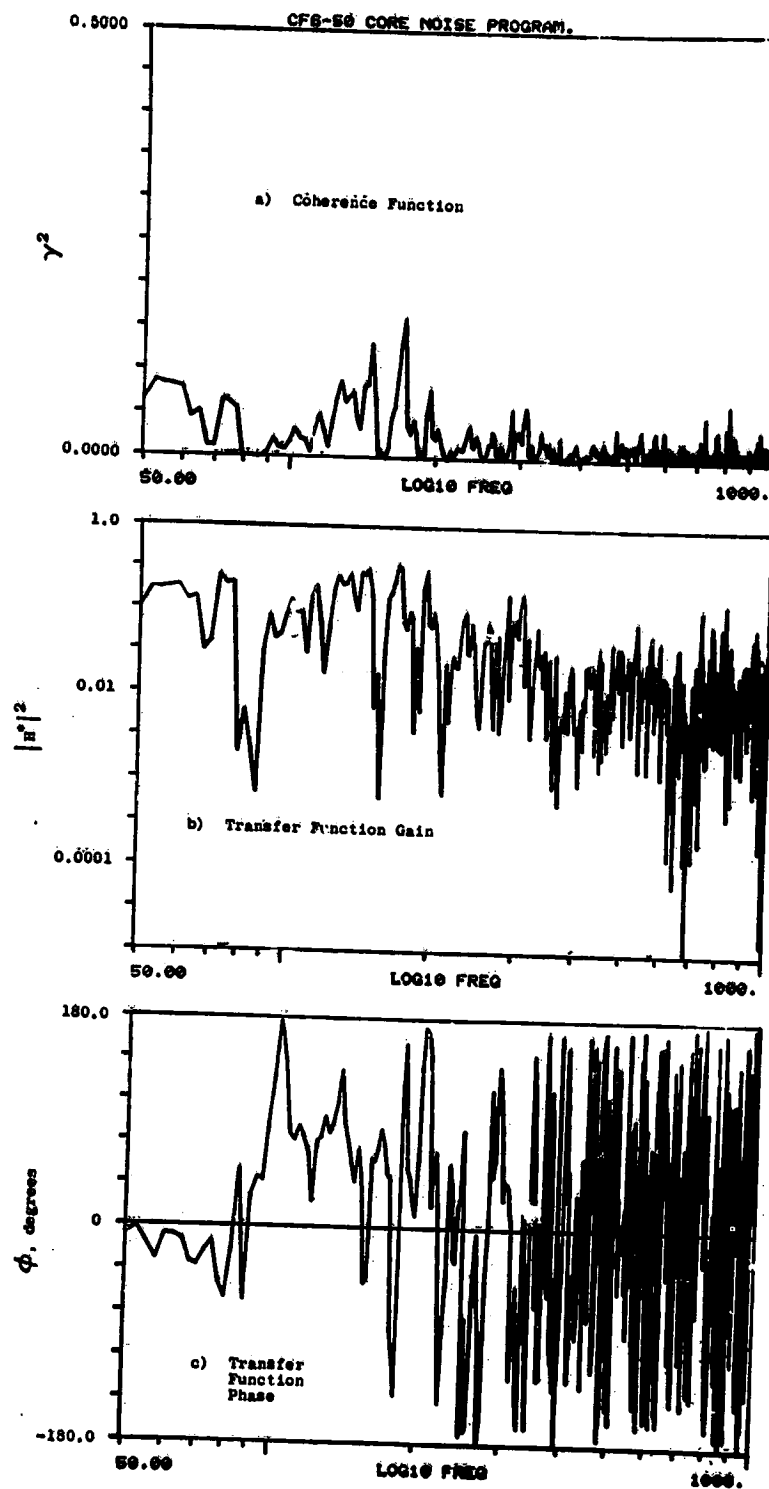


Figure A-220. Coherence and Transfer Functions
for Plane 8.0A (270°) to 140°
Farfield Microphone at 36.5% Thrust.

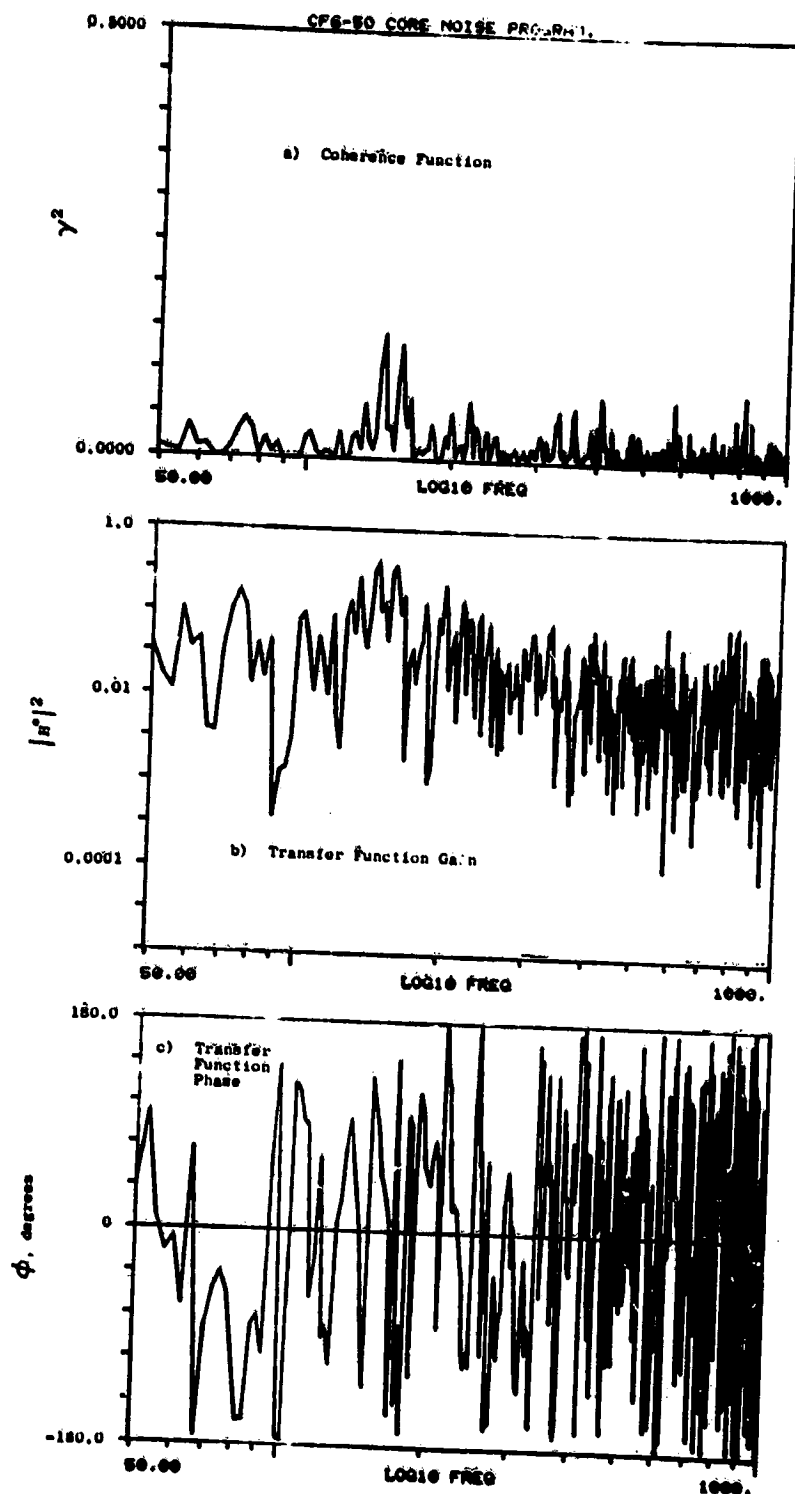


Figure A-221. Coherence and Transfer Functions for Plane 8.0A (270°) to 150° Farfield Microphone at 36.5% Thrust.

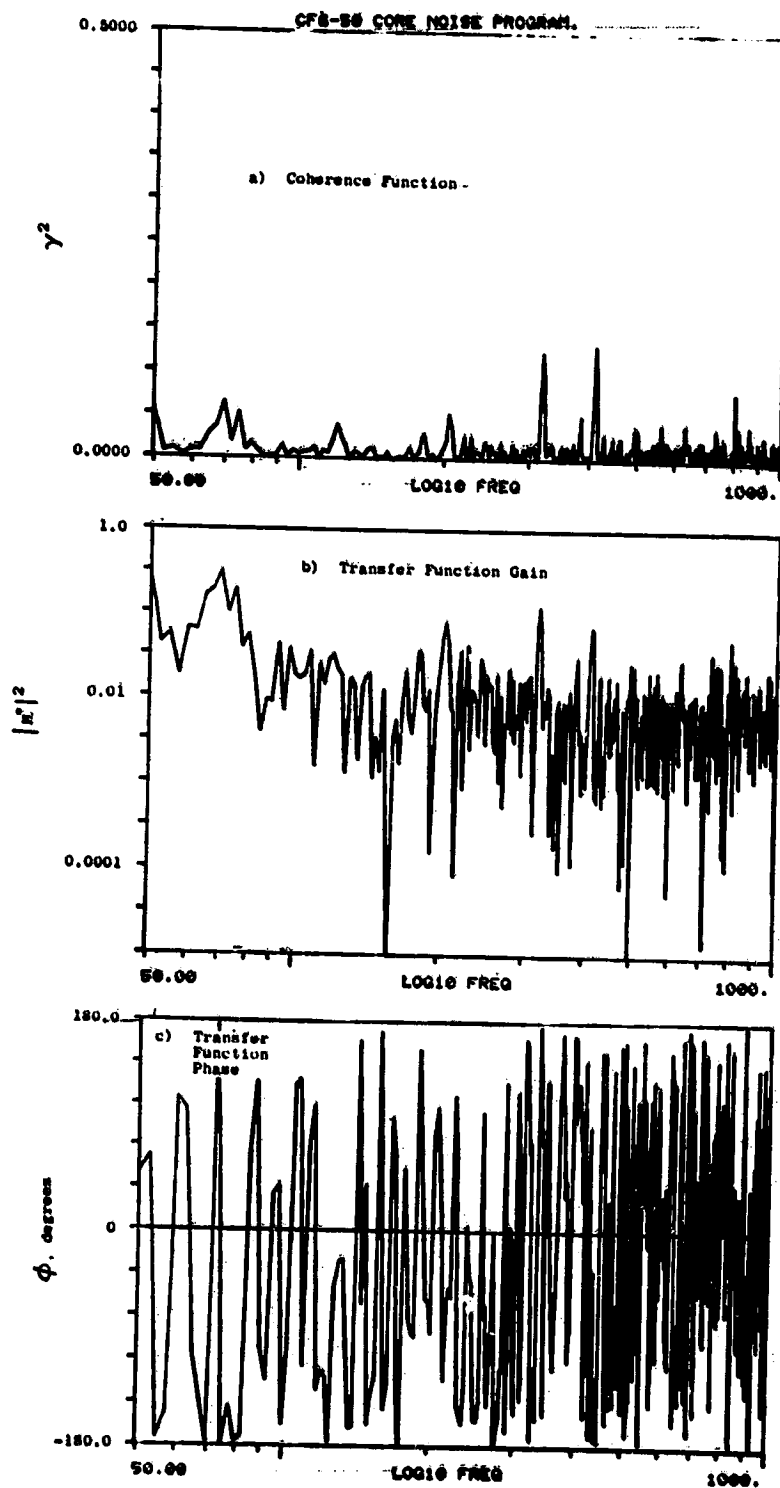


Figure A-222. Coherence and Transfer Functions for Plane 8.0A (270°) to 160° Farfield Microphone at 36.5% Thrust.

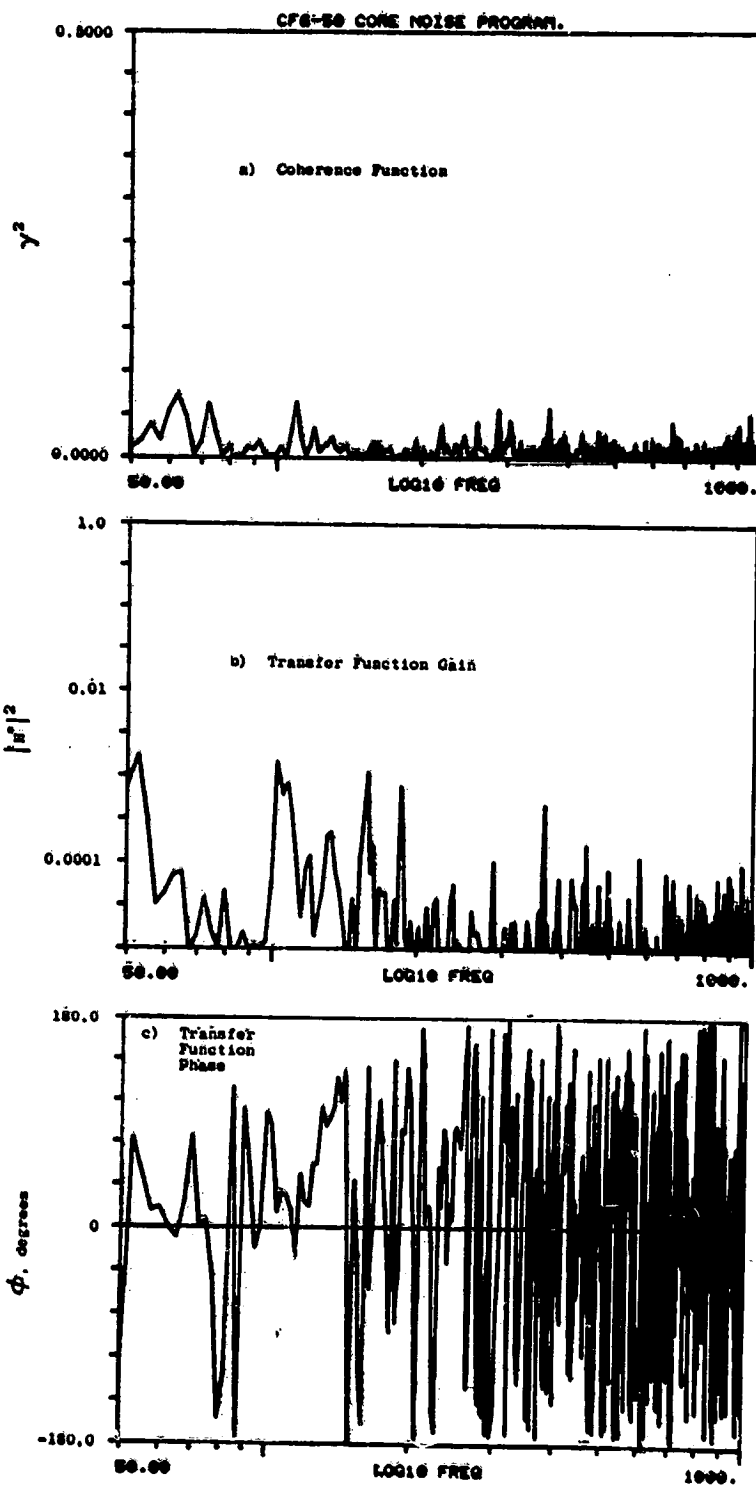


Figure A-223. Coherence and Transfer Functions for Plane 3.5 (102°) to 10° Farfield Microphone at 45.5% Thrust

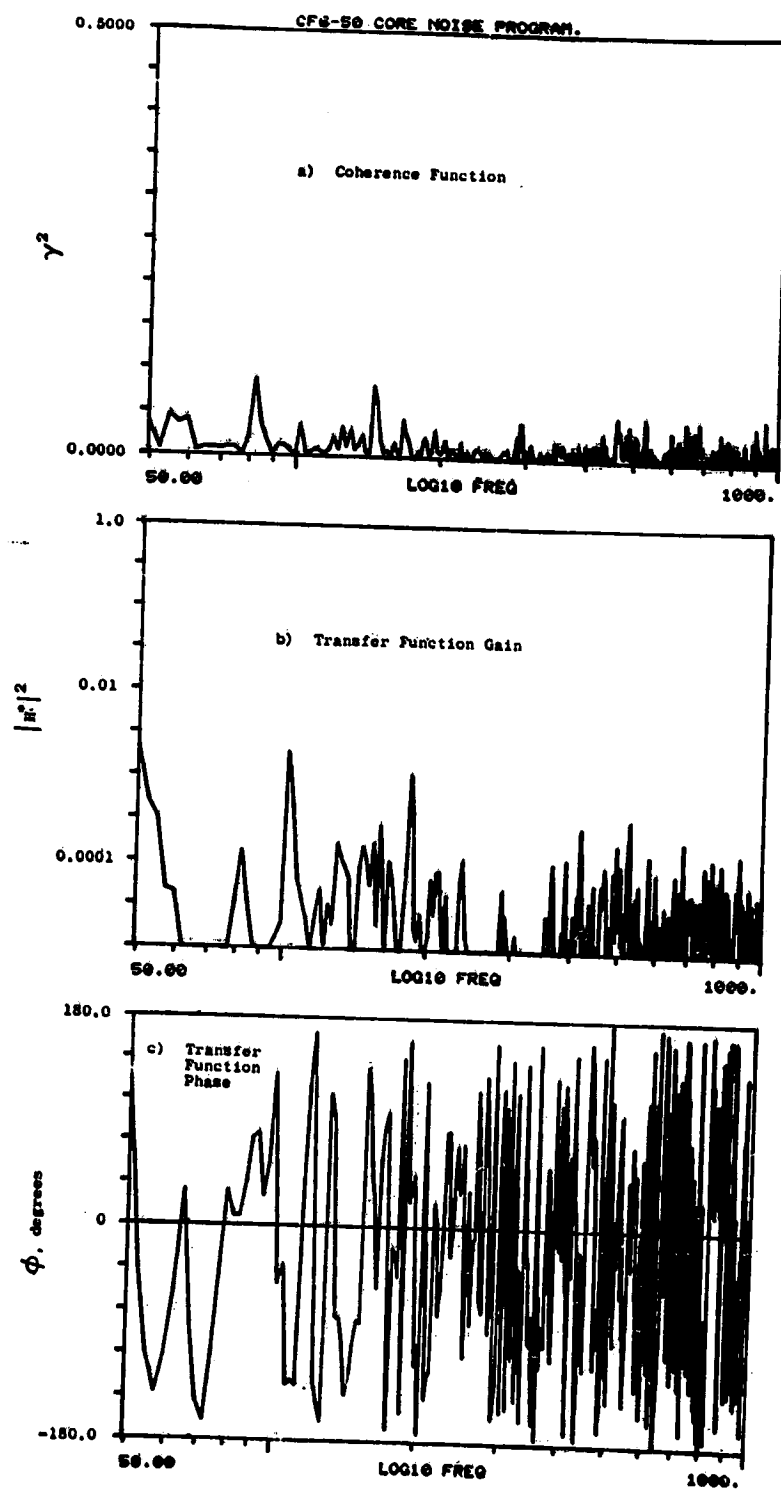


Figure A-224. Coherence and Transfer Functions for Plane 3.5 (102°) to 30° Farfield. Microphone at 45.5% Thrust.

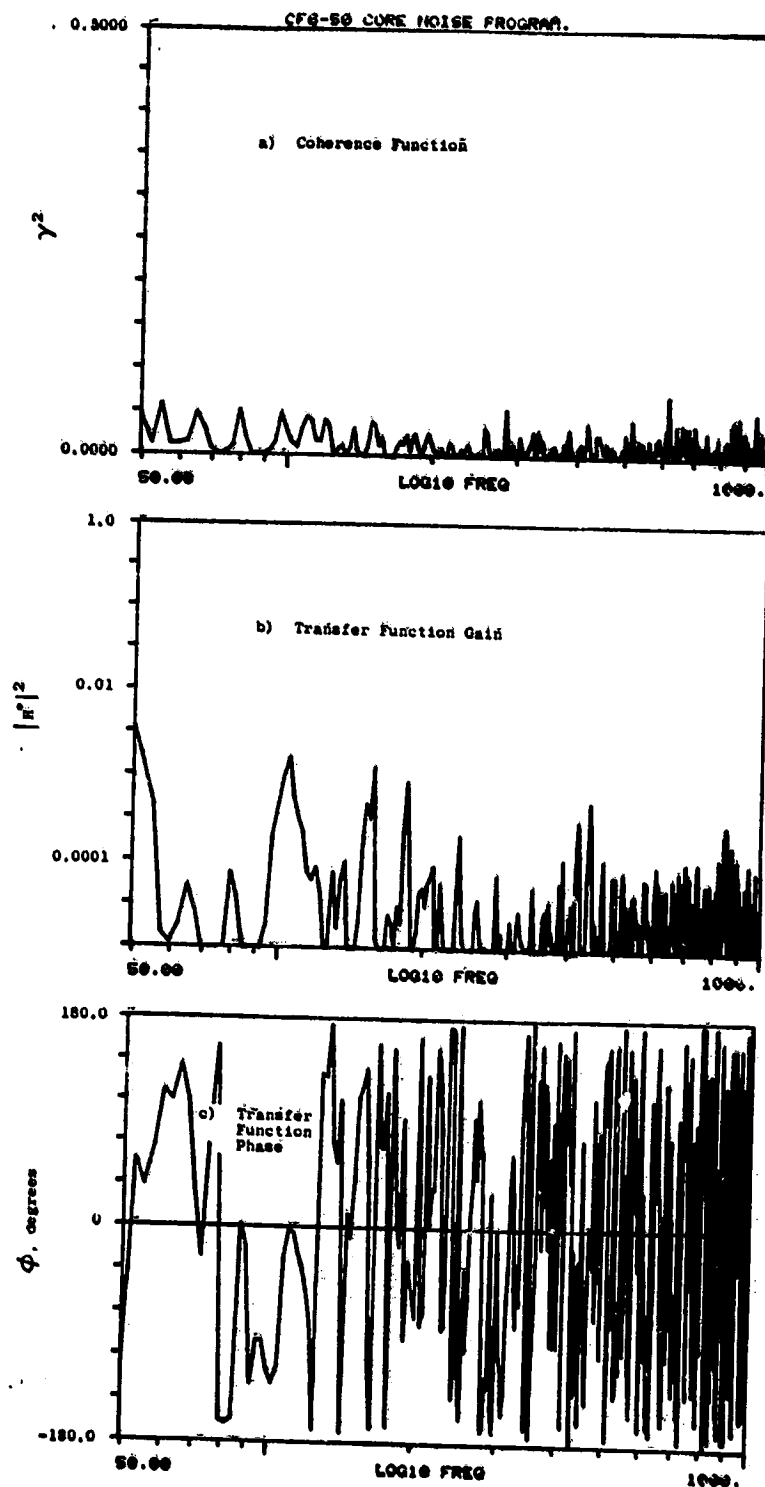


Figure A-225. Coherence and Transfer Functions for Plane 3.5 (102°) to 40° Farfield Microphone at 45.5% Thrust.

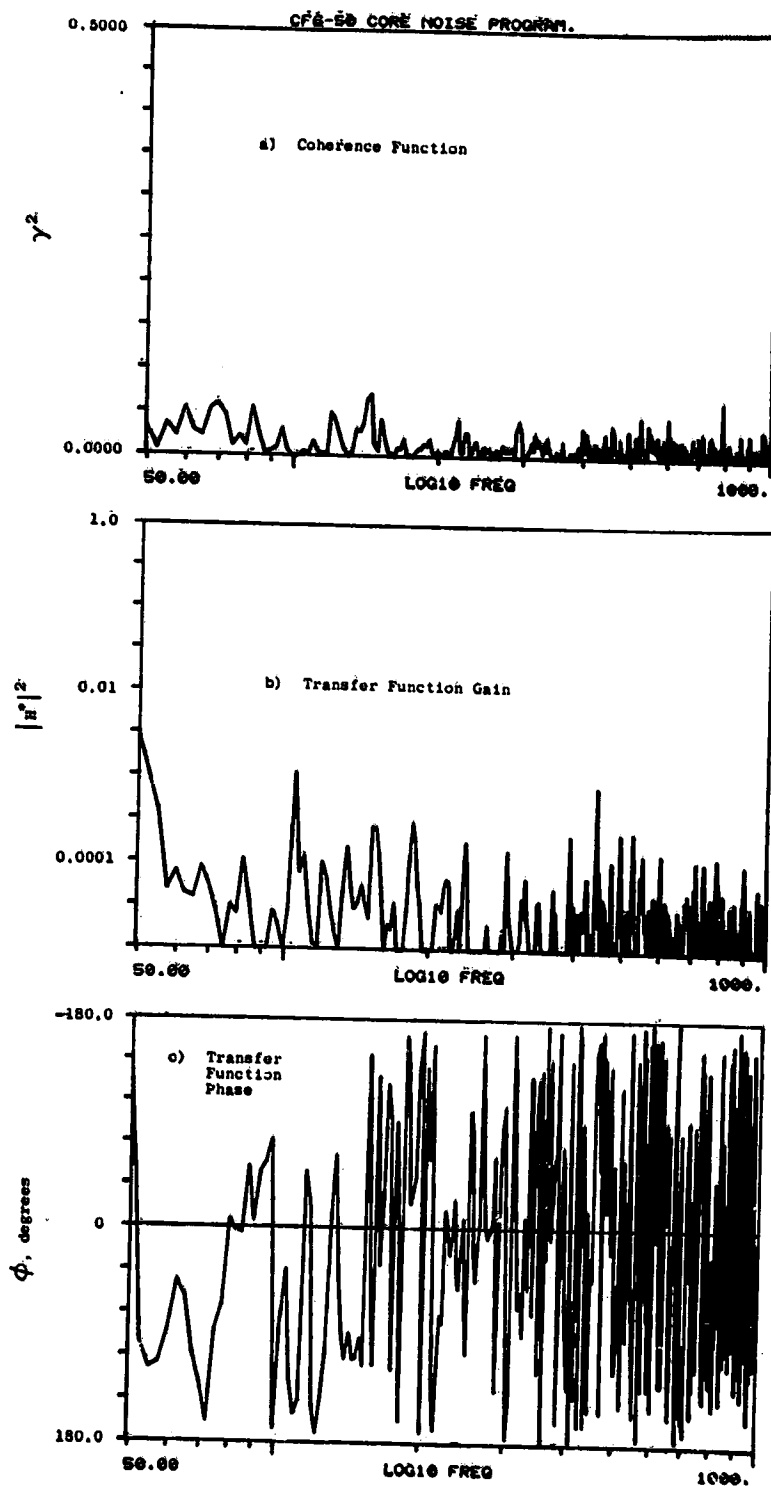


Figure A-226. Coherence and Transfer Functions for Plane 3.5 (102°) to 50° Farfield Microphone at 45.5% Thrust.

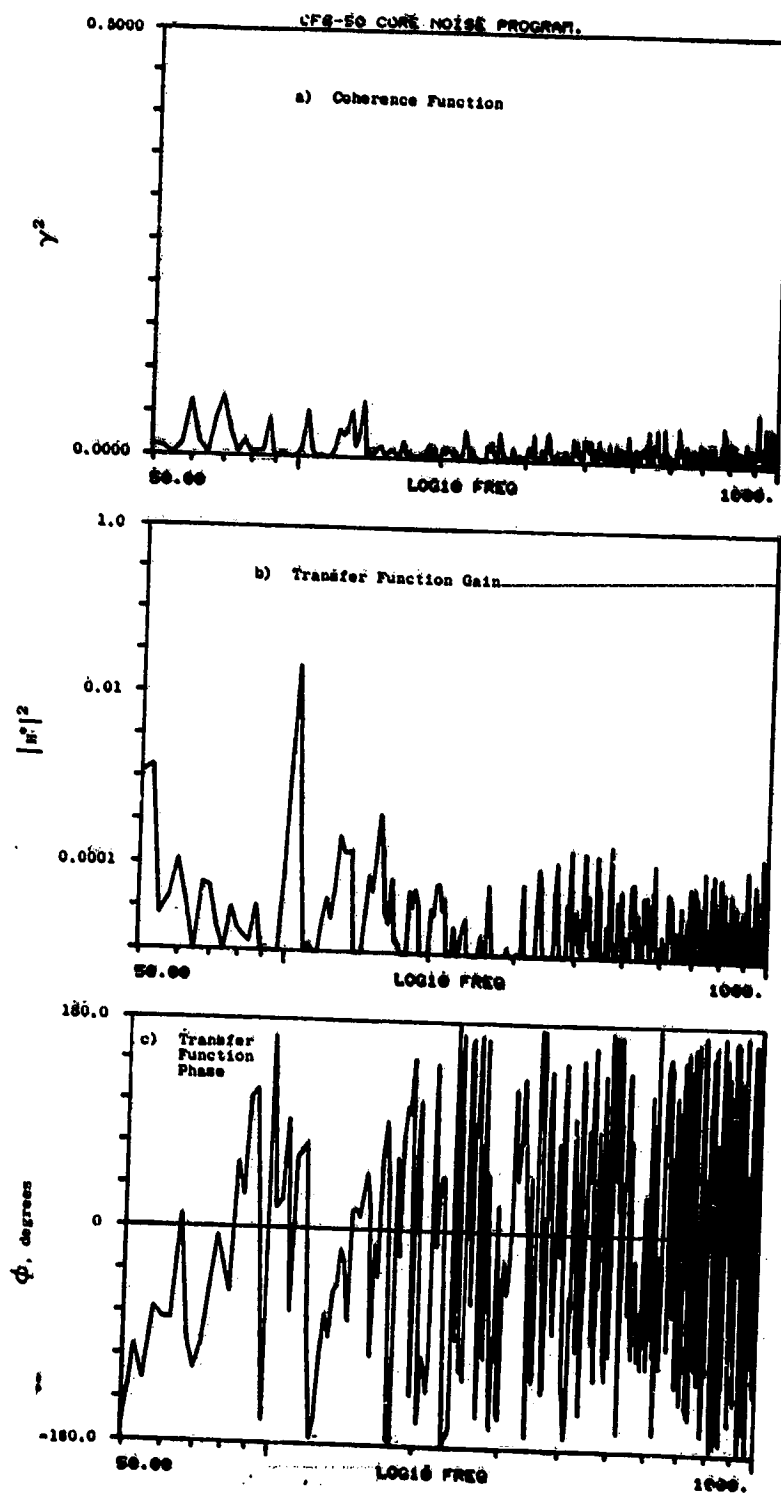


Figure A-227. Coherence and Transfer Functions for Plane 3.5 (102°) to 60° Farfield Microphone at 45.5% Thrust.

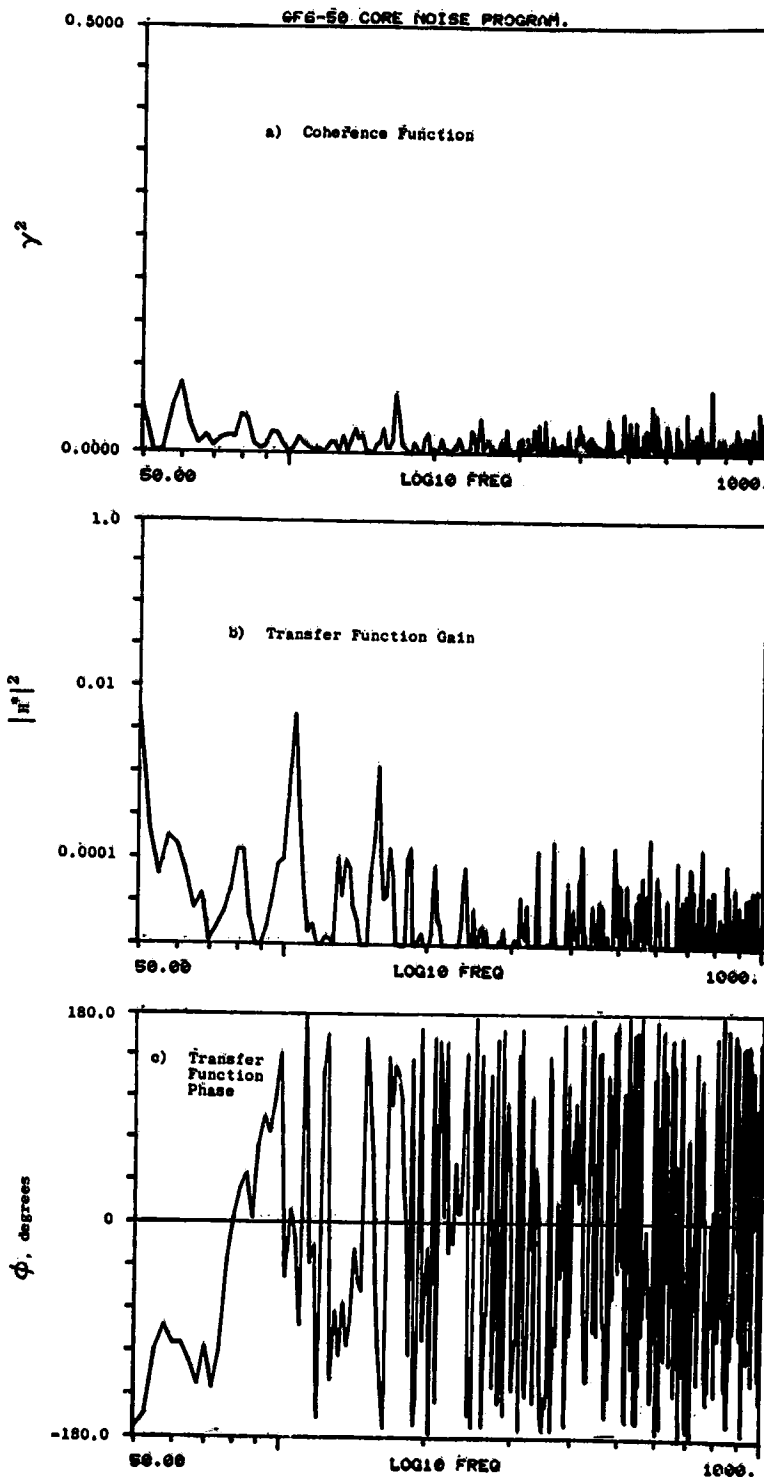


Figure A-228. Coherence and Transfer Functions for Plane 3.5 (102°) to 70° Farfield Microphone at 45.5% Thrust.

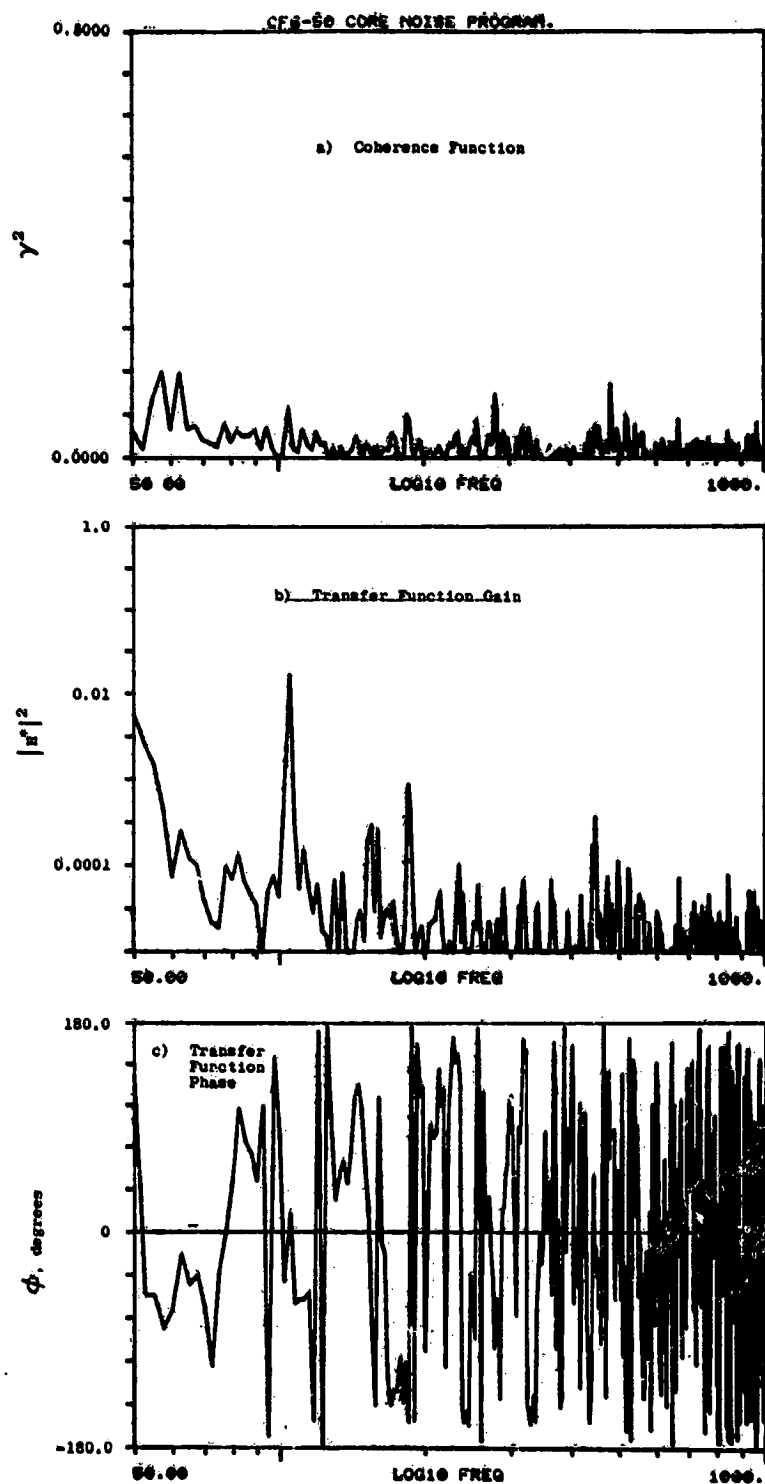


Figure A-229. Coherence and Transfer Functions for Plane 3.5 (102°) to 80° Farfield Microphone at 45.5% Thrust.

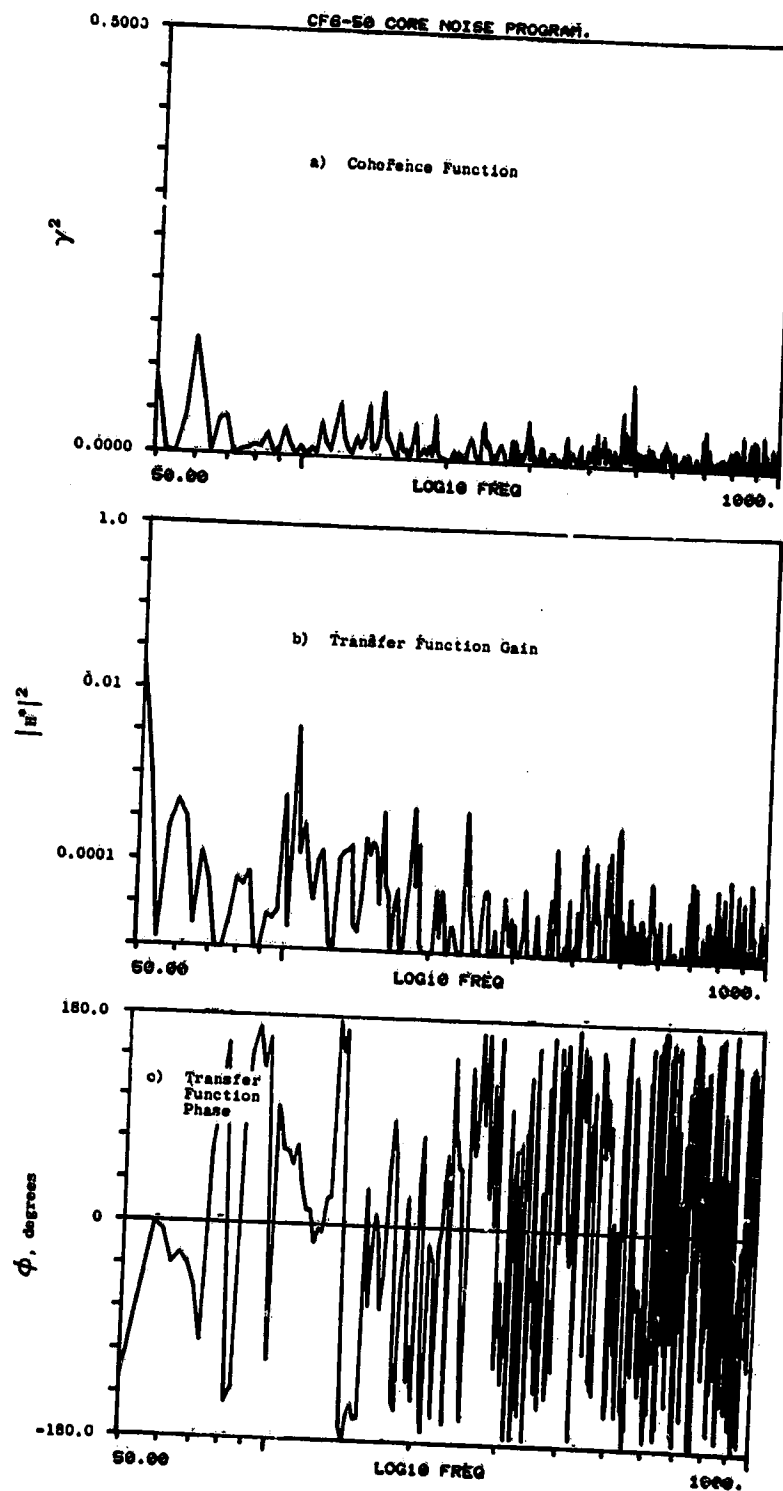


Figure A-230. Coherence and Transfer Functions for Plane 3.5 (102°) to 90° Farfield Microphone at 45.5% Thrust.

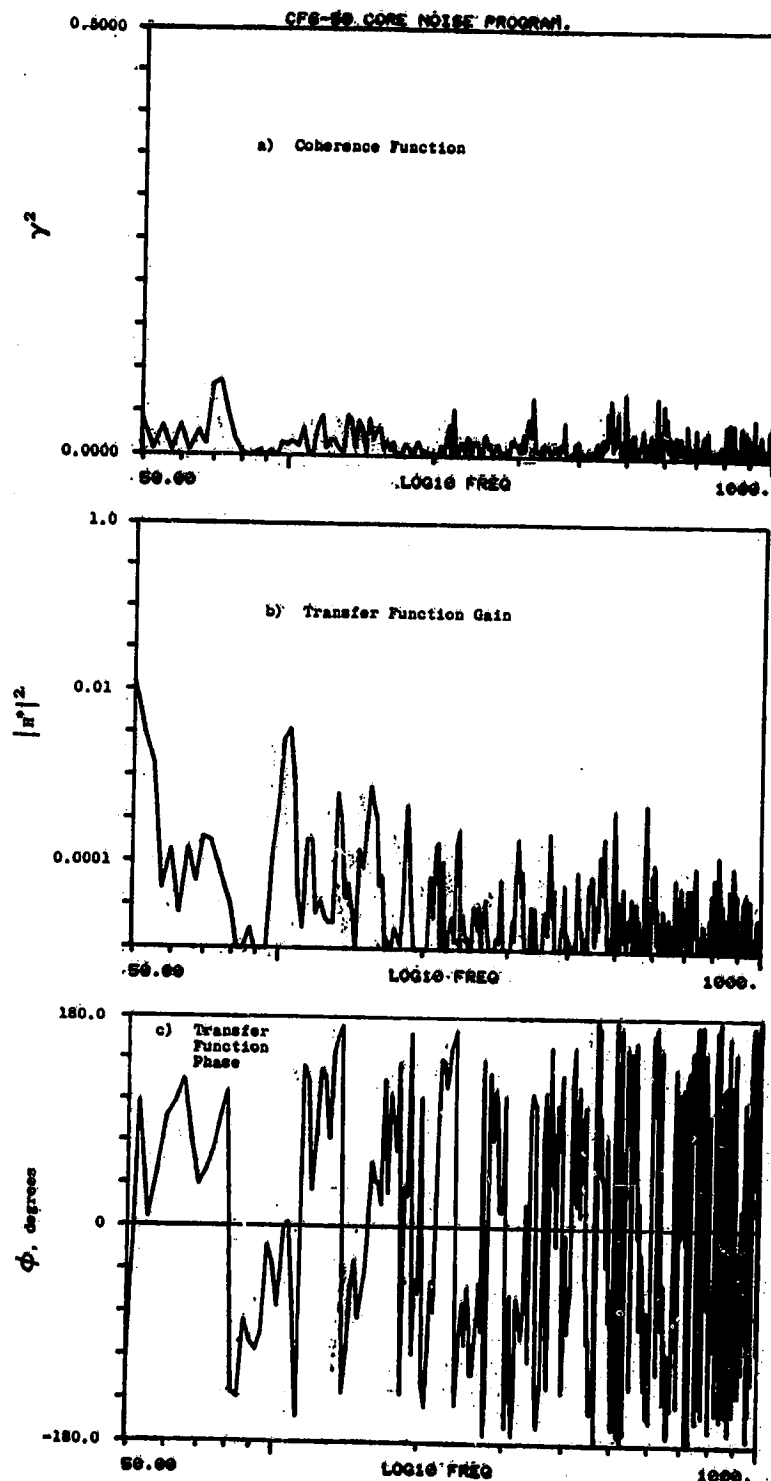


Figure A-231. Coherence and Transfer Functions for Plane 3.5 (102°) to 100° Farfield Microphone at 45.5% Thrust.

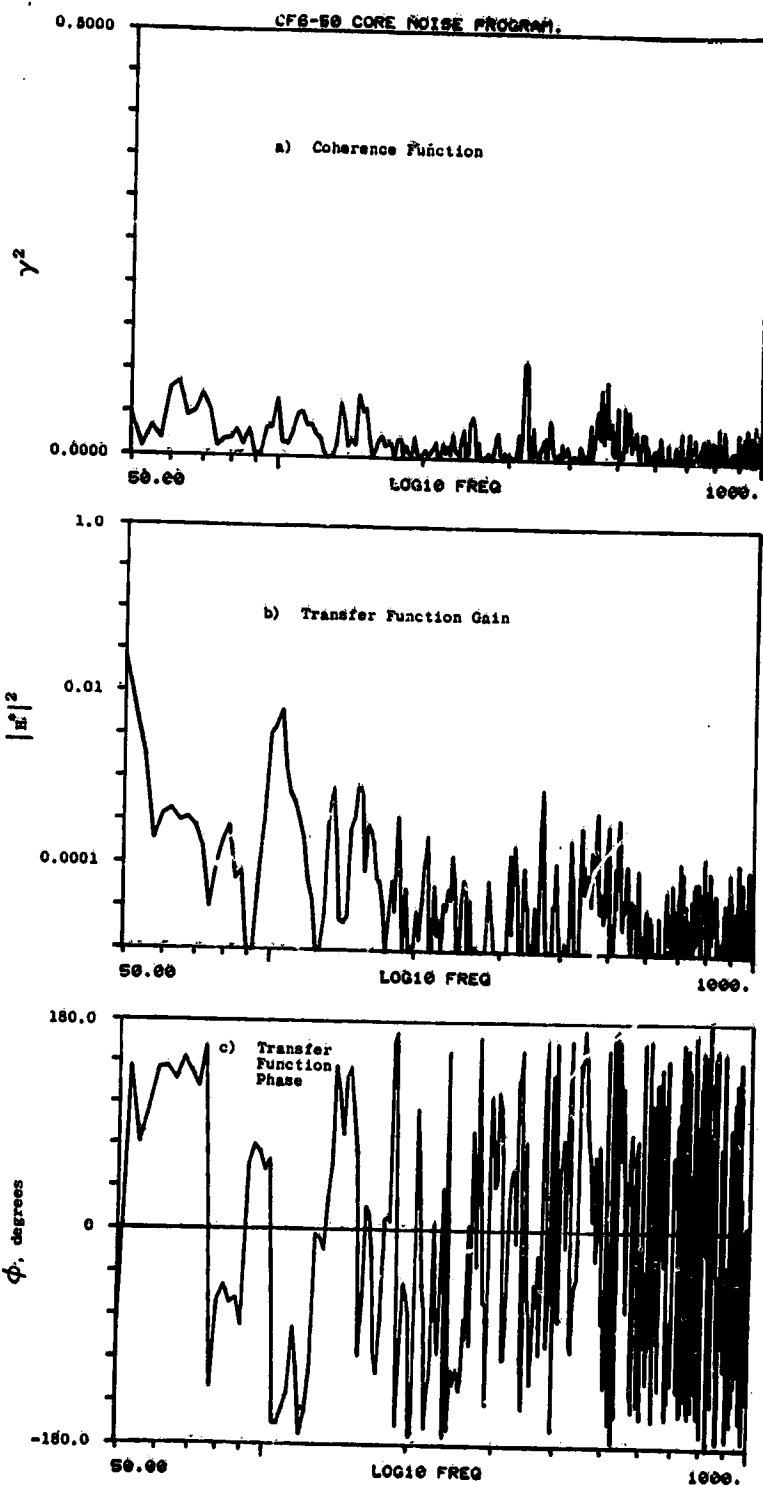


Figure A-232. Coherence and Transfer Functions for Plane 3.5 (102°) to 110° Farfield Microphone at 45.5% Thrust.

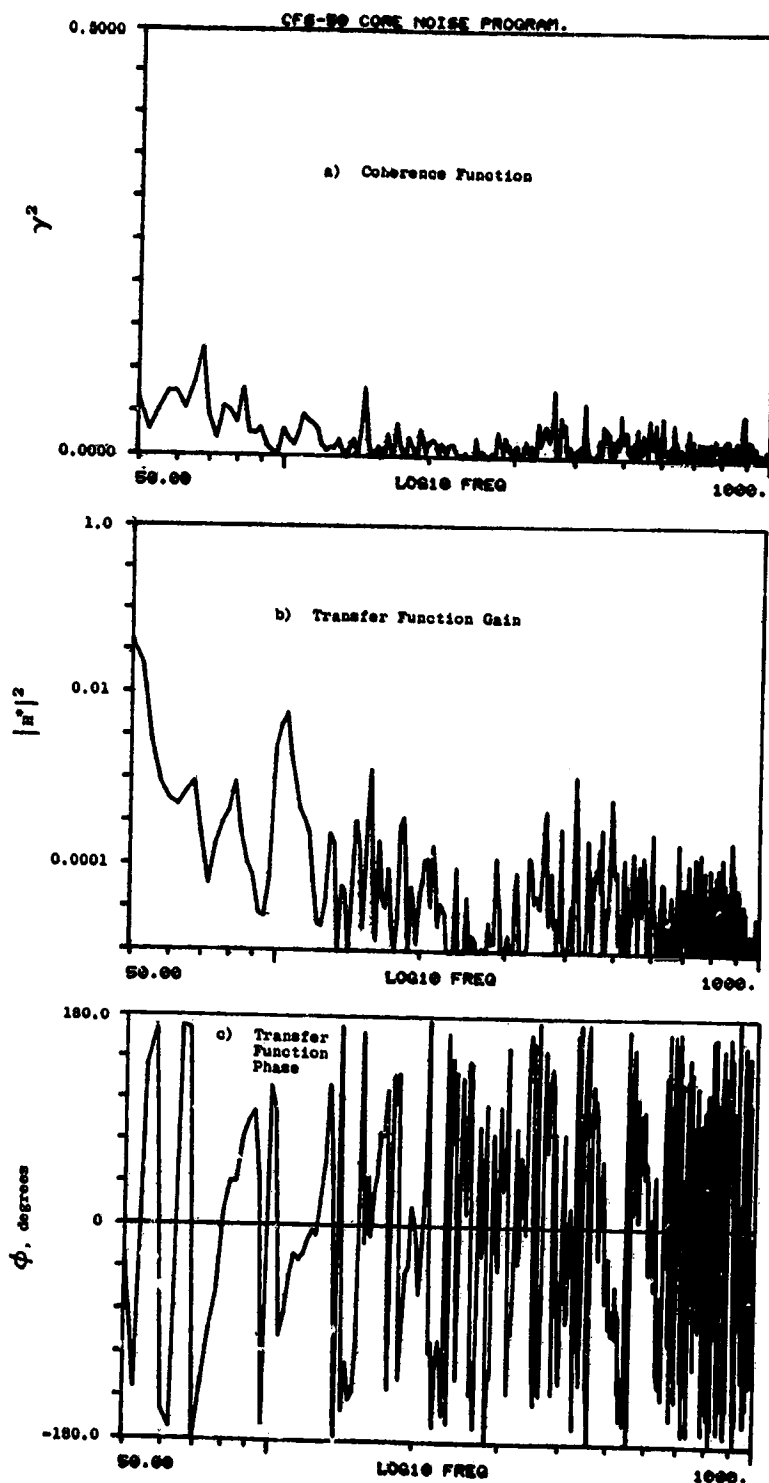


Figure A-233. Coherence and Transfer Functions for Plane 3.5 (102°) to 120° Farfield Microphone at 45.5% Thrust.

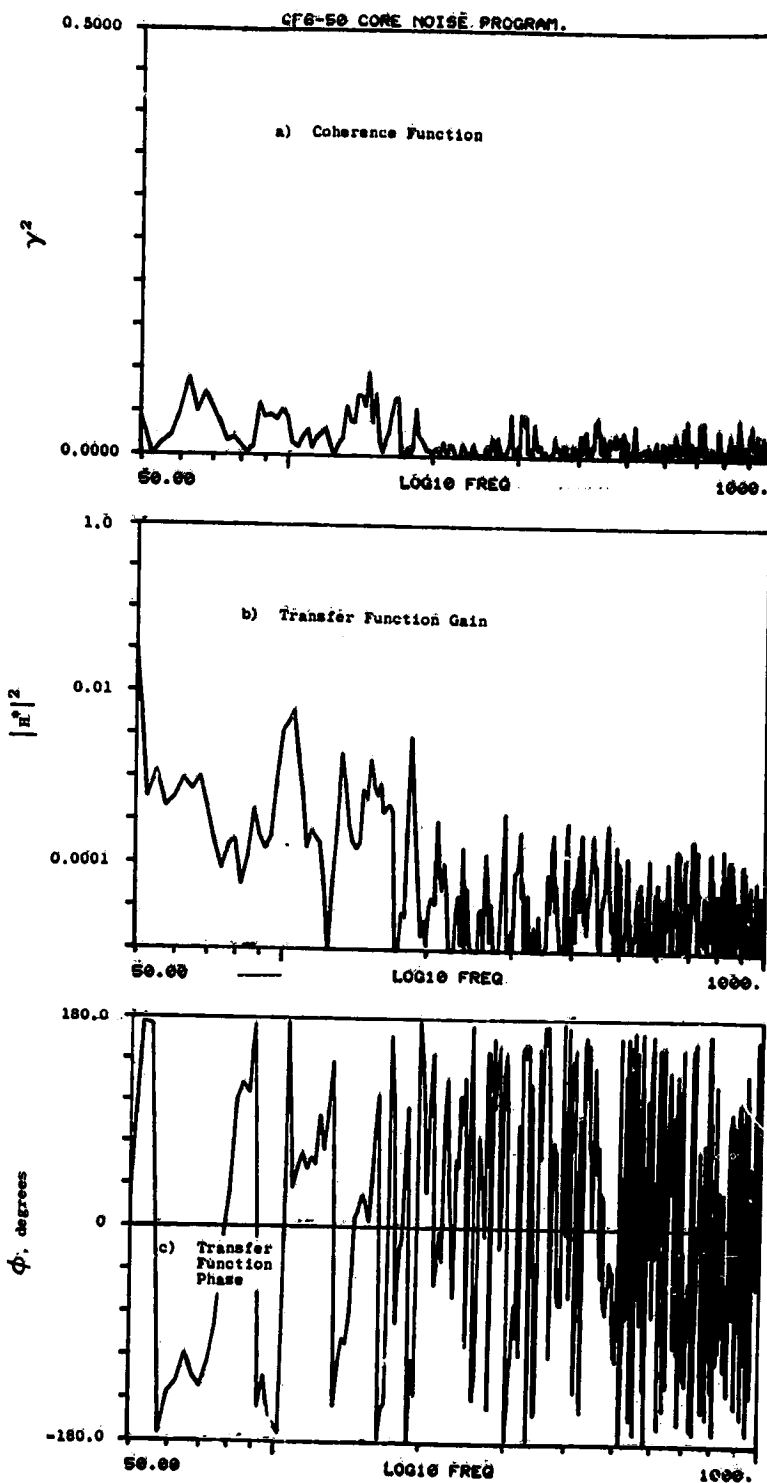


Figure A-234. Coherence and Transfer Functions for Plane 3.5 (102° to 130° Farfield Microphone at 45.5% Thrust.

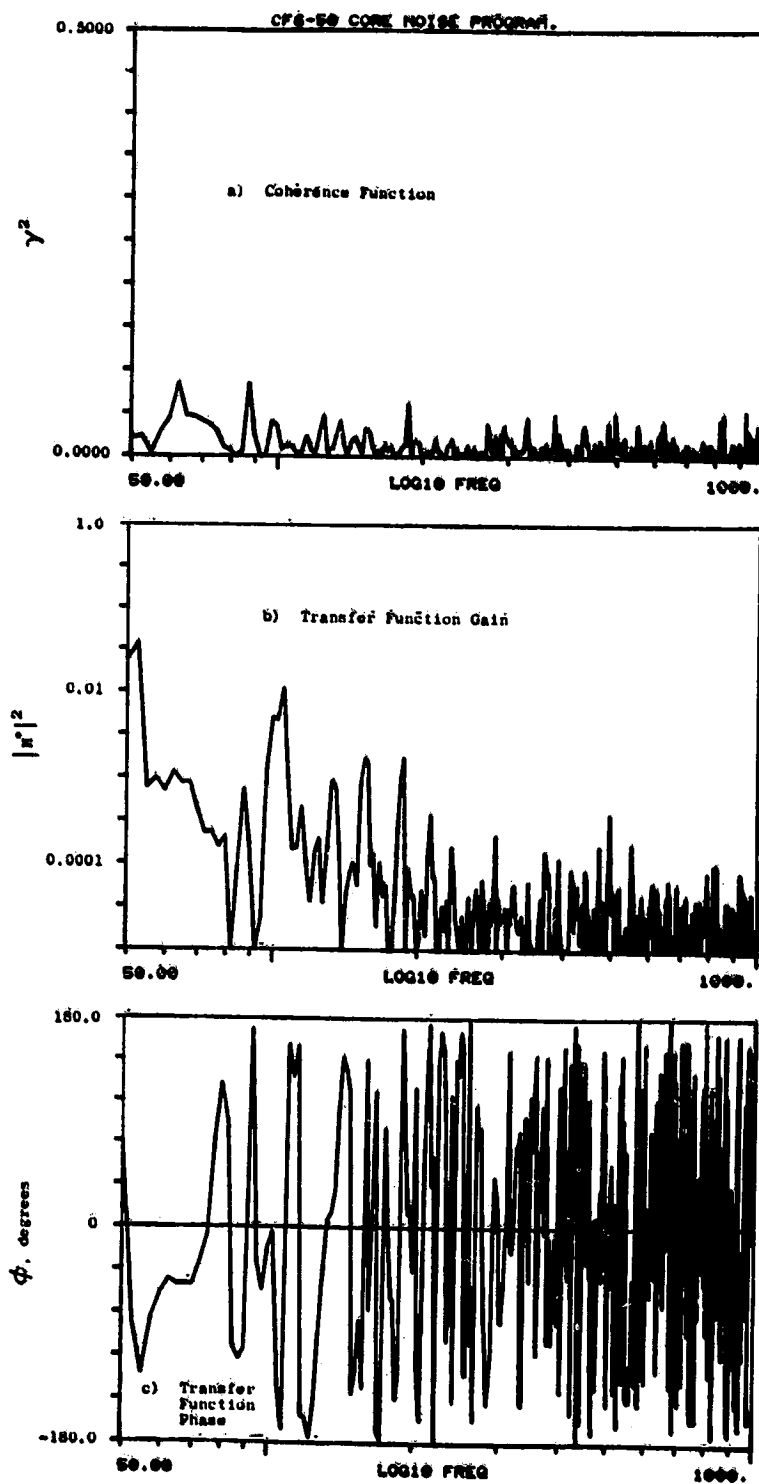


Figure A-235. Coherence and Transfer Functions for Plane 3.5 (102°) to 140° Farfield Microphone at 45.5% Thrust.

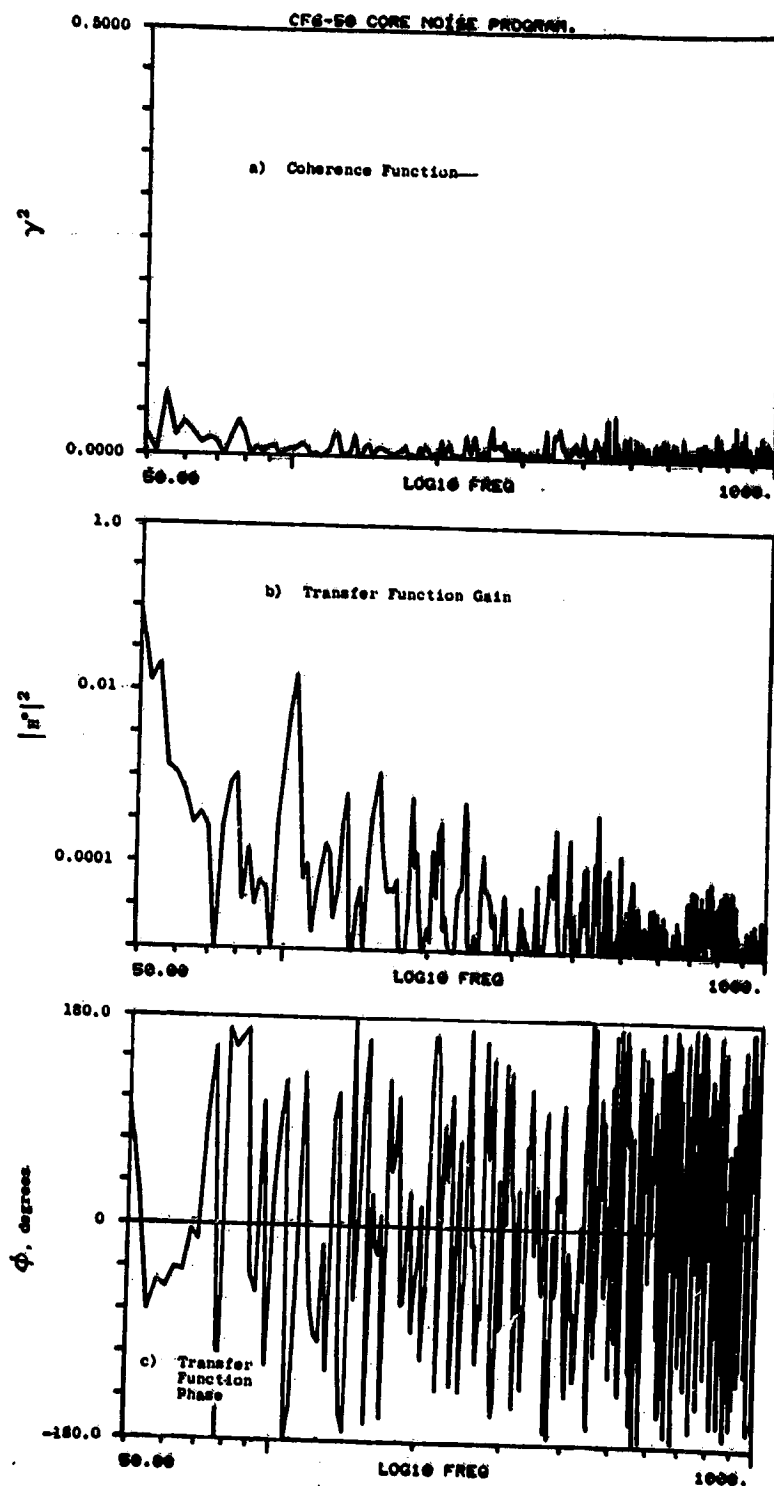


Figure A-236. Coherence and Transfer Functions for Plane 3.5 (102°) to 150° Farfield Microphone at 45.5% Thrust.

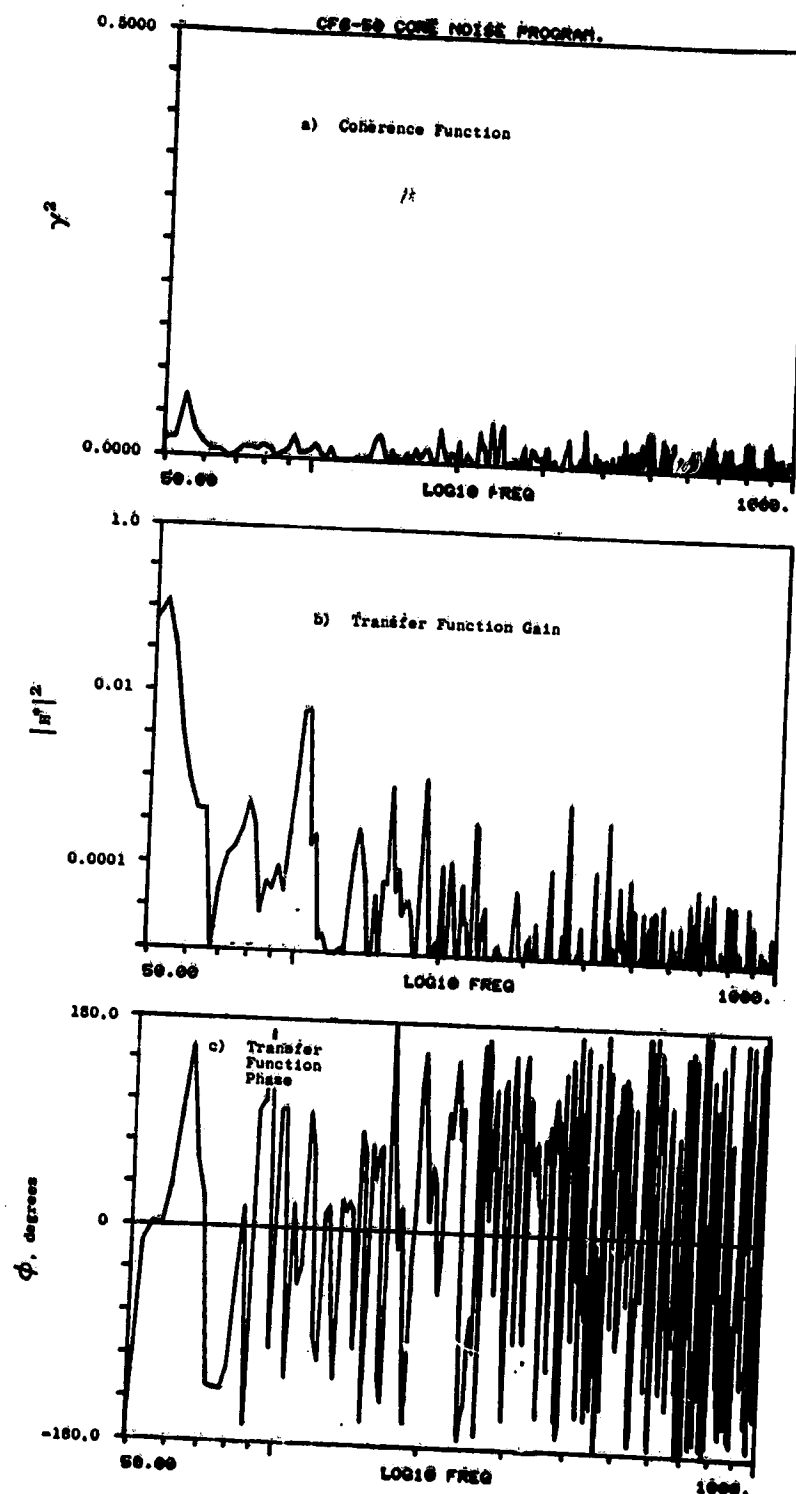


Figure A-237. Coherence and Transfer Functions for Plane 3.5 (102°) to 160° Farfield Microphone at 45.5% Thrust.

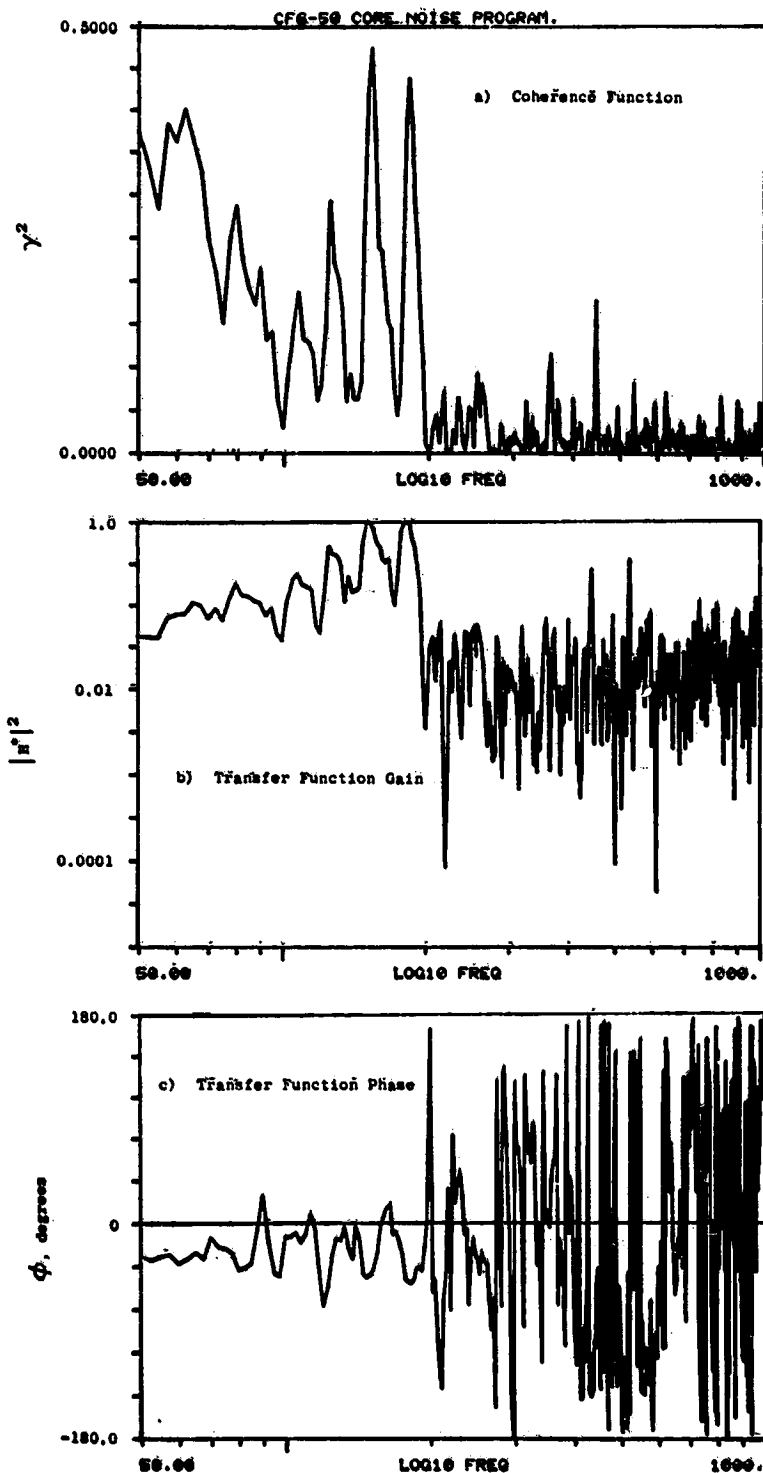


Figure A-238. Coherence and Transfer Functions for Plane 8.0A (270°) to 10° Farfield Microphone at 45.5% Thrust.

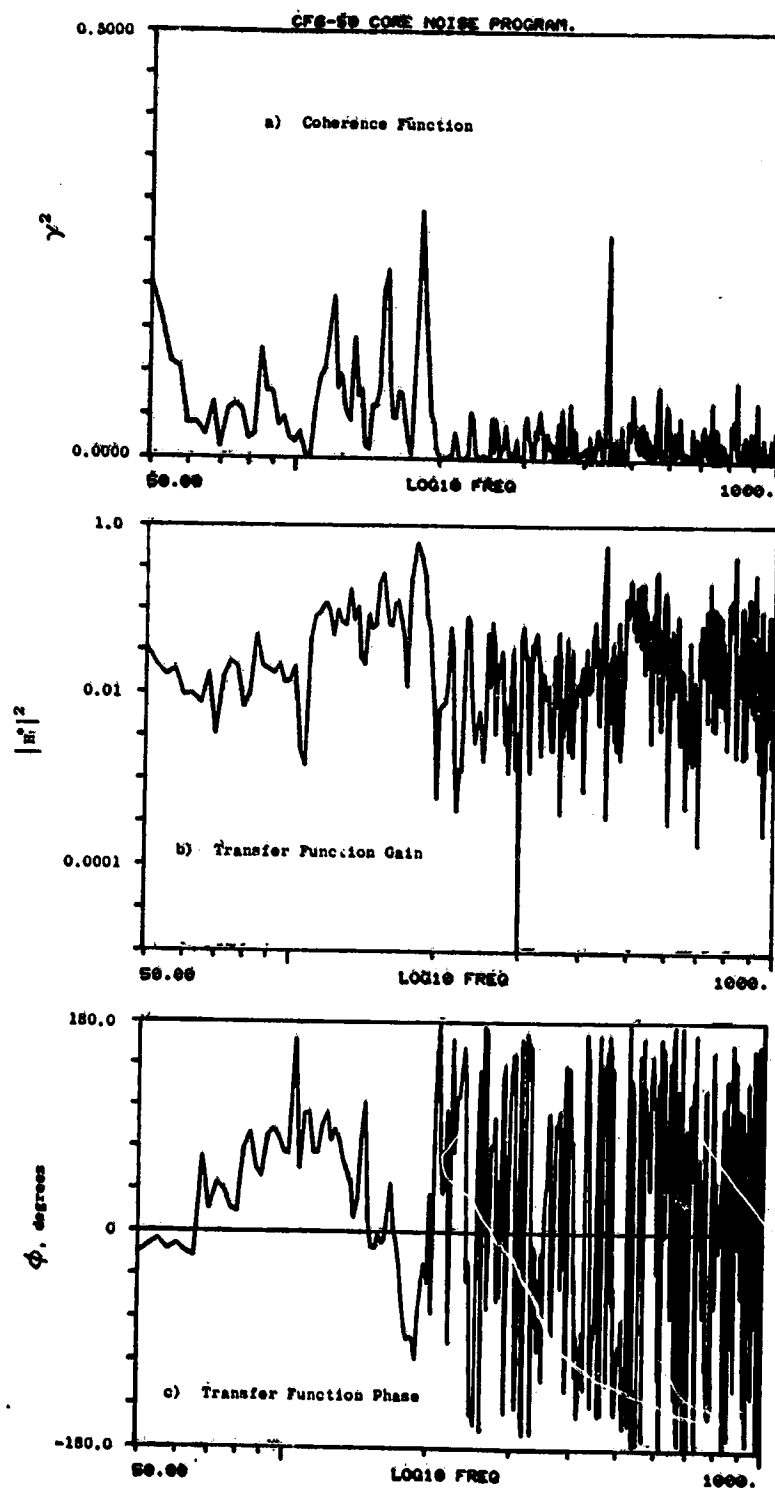


Figure A-239. Coherence and Transfer Functions for Plane 8.0A (270°) to 30° Farfield Microphone at 45.5% Thrust.

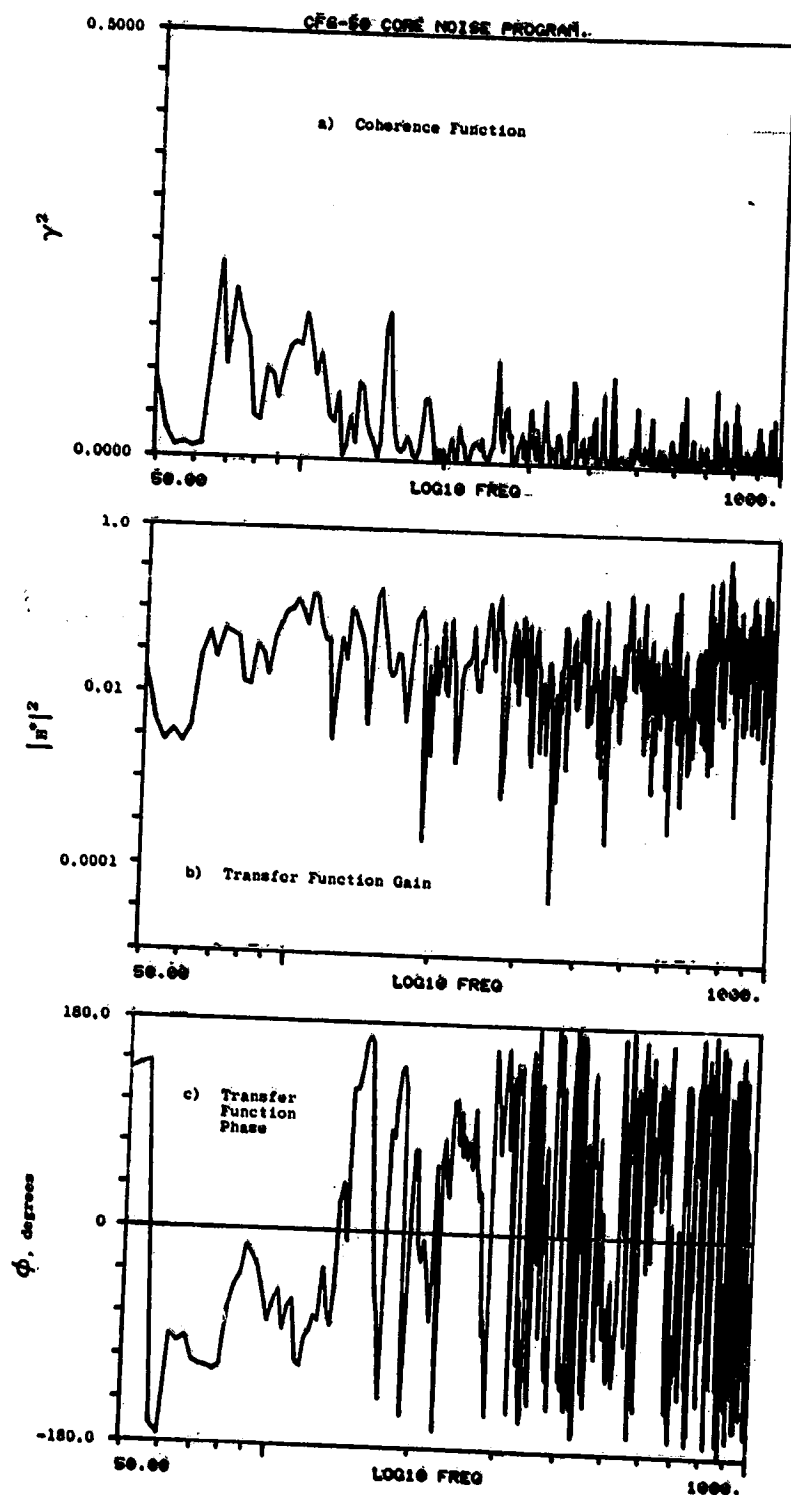


Figure A-240. Coherence and Transfer Functions for Plane 8.0A (270°) to 40° Farfield Microphone at 45.5% Thrust.

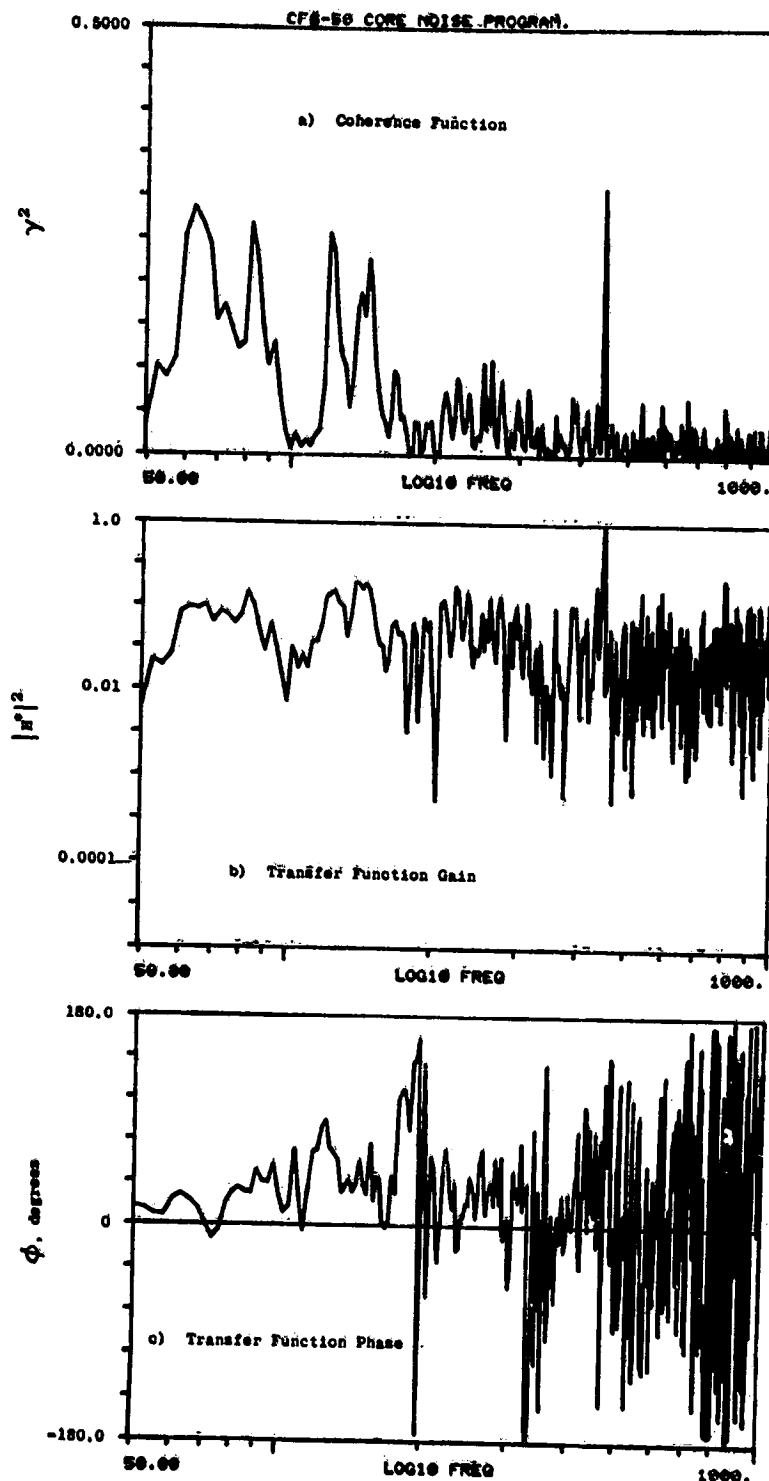


Figure A-241. Coherence and Transfer Functions for Plane 8.0A (270°) to 50° Farfield Microphone at 45.5% Thrust.

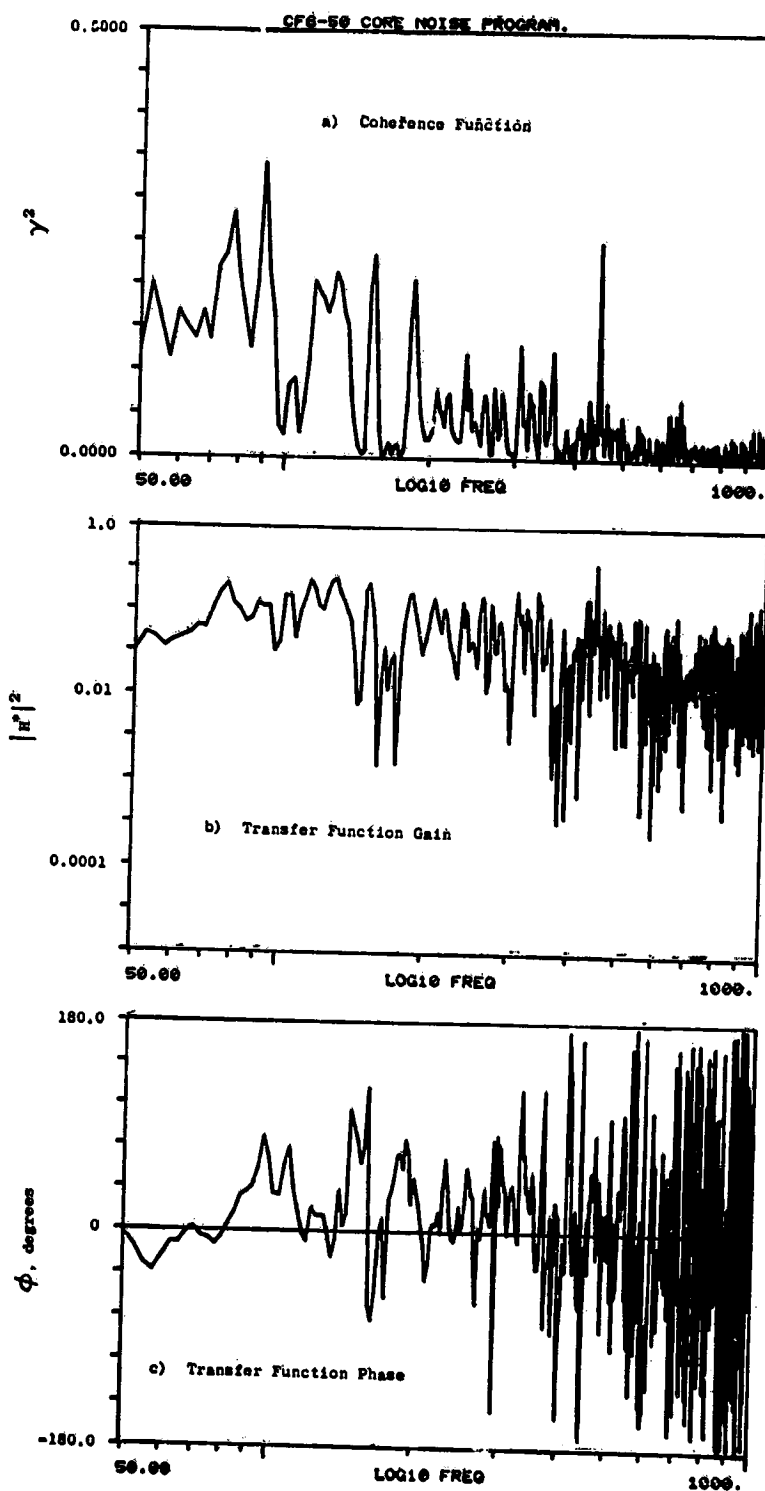


Figure A-242. Coherence and Transfer Functions for Plane 8.0A (270°) to 60° Farfield Microphone at 45.5% Thrust.

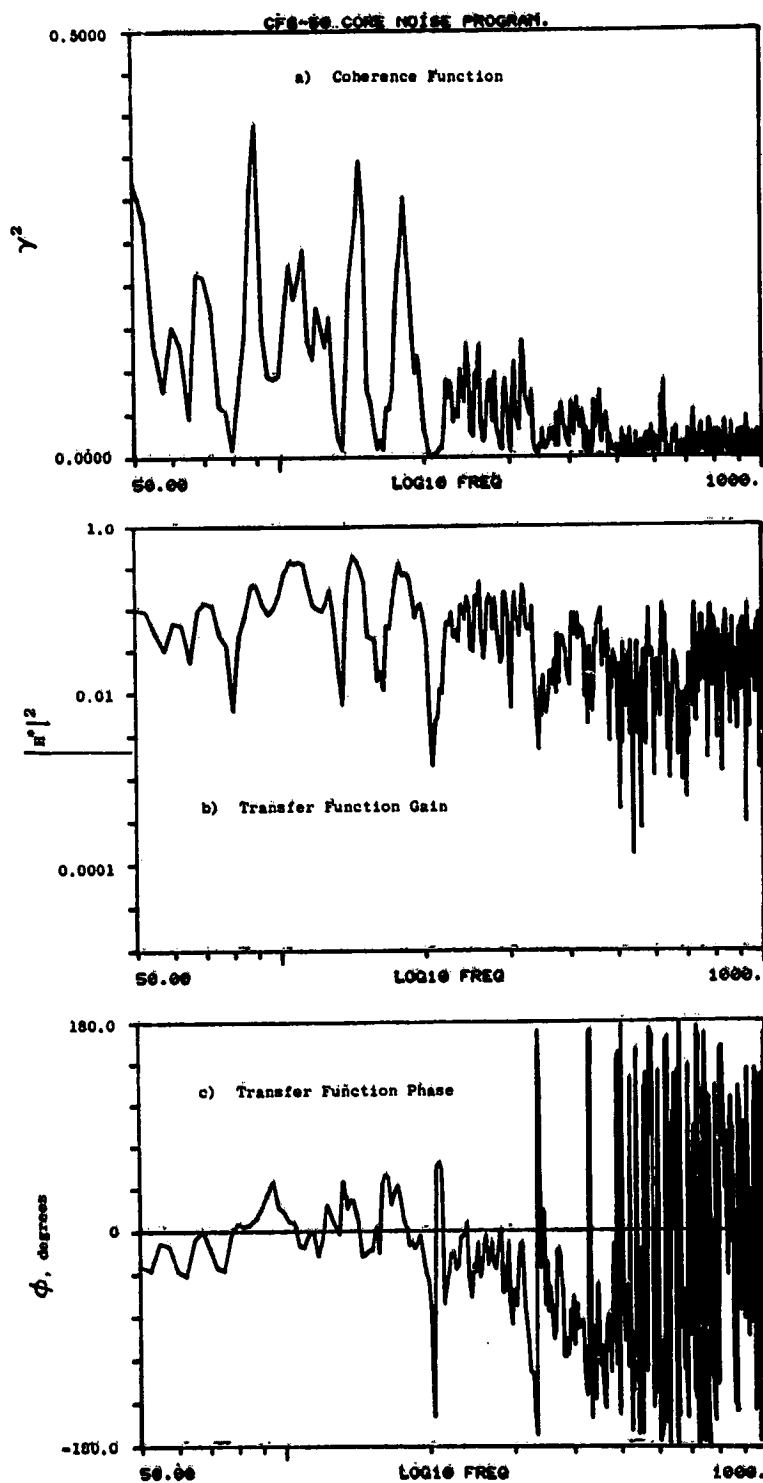


Figure A-243. Coherence and Transfer Functions for Plane 8.0A (270°) to 70° Farfield Microphone at 45.5% Thrust.

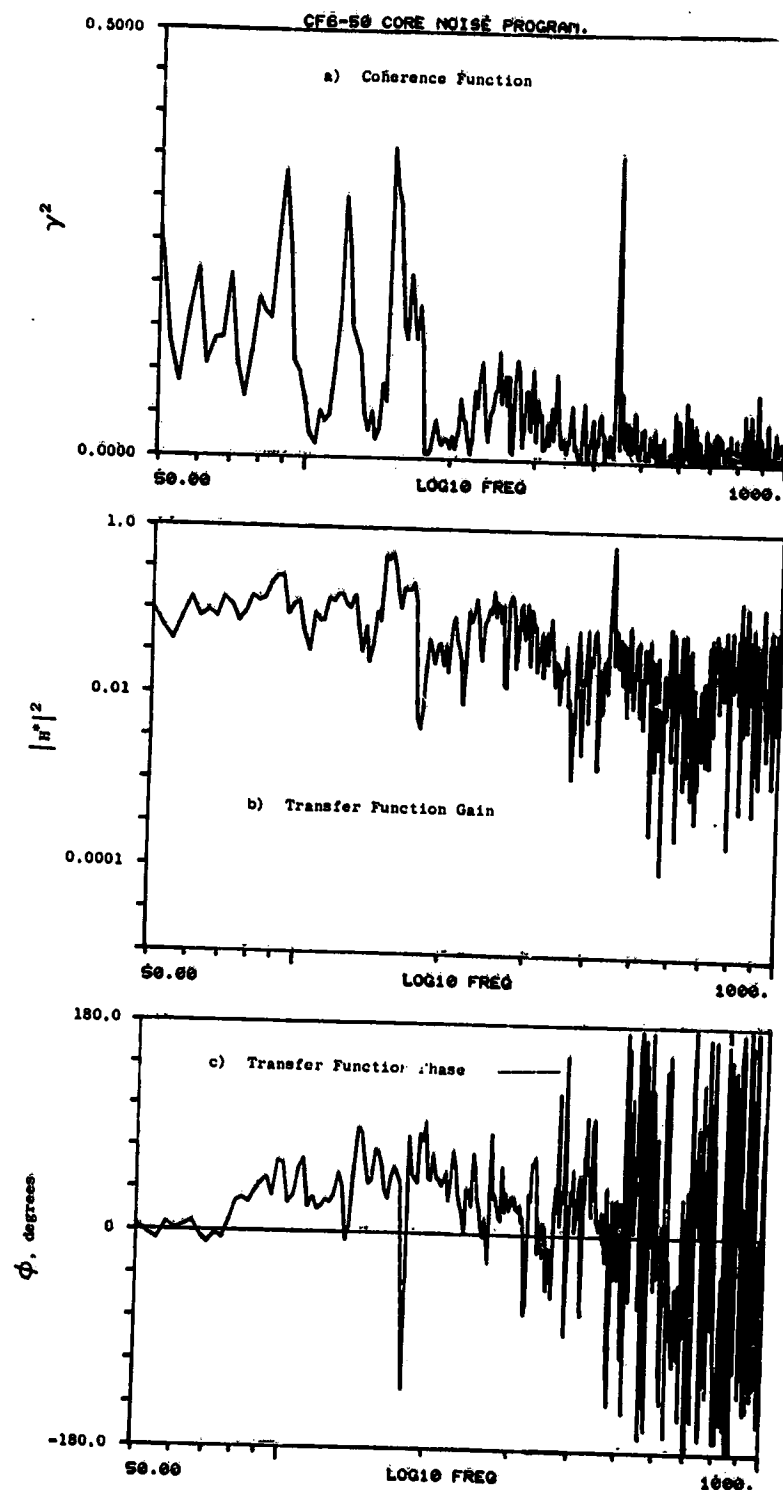


Figure A-244. Coherence and Transfer Functions for Plane 8.0A (270°) to 80° Farfield Microphone at 45.5% Thrust.

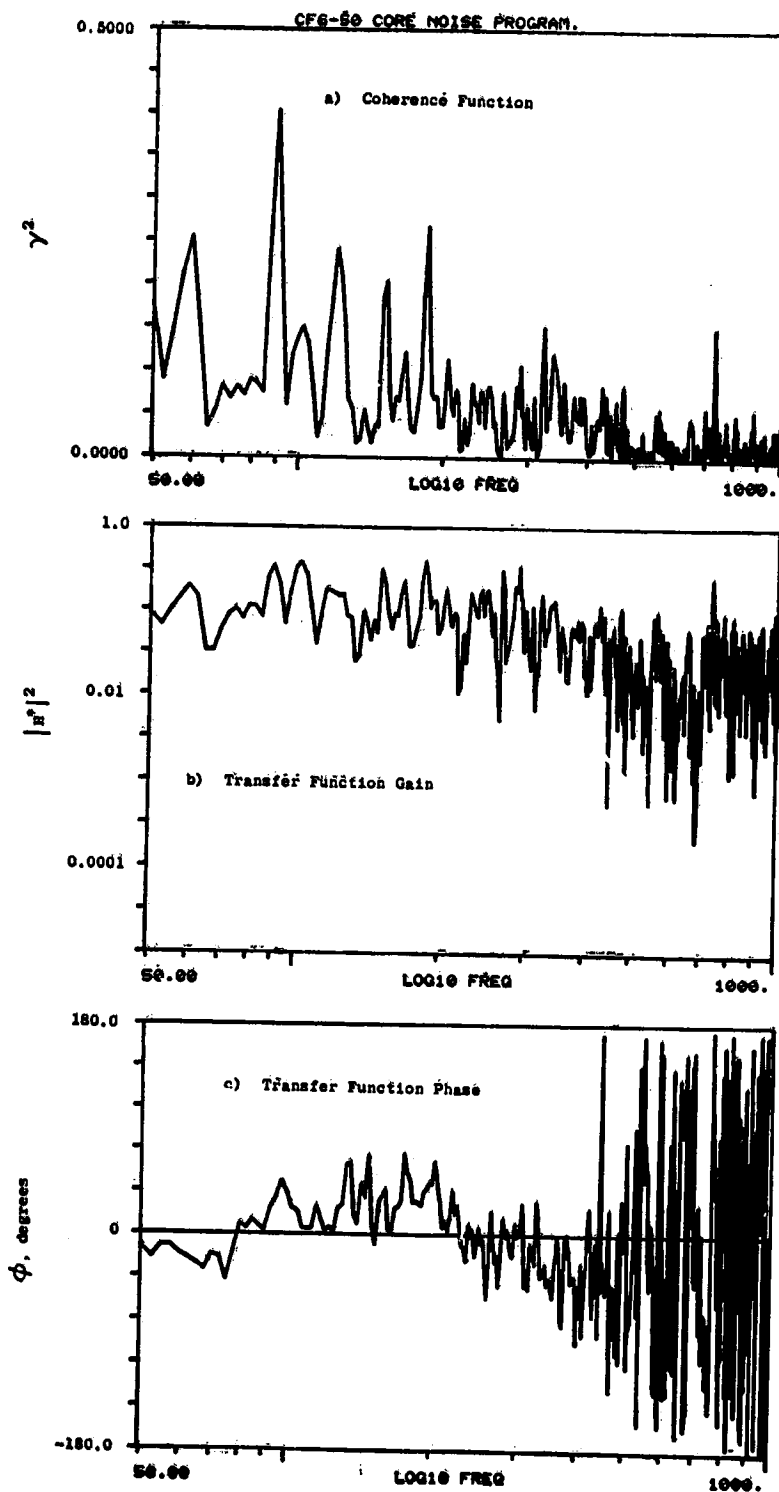


Figure A-245. Coherence and Transfer Functions for Plane 8.0A (270°) to 90° Farfield Microphone at 45.5% Thrust.

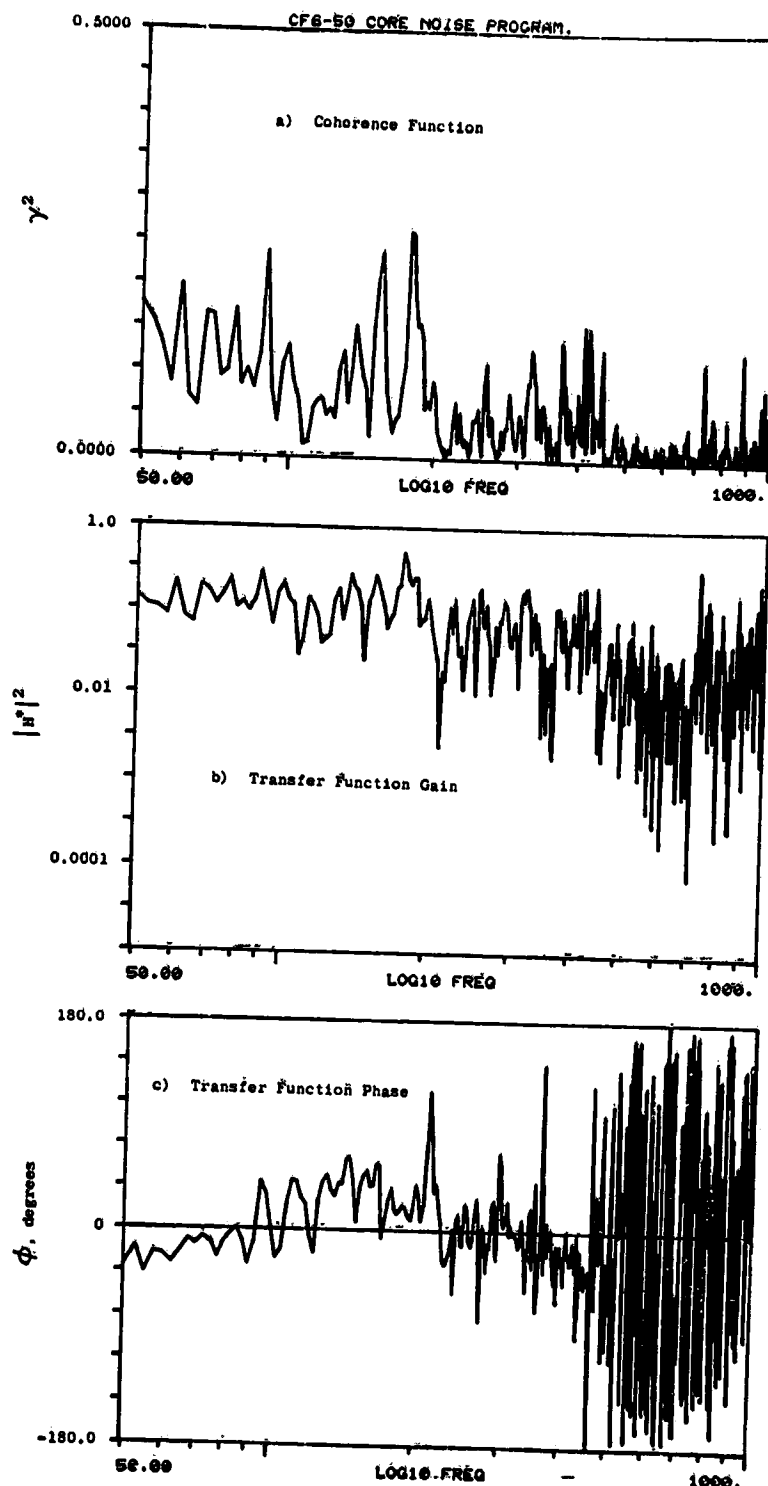


Figure A-246. Coherence and Transfer Functions for Plane 8.0A (270°) to 100° Farfield Microphone at 45.5% Thrust.

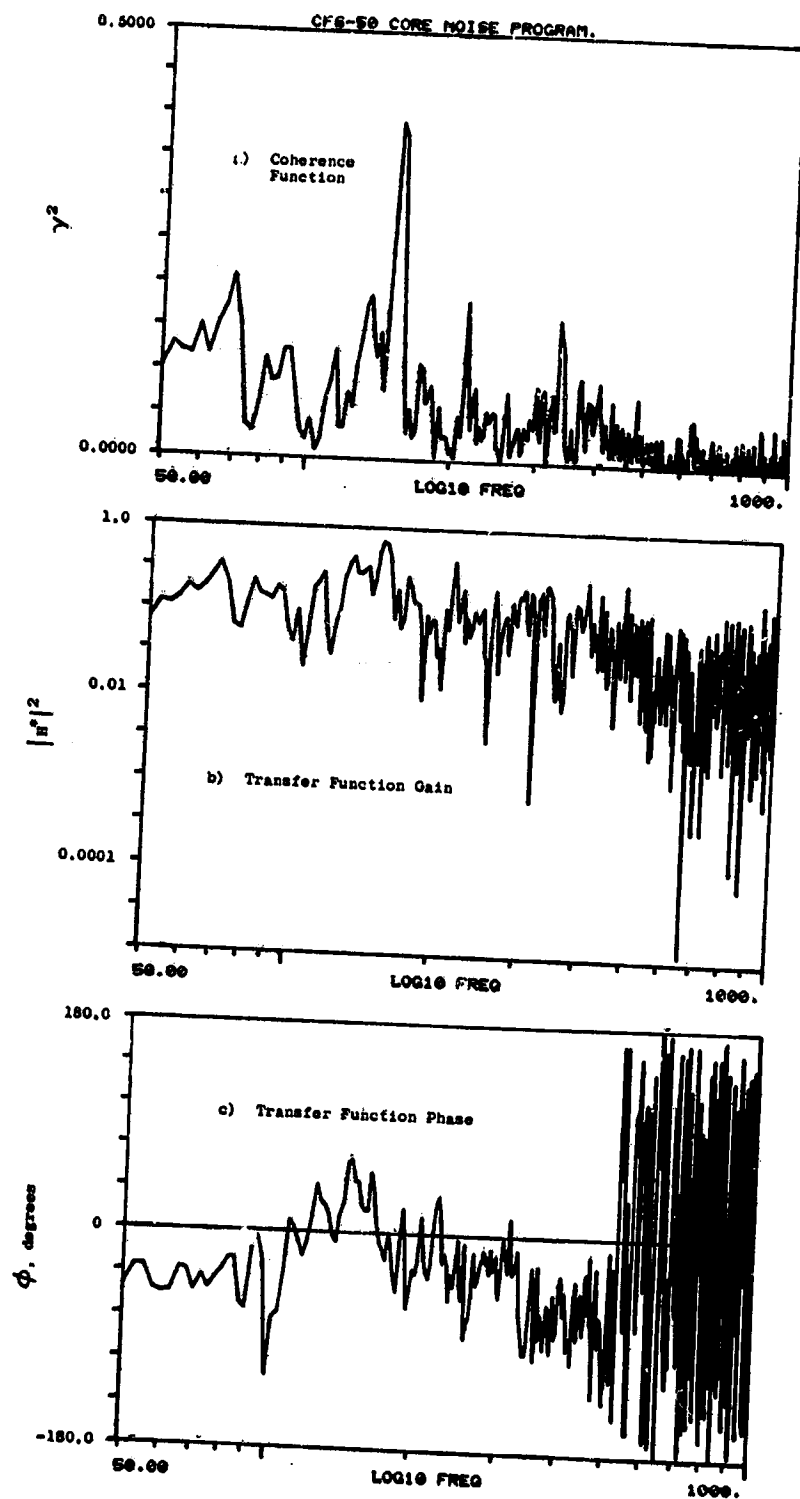


Figure A-247. Coherence and Transfer Functions for Plane 8.0A (270°) to 110° Farfield Microphone at 45.5% Thrust.

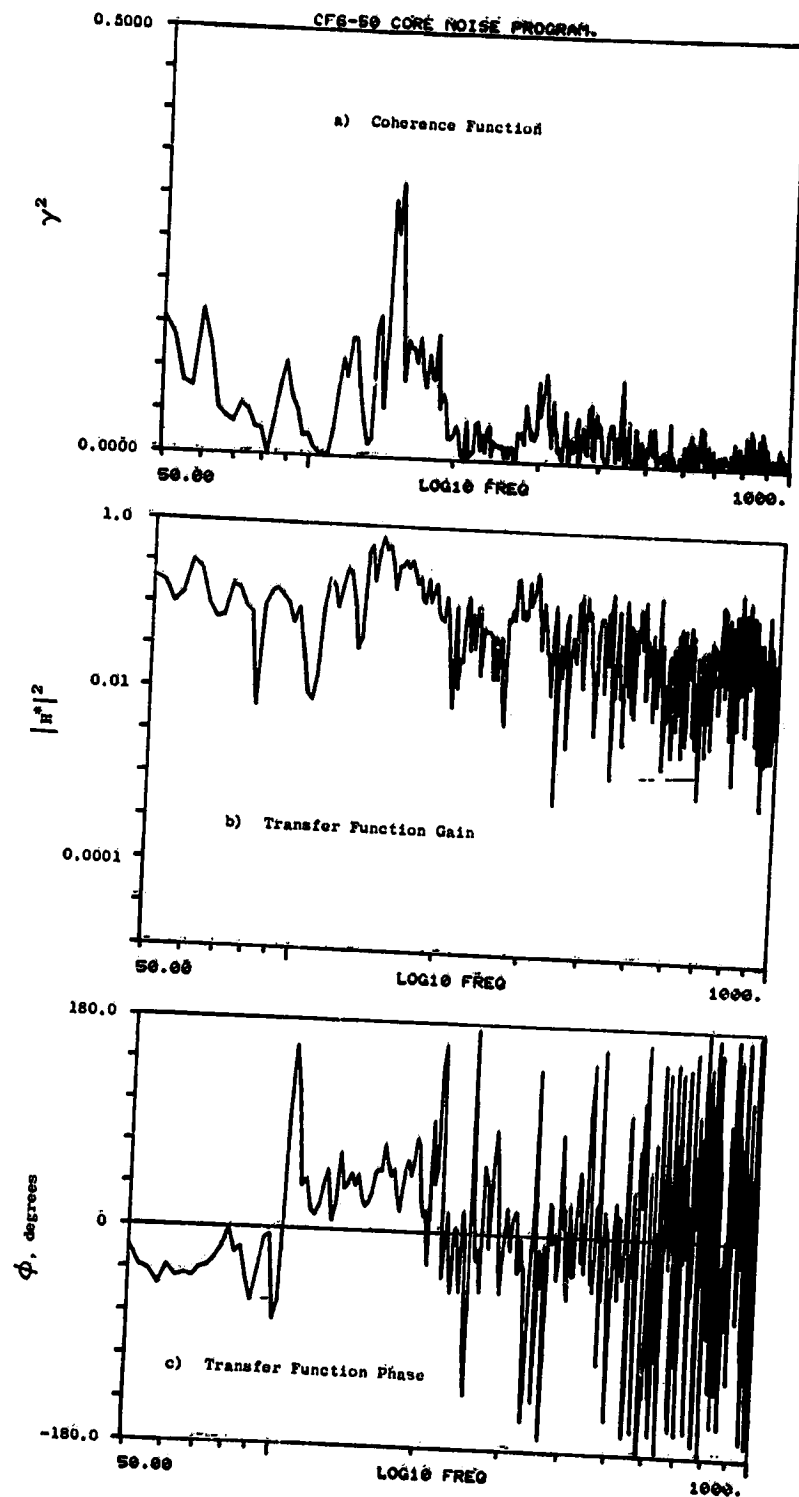


Figure A-248. Coherence and Transfer Functions for Plane 8.0A (270°) to 120° Farfield Microphone at 45.5% Thrust.

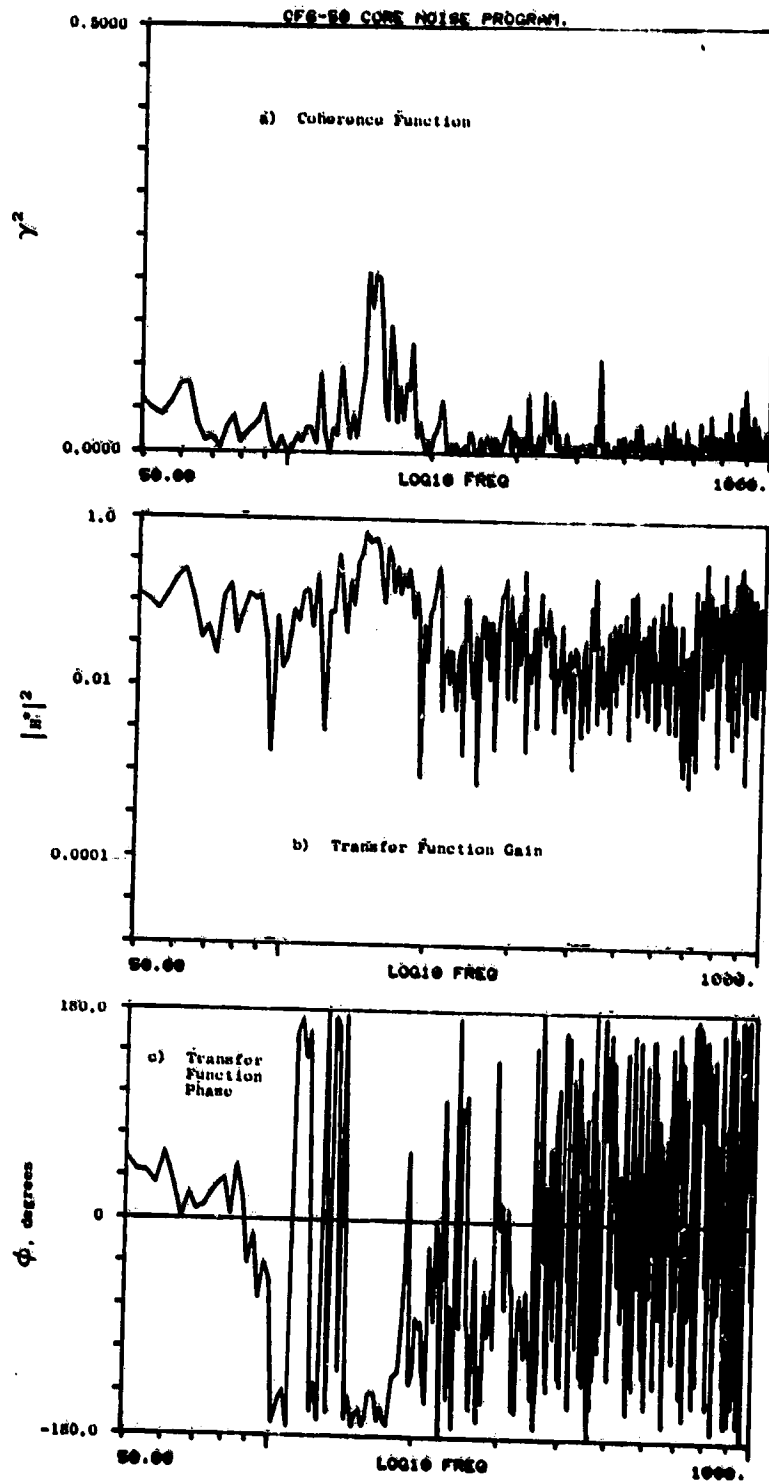


Figure A-249. Coherence and Transfer Functions for Plane 8.0A (270°) to 130° Farfield Microphone at 45.5% Thrust.

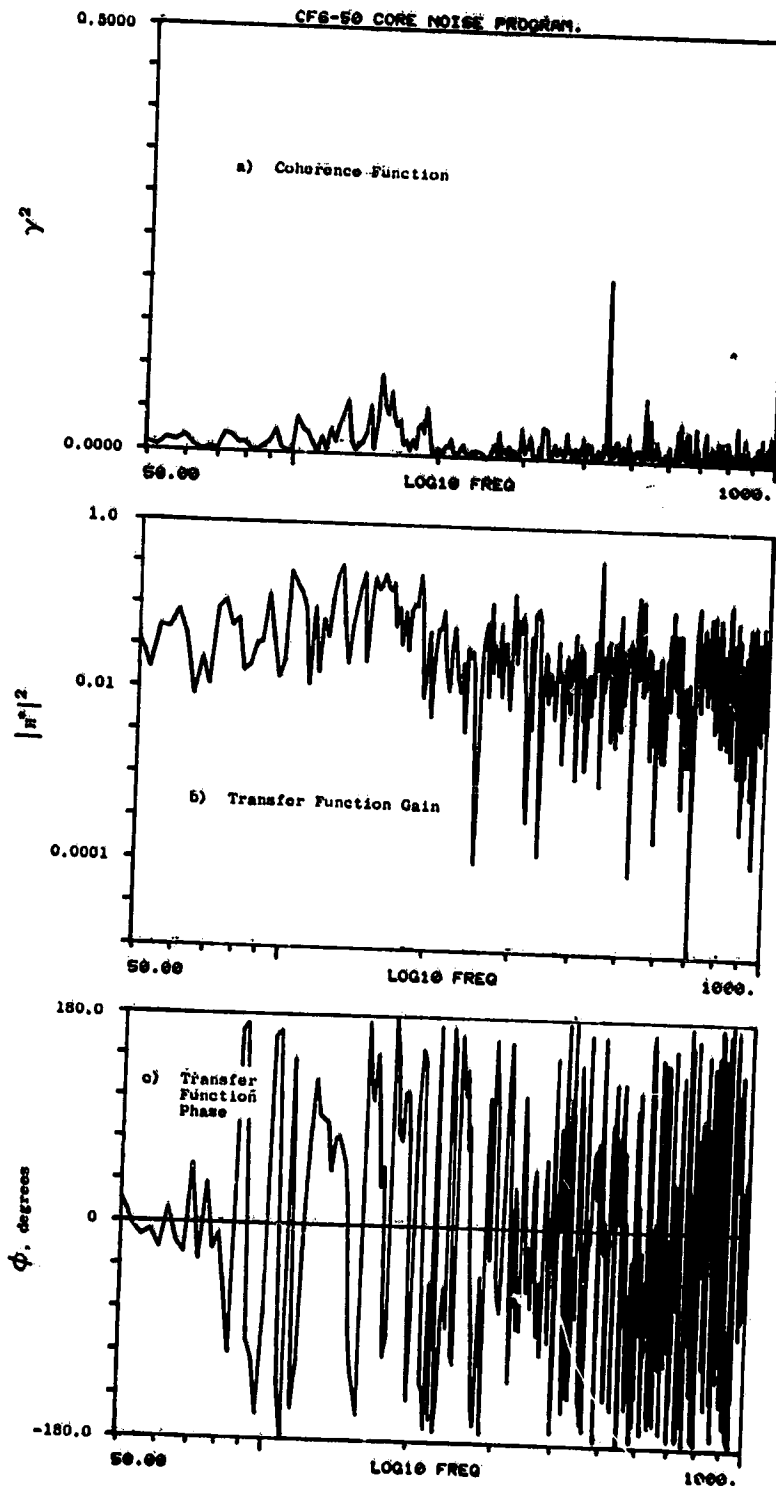


Figure A-250. Coherence and Transfer Functions for Plane 8.0A (270°) to 140° Farfield Microphone at 45.5% Thrust.

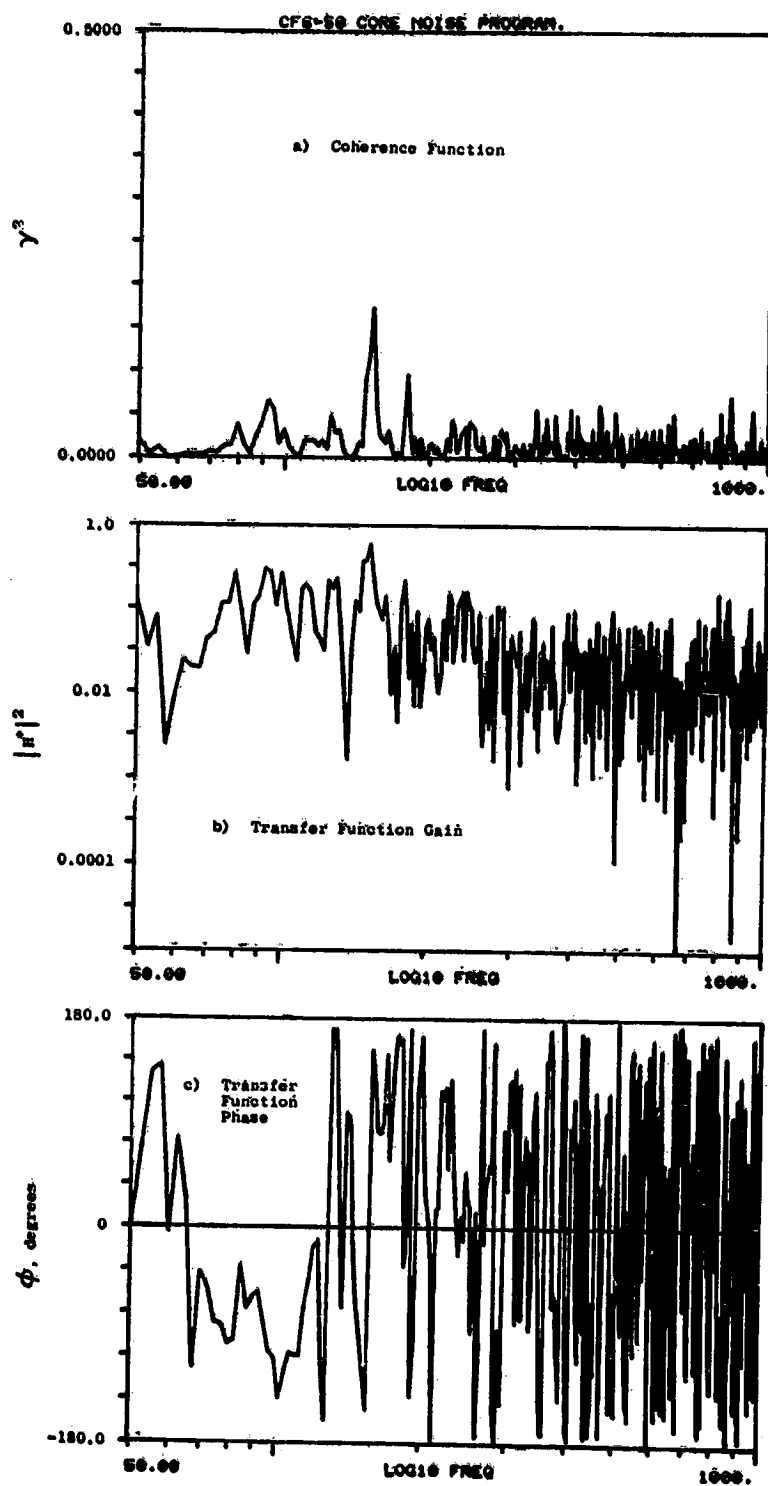


Figure A-251. Coherence and Transfer Functions for Plane 8.0A (270°) to 150° Farfield Microphone at 45.5% Thrust.

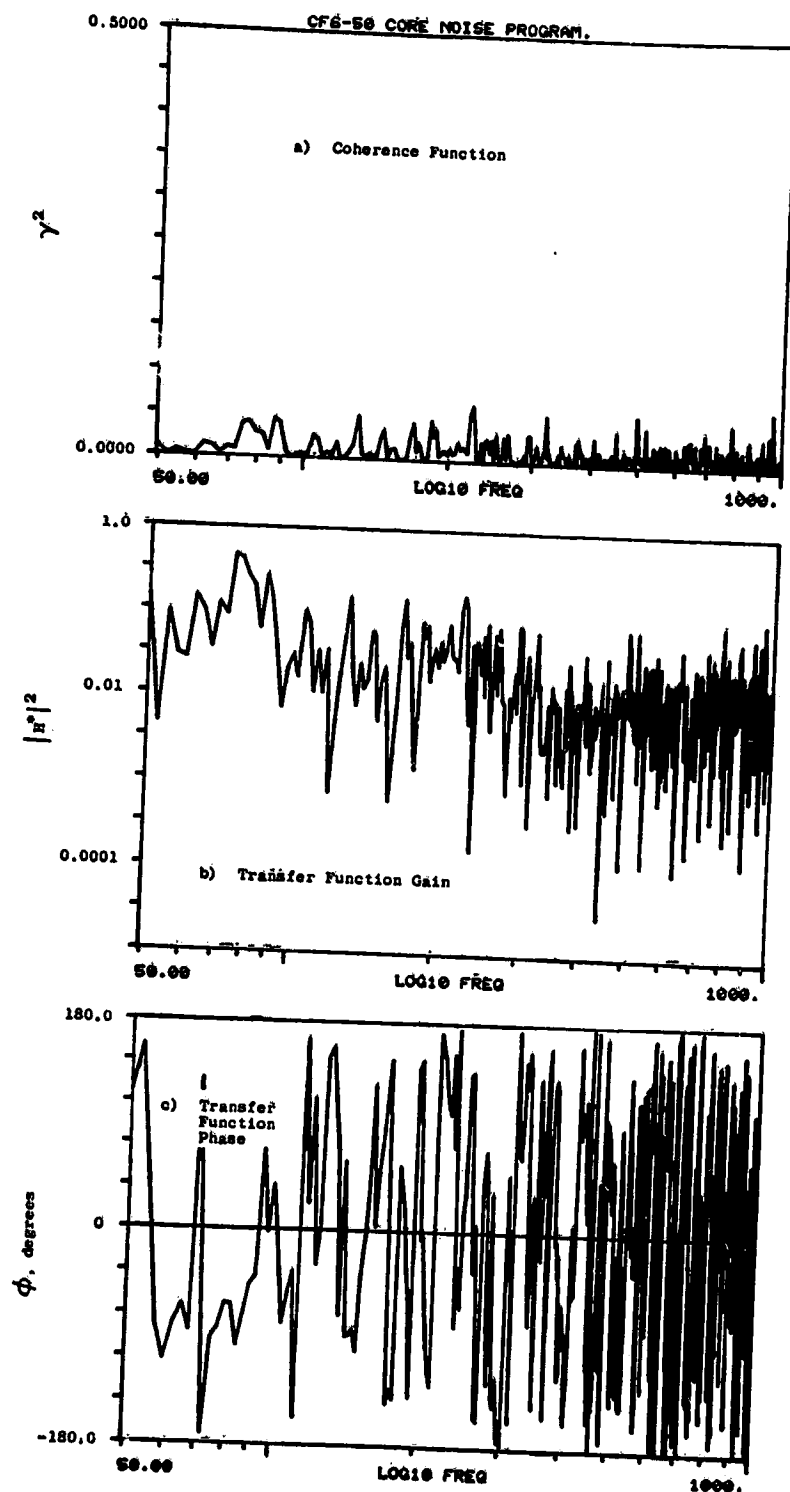


Figure A-252. Coherence and Transfer Functions for Plane 8.0A (270°) to 160° Farfield Microphone at 45.5% Thrust.

APPENDIX B
TURBINE TRANSFER FUNCTION RESULTS.

The turbine transfer function results presented in this appendix are in the form of coherent 1/3-octave-band SPL spectra comparisons at each test condition. Turbine attenuations were obtained between the coherent spectra at Plane 4.0 and the coherent spectra at Plane 8.0, both of which are referenced to Plane 3.5. Noted on the spectra are regions where both spectrum had coherence levels of less than 0.1. The low coherence levels in these regions gave excessive attenuation results. The attenuation results presented are for CF6-50 engine power settings of 3.8, 15.0, 22.8, 26.7, 30.8, 36.5, and 45.5% net thrust.

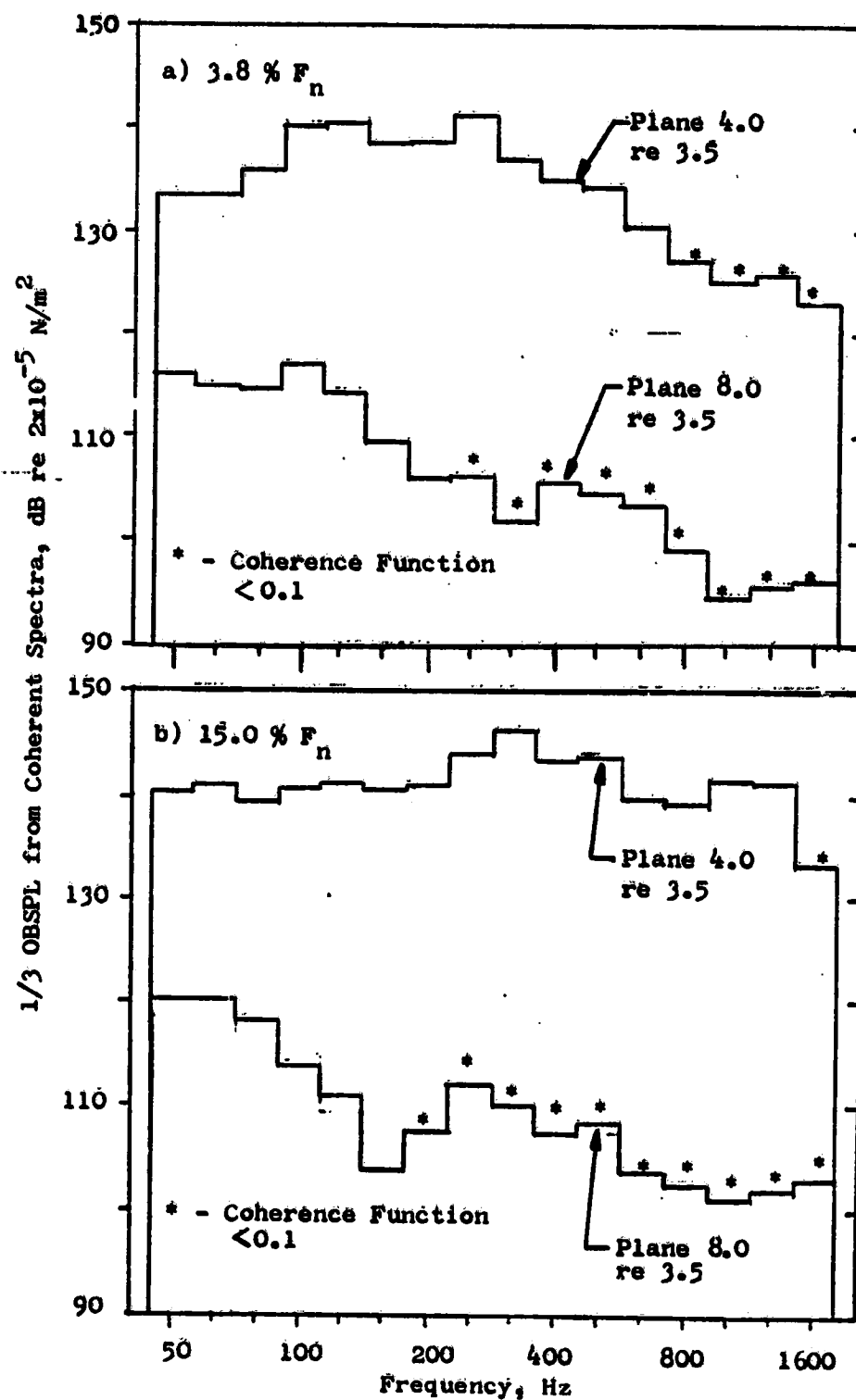


Figure B-1. Turbine Attenuation Comparisons from Coherent Spectra on the CF6-50 Engine.

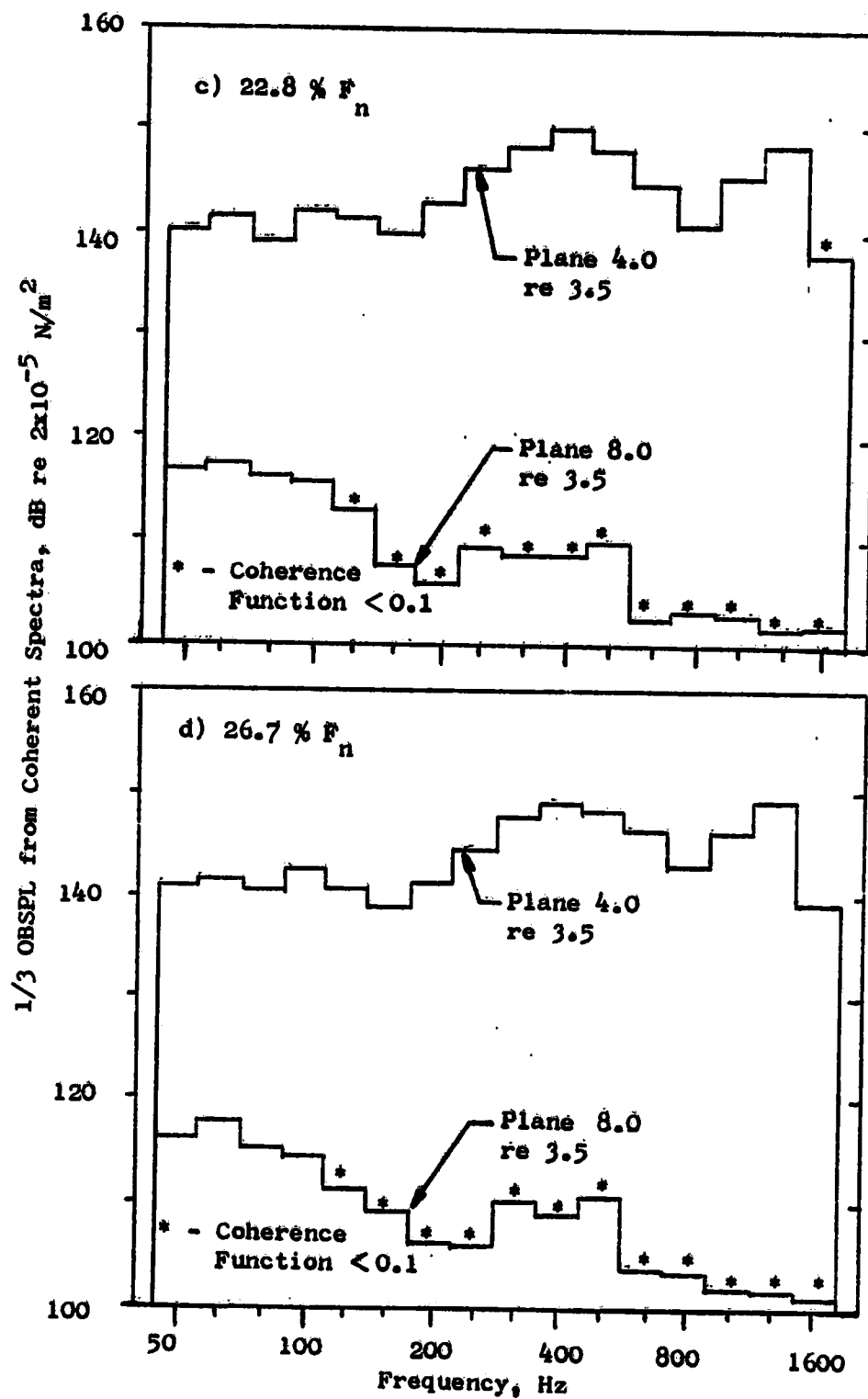


Figure B-1. Turbine Attenuation Comparisons from Coherent Spectra on the CF6-50 Engine (Continued).

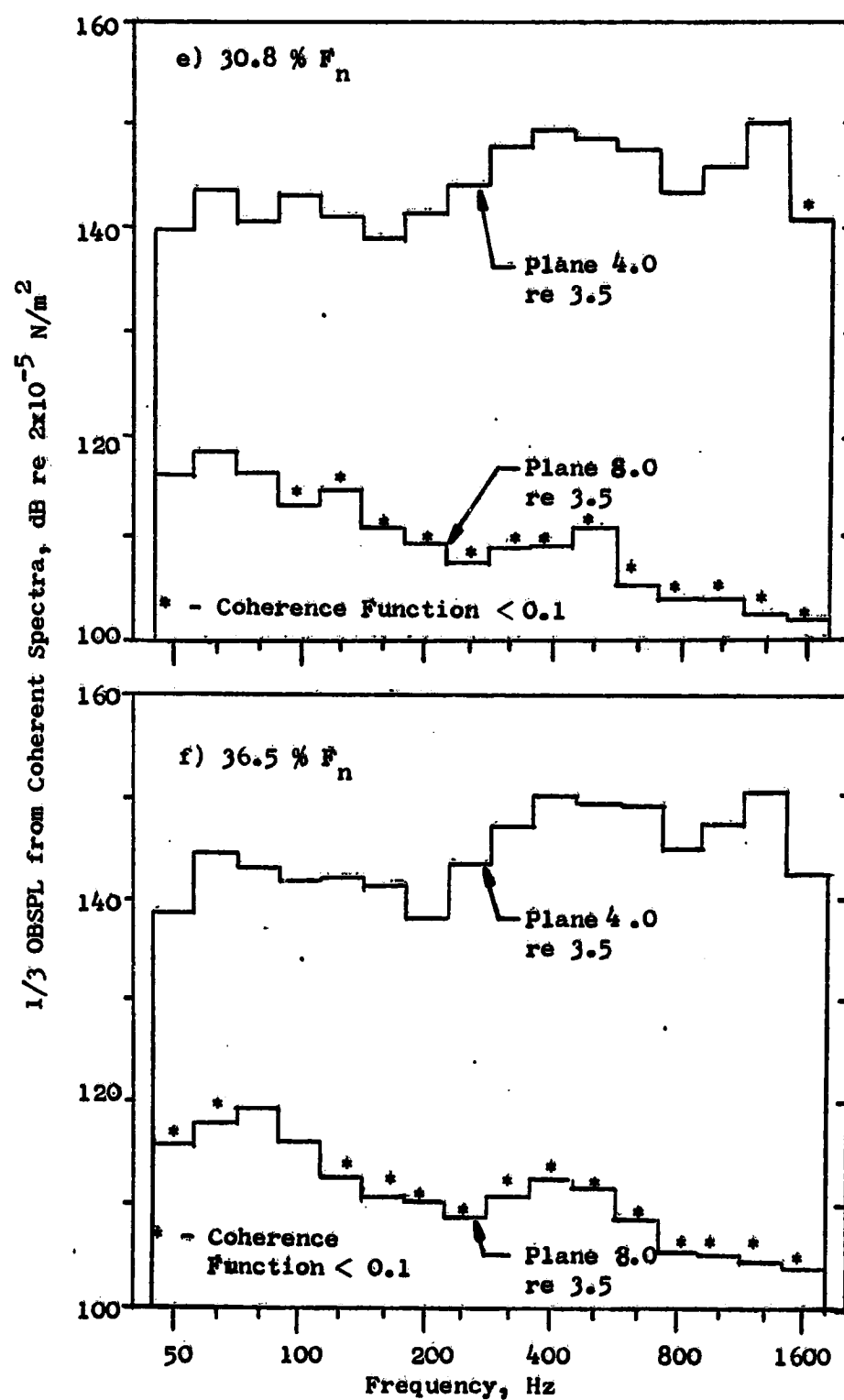


Figure B-1. Turbine Attenuation Comparisons from Coherent Spectra on the CF6-50 Engine (Continued).

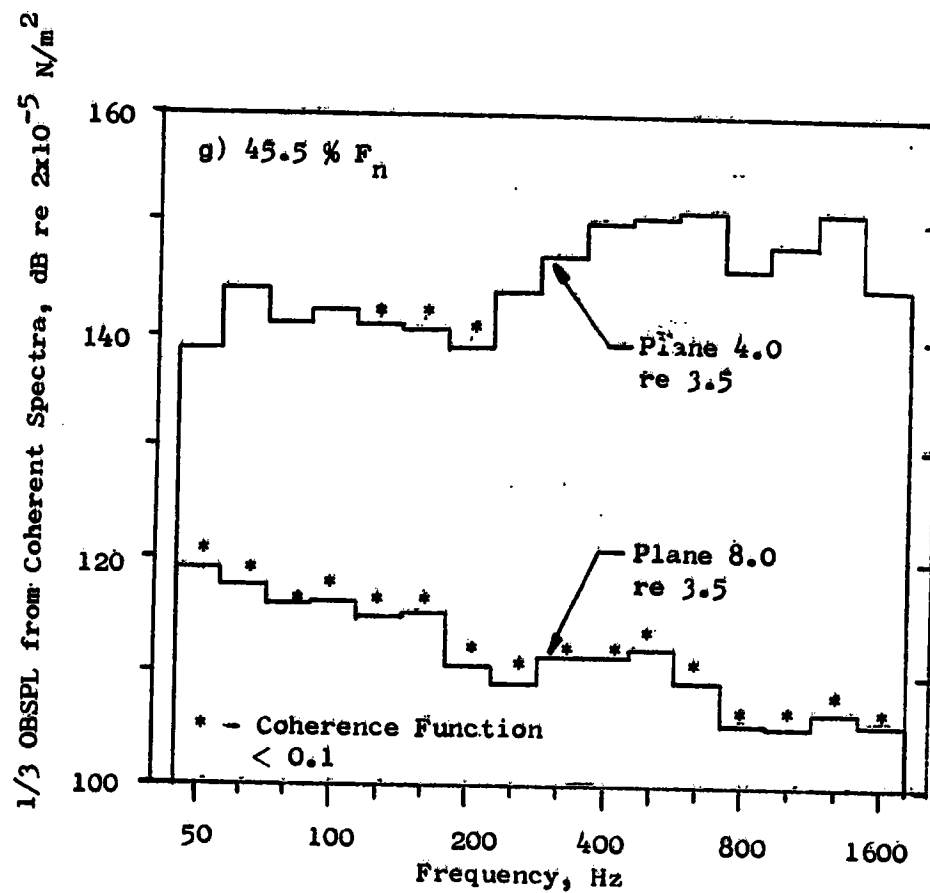


Figure B-1. Turbine Attenuation Comparisons from Coherent Spectra on the CF6-50 Engine (Concluded).

APPENDIX C
COHERENT OUTPUT SPECTRA RESULTS

Appendix C contains the coherent output spectra from the internal sensors at Planes 3.5 (102°) and 8.0A (270°) to each far-field microphone (i.e., $\theta = 10, 30, 40, 50, 60, 70, 80, 90, 100, 110, 120, 130, 140, 150, \text{ and } 160$ degrees). Tabulations of raw and coherent OASPL's and PWL for each set of data are included for the seven power settings selected for this analysis (i.e., 3.8, 15, 22.8, 26.7, 30.8, 36.5, and 45.5% net thrust).

Each of these coherent spectra cover the frequency range of 50 to 1600 Hz with a sample bandwidth of 2.5 Hz, a blocksize of 2048 samples, 100 averages, and a total record length of 40 seconds.

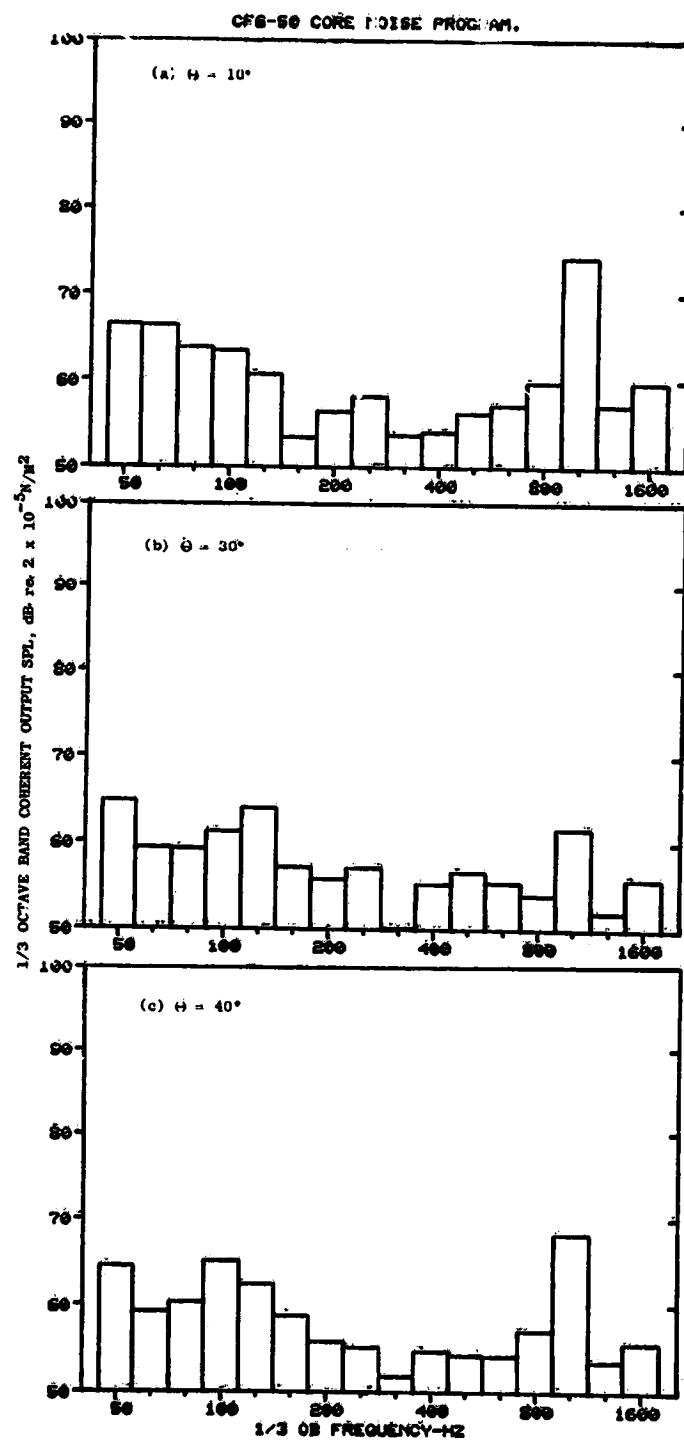


Figure C-1. Coherent Output SPL Spectra from Plane 3.5 (102°) to Farfield Microphones at 3.8% Thrust.

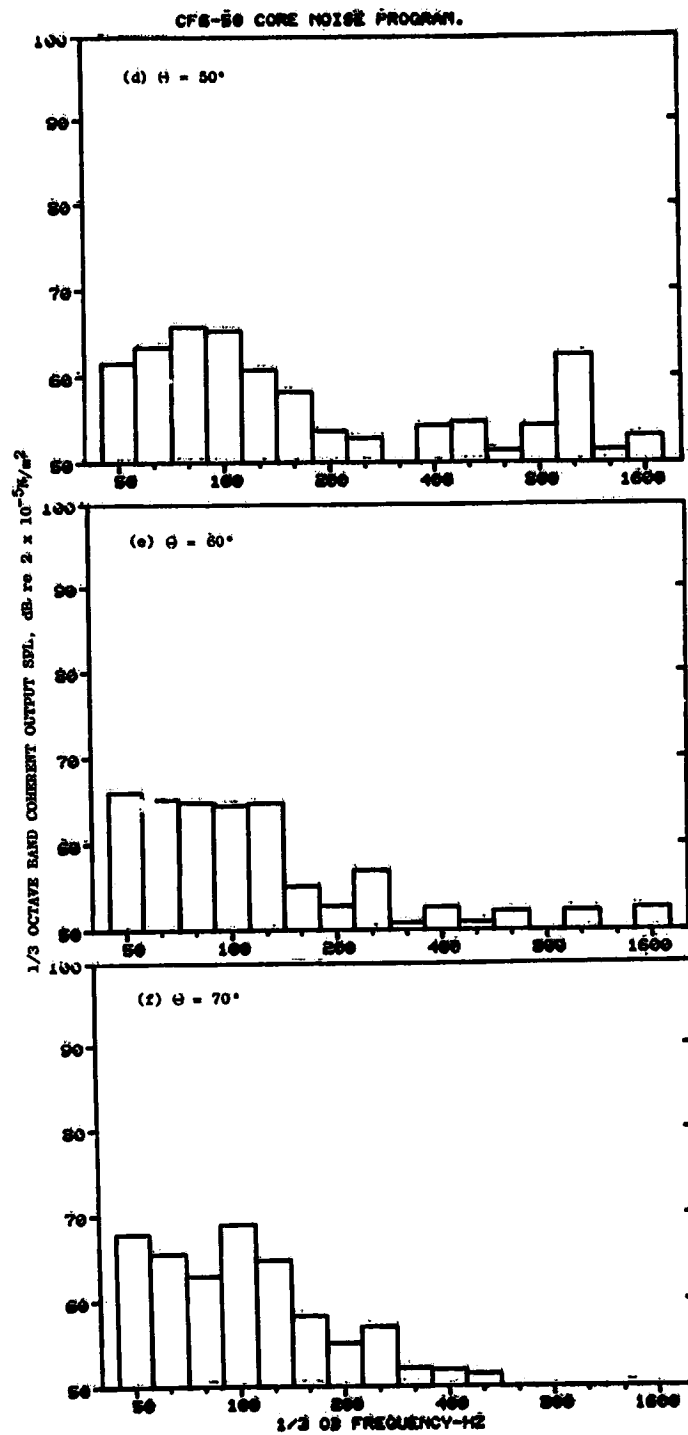


Figure C-1. Coherent Output SPL Spectra from Plane 3.5 (102°) to Farfield Microphones at 3.8% Thrust (Continued).

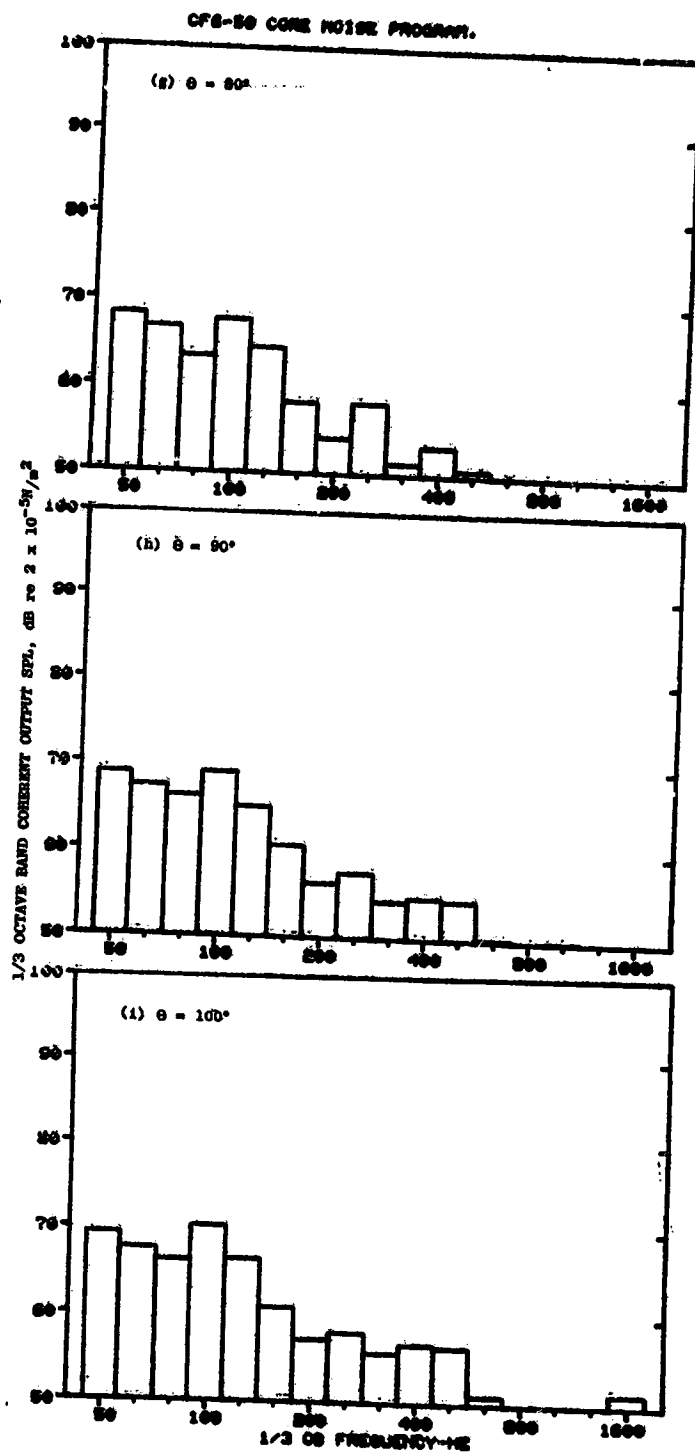


Figure C-1. Coherent Output SPL Spectra from Plane 3.5 (102°) to Farfield Microphones at 3.8% Thrust (Continued).

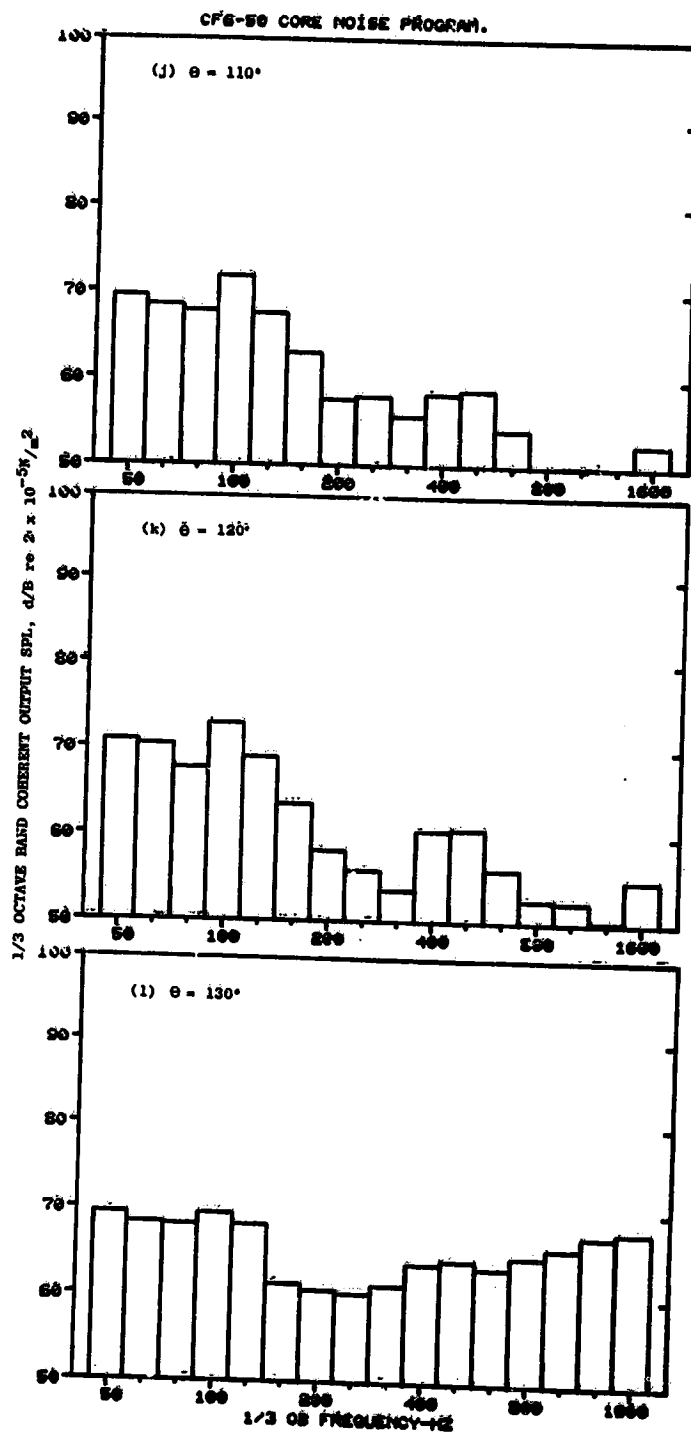


Figure C-1. Coherent Output SPL Spectra from Plane 3.5 (102°) to Farfield Microphones at 3.8% Thrust (Continued).

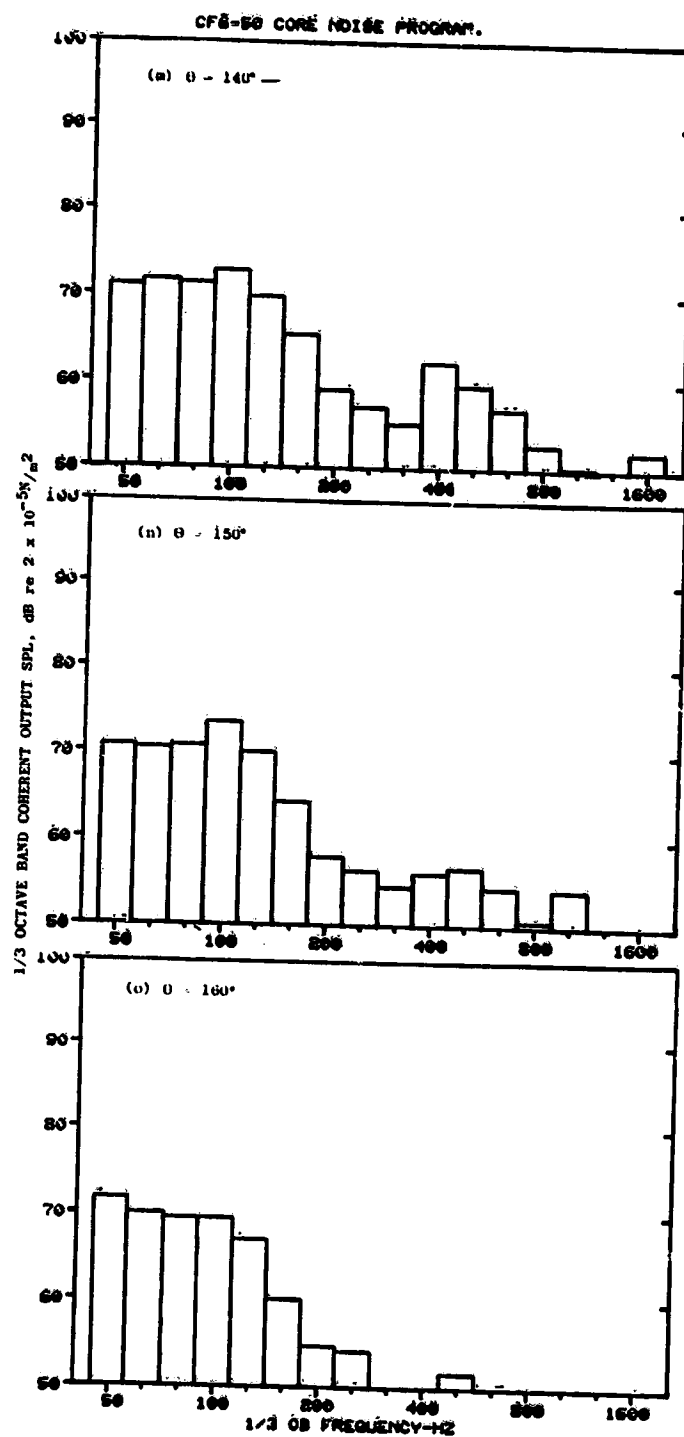


Figure C-1. Coherent Output SPL Spectra from Plane 3.5 (102°) to Farfield Microphones at 3.8% Thrust (Concluded).

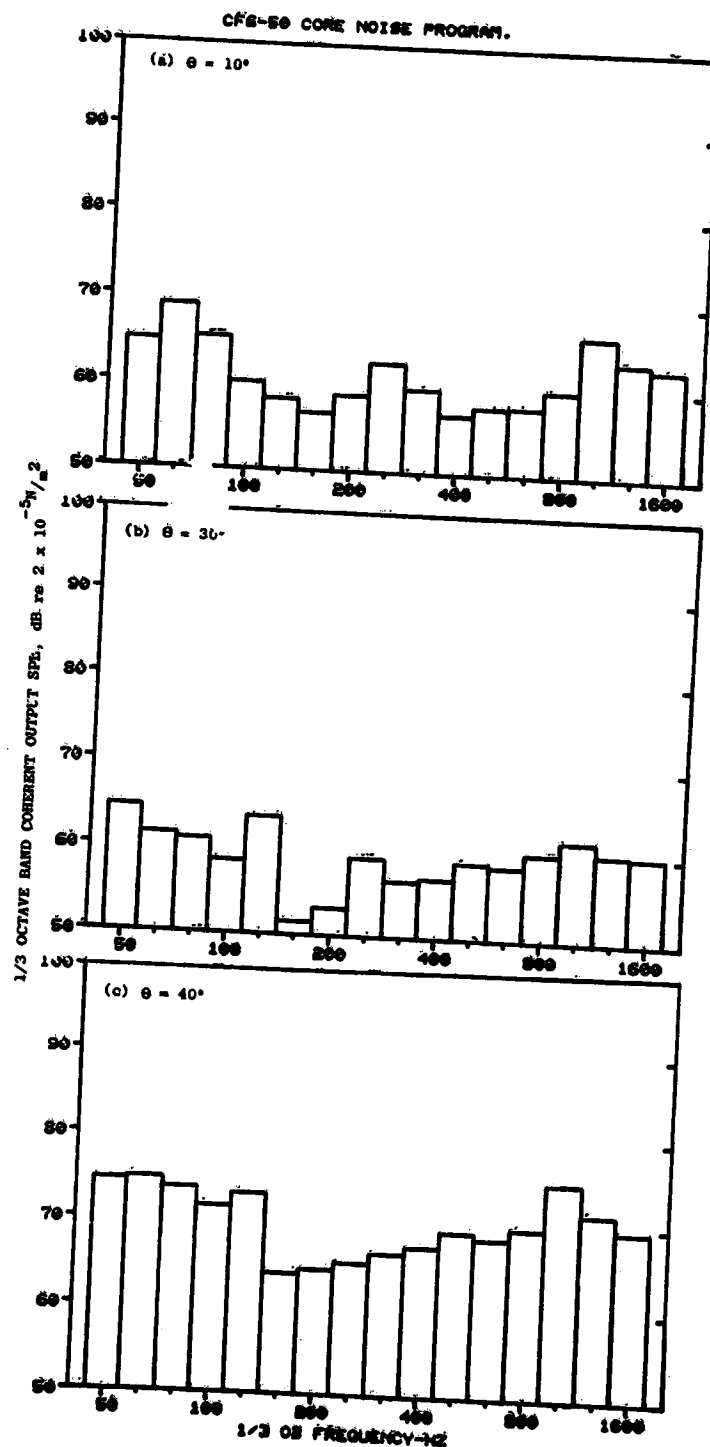


Figure C-2. Coherent Output SPL Spectra from Plane 3.5 (102°) to Farfield Microphones at 15.0% Thrust.

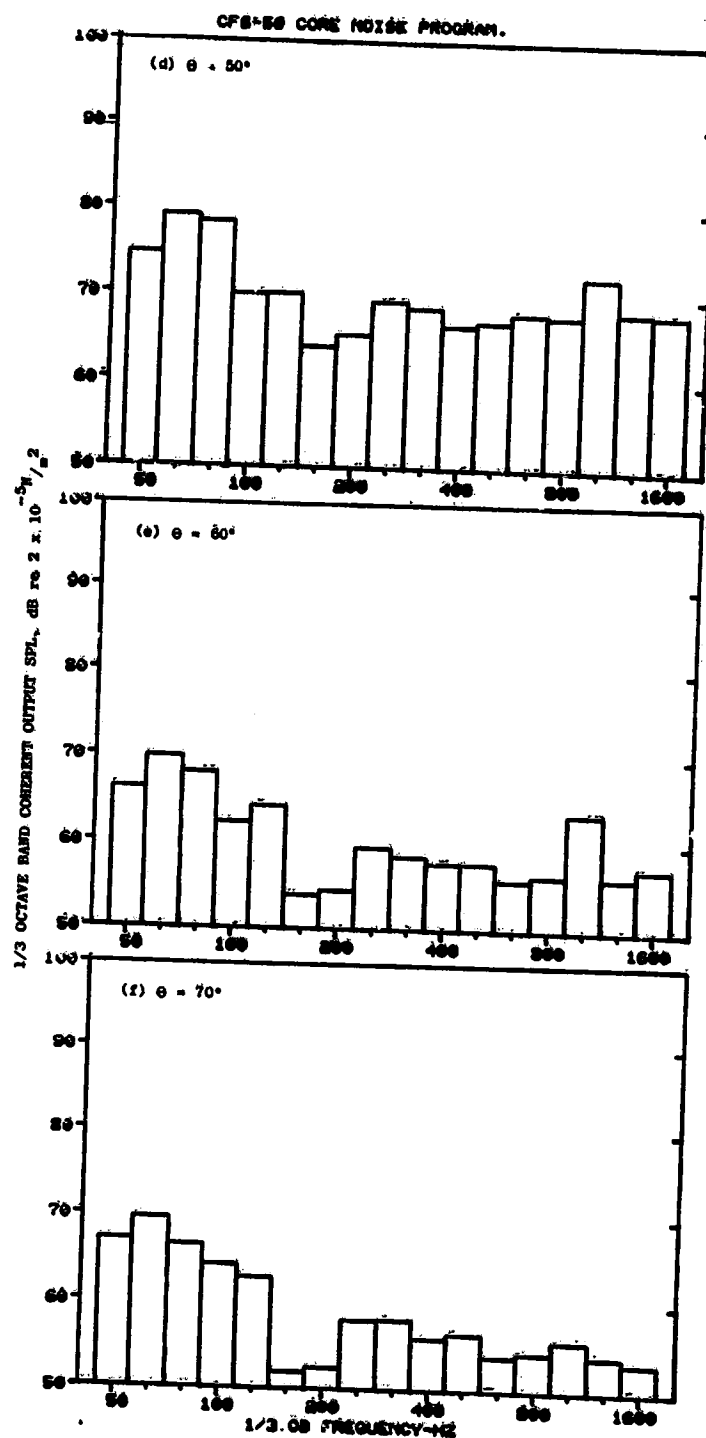


Figure C-2. Coherent Output SPL Spectra from Plane 3.5 (102°) to Farfield Microphones at 15.0% Thrust (Continued).

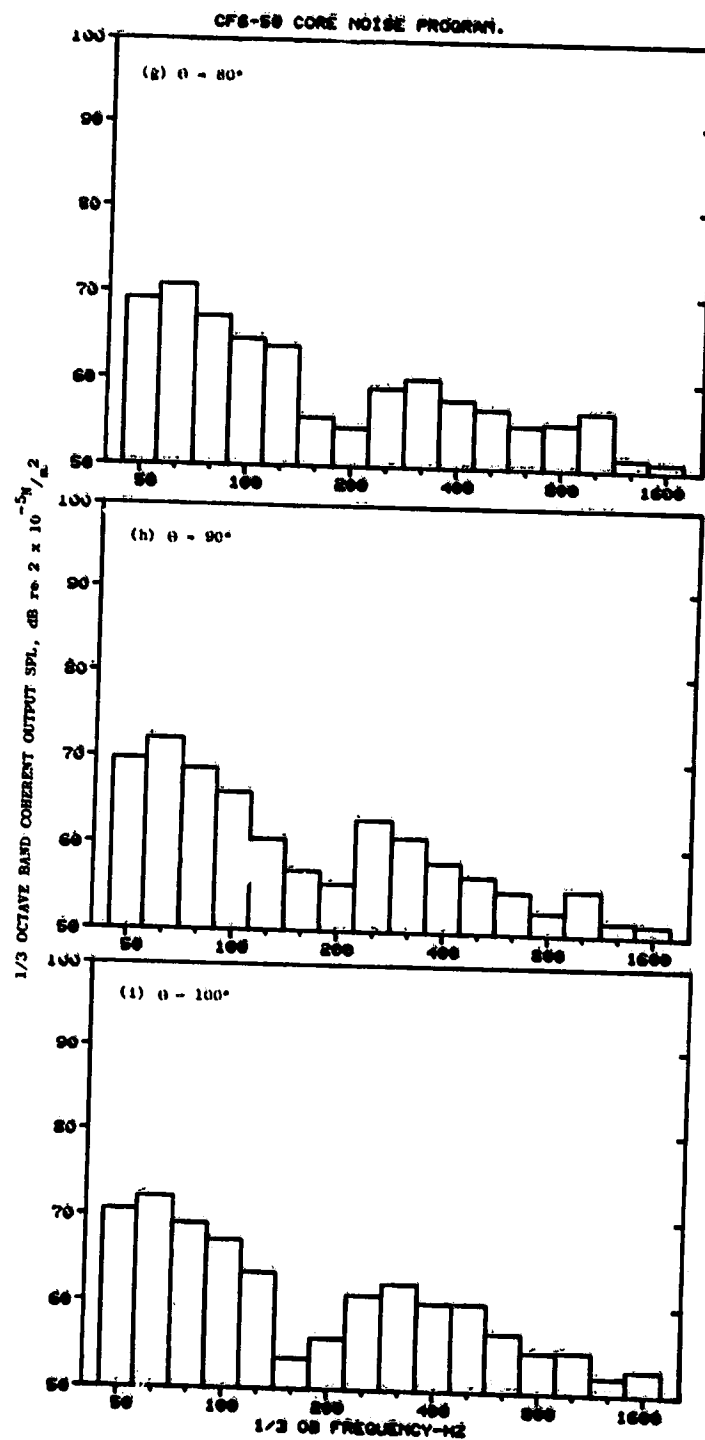


Figure C-2. Coherent Output SPL Spectra from Plane 3.5 (102°) to Farfield Microphones at 15.0% Thrust (Continued).

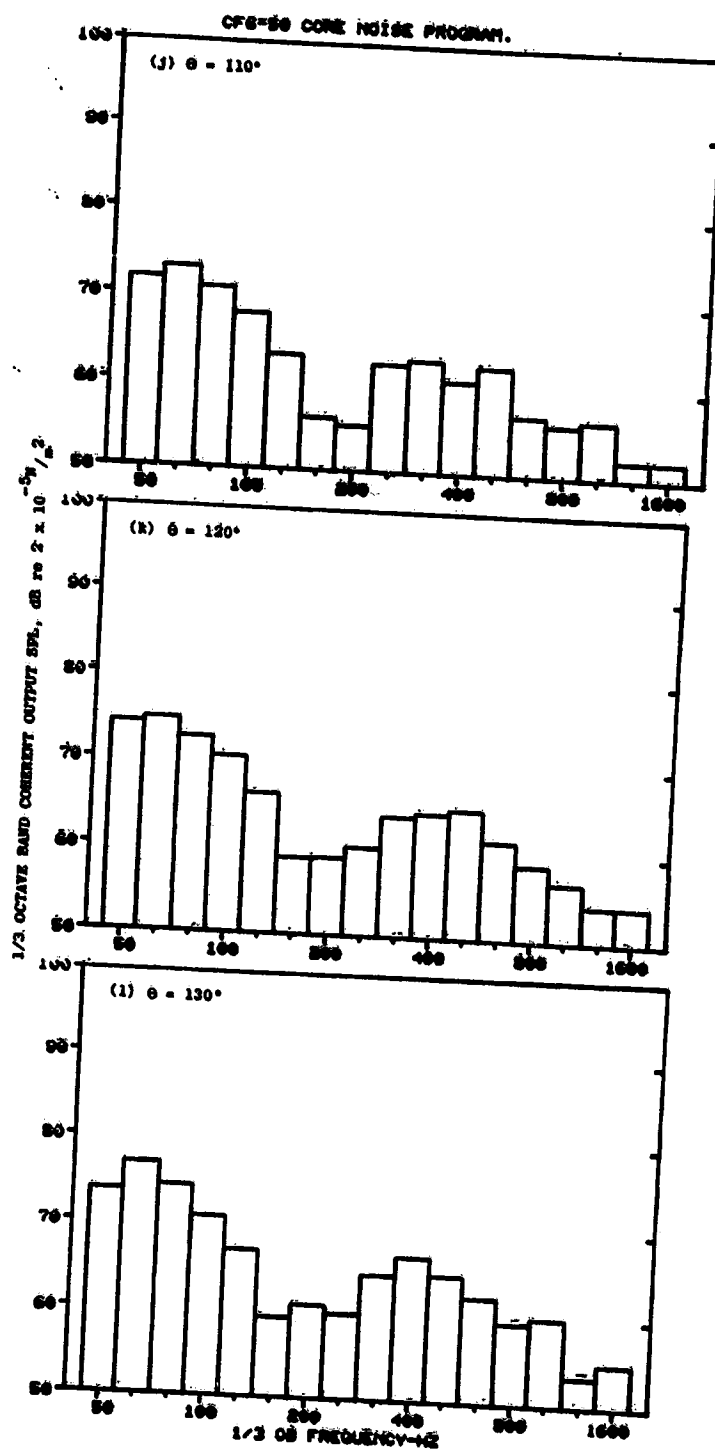


Figure C-2. Coherent Output SPL Spectra from Plane 3.5 (102°) to Farfield Microphones at 15.0% Thrust (Continued).

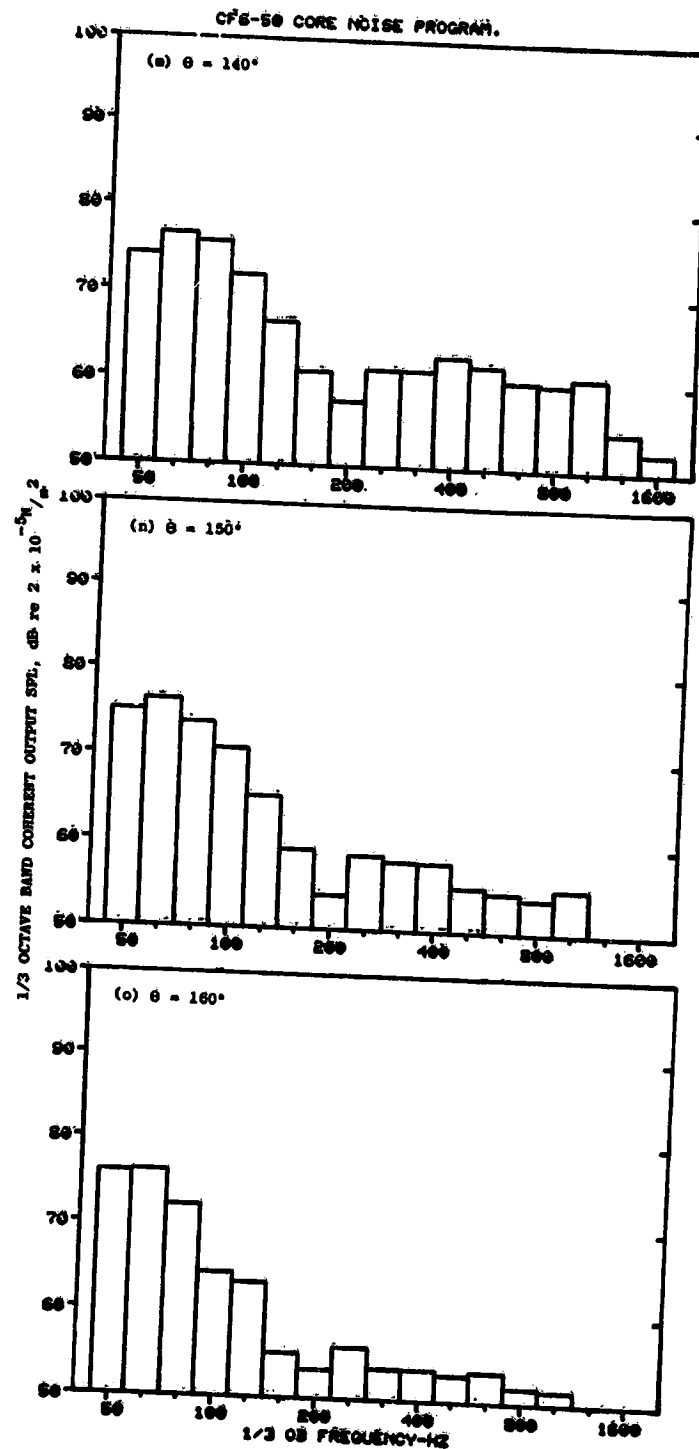


Figure C-2. Coherent Output SPL Spectra from Plane 3.5 (102°) to Farfield Microphones at 15.0% Thrust (Concluded).

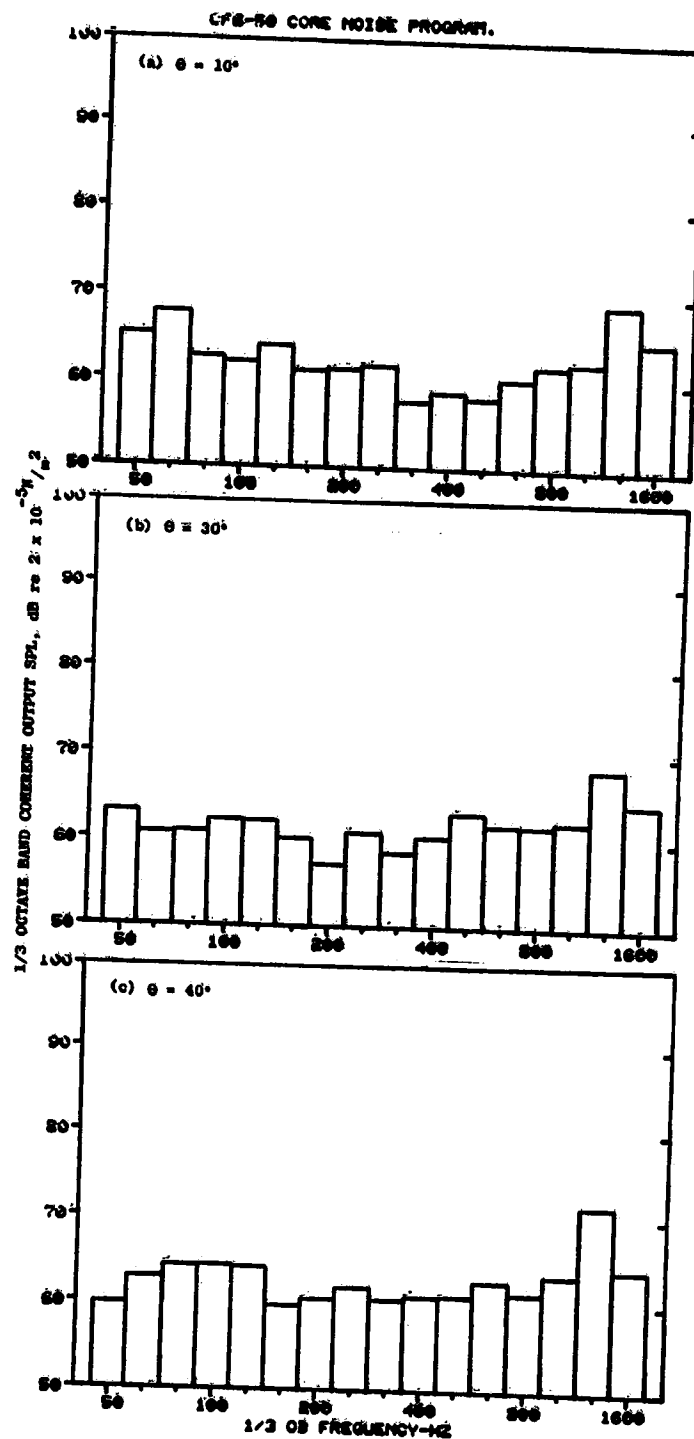


Figure C-3. Coherent Output SPL Spectra from Plane 3.5 (102°) to Farfield Microphones at 22.8% Thrust.

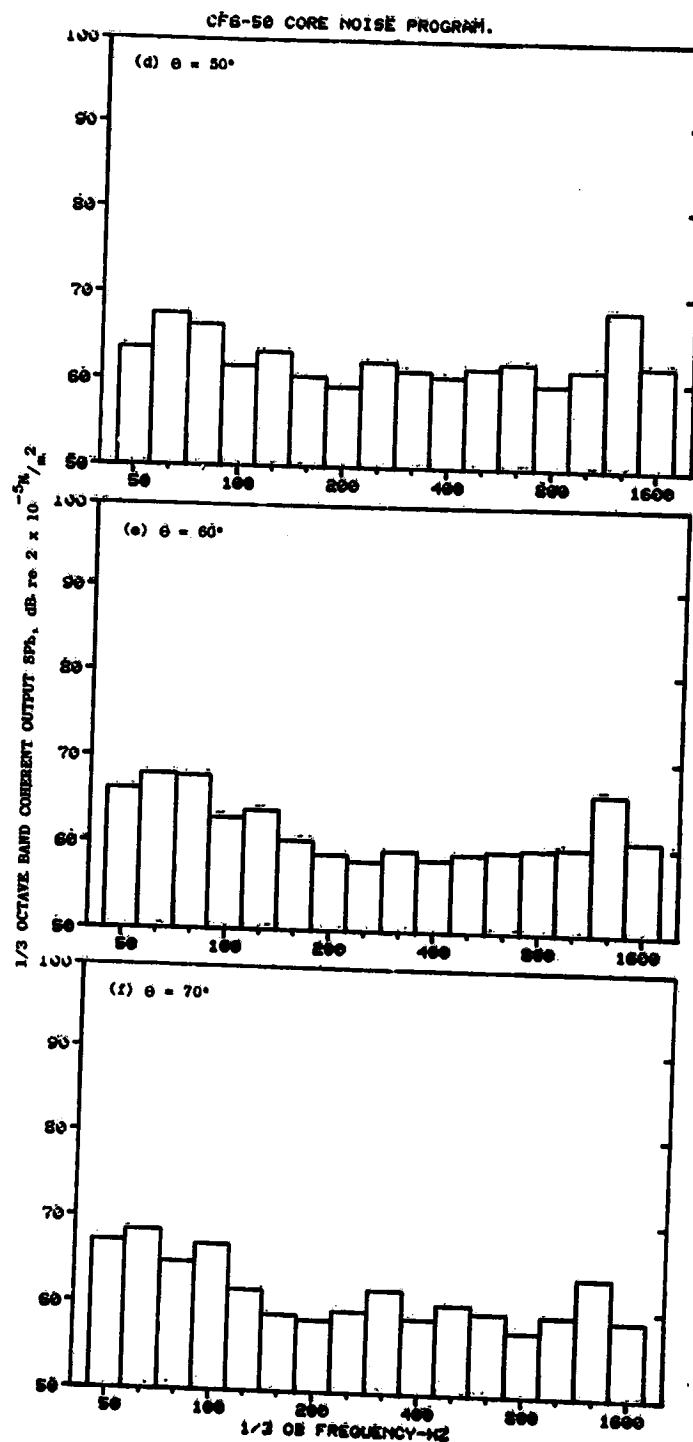


Figure C-3. Coherent Output SPL Spectra from Plane 3.5 (102°) to Farfield Microphones at 22.8% Thrust (Continued).

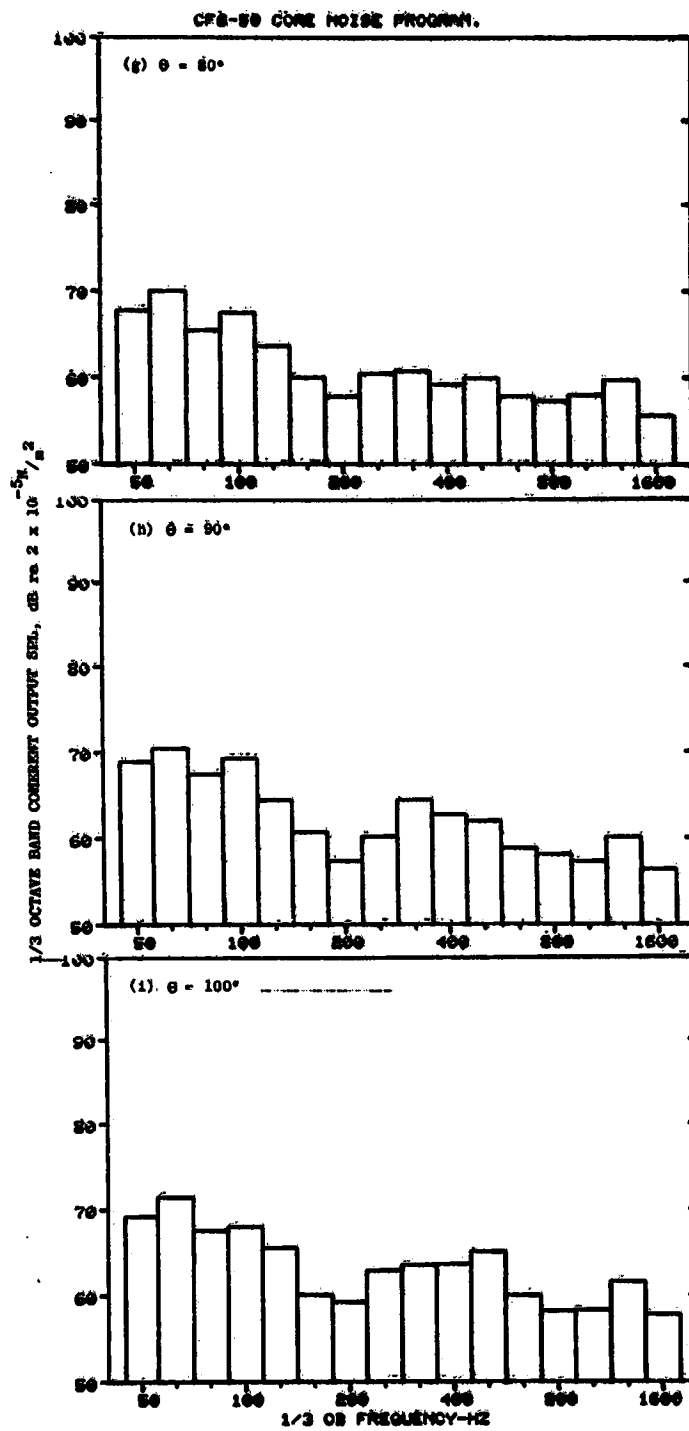


Figure C-3. Coherent Output SPL Spectra from Plane 3.5 (102°) to Farfield Microphones at 22.8% Thrust (Continued).

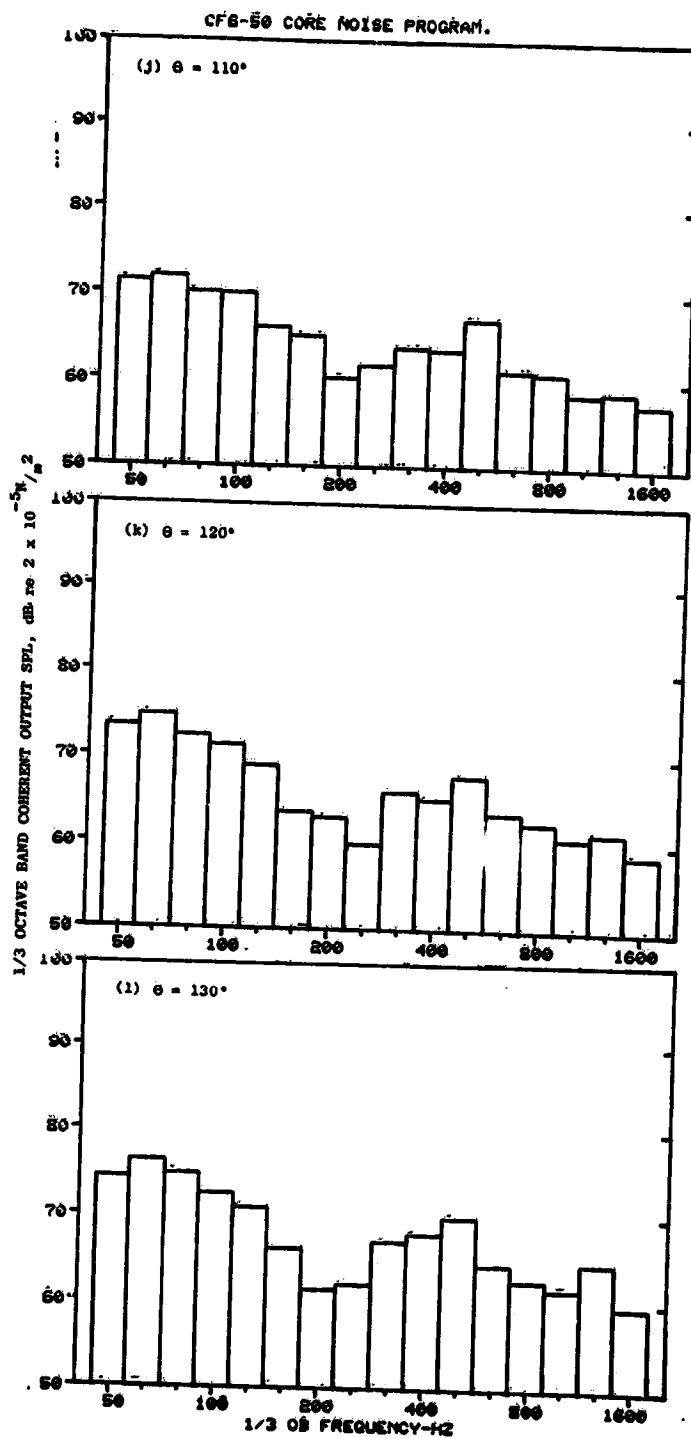


Figure G-3. Coherent Output SPL Spectra from Plane 3.5 (102°) to Farfield Microphones at 22.8% Thrust (Continued).

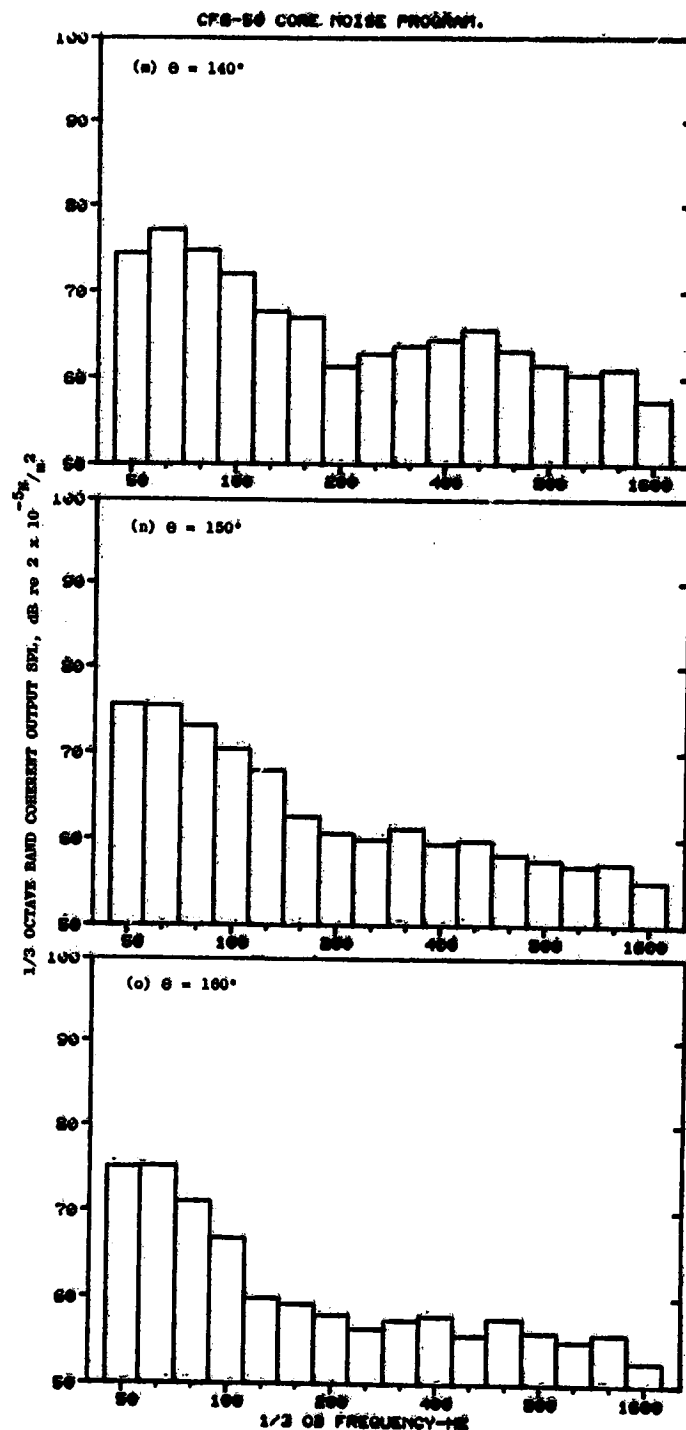


Figure C-3. Coherent Output SPL Spectra from Plane 3.5 (102°) to Farfield Microphones at 22.8% Thrust (Concluded).

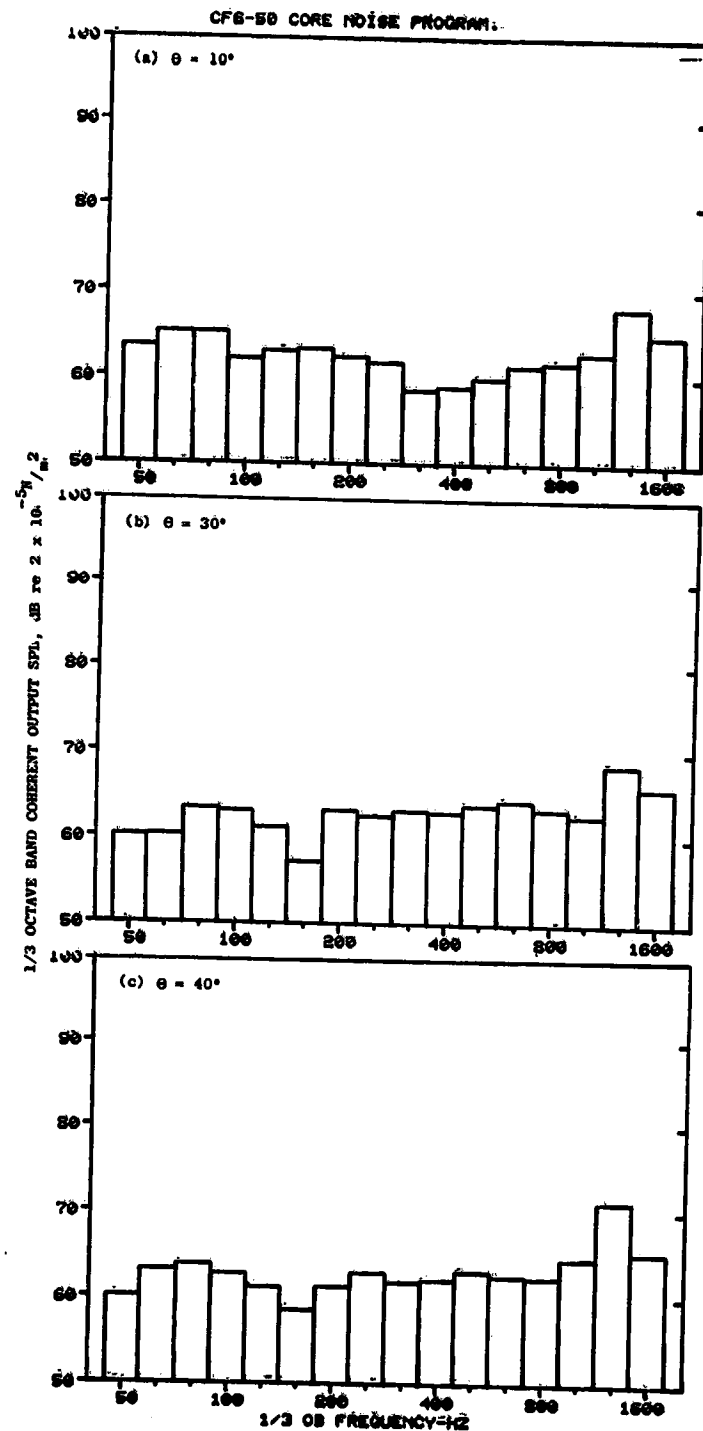


Figure C-4. Coherent Output SPL Spectra from Plane 3.5 (102°) to Farfield Microphones at 26.7% Thrust.

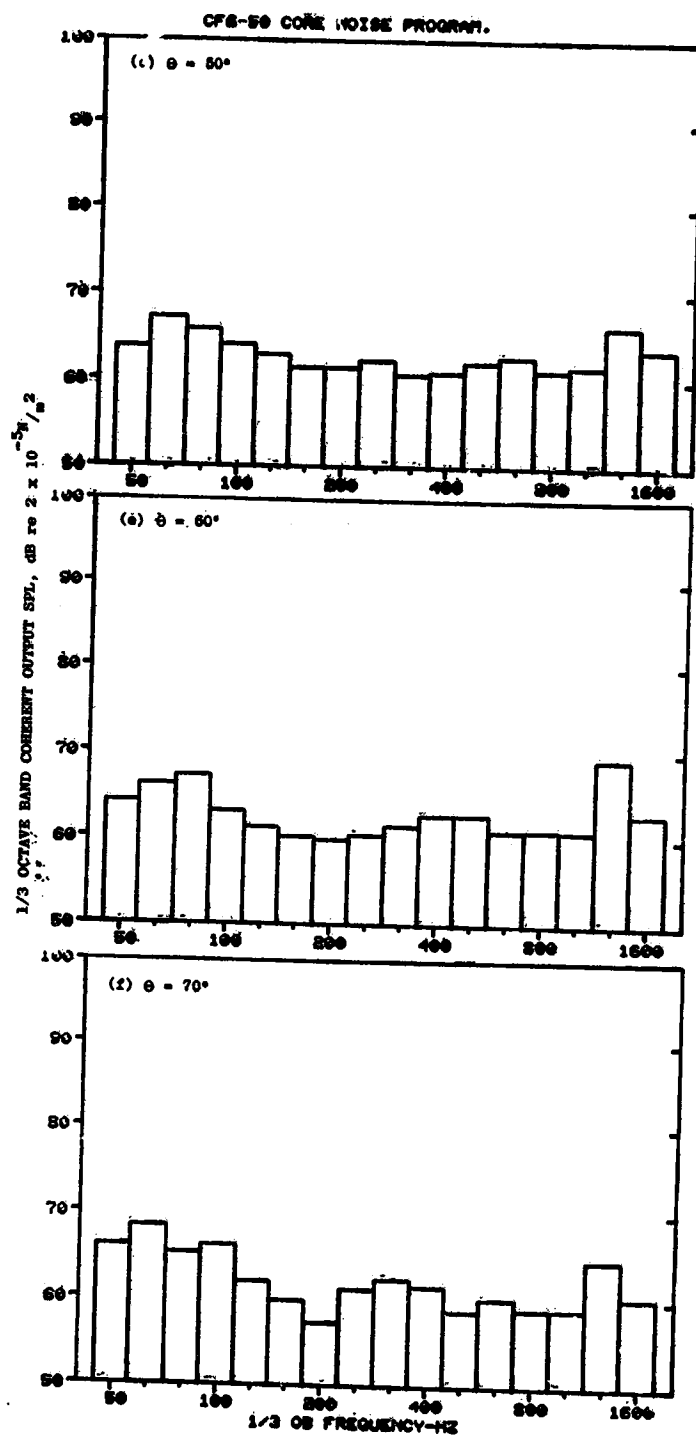


Figure C-4. Coherent Output SPL Spectra from Plane 3.5 (102°) to Farfield Microphones at 26.7% Thrust (Continued).

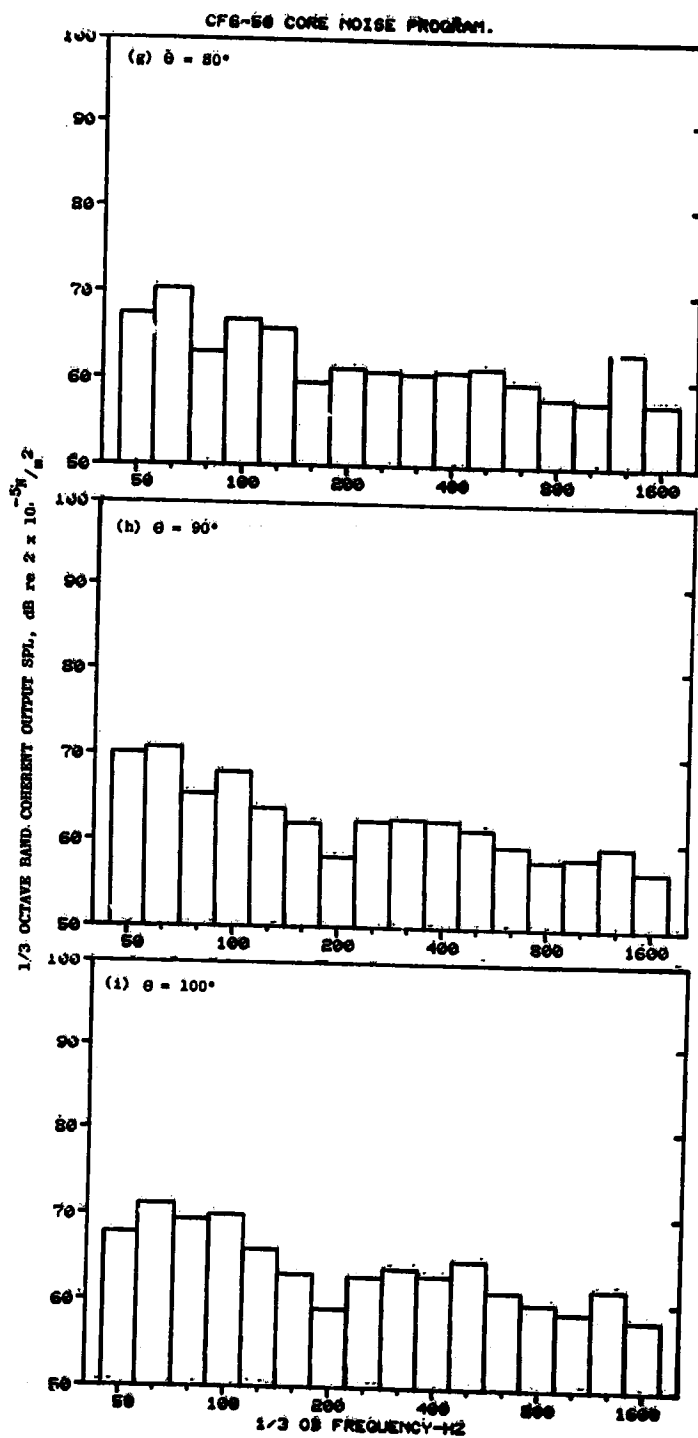


Figure 6-4. Coherent Output SPL Spectra from Plane 3.5 (102°) to Farfield Microphones at 26.7% Thrust (Continued).

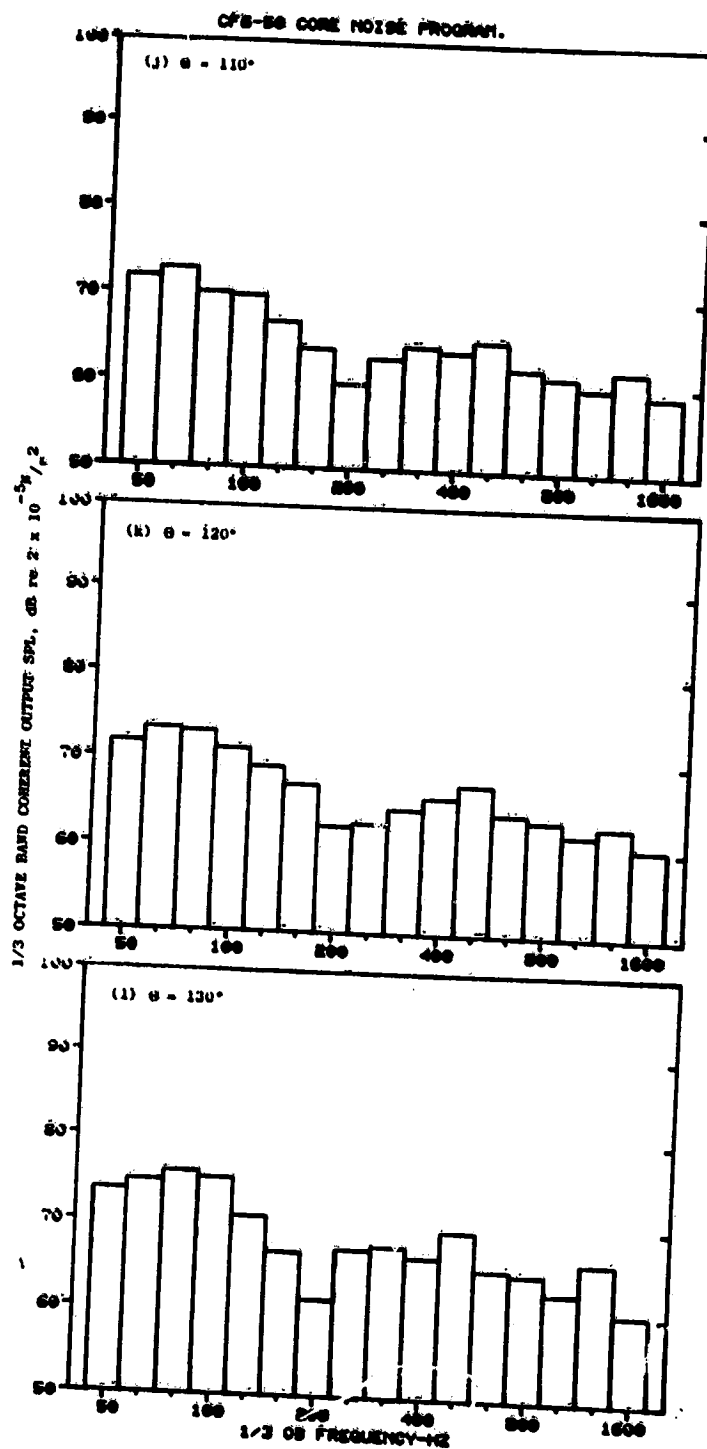


Figure C-4. Coherent Output SPL Spectra from Plane 3.5 (102°) to Farfield Microphones at 26.7% Thrust (Continued).

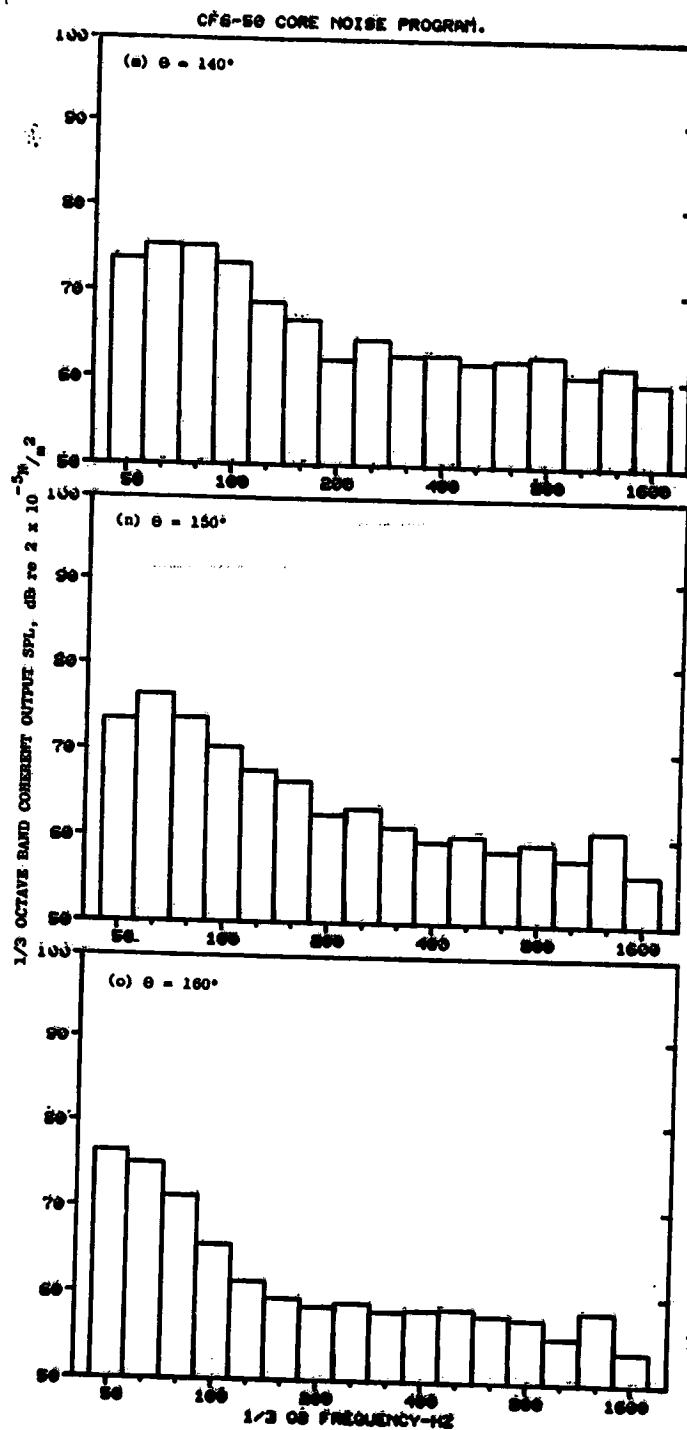


Figure C-4, Coherent Output SPL Spectra from Plane 3.5 (102°) to Farfield Microphones at 26.7% Thrust (Concluded).

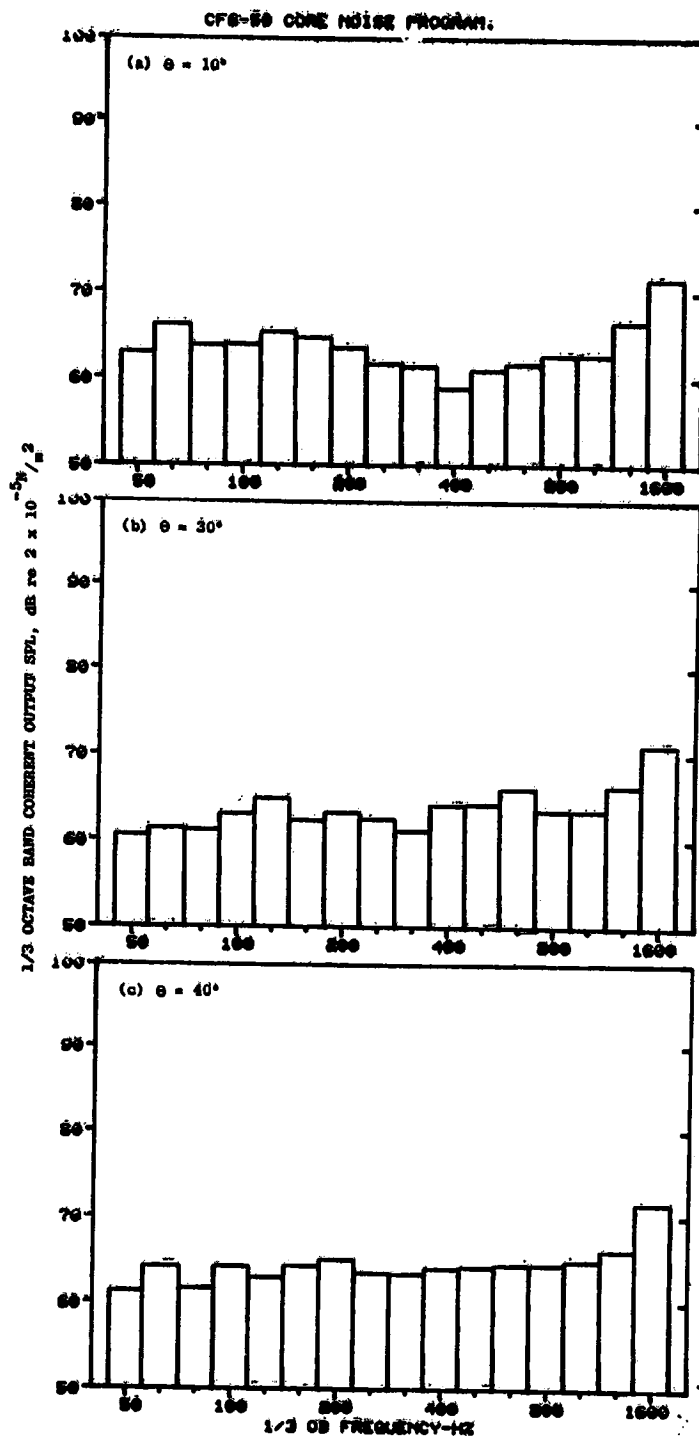


Figure C-5. Coherent Output SPL Spectra from Plane 3.5 (102°) to Farfield Microphones at 30.8% Thrust.

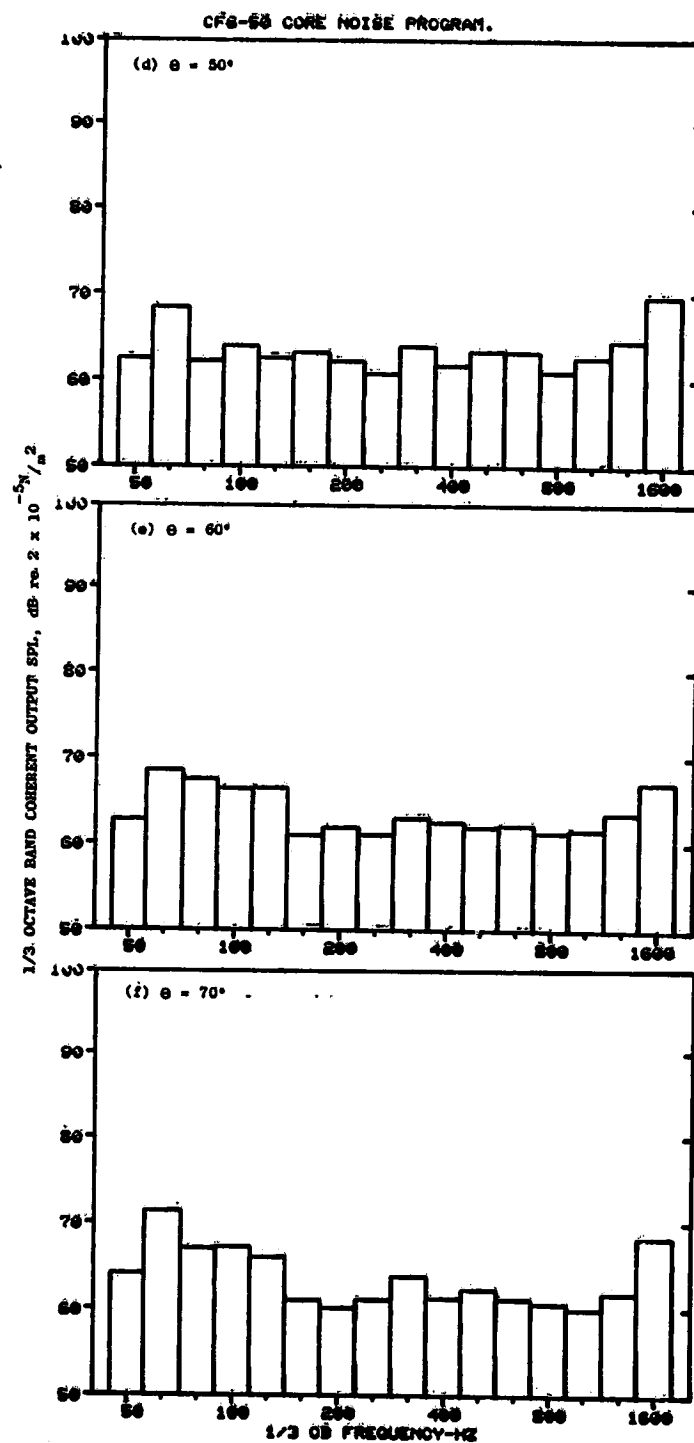


Figure C-5. Coherent Output SPL Spectra from Plane 3.5 (102°) to Farfield Microphones at 30.8% Thrust (Continued).

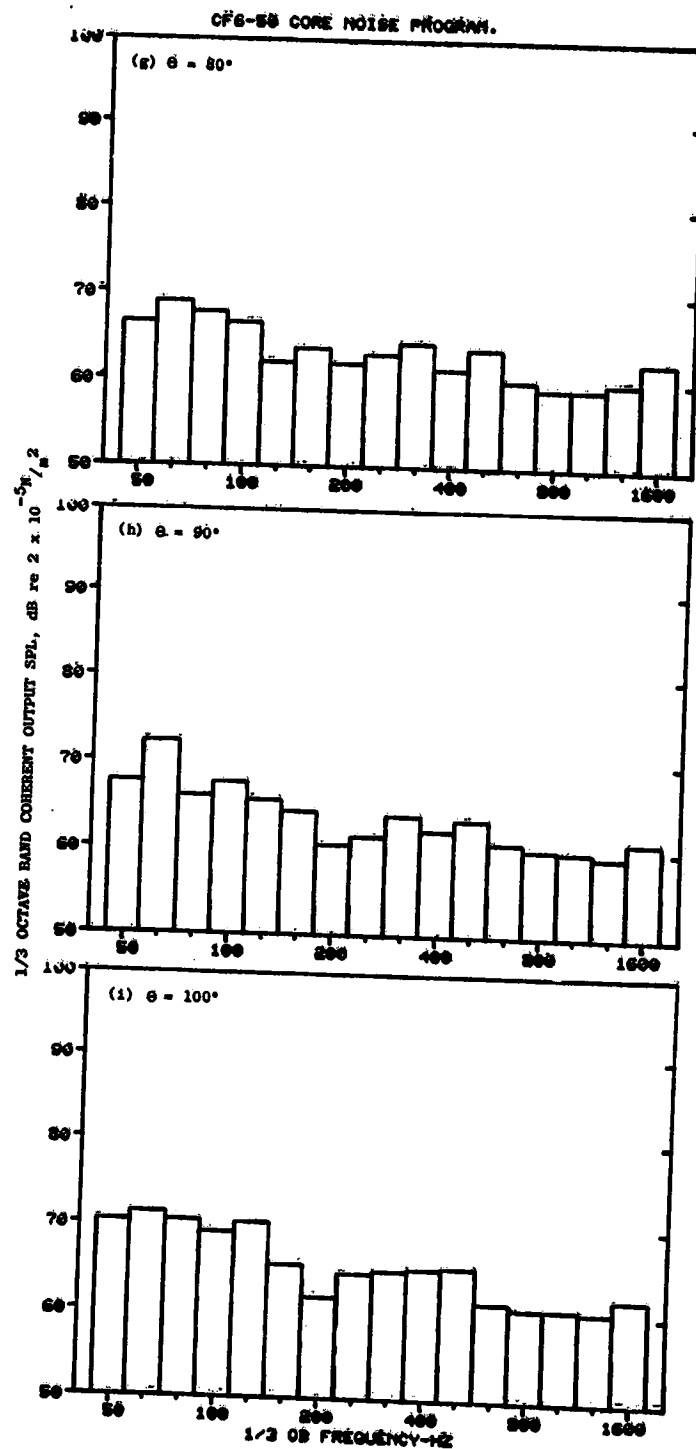


Figure C-5. Coherent Output SPL Spectra from Plane 3.5 (102°) to Farfield Microphones at 30.8% Thrust (Continued).

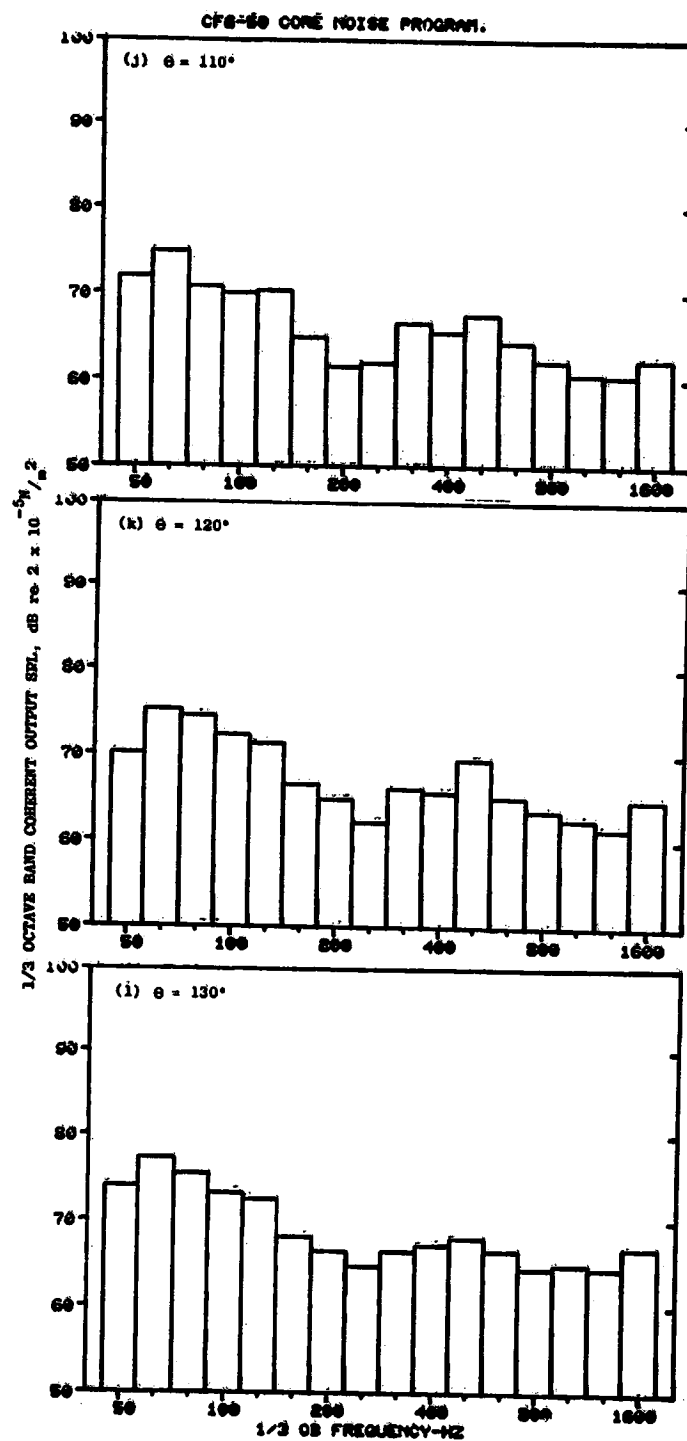


Figure C-5. Coherent Output SPL Spectra from Plane 3.5 (102°) to Farfield Microphones at 30.8% Thrust (Continued).

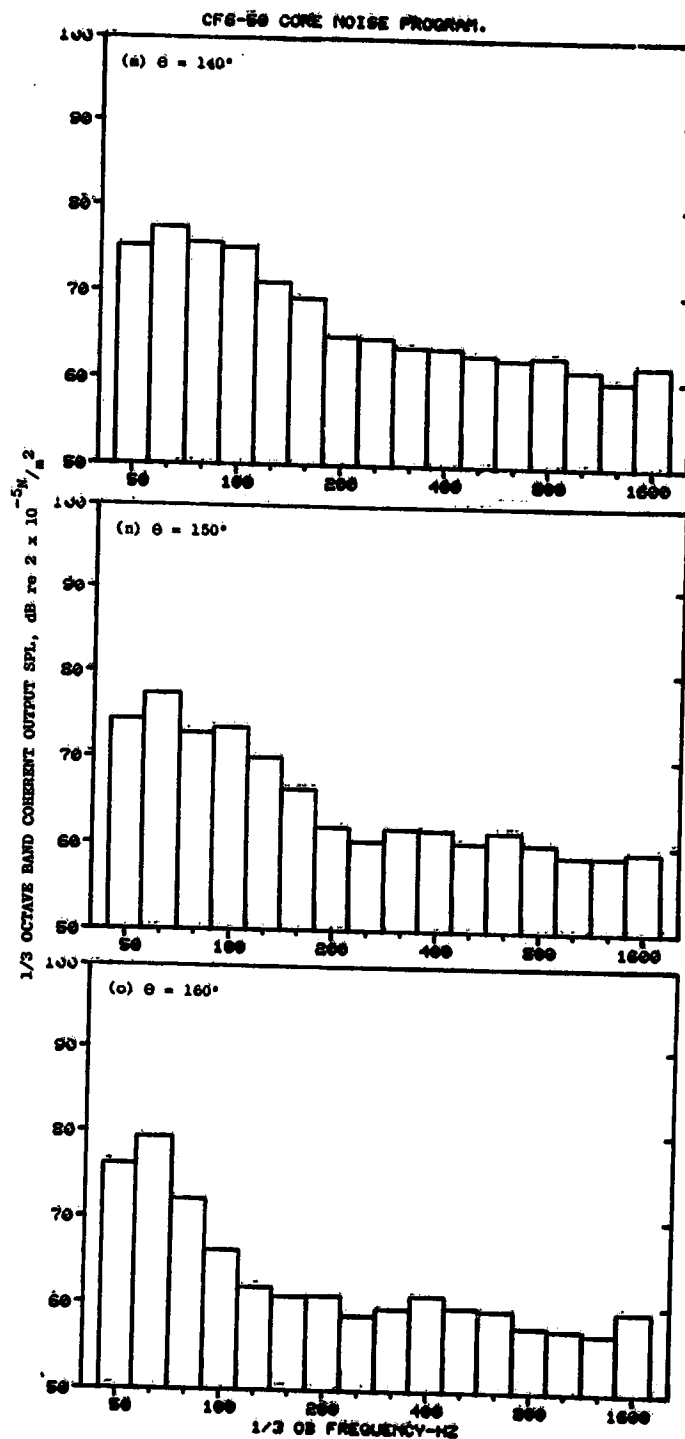


Figure C-5. Coherent Output SPL Spectra from Plane 3.5 (102°) to Farfield Microphones at 30.8% Thrust (Concluded).

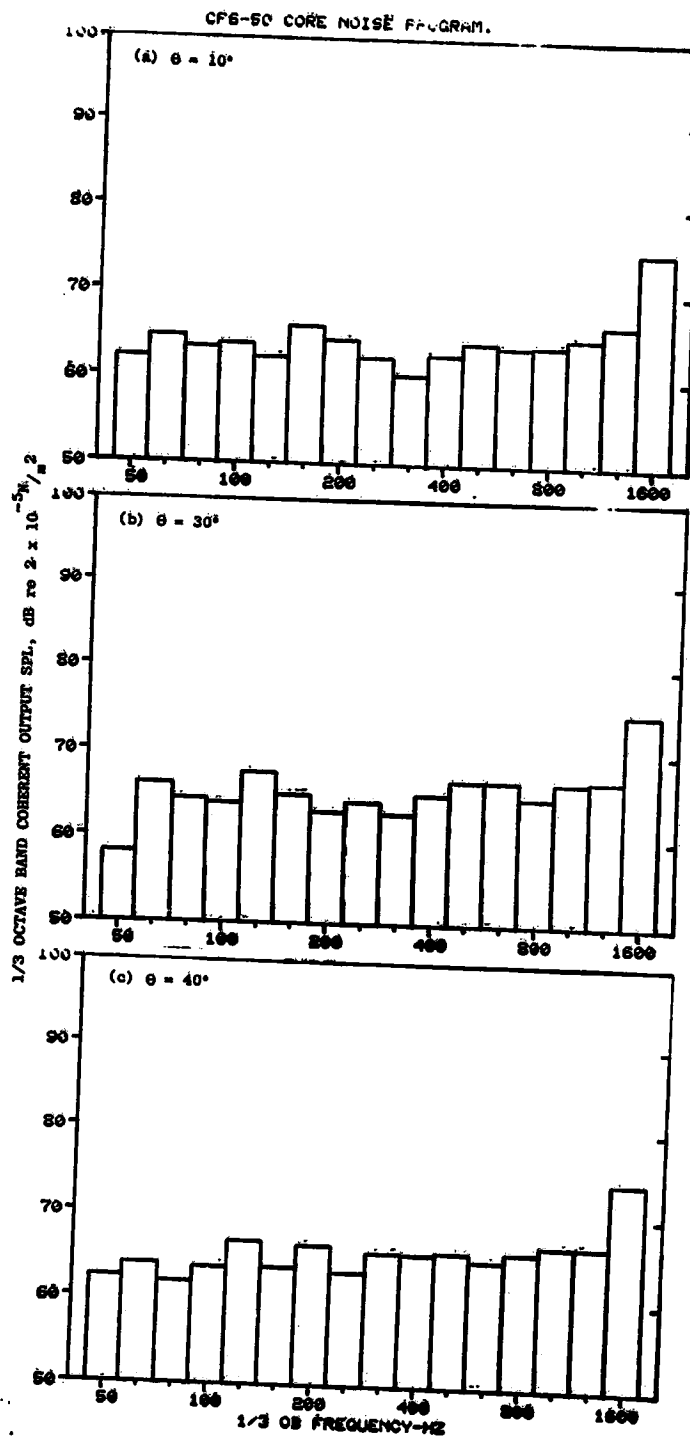


Figure C-6. Coherent Output SPL Spectra from Plane 3.5 (102°) to Farfield Microphones at 36.5% Thrust.

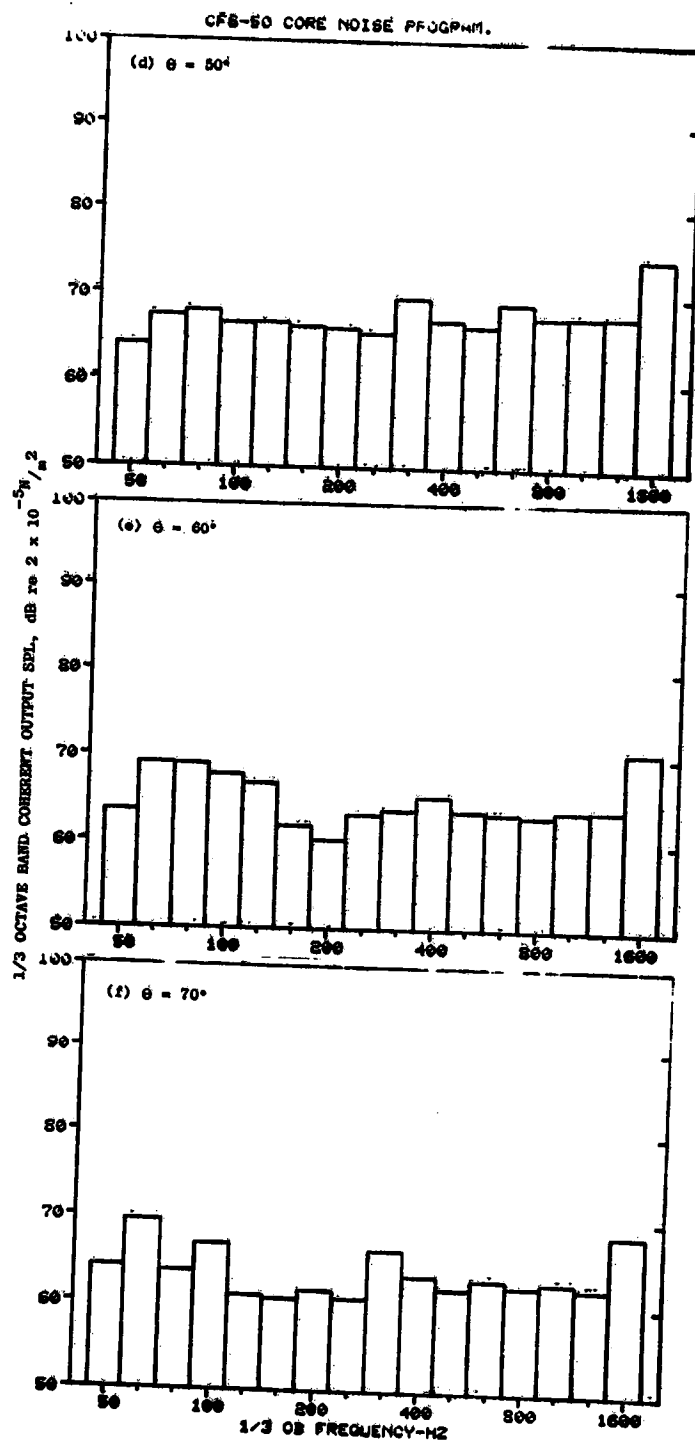


Figure C-6. Coherent Output SPL Spectra from Plane 3.5 (102°) to Farfield Microphones at 36.5% Thrust (Continued).

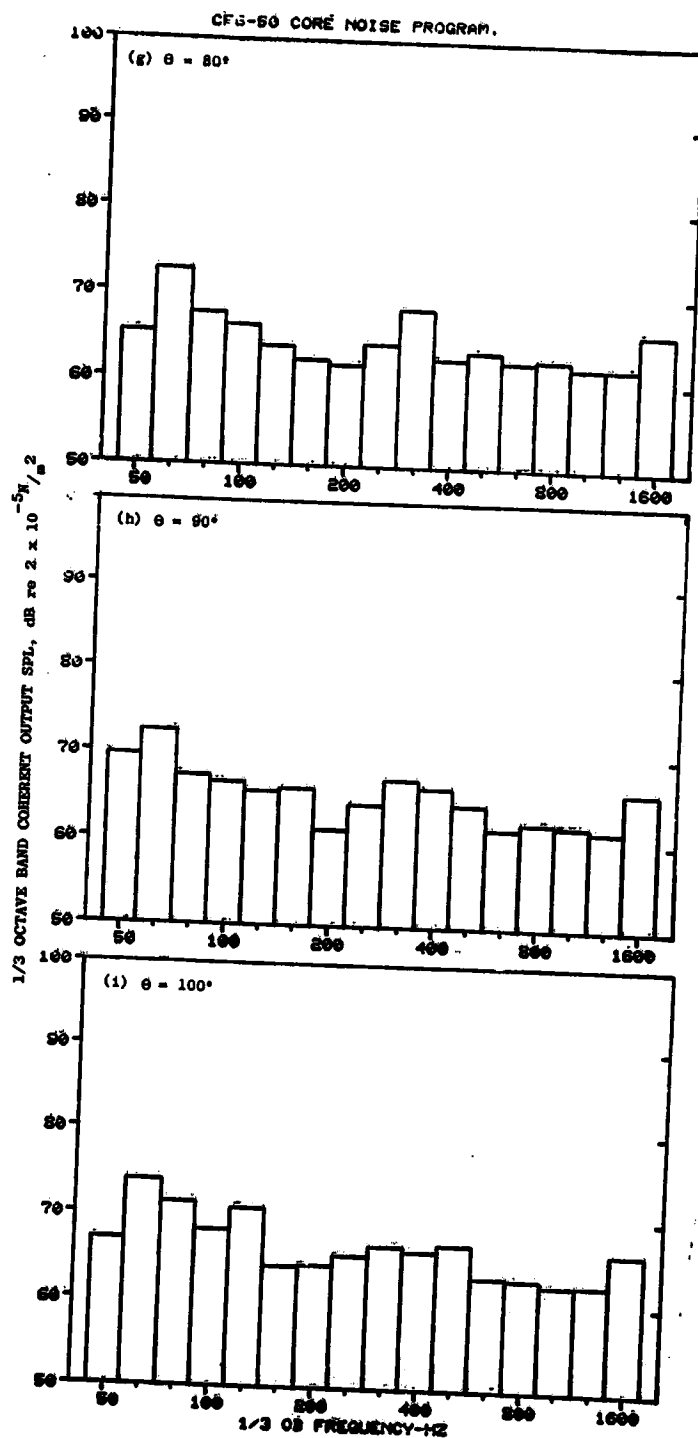


Figure C-6. Coherent Output SPL Spectra from Plane 3.5 (102°) to Farfield Microphones at 36.5% Thrust (Continued).

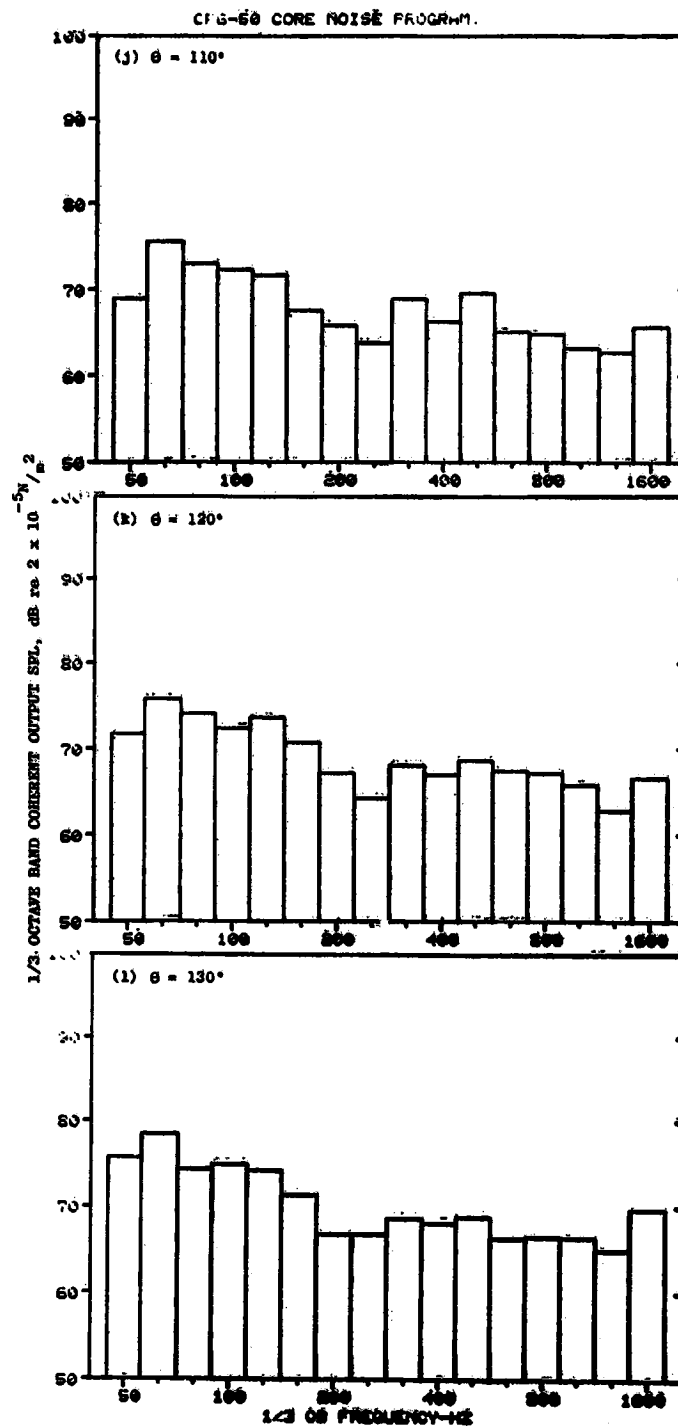


Figure C-6. Coherent Output SPL Spectra from Plane 3.5 (102°) to Farfield Microphones at 36.5% Thrust (Continued).

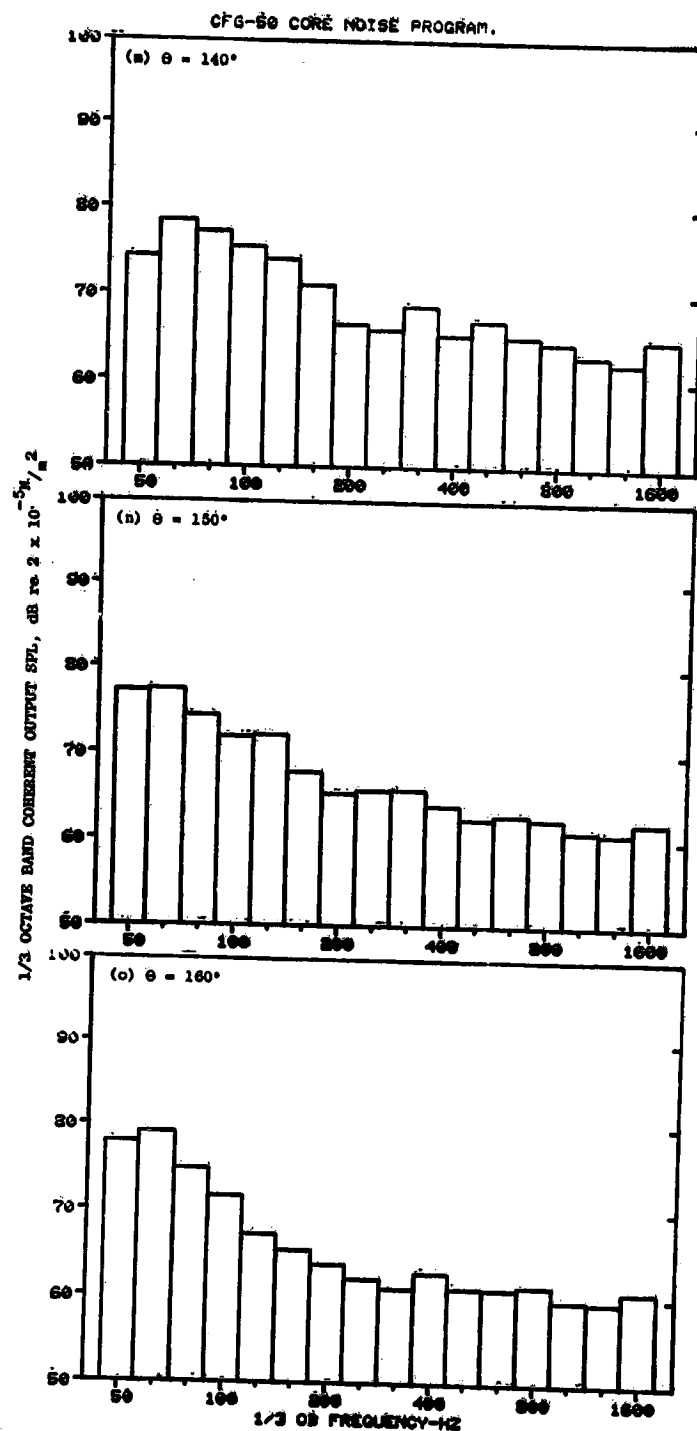


Figure C-6. Coherent Output SPL Spectra from Plane 3.5 (102°) to Farfield Microphones at 36.5% Thrust (Concluded).

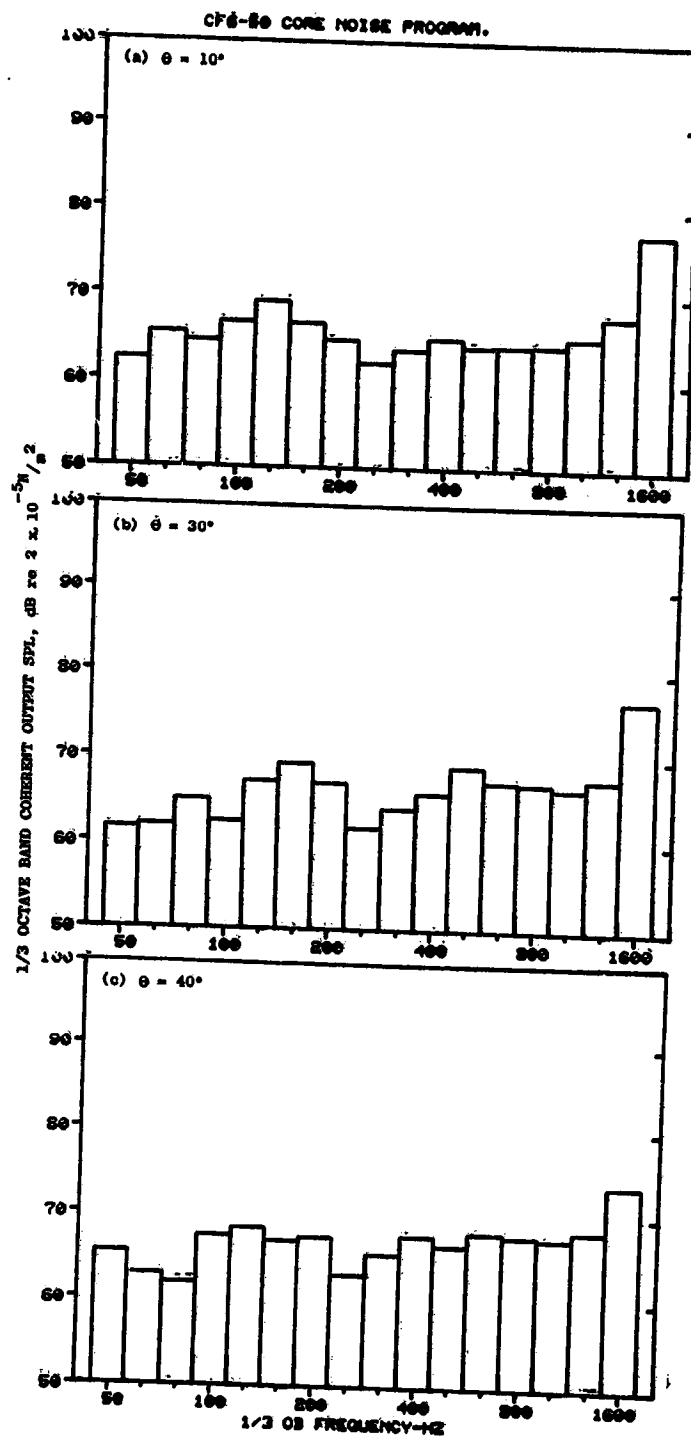


Figure C-7. Coherent Output SPL Spectra from Plane 3.5 (102°) to Farfield Microphones at 45.5% Thrust.

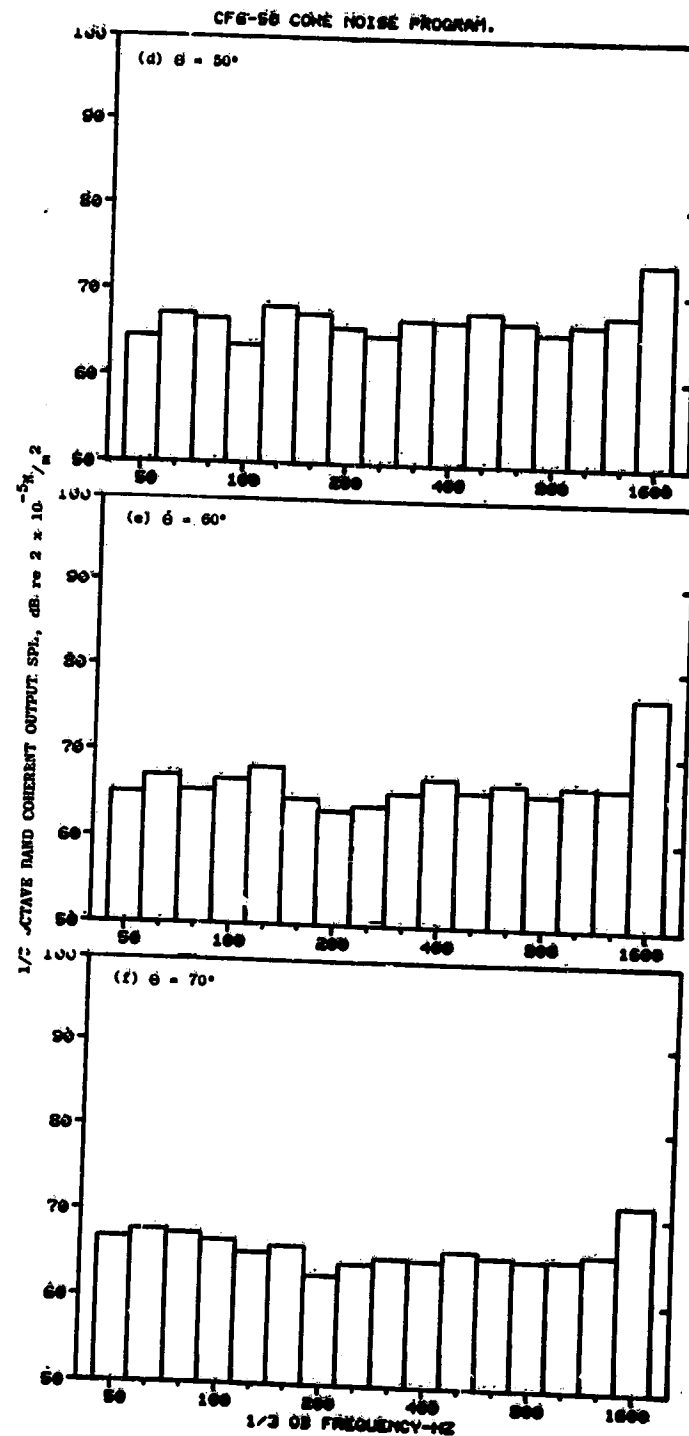


Figure C-7. Coherent Output SPL Spectra from Plane 3.5 (102°) to Farfield Microphones at 45.5% Thrust (Continued).

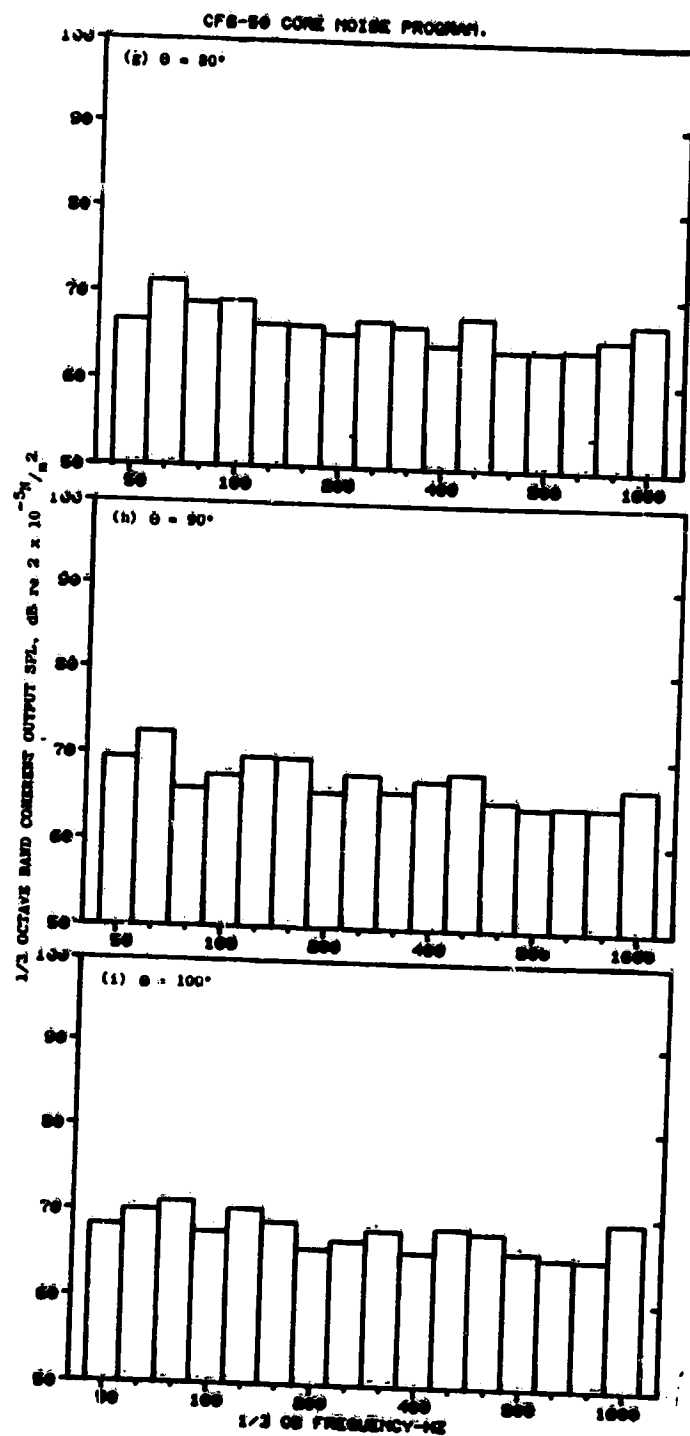


Figure C-7. Coherent Output SPL Spectra from Plane 3.5 (102°) to Farfield Microphones at 45.5% Thrust (Continued).

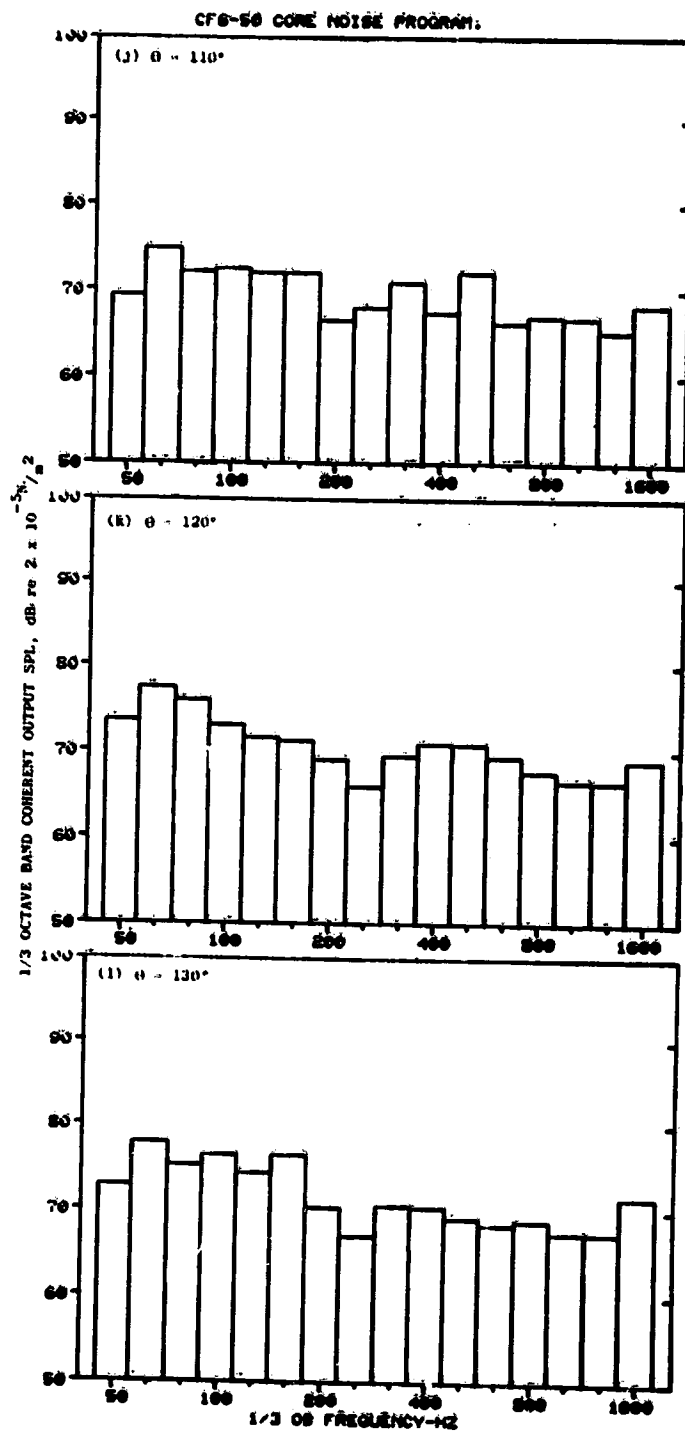


Figure C-7. Coherent Output SPL Spectra from Plane 3.5 (102°) to Farfield Microphones at 45.5% Thrust (Continued).

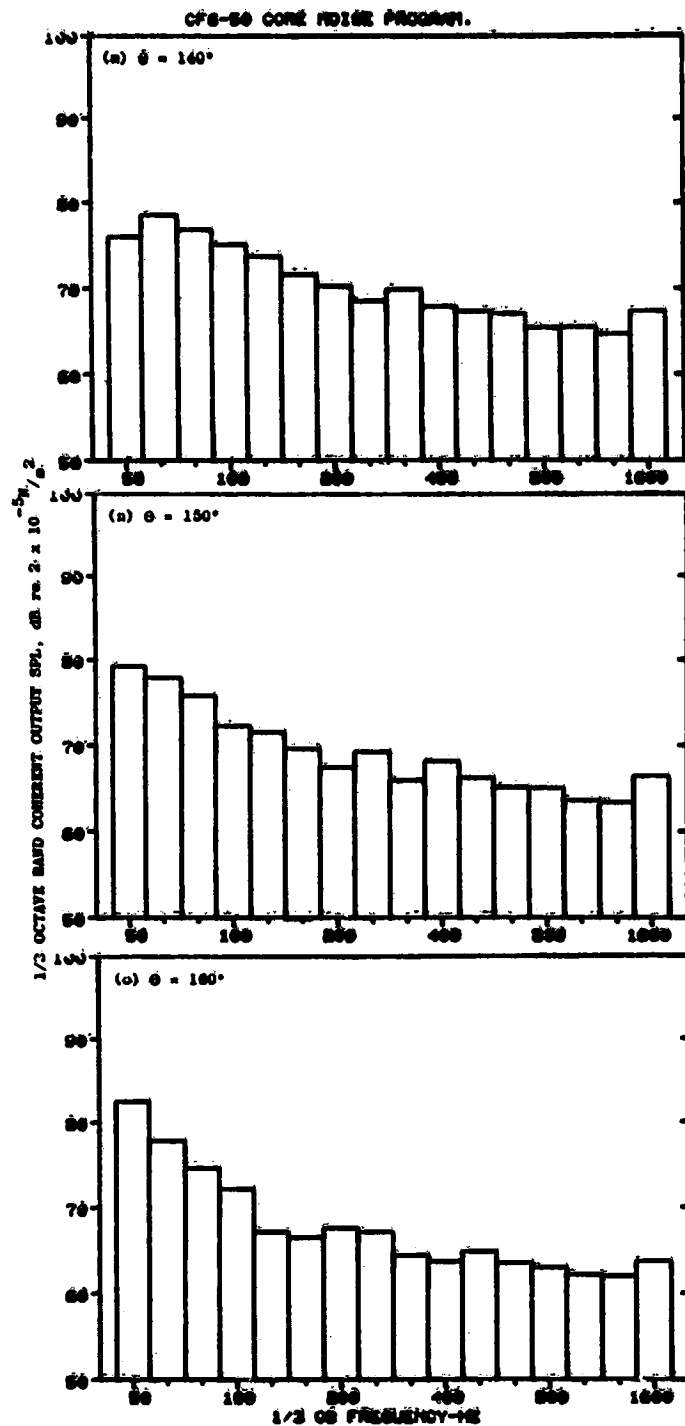


Figure C-7. Coherent Output SPL Spectra from Plane 3.5 (102°) to Farfield Microphones at 45.5% Thrust (Concluded).

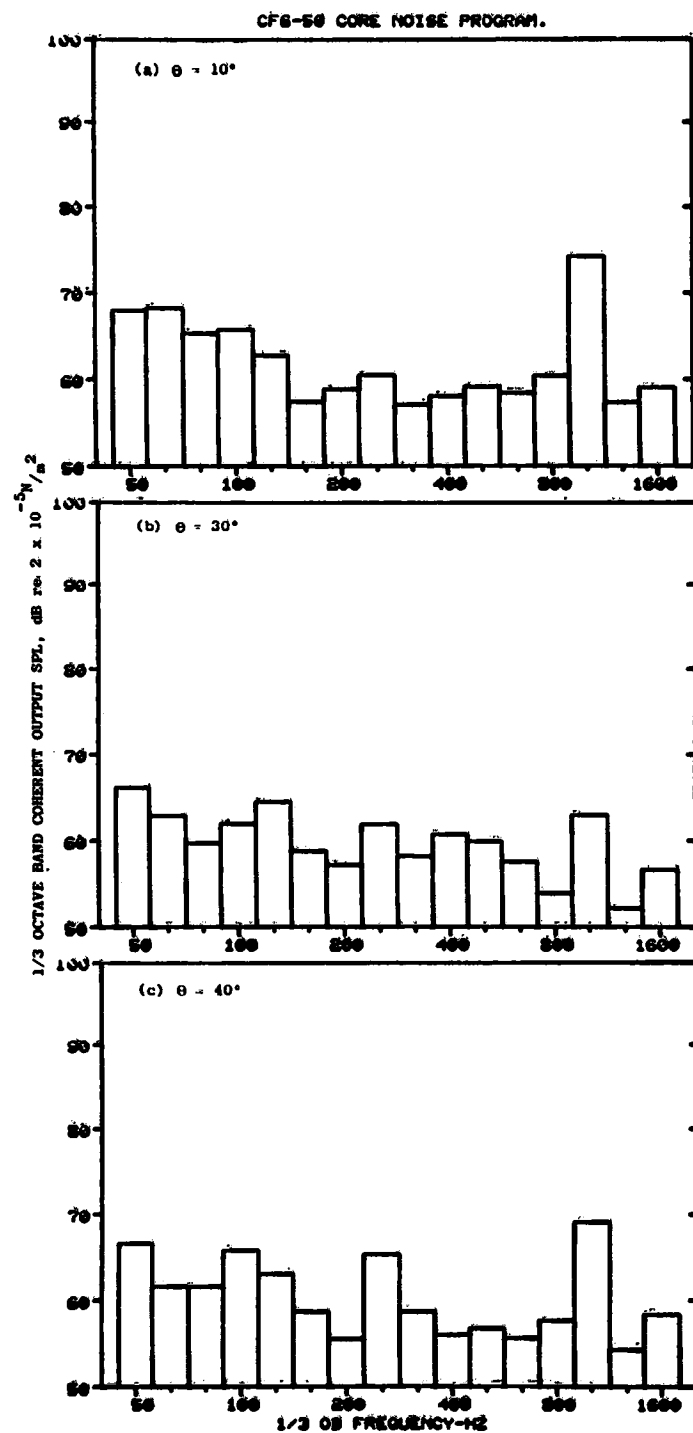


Figure C-8. Coherent Output SPL Spectra from Plane 8.0A (270°) to Farfield Microphones at 3.8% Thrust.

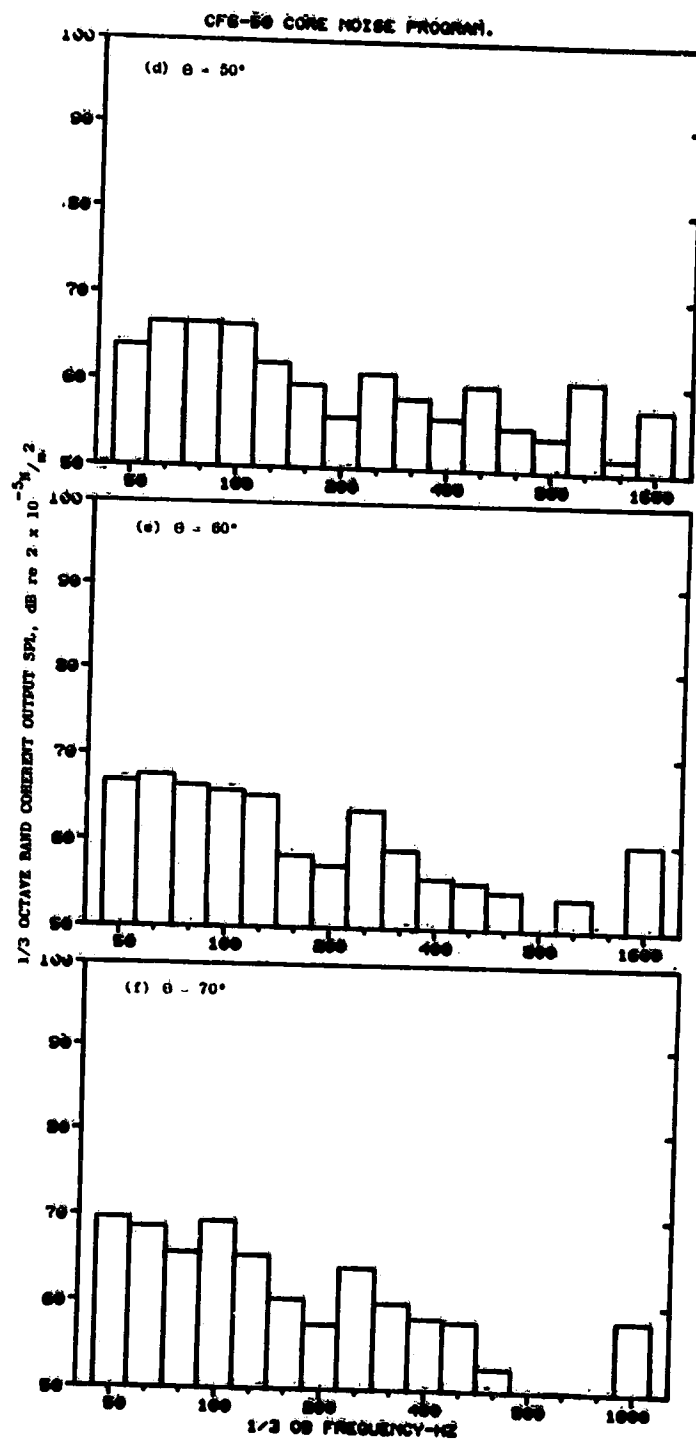


Figure C-8. Coherent Output SPL Spectra from Plane 8.0A (270°) to Farfield Microphones at 3.8% Thrust (Continued).

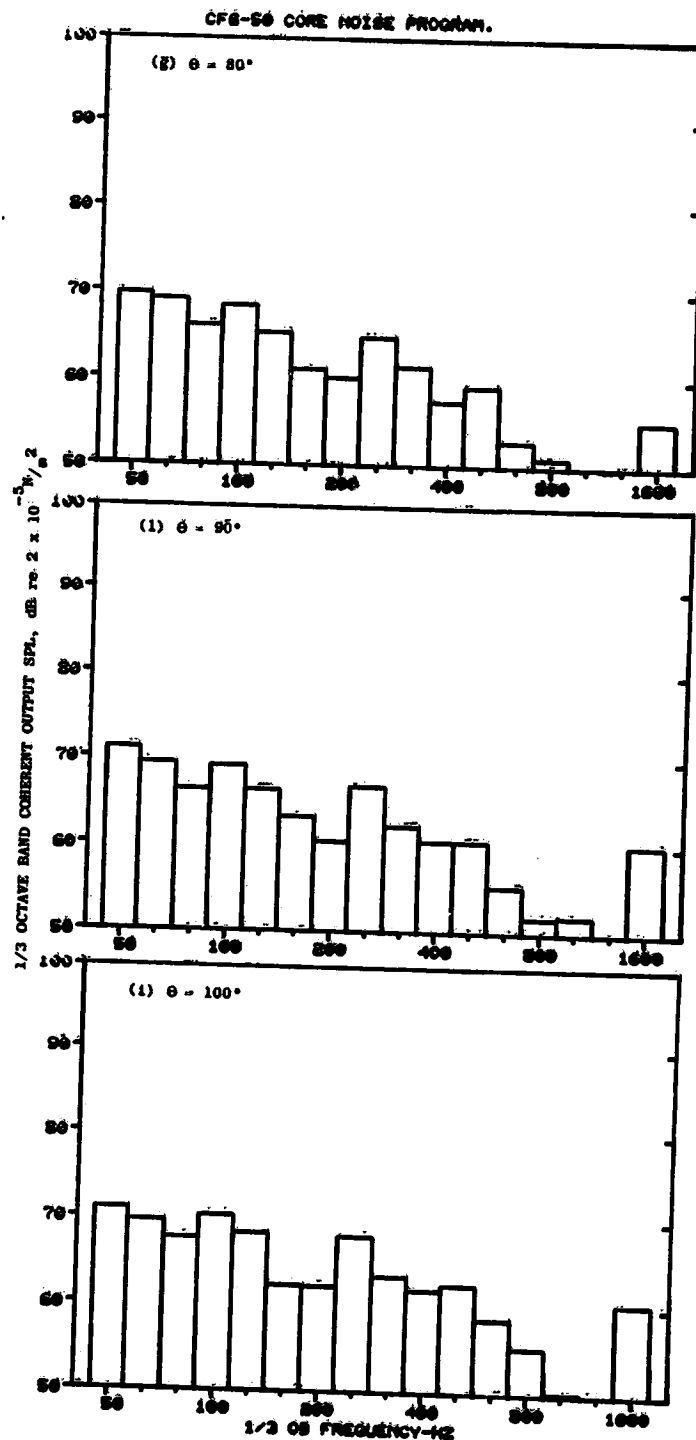


Figure C-8. Coherent Output SPL Spectra from Plane 8.0A (270°) to Farfield Microphones at 3.8% Thrust (Continued).

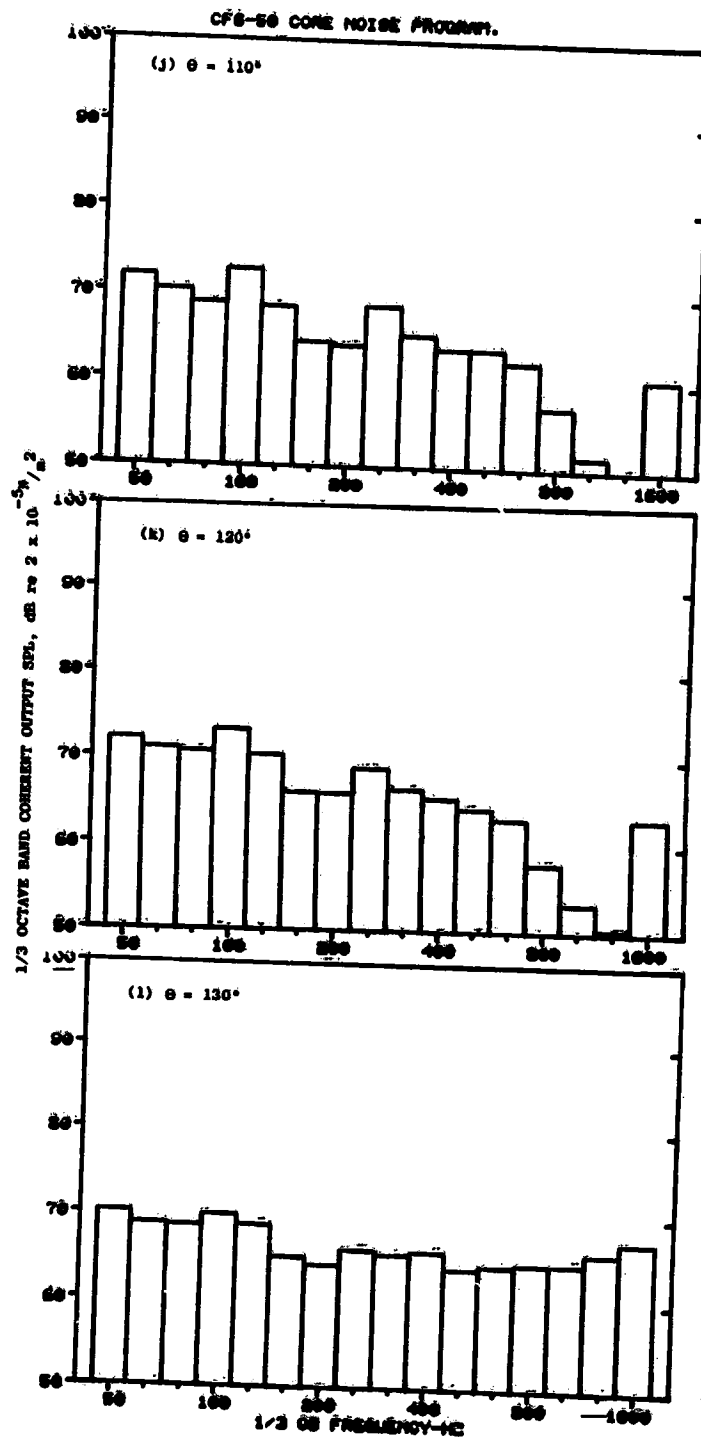


Figure C-8. Coherent Output SPL Spectra from Plane 8.0A (270°) to Farfield Microphones at 3.8% Thrust (Continued).

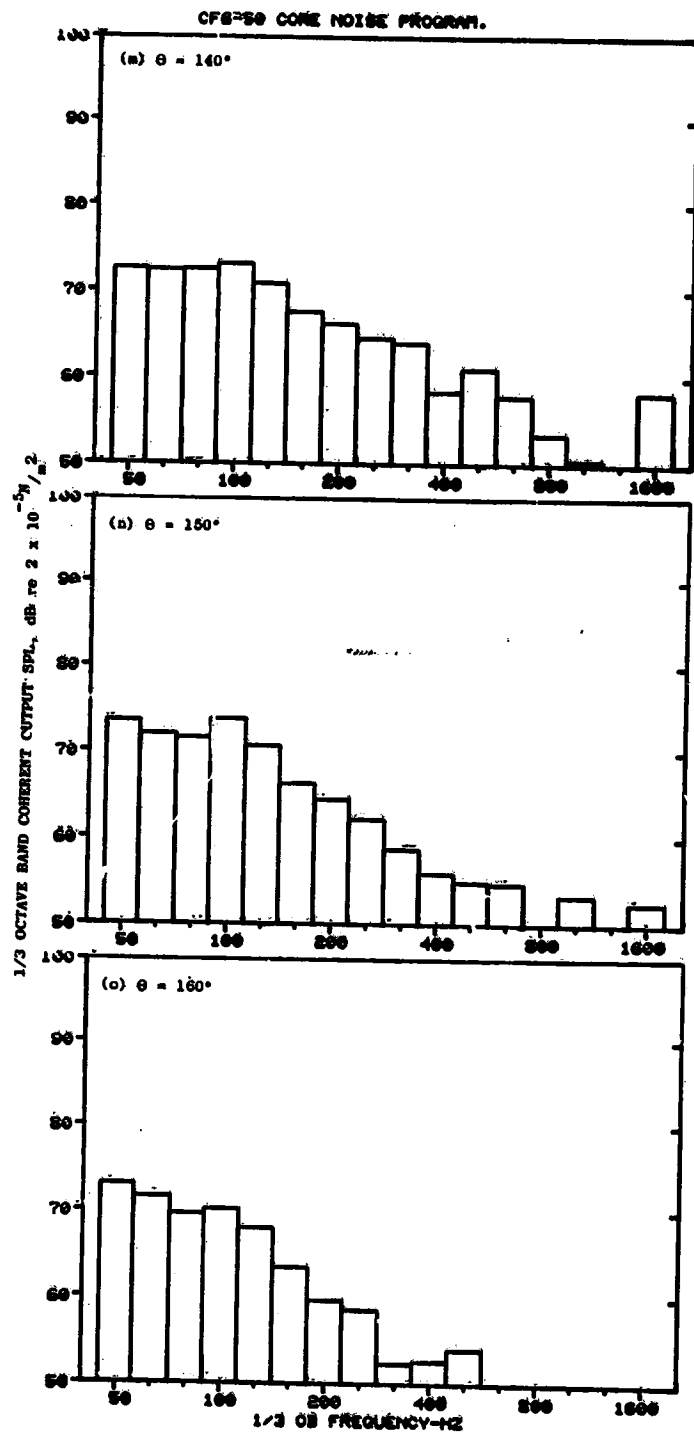


Figure C-8. Coherent Output SPL Spectra from Plane 8.0A (270°) to Farfield Microphones at 3.8% Thrust (Concluded).

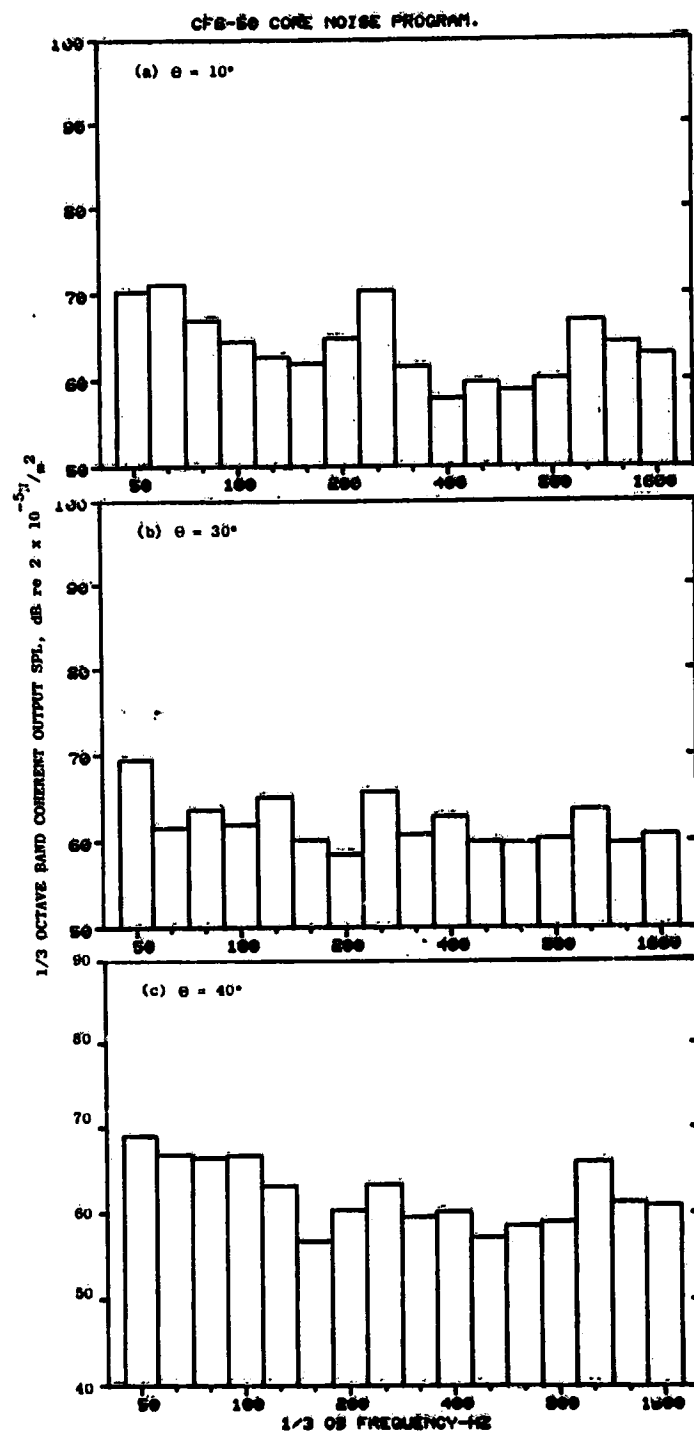


Figure C-9. Coherent Output SPL Spectra from Plane 8.0A (270°) to Farfield Microphones at 15.0% Thrust.

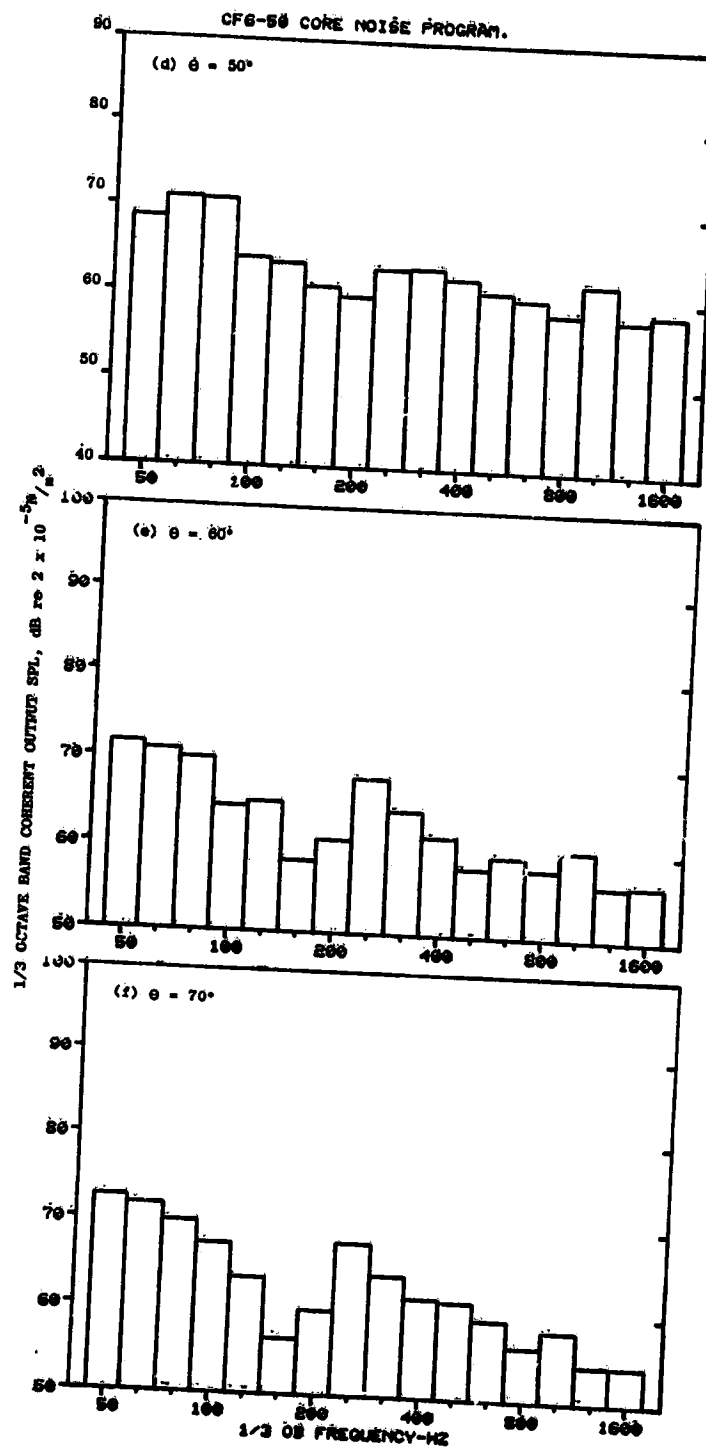


Figure C-9. Coherent Output SPL Spectra from Plane 8.0A (270°) to Farfield Microphones at 15.0% Thrust (Continued).

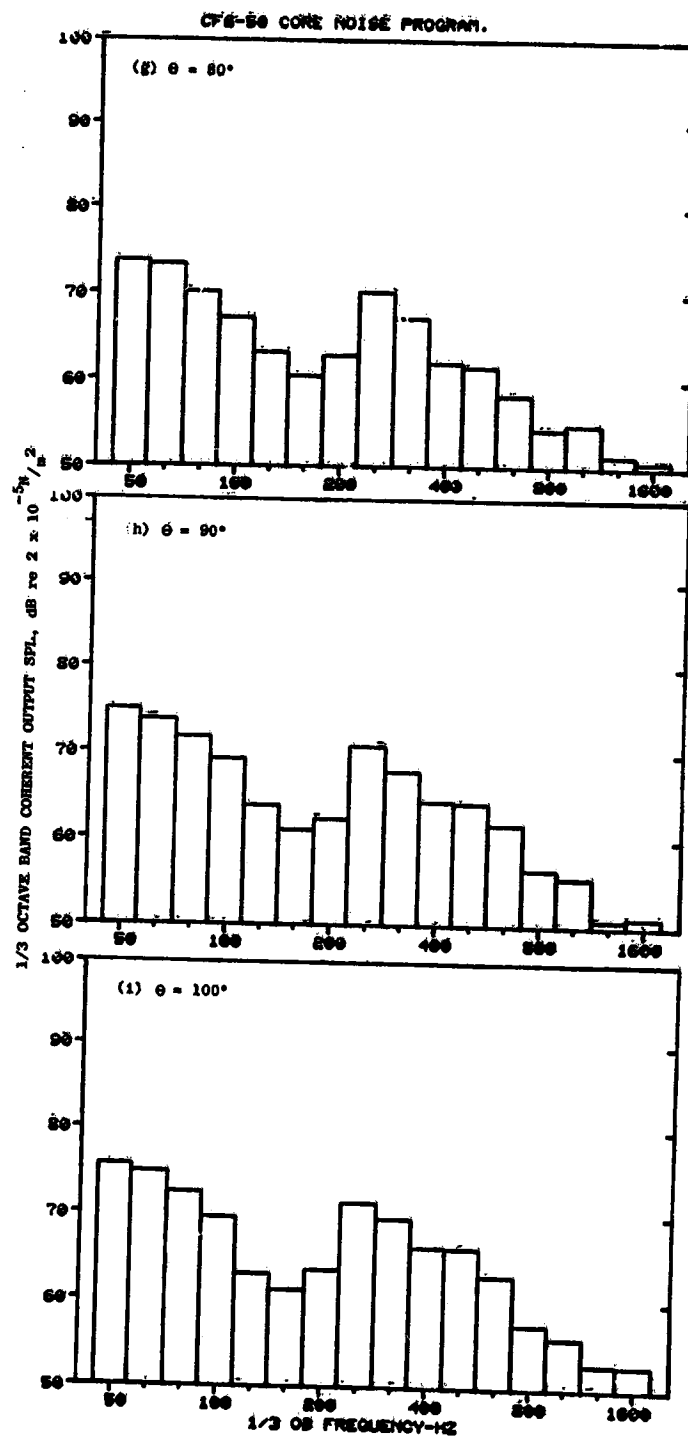


Figure C-9. Coherent Output SPL Spectra from Plane 8.0A (270°) to Farfield Microphones at 15.0% Thrust (Continued).

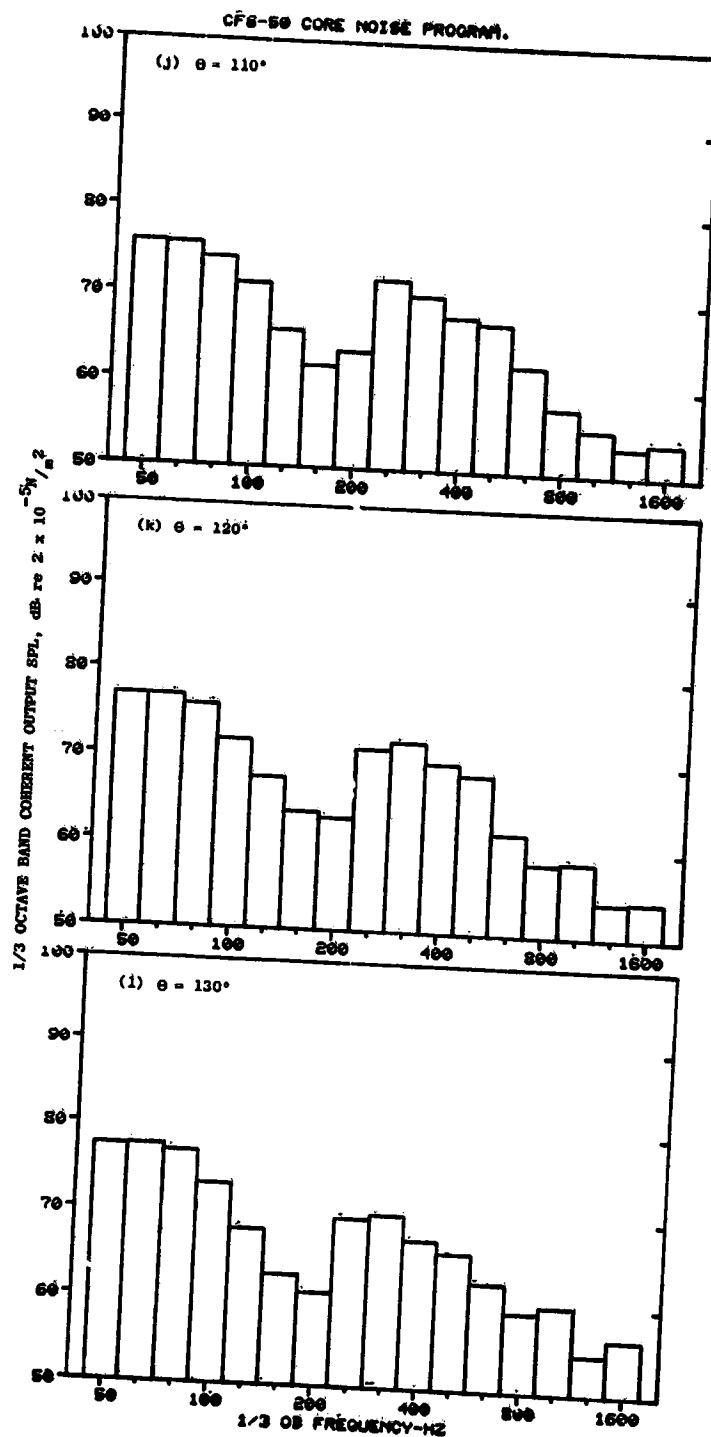


Figure C-9. Coherent Output SPL Spectra from Plane 8.0A (270°) to Farfield Microphones at 15.0% Thrust (Continued).

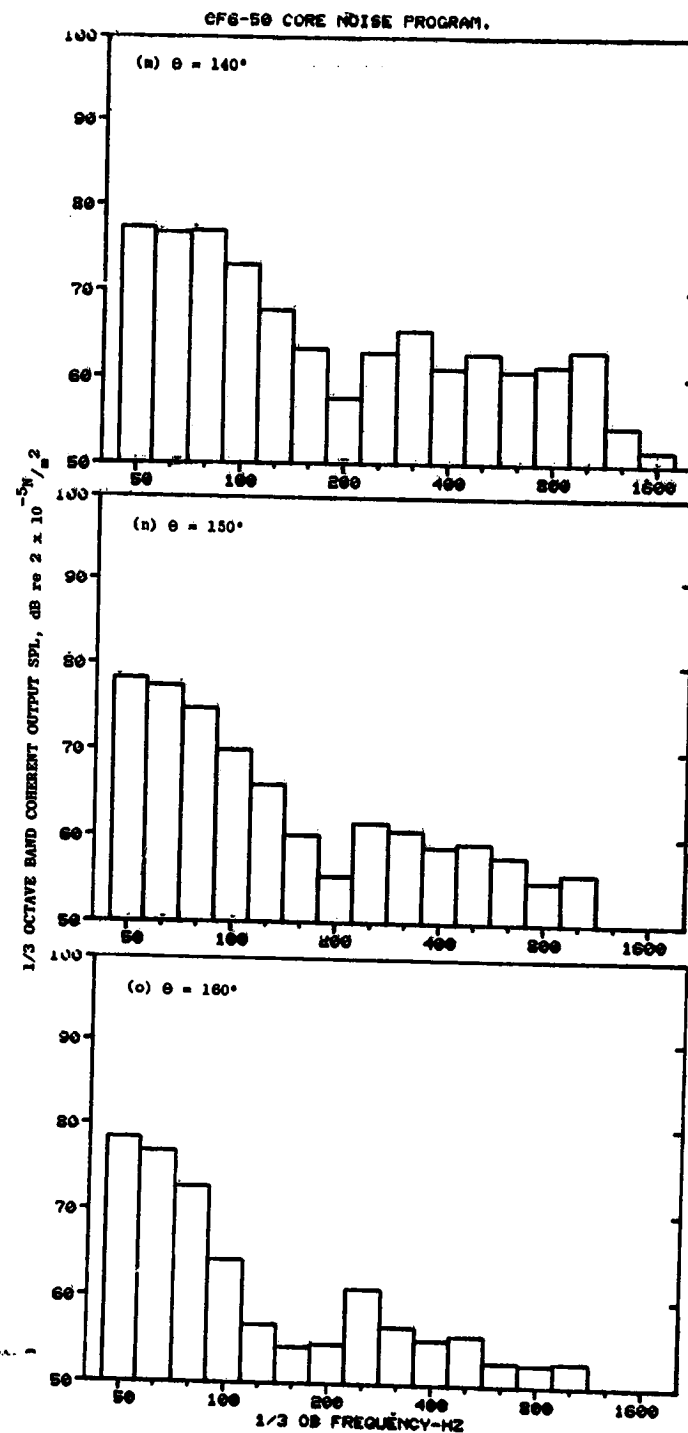


Figure C-9. Coherent Output SPL Spectra from Plane 8.0A (270°) to Farfield Microphones at 15.0% Thrust (Concluded).

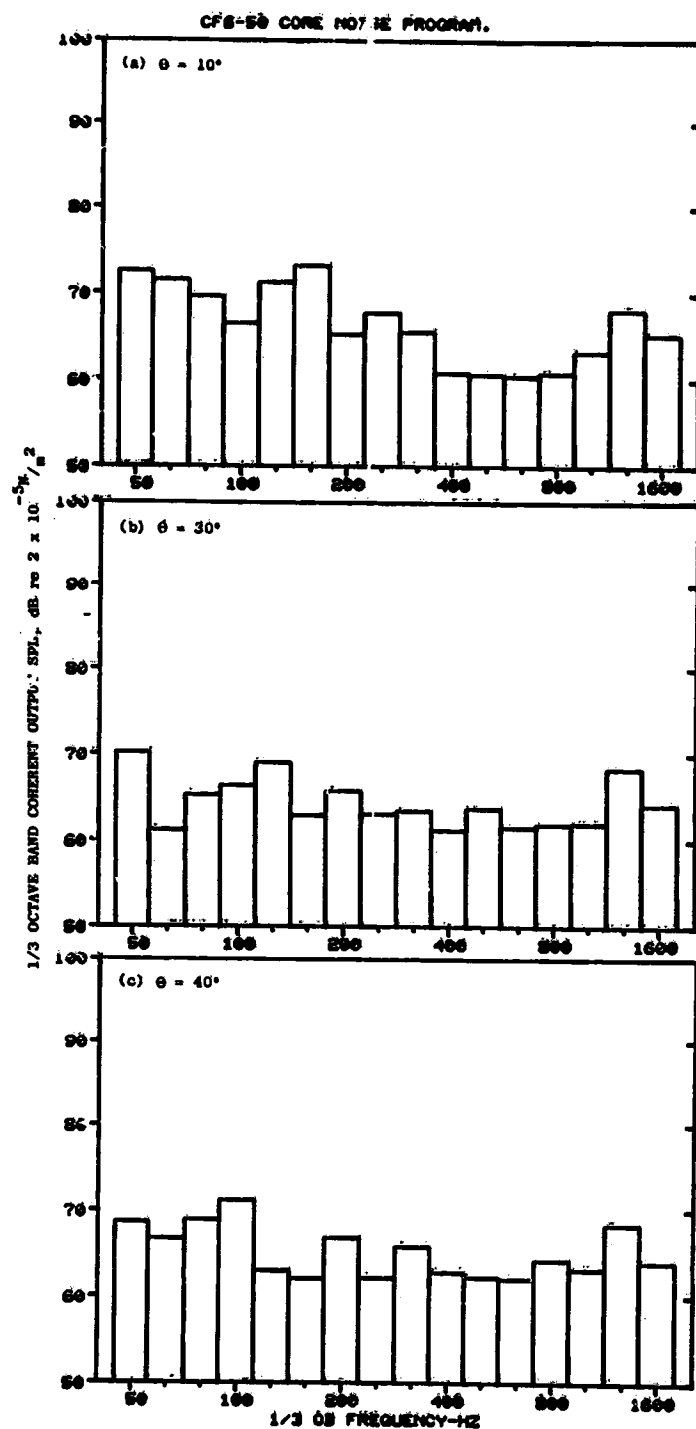


Figure C-10. Coherent Output SPL Spectra from Plane 8.0A (270°) to Farfield Microphones at 22.8% Thrust.

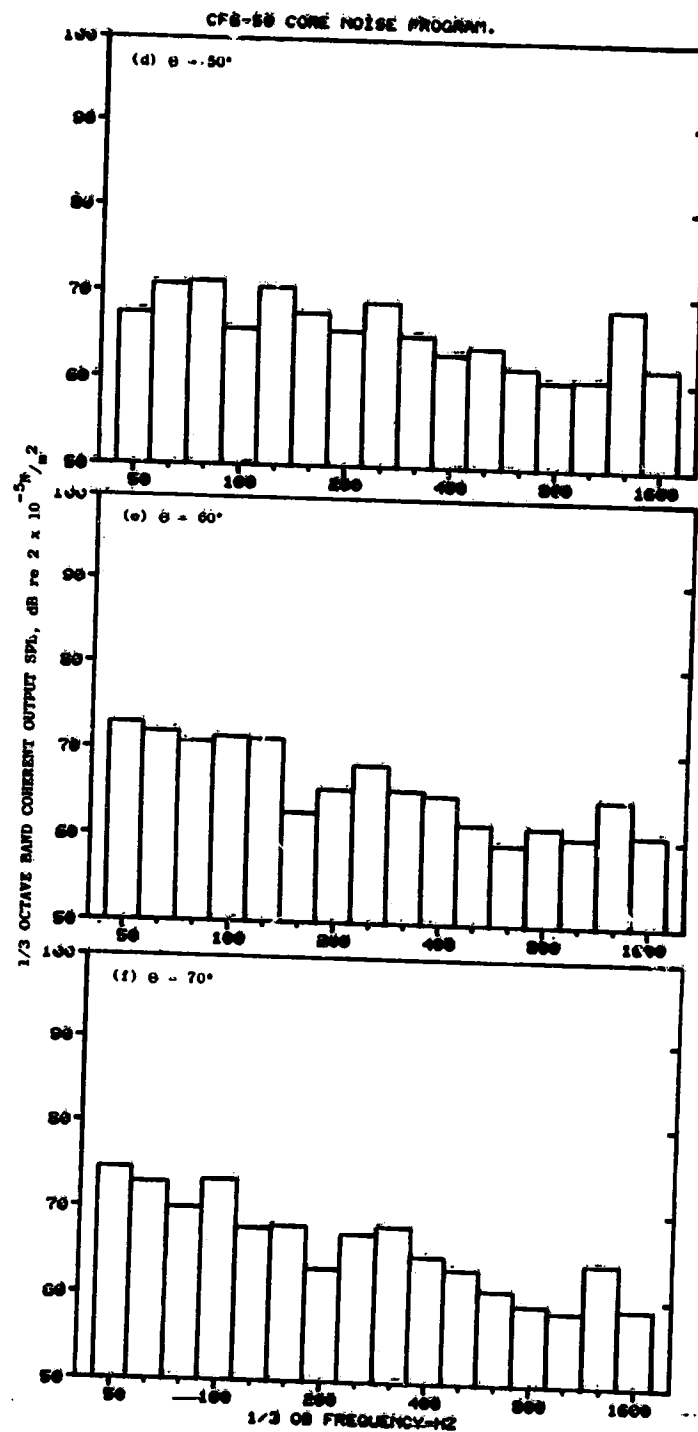


Figure C-10. Coherent Output SPL Spectra from Plane 8.0A (270°) to Farfield Microphones at 22.8% Thrust (Continued).

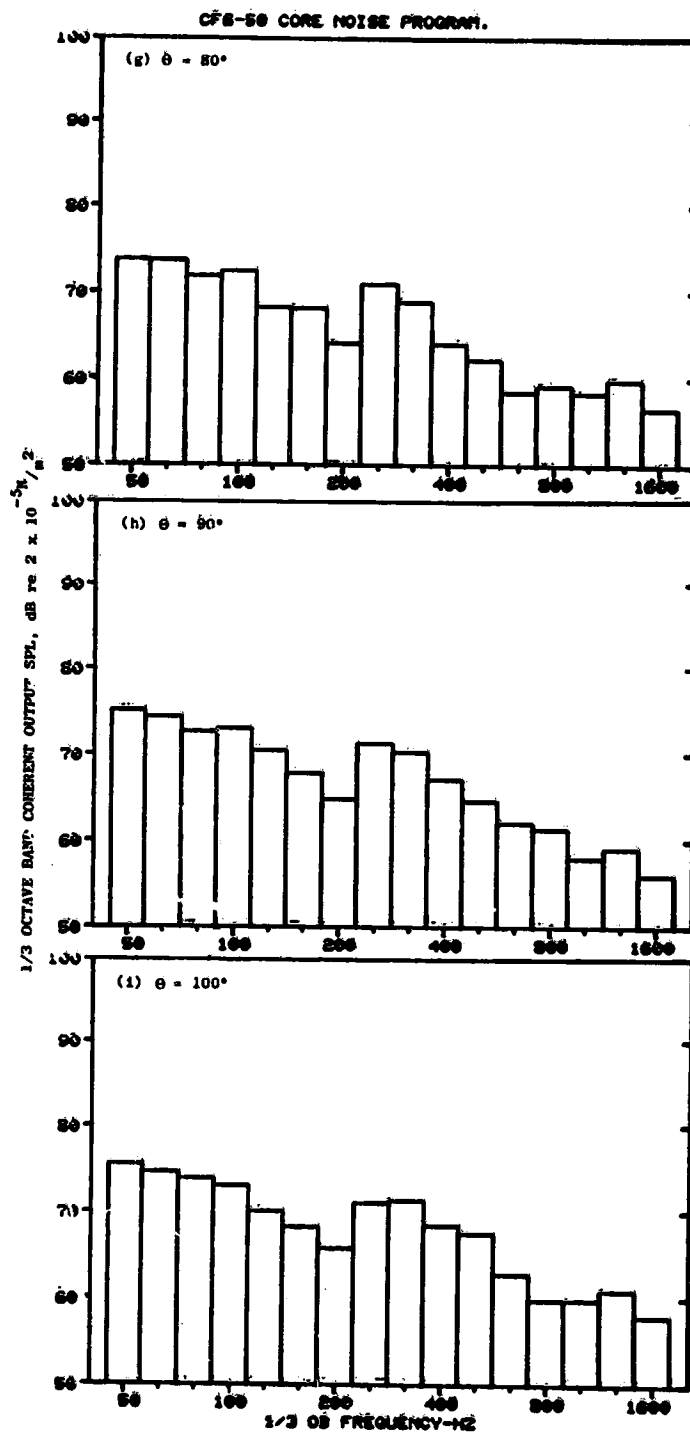


Figure C-10. Coherent Output SPL Spectra from Plane 8.0A (270°) to Farfield Microphones at 22.8% Thrust (Continued).

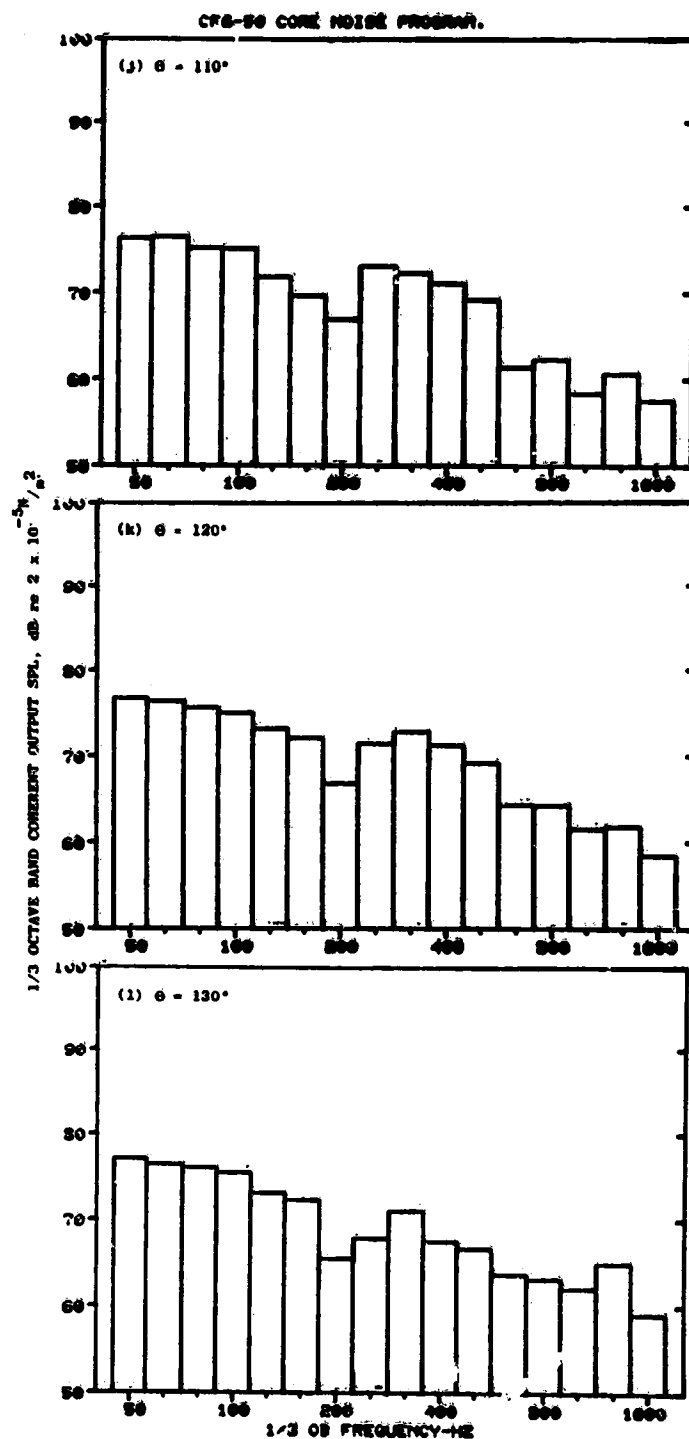


Figure C-10. Coherent Output SPL Spectra from Plane 8.0A (270°) to Farfield Microphones at 22.8% Thrust (Continued).

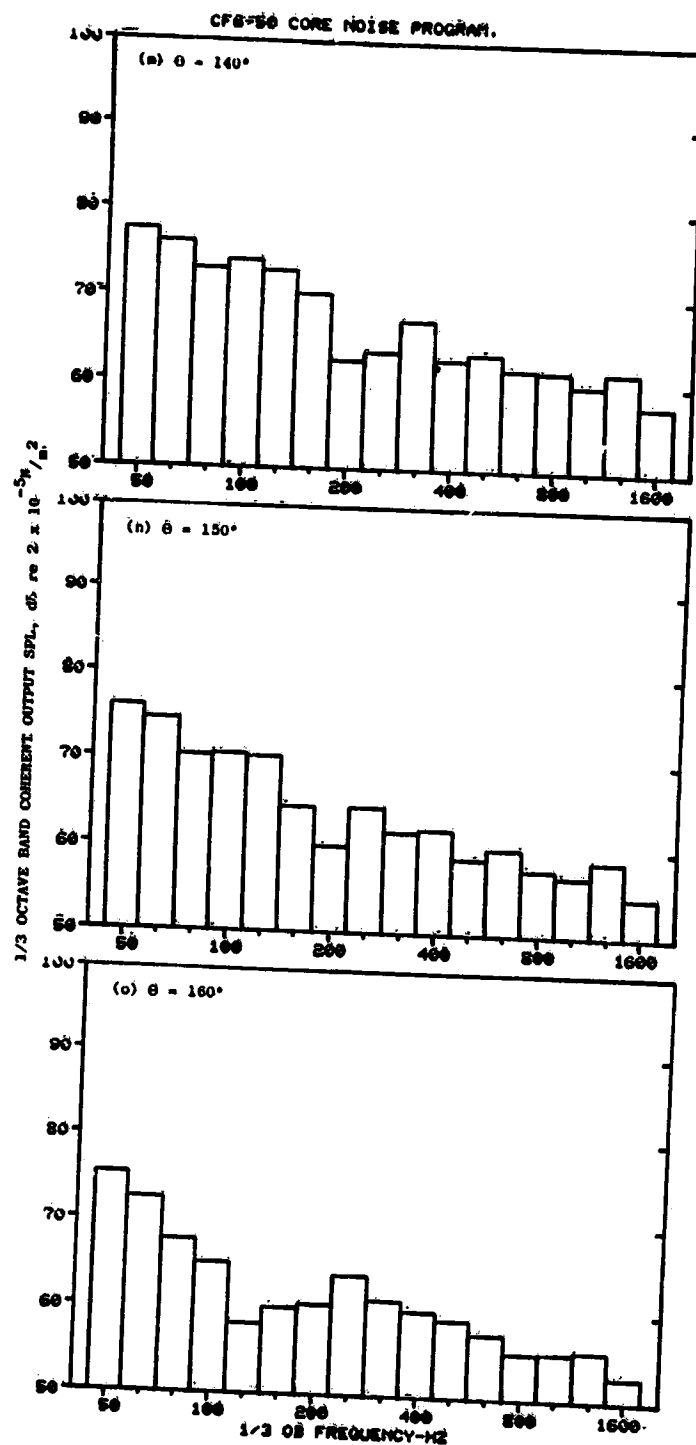


Figure C-10. Coherent Output SPL Spectra from Plane 8.0A (270°) to Farfield Microphones at 22.8% Thrust (Concluded).

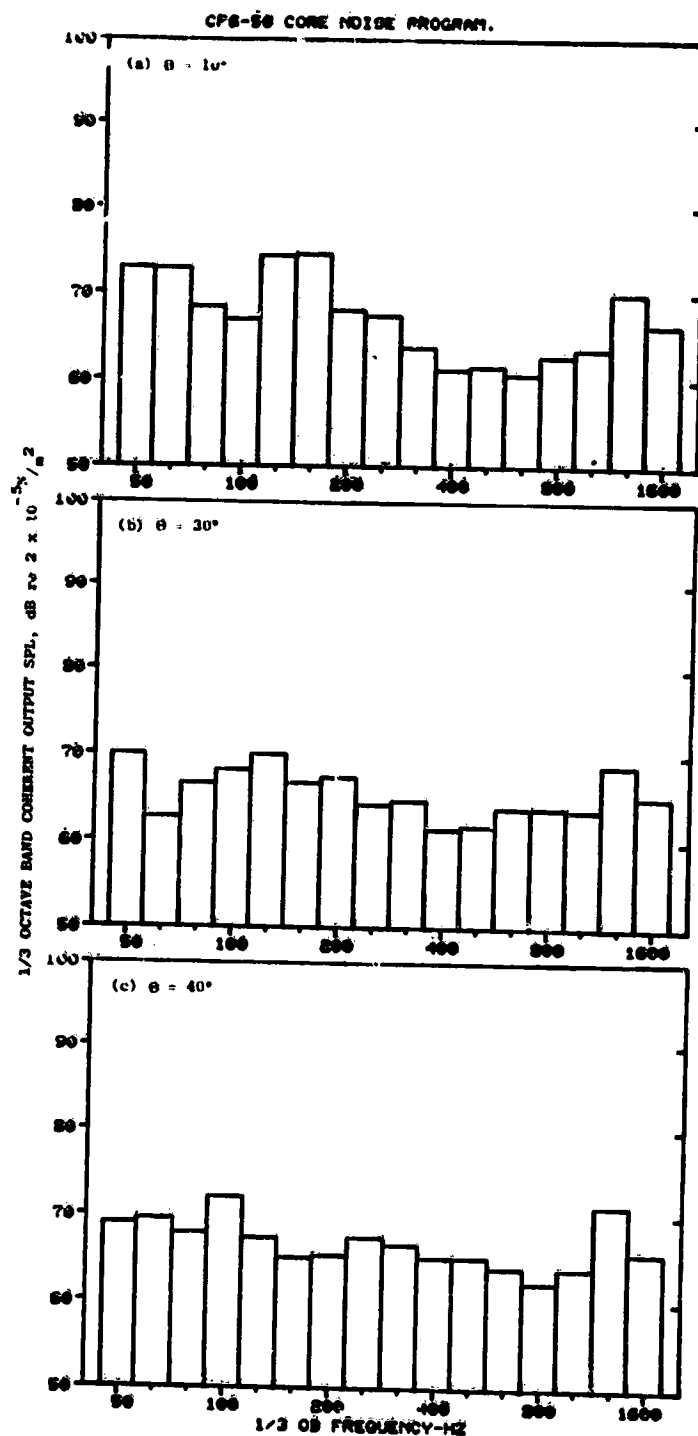


Figure C-11. Coherent Output SPL Spectra from Plane 8.0A (270°) to Farfield Microphones at 26.7% Thrust.

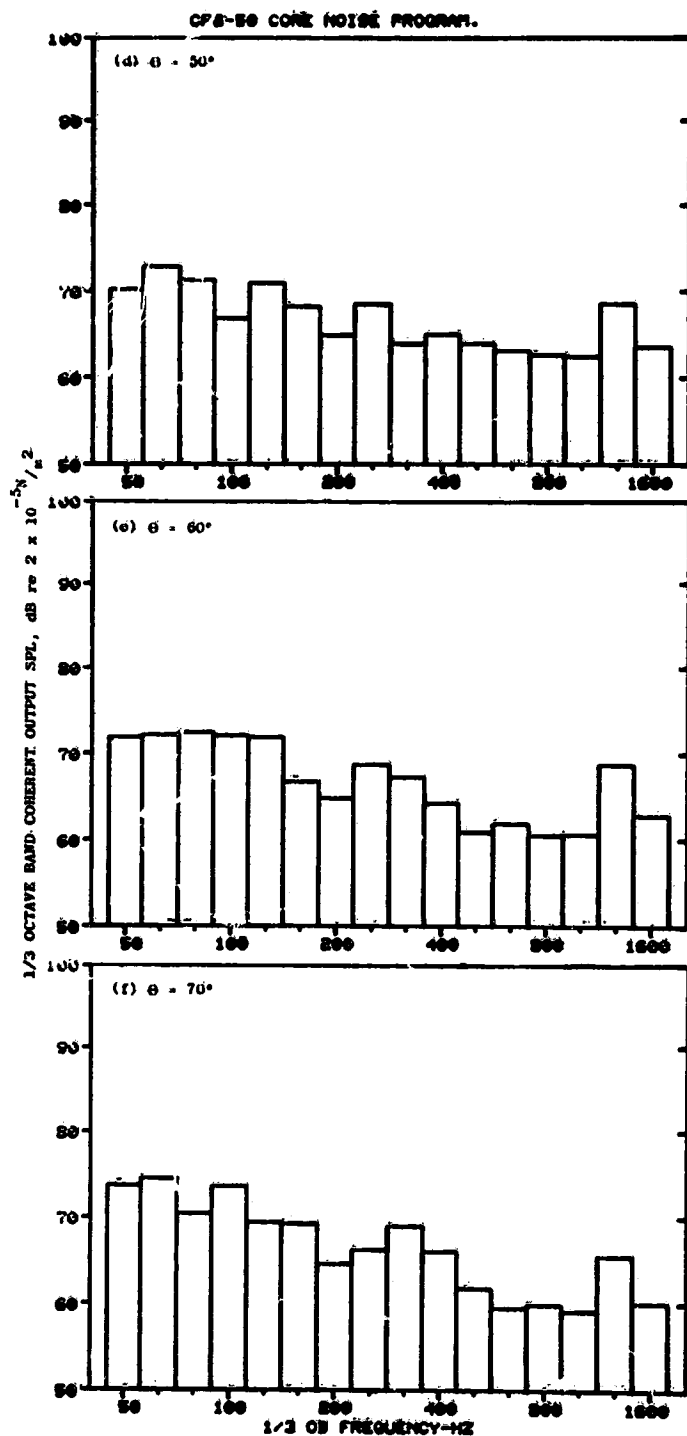


Figure C-11. Coherent Output SPL Spectra from Plane 8.0A (270°) to Farfield Microphones at 26.7% Thrust (Continued).

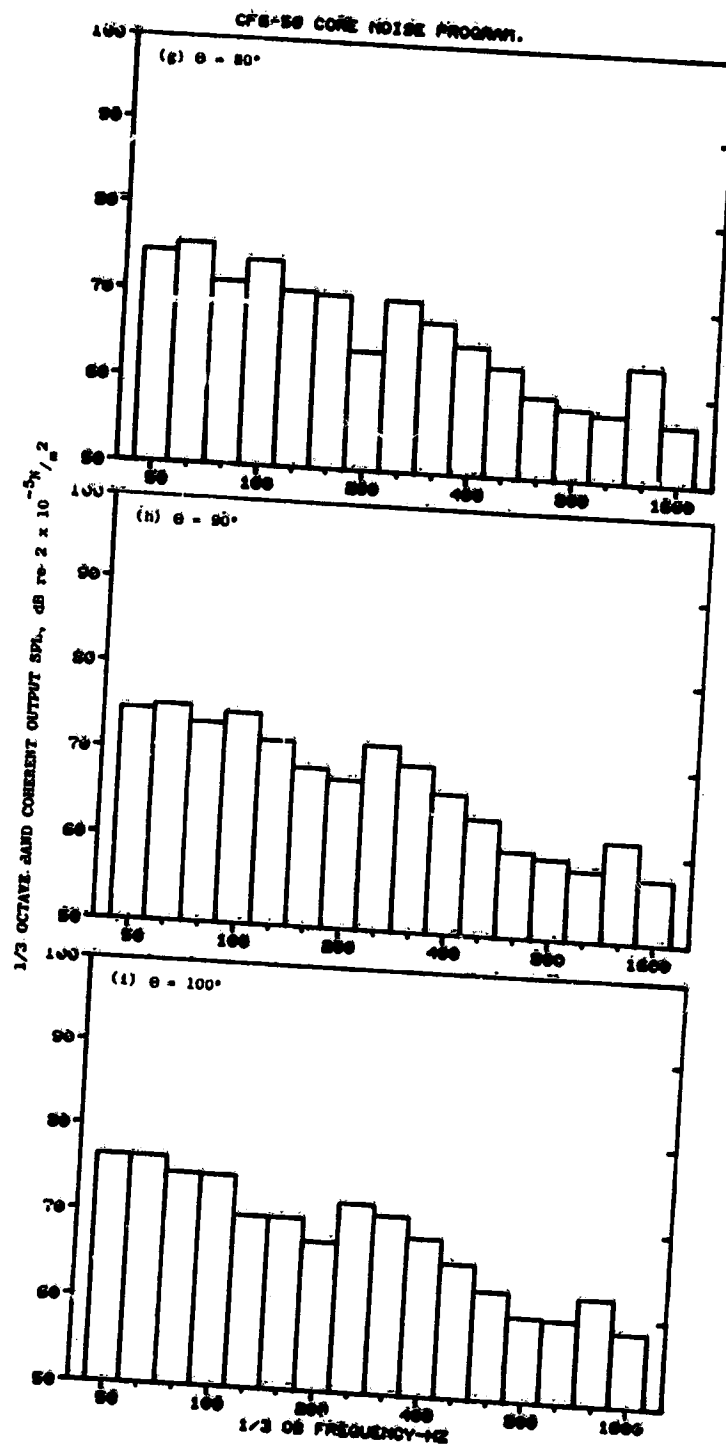


Figure C-11. Coherent Output SPL Spectra from Plane 8.0A (270°) to Farfield Microphones at 26.7% Thrust (Continued).

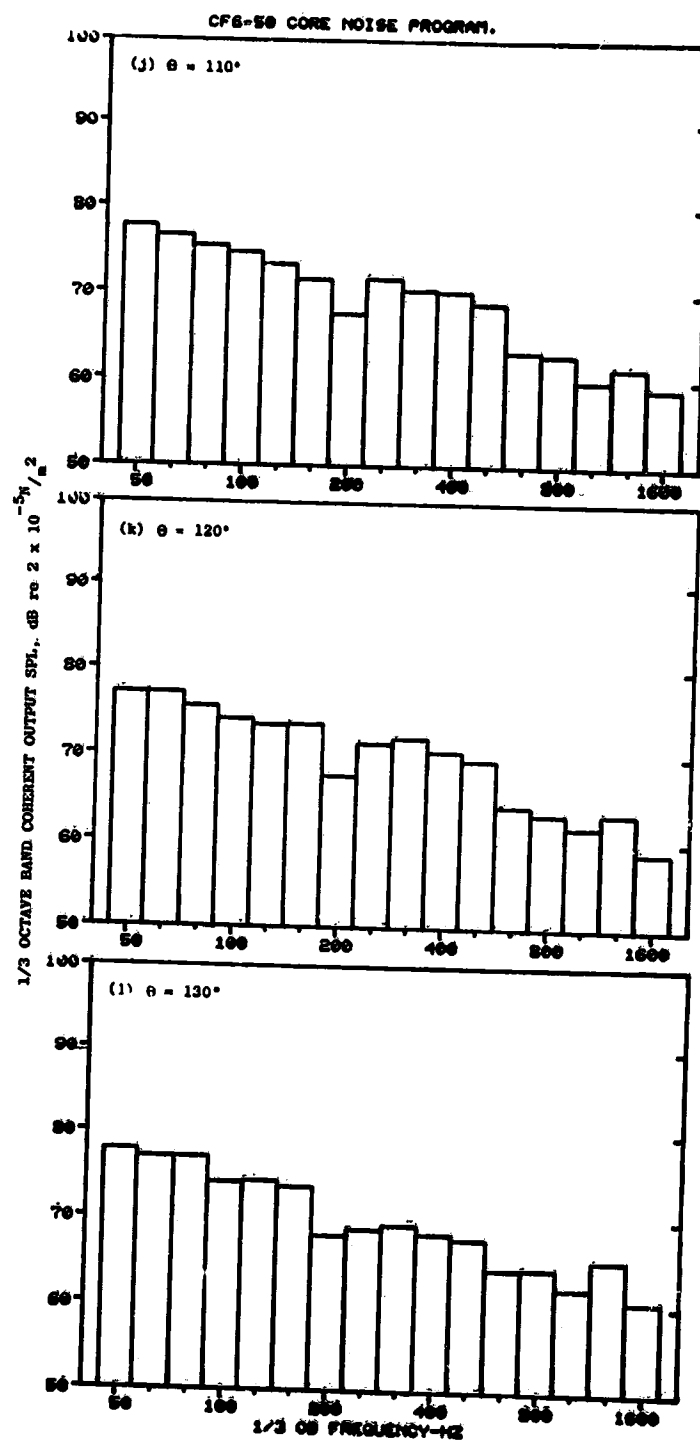


Figure C-11. Coherent Output SPL Spectra from Plane 8.0A (270°) to Farfield Microphones at 26.7% Thrust (Continued).

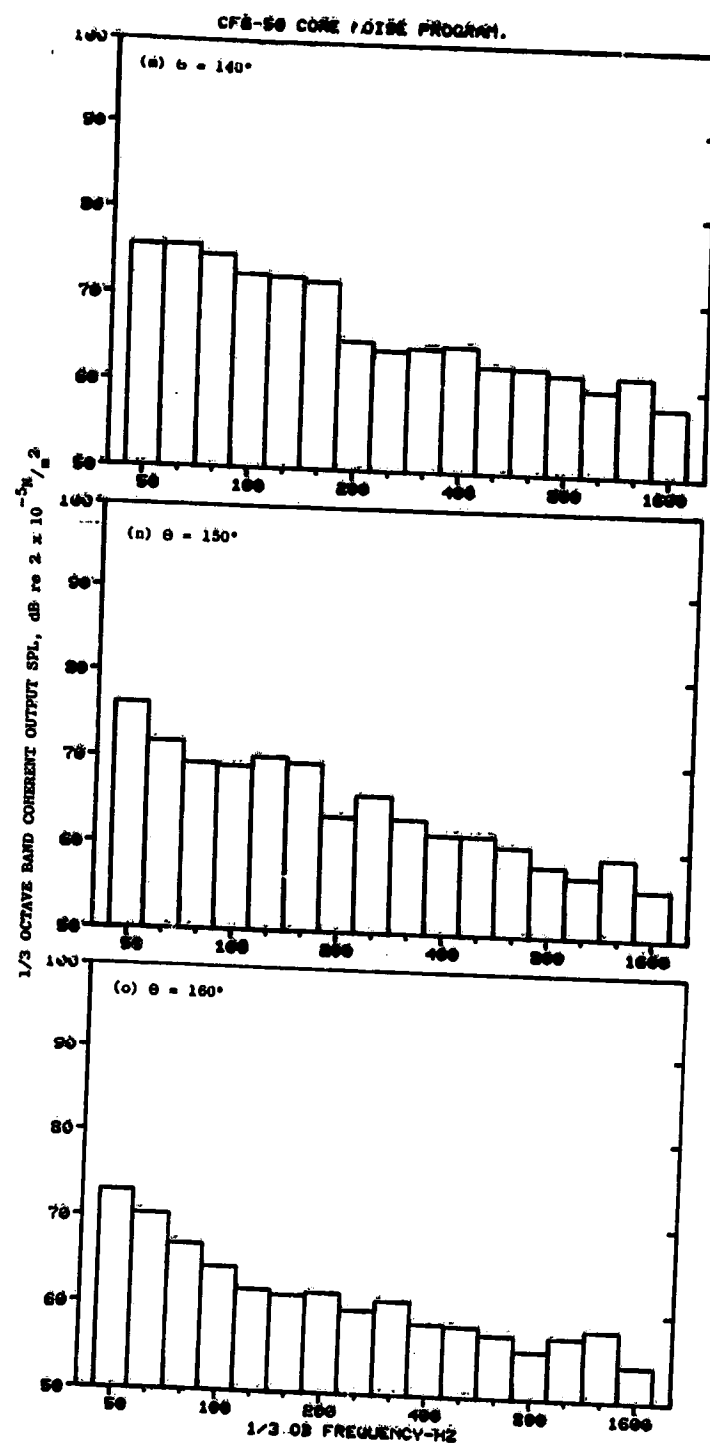


Figure C-11. Coherent Output SPL Spectra from Plane 8.0A (270°) to Farfield Microphones at 26.7% Thrust (Concluded).

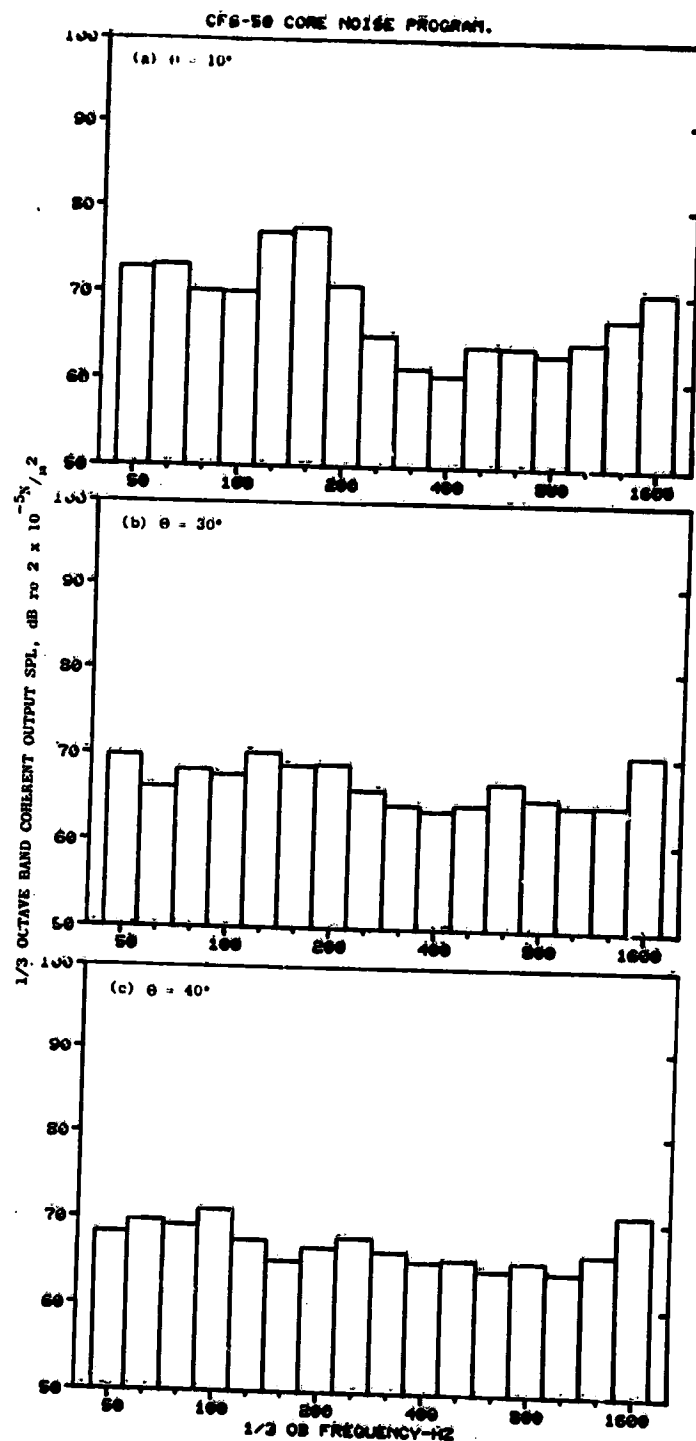


Figure C-12. Coherent Output SPL Spectra from Plane 8.0A (270°) to Farfield Microphones at 30.8% Thrust.

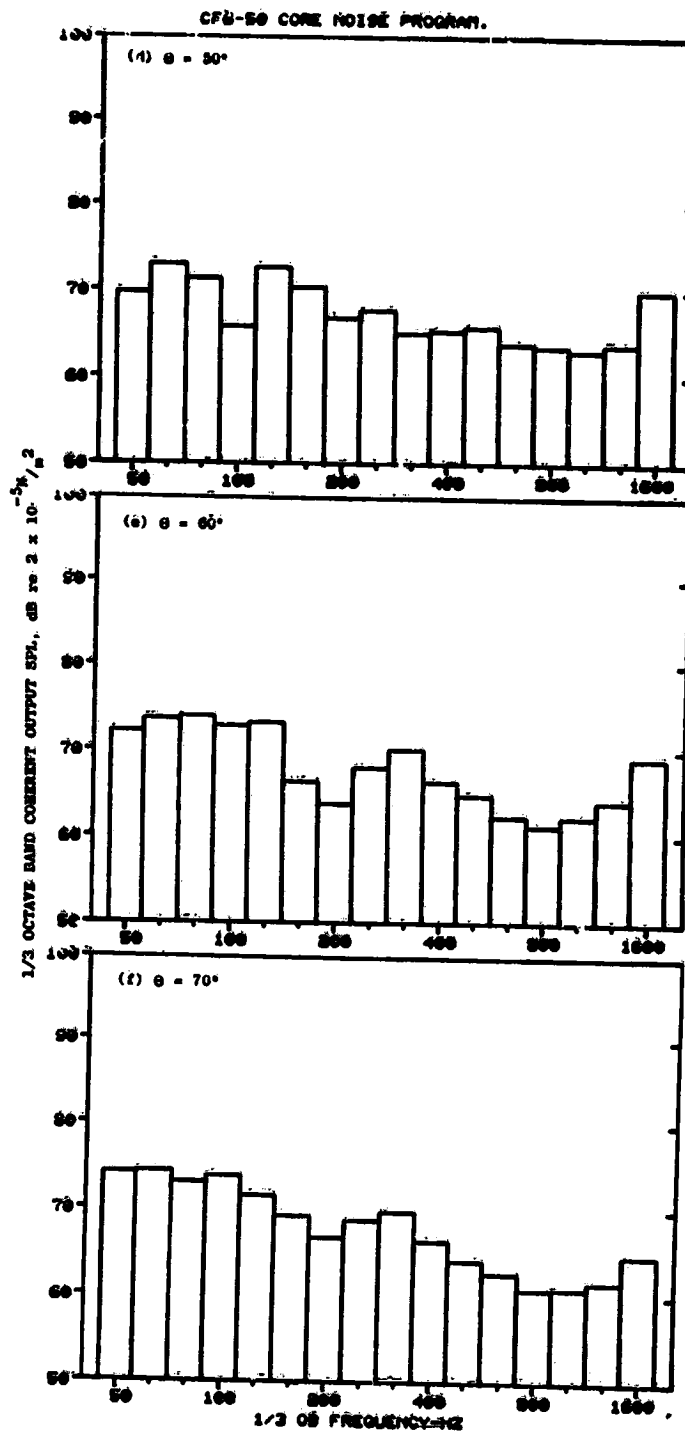


Figure C-12. Coherent Output SPL Spectra from Plane 8.0A (270°) to Farfield Microphones at 30.8% Thrust (Continued).

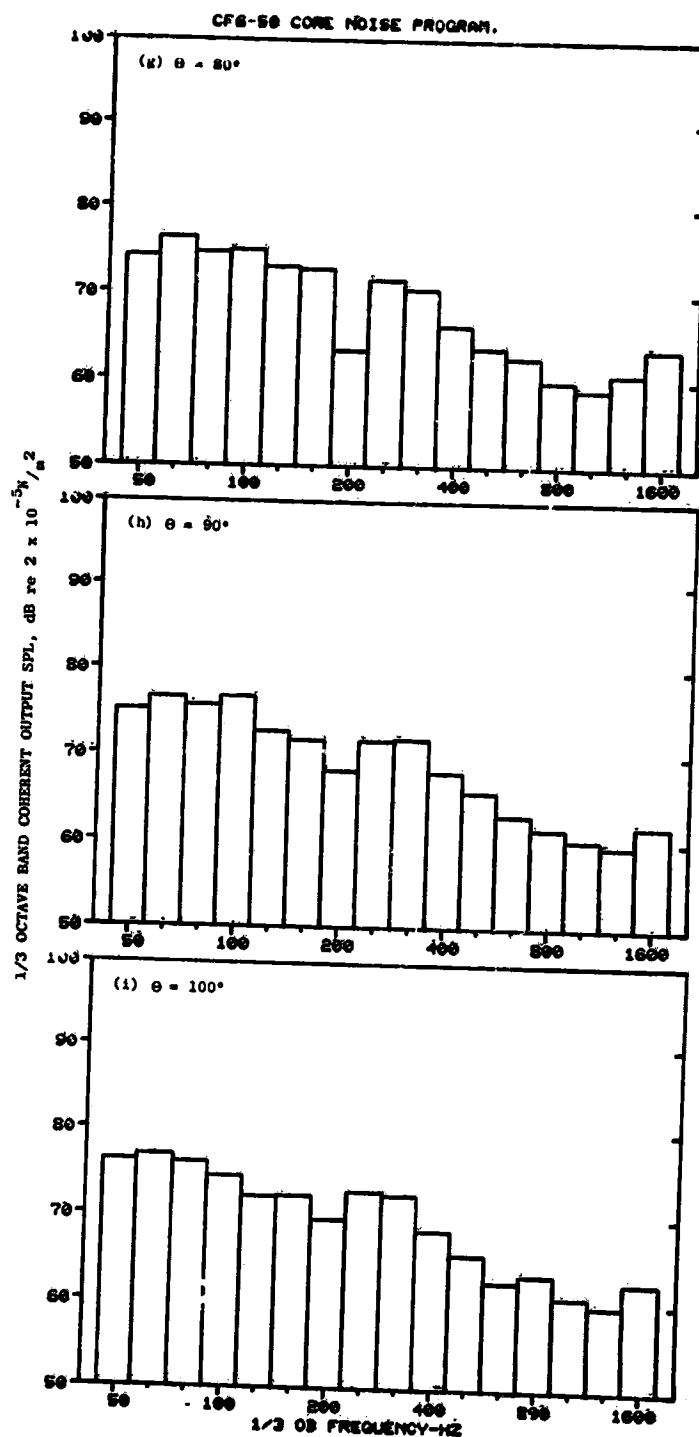


Figure C-12. Coherent Output SPL Spectra from Plane 8.0A (270°) to Farfield Microphones at 30.8% Thrust (Continued).

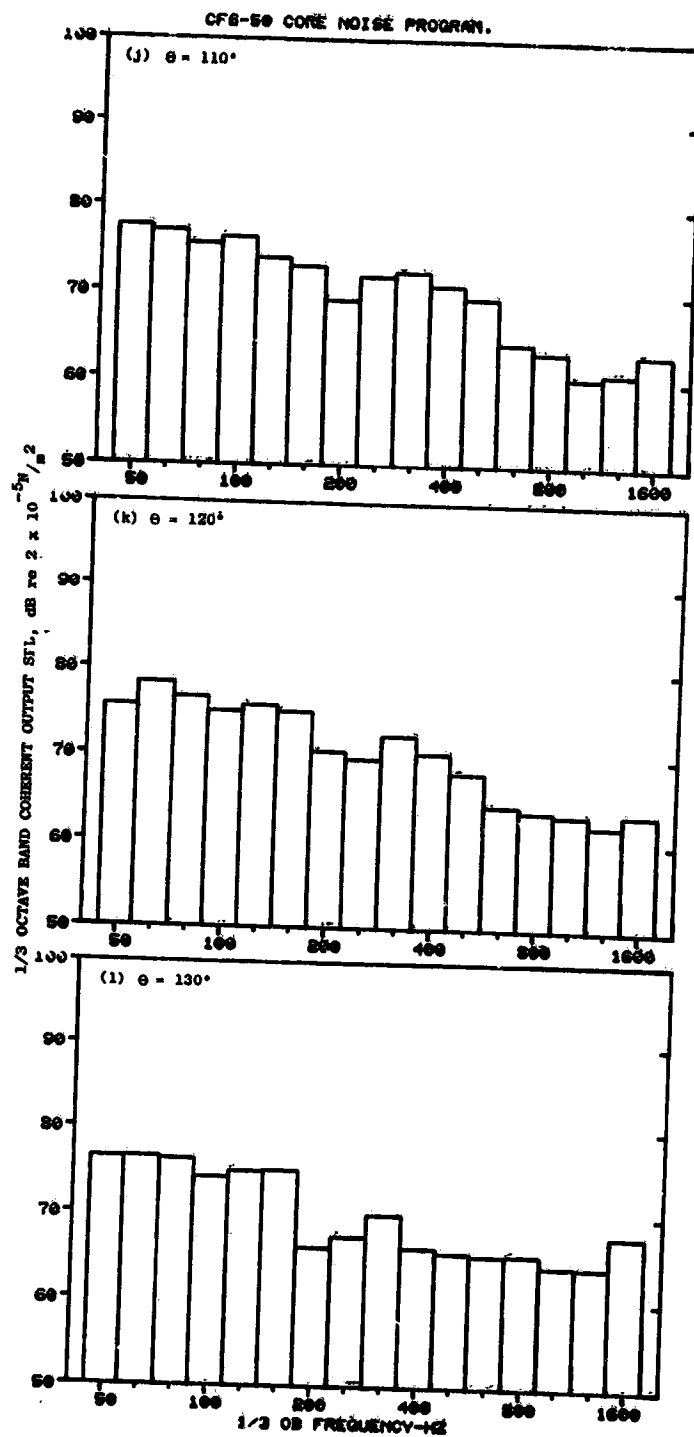


Figure C-12. Coherent Output SPL Spectra from Plane 8.0A (270°) to Farfield Microphones at 30.8% Thrust (Continued).

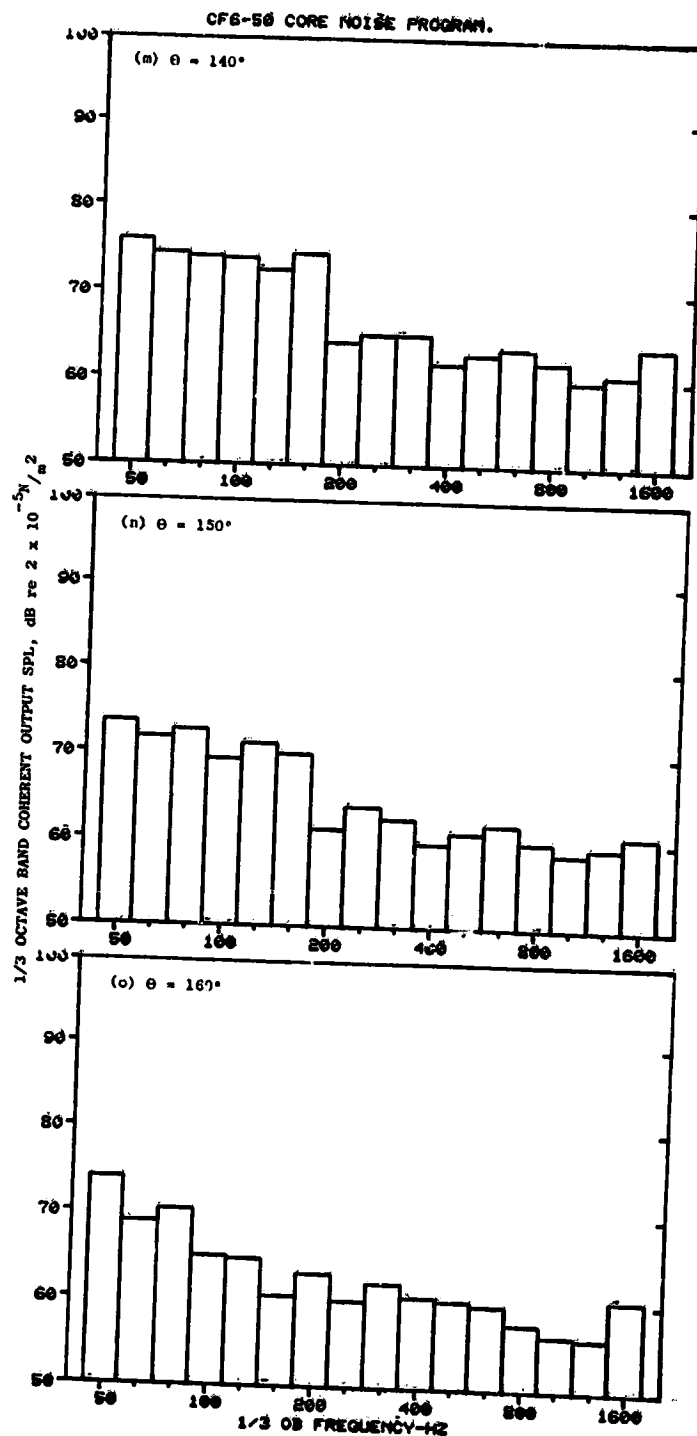


Figure C-12. Coherent Output SPL Spectra from Plane 8.0A (270°) to Farfield Microphones at 30.8% Thrust (Concluded).

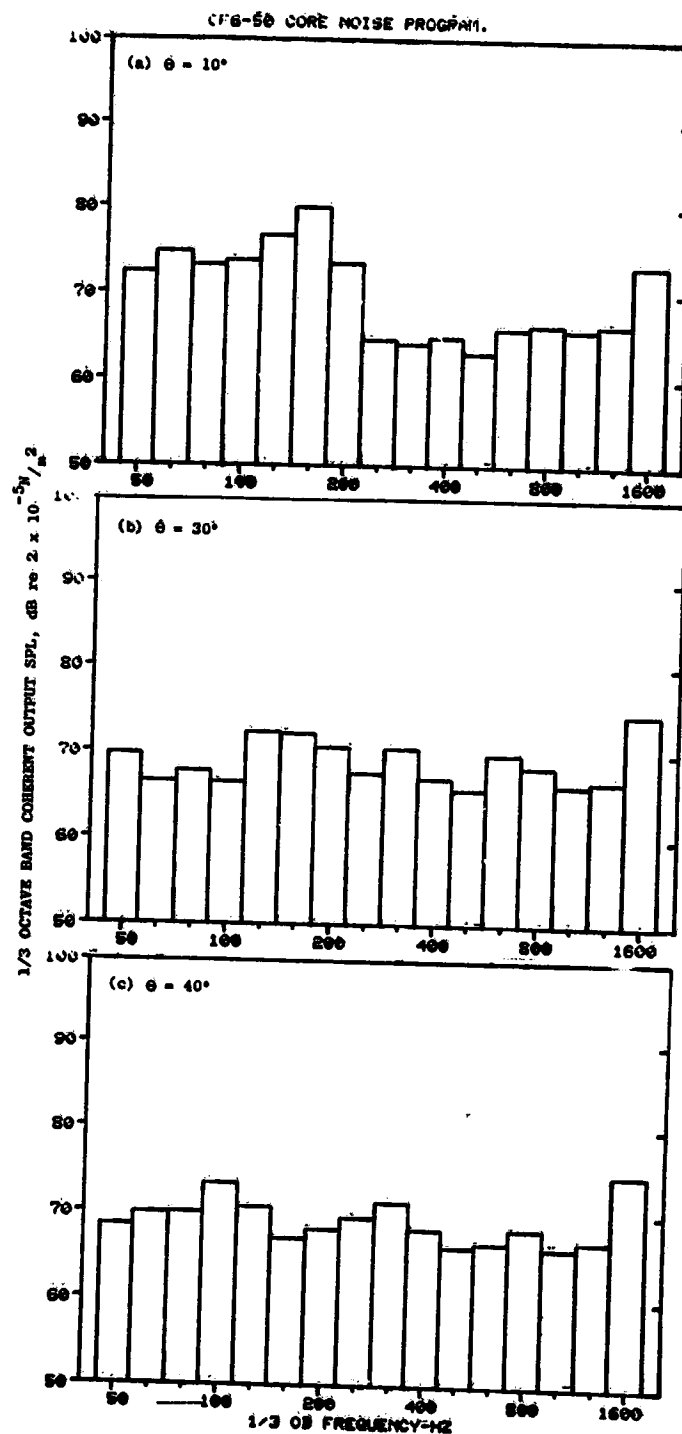


Figure C-13. Coherent Output SPL Spectra from Plane 8.0A (270°) to Farfield Microphones at 36.5% Thrust.

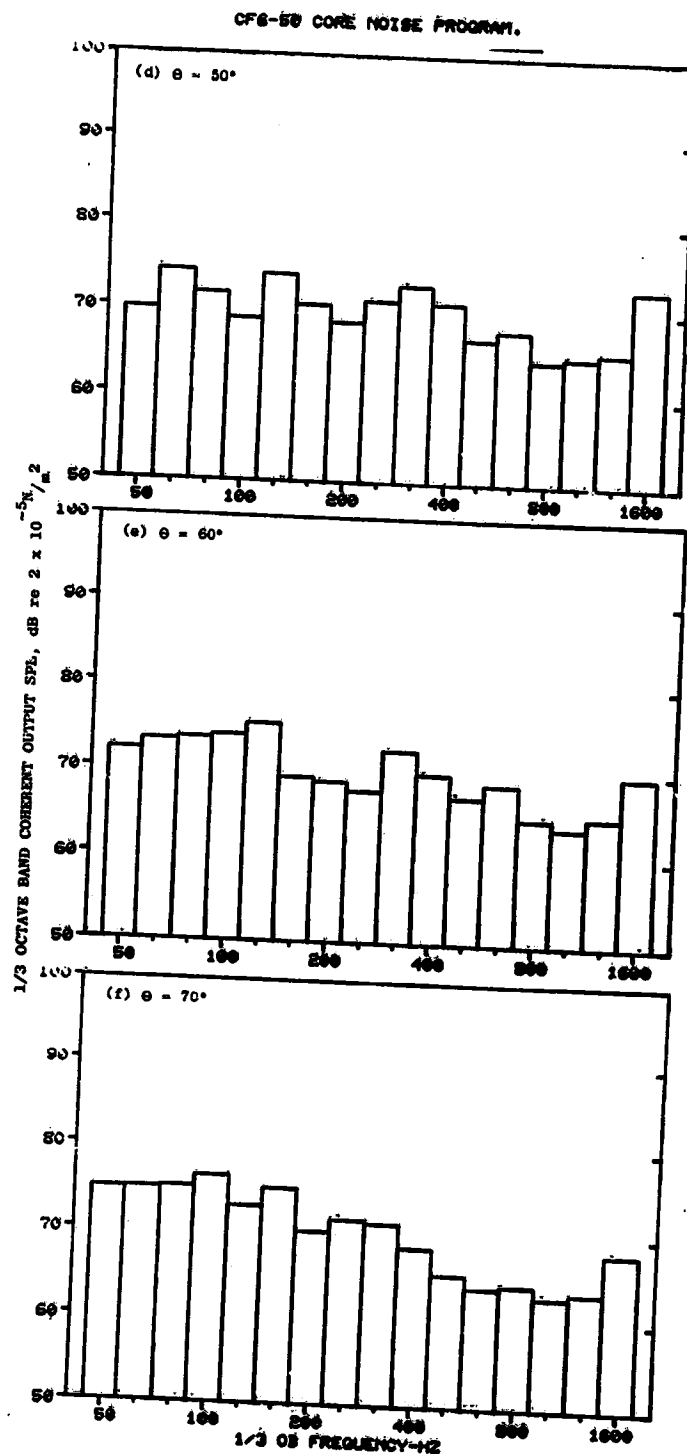


Figure C-13. Coherent Output SPL Spectra from Plane 8.0A (270°) to Farfield Microphones at 36.5% Thrust (Continued).

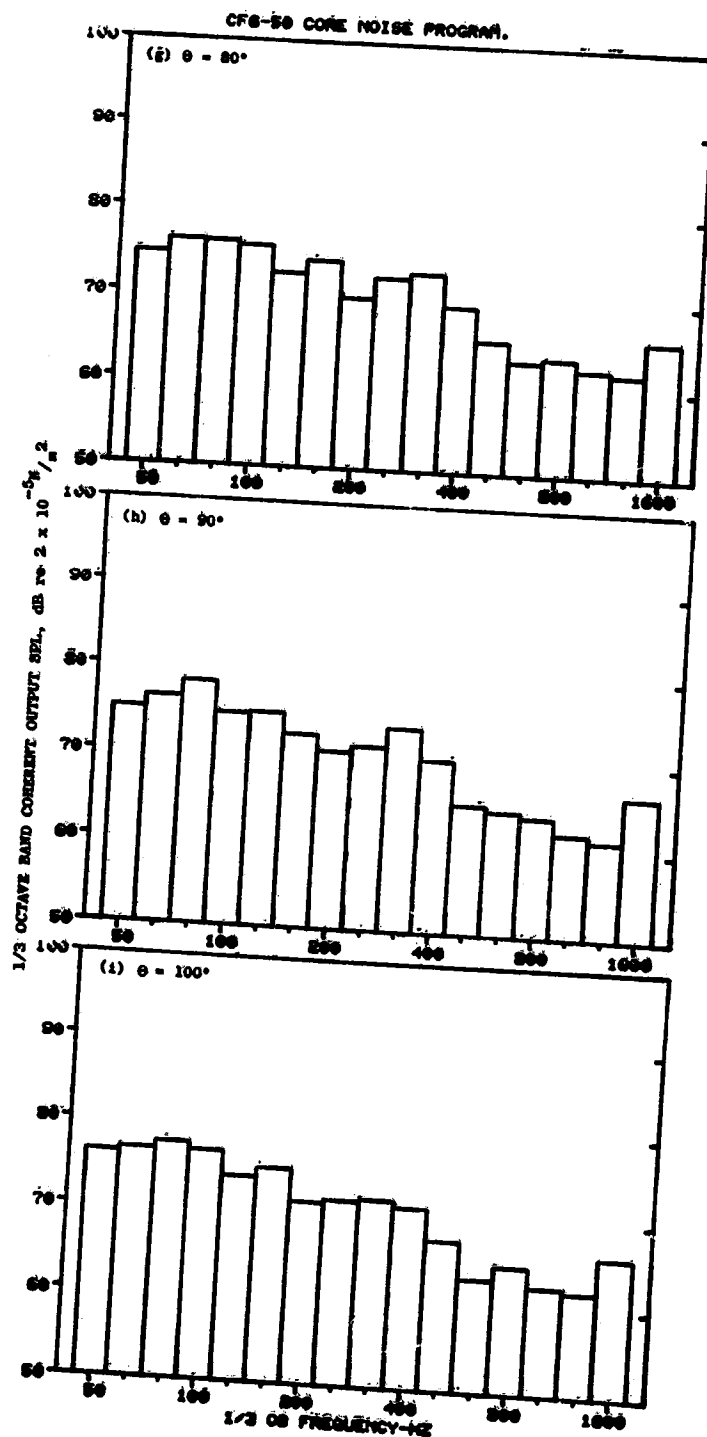


Figure C-13. Coherent Output SPL Spectra from Plane 8.0A (270°) to Farfield Microphones at 36.5% Thrust (Continued).

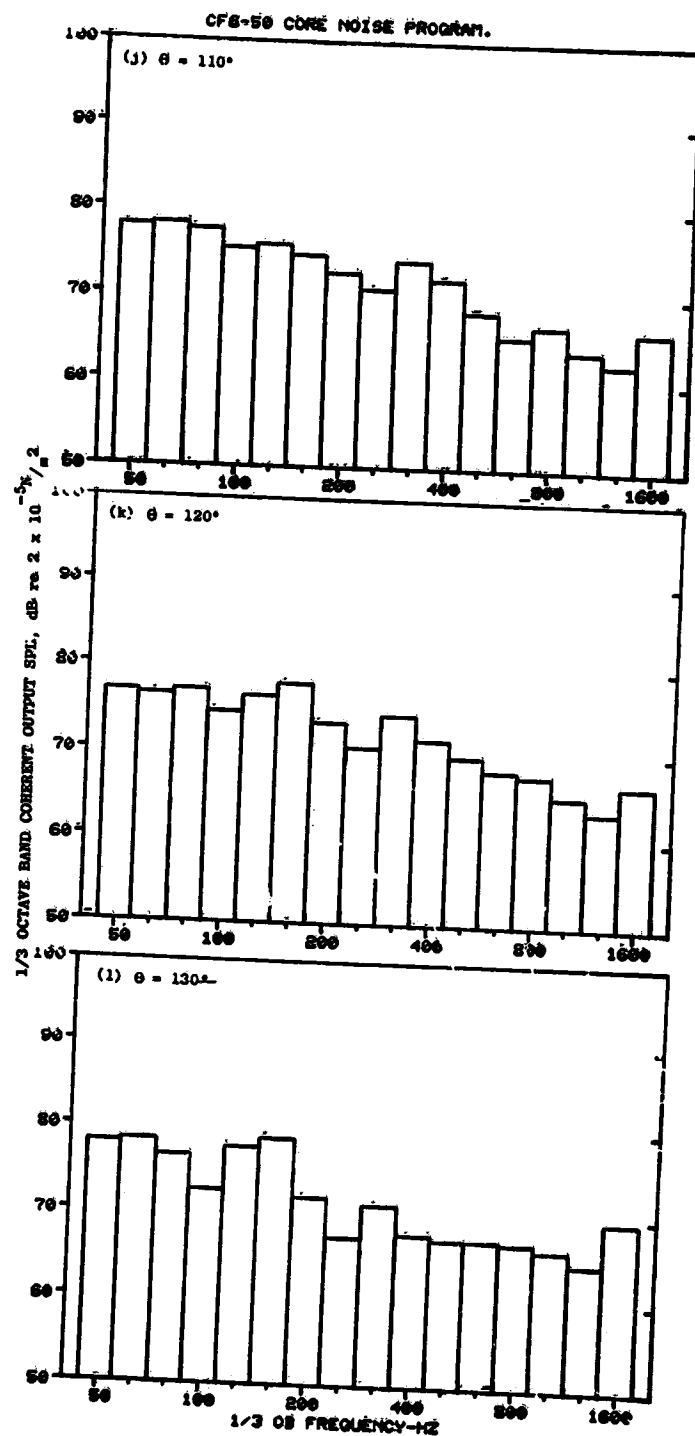


Figure G-13. Coherent Output SPL Spectra from Plane 8.0A (270°) to Farfield Microphones at 36.5% Thrust (Continued).

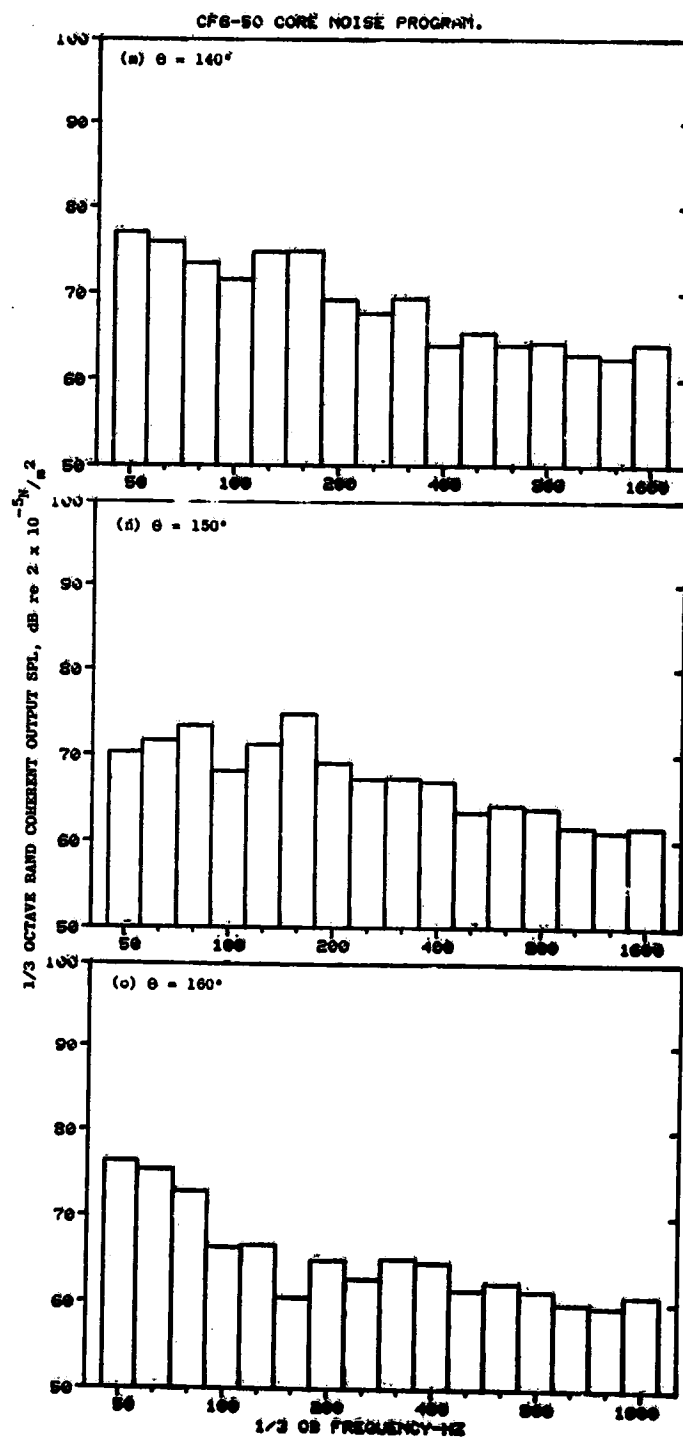


Figure C-13. Coherent Output SPL Spectra from Plane 8.0A (270°) to Farfield Microphones at 36.5% Thrust (Concluded).

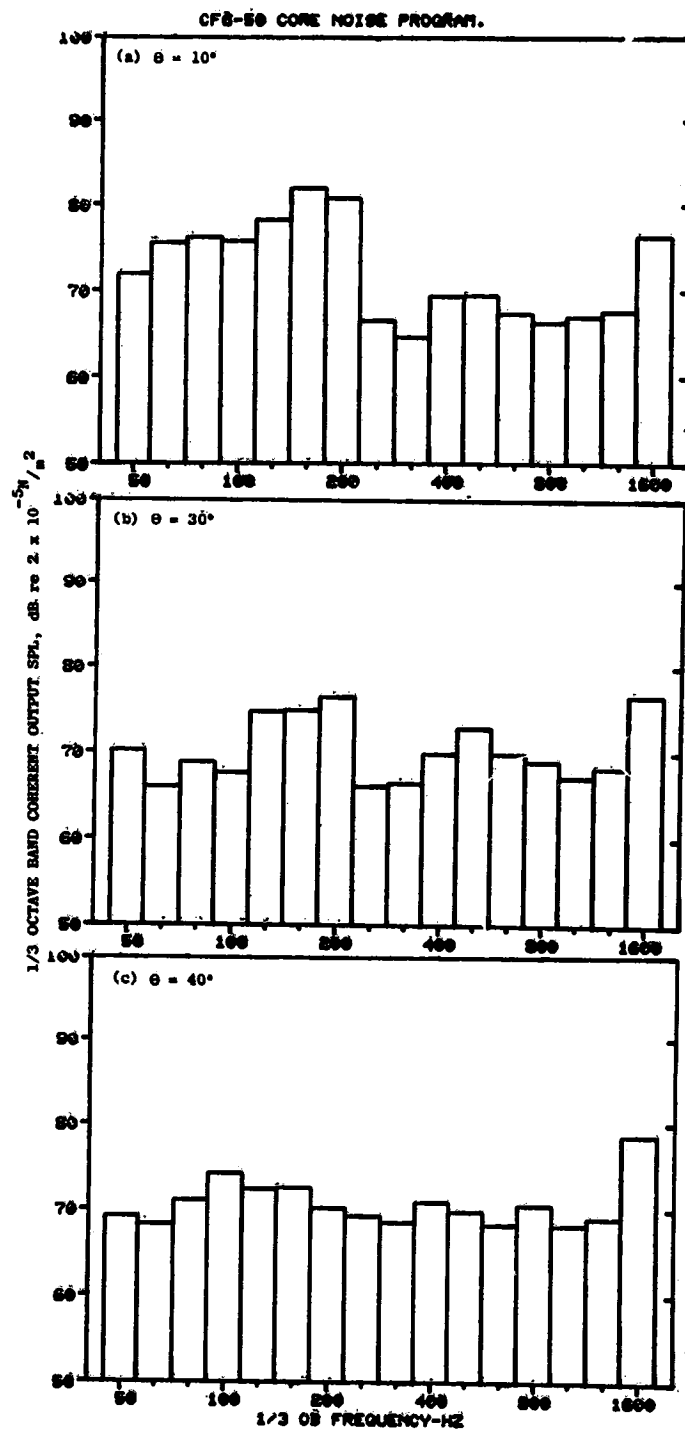


Figure C-14. Coherent Output SPL Spectra from Plane 8.0A (270°) to Farfield Microphones at 45.5% Thrust.

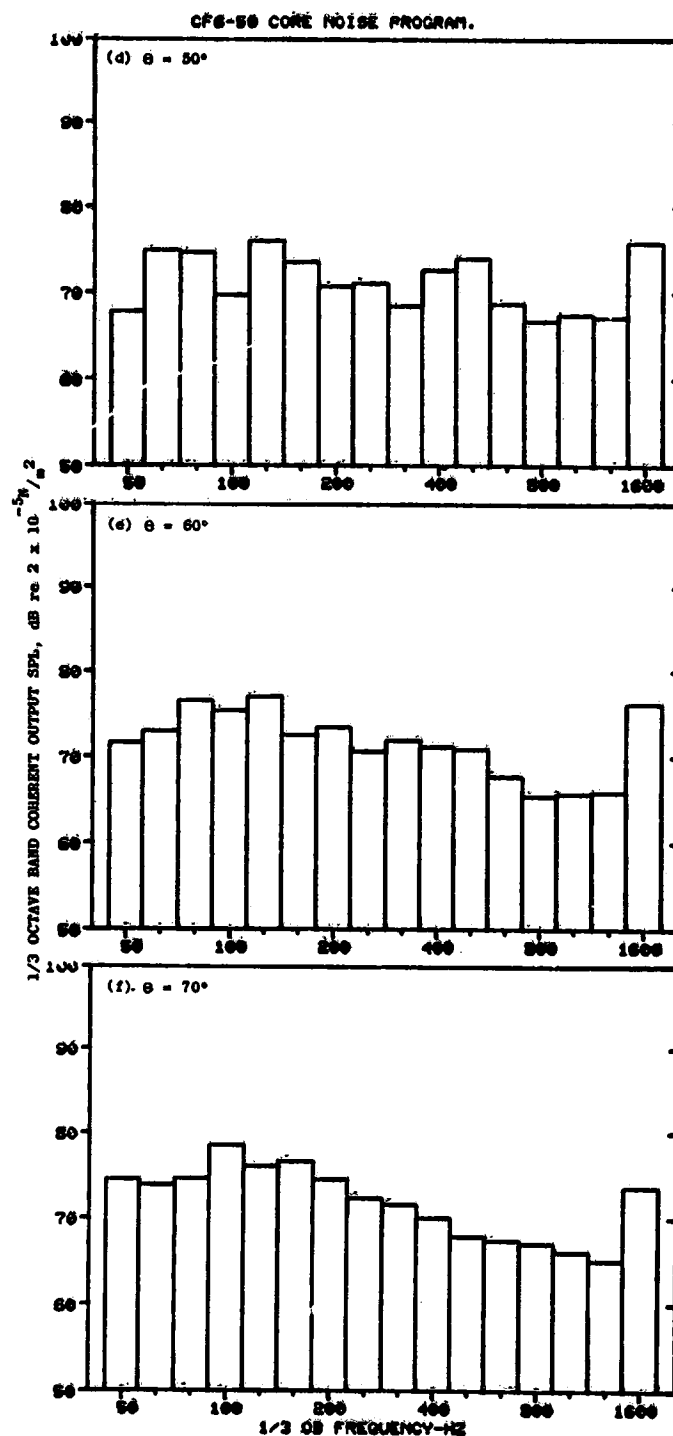


Figure C-14. Coherent Output SPL Spectra from Plane 8.0A (270°) to Farfield Microphones at 45.5% Thrust (Continued).

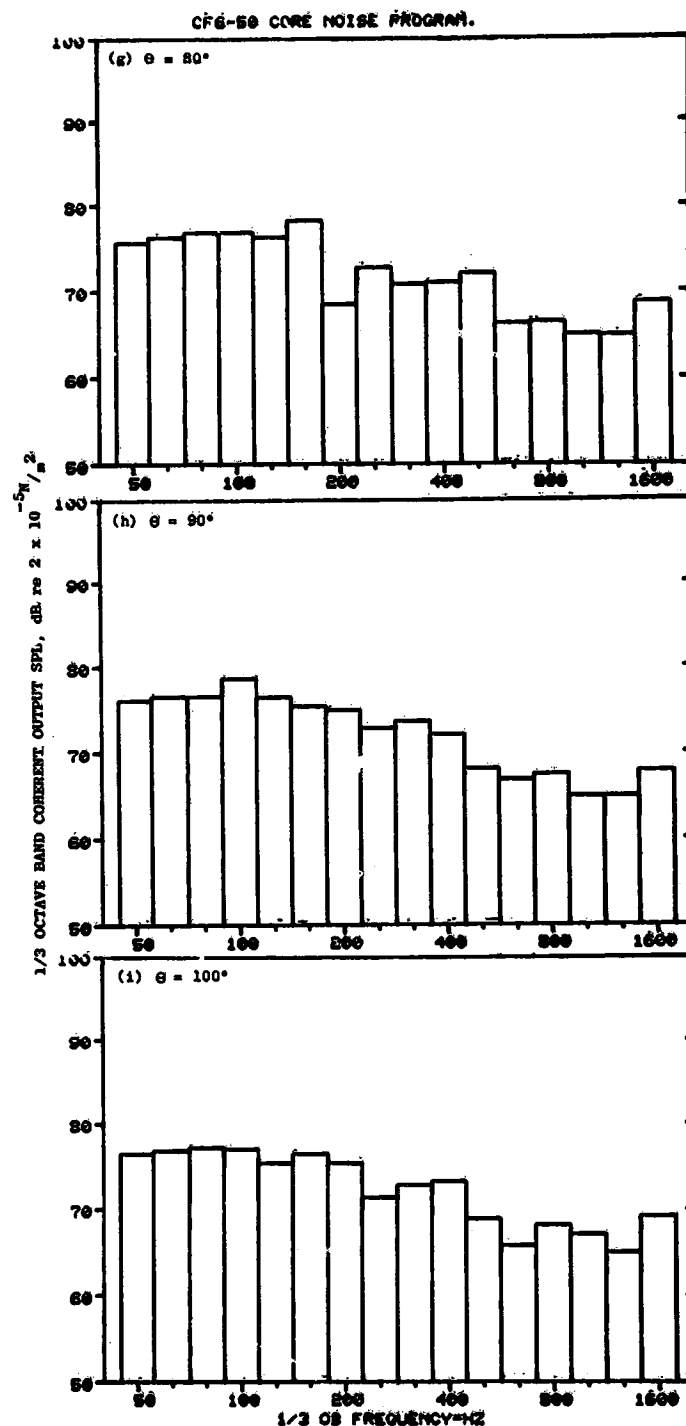


Figure C-14. Coherent Output SPL Spectra from Plane 8.0A (270°) to Farfield Microphones at 45.5% Thrust (Continued).

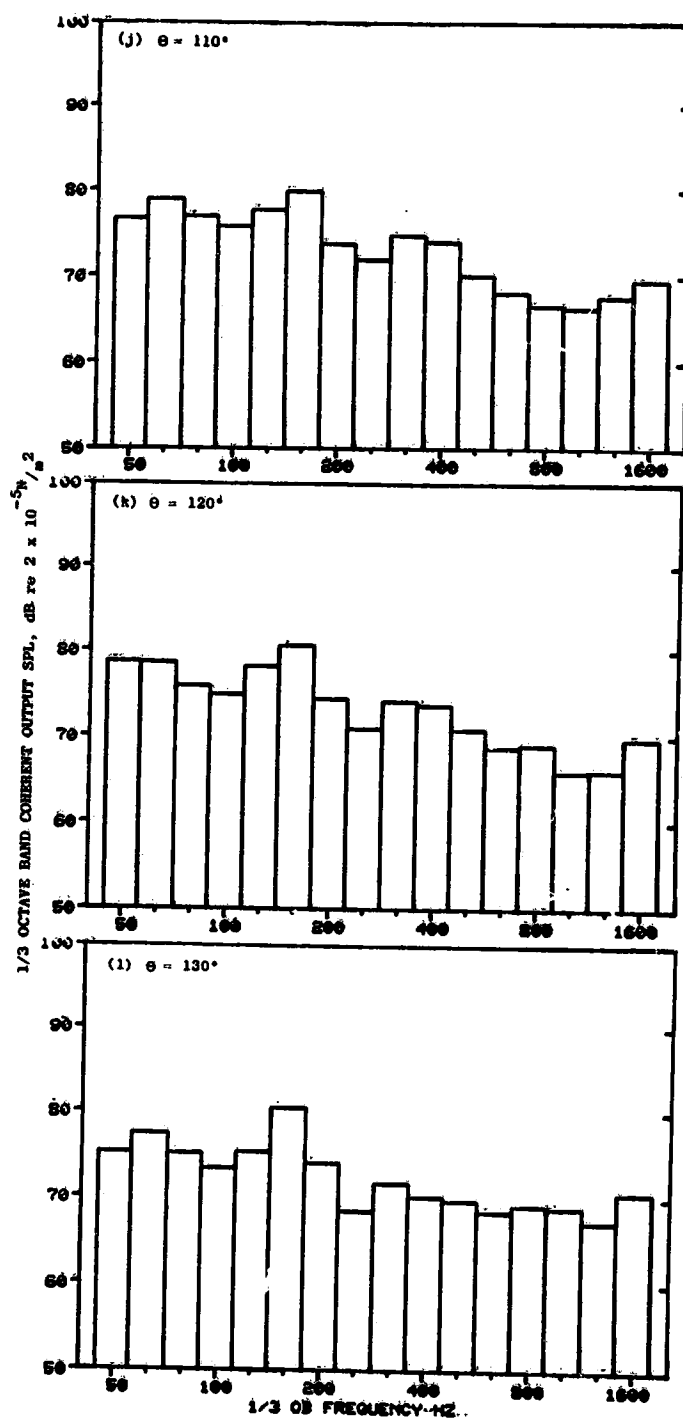


Figure C-14. Coherent Output SPL Spectra from Plane 8.0A (270°) to Farfield Microphones at 45.5% Thrust (Continued).

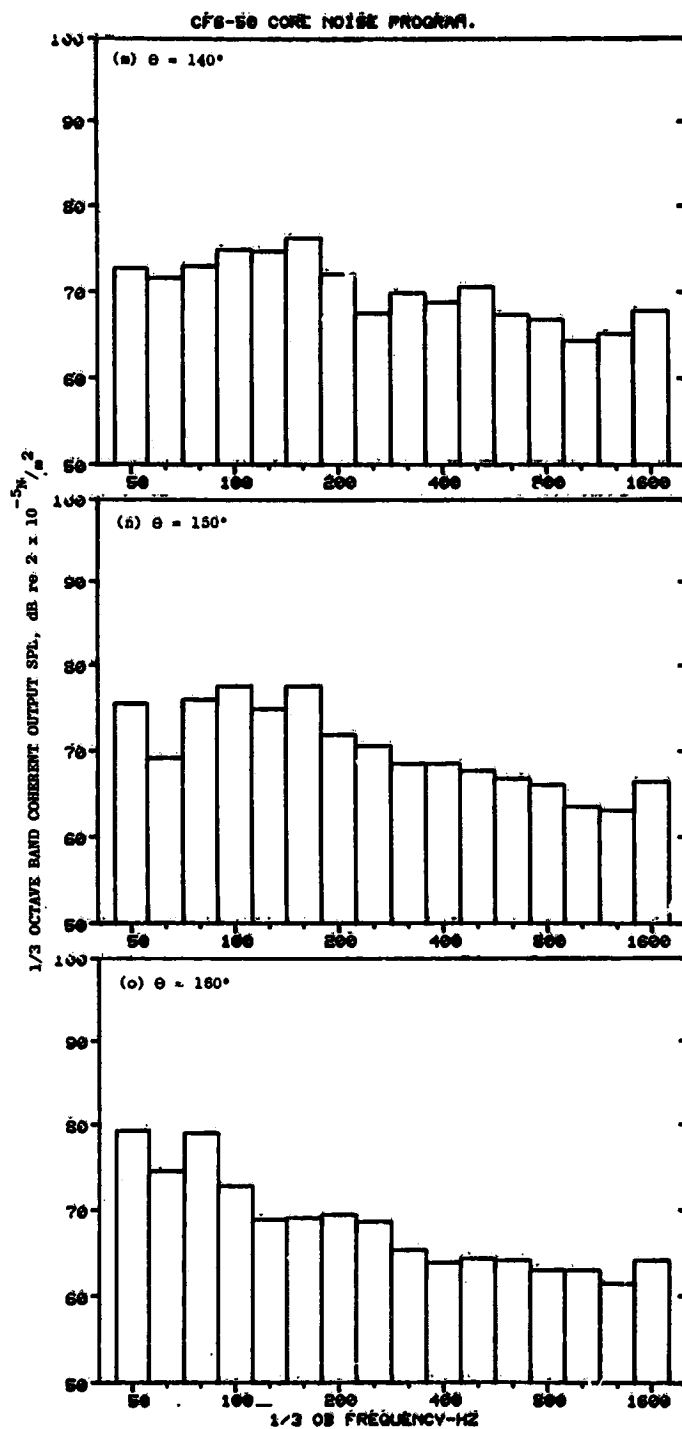


Figure C-14. Coherent Output SPL Spectra from Plane 8.0A (270°) to Farfield Microphones at 45.5% Thrust (Concluded).

Table C-1. Overall Pressure Level from CF6-50 Measurements
Referenced to Plane 3.5.

- OASPL, dB re $12 \times 10^{-5} \text{ N/m}^2$
- $\Delta f = 50\text{-}1600 \text{ Hz}$

$\angle F_n$ OA Level θ (deg)	3.8		15.0		22.8		26.7		30.8		36.5		45.5	
	RAW SPL	COH SPL	RAW SPL	COH SPL	RAW SPL	COH SPL	RAW SPL	COH SPL	RAW SPL	COH SPL	RAW SPL	COH SPL	RAW SPL	COH SPL
10	94.9	76.7	91.5	75.0	94.0	75.7	94.7	75.4	95.6	76.9	98.0	78.4	99.8	80.4
30	86.9	71.4	89.8	72.3	93.6	74.7	94.8	75.7	96.1	76.8	98.1	79.1	99.9	80.5
40	89.5	73.1	90.7	73.4	94.2	76.1	95.1	76.2	96.1	77.2	98.0	78.8	99.9	79.8
50	85.4	72.1	89.1	74.4	93.0	75.6	94.1	75.6	95.2	76.4	99.7	80.4	99.5	79.6
60	82.3	72.6	88.2	75.1	92.1	75.3	93.6	75.8	94.6	76.5	96.5	78.0	99.7	80.4
70	81.1	73.9	86.8	74.4	91.0	75.2	92.2	75.3	93.6	77.1	95.6	76.7	97.9	78.5
80	80.9	74.0	86.5	75.6	90.3	75.6	91.6	76.0	92.8	76.3	94.9	77.9	97.2	79.1
90	82.2	75.1	87.0	76.5	91.0	76.9	91.9	76.7	93.5	77.3	95.3	78.5	97.9	79.9
100	83.4	75.8	87.8	77.1	91.6	77.3	92.5	77.7	94.0	79.0	95.9	79.9	98.4	80.3
110	84.0	76.9	88.5	78.2	92.3	78.7	93.3	79.0	94.8	80.3	96.8	81.6	99.2	82.4
120	86.2	78.0	90.3	80.2	93.5	80.7	94.6	80.4	96.0	81.5	98.0	82.5	100.4	83.9
130	95.1	78.4	91.3	81.3	94.7	82.3	95.6	82.5	97.0	83.1	99.0	84.2	101.4	85.0
140	86.2	79.0	90.8	81.5	93.6	81.9	94.6	81.6	96.3	83.0	98.6	84.2	101.8	84.7
150	84.9	78.6	88.6	80.8	92.5	80.8	93.8	80.8	95.9	81.8	98.6	83.0	102.3	84.3
160	82.5	77.0	87.3	80.2	91.5	79.6	93.1	80.1	95.1	82.1	98.3	83.3	102.1	85.1

Table C-2. Overall Power Level from CF6-50 Measurements
Referenced to Plane 3.5.

- PWL, dB re 10⁻¹³ watts
- Δf = 50-1600 Hz
- Based on Full Spherical Surface

Z F _n OA Level θ(deg)	3.8			15.0			22.8			26.7			30.8			36.5			45.5		
	RAW PWL	COH PWL		RAW PWL	COH PWL		RAW PWL	COH PWL		RAW PWL	COH PWL		RAW PWL	COH PWL		RAW PWL	COH PWL		RAW PWL	COH PWL	
10	130.0	111.8		126.6	110.1		129.1	110.8		129.8	110.5		130.7	112.0		133.1	113.5		134.9	115.5	
30	126.6	111.1		129.5	112.0		133.3	114.4		134.5	115.4		135.8	116.5		137.8	118.8		139.6	120.2	
40	130.2	113.8		131.4	114.1		134.9	116.8		135.8	116.9		136.8	117.9		138.7	119.5		140.6	120.5	
50	126.9	113.6		130.6	115.9		134.5	117.1		135.6	117.1		136.7	117.9		141.2	121.9		141.0	121.1	
60	124.3	114.6		130.2	117.1		134.1	117.3		135.6	117.8		136.6	118.5		138.5	120.0		141.7	122.4	
70	123.5	116.3		129.2	116.8		133.4	117.6		134.6	118.0		136.0	119.5		138.0	119.1		140.3	120.9	
80	123.5	116.6		129.1	118.2		132.9	118.2		134.2	118.6		135.4	118.9		137.5	120.5		139.8	121.7	
90	124.9	117.8		129.7	119.2		133.7	119.6		134.6	119.4		136.2	120.0		138.0	121.2		140.6	122.6	
100	126.0	118.4		130.4	119.7		134.2	119.9		135.1	120.3		136.6	121.6		138.5	122.5		141.0	122.9	
110	126.4	119.3		130.9	120.6		134.7	121.1		135.7	121.4		137.2	122.7		139.2	124.0		141.6	124.8	
120	128.2	120.0		132.3	122.2		135.5	122.7		136.6	122.4		138.0	123.5		140.0	124.5		142.4	125.9	
130	136.1	119.9		132.8	122.8		136.2	123.8		137.1	124.0		138.5	124.6		140.5	125.7		142.9	126.5	
140	126.9	119.7		131.5	122.2		134.3	122.6		135.3	122.3		137.0	123.7		139.1	124.7		142.5	125.4	
150	124.6	118.3		125.3	120.5		132.2	120.5		133.5	120.5		135.6	121.5		138.3	122.7		142.0	124.0	
160	120.5	115.0		125.3	118.2		129.5	117.6		131.1	118.1		133.1	120.1		136.3	121.5		140.1	123.1	
OAPWL	140.2	129.0		141.9	131.0		145.3	131.5		146.7	131.6		147.8	132.7		150.1	133.9		152.8	134.5	

Table C-3. Overall Pressure Level from CF6-50 Measurements
Referenced to Plane 8.0.

- OASPL, dB re 2×10^{-5} N/m²
- $\Delta f = 50-1600$ Hz

$\angle F_n$ OA Level θ (deg)	3.8			15.0			22.8			26.7			30.8			36.5			45.5		
	RAW SPL	COH SPL		RAW SPL	COH SPL		RAW SPL	COH SPL		RAW SPL	COH SPL		RAW SPL	COH SPL		RAW SPL	COH SPL		RAW SPL	COH SPL	
10	194.9	77.6		91.6	78.0		94.0	80.4		94.6	81.6		95.5	83.3		97.8	84.9		99.7	87.5	
30	86.9	73.2		89.9	75.3		93.7	77.4		94.8	78.5		95.9	79.5		98.1	81.8		100.0	83.9	
40	89.4	74.8		90.8	75.9		94.1	78.2		95.2	79.7		96.1	79.8		98.0	81.9		99.9	83.9	
50	85.4	74.0		89.1	77.1		93.0	79.2		94.1	80.0		95.2	80.7		97.4	82.7		99.5	84.4	
60	82.3	74.6		88.2	77.8		92.1	80.1		93.6	80.8		94.5	81.8		96.4	83.0		99.4	85.0	
70	81.5	76.0		86.8	78.3		91.1	80.7		92.2	81.2		93.5	82.0		95.7	84.0		97.8	85.6	
80	81.0	76.1		86.5	79.4		90.3	80.9		91.5	81.8		92.8	83.3		95.0	84.2		97.2	85.8	
90	82.0	77.2		87.1	80.4		91.0	82.0		91.9	82.3		93.4	84.0		95.4	84.7		97.8	86.1	
100	83.2	78.0		87.9	81.3		91.5	82.5		92.6	83.4		94.0	84.1		95.9	85.1		98.3	86.0	
110	84.1	79.3		88.6	82.2		92.4	84.0		93.4	84.2		94.7	84.8		96.8	85.8		99.1	87.0	
120	86.2	80.2		90.3	83.3		93.4	84.2		94.6	84.4		96.0	85.1		98.0	85.9		100.3	87.2	
130	94.1	79.1		91.4	83.6		94.7	84.1		95.6	84.6		96.9	84.3		99.0	86.0		101.4	86.0	
140	86.1	80.2		90.9	82.9		93.8	82.8		94.7	82.3		96.2	82.6		98.6	83.6		101.7	83.7	
150	84.7	80.0		88.8	82.4		92.6	80.7		93.9	80.3		95.8	80.1		98.6	81.2		102.2	84.7	
160	82.5	78.2		87.5	81.6		91.6	78.6		93.0	76.9		95.0	77.9		98.4	81.1		102.4	84.2	

Table C-4. Overall Power Level from CF6-50 Measurements
Referenced to Plane 8.0.

- PWL, dB re 10⁻¹³ watts
- Δf = 50-1600 Hz
- Based on Full Spherical Surface

Z F _n OA Level θ(deg)	3.8		15.0		22.8		26.7		30.8		36.5		45.5	
	RAW PWL	COH PWL	RAW PWL	COH PWL	RAW PWL	COH PWL	RAW PWL	COH PWL	RAW PWL	COH PWL	RAW PWL	COH PWL	RAW PWL	COH PWL
10	130.0	112.7	126.7	113.1	129.1	115.5	129.7	116.7	130.6	118.4	132.9	120.0	134.8	122.6
30	126.6	112.9	129.6	115.0	133.4	117.1	134.5	118.2	135.6	119.2	137.8	121.5	139.7	123.6
40	130.1	115.5	131.5	116.6	134.8	118.9	135.9	120.4	136.8	120.5	138.7	122.6	140.6	124.6
50	126.9	115.5	130.6	118.6	134.5	120.7	135.6	121.5	136.7	122.2	138.9	124.2	141.0	125.9
60	124.3	116.6	130.2	119.8	134.1	122.1	135.6	122.8	136.5	123.8	138.4	125.0	141.4	127.0
70	123.9	118.4	129.2	120.7	133.5	123.1	134.6	123.6	135.9	124.4	138.1	126.4	140.2	128.0
80	123.6	118.7	129.1	122.0	132.9	123.5	134.1	124.4	135.4	125.9	137.6	126.8	139.0	128.4
90	124.7	119.9	129.8	123.1	133.7	124.7	134.6	125.0	136.1	126.7	138.1	127.4	140.5	128.8
100	125.8	120.6	130.5	123.9	134.1	125.1	135.2	126.0	136.6	126.7	138.5	127.7	140.9	128.6
110	126.5	121.7	131.0	124.6	134.8	126.4	135.8	126.6	137.1	127.2	139.2	128.2	141.5	129.4
120	128.2	122.2	132.3	125.3	135.4	126.2	136.6	126.4	138.0	127.1	140.0	127.9	142.3	129.2
130	135.6	120.6	132.9	125.1	136.2	125.6	137.1	126.1	138.4	125.8	140.5	127.5	142.9	127.5
140	126.8	120.9	131.6	123.6	134.5	123.5	135.4	123.0	136.9	123.3	139.3	124.3	142.4	124.4
150	124.4	119.7	128.5	122.1	132.3	120.4	133.6	120.0	135.5	119.8	138.3	120.9	141.9	124.4
160	120.5	116.2	125.5	119.6	129.6	116.6	131.0	114.9	133.0	115.9	136.4	119.1	140.4	122.2
OAPWL	140.0	130.8	142.1	133.8	145.7	134.9	146.4	135.3	147.8	136.1	150.2	137.3	152.7	138.0

APPENDIX D
NOMENCLATURE

<u>Symbol</u>	<u>Description</u>	<u>Units</u>	
		<u>Metric</u>	<u>English</u>
A	Annulus area, cross-sectional area at combustor measurement planes	m ²	(in. ²)
A _{ref}	Combustor reference area	m ²	(in. ²)
B _e	Resolution bandwidth	Hz	(Hz)
BPR	Fan-to-core bypass ratio		
COP	Coherent output power	dB	(dB)
C, c	Acoustic velocity	m/s	(ft/sec)
\bar{C}	Average acoustic velocity	m/s	(ft/sec)
d	Linear distance between Kulites	m	(ft)
dB	Decibel		
DFT	Digital Fourier transform		
DFT ⁻¹	Inverse digital Fourier transform		
DFT*	Complex conjugate of Fourier transform		
DI	Directivity index	m	(in.)
Δd_{PWL}^{dB}	Turbine attenuation based on PWL	dB	(dB)
\hat{e}_p	Unit vector normal to acoustical wave front		
\hat{e}_x	Unit vector, axial component		
f	Frequency	Hz	(Hz)
F	Fourier Transform		
F*	Complex conjugate of Fourier transform		
f/a	Fuel-air ratio		
% F _n	Percent net thrust		
FPL	Fluctuating pressure level re 2 x 10 ⁻⁵ N/m ²	dB	(dB)
FPWL	Power level based on fluctuating pressures re 10 ⁻¹³ watts	dB	(dB)
G _{xx}	Autospectrum		
G _{xy}	Cross-spectrum		
HPT	High pressure turbine		

Symbol	Description	Units	
		Metric	English
HPTN	High pressure turbine nozzle		
HRR	Heat release rate (total fuel flow x heating value of JP5 fuel)		
Hz	Hertz: cycles/second		watts (watts)
H ²	Transfer function		
H ²	Transfer function gain		
H* ²	Transfer function gain less contribution due to spherical divergence		
\vec{I}	Intensity flux vector		
LPT	Low pressure turbine		
M	Sample averages		
M	Mach number		
\bar{M}	Average Mach number		
MADAR	Malfunction, detection, analysis, and recording subsystem		
N	Transform block size		
$N_2/\sqrt{\theta_2}$	Core speed, corrected		
$N_1/\sqrt{\theta_2}$	Fan speed, corrected	rpm	
OACOP	Overall coherent output power level	rpm	
ÖAFPL	Overall fluctuating pressure level	dB	(dB)
OAPWL	Overall sound power level	dB	(dB)
OASPL	Overall sound pressure level	dB	(dB)
1/3 ÖBFPL	One-third octave band fluctuating pressure level	dB	(dB)
1/3 ÖBSPL	One-third octave band sound pressure level	dB	(dB)
P	Acoustic pressure (rms)	dB	(dB)
P _o	Ambient, standard day pressure	kN/m ²	(psia)
P _s	Static pressure	atm	(psia)
P _T	Total pressure	atm	(psia)
$\Delta P_{34}/P_3$	PCT combustor pressure drop relative to upstream pressure	atm	(psia)
ΔP_{34}	Combustor total pressure drop	%	
PWL	Sound power level, re 10 ⁻¹³ watts	atm	(psia)
R	Gas constant for air	dB	(dB)

<u>Symbol</u>	<u>Description</u>	<u>Units</u>	
		<u>Metric</u>	<u>English</u>
R	Reference radius	m	(ft)
RDG, R _{dg}	Reading number	m	(in.)
R _{xx}	Auto-correlation function		
R _{xy}	Cross-correlation function		
r	Arc radius	m	(ft)
SLS	Sea level static		
SR	Sample rate		
S _r	Space rate		
\hat{S}	Coherent output spectrum		
SPL	Sound pressure level, re 2×10^{-5} N/m ²	dB	— (dB)
T	Record Length	sec	
T ₀	Ambient, standard day temperature	K	(° F)
T _S	Static temperature	K	(° R)
T _T	Total temperature	K	(° R)
ΔT_{34}	Combustor total temperature rise	K	(° R)
t	Sample length	sec	
\vec{V}	Absolute flow velocity vector	m/s	(ft/sec)
V ₈	Core jet velocity	m/s	(ft/sec)
V _e	Effective (mixed jet) velocity	m/s	(ft/sec)
V ₁₈	Fan jet velocity	m/s	(ft/sec)
W ₂₅	Core engine airflow rate	kg/sec (lb/sec)	
W ₃	Compressor discharge airflow	kg/sec (lb/sec)	
W ₃₆ , W _c	Total combustor discharge airflow	kg/sec (lb/sec)	
W _{FT}	Total fuel flow	kg/hr (lb/hr)	
$\frac{W_{36} \sqrt{T_3}}{P_3 A_3}$	Combustor discharge flow corrected to combustor inlet conditions		
δ_{02}	Delta (engine inlet)		
θ_{02}	Theta (engine inlet)		
e	Random error		
Δ	Difference, increase or decrease		
γ^2	Ordinary coherence function		
τ	Time delay	sec	

<u>Symbol</u>	<u>Description</u>	<u>Units</u>	
		<u>Metric</u>	<u>English</u>
θ	Far-field angle, circumferential location for internal sensors	deg	
ρ	Density	kg/m ³	(lb/ft ³)
ρ_{xy}	Normalized correlation coefficient		
ϕ	Transfer function phase	deg	
<u>Subscripts</u>			
a	Air		
c	Core		
e	Effective		
f	Fuel, fan		
o	Initial or calibration condition		
1	Largest peak in cross-correlation		
2	Next largest peak in cross-correlation		
3.0	Compressor discharge plane		
3.5	Combustor inlet plane		
4.0	Combustor discharge/turbine inlet plane		
8.0	Core nozzle discharge plane		

REFERENCES

1. Emmerling, J.J., and Bekofski, K.L., "Experimental Clean Combustor Program - Noise Measurement Addendum - Phase II Final Report," Report No. NASA CR-135045, January 1976.
2. Doyle, V.L., "Experimental Clean Combustor Program - Phase III, Noise Measurement Addendum Final Report," Report No. NASA CR-159458, December 1978.
3. Bendat, J.S., and Piersol, A.G., Random Data: Analysis and Measurement Procedures, John Wiley and Sons, Inc., 1971.
4. Doyle, V.L., "Core Noise Investigation of the CF6-50 Turbofan Engine - Data Report," Report No. NASA CR-159598, 1979.
5. Halvorsen, W.G., and Bendat, J.S., "Noise Source Identification Using Coherent Output Power Spectra," Reprint from Sound and Vibration, Magazine, August 1975, pp. 15-24.
6. Bendat, J.S., "Statistical Errors in Measurement of Coherence Functions and Input/Output Quantities," Journal of Sound and Vibration, 1978, pp. 405-421.
7. Bekofski, K., "Attenuation of Acoustic Energy Across a Blade Row," Report No. 73C-342, General Electric Company, December 1973.
8. Reshotko, M., et al., "Core Noise Measurements on a YF-101 Turbofan Engine," NASA TMX-73587 (AIAA Paper No. 77-21), January 1977.
9. Karchmer, A.M., Reshotko, M., and Montegani, F.J., "Measurement of Farfield Combustion Noise from a Turbofan Engine Using Coherence Functions," AIAA Paper 77-1277, October 1977.
10. Matta, R., and Mani, R., "Theory of Low Frequency Noise Transmission Through Turbines," NASA CR-159457, March 1979.
11. Matta, R.K., Sandusky, G.T., and Doyle, V.L., "Core Engine Noise Investigation Program - Low Emission Engines," General Electric Company, DOT/FAA Report No. FAA-RD-77-4, February 1977.